博士論文

Fluid Dynamic Loss
in Aeroengine Transmission Gears

(航空エンジン・ギヤシステムの流体力学的損失に関する研究)

有澤 秀則

Fluid Dynamic Loss

in Aeroengine Transmission Gears

Hidenori Arisawa

Contents

Chapter 1

Introduction

Aircraft engines require the most advanced technology to provide propulsion for a safe mobility that promotes people's global interaction while taking the global environment into consideration. Gas turbines, which have excellent characteristics as aircraft engines, will maintain an important position in the future through the incorporation of environmentally friendly technologies such as sustainable aviation fuel (SAF) and fuel efficiency improvements. To improve fuel efficiency, it is necessary to increase the efficiency of aircraft engines, and therefore, the efficiency of gear systems.

This chapter shows the importance of reducing the fluid dynamic loss of the gear system based on recent trends in aeroengine gear systems, and the possibility and problems of improving the efficiency of the gear system based on the status of conventional research. It also shows the necessity of clarifying and classifying the fluid dynamic loss phenomena to solve these problems and sets research objectives.

1.1 Research Background

1.1.1 Importance of Improving the Gear System Efficiency in the Trend of Shifting to a Geared Aeroengine and Airframe Electrification

1.1.1.1 Overview of the Gear System

(1) Basic Configuration of the Gear System

Figure 1.1-1 shows an example of an aircraft, and Figure 1.1-2 shows an example of an aircraft engine installed under the wing.

Fig. 1.1-1 A typical aircraft (Boeing 787) [1]

Fig. 1.1-2 An aeroengine mounted below an aircraft wing [2]

Figure 1.1-3 shows an example of a lubricating oil system. The systems shown in Fig. 1.1-3 are the oil pressurized by an oil pump (feed oil), in brown; the return oil after lubrication, in green; and the seal air (air flowing from the air passage toward the bearing chamber to seal oil from entering the air passage of the gas turbine), in blue. The main components of the lubricating oil system are an internal gear box that extracts power from the engine shaft with a gear, an accessory gearbox that transmits power from the internal gear box to the auxiliaries, and an oil cooler for cooling the lubricating oil. A schematic of this lubricating oil system is shown in Fig. 1.1-4 .
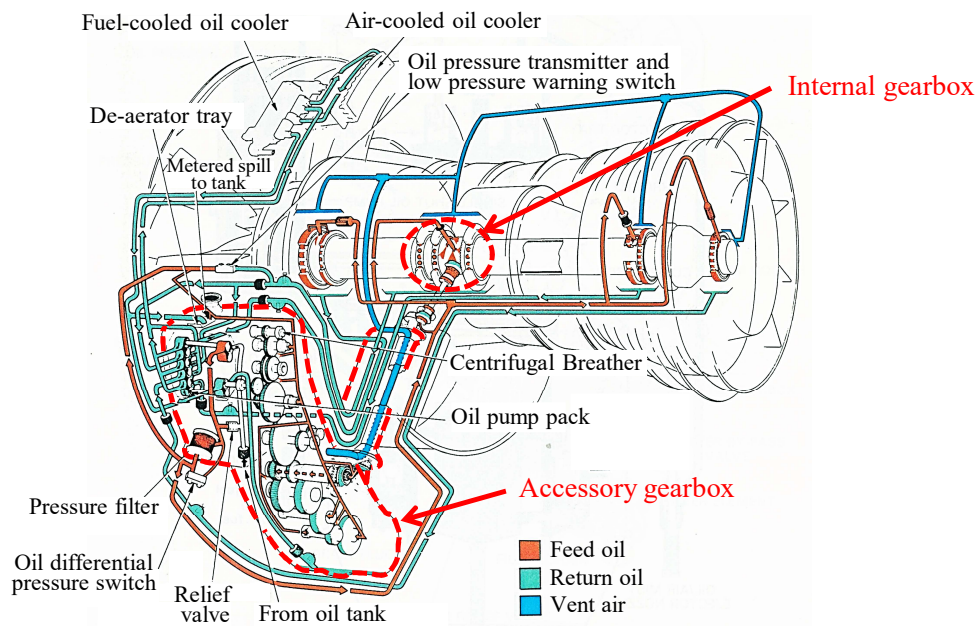
Fig. 1.1-3 A detailed oil system in an aeroengine [3]
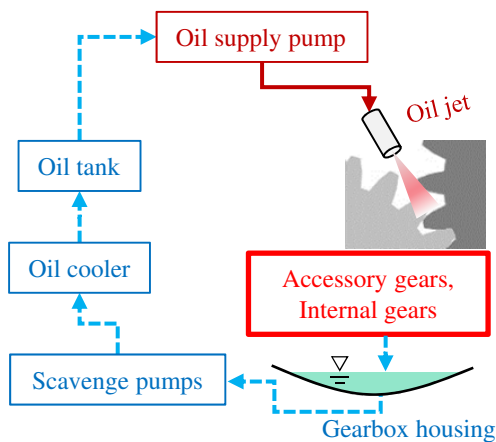
Fig. 1.1-4 Schematic of the oil system
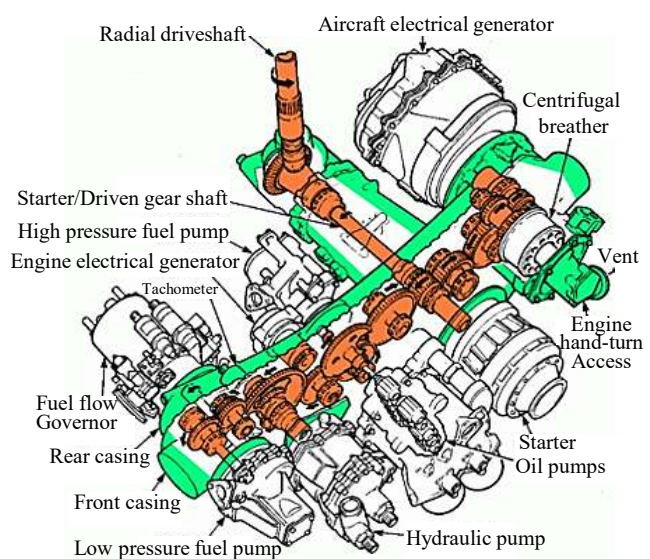
Fig. 1.1-5 Gears and equipment in the accessory gearbox [3]

The oil is sucked from the oil tank by an oil pump, pressurized, and sprayed onto the accessory gear and internal gear. The lubricated oil accumulates in the lower part of the gearbox housing, is sucked out by a scavenge pump, is cooled by an oil cooler, and returns to the oil tank. The oil pump and scavenge pump in Fig. 1.1-4 are included in the "Oil pump pack" in Fig. 1.1-3. The accessory and internal gears in Fig. 1.1-4 correspond to the gears of "Accessory gearbox" and "Internal gearbox" in Fig. 1.1-3, respectively. The oil cooler in Fig. 1.1-4 corresponds to "Fuel-cooled oil cooler" and "Air-cooled oil cooler" in Fig. 1.1-3.

(2)   Basic Gearbox Configuration and Design Parameters

Figure 1.1-5 shows the detailed configuration of the accessory gearbox. The accessory gearbox is powered by a drive shaft (radial driveshaft), changes direction with a bevel gear, and distributes power with spur gears. The accessory gearbox drives the aircraft electrical generator, low-pressure fuel pump, hydraulic pump, oil pump, and centrifugal breather for collecting oil from the seal air flowing into the accessory gearbox.

Figure 1.1-6 shows a simplified version of the basic gearbox configuration from Fig. 1.1-5, including the gear shaft, gear, oil jet, shroud, breather, scavenge pickup, and housing. Figure 1.1-6 also shows the main design parameters, which are outlined below.

- Gear shaft

  The main design parameters are the transmitted power, speed, and torque.
- Gear

  The gear diameter and tooth width are designed to satisfy the durability according to the torque and rotational speed, and the main parameters are gear diameter, tooth width, gear aspect ratio (tooth width / gear diameter), reduction ratio, module, number of teeth, helix angle, and pressure angle.
- Oil jet

  An oil supply jet is installed to lubricate the friction surface (to reduce the coefficient of friction at the contact surface and protect it) and to cool the heat generated on the friction surface. The maximum oil temperature is set to prevent the oil from deteriorating or igniting due to heat. The temperature of the oil supply jet and the temperature difference between the oil supply and the exhaust oil are determined so that the oil temperature does not exceed the maximum allowable. The oil supply pressure is designed so that the oil can reach the tooth surface of the gear rotating at high speed.
- Shroud

  In aeroengine gears, a high gear peripheral speed (gear rotational speed) is set to reduce the torque and miniaturize the gear. Therefore, the relative speed of the contact surface between the gears increases, and the frictional heat generation increases. A large amount of oil must be supplied to reduce the generated heat and to satisfy the restriction of the difference in oil supply and scavenged temperature to prevent the deterioration of the oil [4]. Therefore, in the gearbox, a power loss (fluid dynamic loss of air and oil) occurs due to the high-speed air flow generated by the gear churning a large amount of oil. In extreme cases, oil accumulates inside the gearbox, causing the oil level of the oil tank to drop abnormally (the "oil gulping" phenomenon). To suppress this fluid dynamic loss and prevent the oil gulping phenomenon, a shroud is set in the gear.
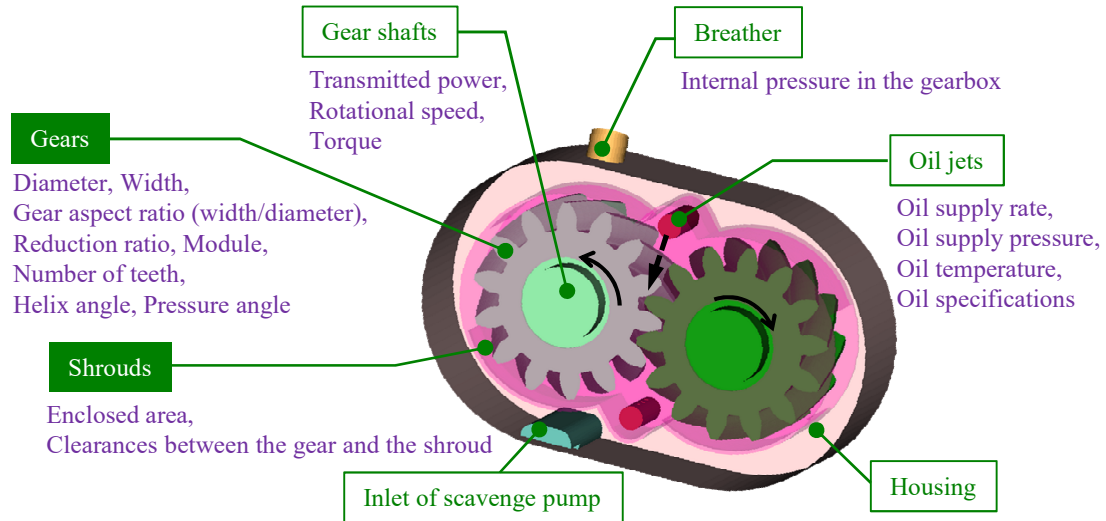
Fig. 1.1-6 Schematic configuration and typical design parameters in a gearbox

- Breather

  The breather exhausts air out of the engine after oil is collected from the seal air. In general, oil and air are separated by the rotational centrifugal force, which causes exhaust pressure resistance. This exhaust pressure resistance increases the pressure inside the gearbox. When the pressure inside the gearbox is high, the engine power to ensure the flow rate of the seal air increases. Therefore, it is desirable that the exhaust pressure resistance of the breather be small.

- Scavenge pump inlet

  One scavenge pump inlet is provided for each scavenge pump, and the position of the scavenge pump inlet is designed so it can suck in oil even if the aircraft attitude changes.

- Housing

  The weight and size of the housing must be minimized to improve fuel economy and ensure mountability on the aircraft. However, if the clearance between the gear and the housing is too small, the increase in fluid dynamic loss of air and oil and the occurrence of oil gulping phenomena are of concern. Therefore, an appropriate design is necessary.

To reduce the fluid dynamic loss in the gearbox, the gear and shroud design is important and will be described in this chapter.

(3)   Characteristics of Power Loss in the Gearbox

Figure 1.1-7 shows an example of the loss fraction in a gearbox. The power loss of a gearbox is mainly classified into gear friction loss, bearing friction loss, and fluid dynamic loss. The fluid dynamic loss is the loss generated by churning air and oil in an area other than the gear contact surface (the internal area of the housing including the gear periphery). In the design of aeroengine gears, the peripheral speed of the gear generally exceeds 50 m/s to reduce torque and to minimize the gear. From Fig. 1.1-7 , it can be observed that the fraction of fluid dynamic loss exceeds half of the total loss when the peripheral speed exceeds 50 m/s. Therefore, a reduction in the fluid dynamic loss is important for improving the efficiency of high-speed gear systems.
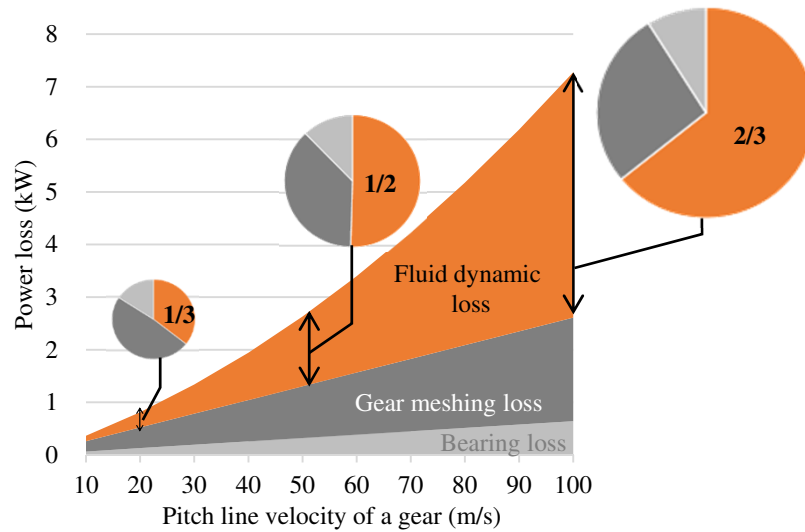
Fig. 1.1-7 Breakdown of power loss in the gearbox (10–50 m/s: experimental results [5], 50–100m/s: extrapolation)

1.1.1.2 Impacts on Engine Efficiency of Improvement in Gear System Efficiency of Geared Engines

The geared engine is part of a trend toward higher engine efficiency. This section describes the fuel consumption reduction effect of a geared engine and the importance of improving the gear system efficiency. Figure 1.1-8 shows a geared turbofan, which is a turbofan engine with a reduction gear installed between the fan and the low-pressure turbine.

Figure 1.1-9 shows the fuel consumption reduction effect of the higher bypass ratio of geared turbofans. Figure 1.1-9 depicts the bypass ratio on the horizontal axis and the fuel consumption on the vertical axis, comparing the fuel consumption reduction effect of a conventional turbofan (direct drive turbofan) with that of a geared turbofan. To achieve the higher bypass ratio, it is necessary to increase the ratio of the flow rate of the fan to the flow rate of the engine core (gas turbine). To increase the flow rate of the fan, the fan diameter must be increased, but the fan speed must be reduced so that the tip of the fan does not exceed the speed of sound. To reduce the fan speed, it is necessary to reduce the speed of the low-pressure turbine, but due to the reduction in blade load, the radius of the turbine (or the number of turbine stages) will increase. Therefore, the increase in weight will adversely affect fuel consumption (red line in the figure). The geared turbofan can reduce the weight penalty of the low-pressure core by increasing the rotation speed of the low-pressure turbine while reducing the fan speed. Thus, fuel consumption can be reduced by increasing the bypass ratio even further (red dashed line in the figure). As a result, the point of minimum fuel consumption decreases from "A" to "B" in the figure.

Further, geared turbofans suffer from power losses in the fan drive gear system itself and they increase in the oil coolers that reduce the heat generated in the gear system. Figure 1.1-10 shows a comparison of the fuel efficiency reduction effects of the geared turbofan and direct-drive turbofan. From the figure, power losses in the gearbox ("Gearbox" in the figure) and power losses in heat exchangers ("Frame & heat exchanger losses" in the figure) are estimated to be as large as the effects of a geared engine ("Improved BPR, Fan, and LPT efficiency" in the figure). In the oil system, fuel-cooled oil coolers (FCOCs) and air-cooled oil coolers (ACOCs) are equipped as oil coolers. The FCOC also preheats the fuel and makes effective use of exhaust heat from the gear system. However, the oil cooling performance of the FCOC tends to decrease owing to the improvement

in fuel efficiency. If the heat input to the oil increases, it is necessary to increase the heat transfer area of the ACOC, which increases the size of the oil cooler and increases the resistance of the engine, resulting in poor fuel economy. The feasibility of an oil system including oil coolers is an important issue related to the feasibility of a geared engine.

A reduction in power loss of the gear system reduces the loss of the gear system itself and also reduces the increase of the oil cooler. Assuming that the efficiency of a 40000 hp (30000 kW) class fan drive gear system for turbofans is approximately 99.3% (0.7% loss) [8], a large 280 hp (210 kW) oil cooler would be required. Meanwhile, if the power loss of the gear system could be reduced by 20%, a loss reduction of 40 kW in the gear system and a reduction in oil cooler capacity would be possible. The effect of improving the engine efficiency by reducing the power loss and oil cooler capacity of this gear system is equivalent to 0.3% (= 20% × (gearbox loss 0.7% + oil cooler loss 0.9%)). Therefore, it can be seen that a geared engine requires a large-capacity oil cooler and is effective in reducing the power loss of the gear system.

1.1.1.3 Impact of Improvement in Gear System Efficiency on Engine Efficiency in Electrification of Airframe

As shown in Fig. 1.1-2 , an accessory gearbox is powered by an internal gear connected to the engine shaft through a radial driveshaft. As shown in Fig. 1.1-5 , an accessory gearbox is a power transmission mechanism for driving auxiliary equipment such as the generator for the airframe, fuel pump, and hydraulic pump. In recent years, the airframe has become more electrified in order to reduce its weight, and in particular the power generation capacity has increased. The increase in power generation capacity is illustrated in Fig. 1.1-11 . As the transmission power of the internal and accessory gearboxes depends on the power required by the auxiliary equipment, the loss of these gearboxes increases as the power generation capacity increases.
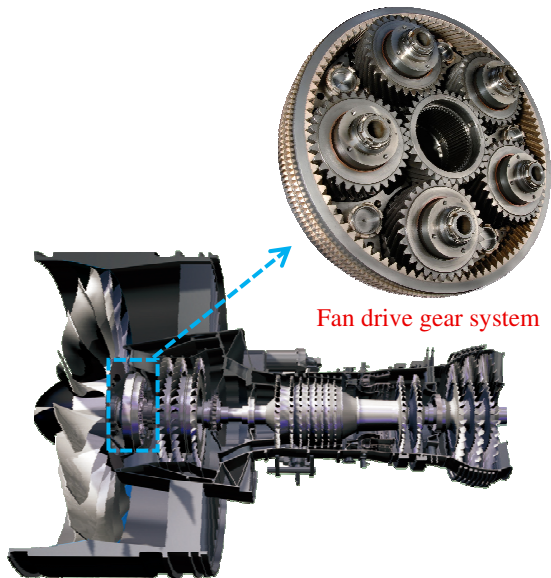
Fig. 1.1-8 Geared Turbofan™ [6]
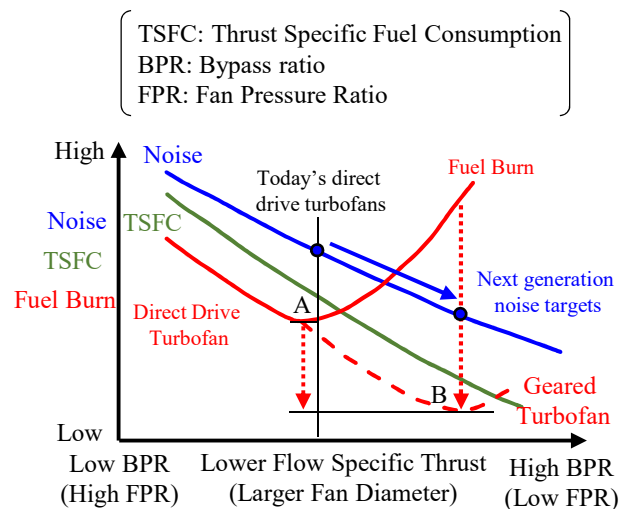
Fig. 1.1-9 High bypass ratio and low fuel burn with Geared turbofan™ (concept) [7]
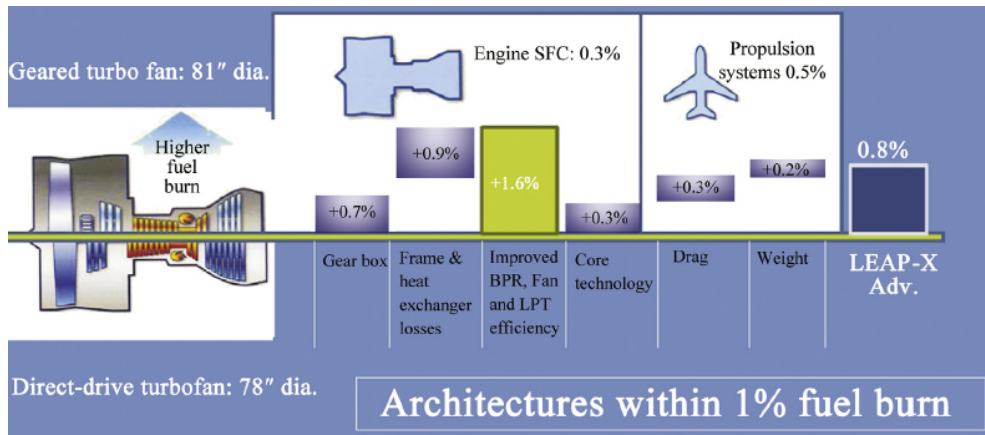
Fig. 1.1-10 Relative comparison of fuel efficiency between a geared turbofan and direct-drive turbofan in the same generation (estimation obtained using engine models constructed with publicly available data) [9]
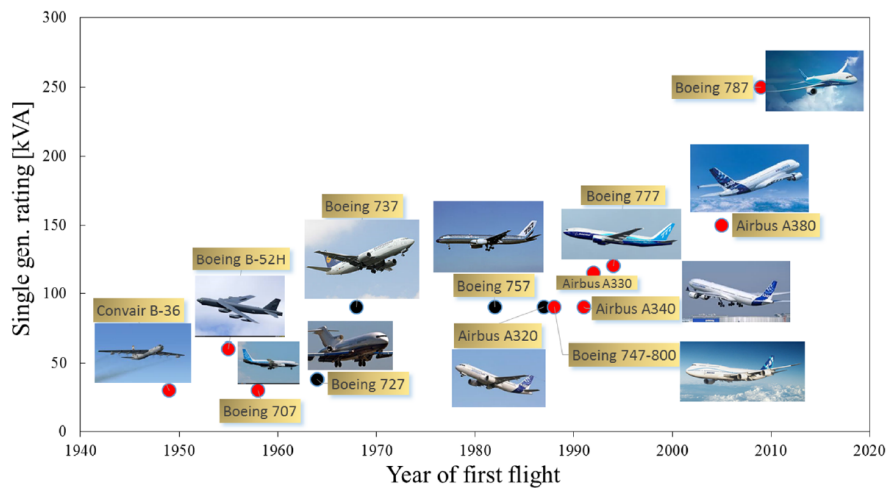
Fig. 1.1-11 Increase in aircraft power generation capacity (the black circles represent short to medium haul and the red circles represent medium to long haul) [10]

For example, one engine has a generating capacity of 500 kW, and two sets of bevel gears (in the internal and accessory gear boxes) and one set of spur gears (in the accessory gear box) are considered as the main gears for driving the generator. The efficiency of each of the two sets of bevel gears and the set of spur gears is assumed to be 96%. Assuming that the efficiency of the gear system is improved by 20%, the power loss will be reduced by 12 kW. In addition, the efficiency of the gear system can be improved to reduce the cooler capacity. If the current airframe is electrified in a similar manner to that of the B787 in the next generation of small and medium-class aircraft, it has been estimated that the deterioration of the engine fuel economy will be approximately 1% [11]. Therefore, it is important to improve the efficiency of the gear system.

1.1.2   Development of Gear Systems in Aeroengines

This section describes the development of the "propeller driven / fan drive gear system," which transmits engine power to the propeller or fan via the gear system, the "accessory gear system," which drives auxiliary equipment, and the "special gear system," which adds special functions to the airframe.

1.1.2.1   Development of Propeller Driven / Fan Driven Gear Systems

Many of the power gear systems that reduce engine speed and transmit power to the propeller or fan use epicyclic gear systems (star gear or planetary gear systems), which are small in size and have a large reduction ratio. This section briefly describes the development of the gear system, focusing on the example of the epicyclic gear system. The development, from the 1920s to the appearance of geared turbofans in recent years, is shown in Fig. 1.1-12 . In the figure, the gear systems that have been used in commercial or defense applications are shown.
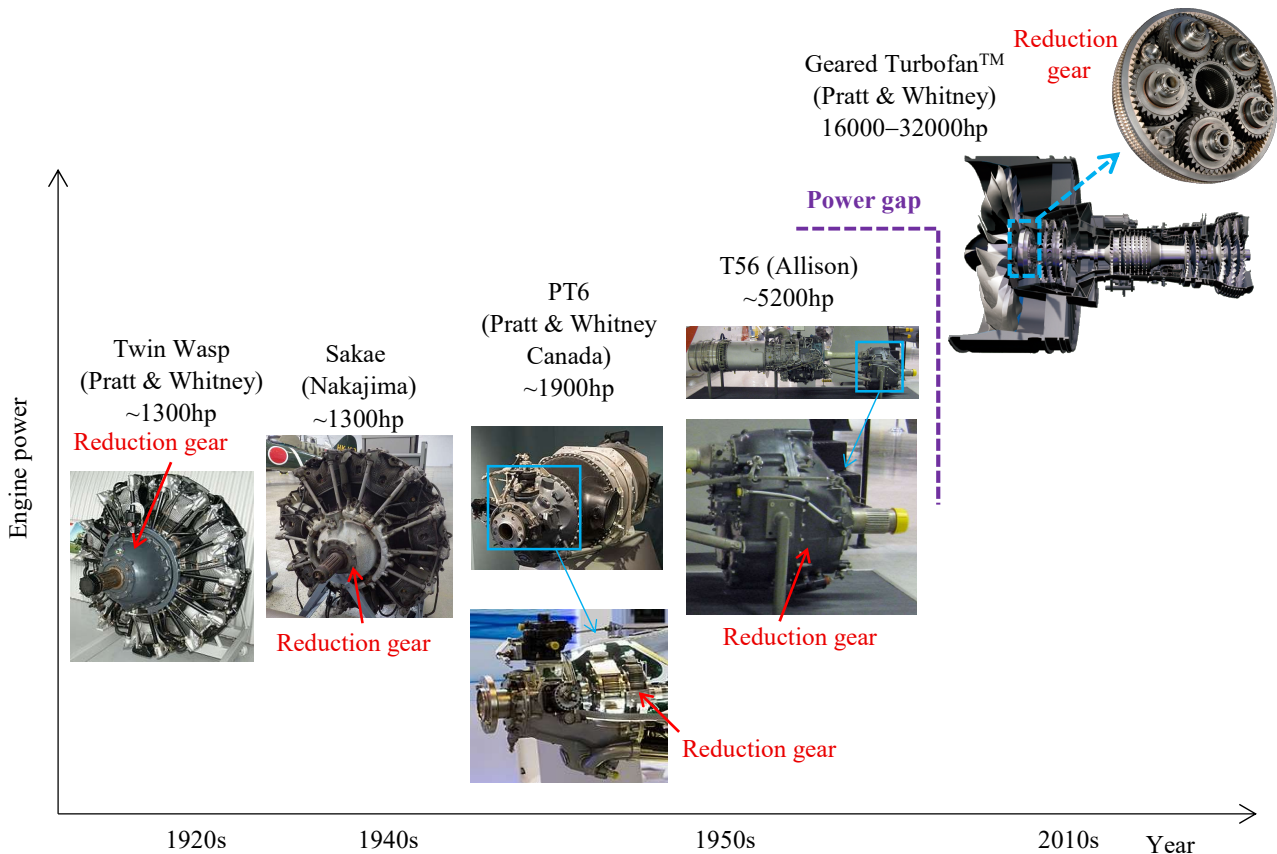
Fig. 1.1-12 History of the engines with a planetary gear system for propeller drive or fan drive [6][12][13][14][15]

The epicyclic gear system of the Twin Wasp engine in the 1920's and that of the Sakae engine in the 1940's are typical examples. Both were of approximately 1000 hp. The subsequent PT6 was of approximately 2000 hp. The maximum power of the engine before the appearance of the geared turbofan ranged from 2000 to 5200 hp of the T56 engine[*1]. There was a large power gap between the gear system of the geared turbofan and that of the

---

[*1] There is a 14000 hp D-27 turbofan engine that uses an epicyclic gear system with a larger output, but the number of produced

conventional gear systems, because the gear system of the geared turbofan ranges from approximately 16000 to 32000 hp.

To overcome this power gap, the technology had to be matured through several engine prototypes. Figure 1.1-13 shows the history of the maturation of gear systems through some demonstrator engines equipped with fan-driven gear systems. The horizontal axis in the figure indicates the age, and the vertical axis indicates the risk. From the 1980s, Pratt & Whitney began the development to install gear systems in engines, and in 1987, they produced a prototype 13000 SHP prop fan demo engine. Since then, they have produced a prototype 40000 SHP ADP demo engine [8] in 1993, a 11000 SHP ATFI (advanced technology fan integrator) demo engine in 2001, and a 31000 SHP GTF (geared turbo fan) demo engine in 2007 (renamed to the PW 1000G in 2008). It took about 30 years from the start of development until the PW 1100G installed in the Airbus A320 started operation in 2015, which indicates that there was a large technology gap in the use of high power gear systems.

From the above, it can be seen that the range of application of propeller drive and fan drive gear systems has been extended by dramatically improving the drive power through many operational experience and demo engines.
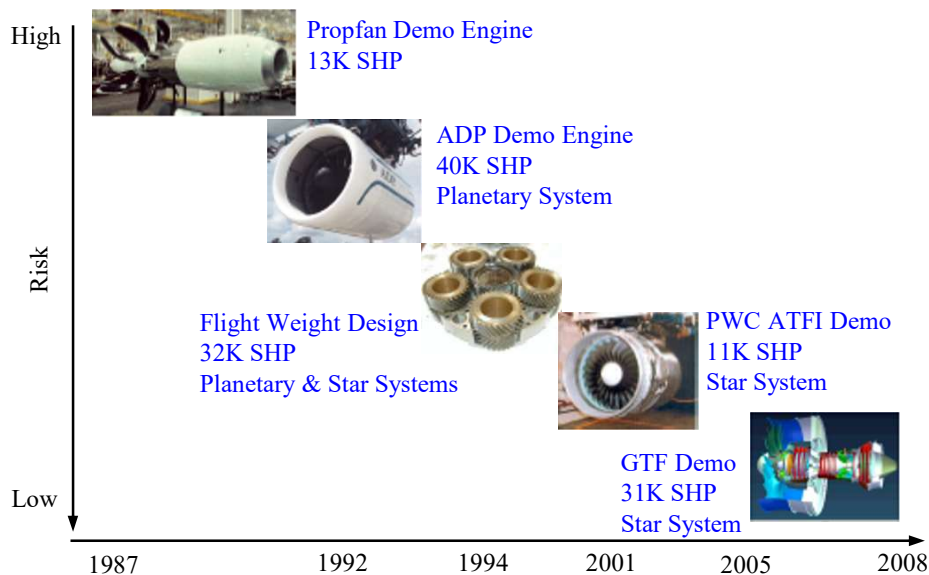
Fig. 1.1-13 Development history of the Geared Turbofan™ [7]

1.1.2.2 Development of the Accessory Gear System

The accessory gearbox of an aircraft engine is basically constructed so that the engine shaft and the auxiliary equipment are directly connected by a combination of gears. As a result, when the engine speed changes, the engine speed of the auxiliary equipment also changes. As an exception, the generator is generally equipped with a transmission mechanism for generating electricity at a constant frequency (rotating the generator at a constant speed).

Figure 1.1-14 shows an example of a constant-speed generator (integrated drive generator, IDG). A schematic of the transmission mechanism built into the constant-speed generator is shown in Fig. 1.1-15 [16][17]. The input gear is connected to an engine-driven accessory gear, and power is supplied. The rotational speed varies

---

engines is small and it cannot be said that it has a sufficient track record.

according to the engine speed. The input gear is input to the epicyclic gear unit (① in Fig. 1.1-15). This power is transmitted to the hydraulic pump side of the hydraulic unit (② in Fig. 1.1-15). The oil discharge flow rate of the hydraulic pump is adjusted by the control cylinder. The hydraulic motor rotates at a speed corresponding to the oil discharge flow rate. By the combination of this hydraulic pump and hydraulic motor, the rotational speed can be changed. The output gear of the hydraulic motor rotates the ring gear on the input gear side of the planetary gear unit (③ in Fig. 1.1-15). The rotation of the ring gear on the output gear side of the planetary gear unit is determined according to the rotation of the ring gear on the input gear side. The ring gear on the output gear side drives the output gear (④ in Fig. 1.1-15). The output gear drives the generator. As described above, the IDG drives the generator at a constant speed by controlling the discharge flow rate of the hydraulic pump.
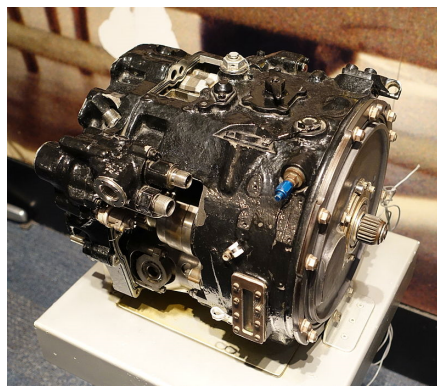
Fig. 1.1-14 Integrated drive generator (IDG) [16]
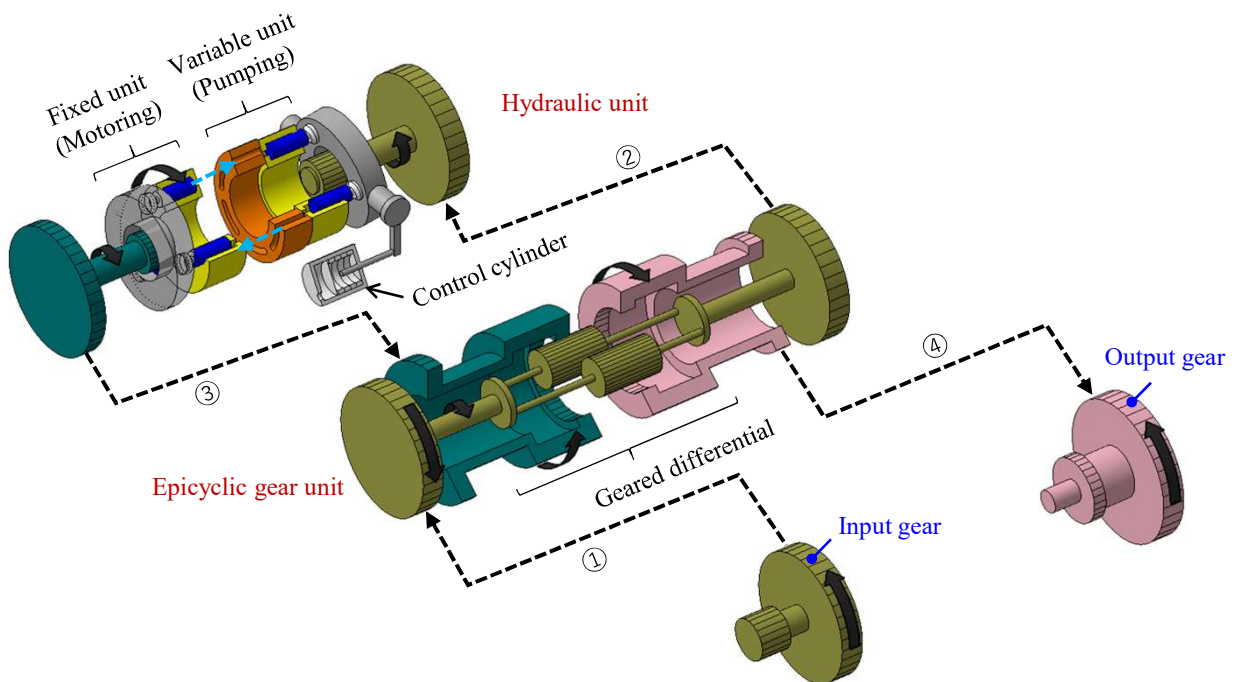
Fig. 1.1-15 Schematic of the constant speed drive mechanism of IDG [17]

A constant-speed generator with a different transmission mechanism is the traction drive IDG (T-IDG) [18]. This is shown in Fig. 1.1-16 . In Fig. 1.1-16 (a), power is supplied from an engine-driven accessory gear. This power is divided into a transmission mechanism (①a in Fig. 1.1-16 (a)) and an epicyclic gear (①b in Fig. 1.1-16 (a)). This power division is intended to minimize the weight and size of the transmission mechanism by reducing the load on it. Figure 1.1-16 (b) shows the transmission mechanism. The transmission is performed by connecting different radii of one pair of opposed disks (r_1 and r_2 in Fig. 1.1-16 (b)) with power rollers. The power input to the transmission mechanism (①a in Fig. 1.1-16) is changed in speed by the transmission mechanism (② in Fig. 1.1-16). This power is combined with the power shown in ①b in Fig. 1.1-16 through the epicyclic gear and is output to the generator (③ in Fig. 1.1-16). As described above, the T-IDG uses a transmission mechanism that combines a disk and a roller to drive the generator at a constant speed.

(a) Power transmission path

(b) Speed change mechanism
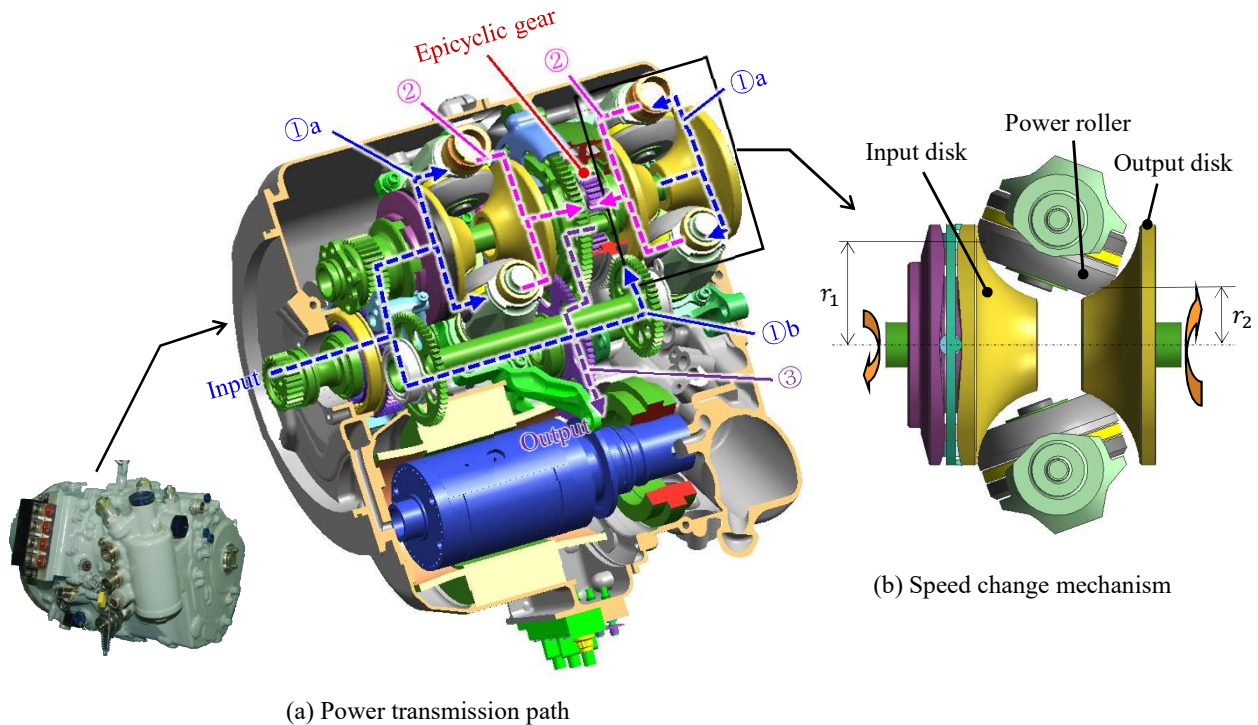
Fig. 1.1-16 Traction drive IDG (T-IDGⓇ) [18] and the constant speed drive mechanism

1.1.2.3 Special Gear System

Examples of gearboxes that add special performance to the aircraft are the V -22 Osprey for tiltrotor vertical take-off and landing aircraft and the F-35 B for short takeoff vertical landing (STOVL) aircraft.

Figure 1.1-17 shows the gear system of the V-22 Osprey equipped with a tilt rotor [19]. The V-22 Osprey takes off and lands vertically in the same manner as a helicopter, and after takeoff, it flies with the rotor shaft directing forward. With this system, the helicopter does not require a runway, but has a flight speed and a flight range approximately two times that of the CH-53 E, a helicopter of the same scale currently used by the U.S. military. A key contributor to this realization is the tilt-rotor gear system shown in the right figure in Fig. 1.1-17 , which has a function to rotate the propeller shaft, a function to cancel the rotational moment of the propeller by synchronizing the left and right propeller shafts, and a fail-safe function to drive both propellers with the other engine even if one engine fails. This system has "Midwing gearbox assembly" in Fig. 1.1-17 to connect the left

and right gearboxes and "Idler gears" in "Proprotor gearbox" to connect the engine and propeller rotor shafts, that increase the power loss of the gear system, in addition to a typical turboprop engine. Therefore, reducing the power loss of the gear system is thought to be effective in improving the engine fuel efficiency.
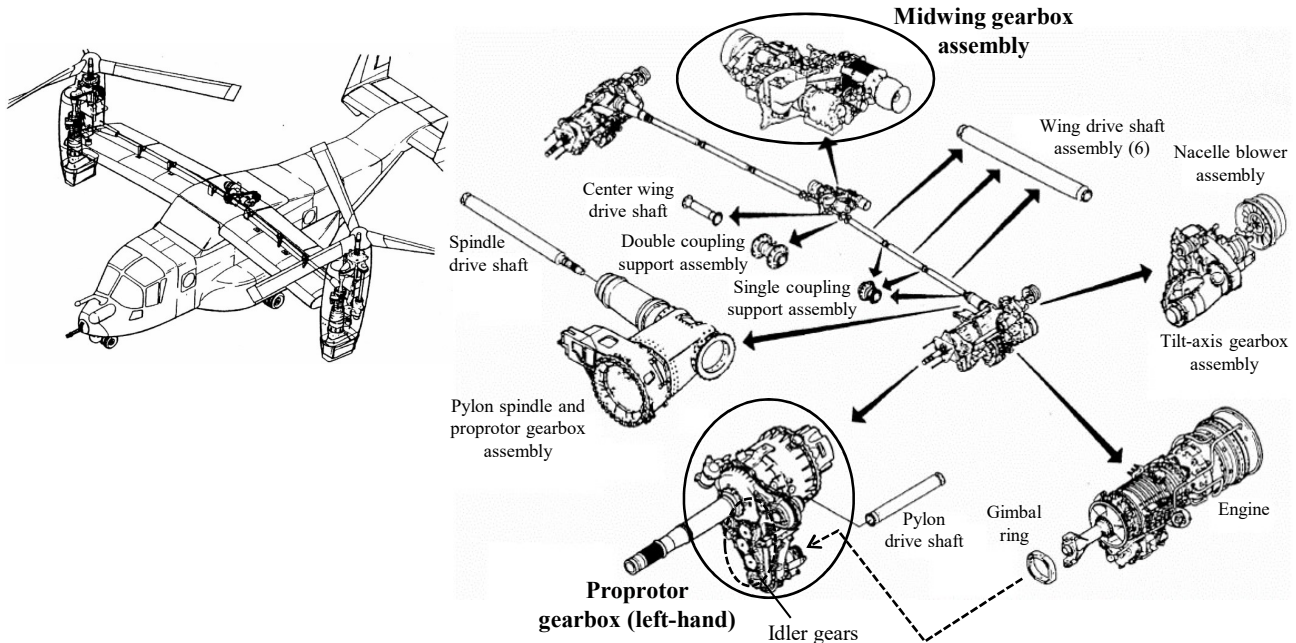
Fig. 1.1-17 The tilt rotor gear system of V-22 Osprey [19]
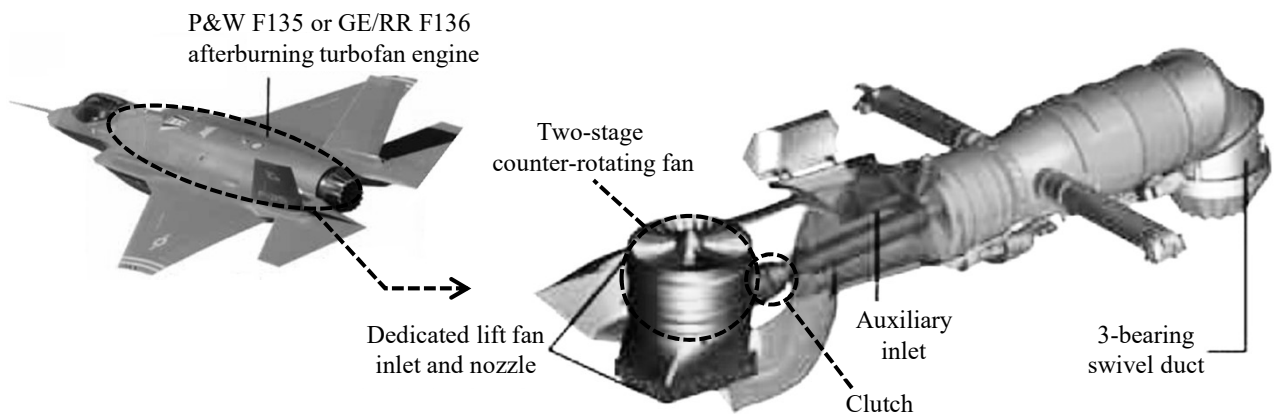
Fig. 1.1-18 The lift fan gear system of F35 fighter to assist the vertical takeoff and the landing [20][21]

Figure 1.1-18 shows the gear system of the F35B Lightning Ⅱ aircraft equipped with a system to drive a fan for vertical takeoff and landing assistance [20] [21]. The F35B is stealthy and does not require a long runway, so it is expected to improve the defense capability. The F35B takes off and lands while maintaining a balance between front and rear by directing the engine nozzles downward and forcing air to flow downward from the fan (lift fan) behind the cockpit. The front fan and rear engine are connected by a shaft, and the fan is driven by the engine through a clutch when necessary. The lift fan consists of a double inversion fan and is equipped with bevel gears that face each other and rotate in reverse to drive the fan. This bevel gear has a high rotation speed. Therefore, reducing the power loss of the gear system is considered to be effective in improving the fuel efficiency of the engine.

1.1.3　Research on the Power Loss of the Gear System

1.1.3.1　Research on Sliding and Rolling Losses in Tribology at the Gear Contact Surface
(1)　Research on the Phenomenon of Power Loss at the Gear Contact Surface
（ⅰ）　Phenomenon at the Gear Contact Surface

From the conventional research on the phenomenon at the gear contact surface (e.g., [22] [23]), the phenomenon at the gear contact surface is explained. Figure 1.1-19 shows a schematic of the gear contact condition. Figure 1.1-19 (a) depicts the gear contact condition on the contact line. The number of teeth that are engaged changes according to the phase and moves up and down between two integers (see Appendix B.1.1 for details). In this example, the case of going up and down between 2 tooth engagement and 1 tooth engagement is shown. When the number of teeth changes, the load on the contact surface changes because the number of teeth that take the load changes. Figure 1.1-19 (b) presents a schematic of the phenomenon at the gear contact position. At the gear contact position, the material is deformed by the Hertz contact pressure and the surface comes into contact with a finite width. Oil film exists between the surfaces. As shown in Fig. 1.1-19 (b), friction power loss due to the sliding speed of the contact surface (hereinafter, sliding power loss or sliding loss) and power loss due to the pumping of oil at the rolling speed of the contact surface (hereinafter, rolling power loss or rolling loss) occur on the gear contact surface. To calculate the power loss at the gear contact surface with high accuracy, it is important to construct a formula corresponding to each phenomenon of sliding power loss and rolling power loss, and to simulate the contact condition with different loads and speeds depending on the place of contact.

（ⅱ）　Research on Sliding Power Loss at the Gear Contact Surface

The sliding power loss at the gear contact surface is calculated by the following expression: friction coefficient × tangential load × peripheral speed (peripheral speed = rotational radius × angular speed). In estimating the sliding power loss, it is important to estimate the friction coefficient. Figure 1.1-20 shows the Stribeck curve, which is commonly used as the relationship between the lubrication condition of the contact surface and the friction coefficient. In the boundary lubrication condition (left side of Fig. 1.1-20), the friction due to the metal contact of the surface roughness protrusions becomes dominant. In this case, the oil film is thinner than the surface roughness, so the effect on the friction coefficient is small. In the hydrodynamic lubrication condition (right side of Fig. 1.1-20), the oil shear resistance becomes dominant because the thickness of the oil film is sufficiently thicker than the surface roughness. The lubrication condition of the gear contact surface is mixed, between the boundary and the hydrodynamic lubrication conditions, as illustrated in Fig. 1.1-21 . In the gear contact surface, the oil film thickness is in the same order as the surface roughness, as shown in Fig. 1.1-21 . The boundary lubrication condition caused by the contact of the surface roughness protrusions and the hydrodynamic lubrication in which the contact surface is separated by the oil film coexist. The friction coefficient in the mixed lubrication condition is affected by the load, sliding speed, and viscosity of the fluid, as shown by the horizontal axis parameter in Fig. 1.1-20 . Many studies have been conducted on the estimation method of the sliding friction coefficient at the gear contact surface. For example, Anderson et al. [22] constructed a model using the log function to estimate the friction

coefficient of the unsteady contact condition at a certain phase and location. In addition, Li and Kahraman et al. [23] constructed a model that approximates the real phenomenon of sudden changes in the number of gear teeth meshing using transient elastohydrodynamic lubrication (Transient EHL). In both cases, there are experimental constants for fitting the friction coefficient to the experimental results.

(a) Gear meshing

(b) Sliding and rotating losses between contact surfaces
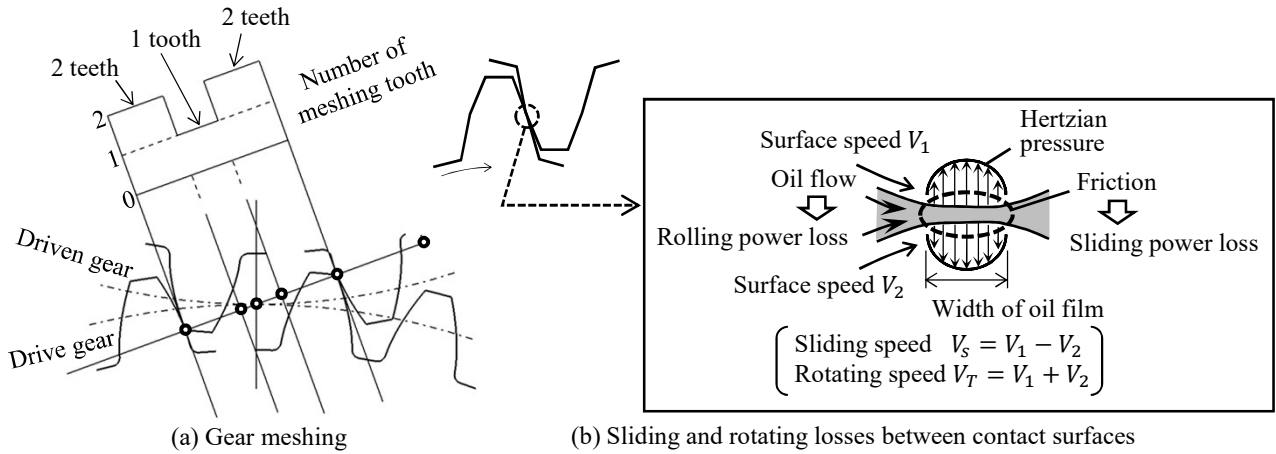
Fig. 1.1-19 Schematics of gear contacts
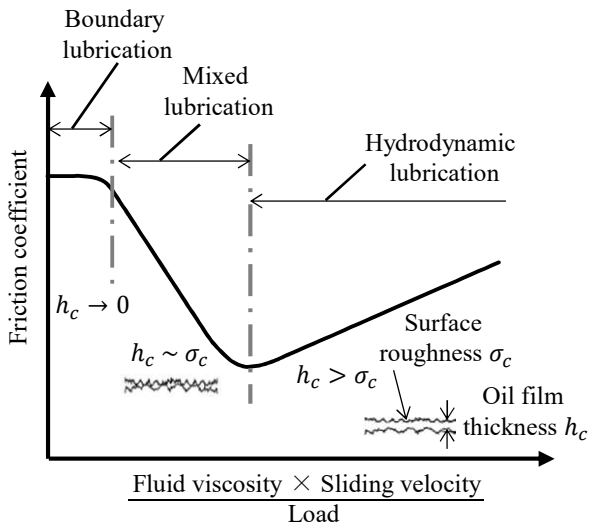
Fig. 1.1-20 A Stribeck curve [24]
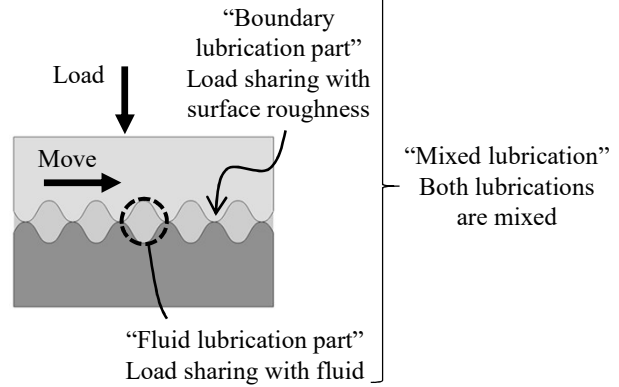
Fig. 1.1-21 Schematic of mixed lubrication

(iii) Research on Rolling Power Loss at the Gear Contact Surface

As shown in Fig. 1.1-19 (b), the rolling power loss at the gear contact surface is a loss generated by the pumping action between the contact surfaces. The rolling power loss is proportional to the flow rate of oil (= distance between the contact surfaces (oil film thickness) × contact surface length × rolling speed). Estimating the oil film thickness is important in estimating the rolling power loss. Numerous studies have also been conducted on methods for estimating the oil film thickness. For example, Anderson et al. [22] constructed an empirical formula for estimating the rolling power

loss by calculating the oil film thickness, taking into consideration the load, speed, material, radius of curvature, etc. of the contact surface. A method for directly solving the Reynolds equation to determine the oil film thickness (Li and Kahraman et al. [23]) has also been proposed.

(2)   Research on Reduction of Power Loss at the Gear Contact Surface

As methods for reducing power loss at the gear contact surface, reduction of the gear module (reduction of tooth height), super finish of the tooth surface, and change of oil are mentioned.

Figure 1.1-22 presents an example in which a gear module is reduced in size [5]. Compared to the gear on the left side, the gear module on the right side is smaller. Smaller gear modules reduce power losses because the distance from the pitch circle to the tip of the tooth and the distance from the pitch circle to the base of the tooth decrease, and the relative speed between the tooth surfaces decreases. Figure 1.1-23 shows an example of super finish of the tooth surface. The power loss is reduced when the tooth surface is super finished because the area in the boundary lubrication decreases, thereby reducing the coefficient of friction on the contact surface. In the example of Petry-Johnson and Kahraman [5], the power loss reduction effects of smaller gear modules and tooth surface super finishing were experimentally shown.

Fig. 1.1-22 Example of the reduction of the gear module for small sliding loss on gear contact surfaces [5]
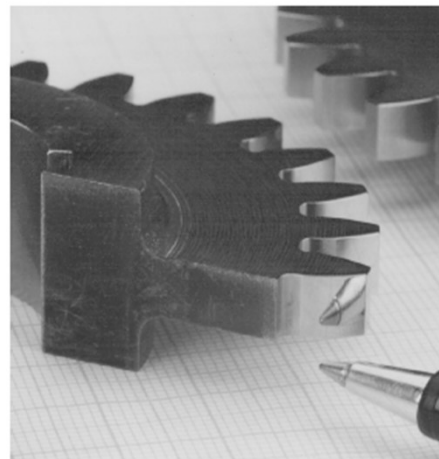
Fig. 1.1-23 Example of super finished tooth surfaces [25]

Regarding the change of oil, when the viscosity of oil is lowered, the sliding friction coefficient at the gear contact surface and sliding power loss tend to increase because the mixed lubrication condition of the Stribeck curve (Fig. 1.1-20) approaches the boundary lubrication condition, while the rolling power loss tends to decrease because the oil film thickness becomes thinner. It was experimentally shown that whether the increasing trend or decreasing trend is dominant depends on the surface conditions of the tooth surface such as the surface roughness of the gear [5].

1.1.3.2   Research of Fluid Dynamic Loss of Air and Oil in Areas Other than Gear Contact Surfaces

This section summarizes the previous research on the fluid dynamic loss of air and oil in the area around the gear other than the gear contact surface (including all areas other than the gear contact surface).

(1)   Overview of Research on the Fluid Dynamics of Air and Oil

Figure 1.1-24 presents a summary of previous studies. As indicated in Section 1.1.1.1, the fraction of fluid dynamic loss increases under conditions where the gear peripheral speed exceeds 50 m/s. Therefore, the previous research under this condition was summarized.

The horizontal axis in the figure is divided into three parts according to the number of gears of the research target. The left area corresponds to a single gear, the middle area to two gears (one meshing), and the right area to three or more gears (two or more meshings). In each area, the research on the right side is more recent. The gear is composed of two or more meshing gears for power transmission purposes, so the research on them seems to be dealing with phenomena equivalent to those of a real gearbox. The larger the number of gears, the more complicated the phenomena, and the more difficult the research is. The areas in the figure are divided according to these concepts. The higher the peripheral speed, the more complicated the phenomena, and the more difficult the research becomes. The maximum values of the peripheral speed in each research are also shown.

In the upper table of Fig. 1.1-24 , the meanings of symbols are shown. With regard to experiments ($\bigcirc$ and ● in the figure), there are many studies on single gears, two gears, and a gear system, and at the same time, power loss models ($\square$ and ■ in the figure) have often been proposed. With regard to flow visualization (Δ and ▲ in the figure), there are some examples using single gears, but there are few examples using two gears, and no examples using more than three gears are found. With regard to velocity measurement of air flow (∇ in the figure) and two-phase flow measurement (measurement of oil fraction and mixture velocity, shown as ◆ in the figure), there are examples using single gears, but no examples using more than two gears are found. With regard to numerical simulations (computational fluid dynamics, ☆ and ★ in the figure), there are simulations with airflow or two-phase flow using single gears, and the airflow simulations focused around the gear meshing area. There seems to be no simulations with two-phase flow of air and oil using two or more gears.

The following sections describe the following in detail: (2) method for measuring fluid dynamic loss, (3) visualization of air and oil flows, (4) measurement of oil fraction and mixture velocity of two-phase flow, (5) fluid dynamic loss model, (6) theory of fluid dynamic loss, (7) numerical simulation method of fluid dynamic loss, (8) research on reduction of fluid dynamic loss, (9) reference cases of fluid dynamic loss, and (10) summary of the studies on fluid dynamic loss.

(2)   Method for Measuring Fluid Dynamic Loss

To measure the fluid dynamic loss of a gear system, first the total power loss of the gear system is measured. Total power loss includes friction power loss (at the gear contact surfaces, bearings, and seals) and fluid dynamic loss. Therefore, the fluid dynamic loss is calculated by subtracting the friction power loss from the total power loss.

(i)   Measurement of the Total Power Loss of the Gear System

There are four methods for measuring the total power loss of a gear system. Figure 1.1-25 shows the schematic of ①–③.

①   Oil Temperature Difference Method of Oil Supply and Scavenged Oil Temperatures

In this method, the fluid dynamic loss is obtained from the measurement results of the difference between the oil supply and scavenged oil temperatures of the gear system and the oil supply flow

	Experiment				Loss model	Computational fluid dynamics
	Loss measurement	Visualization	Velocity measurement	Two-phase flow measurement		
Air	○	△	▽		□	☆
Two-phase (air, oil)	●	▲	None	◆	■	★

Superscript: none: Spur or helical gear(s), b : Bevel gear(s),
*: Estimation of rotational speed
CFD: Computational Fluid Dynamics, PIV: Particle Image Velocimetry

No paper with two gears or more
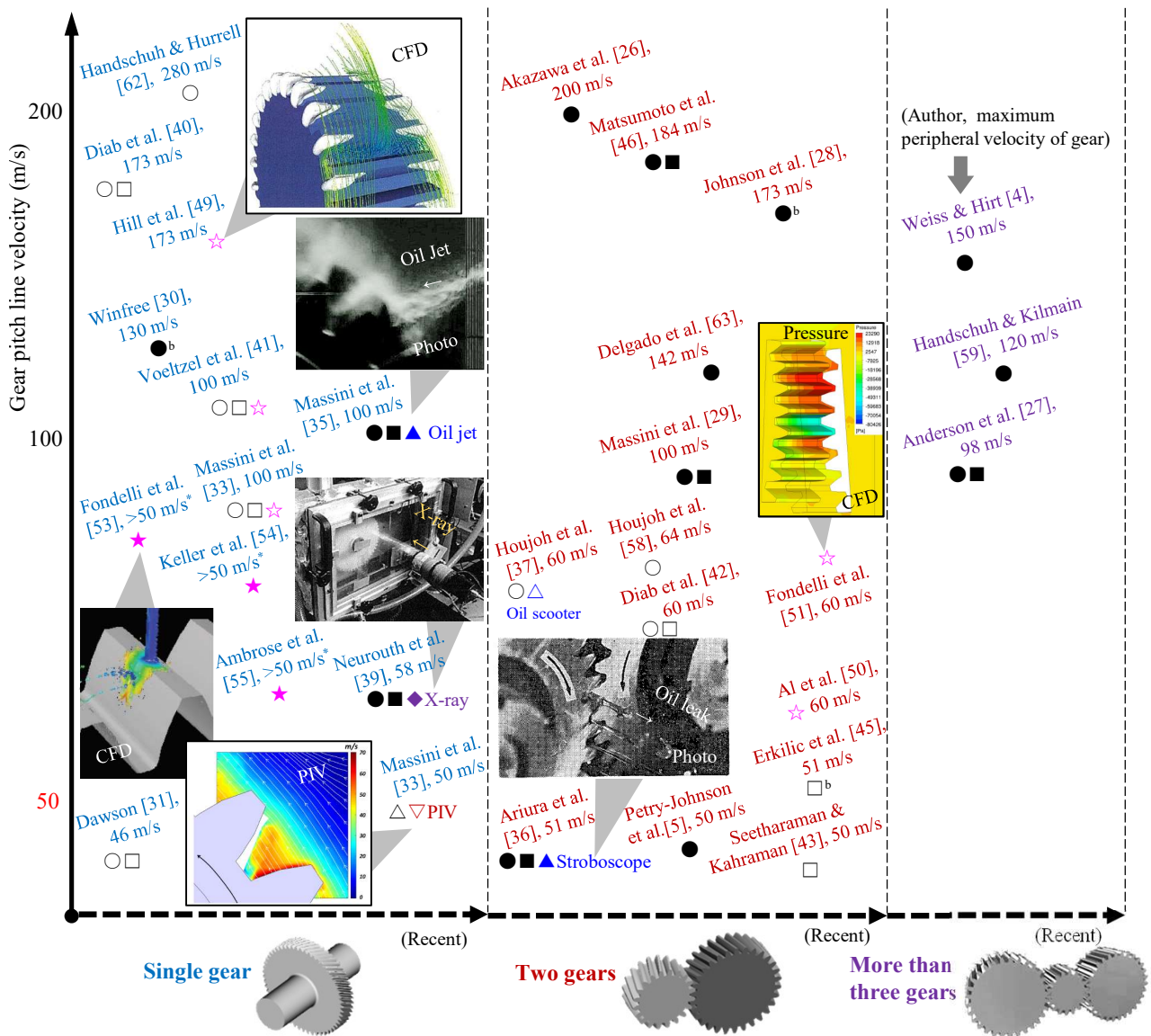
Fig. 1.1-24 Summary of previous studies

17

rate (e.g., Akazawa et al. [26] and Anderson et al. [27]). The method is affected by the temperature measurement error of the thermocouple and other devices, the error due to the heat radiation from the gearbox, and the error due to the time delay of the temperature change between the oil supply and scavenged oil temperatures, but is widely used as a simple method.

② Measurement Method by Torque Meter

In this method, the torque generated by the power loss is directly measured using a torque meter (e.g., Johnson et al. [28] and Massini et al. [29]). It is affected by the error of the torque meter and the power loss between the location of the torque meter and the gearbox (intermediate bearing, for example), but relatively high accuracy measurement is possible.

③ Method for Measuring Power Loss of Driving Motor

This method uses the efficiency of the driving motor (e.g., Winfree [30]). Although it is simple, the accuracy of the efficiency of power loss in the motor is relatively low. Thus, measurement errors are large, and it is often used for the rough evaluation of power loss.

④ Measuring Method from Change in Moment of Inertia during Free Deceleration

In this method, angular acceleration is obtained from the relationship between the time change of the rotational speed after the motor driving force is turned off, and power loss torque is obtained by multiplying the angular acceleration by the moment of inertia of the gear (e.g., Dawson [31] and Delgado et al. [32]). This method appears to be infrequent and less common.
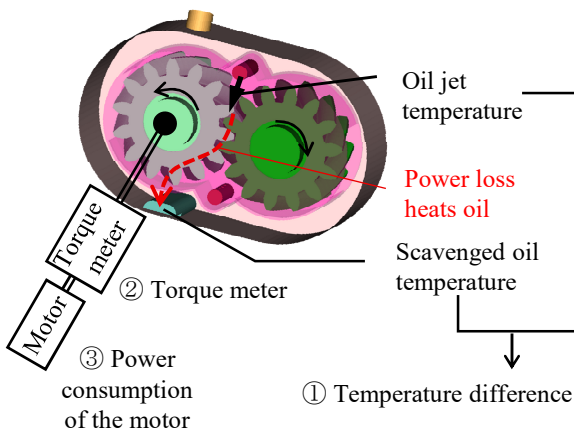
Fig. 1.1-25 Schematic of the power loss measurement method
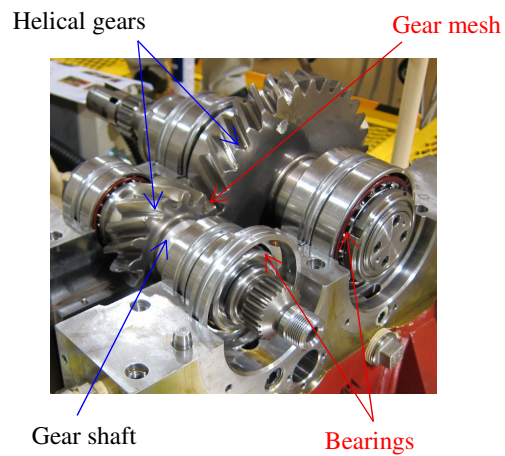
Fig. 1.1-26 Examples of gear shafts and bearings

(ii) Evaluation of Friction Power Loss in Gear Contact Surfaces, Bearings, and Seals

Figure 1.1-26 shows an example of a gearbox for evaluating the power loss at gear contact surfaces, bearings, and seals. In high-speed gearboxes, gears and bearings are often placed close to each other to increase the natural frequency of the shaft. Power loss at gear contact surfaces is evaluated in Section 1.1.3.1 (or Appendix B.1 for details). The following methods are used to evaluate power losses in bearings and seals.

① Method using Power Loss Evaluation Equations for Each Gear Contact Surfaces, Bearings, and Seals

In this method, the power loss is calculated according to the load and rotational speed using the power loss evaluation equation for each gear contact surfaces, bearings, and seals (e.g., [5]). The

loss evaluation equations are often provided by manufacturers. This method is widely used because it is easy to use.

② Method using Power Loss Measurement Results without Gear

In this method, power loss measurement results without gears, that is, with shafts, bearings, and seals only, are used for evaluating bearing and seal losses (e.g., Johnson n et al. [28] and Delgado et al. [32]). This method is used for single gear tests because it is limited to drive gears only (driven gears cannot rotate).

③ Method for Separating the Gear Chamber from the Bearing and Seal Chamber

In this method, the gear chamber and the bearing and seal chamber are separated, and in each chamber, the power loss of only the gear can be calculated by using the oil supply and scavenge temperature difference method described in (ⅰ)① (e.g., Akazawa et al. [26]). This power loss includes the power loss at the gear contact surface, so it must be subtracted by another method. This method is not common because the gearbox needs to be specially designed.

(ⅲ) Separation of Fluid Dynamic Loss into Aerodynamic Loss and Oil Dynamic Loss

The fluid dynamic loss calculated using either of the above methods can be further divided into the aerodynamic loss and the oil dynamic loss. As a method for separating the aerodynamic loss and the oil dynamic loss, the oil dynamic loss is calculated by subtracting the loss at zero oil supply (which is equal to an oil dynamic loss of zero) from the total loss, and the aerodynamic loss is calculated by subtracting the loss at the gear contact surfaces, bearings, and seals from the remaining loss (e.g., Johnson et al. [28]).

(3) Visualization of Air and Oil Flows

Examples of visualization of airflow and oil flow are shown in Fig. 1.1-27 .

(ⅰ) Visualization of Airflow

Regarding the visualization of airflow, Massini et al. [33] used particle image velocimetry (PIV) to visualize the flow around the spur gear (Fig. 1.1-27 (a)). In Fig. 1.1-27 (a1), the velocity near the tip of the tooth is close to the peripheral velocity of the tooth tip, whereas the velocity tends to decrease sharply with radial distance from the tooth tip. In Fig. 1.1-27 (a2), the flow in the axial direction is generated from the edge of the tooth toward the center, and after colliding near the center, the flow ejected in the radial direction is captured.

(ⅱ) Visualization of Oil Flow

The visualization of oil flow in the gearbox is generally conducted by making the housing of the gearbox transparent and capturing images using stroboscopic photography or a high-speed camera. Figure 1.1-27 (b) to (e) show examples of oil flow visualization.

① Visualization of Oil Jet for Lubrication to Gear Tooth Surface

Visualization of oil jets for lubrication of gear tooth surfaces can be conducted by stroboscopic photography at the same time as oil jet injection (Townsend et al. [34]) or a high-speed camera (e.g., Massini et al. [35]; shown in Fig. 1.1-27 (b)), which captures the tangential scattering of oil after it reaches the tooth surface.

(a1) Peripheral
velocity, 50 m/s*

(a2) Axial velocity, 100 m/s*

(a) PIV measurement results
with a spur gear (Massini et al. [33])

(b) A visualization of the oil jet
with a spur gear, 100 m/s*
(Massini et al. [35])

(c) A visualization of oil flow
discharging from the shroud slot
with a bevel gear, 50 m/s*
(Johnson et al. [28])

(* Gear
peripheral
speed)

(d1) 300 rpm, 120 cc/s

Oil bending
(d2) 440 rpm, 40 cc/s

(d) Visualizations of oil from the gear mesh
of spur gears, 50 m/s* (Ariura et al. [36])

(e) Hand sketches of oi supplied from both ends,
helical gears, 60 m/s* (Houjoh et al. [37])

Fig. 1.1-27 Examples of flow visualization

② Visualization of Oil Outflow from the Gear Shroud (Gear Enclosure to Reduce Fluid Dynamic Loss)

Regarding visualization of oil flow from a gear shroud, there is an example of visualization of oil flow from a bevel gear shroud (Fig. 1.1-27 (c)) by Johnson et al. [28]. The oil adhering to the inner surface of the gear shroud is observed to flow tangentially from the shroud opening.

③ Visualization of Oil Behavior in the Gear Meshing Part

Regarding visualization of the behavior of oil in the gear meshing part, Ariura et al. visualized the outflow of oil from the spur gear meshing by stroboscopic photography [36] (Fig. 1.1-27 (d)). They observed the oil jetting out in the axial direction from the gap between the tip clearance of the gear (the gap between the tip and the valley of the gear). In another example [37] (Fig. 1.1-27 (e)), in which Houjoh et al. visualized the flow of oil in the helical gear meshing part by injecting dye, dye injected from the leading side of the helical gear teeth flowed in the axial direction, while dye injected from the opposite side (trailing side) flowed in a limited area.

(4) Measurement of Oil Fraction and Mixture Velocity of Two-Phase Flow

Regarding the flow velocity measurement of airflow, the velocity distribution was measured by the PIV measurement [33] of Massini et al. described above. For the measurement of the oil fraction and the mixture velocity of two-phase flow of air and oil, there are examples of LePrince et al. [38] and Neuroth et al. [39] (peripheral speed of approximately 60 m/s) measuring the aeration rate of the oil stagnating in the lower part of the gearbox by X-ray. This measurement setting is shown in Fig. 1.1-28 . In this example, as
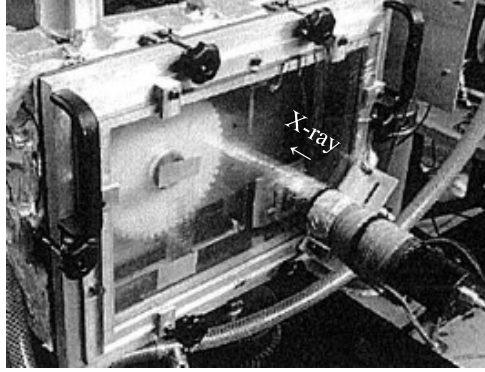
Fig. 1.1-28 A setting of the oil aeration measurement with a X-ray sensor for a spur gearbox, max gear peripheral speed of 58 m/s (Neurouth, et al. [39])

the oil supply to the gear is conducted by churning up the oil (which is called oil bath lubrication, splash lubrication, or dip lubrication), a large amount of oil exists in the lower part of the gear box, and the maximum aeration rate in the oil reaches approximately 20% in the maximum peripheral speed, 60 m/s. It was shown that the higher the aeration rate into oil was, the higher the liquid level and the larger the fluid dynamic loss of the gear.

There seems to be no research in which the oil fraction and mixture velocity of the two-phase flow of air and oil were measured around the oil jet, gear meshing part, or shroud.

(5)   Fluid Dynamic Loss Model

The fluid dynamic loss model, whose main purpose is the prediction of loss, consists of a base loss equation and experimental constants to fit the experimental results. The following shows power loss models for aerodynamic loss and oil dynamic loss in previous studies, and compares the breakdown of power loss in the loss model. The units of symbols in the equation are SI units unless otherwise indicated.

(i)   Aerodynamic Loss Model

① Difference between the Gear Meshing and Gear Peripheral Parts

Regarding the phenomenon of the gear meshing part, Houjoh et al. [37] measured the transient pressure at the tooth bottom and showed that the pressure rose sharply near the start of the tooth meshing and dropped sharply near the end of it. Because of this transient pressure, the aerodynamic loss of the meshing gear is greater than the sum of the aerodynamic loss of two gears. For example, Delgado et al. [32] reported that the loss of the meshing spur gear is 6–12 times larger than the sum of the loss of the two gears. Therefore, it is necessary to consider the gear meshing part and the gear peripheral part separately.

② Aerodynamic Loss Model around Gear Periphery (or Single Gear)

Dawson [31], Diab et al. [40], and Massini et al. [33] present examples of empirical equations for the aerodynamic loss in a single spur gear.

Dawson's empirical equation for the aerodynamic loss of a spur gear [31] is shown below.

$$P = N^{2.9} \left(0.16 D_f{}^{3.9} + D_f{}^{2.9} B^{0.75} M_g{}^{1.15} \right) \times 10^{-20} \Phi \lambda \tag{1.1}$$

where P is the aerodynamic loss (for $\Phi = 1$) (kW), N is the rotational speed (rpm), D_f is the

tooth bottom diameter (mm), B is the tooth width (mm), M_g is the gear module (mm), Φ is the ratio of fluid density to air density (for air, $\Phi = 1$), and λ is the shroud coefficient (= aerodynamic loss when the gear is shrouded / aerodynamic loss without shroud).

The empirical equation for the aerodynamic loss of a spur gear by Diab et al. [40] is shown below.

$$P = T\omega = C_M \frac{1}{2}\rho_{air}\omega^3 r_p{}^5 \tag{1.2}$$

$$C_M = 60 \, \text{Re}^{-0.25} \left(\frac{B}{r_p}\right)^{0.8} z^{-0.4} c_{flange} \tag{1.3}$$

$$\text{Re} = \frac{\omega r_p{}^2}{\nu_{air}} \tag{1.4}$$

where T is the torque, ω is the rotational angular velocity, C_M is the rotational moment coefficient, ρ_{air} is the air density, r_p is the pitch radius, Re is the rotational Reynolds number, B is the tooth width, z is the number of teeth, c_{flange} is the coefficient of influence of the flange (disk) close to the gear side wall ($c_{flange} = 1$ without the flange), and ν_{air} is the kinematic viscosity of air. Massini et al. [33] obtained the rotational moment coefficient C_M from the experimental result of the spur gear, and it was compared with the experimental Eq. 1.3 of Diab et al. The results showed that it deviated from the experimental result by the setting way of the flange influence coefficient c_{flange}.

Regarding the aerodynamic loss in helical gears and spur gears, Dawson [31] showed from experimental results that the aerodynamic loss in a helical gear is smaller than that in a spur gear. Meanwhile, Voeltzel et al. [41] showed that comprex experimental results on the influence of the helix angle exist, in which the aerodynamic loss of the helical gear becomes larger or smaller than that of a spur gear. Thus, the aerodynamic loss in a helical gear has not been sufficiently investigated.

③ Aerodynamic Loss Model in the Gear Meshing Part

Regarding the aerodynamic loss model of the gear meshing part, there is a method of solving the aerodynamic loss caused by the volume change between the teeth in the gear meshing by constructing a control volume of inviscid compressible air in a network. As an example of this network, an application to spur gears of Diab et al. [42] is shown in Figure 1.1-29 .

(a) Air trapping phenomena (b) An example of the flow network in a gear mesh
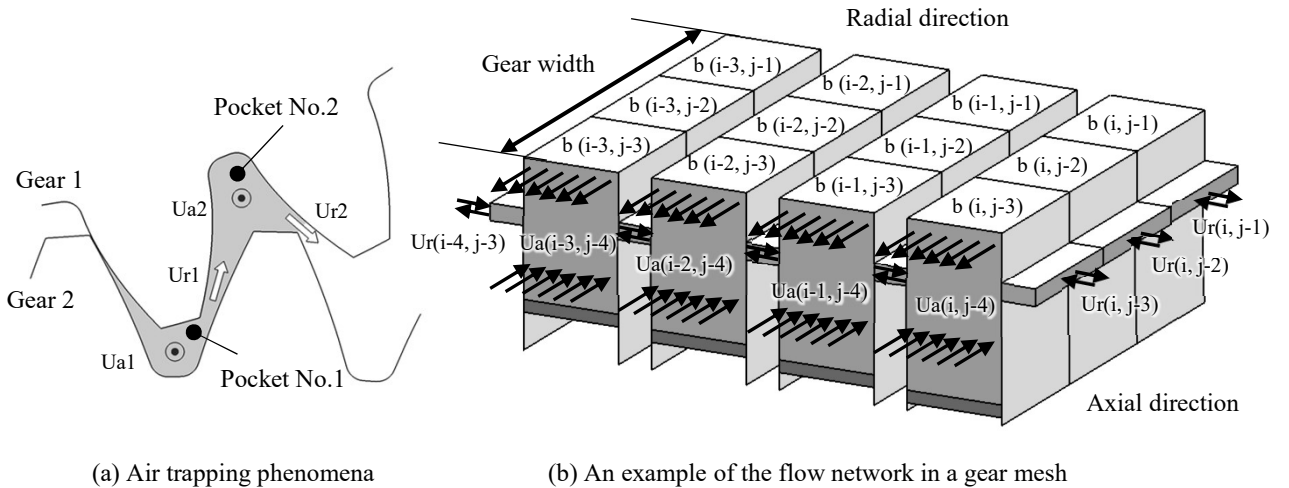
Fig. 1.1-29 Air trapping phenomena and an example of the flow network in a gear mesh (Diab, et al. [42])

The aerodynamic loss is calculated as the loss caused by the inflow and outflow from the gear side through the calculation of the unsteady pressure of each volume in the isentropic process. Similar examples are presented in Seetharaman [43] (spur gear), Talbot [44] (helical gear), and Erkilic [45] (bevel gear). Diab et al. [42] named the aerodynamic loss in gear meshing as "Trapping loss" and Seetharaman et al. [43], Talbot et al. [44], and Erkilic et al. [45] named the loss as "Pocketing loss."

(ii) Oil Dynamic Loss Model

Regarding the oil dynamic loss model, the gear meshing part and the gear peripheral part are considered separately as in the aerodynamic loss model.

① Oil Dynamic Loss Model at the Gear Periphery (Single Gear)

The fluid dynamic loss of air and oil in the gear periphery of Matsumoto et al. [46] is given by the following equation.

$$P = 3.80 \times 10^{-22} N^3 D_p{}^5 \left\{ 0.006 + 0.02 \left(\frac{B}{D_p} \right)^{0.8} + \left(\frac{h}{D_p} \right) \right\} \Phi' \tag{1.5}$$

where N is the rotational speed (rpm), D_p is the pitch diameter (mm), B is the tooth width (mm), h is tooth height (mm), and Φ' is the density of the surrounding fluid (kgf/mm^3). In the above equation, the estimation of Φ' is important; however, the calculation equation for Φ' is not shown. Massini et al. [35] showed the experimental results of the rotational moment coefficient C_M (defined as Eq. 1.3) when an oil jet was injected into a single spur gear. However, no experimental equation was shown.

② Oil Dynamic Loss Model in the Gear Meshing Part

Ariura et al. [36] compared the oil dynamic loss in a set of spur gears at a speed of up to 50 m/s with the theoretical calculation result that the oil injected was accelerated to the gear peripheral speed by gear meshing. The result showed that the calculated results agreed with the experimental results when the oil supply flow rate was small. This is the oil dynamic loss due to the acceleration of the oil when the oil is injected in the tangential direction of the gear meshing, and the oil that has flowed into the gear tip clearance at the oil jet speed v_{jet} is blown off at the gear peripheral speed v_p. It is theoretically obtained as the change in momentum when the oil is accelerated. This is shown in the following equation [36].

$$P = T\omega = \rho_{oil} Q_s r_p \omega \left(v_p - v_{jet} \right) \tag{1.6}$$

where ρ_{oil} is oil density and Q_s is the volumetric flow rate of oil.

Matsumoto et al. [46] modeled the oil dynamic loss in the gear meshing part as the loss caused by the acceleration of oil in the part for a pair of helical gears with a peripheral speed of 90 to 180 m/s. The equation for the oil dynamic loss was constructed based on the theoretical Eq. 1.6, and an experimental coefficient was introduced to fit it to the experimental results.

③ Oil Dynamic Loss Model including the Gear Meshing and Gear Peripheral Parts

In the fluid dynamic loss model of air and oil including gear meshing part and gear peripheral part, the loss calculation equation (per gear) for a pair of meshed spur gears obtained experimentally by Anderson et al. [47] is shown below.

$$P = 2.82 \times 10^{-7} \left(1 + 2.3 \frac{B}{r_p} \right) N^{2.8} r_p{}^{4.6} \left(0.028 \mu_{oil} + 0.019 \right) \tag{1.7}$$
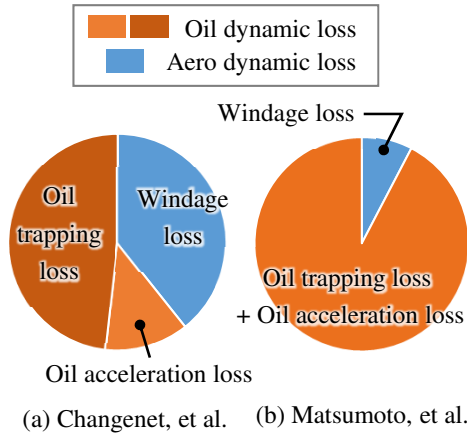
Fig. 1.1-30 Comparison of loss components (estimation obtained using loss models) [46][48]

Table 1.1-1 Gearbox conditions for comparison of loss components

		Changenet, et al.		Matsumoto, et al.	
Parameter	Unit	Pinion	Wheel	Pinion	Wheel
Pitch line velocity	m/s	162		166	
Gear type	-	Single helical		Double helical	
Number of teeth	-	32	113	34	99
Module	mm	6.8		6	
Pitch diameter	mm	219.5	775	225	655
Tooth face width	mm	390	400	190 × 2	
Pressure angle	°	20		20	
Helix angle	°	7.5		24.9	

where B is the tooth width, r_p is the pitch radius, N is the rotational speed (rpm), and μ_{oil} is the oil viscosity (cP). Support bearing loss was also included in Eq. 1.7. The total loss can be calculated by summing the loss using Eq. 1.7 for each gear.

(ⅲ) Comparison of Loss Breakdown of the Fluid Dynamic Loss Model

Figure 1.1-30 shows an example of the breakdown of fluid dynamic losses. In Fig. 1.1-30 (a), the breakdown of losses by Changenet et al. [48] is shown. In Fig. 1.1-30 (b), the breakdown of losses by Matsumoto et al. [46] is exhibited. Table 1.1-1 presents a comparison of the experimental conditions (a) and (b) in Fig. 1.1-30 . From this table, both conditions are considered to be approximately equivalent.

In Fig. 1.1-30 , "Oil trapping loss" and "Oil acceleration loss" are the oil dynamic loss[*2], and "Windage loss" is the aerodynamic loss containing oil mist.

A comparison of (a) and (b) in Fig. 1.1-30 shows a significant difference in the fraction of the oil dynamic loss and aerodynamic loss, which is considered to depend on which experimental coefficient is used to fit to the experimental results because both the oil dynamic loss and the aerodynamic loss contain experimental coefficients.

(6) Theory of Fluid Dynamic Loss

The theory of aerodynamic loss using the rotational moment coefficient is presented above in (5) (Eq. 1.3). The theory of oil dynamic loss is the theoretical equation of the loss due to acceleration of oil, as presented above in (5) (Eq. 1.6).

(7) Numerical Simulation Method of Fluid Dynamic Loss

Figure 1.1-31 shows an example of conventional studies on the numerical simulation (computational fluid

---

[*2] In the loss breakdown of Matsumoto et al. [46], the oil acceleration loss is divided into the peripheral acceleration and the axial acceleration. The peripheral acceleration corresponds to the "oil acceleration loss" in the loss breakdown of Changenet et al. [48]. The axial acceleration is considered to be substantially similar to the "Oil trapping loss" caused by the axial inflow and outflow.

(a1) Calculation mesh
(overset grid)

(a2) Relative streamlines and
isosurface of a high pressure region

(a) A CFD result around a spur gear,
173 m/s* (Hill et al. [49])

(b1) Calculation mesh
(morphing and remeshing grid)

(b2) Pressure contour

(b) A CFD result around a gear mesh,
60 m/s* (Fondelli et al. [51])

(c1) Calculation mesh
(Adaptive mesh refinement)

(c2) Isosurface of oil
with speed contour

(c) A CFD result of an oil jet to gear tooth, > 50 m/s*
(Fondelli et al. [53])

(d1) Calculation mesh
(morphing and
remeshing grid)

(d2) Isosurface of oil with speed contour
and path line

(d) A CFD result of dipped lubrication gears,
38 m/s* (Concli & Gorla [56])

(* Gear peripheral speed)

Fig. 1.1-31 Examples of previous CFD results

dynamics, CFD) of a gearbox. In the following, the numerical simulation methods are classified into those of airflow for a single gear, airflow for a meshing gear pair, two-phase flow of air and oil for a single gear, and two-phase flow of air and oil for a meshing gear pair.

(i)　Numerical Simulation Method of Airflow for a Single Gear

Numerical simulation of the airflow for a single gear can be conducted by either modeling a part of the gear to reduce calculation time and solving it by setting a periodic condition at the peripheral direction boundary (e.g., Voeltzel et al. [41]) or solving it for the whole gear (Hill et al. [49] (Fig. 1.1-31 (a)), Massini et al. [33]).

When the whole gear is solved, the boundary condition of the gearbox can be modeled. Massini et al. [33] showed that the gearbox boundary conditions caused asymmetrical flow in the width direction of the spur gear, which was in good agreement with the PIV measurement results (Fig. 1.1-27 (a2)).

(ii)　Numerical Simulation Method of Airflow for a Meshing Gear Pair

As an example of simulating only the gear meshing part of the meshed gear, Al et al. [50] and Fondelli et al. [51] (Fig. 1.1-31 (b)) used the method of morphing and remeshing the calculation mesh as the gear moves, and they showed that the change in pressure at the tip clearance in the gear meshing part

agreed well with the measurement by Houjoh et al. [37].

Concli et al. [52] provided an example of a simulation of a whole gear including meshing using this method. In this example, the peripheral speed was of up to 38 m/s, which is lower than the 50 m/s targeted in this research. There seems to be no example of a simulation of a whole gear including meshing with a peripheral speed of more than 50 m/s. This is considered to occur because the computational load in the gear meshing part is high, and the numerical convergence of the calculation deteriorates when the phenomenon becomes complicated as the peripheral speed increases.

The method of solving the equations for inviscid compressible air by setting the control volume at the gear meshing part shown in Fig. 1.1-29 can be regarded as local CFD at the gear meshing part. The reason is that the method numerically solves the governing equations for fluid dynamics, as in CFD.

(iii) Numerical Simulation Method of Two-Phase flow of Air and Oil for a Single Gear

An important design aspect for a two-phase flow of air and oil is how the oil jet reaches the tooth surface to allow its lubrication and cooling.

Figure 1.1-31 (c) shows an example [53] of Fondelli et al., in which the advection equation of the volume fraction of oil was solved by adding the volume of fluid (liquid) information to the calculation cell (volume of fluid (VOF) method), and the mesh size of the gas–liquid interface was automatically refined in the calculation mesh (adaptive mesh refinement (AMR) method). The oil jet impinged on the tooth surface, and then the spread of the oil film in the tooth root and tooth width directions was calculated. Examples of other simulation methods for the oil jet are the smoothed particle hydrodynamic (SPH) method used by Keller et al. [54] and the lattice Boltzmann method used by Ambrose et al. [55].

(iv) Numerical Simulation Method of Two-Phase Flow of Air and Oil for a Meshing Gear Pair

Figure 1.1-31 (d) shows an example of Concli et al. [56] using the VOF method for the gas–liquid interface and morphing/remeshing for the boundary fitting mesh. This example also has a peripheral speed of up to 38 m/s, which is lower than the 50 m/s targeted in this research. As a result of the calculation, the phenomenon that the oil surface is splashed up by the gear can be simulated. Liu et al. [57] also simulated using the SPH method (peripheral speed of 20 m/s). The SPH method does not require a calculation grid, making it easy to model the gear meshing part. The SPH method requires that all regions have the same particle size, and the particle size must be smaller than the tip clearance in order for the particles to enter the gear mesh.Therefore, the calculation time increases.

All of the above are examples with peripheral speeds of 50 m/s or less, and there seems to be no example of simulating the two-phase flow of whole gears including gear meshing part at a peripheral speed of 50 m/s or more. This is considered to be because the computational load in the gear meshing part is high and the numerical convergence of the calculation deteriorates when the phenomenon becomes complicated as the peripheral speed increases. This simulation is more complex than airflow simulation because a two-phase flow is solved.

(8) Research on Reduction of Fluid Dynamic Loss

In the research on the reduction of fluid dynamic loss, the effective loss reduction effect was obtained through experiments of a single gear and a gear system simulating a real gearbox for aeroengines. The research is divided into the reduction of aerodynamic loss and the reduction of fluid dynamic loss of air

and oil.

（ⅰ） Reduction of Aerodynamic Loss

To reduce the aerodynamic loss, it is effective to enclose the gear with a shroud and to reduce the air pressure inside the gearbox.

① Reduction of Aerodynamic Loss by Enclosing Gear in Shroud

Figure 1.1-32 (a1) shows an example of a shroud installed on a single spur gear (Dawson [31]). Installation of the shroud has been shown to reduce the aerodynamic loss by up to 66%[*3]. As a mechanism for reducing the loss of the shroud, it has been shown that the shroud suppresses the pumping work of the gear shown in Fig. 1.1-32 (a2) (intake of air from the axial direction and discharge of air to the radial direction).

② Reduction of Aerodynamic Loss by Reducing Air Pressure inside the Gearbox

With regard to the reduction of aerodynamic loss by reducing the internal pressure in the gearbox, Weiss et al. [4] conducted an experiment with a double helical gear pair and a peripheral speed of 150 m/s with a vacuum pump. As a result of decompressing the inside by the vacuum pump, it was shown that the fluid dynamic loss of air and oil was reduced by 1/3 and the total power loss including friction power loss was reduced by half.

Houjoh et al. [58] showed that a reduction in aerodynamic loss approximately proportional to the air pressure reduction inside the gearbox can be obtained by setting the inside of the gearbox to negative pressure[*4] using an external vacuum pump (an experiment with a spur gear pair, with peripheral speed of 60 m/s).

The aeroengine gearbox can reduce the aerodynamic loss when the gearbox internal pressure is lowered in accordance with the external pressure during cruising at high altitude.

（ⅱ） Reduction of Fluid Dynamic Loss of Air and Oil

To reduce the fluid dynamic loss of air and oil, it is effective to enclose the gear with a shroud. Nevertheless, it is necessary to have an oil discharge opening to prevent oil from stagnating inside the shroud. The effect of reducing the loss depends on the shape and location of the opening. In addition, reducing the oil supply flow rate is another effective method for reducing the loss.

① Reducing the Fluid Dynamic Loss of Air and Oil by Enclosing the Gear with a Shroud with Appropriate Oil Discharge Openings

An example of installing a shroud in a single bevel gear (peripheral speed of 140 m/s) is shown in Fig. 1.1-32 (b) (Johnson et al. [28]). It has been shown that the design of appropriate oil discharge openings in the shroud reduces the fluid dynamic loss of air and oil by approximately 23%. However, the reduction rate of loss is smaller when the oil discharge openings in the shroud are too small or too large.

[*3] Although the peripheral speed is 30 m/s, the rotational Reynolds number is equivalent to that of an aeroengine gear because the gear diameter is larger (300 to 1160 mm) than that of a general aeroengine gear (approximately 100 to 200 mm). Therefore, Dawson's results are considered applicable to aeroengine gears.

[*4] It has been reported that negative pressure inside the gearbox can be produced by the pumping work of the gear itself instead of that of the vacuum pump. However, the aerodynamic loss increases in this case.

An example of installing a shroud in a helical gear train for a tiltrotor aircraft (five meshing helical gears, peripheral speed of 120 m/s) is shown in Fig. 1.1-32 (c) (Handschuh et al. [59]). It was shown that installing a shroud reduces the fluid dynamic loss of air and oil by approximately 40%. Figure 1.1-32 (d) presents an example of a shroud installed in a gear system that simulates the F-35 STOVL's bevel gear system for driving the lift fan (three bevel gears, peripheral speed of 130 m/s, Winfree [30]). The installation of the shroud reduces the fluid dynamic loss of air and oil by up to 70%*5. The large loss reduction effect is thought to be due to the fact that the counter-rotating bevel gears are installed facing each other and close to each other, so that when there is no shroud, the surrounding fluid flow generated by gear rotation is large.

The shape for loss reduction in the epicyclic reduction gear system*6 for geared turbofans is shown in Fig. 1.1-32 (e) (Sheridan et al. [60]). The fluid dynamic loss can be reduced by installing a baffle between the star gears and by surrounding the ring gear with a gutter.

−66% (Aerodynamic loss)

(a1) Gear shroud   (a2) Pumping effect of gear

(a) A shroud for a spur gear (Dawson [31])

−23% (Fluid dynamic loss)

(b) A shroud with a slot for a bevel gear (Johnson et al. [28])

Tiltrotor aircraft   Helical gears

−40% (Fluid dynamic loss)

Gear shrouds

(c) Shrouds for a helical gear train (Handschuh & Kilmain [59])

F35 lift fan (Hamstra [20])

Lift fan

−70% (Fluid dynamic loss)

Gear test rig

Lower baffle

Gear shrouds

(d) Shrouds for a bevel gear train (Winfree [30])

Fan drive gear system

Star   Gutter

Baffle   Scavenge oil

Reduction of fluid dynamic loss

Baffle and gutter

(e) Baffles and a gutter for a star gear system (Sheridan et al. [60])

Fig. 1.1-32 Examples of experimental reduction of fluid dynamic loss by shrouding [6][28][30][31][59][60]

②   Reduction of Fluid Dynamic Loss of Air and Oil by Reduction of Oil Supply Flow Rate

Regarding the fluid dynamic loss of air and oil due to the reduction of oil supply flow rate, the example of Reynolds et al. [61] is shown in Fig. 1.1-33 . In the cruising operation range of an aircraft ("Typical cruise power range" in the figure), the fluid dynamic loss of air and oil ("Windage churning and pumping" in the figure) could be reduced by reducing the oil supply flow rate in accordance with the decrease in transmission power.

---

*5 The test gears were not meshed (the tooth tip circles were close together) and were driven separately by a motor or another gear.

*6 It consists of a sun gear, star gears, and a ring gear. The star gears do not revolve.

(a) Standard oil supply rate

(b) Reduction of oil supply rate at low power condition
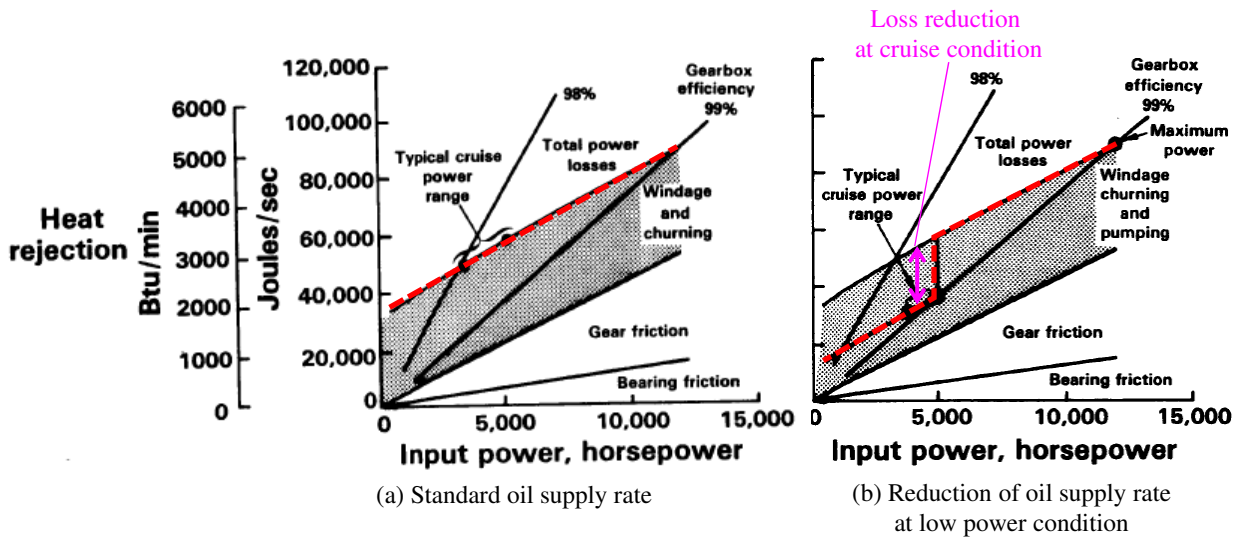
Fig. 1.1-33 Examples of reduction in fluid dynamic loss achieved by reducing the oil flow rate (estimation obtained using lubrication system model) [61]

(9)   Reference Cases of Fluid Dynamic Loss

Examples of fluid dynamic losses investigated are a single helical gear with peripheral speed of 280 m/s for the experiment of aerodynamic loss (by Handschuh et al. [62]) and a spur gear pair with peripheral speed of 142 m/s for the experiment of fluid dynamic loss of air and oil (Delgado et al. [63]).

(10)   Summary of the Studies on Fluid Dynamic Loss

A classification of fluid dynamic loss and loss reduction methods based on previous studies is presented in Fig. 1.1-34 .
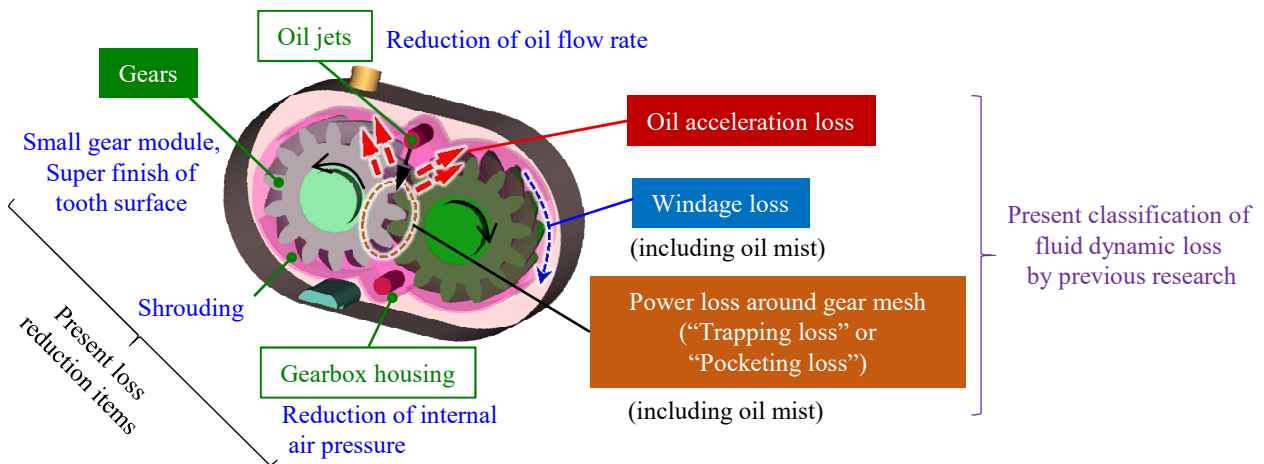
Fig. 1.1-34 Classification of fluid dynamic loss and methods for loss reduction in a high-speed gearbox

As shown in the right half of the figure, fluid dynamic losses are classified into oil acceleration loss caused by oil acceleration in the gear meshing part, aerodynamic loss (or windage loss) at the gear periphery, and fluid dynamic loss at the gear meshing part (sometimes called "Power loss around gear mesh," or "Trapping loss," or "Pocketing loss"). As shown in the left half of the figure, the methods for reducing fluid dynamic

29

loss include making the gear module smaller, super finishing of the tooth surface, installing a shroud to the gear, reducing the air pressure in the housing, and reducing the oil supply flow rate.

1.1.4 Examples of Research in Other Industries

(1) Reduction Gear System for Industrial Gas Turbines

In industrial gas turbines, a reduction gearbox is equipped between the turbine shaft and the motor because there is a difference between the optimal rotational speed of the turbine and the optimal rotational speed of the motor. The examples already shown in Weiss et al. [4] (maximum peripheral speed of 150 m/s), Akazawa et al. [26], and Matsumoto et al. [46] (peripheral speed of 100–200 m/s) are examples of reduction gearboxes for industrial gas turbines. In these reduction gearboxes, the gear of the reduction gear exceeds 50 m/s because the rotational speed of the turbine shaft is high. Therefore, the research results on reduction gearboxes for industrial gas turbines are thought to be applicable to aeroengine gear systems and are introduced in the above section on previous research.

(2) Automotive Field

As the gear peripheral speed of automobile transmissions is approximately 20 m/s or less, the fraction of friction power loss on the tooth surface to the total power loss is large, and the fraction of fluid dynamic loss is small. However, research on reducing fluid dynamic loss has been actively conducted owing to the fierce competition for fuel economy.

In automotive transmissions, oil is stored in the lower part of the housing, and the gears and bearings are lubricated by scooping up of oil with gear rotation (splash lubrication or dip lubrication). In splash lubrication, it is important to control the lubrication condition of each bearing by scooping up of oil and to minimize the power loss due to oil churning.

Luke et al. [64] (a single spur gear with peripheral speed of 30 m/s was examined for different oil and liquid levels), Kolekar et al. [65] (a simple spur gear with a peripheral speed of 30 m/s was examined by changing the internal pressure from vacuum to 2 atm), and Seetharaman et al. [66] [67] (a meshing spur gear pair with 20 m/s peripheral speed was examined for different liquid levels and gear speeds) present examples of equations based on experimental measurements of the fluid dynamic loss of splash lubrication. Regarding the numerical simulation for splash lubrication, Concli et al. [56] (peripheral speed of 38 m/s) and Liu et al. [68] (peripheral speed of 20 m/s) used the finite volume method to solve fluid conservation equations, the VOF method to capture the liquid surface, and the boundary fitting calculation mesh (the mesh is moved (morphed) and reconstructed (remeshed) as the gear rotates). As a result, the fluid dynamic loss agreed well with the experimental results.

As an example of numerical simulation using methods other than the finite volume method, Liu et al. [57] (peripheral speed of 20 m/s) used the SPH method to simulate the splash lubrication of a spur gear pair (described in Section 1.1.3.2 (4) (iv)).

As an example of measuring the aeration rate into oil in a two-phase flow of air and oil, LePrince et al. [38] and Neuroth et al. [39] measured the aeration rate of oil remaining in the lower part of the gearbox by X-ray (both measured at a peripheral speed of approximately 60 m/s) (described in Section 1.1.3.2 (4)).

An example of velocity measurement in a two-phase flow of air and oil is provided in Hartono et al. [69]

(peripheral velocity of 1.6 m/s). In this example, PIV was used to measure the flow velocity distribution around the gear and the air bubbles around the gear as it rotated.

(3)   Nuclear Power, Mineral Resources, and Environmental Measurement (Multiphase Flow Measurement) Fields

Multiphase flow measurement is important for heat transfer phenomena in nuclear reactors in the field of nuclear power, flotation machines in the field of mineral resources, and dust measurement in the field of environmental measurement.

Isokinetic suction, a type of multiphase flow measurement, is a method for adjusting the suction velocities of a probe to be equal to the surrounding flow velocities, which is used in dust measurement. An example is presented in Makino et al. [70] (average particle diameter of 2–4.5 µm, air flow rate of 6–21 m/s). Makino et al. also investigated the influence of non-isokinetic suction (where the suction velocity and the flow velocity differ).

Yang et al. [71] (liquid volume fraction of 86%–96%, flow rate of 6 m/s) and Namie et al. [72] (liquid volume fraction less than 0.15%, flow rate of 34–63 m/s) provide examples of applications of the isokinetic suction method to gas–liquid two-phase flows.

Other gas–liquid flow measurement methods include the optical method (using two optical fibers to detect changes in light transmittance) and the electrical resistance method. Ishikawa et al. [73] (liquid volume fraction of 30% to 70%, flow rate of 1–16 m/s) conducted experiments with these methods.

1.2   Possibility and Challenges of Improving the Gear System Efficiency

Under the circumstances where various efforts have been made to reduce the power loss of gear systems, the scope and method for further reducing the loss is described in this section.

1.2.1   Possibility of Low-Power-Loss Design in Gear-Strength and Lightweight Designs

The possible design parameters that can be changed for low-power-loss design are the gear aspect ratio and shroud shape, and the possibility of low-power-loss design by the optimization of these parameters is presented.

(1)   Possibility of Low-Power-Loss Design by Optimization of Gear Aspect Ratio

（ⅰ） Selectivity of Gear Design Parameters in AGMA[*7] Gear Strength Design Standard

Figure 1.2-1 shows various failure regimes encountered by gear teeth. In the low-speed gear, wear becomes important, and in the high-speed gear, tooth surface fatigue (pitting) or tooth surface scoring become important. Tooth surface scoring can be mitigated by reducing the gear module (gear tooth height) or the surface roughness of the tooth surface. Therefore, tooth surface fatigue is considered to be the most important design criteria.

As an index for the magnitude of the surface pressure load on the gear tooth surface, there is a K value shown by the following equation (from AGMA Standard 218.01 [75]).

$$K = \frac{2T}{BD_p{}^2}\left(\frac{m_G + 1}{m_G}\right) \tag{1.8}$$

[*7] American Gear Manufactures Association

where T is the torque, D_p is the pitch circle diameter of the pinion gear, B is the tooth width, and m_G is the gear ratio (= number of wheel gear teeth / number of pinion gear teeth > 1.0). From Eq. 1.8, it can be observed that the K value depends on the gear specifications and the transmitted load. To avoid gear tooth surface fatigue, the K value is designed not to exceed the recommended value (e.g., that presented in Dudley [76]) determined by applications, materials, life, machining accuracy, and achievements. Transmitted load and gear ratio are required specifications in many cases, and it is difficult to change them. Meanwhile, under the condition that $BD_p{}^2$ (tooth width × pitch circle diameter^2) is constant, designers can select the tooth width and pitch circle diameter (or gear aspect ratio = tooth width / pitch circle diameter). That is, it is possible to select the gear aspect ratio so as to have a low power-loss.
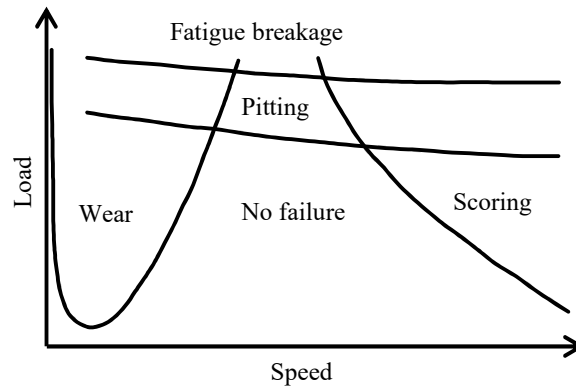
Fig. 1.2-1 Various failure regimes encountered by gear teeth [74]

(ii) Selectivity of Gear Design Parameters in Gear Weight Calculation

Figure 1.2-2 shows a cross section of a general aeroengine gear. In Fig. 1.2-2 (b), for reducing the weight, the width of the web is smaller than the width of the teeth, and a weight reduction hole is set on the web. The outline of each dimension is shown below with reference to Bhandari [77].
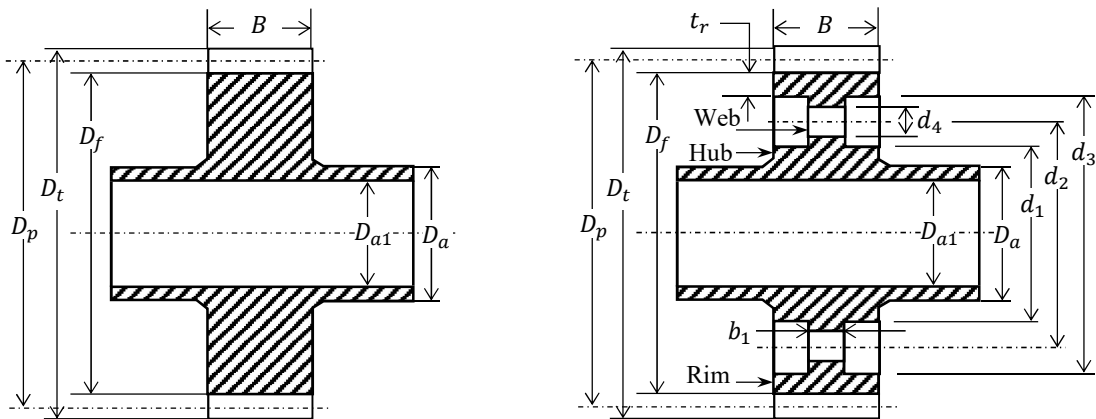
(a) Typical gear (Gear A)   (b) Typical gear with rim, hub, web, and weight reduction holes (Gear B)

Fig. 1.2-2 Typical gear parameters

- Pitch circle diameter $D_p = M_g z$ (M_g is the gear module, z is the number of teeth)
- Tooth tip diameter $D_t \simeq M_g(z+2)$

- Tooth base diameter $D_f \simeq M_g(z - 2.5)$
- Shaft outer diameter D_a, shaft inner diameter D_{a1}
- Tooth Width B
- Rim thickness $t_r = 2M_g \sim 3M_g$
- Web thickness $b_1 = 0.2B \sim 0.3B$
- Hub outer diameter $d_1 = 1.5D_a \sim 2.0D_a$
- Rim inner diameter $d_3 = D_f - 2t_r$
- Diameter of weight reduction hole on web $d_4 = (d_3 - d_1)/4$, number of holes n_h
- Pitch circle diameter of weight reduction holes $d_2 = (d_3 + d_1)/2$

The weight of Figure 1.2-2 (a) is given by the following equation.

$$\text{Weight of Gear A} = \frac{\pi}{4}\left(D_p{}^2 - D_{a1}{}^2\right)B \tag{1.9}$$

Similarly, the weight of Fig. 1.2-2 (b) is given by the following equation. Except for the weight of the shaft, the median value was used if it has a range of values.

$$\text{Weight of Gear B} = \frac{\pi}{4}\left(D_p{}^2 - D_{a1}{}^2\right)B - \frac{\pi}{4}\left\{(D_p - 2 \times 2.5M_g)^2 - (1.75D_a)^2\right\}(B - 0.25B)$$
$$- n_h\frac{\pi}{4}\left(\frac{D_p - 2 \times 2.5M_g - 1.75D_a}{4}\right)^2 \times 0.25B \tag{1.10}$$

The second term on the right side is the weight reduction effect of reducing the thickness of the web, and the third term is the weight reduction effect of the weight reduction holes on the web. The shaft outer diameter D_a and shaft inner diameter D_{a1} are considered not to be changed if they are the same transmitted power. Equations 1.9 and 1.10 are approximately proportional to $BD_p{}^2$, assuming that the module M_g and the number of weight reduction holes n_h are the same. That is, if $BD_p{}^2$ (tooth width $\times$ pitch circle diameter^2) is constant, the weight of the gear becomes almost constant. Therefore, under the condition that $BD_p{}^2$ (tooth width $\times$ pitch circle diameter^2) is constant, the designer can select the tooth width and pitch circle diameter (or gear aspect ratio = tooth width / pitch circle diameter). That is, it is possible to select the gear aspect ratio so as to have a low power-loss.

(iii)   Possibility of Low-Power-Loss Design by Optimization of Gear Aspect Ratio

As described above, the strength and weight of the gear can be maintained by keeping the tooth width $\times$ pitch circle diameter^2 constant in the gear strength design standard and the gear weight calculation equation. Therefore, under the condition that the tooth width $\times$ pitch circle diameter^2 is constant, the designer can select the tooth width and pitch circle diameter (or the gear aspect ratio = tooth width / pitch circle diameter). Optimization of the gear aspect ratio can be considered one of the important points of low-power-loss design and will be discussed in this research.

(2)   Possibility of Low-Power-Loss Design by Shroud Optimization

Among the aspects of design improvement shown in the summary of loss reduction methods (Fig. 1.1-34), the installation of the shroud can be relatively easily included in the design because the design of the housing is not changed and the weight penalty is small. As shown in Fig. 1.1-32 , the optimal shroud shape needs to be obtained depending on the gear specification. The optimization of the shroud is considered to be an important point of the low-power-loss design, and will be discussed in this research together with the

optimization of the gear aspect ratio.

1.2.2 Challenges in Low-Power-Loss Design of Gear Systems in Preliminary Design of Aeroengines

The gear aspect ratio optimization, which was shown as one of the key points of the low-power-loss design, has a large impact on the surrounding structure, and it includes aspects such as a change in axial distance of shafts and a change in the gearbox housing. Thus, it is important to consider it in the preliminary design stage of the gear system. For gear strength design, there are practical standards that include theoretical equations with empirical constants based on real phenomena, such as design standards for tooth surface strength and bending strength (e.g., AGMA 218.01 (1982) [78]) or design standards for tooth surface scuffing (e.g., AGMA 217.01 (1965) [79]). These standards ensure high reliability and accuracy by accumulating continuous improvements (e.g., AGMA 2001-D04 (2004) [80] for tooth surface strength and root bending strength, and AGMA 925-A03 (2003) [81] for tooth surface scuffing). For the lightweight design of gears, structural optimization based on strength analysis and vibration analysis enables examination of lightweight shapes with high accuracy. For the low-power-loss design, the conventional research described in Section 1.1 clarifies certain phenomena and reduces losses. However, as there is no standard with high accuracy and reliability such as the AGMA strength design standard, strength and lightweight designs tend to be prioritized. Therefore, there is room to reduce losses through an overall optimal design, including a low-power-loss design, from the preliminary design stage.

Standardization of low-power-loss designs is necessary to establish the corresponding standards, and understanding of loss phenomena is indispensable for the standardization. Regarding gear friction loss and power loss in bearings and seals, as described in Section 1.1.3.1, it can be considered that the standard loss calculation methods have been generally constructed based on understanding of these phenomena. However, regarding fluid dynamic loss, as described in Section 1.1.3.2, the difficulty in understanding it is extremely high due to the nonlinearity of the two-phase flow of air and oil and the complicated boundary conditions of meshed gears. Consequently, there is no common understanding of fluid dynamic loss phenomena, which is important for standardization of low-power-loss designs. In the next section, the problem of understanding fluid dynamic loss phenomena will be clarified.

1.3 Issues in Understanding the Phenomena of Fluid Dynamic Loss

For the inclusion of low-power-loss design from the preliminary design stage of a gearbox, it is necessary for the low-power-loss design standard to have the same accuracy and reliability as the strength design standard. Therefore, it is important to understand the phenomena of fluid dynamic loss of the gearbox. To understand the fluid dynamic loss phenomena, their classification is the first priority. For this purpose, a theory of fluid dynamic loss, a loss model, an experimental measurement method, and a numerical simulation method are necessary. The corresponding issues are described below.

1.3.1 Issues in the Classification of Fluid Dynamic Loss

As shown in Fig. 1.1-34 , fluid dynamic loss is generally classified into "Oil acceleration loss," "Windage loss," and "Trapping loss or Pocketing loss." To standardize these loss categories to a level where differences in opinion among researchers (e.g., Fig. 1.1-30) do not occur, it is necessary to understand the phenomenon of fluid

dynamic loss. However, neither the theory of fluid dynamic loss, the loss model, the experimental measurement method, nor the numerical simulation method have reached the required level to understand the phenomena. This is because of the extremely high difficulty due to the high-speed two-phase flow of air and oil and the complicated boundary conditions of gears including gear meshing. That is, it seems to be difficult to understand the phenomena by any single method, including theory, experimental measurement, or numerical simulation. Therefore, it is necessary to use these methods complementarily to collect clues to understand phenomena and to increase the reliability of loss classification.

1.3.2   Issues in the Fluid Dynamic Loss Theory and Loss Model

Regarding the theory of fluid dynamic loss, as described in Section 1.1.3.2 (5) and (6), there are methods using the rotational moment coefficient and the theoretical equation for the oil acceleration loss. Meanwhile, as described in Section 1.1.3.2 (5), it is considered necessary to divide the fluid dynamic loss of the gear into the loss at the gear meshing part and that at the gear peripheral part because the difference in the loss of each part is large. Therefore, it is necessary to construct a theory at the gear meshing part and the peripheral part, for both aerodynamic loss and oil dynamic loss.

As presented in Section 1.1.3.2 (5), various empirical equations have been proposed for fluid dynamic loss models. These equations focus on fitting the total loss with that in the experimental results, and the knowledge on the classification of fluid dynamic loss is not sufficient.

1.3.3   Issues in the Experimental Measurement Methods for Fluid Dynamic Loss

To understand the phenomena of fluid dynamic loss, we need an "experimental measurement method of the loss" to understand the phenomena from the characteristics of the loss, a "flow visualization method" to understand the phenomena qualitatively, a "measurement method of oil fraction and mixture velocity of two-phase flow" to understand the two-phase flow of air and oil quantitatively, and an "experimental classification method of the loss" to validate the loss model based on the classification of fluid dynamic loss. Each issue with the method is described below.

(1)   Issues in the Experimental Measurement Method of Fluid Dynamic Loss
As shown in Fig. 1.1-7 , the fraction of fluid dynamic loss increases in high-speed gearboxes. Nonetheless, friction loss of gears, bearings, and seals still accounts for a certain fraction. Therefore, measurement errors in the friction loss cause measurement errors in fluid dynamic loss, as detailed below.

（ⅰ） Fraction of Friction Loss of Gears, Bearings, and Seals to Total Power Loss in a Gearbox
As for the fraction of bearing loss, for example, Reynolds [61] (Fig. 1.1-33) and Changet et al. [48] showed that bearing power loss accounts for approximately 20% of the total power loss. The fluid dynamic loss of the gearbox is calculated by subtracting the friction loss of the gears, bearings, and seals from the total power loss of the gearbox. Therefore, it is necessary to measure the friction loss of the gears, bearings, and seals accurately.

（ⅱ） Temperature Dependence of Friction Loss of Gears, Bearings, and Seals
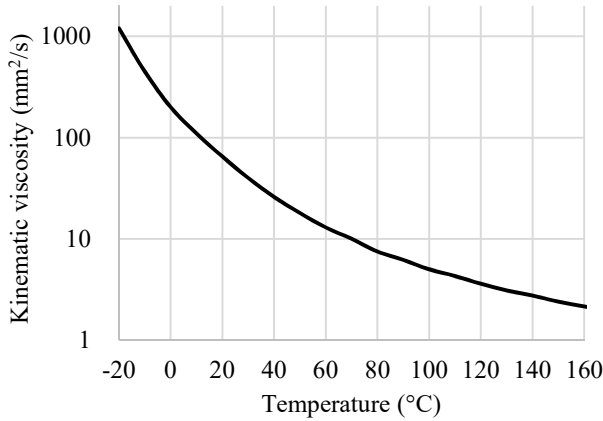
Fig. 1.3-1 Kinematic viscosity vs. oil temperature (experimental results, oil type: MIL-PRF-23699)
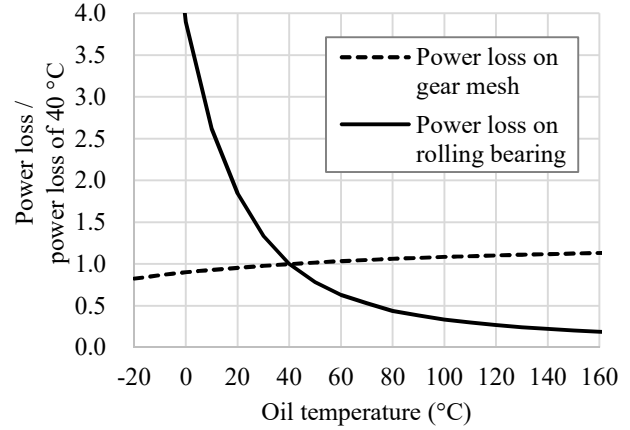
Fig. 1.3-2 Temperature dependences of power loss on a gear mesh and rolling bearing (Experimental equations are used. See Appendix B for more detail.)

The equation of ASTM[*8] D341-77, which is the relationship between temperature and kinematic viscosity of oil, is shown below.

$$\log_{10}\left\{\log_{10}\left(\nu + 0.7\right)\right\} = A - B \times \log_{10}\left(\mathscr{T} + 273.15\right) \tag{1.11}$$

where ν is the kinematic viscosity of oil, A and B are the coefficients of the lubricant, and $\mathscr{T}$ is the temperature (°C). Solving this equation for the kinematic viscosity ν gives the following equation.

$$\begin{aligned}
\nu(\mathscr{T}) &= 10^{10^{C_\nu}} - 0.7 \\
C_\nu &= A - B \times \log_{10}\left(\mathscr{T} + 273.15\right)
\end{aligned} \tag{1.12}$$

Figure 1.3-1 shows an example of the relationship between oil temperature and kinematic viscosity. It can be observed that the kinematic viscosity varies largely with temperature.

According to the simplified equation of Höhn et al. ([82], see Appendix B.1.2 for details), the friction loss of gear mesh is proportional to the −0.05th power of the viscosity of oil. Therefore, the friction loss of gear mesh changes as the temperature changes and the viscosity of oil changes. According to the simplified equation of Palmgren [83], the friction loss of a rolling bearing is proportional to the 2/3 power of the kinematic viscosity of oil (see Appendix B.2 for details). The temperature dependence of the friction loss of a seal depends on the product. In the case of mechanical seals, thermal deformation occurs due to the temperature changes of gear shafts and gearbox housing, which changes the extension of the spring and the spring load. The changes in spring condition may cause friction loss change in the seal (see Appendix B.3 for details.). Figure 1.3-2 shows the oil temperature dependence of the friction loss of the gear and the rolling bearing. The friction loss is shown as a relative value based on that at 40°C using the viscosity chart of oil shown in Fig. 1.3-1 . The simple equation [82] of Höhn et al. was used to calculate the friction loss of the gear mesh, and the simple equation [83] of Palmgren was used to calculate the friction loss of the bearing. It can be observed from the figure that the temperature dependence of the friction loss of the bearing is large.

[*8] ASTM International, formerly American Society for Testing and Materials

(iii)   Temperature Error due to the Effect of the Heat Capacity of the Gearbox

It takes time for the gearbox to reach the steady temperature because of its large heat capacity. In particular, it is difficult to reach a constant temperature distribution in the periphery of the gearbox because the temperature increases slowly in the periphery. This is because the heat input is small compared with the heat capacity. Therefore, it is often determined that the temperature distribution has reached a steady state when the temperature change in the high-temperature part of the gearbox becomes moderate (e.g., [59]). In this case, the temperature of the bearings and seals at the periphery of the gearbox may differ owing to the influence of ambient temperature, operating conditions, operation history, etc. Differences in temperature lead to measurement errors in the friction loss of bearings and seals, as described in (ii) above.

From the above, it was found that the development of a measurement method that can decrease the measurement error of the power loss due to the friction between the gears, bearings, and seals was an issue for high-accuracy measurement of the fluid dynamic loss of the gearbox.

(2)   Issues in Flow Visualization Methods

For the PIV method [33], one of the methods for visualizing airflow, the laser light sheet should not be blocked by the oil mist. In the conventional research of methods for visualizing oil flow in a gearbox [28][35][36][37] (Section 1.1.3), a gearbox housing with a sufficiently wide space around the gear was used to prevent the oil mist in the gearbox from blocking the camera's sight. However, the gearbox of an actual machine has a small housing owing to its compact size and light weight, and a large amount of oil mist is thought to be circulating in a narrow space around the gear. Therefore, when visualizing a condition close to the flow in the gearbox of an actual aeroengine, the development of a method for visualizing the inside of the gearbox in a condition where the oil mist is thick is an issue.

(3)   Issues in the Measurement Method of Oil Fraction and Mixture Velocity of a Two-Phase Flow

The method [38] [39] (Section 1.1.3) for measuring the oil fraction of two-phase flow using X-rays is not suitable for measuring the two-phase flow in the gearbox because it requires an X-ray oscillation probe and a receiver to be installed in pairs, and because the spatial resolution is poor due to large sensing part of the probe. The optical two-phase flow measuring method [73] (Section 1.1.4) is not suitable for measuring the two-phase flow in a gearbox because it is not possible to measure oil particles smaller than the distance between the optical fibers, and because there is the possibility of breakage of the fibers due to high-speed flow. The electrical resistance method is not applicable because oil is non-conductive.

The isokinetic suction method has a narrow measurement experience for the gas–liquid ratio and the mixture velocity in the measurement examples [71] [72], but it is possible to correct the error even in the case of non-isokinetic suction [70]. Because the probe is sufficiently rigid to withstand a high-speed flow, it is highly possible that the isokinetic suction method can be applied to the measurement of a two-phase flow of air and oil in a gearbox. Therefore, the development of a measurement method that can be applied to a wide range of gas–liquid ratio and mixture velocity conditions for two-phase flow in a gearbox is an issue.

(4)   Issues in the Experimental Classification Methods of Fluid Dynamic Loss

The loss model of fluid dynamic loss in conventional studies is composed of loss equations and experimental coefficients to fit the experimental results, and the difference in the loss fraction may be caused by the selection of the experimental coefficients to be used to fit the experimental results (Section 1.1.3.2 (5)). This difference in the loss fraction is considered to be due to the insufficient individual validation of the loss elements of fluid dynamic loss. However, the experimental results of the elements of fluid dynamic loss, which are necessary for the individual validation of these loss elements, do not seem to be available. Therefore, the issue is to develop a method for experimentally classifying the fluid dynamic loss into loss elements.

1.3.4   Issues in the Numerical Simulation Method for Fluid Dynamic Loss

(1)   Issues of Numerical Stability and Calculation Speed in the Numerical Simulation Method

A numerical simulation method that can solve a two-phase flow of air and oil with a boundary condition including a gear meshing part is required in a real gearbox because oil jets are injected into multiple meshing gears. However, no previous research has conducted such a numerical simulation (Fig. 1.1-24). Therefore, it is an issue to develop a numerical simulation method that overcomes the problems in previous studies. In general, for the simulation of the gas–liquid interface, numerical pressure vibration occurs when the liquid surface collides with a wall surface (e.g., [84]), which leads to numerical instability. In high-speed two-phase flow in a gearbox, this numerical instability may be an essential cause. Furthermore, when applied to a real gearbox, further numerical instability may occur by dispersing the gas–liquid interface throughout the gearbox.

The VOF [53], SPH [54], and lattice Boltzmann [55] methods are used for numerical simulation of the gas–liquid interface. For the calculation mesh system, the method of deformation (morphing) and reconstruction (remeshing) of the mesh as the gear moves [50] [51] [52] and the SPH method [57], which is a calculation method that does not require a calculation mesh, are used. To apply these methods to a real gearbox, it is necessary to use a high-speed calculation method because the size of the calculation mesh increases due to the wide calculation area in the gearbox.

From the above, the numerical simulation method requires numerical stability to calculate the high-speed two-phase flow in the gearbox and calculation speed to solve the wide area in a gearbox.

(2)   Issues in the Evaluation Method of the Numerical Simulation and Issues in the Loss Classification Method using Numerical Simulation

Numerical simulation should be useful not only for prediction of fluid dynamic loss in real gearbox, but also for clarifying phenomena and developing loss models. For example, numerical simulation is thought to be able to clarify the characteristics of the behavior of airflow and oil flow in the gear meshing part and gear peripheral part, and the relation with fluid dynamic loss. By modeling the relation between the characteristics of phenomena and loss, a loss model based on the phenomena can be developed. To achieve this, the construction of a proper evaluation method of the simulation results is an issue for utilizing numerical simulation to understand phenomena and develop loss models.

To validate the loss model developed for each element of fluid dynamic loss, it is also necessary to develop

a classification method of fluid dynamic loss into loss elements using numerical simulation.

1.4 Research Objectives

1.4.1 Research Objectives

Although various efforts have been made to design the power loss of gear systems, we believe that the standardization of designs with low power-loss has the potential to reduce losses. Strength and weight designs are prioritized because there are no standards for general use with high accuracy in low-power-loss designs. To standardize low-power-loss designs, the classification of fluid dynamic losses is important, and in this research we will obtain evidence on the principle of phenomena for classification. The research objective of this research is set to "Clarification and Classification of Fluid dynamic loss Phenomena of Two-Phase Flow of Air and Oil for Standardization of Low-Power-Loss Design of High-Speed Gear Systems."

In addition, to show the effect of standardization of low-power-loss designs, the following aspects are also presented: a proposal of loss model based on the result of understanding of phenomena and classification of fluid dynamic loss, the effect of representative parameters of the gearbox on fluid dynamic loss, and a practical example of low-power-loss design by optimization of parameters.

The key points of understanding the phenomena of fluid dynamic loss and the key points of low-power-loss design are explained in the next section as the concrete problems raised in this research.

1.4.2 Key Points of Understanding the Phenomena of Fluid Dynamic Loss and Key Points of Low-Power-Loss Design (Raised Problems)

To concretize and clarify the research objectives, Fig. 1.4-1 shows the key points of understanding the phenomena of fluid dynamic loss and the key points of low-power-loss design. The loss classification based on the phenomena ("Q1" in Fig. 1.4-1) is the most important point for understanding these phenomena.

To standardize low-power-loss designs, a fluid dynamic loss model based on loss classification is required. The fluid dynamic loss model includes model coefficients, which can be analyzed to clarify the main features of loss ("Q2" in Fig. 1.4-1).

As key points of design improvement to show the effect of standardization of low-power-loss design, optimization of the gear aspect ratio (tooth width / gear diameter (gear diameter $\sim$ pitch circle diameter)) ("Q3" in Fig. 1.4-1) and shroud optimization ("Q4" in Fig. 1.4-1) are selected and their effects are shown. Optimization of the gear aspect ratio is considered to be possible for low-power-loss optimization because the gear tooth surface strength and weight are approximately proportional to tooth width $\times$ gear diameter^2. Optimization of the shroud is considered to be possible because the weight penalty of the shroud is small and therefore, it can be installed relatively easily.

Table 1.4-1 presents the progress of the fluid dynamic loss model and model coefficients developed in this research with respect to the conventional research. In Table 1.4-1 , the gear area is divided into the gear meshing part and gear peripheral part. From conventional studies, in the gear meshing part there is an air pocketing loss (or air trapping loss) as aerodynamic loss and an oil acceleration loss as oil dynamic loss. In the gear peripheral part, there is windage loss including aerodynamic loss and oil dynamic loss. The theory, loss model, and coefficients to be developed in this research are as follows.

- For air pocketing loss (or air trapping loss), only a numerical analysis method has been proposed, so we propose a new theory, loss model, and coefficient in this research.
- A part of the oil acceleration loss can be calculated by theoretical equations [36], and it is known that the other parts can be modeled by the experimental coefficients using the theoretical equations [46]. However, no experimental coefficients including the effects of shrouds were found, so we propose new experimental coefficients in this research.
- On windage loss, an empirical equation has been proposed [31] for the aerodynamic loss excluding oil mist. Nonetheless, as the coefficient of the empirical equation has dimension and is not common, the empirical equation is reformulated by introducing the conventional rotational moment coefficient of a cylinder or disk.
- It has been proven that the oil dynamic loss in windage loss can be modeled using a magnification coefficient for the aerodynamic loss [46]. However, an empirical formula for the coefficient was not found, so we propose a new one in this research.

In the future, a rational design method based on phenomena will be important for special gears with a peripheral speed exceeding 50 m/s for aeroengines. We will improve the outlook through the "key points for understanding phenomena" and "key points for improving designs" mentioned above. The solution to the problem in Fig. 1.4-1 is presented in Section 9.2.

1.5 Positioning from the Viewpoint of Tribology to Fluid Dynamic Loss for the Subject of this Research

In this section, we show that the tribology of the torque transmission surface in the gear tooth and the fluid dynamic loss in this research can be dealt with separately, and that the effect of the pressure applied to the tooth surface for torque transmission on the global flow field is considered to be small.

(1) Difference between Gear Tribology and Fluid Dynamic Loss

The object of the tribology of the gear is the torque transmission surface (contact surface), and the object of the fluid dynamic loss research is the tooth surface and peripheral region, except for the torque transmission surface.

The phenomena researched in the tribology of the gear are friction by the relative motion of the contact surface and oil pumping work by the intake of oil into the contact surface (e.g., [22] [23]), as shown in Fig. 1.5-1 . When the tooth surface comes into contact, the tooth surface deforms, and the pressure due to Hertzian contact is generated with the width of the oil film ("Width of oil film" in Fig. 1.5-1). When there is a relative velocity between the Hertzian contact surfaces (separated by the oil film thickness), power loss due to friction occurs ("Sliding power loss" in Fig. 1.5-1). As the Hertzian contact surfaces are separated by the thickness of the oil film, power loss occurs due to oil drawing ("Rolling power loss" in Fig. 1.5-1) into the Hertzian contact surfaces. Both the power losses are phenomena occurring at the Hertz contact surface.

Gear shafts · Breather · Gears · **Gear aspect ratio (width/diameter)** · Oil jets · Oil acceleration loss · Windage loss (including oil mist) · Shrouds · **Clearances between gear and shroud, shroud opening** · Power loss around gear mesh ("Trapping loss" or "Pocketing loss") (including oil mist) · Inlet of scavenge pump · Housing

Key points for low-power-loss design

Q3. Optimization of gear aspect ratio (width / diameter)

The optimal aspect ratio can be determined by using the equations of tooth surface strength and gear weight, which are approximately proportional to tooth width $\times$ gear diameter^2.

Q4. Optimization of shroud shape

It can be optimized flexibly, because the weight penalty is small.

Key points for understanding the phenomena of fluid dynamic loss

Q1. Phenomenon-based loss classification*

* Most important

Q2. Development of **fluid dynamic loss models** with **model coefficients**

Understanding the **key parameters** in loss

Fig. 1.4-1 Key points for understanding the phenomena of fluid dynamic loss and for low-power-loss design

Table 1.4-1 Key points in developing fluid dynamic loss models and model coefficients

☐ : Need to be developed
☐ : Need to be reformulated

Location	Air	Oil	Previous research		
			Classification	Theory, model	Coefficients
Gear meshing	✓		Air pocketing loss (or Air trapping loss)*	No previous research (Numerical methods only)	No previous research
		✓	Oil acceleration loss	A theoretical equation (Ariura et al. [36])	—
				A theoretical equation × experimental coefficients (Matsumoto et al. [46]**)	Experimental coefficients, 9 types of helical gears, without shrouding (Matsumoto et al. [46]) ⇒ New coefficient considering shroud effect is suggested.
Gear periphery	✓		Windage loss (including oil mist)	An experimental equation for single spur gears (Dawson [31]**)	Experimental coefficients, 22 types of spur gear, 7 types of shrouds (Dawson [31]**)
		✓		An experimental equation for air-only windage loss × an experimental coefficient	No previous research

* Since the effect of oil has not been validated, only air should be included.
** The researches with the largest scope of validation were chosen.

41
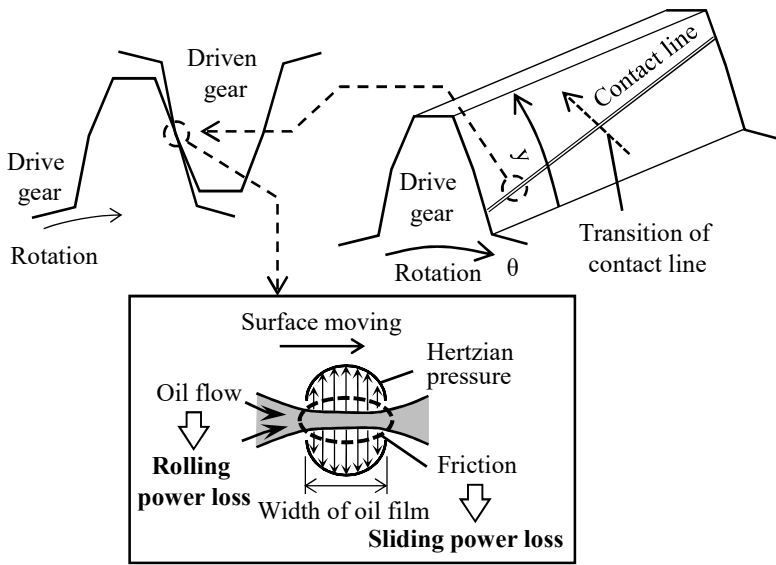
Fig. 1.5-1 Features of tribology on meshing gears (friction and oil flow between contact surfaces)

Fig. 1.5-2 Features of fluid dynamics around a gear mesh (an experimental result for oil jetting from a gear mesh [36])

In the research of fluid dynamic loss, all areas other than the Hertzian contact surface are investigated. For example, the phenomenon of oil flow in gear meshing is shown in Fig. 1.5-2 . In the into-mesh of gear meshing, the volume between the gear and the gear decreases rapidly. As a result, oil jetting occurs from the tip clearance ("Oil jetting from tooth tip clearance" in Fig. 1.5-2). In this case, the sudden change in the flow caused by a sudden change in the gap between the teeth is important.

The differences between the above gear tribology and fluid dynamic loss are summarized in Table 1.5-1 .

Table 1.5-1 Differences in gear tribology and fluid dynamic loss between the gears

Items	Tribology on gears		Fluid dynamics on gears
Target area	Contact surfaces (torque transmission surfaces)		All surfaces except for contact surfaces
Phenomena on power loss	Friction due to relative motion between the contact surfaces	Pumping work due to oil flow between the contact surfaces	Flow dynamics of air and oil
Feature	Phenomena in oil film between contact surfaces		Sudden change in flow around gear meshing area (for example)

(2)　Locality of Sliding Phenomenon at the Gear Contact Surface

An image of the area of Hertzian contact surface on the gear tooth surface is shown in Fig. 1.5-1 as "Contact line." The Hertzian contact surface is called a contact line because its width is minimal. We examine the locality of tribology from the area of the contact line.

Figure 1.5-3 shows a schematic of a connection to gears to explain the torque transmission condition.

(a) Connection at full load   (b) Connection at no load
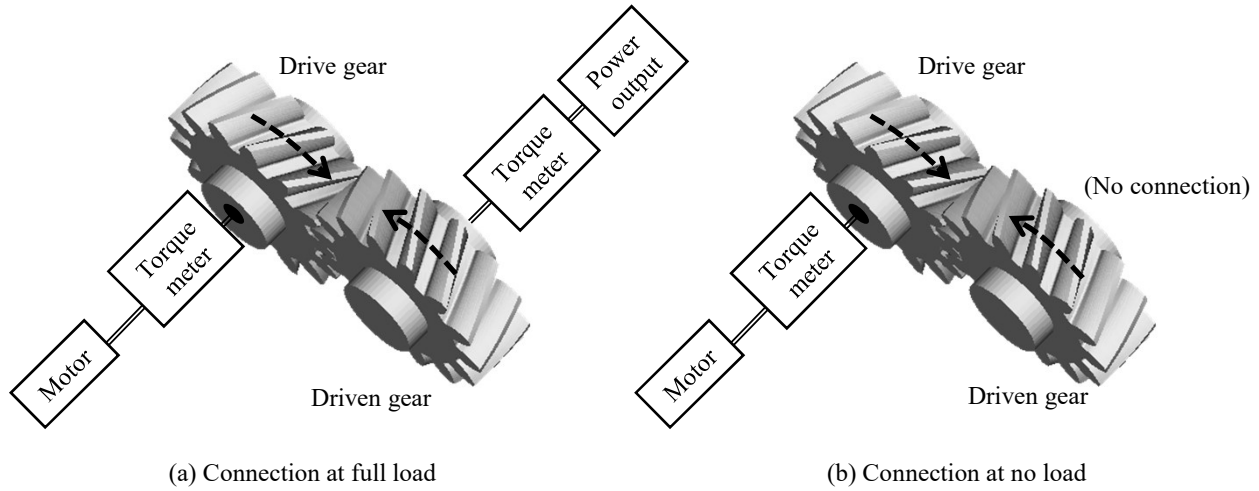
Fig. 1.5-3 Connection patterns for power transmission

Figure 1.5-3 (a) shows a connection configuration for measuring the power transmission characteristics of a gear box for a full load condition. The drive gear is rotated from a motor (power source) via a torque meter. The drive gear rotates the driven gear and transmits power. The driven gear transmits power to the output that consumes power via a torque meter. The power transmission characteristics of the gearbox are measured using the difference between the torque measured by a torque meter connected to the drive gear and the torque measured by a torque meter connected to the driven gear. Figure 1.5-3 (b) shows the connection of no-load condition. The configuration is the same as that of the full load conditions except that nothing is connected to the shaft of the driven gear. The purpose of this configuration is to minimize the friction loss of the gear contact surface in order to measure the loss characteristics other than that at the gear contact surface. The transmission characteristics are measured by a torque meter connected to the drive gear.

The contact conditions are examined for the tooth surfaces of each of the two configurations shown in Fig. 1.5-3 (a) and (b). The calculation conditions are presented in Table 1.5-2 . The conditions of two-axis helical gears are used in this research (see Chapter 3 for details). The results of the calculation under the conditions of Table 1.5-2 are shown in Fig. 1.5-4 . The friction loss calculation program was used for the gear contact surfaces (see Appendix B.1.3 for details), and it was prepared based on the existent research [22].

Figure 1.5-4 (a) shows the pressure distribution under full load conditions. The horizontal axis is the direction of tooth height (coordinate y in Fig. 1.5-1), and the center is enlarged to show the contact position ($y = 0$). The vertical axis shows the pressure on the tooth surface in logarithmic scale. For comparison with the pressure order outside the contact position, the typical pressure (which is the result of numerical simulation, see Chapter 5 for details) under the conditions in Table 1.5-2 is shown. From this figure, it can be observed that a high pressure is generated at the contact position $y = 0$ with a contact width, and the order of the pressure is different from those outside the contact width. The contact width is as small as 0.2 mm. This is because the gear material for an aeroengine is relatively rigid and the deformation of the tooth surface is small. In this case, the fraction of the contact line area to the area of one tooth surface is 3%.

Figure 1.5-4 (b) shows the pressure distribution under the no-load condition. The horizontal and vertical

axes are the same as those in (a) in the figure. The gear pressure and contact width at the contact surface under the no-load condition are smaller than those under the full load condition. This is because the deformation of the material is smaller owing to the reduced surface pressure. In this case, the fraction of the contact line area to the area of one tooth surface is 0.4%.

These results indicate that pressure is generated locally at the gear contact position for torque transmission under the full load and no-load conditions, and that the fraction of the contact area (contact line area) to the tooth area is small. The small fraction is an evidence that the phenomena at the gear contact surface is local.

Table 1.5-2 Calculation conditions to evaluate the locality of a gear contact

(a) Gear specifications

Item	Unit	Input gear	Output gear
Module	mm	5	
Number of teeth	–	33	14
Pitch diameter	mm	191	81
Face width	mm	34	
Helix angle	deg	30	

(b) Operation conditions

Item	Unit	Input gear	Output gear
Rotational speed	rpm	10000	23913
Pitch line speed	m/s	100	
Transmitted power (Full load)	kW	570	
Transmitted power (No load)	kW	13	
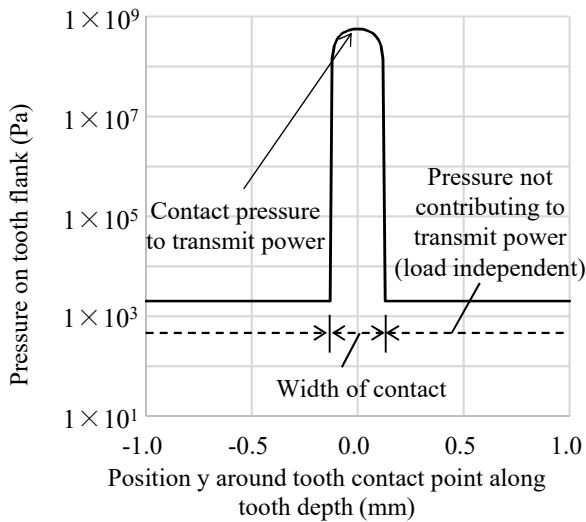
(a) Pressure on gear frank at full load condition
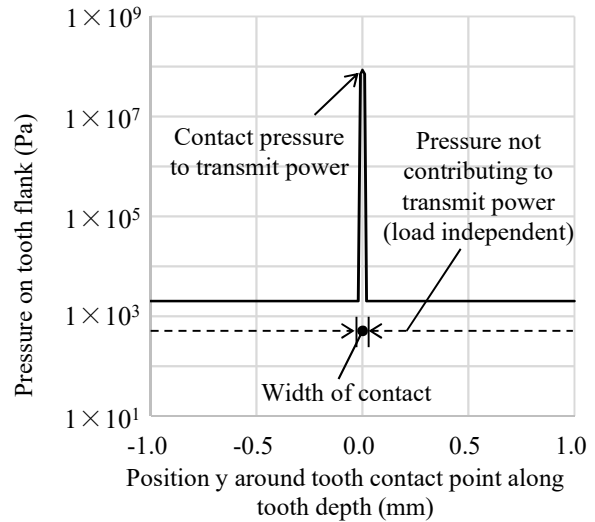
(b) Pressure on gear frank at no load condition

Fig. 1.5-4 Gear pressure around the contact point along the tooth depth (calculations conducted using empirical model)

(3)   Locality of Rolling Phenomenon at the Gear Contact Surface

Given that the rolling loss is the pumping work caused by the oil entrainment into the gear contact surface, the locality of the rolling phenomenon is examined by the fraction of the flow rate generated by the pumping work to the oil supply flow rate. The calculation conditions are the same as those in Table 1.5-2 (the conditions of the two-axis helical gearbox in this research, see Chapter 3 for details). For the calculation of the rolling loss, a calculation program prepared based on the existent research [22] (see Appendix B.1.3

for details) was used. The oil supply flow rate was 7.4 L/min, which is the flow rate in the two-axis helical gearbox referred to in Table 1.5-2 .

The rolling loss (loss due to pumping work) at the gear contact surface under full load conditions was 0.30 kW. Dividing this by the maximum pressure at the contact surface of 5.6×10^8 Pa (peak pressure in Fig. 1.5-4 (a)) gives a pump flow rate of 0.032 L/min, which is 0.4% of the oil supply flow rate of 7.4 L/min to the gear mesh.

The rolling loss (loss due to pumping work) at the gear contact surface under the no-load condition was 0.39 kW. Dividing this by the maximum pressure at the contact surface of 8.5×10^7 Pa (peak pressure in Fig. 1.5-4 (b)) gives a pump flow rate of 0.28 L/min, which is 4% of the oil supply flow rate of 7.4 L/min to the gear mesh.

The small fraction of the pump flow rate to the oil supply flow rate at the gear contact surface is considered to be an evidence that the phenomena at the gear contact surface is local.

(4) Effect of Gear Contact Surface Phenomena on the Global Flow Field

Although there is no research to verify the effect of the phenomenon of the gear contact surface on the global flow field, a conventional research of the gear contact surface (e.g., [22] [23] [85]) has shown that the loss at the gear contact surface is estimated only by the condition at this surface, and that it is consistent with the experimental results.

In addition, from the locality of the phenomena at the gear contact surface shown in (2) and (3) above, it is considered that the effect of the pressure applied to the tooth surface for torque transmission on the global flow field is small.

1.6 Structure of the Thesis

This thesis consists of nine chapters.

In Chapter 1, the background of this research was described. Based on this background, the possibility of improving the gear system efficiency was presented and the issue of clarifying the phenomena of fluid dynamic loss was shown. Then, the issue of clarifying the phenomena was decomposed, and "Clarification and Classification of Fluid Dynamic Loss Phenomena of Two-Phase Flow of Air and Oil for Standardization of Low-Power-Loss Design of High-Speed Gear Systems" was set as the research objective.

The progression from Chapter 2 (Theory of Fluid Dynamic Loss) to Chapter 5 (Clarification and Classification of Fluid Dynamic Loss Phenomena) is summarized in Table 1.6-1 .

In Chapter 2, the theory of fluid dynamic loss is divided into aerodynamic loss and oil dynamic loss, and into the gear meshing part and gear peripheral part, and is arranged as the difference of the proportional exponent of aerodynamic loss or oil dynamic loss to the gear peripheral speed. The theory is used to understand the phenomena of fluid dynamic loss.

Chapter 3 describes the experimental measurement method of fluid dynamic loss and the validation of its applicability to the understanding of fluid dynamic loss phenomena. It also provides the validation data for the numerical simulation method and fluid dynamic loss model. To do this, the test gearbox uses a two-axis helical gearbox and proposes/validates a method to maintain the bearing temperature of the gearbox constant as a

high-accuracy measurement method of power loss. It also proposes/validates an oil fraction and mixture velocity measurement method, a visualization method of oil particles, and an image measurement method of oil particle velocity.

Chapter 4 describes the numerical simulation method of fluid dynamic loss and the validation of its applicability to the understanding of fluid dynamic loss phenomena. It shows that the VOF method is used for the calculation of the gas–liquid interface, the rectangular mesh is used for the calculation mesh, and the porosity method (where the boundary condition of the gear is modeled with the immersed boundary method) is used for modeling the gear shape. In addition, it shows the special modeling method for a gearbox. As the validation of the applicability of the numerical simulation method to the understanding of fluid dynamic loss phenomena, it shows that the simulation results of fluid dynamic loss qualitatively agree with the experimental results. In addition, the airflow and the oil flow are validated individually. The validation of the airflow simulation is carried out through the validation of the airflow in the gear meshing part, the validation of the airflow in the gear peripheral part, and the validation of the effect of the shroud on the airflow. The validation of the oil flow simulation is carried out through the validation of the oil flow in the gear meshing part, in the gear peripheral part, and between the gear and the shroud.

In Chapter 5, the aerodynamic and oil dynamic losses are clarified by considering the results of the numerical simulation. From the results, fluid dynamic losses are classified. Fig. 1.6-1 shows an outline of the method of understanding the phenomena. To understand the fluid dynamic losses, it is necessary to understand the phenomena that constitute them. The fluid dynamic loss occurs through a flow field and a pressure field around the gear due to the rotation of the gear. Pressure and shear force are generated on the gear surface, and torque is generated on the gear. The torque causes the fluid dynamic loss. The gear shroud is thought to affect them. Further, validation of the theory of fluid dynamic losses also leads to clarification of the phenomena. The validation of the theory of fluid dynamic losses is carried out through the evaluation of the characteristics of changes in losses with respect to rotational speed, and the evaluation of non-dimensional parameters.

The progression from Chapter 6 (fluid dynamic loss model) to Chapter 8 (contribution to standardization of low-power-loss design) is summarized in Table 1.6-2 .

In Chapter 6, we propose a fluid dynamic loss model, which is necessary for the standardization of low power-loss, and a method to classify the fluid dynamic losses experimentally and analytically for the validation of the loss model. The fluid dynamic loss model is validated using the experimental results and the experimentally validated simulation results. From the coefficients included in the loss model, we extract the main parameters of the loss elements of fluid dynamic loss.

Chapter 7 examines the effects of gearbox design parameters, such as gear diameter, tooth width, gear aspect ratio, and shroud effects, on fluid dynamic losses in order to demonstrate the effectiveness of the standardization of low-power-loss design. In addition, the effect of optimizing the gear aspect ratio and optimizing the shroud shows that the improvement in efficiency of the gearbox described in Chapter 1 is realistic.

Chapter 8 describes the proposal of standardization of low-power-loss design and the contribution of this research to the standardization, based on the gear strength design standard.

Finally, Chapter 9 summarizes the achievements of this research and describes its scope and future progression.

Table 1.6-1 Structure of the thesis up to the understanding of fluid dynamic loss phenomena

Gearbox No.	Development of theory (Chapter 2 (Theory), Chapter 5 (Validation))	Development of experimental measurement method (Chapter 3)	Development of numerical simulation method (Chapter 4)	Understanding of phenomenon, loss classification (Chapter 5)	Gearboxes	Target phenomena – Fluid dynamic loss	Target phenomena – Air flow	Target phenomena – Oil flow	Target areas – Gear meshing part	Target areas – Gear peripheral part	Target areas – Gear shroud	Methods – Experiments	Methods – Numerical simulation
GA	Theory of fluid dynamic loss, loss characteristics for rotational speed				Two-axis helical gearbox for understanding fluid dynamic loss and validating numerical analysis	✓			✓	✓	✓		✓
GA		Validation of highly accurate measurement method of fluid dynamic loss	Validation of fluid dynamic loss	Understanding of fluid dynamic loss, loss classification		✓			✓	✓	✓	✓	✓
GX1			Validation of air pressure in gear mesh		Two-axis helical gears for validating air pressure in gear mesh		✓		✓			By Diab et al.	✓
GX2			Validation of aerodynamic loss with a single gear		One-axis spur gear for validating aerodynamic loss with a single gear		✓			✓	✓	By Dowson	✓
GB1			Validation of oil jet flow into gear mesh		Two-axis spur gearbox for validating oil jet flow into gear mesh			✓	✓			✓	✓
GB2-1		Validation of visualization method for oil particles			One-axis spur gearbox for validating flow visualization of oil jet into gear tooth surface			✓		✓		✓	✓
GB2-2			Validation of oil spray flow on gear tooth surface		One-axis spur gearbox for validating oil spray flow on gear tooth surface			✓		✓		✓	✓
GB3		Validation of the image measurement method for the velocity of oil particles	Validation of oil flow between gear tips and shroud wall		One-axis spur gearbox for validating the image measurement method for the velocity of oil particles and oil flow between gear tips and shroud wall			✓		✓	✓	✓	✓
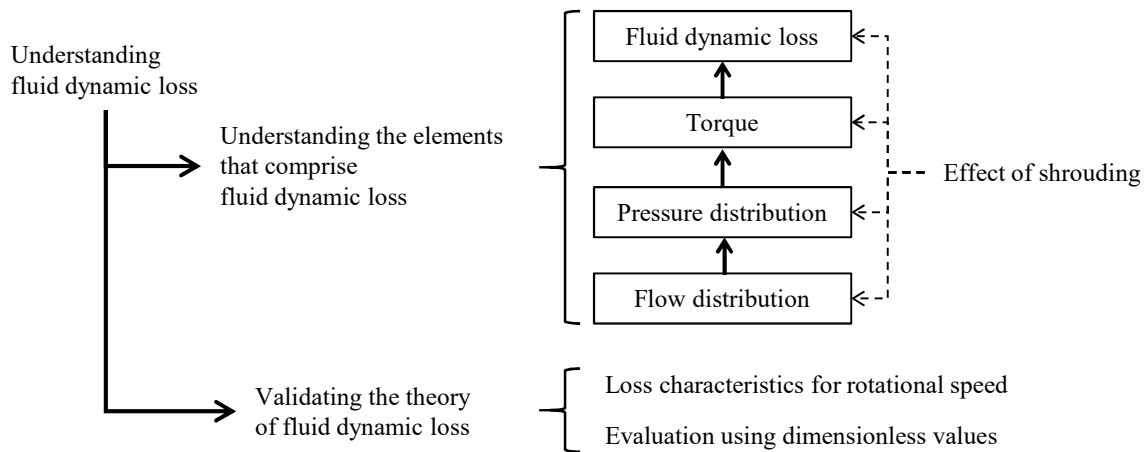
Fig. 1.6-1 Outline for the understanding of fluid dynamic loss

Table 1.6-2 Structure of the thesis for the standardization of low-power-loss design

Section	Fluid dynamic loss model	Experimental measurement method	Numerical simulation method	
Chapter 6	Suggestion of fluid dynamic loss model	Experimentally implementing method for the classification of fluid dynamic loss	Analytically implementing method for the classification of fluid dynamic loss	
	Validation of fluid dynamic loss model			Appendix B
Chapter 7	Influence and optimization of gearbox design parameters			Calculation method for the power loss on gear contact surfaces
Chapter 8	Contribution to the standardization of low-power-loss design for high-speed gear systems			

Chapter 2

Theory of Fluid Dynamic Loss

This chapter describes the theory of fluid dynamic loss, which is necessary for the consideration of fluid dynamic loss and development of loss models. First, the flow behaviors of the air and oil around the gear are estimated for theoretical study. Thereafter, the theories of aerodynamic loss and oil dynamic loss are studied. The results reveal that the gear meshing and gear peripheral parts have different characteristics, and that the flow rate of the fluid accelerated by the gear and fluid dynamic loss are characterized by the exponent of the gear rotational speed (peripheral speed) to which the loss is proportional. The estimated flow pattern and validity of the constructed theory are confirmed in Chapter 5.

2.1 Estimation of Air and Oil Behaviors around Gears, and Categorization of Region around Gears

To construct a theory of fluid dynamic loss, the flow behavior of air and oil around the meshing gears is estimated. The flow assumption around the gear pair is illustrated in Fig. 2.1-1 . Figure 2.1-1 (a) (upper left) shows the flow estimation at the gear meshing part, whereas Fig. 2.1-1 (b) (upper right) shows the flow estimation at the gear peripheral part (the peripheral part of the gear excluding the gear meshing part).

(1) Continuous and Dispersed Phases

In the case of a high-speed gear, the airflow rate around the gear is high because the airflow speed is high. In comparison to the high airflow rate, the oil supply flow rate is insignificant, and it is presumed that the oil droplets are dispersed in the airflow. Therefore, air becomes a continuous phase, and oil becomes a dispersed phase. In general, when the particle size of the dispersed phase is small, the particle flow speed of the dispersed phase is homogeneous (equal to the continuous phase speed); however, when the particle size of the dispersed phase is large, the particle flow speed of the dispersed phase is inhomogeneous [86]. In addition, there are cases in which only the motion of the dispersed phase (oil droplets) is considered, and the effect of the continuous phase of air is ignored [87]. To estimate the flow behavior of air and oil around the gear, in addition to understanding these phenomena, it is necessary to understand the effects of boundary conditions, such as gear meshing.

(2) Estimation of Airflow Behavior

An estimation of the airflow at the gear meshing part is shown in Figs. 2.1-1 (a) and (a-1). The gear is considered to be a cylinder with a large surface roughness, and a simple model is constructed as a cylinder

(a) Flow around gear meshing part

(b) Flow around gear peripheral part

(a-1) Anticipated airflow pattern around gear meshing part

(b-1) Airflow pattern around gear peripheral part

(a-2) Anticipated oil-particle behavior into gear meshing part

(b-2) Anticipated oil-particle behavior around gear peripheral part
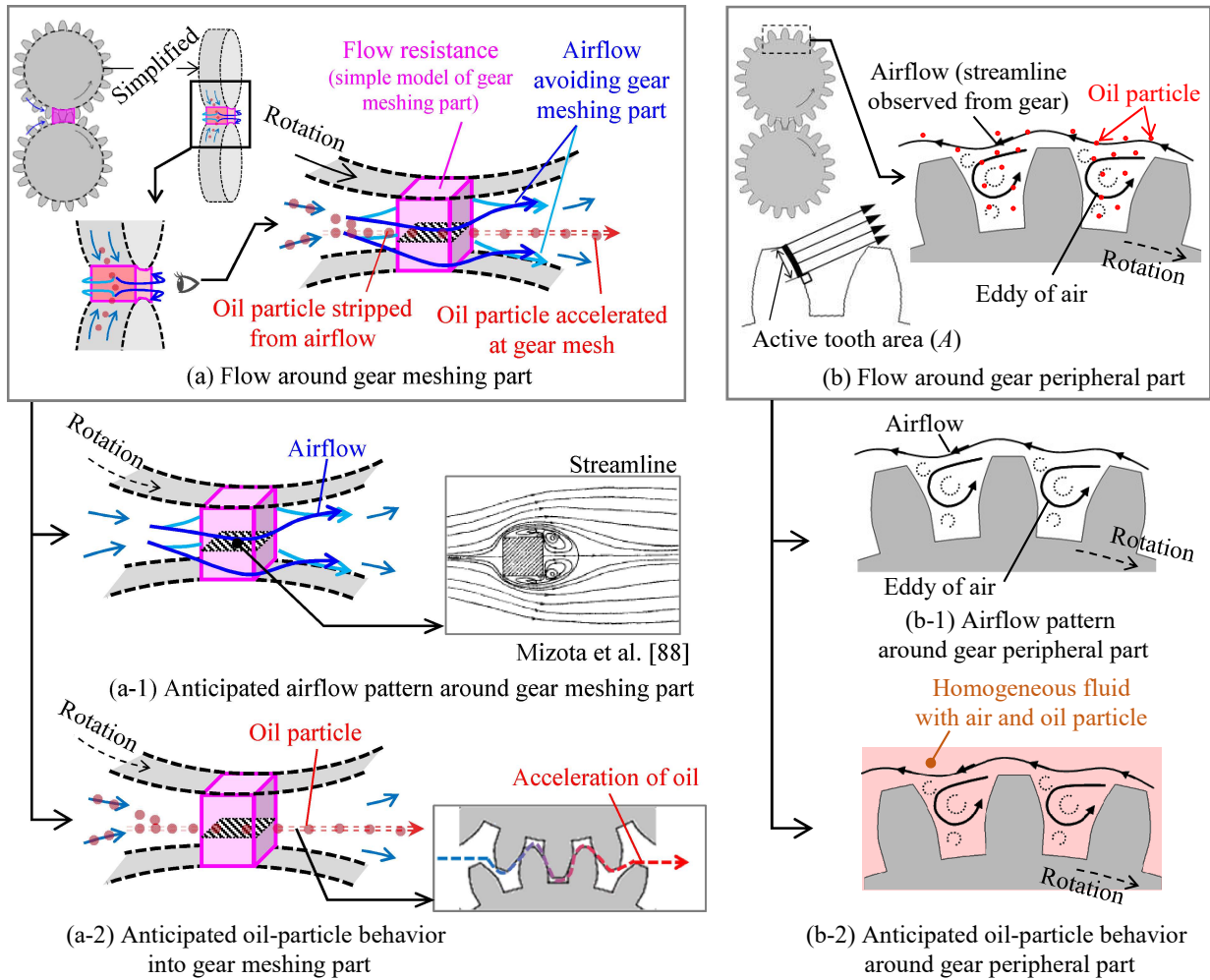
Fig. 2.1-1 Anticipated flow around a gear pair

whose diameter is that of the tooth bottom circle. The gear meshing part becomes flow resistant because the space between the teeth is small, and the gear meshing part is modeled as a flow-resistant element ("Flow resistance" in Fig. 2.1-1 (a)). The airflow from the gear periphery is considered to avoid the gear meshing part and flow in the gear axial direction ("Airflow avoiding gear meshing part" in Fig. 2.1-1 (a)) from the analogy with the flow through the rectangular column [88]. The flow pattern with the airflow is shown in Fig. 2.1-1 (a-1).

The airflow around the gear periphery is estimated as shown in Figs. 2.1-1 (b) and (b-1). Because the fraction of oil particles in the space is small (the oil supply flow rate is less than the airflow rate around the gears), the effect of the oil particles on the airflow is considered insignificant. Therefore, airflow and oil flow can be considered separately. As Hill et al. [89] reported, the flow pattern of air in the gear periphery results from the air vortices generated in the cavity between the teeth ("Eddy of air" in Fig. 2.1-1 (b-1)).

(3)   Estimation of Oil Flow Behavior

An estimation of oil flow in the gear meshing part is shown in Figs. 2.1-1 (a) and (a-2). Oil particles carried by the airflow taken from the gear periphery cannot follow the sudden change in the direction of the airflow. As they avoid the gear meshing part, they may be separated from the air flow ("Oil particle stripped from airflow" in Fig. 2.1-1 (a)). Subsequently, the oil particles that enter between the gear teeth are accelerated to the gear peripheral speed in the gear meshing part and scatter to the out-of-mesh side of the gear ("Oil particle accelerated at gear mesh" in Fig. 2.1-1 (a)). The acceleration of the oil particles in the gear meshing part is extracted, as shown in Fig. 2.1-1 (a-2). Therefore, it is necessary to consider the motion of the oil particles separately from the airflow.

An estimation of oil flow around the gear periphery is shown in Figs. 2.1-1 (b) and (b-2). It is assumed that the oil particles around the gear periphery move in accordance with the airflow. As a model of this oil behavior, we assume a homogeneous flow in which air and oil particles are uniformly mixed, as shown in Fig. 2.1-1 (b-2). In this case, the oil particles apparently increase the fluid density.

(4)   Categorization of the Region around Gears by Locations of Fluid Dynamic Loss and Types of Fluid

As shown in Fig. 2.1-1 , the flow pattern is different at the gear meshing and gear peripheral parts. Therefore, we categorize the region around the gears into gear meshing and gear peripheral parts. In addition, it was shown that air and oil should be considered separately because of the differences in their behaviors. Therefore, the fluid dynamic loss is categorized as "aerodynamic loss in the gear meshing part," "aerodynamic loss in the gear peripheral part," "oil dynamic loss in the gear meshing part," and "oil dynamic loss in the gear peripheral part." The theories explaining these categories are described below.

2.2   Theory of Aerodynamic Loss (Common in the Gear Meshing Part and Gear Peripheral Part)

As described in the previous section, the oil droplets are dispersed in the air in the case of a high-speed gear because the oil supply flow rate is less than the airflow rate around the gear. Therefore, the effect of the oil droplets on the air flow is ignored, and only the fluid dynamic loss of air, as shown in Figs. 2.1-1 (a-1) and (b-1), is considered. Air molecules are continuously distributed in space; therefore, it is possible to treat them as a continuum regardless of their flow pattern. The equation of motion is expressed as follows [90] [91]:

$$\rho_{air}\frac{Dv_i}{Dt} = \mathcal{K}_{air,i} + \frac{\partial t_{air,ij}}{\partial x_j} \tag{2.1}$$

where ρ_{air} denotes the air density, D is the material derivative (in Lagrangian notation), v is the flow velocity, t is the time, $\mathcal{K}_{air,i}$ is the force per unit volume of air, $t_{air,ij}$ is the stress tensor of air flow, and x is the spatial coordinate. If the density change of air is 5% or less, air can be considered an incompressible fluid; if it is more than 5%, the compressibility of air must be considered. The Mach number (velocity / speed of sound) corresponding to a density change of 5% was approximately 0.3. For the condition of air in the gearbox, if the temperature is 80°C and the air pressure is 1 atm, the speed of sound is 380 m/s, and the Mach number 0.3 is equivalent to 114 m/s. As the peripheral speed of an aeroengine gear is less than this speed, the air in the gearbox is considered an incompressible fluid. In addition, considering the viscosity of air, the following equation of motion (momentum conservation equation for an incompressible viscous fluid) is derived from Eq. 2.1 [90] [91]:

$$\frac{\partial v_i}{\partial t} + v_j \frac{\partial v_i}{\partial x_j} = -\frac{1}{\rho_{air}} \frac{\partial p}{\partial x_i} + \nu \frac{\partial^2 v_i}{\partial x_j \partial x_j} + \mathcal{K}_i \tag{2.2}$$

where p denotes pressure and ν represents kinematic viscosity. Thereafter, the force F_{air} that the gear receives when it accelerates the air around it (volume ΔV) in the gear peripheral direction l is considered. When the term of the pressure gradient at acceleration $-\frac{1}{\rho_{air}} \frac{\partial p}{\partial x_i}$ and that of the effect of viscosity $\nu \frac{\partial^2 v_i}{\partial x_j \partial x_j}$ are ignored at a steady flow $\frac{\partial v}{\partial t} = 0$, and the volume force $\mathcal{K}_l$ is exerted on the air by the gear, the velocity difference between before and after acceleration Δv_l and the volume $\Delta V = A\Delta x_l$ of air subjected to acceleration (A denotes the area contributing to the acceleration, as shown in Fig. 2.1-1 (b), and Δx_l denotes the acceleration distance) are considered in Eq. 2.2, the force F_{air} is expressed as follows:

$$F_{air} = \mathcal{K}_l \Delta V = \rho_{air} \left(\frac{\partial v_l}{\partial t} + v_l \frac{\partial v_l}{\partial x_l} \right) \Delta V = \rho_{air} \left\{ \frac{1}{2} \frac{(\Delta v_l)^2}{\Delta x_l} \right\} (A\Delta x_l) = \frac{1}{2} \rho_{air} A (\Delta v_l)^2 \tag{2.3}$$

where the relation $v_l \frac{\partial v_l}{\partial x_l} = \frac{1}{2} \frac{(\Delta v_l)^2}{\Delta x_l}$ is used. The aerodynamic loss P_{air} due to the force F_{air} applied to the gear is derived from the following equation:

$$P_{air} = T_{air}\omega = F_{air} r_p \omega = F_{air} v_p = \left\{ \frac{1}{2} \rho_{air} A (\Delta v_l)^2 \right\} v_p$$

$$\simeq \left\{ \frac{1}{2} \rho_{air} A v_p^2 \right\} v_p = \frac{1}{2} \left(\rho_{air} A v_p \right) v_p^2 = \frac{1}{2} \dot{m}_{air} v_p^2 \tag{2.4}$$

where T_{air} denotes the torque, ω is the rotational angular velocity of the gear, r_p is the rotational radius (pitch circle radius), v_p is the pitch circle velocity, $\Delta v_l \simeq v_p$ (assuming that the velocity accelerates from zero to v_p), and $\dot{m}_{air} = \rho_{air} A v_p$ is the mass flow rate at which the gear accelerates.

Assuming that the mass flow rate $\dot{m}$ at which the gear accelerates is proportional to the peripheral speed (rotational speed), the aerodynamic loss P_{air} is proportional to the third power of the rotational speed. If the airflow is affected by the compressibility of the air, the mass flow rate $\dot{m}$ at which the gear accelerates with an increase in the rotational speed increases more than the rotational speed proportionality, and the rotational speed exponent to which the aerodynamic loss is proportional is considered to exceed three. In contrast, in an experimental example of the fluid dynamic loss of a real gear, the rotational speed exponent does not exceed three, even at a peripheral speed of 200 m/s (Mach 0.5) [46][*1]. Therefore, the effect of air compressibility is considered to be negligible. In this example, the rotational speed exponent is three; therefore, the mass flow rate at which the gear accelerates is estimated to be proportional to the rotational speed.

2.3 Theory of Oil Dynamic Loss

The behavior of oil particles can be distinguished as described in Section 2.1, when oil particles are accelerated at the gear meshing part (Fig. 2.1-1 (a-2)), and when a flow containing oil particles at the gear periphery is regarded as a homogeneous fluid (Fig. 2.1-1 (b-2)). For each case, a theory is presented in this section.

[*1] In this example, oil dynamic loss is also included. Because the oil dynamic loss is proportional to the second to third power of the rotational speed, as described in Section 2.3, the rotational speed exponent to which the fluid dynamic loss of the two-phase flow of air and oil is proportional, including the oil dynamic loss, is not expected to exceed three if the effect of air compressibility is insignificant.

2.3.1 Theory of Loss due to Acceleration of Oil Particles in the Gear Meshing Part

Power loss occurs when oil particles entering the gear meshing are accelerated to the gear peripheral speed by the meshing. In this case, the oil particles are accelerated as mass particles, and the power loss $P_{oil,par}$ (subscript par represents the particles) is expressed by the following equation [36] [87] :

$$P_{oil,par} = T_{oil,par}\omega = F_{oil,par}r_p\omega = F_{oil,par}v_p \tag{2.5}$$

where $T_{oil,par}$ denotes the torque and $F_{oil,par}$ denotes the force.

The force $F_{oil,par}$ exerted on the oil particle is the sum of the forces acting on all oil particles accelerated by the gear meshing. This is illustrated in Fig. 2.3-1 . Figure 2.3-1 shows that the force loaded by the acceleration $\frac{Dv_l}{Dt}$ on the oil mass particles $m_{oil,i}$ (where i denotes the number of particles) dispersed in the volume ΔV at density ρ_{oil} (shown on the left side of the figure) is equal to the force causing the mass flow rate of oil $\dot{m}_{oil}$ through the cross-section to change Δv_l (shown on the right side of the figure).

Assuming that the velocity change is $\Delta v_l \simeq v_p$ and the oil supply flow rate is Q_s (constant), the following equations are provided for force $F_{oil,par}$ loaded on the oil particles and power loss $P_{oil,par}$ due to oil acceleration:

$$P_{oil,par} = F_{oil,par}v_p = \left(\sum_{i\in\Delta V} m_{oil,i}\frac{Dv_l}{Dt}\right)v_p = (\dot{m}_{oil}\Delta v_l)\,v_p = (\rho_{oil}Q_s\Delta v_l)\,v_p \simeq \rho_{oil}Q_s v_p^2 \tag{2.6}$$

Equation 2.6 shows that the oil dynamic loss is proportional to the square of the peripheral speed (rotational speed) when the oil is forcibly accelerated in the gear meshing part with a constant oil flow rate (oil supply flow rate).
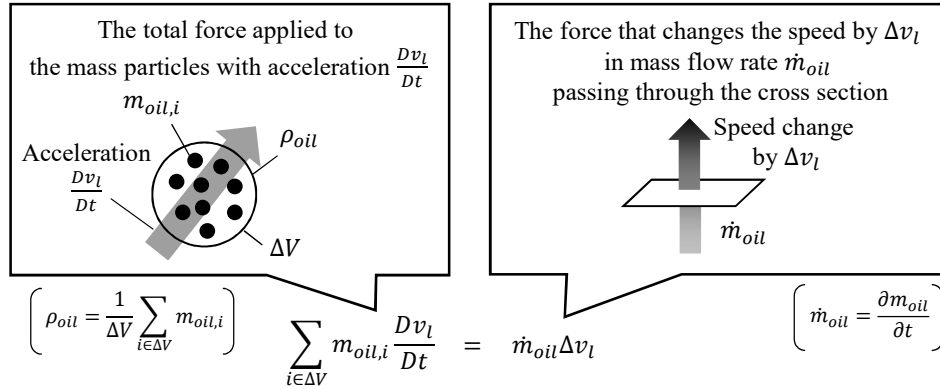
Fig. 2.3-1 Schematic of the force needed to accelerate the group of oil particles

2.3.2 Theory of Loss due to the Flow of Oil Particles in the Gear Peripheral Part

The loss due to the flow of oil in the case where a flow containing oil particles is regarded as a homogeneous fluid in the gear peripheral part [92] was considered. The oil dynamic loss $P_{oil,hom}$ in homogeneous flow of air and oil was obtained by replacing the air density ρ_{air} with spatially-averaged oil density $\alpha_{oil}\rho_{oil}$ (α_{oil} is the oil fraction) in Eq. 2.4. The resulting equation is

$$P_{oil,hom} \simeq \frac{1}{2}\left(\alpha_{oil}\rho_{oil}Av_p\right)v_p{}^2 = \frac{1}{2}\dot{m}_{oil}v_p{}^2 \tag{2.7}$$

Assuming that the mass flow rate of the oil $\dot{m}_{oil}$ accelerated by the gear is proportional to the peripheral speed (rotational speed) and air, the power loss due to the flow of oil particles is proportional to the third power of the rotational speed.

2.4 Difference in the Characteristics of Rotational Speed Changes on Fluid Dynamic Loss

To validate the theory developed in this chapter, a summary of the rotational speed exponent to which the flow rate caused by gear rotation is proportional and the rotational speed exponent to which the fluid dynamic loss is proportional is presented in Table 2.4-1 .

In the theory of aerodynamic loss, the airflow rate around the gear is proportional to the rotational speed, and aerodynamic loss is proportional to the third power of the rotational speed. The difference between the rotational speed exponent to which the airflow rate around the gear is proportional and the rotational speed exponent to which the aerodynamic loss is proportional was two.

In the theory of oil dynamic loss, two cases exist: 1) the oil flow rate around the gear is constant, and the oil dynamic loss is proportional to the square of the rotational speed, and 2) the oil flow rate around the gear is proportional to the rotational speed, and the oil dynamic loss is proportional to the third power of the rotational speed. The difference between the rotational speed exponent to which the oil flow rate around the gear is proportional and the rotational speed exponent to which the oil dynamic loss is proportional was two in both cases. In the oil dynamic loss in the entire gear (including the gear meshing and gear peripheral parts) summed by the above two cases, the oil flow rate is proportional to the power of 0–1 of the rotational speed and the oil dynamic loss is proportional to the power of 2–3 of the rotational speed.

The theory of fluid dynamic loss is validated by the agreement between the aforementioned rotational speed exponent in the theory and that in the experimental results.

Table 2.4-1 Summary of the fluid dynamic loss characteristics with respect to speed changes

Classification		Exponent of speed for the airflow rate around gear	Exponent of speed for the oil flow rate around gear	Exponent of speed for the power loss	Difference of exponents
Aerodynamic loss		1	–	3	2
Oil dynamic loss	Total	–	0–1	2–3	2
	Gear meshing part	–	0 (Constant flow rate)	2	
	Gear peripheral part	–	1	3	

2.5   Summary of Chapter 2

The fluid dynamic loss theory described in this section is summarized in Table 2.5-1 . Owing to the difference in flow patterns, we divided the area into the gear meshing part and the gear peripheral part, and also considered the air and oil separately because of their differences in behavior. Therefore, the fluid dynamic loss is categorized as "aerodynamic loss in the gear meshing part," "aerodynamic loss in the gear peripheral part," "oil dynamic loss in the gear meshing part," and "oil dynamic loss in the gear peripheral part," and developed the theory. The results are as follows.

1. In "aerodynamic loss in the gear meshing part" and "aerodynamic loss in the gear peripheral part," based on the theory of conservation of momentum of a continuum, the flow rate at which the gear accelerates the air in the peripheral direction is proportional to the rotational speed, and the aerodynamic loss is proportional to the cube of the rotational speed.
2. In "oil dynamic loss in the gear meshing part," as the flow rate at which the gear accelerates the oil is equal to the supplied oil flow rate (constant) and based on the theory of conservation of momentum of mass particles, the oil dynamic loss is proportional to the square of the rotational speed.
3. In "oil dynamic loss in the gear peripheral part," according to the continuum momentum conservation theory (assuming that the oil particles in the air flow behave like a continuum), the flow rate at which the gear accelerates the oil in the peripheral direction is proportional to the rotation speed, and the oil dynamic loss is proportional to the cube of the rotation speed.

Table 2.5-1 Summary of the theories on fluid dynamic loss

Classification		Working fluid or particle	Mass flow rate around gear	Exponent of speed for the flow rate around gear	Fluid dynamic loss	Exponent of speed for the power loss
Aero- dynamic loss	Gear meshing part	Air	$\rho_{air} A v_p$	1	$\frac{1}{2}\rho_{air} A v_p{}^3$	3
	Gear peripheral part					
Oil dynamic loss	Gear meshing part	Oil particle	$\rho_{oil} Q_s$	0 (Constant flow rate)	$\rho_{oil} Q_s v_p{}^2$	2
	Gear peripheral part	Oil particles uniformly distributed in the air	$\alpha_{oil}\rho_{oil} A v_p$	1	$\frac{1}{2}\alpha_{oil}\rho_{oil} A v_p{}^3$	3

Chapter 3

Experimental Measurement Method of Fluid Dynamic Loss

In this chapter, experimental measurement methods for clarifying the phenomena of fluid dynamic loss are described. First, a two-axis helical gearbox to validate fluid dynamic loss and various gearboxes to validate experimental measurement and numerical simulation methods are described. Next, a high-accuracy method for measuring fluid dynamic loss, a method for measuring oil fraction and mixture velocity, and a method for visualizing oil particles and measuring their speed are presented. Finally, the results of the validation of the applicability of the experimental measurement methods for fluid dynamic loss phenomena are presented.

3.1 Test Gearboxes and Measurement Conditions

3.1.1 Two-axis Helical Gearbox (GA) to Clarify Fluid Dynamic Loss Phenomena and Validate Numerical Simulations

The system diagram of the experimental apparatus is shown in Fig. 3.1-1 . The input shaft of the gearbox was driven by a motor, and the rotational speed and torque were measured using a torque meter. A no-load condition (no connection to the output shaft) was applied to sufficiently reduce the friction loss of the gear mesh. The gearbox was connected to an oil supply unit to lubricate the gear meshing, bearings, and seals. The oil supply unit supplied oil at a constant pressure and temperature. A vacuum pump was connected to reduce the internal pressure of the gearbox.

The test gearboxes are shown in Fig. 3.1-2 , and their specifications are listed in Table 3.1-1 . These specifications are generally used for aeroengine gears. Each gear shaft was supported by ball bearings and sealed with carbon mechanical seals. Oil was supplied to the bearings and seals from oil jet nozzles installed in the spacer. The supplied oil was discharged from the lower opening of the spacer into the gearbox to avoid affecting the fluid dynamic loss of the gears. The oil supply temperature, temperature of the discharged oil from the gearbox, temperature of the bearings and seals, and temperature of the gearbox housing were measured.

Two types of gear shrouds with oil jet nozzles are shown in Fig. 3.1-3 . As shown in Fig. 3.1-3 (a), Shroud 1 had six openings at the gear peripheral surface and clearance between the shroud and shaft. There are two oil jet nozzles, one toward the into-mesh side and the other toward the out-of-mesh side of the gear mesh. Shroud 2 shown in Fig. 3.1-3 (b) was the same as Shroud 1, except that the gear peripheral surface had two openings. Sections and representative dimensions are shown in Fig. 3.1-4 . The measurement conditions are shown in Table

3.1-2 . Experiments were conducted by changing the oil-supply flow rate, gear rotational speed, and internal pressure of the gearbox.
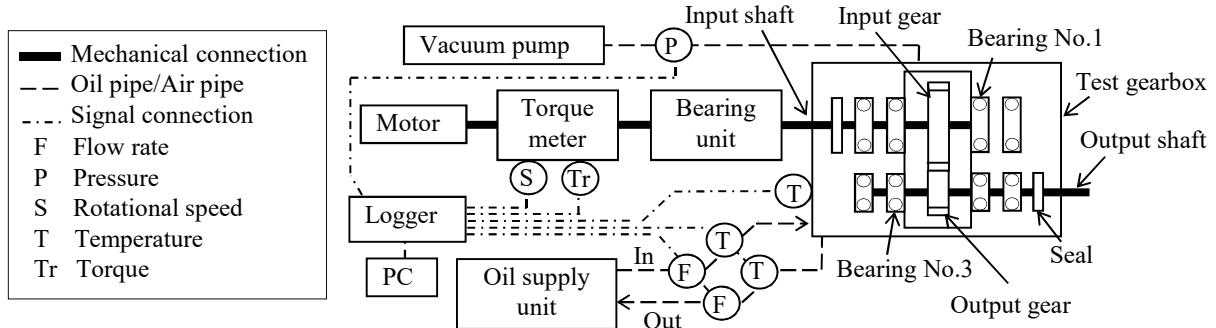
Fig. 3.1-1 Connections in a two-axis helical gearbox (GA)

Fig. 3.1-2 Two-axis helical gearbox (GA)

Table 3.1-1 Specifications of the two-axis helical gearbox (GA)
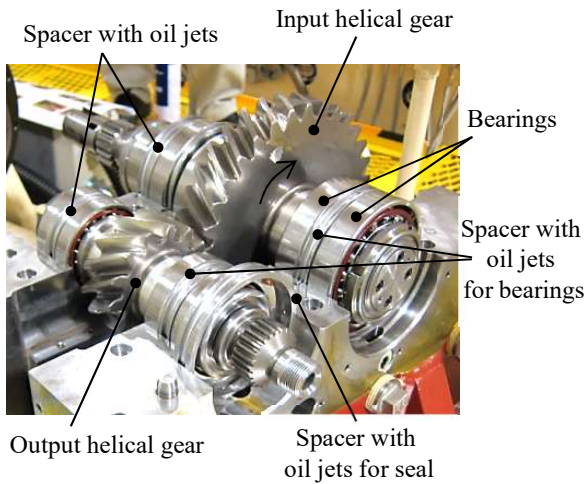
Items	Input gear	Output gear
Type	Single helical	
Number of teeth	33	14
Module (normal)	5 mm	
Pitch diameter	190 mm	80 mm
Face width	34 mm	
Pressure angle (normal)	20°	
Helix angle, direction	30°, right hand	30°, left hand
Tooth surface roughness	~0.2 μm (Ra), ~1.0 μm (Ry)	
Side surface roughness	~1.0 μm (Ra), ~10 μm (Ry)	
Root fillet radius	1.0 mm	
Shaft diameter	ϕ70 mm	ϕ51 mm
Material	SCM420	
Shore hardness	79–87 HS	
Backlash (axial)	0.14–0.31	
Tooth contact ratio	2.54	
Rotational direction	Upward at gear mesh	
Maximum speed	10000 rpm	23000 rpm
Peripheral speed	100 m/s at 10000rpm of input gear	
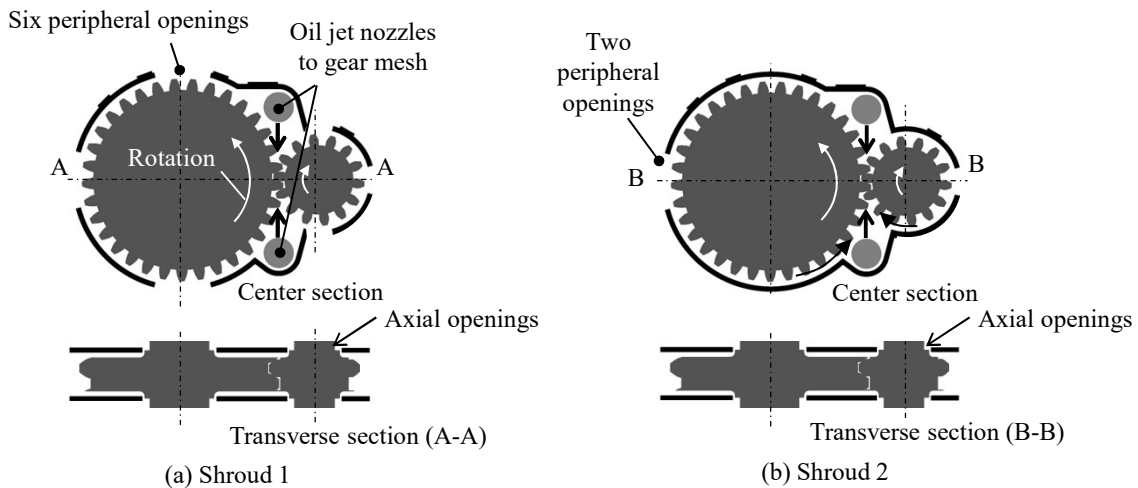
(a) Shroud 1

(b) Shroud 2

Fig. 3.1-3 Shape of shrouds for the two-axis helical gearbox (GA)

(a) Vertical cross-section view
at center of gear width (view A-A)

(c) Vertical cross-section view
of input gear (view C-C)

(b) Horizontal cross-section view (view B-B)

(d) Vertical cross-section view
of output gear (view D-D)
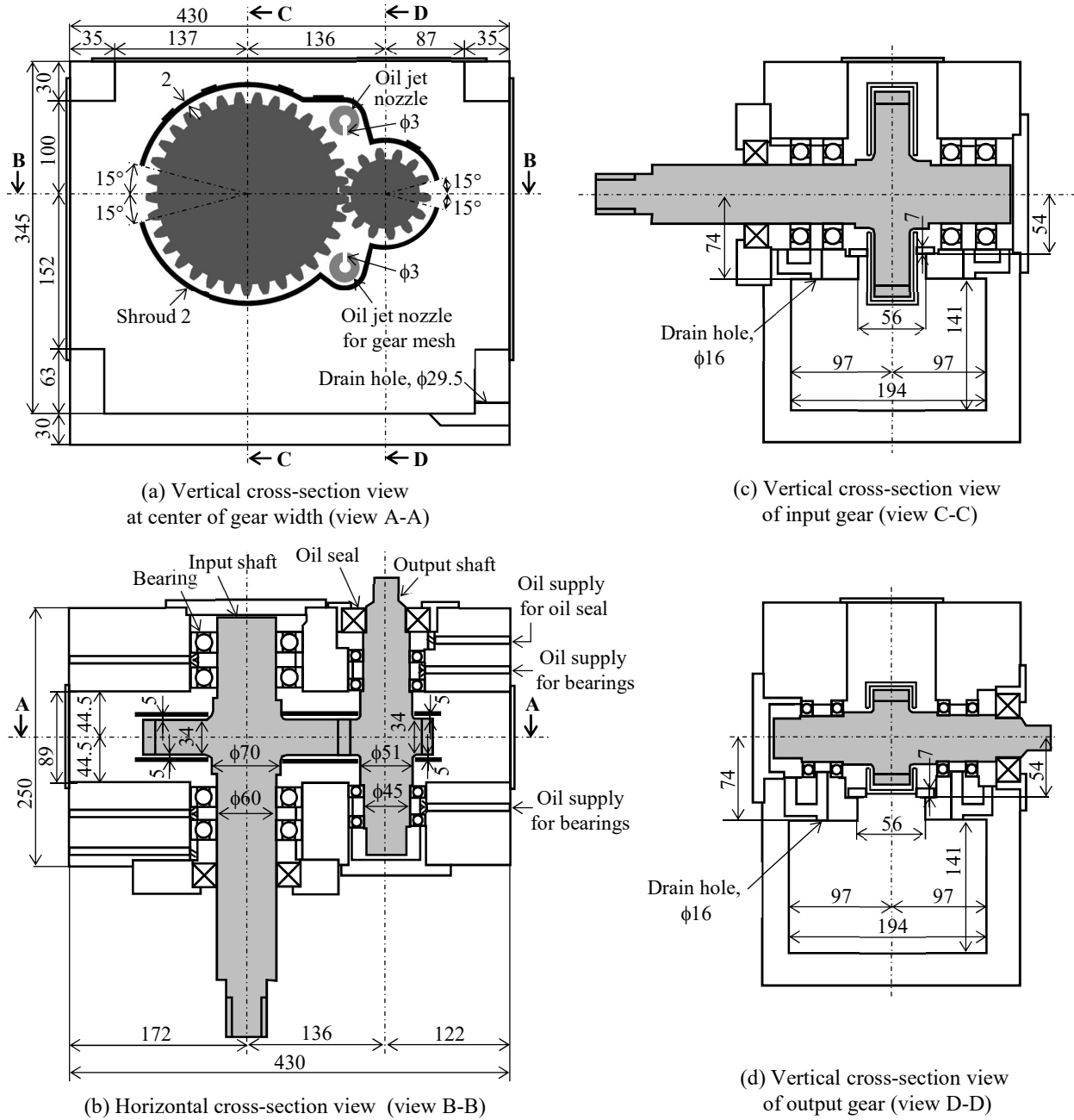
Fig. 3.1-4 Sections and representative dimensions of the two-axis helical gearbox (GA)

Table 3.1-2 Test conditions for the two-axis helical gearbox (GA)

Items	Conditions
Load condition	No load
Oil type, temperature	MIL-PRF-23699, 40°C
Oil density	981 kg/m^3 at 40°C
Oil viscosity	27.6 mm^2/s at 40°C
Oil jet direction	Into-mesh, out-of-mesh
Oil jet supply rate to gears (total)	1.48–7.40 L/min
Oil jet supply rate to bearings and seals	1.0 L/min each (constant)
Jet nozzle diameter	2.0 mm for two nozzles
Input speed	7000–10000 rpm
Internal pressure	0.5 bar, 1.0 bar (absolute)

3.1.2 Various Gearboxes to Validate Experimental Measurement and Numerical Simulation Methods

This section presents three types of gearboxes to validate experimental measurement and numerical simulation methods. Each gearbox was a partial replacement of the helical gearbox described in the previous section.

3.1.2.1 Two-axis Spur Gearbox (GB1) to Validate Oil Jet Flow to Gear Meshing Part

The test gearbox is shown in Fig. 3.1-5 . This gearbox was designed to visualize the inflow of oil jet to the into-mesh or out-of-mesh sides of the gear to validate the numerical simulation method. As shown in Fig. 3.1-5 (a), the input gear of the two-axis spur gears was driven by a motor. The output shaft was set free (no connection). A borescope from the side of the gear was installed to visualize the gear meshing. Figure 3.1-5 (b) shows the gear rotation direction for the into-mesh jet. The oil jet was injected from above the gear meshing. For the into-mesh jet, the rotational directions of the gears were set such that the gear meshing moved from top to bottom.
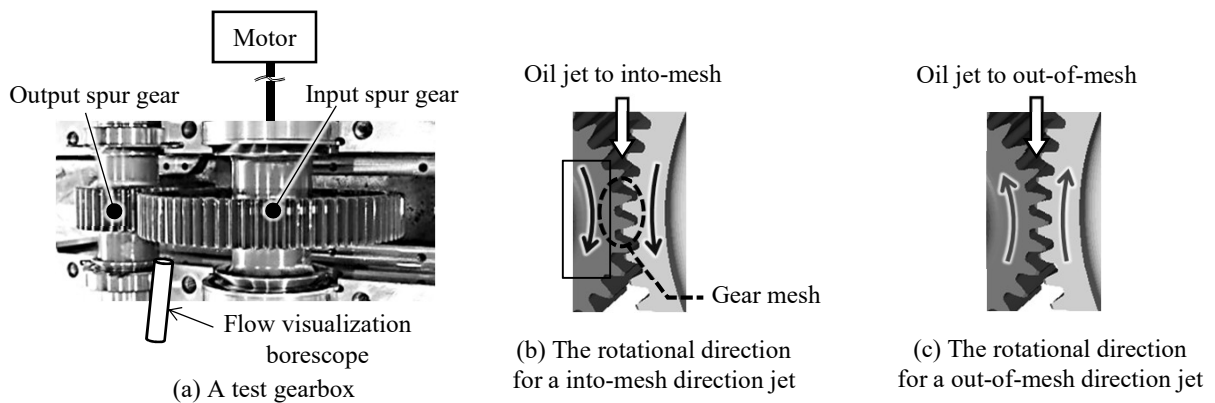
Fig. 3.1-5 Two-axis spur gearbox to visualize an oil jet to the gear mesh (GB1)

Table 3.1-3 Specifications of two-axis spur gearbox for the visualization of an oil-jet to the gear mesh (GB1)

Items	Input gear	Output gear
Type	Spur	
Number of teeth	76	33
Module (normal)	2.5 mm	
Pitch diameter	190 mm	82.5 mm
Face width	34 mm	
Pressure angle (normal)	20°	
Tooth surface roughness	$\sim$0.2 μm (Ra), $\sim$1.0 μm (Ry)	
Side surface roughness	$\sim$1.0 μm (Ra), $\sim$10 μm (Ry)	
Root fillet radius	1.0 mm	
Shaft diameter	ϕ70 mm	ϕ51 mm
Material	SCM420	
Shore hardness	79–87 HS	
Backlash	0.14–0.31	
Tooth contact ratio	1.75	
Rotational direction	Upward at gear mesh	
Maximum speed	10000 rpm	23030 rpm
Peripheral speed	100 m/s at 10000rpm of input gear	

Table 3.1-4 Test conditions of two-axis spur gearbox for the visualization of an oil-jet to the gear mesh (GB1)

Items	Into-mesh jet	Out-of-mesh jet
Speed	500, 4000 rpm	1600
Pitch line velocity	5.0, 40 m/s	16 m/s
Oil specification	MIL-PRF-23699	
	989 kg/m^3, 40 mm^2/s at 30°C	
Oil flow rate	3.8 L/min	
Oil jet nozzle diameter	3.0 mm	
Oil jet speed	9 m/s	
Oil inlet temperature	30 °C	

Figure 3.1-5 (c) shows the gear rotation direction for the out-of-mesh jet. The position of the oil jet was the same as that in (b) in the figure, and the rotational directions of the gears were set such that the gear meshing moved from bottom to top. Table 3.1-3 shows the gear specifications, and Table 3.1-4 shows the experimental conditions. For the into-mesh jet, the phenomenon was switched according to the gear peripheral speed; therefore the rotational speed was set to two conditions. For the out-of-mesh jet, the maximum rotational speed at which the gear meshing could be visualized was set, because visibility was reduced by the oil mist.

3.1.2.2 One-Axis Spur Gearbox to Validate the Visualization of Oil Jet Inflow to Gear Tooth Surface (GB2-1), One-Axis Spur Gearbox to Validate Oil Spray Inflow to Gear Tooth Surface (GB2-2)

The purpose of this gearbox was to visualize the tooth surface inflow of oil jets or oil sprays to validate the numerical simulation method. The test gearbox is shown in Fig. 3.1-6 . A single spur gear was driven by a motor. The gear specifications is shown in Table 3.1-5 . The nozzle (oil jet or oil spray nozzle) was installed toward the gear radial direction. The oil jet or oil spray was observed from the side of the gearbox through a borescope (the visualization method is described in Section 3.4), and images were captured at 60000 frames per second (fps).
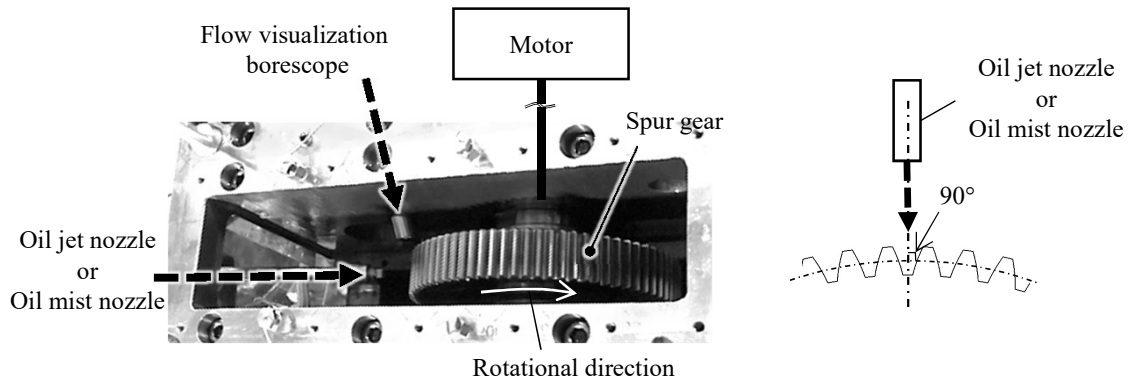
Fig. 3.1-6 One-axis spur gearbox to visualize an oil-jet impingement (GB2-1) or oil-mist impingement (GB2-2)

Table 3.1-5 Specifications of one-axis spur gearbox to visualize an oil-jet impingement (GB2-1) or oil-mist impingement (GB2-2)

Items	Specifications
Type	Spur
Number of teeth	76
Module (normal)	2.5 mm
Pitch diameter	190 mm
Face width	34 mm
Pressure angle (normal)	20°
Tooth surface roughness	∼0.2 μm (Ra), ∼1.0 μm (Ry)
Side surface roughness	∼1.0 μm (Ra), ∼10 μm (Ry)
Root fillet radius	1.0 mm
Shaft diameter	ϕ70 mm
Material	SCM420
Shore hardness	79–87 HS
Backlash	0.14–0.31
Maximum speed	10000 rpm
Peripheral speed	100 m/s at 10000rpm

Table 3.1-6 Test conditions of one-axis spur gearbox to visualize an oil-jet impingement (GB2-1) or oil-mist impingement (GB2-2)

Items	GB2-1	GB2-2
Nozzle type	Oil jet nozzle	Oil mist nozzle
Oil jet nozzle diameter	1.0 mm	1.1 mm
Oil jet speed	15 m/s	64 m/s
Oil flow rate	0.7 L/min	0.048 L/min
Oil specification	MIL-PRF-23699	
	981 kg/m^3, 26 mm^2/s at 40°C	
Oil temperature	40°C	
Air flow rate(Normal)	-	10 L/min
Air temperature	-	40°C
Rotational speed	10000 rpm	2500, 7500 rpm
Pitch line velocity	100 m/s	25, 75 m/s

The one-axis spur gearbox (GB2-1) to validate the visualization of an oil jet inflow to the gear tooth surface and the one-axis spur gearbox (GB2-2) to validate an oil spray inflow to the gear tooth surface used different nozzles and operating conditions. The oil supply and operating conditions are shown in Table 3.1-6 . For the oil spray nozzle, a two-fluid nozzle (MMA10, Kyoritsu Gokin Co., LTD.) was used. The nozzle was a coaxial cylinder, in which oil was ejected from the center cylinder, and air was ejected from the outer cylinder. The air pressure was kept constant at 0.3 MPa.

3.1.2.3   One-Axis Spur Gearbox to Validate Oil Flow between Gear Tooth Tip and Shroud Wall and to Validate the Image analysis Method of Velocity of Oil Particles (GB3)

The test apparatus is shown in Fig. 3.1-7 . The gearbox was designed to measure the oil fraction and mixture velocity around the gear to validate the visualization and image analysis methods of the discharge flow of oil from the shroud opening and to validate the numerical simulation method of the flow. The spur gear was driven by a motor. The gear was enclosed by a shroud and had one opening on the peripheral surface. Oil was supplied from 16 nozzles located at eight positions in the peripheral direction on both sides near the gear shaft. The oil hole of the nozzles was 3.0 mm in diameter. The direction of the nozzle was perpendicular to the side surfaces. A two-phase flow probe for measuring the oil fraction and mixture velocity was inserted in the radial direction from a hole provided directly above the shroud and in the center of the width. The probe position was close to the shroud opening and upstream from the opening; thus, it was considered possible to capture the outflow characteristics from the shroud opening. The visualization borescope was installed in two locations: where the shroud opening could be viewed from the radial direction (top view), and where the shroud opening could be viewed from the axial direction (side view).

The gear specifications are shown in Table 3.1-7 , and the operating conditions are shown in Table 3.1-8 . When compared with the conditions of the two-axis helical gearbox to simulate the general conditions of an aeroengine gearbox, the spur gear without gear meshing, and large oil-supply flow rate were different. The spur gear without gear meshing was adopted to simplify the flow and facilitate flow evaluation using the two-phase flow probe. The oil-supply flow rate was increased to facilitate observation with the visualization borescope.
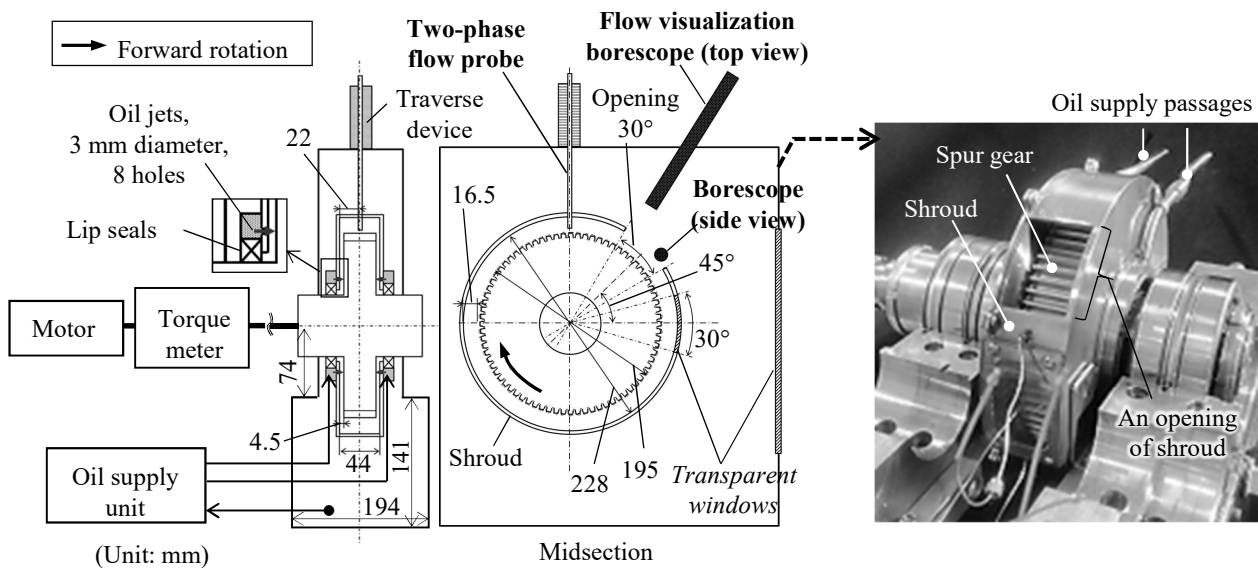
Fig. 3.1-7 One-axis spur gearbox to visualize and measure the two-phase flow (GB3)

Figure 3.1-8 shows the details of the attachment of the two-phase flow probe to the shroud. As shown in the figure, the two-phase flow probe had an outer diameter of 5 mm with a measurement hole diameter of 1 mm near the tip. The measurement was performed by directing this hole against the flow direction. The probe could be traversed in the radial direction and rotated for the center of the probe axis. The two-phase flow probe was equipped with a two-phase flow probe measurement system. The details of the two-phase flow probe measurement system are described later in Section 3.3, and those of the visualization borescope in Section 3.4.
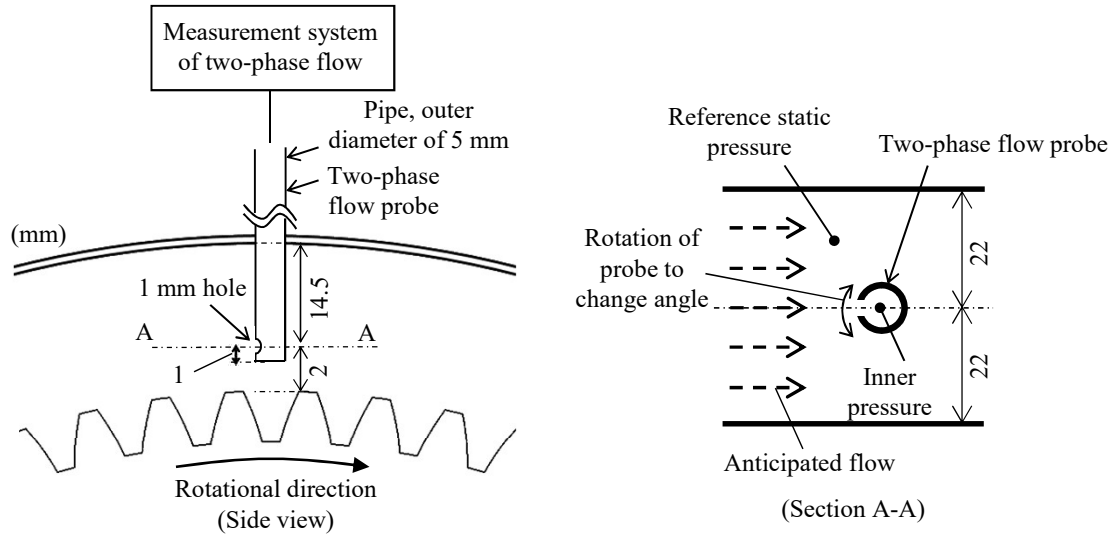
Fig. 3.1-8 Probe settings of one-axis spur gearbox to visualize and measure the two-phase flow (GB3)

Table 3.1-7 Specifications of one-axis spur gearbox to visualize and measure the two-phase flow (GB3)

Items	Specifications
Type	Spur
Number of teeth	76
Module (normal)	2.5 mm
Pitch diameter	190 mm
Face width	34 mm
Pressure angle (normal)	20°
Tooth surface roughness	~0.2 μm (Ra), ~1.0 μm (Ry)
Side surface roughness	~1.0 μm (Ra), ~10 μm (Ry)
Root fillet radius	1.0 mm
Shaft diameter	ϕ70 mm
Material	SCM420
Shore hardness	79–87 HS
Backlash	0.14–0.31
Maximum speed	10000 rpm
Peripheral speed	100 m/s at 10000rpm

Table 3.1-8 Test conditions of one-axis spur gearbox to visualize and measure the two-phase flow (GB3)

Items	Conditions
Speed	7000 – 10000 rpm
Oil specification	MIL-PRF-23699
	981 kg/m^3, 26 mm^2/s at 40°C
Oil flow rate	20 L/min
Oil jet nozzle diameter	1 mm
Oil jet speed	15 m/s
Oil inlet temperature	40°C

3.2 High-Accuracy Measurement Method of Fluid dynamic loss (In-Situ Measurement Method)

3.2.1 In-Situ Measurement Method of Friction Loss of Gears, Bearings, and Seals

For key points to remember when measuring the fluid dynamic loss of the gearbox with high accuracy, the following are mentioned from Section 1.3.3.

- The friction loss of gears, bearings, and seals that occupy a certain percentage of loss of the high-speed gearbox must be measured with high accuracy.
- The cause of the decrease in measurement accuracy is considered to be the temperature dependence of friction power loss in bearings and seals.
- It is difficult to accurately reflect the bearing temperature in the actual gearbox in the power loss estimation using the equations based on the single unit test of bearing and seal; therefore, errors may occur.

Therefore, to increase the accuracy of measuring friction power loss, it is necessary to measure the friction loss of the gear, bearing, and seal simultaneously as the fluid dynamic loss measurement, and to set the temperature of the bearing and seal to a constant value under each test condition. In this section, we propose an in-situ measurement method that includes high-accuracy temperature control for high-accuracy measurement of friction loss of gears, bearings, and seals.

(1) In-Situ Measurement Method of Friction Loss of Gears, Bearings, and Seals

The friction loss of gears, bearings, and seals is estimated through extrapolation to the power loss at zero air pressure and zero oil-supply flow rate. This is because the aerodynamic loss is excluded at zero air pressure, and the oil dynamic loss is excluded at zero oil-supply flow rate. An image of this estimation method is shown in Fig. 3.2-1 .

Figure 3.2-1 (a) shows the power loss at zero oil-supply flow rate ($P_{zero-oil}$) estimated by extrapolation from the setting conditions (power loss P_{set}) by changing the oil-supply flow rate. The loss at zero oil-supply flow supply rate is evaluated through extrapolation because direct measurement of the loss at zero oil-supply flow rate causes gear damage. Subsequently, the air pressure in the gearbox is changed (e.g., 0.5 bar), the oil-supply flow rate is changed again, and the power loss at zero oil-supply flow rate ($P_{zero-oil,0.5bar}$) is calculated through extrapolation.
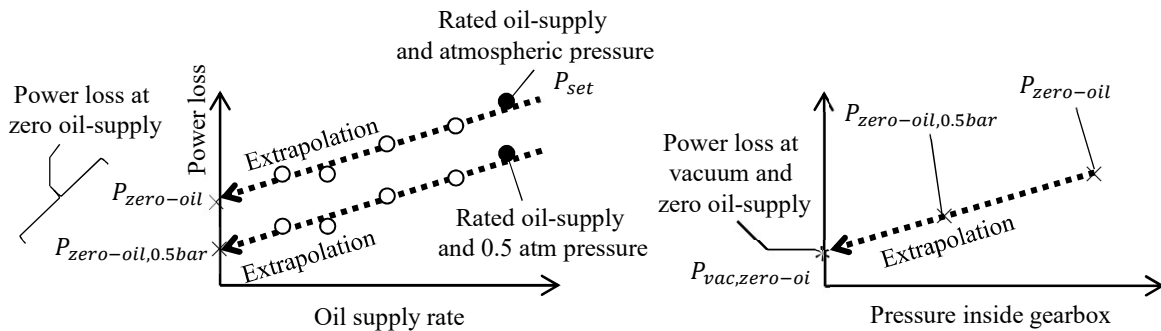
(a) Evaluation of power loss at zero oil-supply   (b) Evaluation of power loss at vacuum and zero oil-supply

Fig. 3.2-1 In-situ measurements of friction power losses on gears, bearings, and seals

63

Using the loss at zero oil-supply flow rate when these air pressures are changed, the losses at the zero oil-supply flow rate and zero air pressure ($P_{vac,zero-oil}$) can be estimated by extrapolating (Fig. 3.2-1 (b)). This $P_{vac,zero-oil}$ corresponds to the friction loss of the gears, bearings, and seals.

(2)　High-Accuracy Temperature Control Method for Gears, Bearings, and Seals

To minimize the error caused by the difference in the temperature of the bearing and seal of the gearbox, the temperature of the bearing and seal of the gearbox should be monitored and measured. The friction loss of the gears is minimized by operating the gearbox with the no-load condition; thus, the temperature of the gears need not be considered. The measurement procedure is described below.

（ⅰ）　Preparation of the Measurement

1. At the upper or lower limits of the rotational speed in the measurement, the bearing temperatures are measured until the temperatures become approximately constant. The median of these temperatures is set as the target temperature. For example, the median of the temperature at the lower limit of 7000 rpm and that at the upper limit of 10000 rpm is set as the target temperature.

2. Change the rotational speed to set the bearings and seals at each target temperature. For example, if the temperatures are low, increase the rotational speed to increase the temperatures closer to the target temperatures.

3. Set the rotational speed to the value in the measurement condition (target rotational speed). Here, the changing of the temperatures of the bearings and seals are monitored. For example, the temperature at 7000 rpm tends to decrease from the target value, while that at 10000 rpm tends to increase from the target temperature.

4. Repeat steps 2 and 3 at the rotational speed in each measurement condition.

（ⅱ）　Acquisition of Measurement Data

1. After the measurement is started, the gearbox speed is changed to achieve the approximate target temperature (warm-up operation).

2. If the temperature changing trend at the target rotational speed (already obtained in "3 in (i) Preparation of the Measurement" described above) is decreasing at the target temperature, increase the temperature by a few degrees Celsius from the target temperature. In contrast, if the temperature changing trend at the rotational speed in the measurement condition is increasing at the target temperature, decrease the temperature by a few degrees Celsius from the target temperature.

3. Set the rotational speed to the target value.

4. When the temperature gradually changes and the temperature of the bearings and seals reaches the target value, the torque is sampled for 3 s , and the average torque for these 3 s is used as the measurement torque under the rotational speed condition.

5. Repeat steps 2– 4 at each target rotational speed.

An example of this measurement is shown in Fig. 3.2-2 . In this scenario, the temperatures of the bearings and seals at the target rotational speed have an increasing trend. First, by reducing the rotational speed, the temperature of the bearing or seal is lowered by several degrees Celsius from the target value ("Cooling phase" in the figure). Next, the rotational speed is set to the target value and until the temperature begins to increase ("Measurement phase" in the figure). When the temperatures of the bearings and seals reach the

target values ("Target temperature" in the figure), measurement sampling is performed ("Measurement" in the figure). If all temperatures of the bearings and seals are within the target temperature scope, the measurement results are adopted.

The above discussion shows that high-accuracy friction loss can be measured using the temperatures of the bearings and seals in the gearbox within the target temperature scope under each experimental condition.
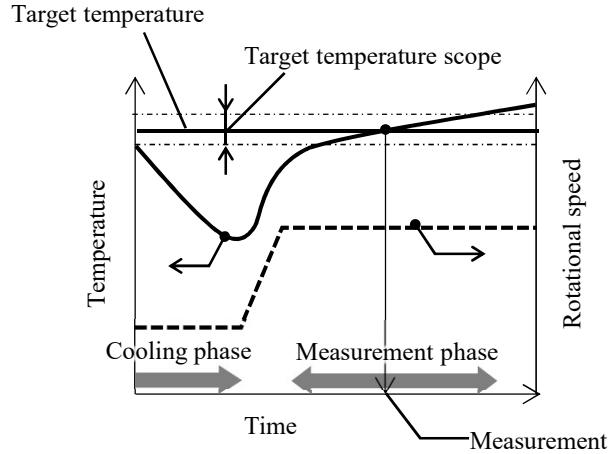
Fig. 3.2-2 Procedure of the in-situ measurement of the friction power losses

3.2.2 Separation Method to Aerodynamic and Oil Dynamic Losses

A method of separating the fluid dynamic loss into aerodynamic and oil dynamic loss is shown in Fig. 3.2-3 . This separation method uses the loss at the zero oil-supply flow rate ($P_{zero-oil}$), the loss at the zero air pressure and zero oil-supply flow rate ($P_{vac,zero-oil}$), and total power loss under the target condition (P_{set}). These losses are obtained using the in-situ measurements shown in Fig. 3.2-1 .

Oil dynamic loss	$P_{set} - P_{zero-oi}$
Aerodynamic loss	$P_{zero-oil} - P_{vac,zero-oil}$
Friction power loss on gear mesh, bearings, and seals	$P_{vac,zero-oi}$

Power loss at vacuum and zero oil-supply condition $P_{vac,zero-oil}$

Power loss at zero oil-supply condition $P_{zero-oil}$

Power loss at setting condition P_{set}
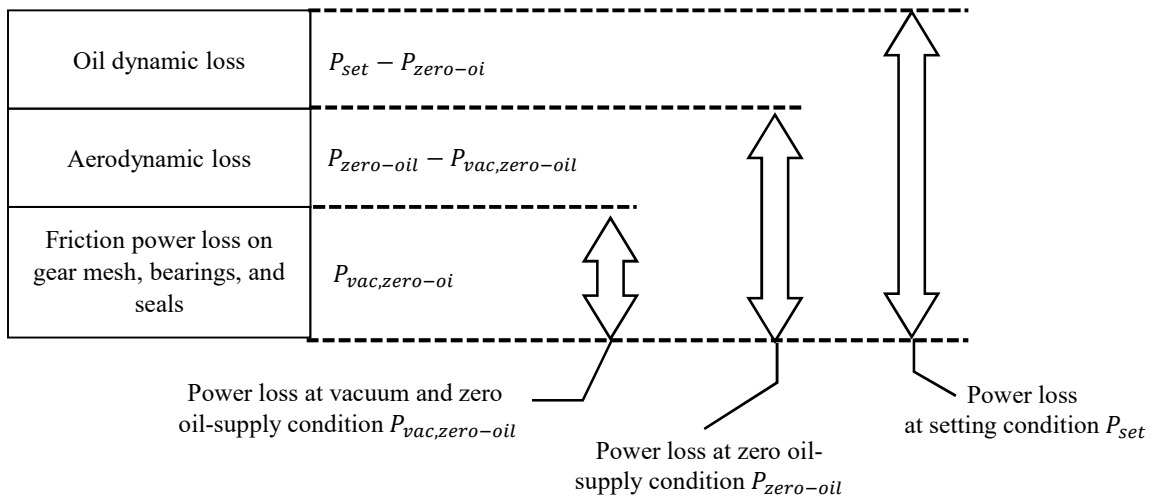
Fig. 3.2-3 Separation method of total power loss into aerodynamic and oil dynamic losses

65

The aerodynamic loss (P_{air}) is obtained by subtracting $P_{vac,zero-oil}$ from $P_{zero-oil}$. The oil dynamic loss (P_{oil}) is obtained by subtracting $P_{zero-oil}$ from P_{set}. These are shown in the following equations.

$$P_{air} = P_{zero-oil} - P_{vac,zero-oil} \tag{3.1}$$

$$P_{oil} = P_{set} - P_{zero-oil} \tag{3.2}$$

3.2.3 Evaluation Methods and Targets of Measurement Error

The repeatability error of the measurement is evaluated using the standard error $E_{2\sigma_{rep,P}}$ of 2σ (σ is the standard deviation), which is shown in the following equation.

$$E_{2\sigma_{rep,P}} = 2\sigma_{rep,P}/\sqrt{\mathcal{N}_{rep}}$$
$$\sigma_{rep,P} = \sqrt{\frac{1}{\mathcal{N}_{rep}} \sum_{i=1}^{\mathcal{N}_{rep}} (P_i - \hat{P})^2} \tag{3.3}$$

where $\mathcal{N}_{rep}$ is the iteration number of measurement, P_i is the measured value of power loss, and $\hat{P}$ is the ensemble-averaged value. By using the standard error of 2σ, the true value exists in the range of the mean value $\pm E_{2\sigma_{rep,P}}$ with a probability of 95%. The target of the measurement error is set to 0.1 kW or less, which is equivalent to the measurement error of the torque meter, as the measurement error in the scenario in which the influence of the temperature deviation of bearings and seals is negligible.

3.3 Measurement Methods for Oil Fraction and Mixture Velocity

In this section, we describe methods for measuring oil fraction and mixture velocity to obtain validation data for both the visualization and numerical simulation methods.

3.3.1 Measurement Methods for Oil Fraction and Mixture Velocity

3.3.1.1 Measuring Oil Fraction and Mixture Velocity Using the Isokinetic Suction Method

The oil fraction is the volume fraction of oil in a two-phase flow of air and oil, and the mixture velocity is the apparent velocity when the air and oil velocities are considered to be the same. Both parameters are important for understanding the phenomenon of two-phase flow. As shown in Section 1.3.3, the isokinetic suction method has the highest possibility of being applied to measure the oil fraction and mixture velocity of two-phase flow in a gearbox.

The isokinetic suction method is shown in Fig. 3.3-1 [70]. The isokinetic suction method is a method of sampling the dispersed phase (oil, dust, etc.) contained in the external flow by making the suction speed of the probe the same as the flow speed of the external flow toward the probe (Fig. 3.3-1 (a)). For suction at an isokinetic speed, the pressure of the external flow ($P_{outside}$) must be balanced with the pressure in the probe (P_{inside}). When this balance is lost, as shown in (b) and (c) in the figure, non-isokinetic suction occurs. Figure 3.3-1 (b) shows the scenario of high-speed suction, in which the flow speed in the probe is higher than the external flow speed because the pressure in the probe is lower than the outside pressure. Here, the amount of sampled particles would be underestimated because larger particles would not follow the flow toward the probe. Figure 3.3-1 (c) shows the scenario of low-speed suction, in which the flow speed in the probe is lower than the external flow speed because the pressure in the probe is higher than outside pressure. Here, the amount of

sampled particles would be overestimated because larger particles would not follow the flow away from the probe. The mixture velocity (u_m) is obtained using the following equation using the stagnation point pressure (p_{stag}) and values measured using the isokinetic suction method (the oil fraction (α_{oil}), air density (ρ_{air}), oil density (ρ_{oil}), and apparent two-phase flow density (ρ_m)).

$$u_m = \sqrt{\frac{2p_{stag}}{\rho_m}} = \sqrt{\frac{2p_{stag}}{\alpha_{oil}\rho_{oil} + (1 - \alpha_{oil})\rho_{air}}} \tag{3.4}$$

One of the challenges of the isokinetic suction method is the development of a measurement method that can be applied to a wide range of oil fractions and mixture velocities for two-phase flow in the gearbox. In the following, we propose a measurement method for oil fraction and mixture velocity and a calibration method to apply it to a wide range of oil fractions and mixture velocities, considering the characteristics shown in Figure 3.3-1 .
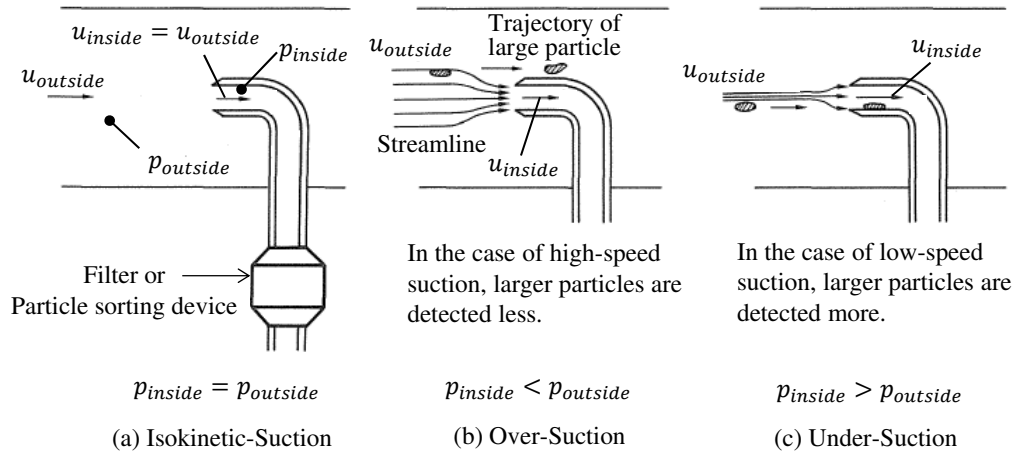
Fig. 3.3-1 Schematics of isokinetic sampling compared with non-isokinetic sampling [70]

3.3.1.2 Apparatus for Measuring Oil Fraction and Mixture Velocity

An apparatus using a two-phase flow probe for measuring oil fraction and mixture velocity is shown in Figure 3.3-2 . The probe is a cylindrical tube with an outer diameter of 5 mm and has a measurement hole of 1 mm at the tip, and a pressure adjusting pipe is installed inside. The probe is not shaped like a pitot tube to enable it to be easily installed in a gearbox if the gearbox has only a small opening on the gearbox wall (or shroud wall). Figs. 3.1-7 and 3.1-8 show the installation of the two-phase flow probe in the gearbox.

The measurement system consists of a two-phase flow suction line, a pressure control line in the probe and an oil purge line. The two-phase flow suction line is used to suck air and oil through the measurement hole. It is connected to a pressure control valve, a vacuum tank supported by a weight meter, a vacuum pump, and an air flow meter. The pressure control line is used to adjust the pressure in the probe to be equal to the outside pressure, and a pressure gauge is connected. The oil purge line is used to purge air from the two-phase flow suction line and the pressure control line before measurement of oil fraction and mixture velocity, thereby eliminating measurement errors due to surface tension at the gas–liquid interface in the pipe.
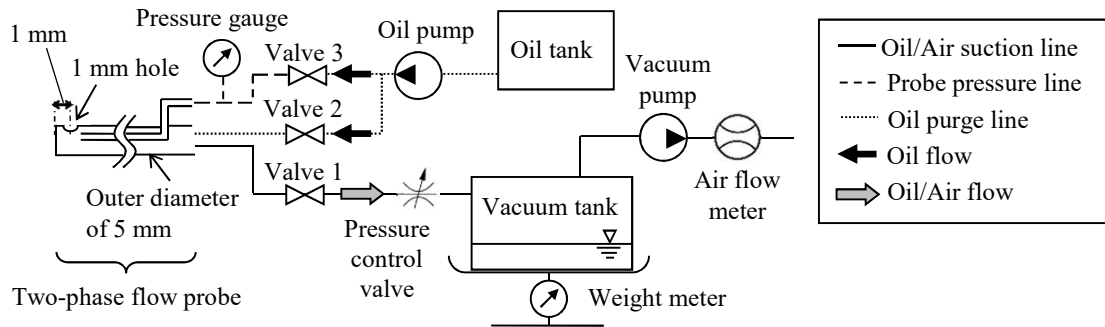
Fig. 3.3-2 Measurement system for two-phase flow probe

3.3.1.3 Procedure for Measuring Oil Fraction and Mixture Velocity

The procedures for measuring the oil fraction and mixture velocity are described below. In the procedures, "Valve" and "Line" refer to those in Figure 3.3-2 .

(1)   Measurement of Oil Fraction

A1   Open "Valve 3" and close "Valve 1" and "Valve 2." Oil is supplied by the "Oil pump," which purges air from the "Probe pressure line" and fills it with oil.

A2   Open "Valve 1," close "Valve 2" and "Valve 3," and turn "Vacuum pump" on. The two-phase flow is sucked from the "Oil/Air suction line. "

A3   Using the "Pressure control valve," the pressure at the inner pressure of the probe measured by the "Pressure gauge" is adjusted to be equal to the static pressure of the external flow. In this research, the static pressure of the external flow is assumed to be atmospheric pressure.

A4   Calculate the oil fraction using the weight of the oil measured with a weight meter and the air flow rate measured with an air flow meter.

A5   Repeat steps A1 to A4 until the standard error of the measurement results is less than or equal to the target value. The standard error is $\sigma/\sqrt{\mathcal{N}_{rep}}$ (σ is the standard deviation, and , $\mathcal{N}_{rep}$ is the number of repetitions). The minimum number of repetitions at each measurement position is set to 3. The oil fraction of the ensemble-averaged value of the measured values obtained through repeated measurements is the oil fraction under the conditions before calibration.

(2)   Measurement of Mixture Velocity

B1   Open "Valve 2" and "Valve 3," close "Valve 1," and fill "Two-phase flow probe" and "Probe pressure line" with oil.

B2   Close "Valve 2" and "Valve 3" ("Valve 1" remains closed), and measure the stagnation pressure (p_{stag}) using the "Pressure gauge".

B3   Calculate the mixture velocity using p_{stag} and Eq. 3.4.

B4   Repeat steps B1 to B3 until the standard error of the measurement results is equal to or less than the target value. The minimum number of repetitions at each measurement position is set to 3. The mixture velocity of the ensemble-averaged value of the measured values obtained through repeated measurements is the mixture velocity under the conditions before calibration.

3.3.2 Calibration Methods for Oil Fraction and Mixture Velocity

3.3.2.1 Apparatus for Calibrating Oil Fraction and Mixture Velocity

(1) Apparatus for Calibrating Oil Fraction and Mixture Velocity Suitable for High-Speed Two-Phase Flow

The calibration apparatus to be applied to calibrate the oil fraction and mixture velocity of high-speed two-phase flow in this research is shown in Fig. 3.3-3 (a). The oil is pumped from the oil tank and injected into the mixing chamber ("Oil supply passage" in Fig. 3.3-3 (a)). Air is blown into the mixing chamber by the compressor ("Air supply passage" in Fig. 3.3-3 (a)). Each flow rate is controlled by flow control valves and flow meters. The two-phase flow of air and oil is injected toward the two-phase flow probe through a supply pipe (inner diameter 4 mm, length 300 mm) located directly below the mixing chamber. The distance between the supply pipe outlet and the probe is 10 mm, which is a distance at which the width of two-phase flow is seemed almost no expands from the lower end of the supply pipe. (The diameter of the two-phase flow at the probe position is seemed to be equivalent to the inner diameter of the pipe.)

Figure 3.3-3 (b) shows an image of the state of bubbles in a high-speed two-phase flow in the supply pipe. The air supplied to the mixing chamber ("A" in Fig. 3.3-3 (a)) temporarily dissolves in the oil owing to an increase in pressure in the middle of the pipe ("B" in Fig. 3.3-3 (b)) and is separated again toward the outlet of the supply pipe ("C" in Fig. 3.3-3 (b)). Because the pressure at the outlet of the supply pipe is atmospheric, the bubbles are considered to be completely separated ("D" in Fig. 3.3-3 (b)).
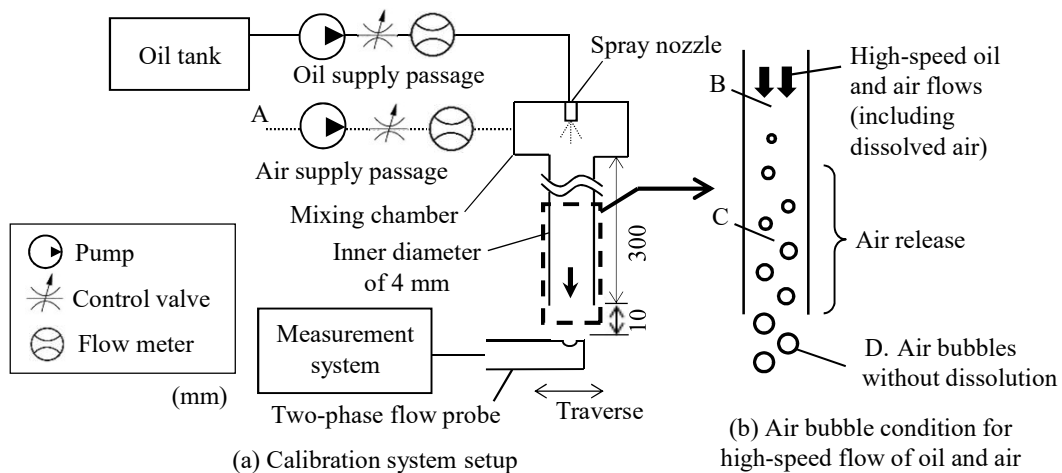
Fig. 3.3-3 Calibration system setup for a two-phase flow probe

For this phenomenon of bubble dissolution and separation, the bubble solubility in oil and water with respect to pressure changes are shown in Fig. 3.3-4 [93]. As shown in this figure, for example, when the atmospheric pressure doubles, the volume of dissolved air in oil doubles (Henry's law). In addition, the air solubility in water at atmospheric pressure (1 atm) is 3.7%, whereas the air solubility in oil is 9.4%, which is about twice as high. The surface tension of oil is smaller than that of water [94] [95]; thus, the bubbles become finer and they are considered to dissolve rapidly in oil.

Based on this basic characteristic, the change in air dissolution in the calibration apparatus is explained. The upper part in Fig. 3.3-5 shows an image of the change in the capacity to dissolve air and the change in the actual dissolved air. The lower part in Fig. 3.3-5 shows an image of the change in air mass in

the separated condition (air bubble). "A", "B", "C", and "D" in Fig. 3.3-5 correspond to "A", "B", "C", and "D" in Fig. 3.3-3 . As shown in the upper part in Fig. 3.3-5 , upstream of the pipe (B), the capacity of bubble dissolution increases with the increase in pressure, and the mass of the actual dissolved air increases with the increase in pressure in the pipe. At the middle of the pipe (C), the mass of dissolved air increases with time. In contrast, as shown in the lower part of Fig. 3.3-5 , the mass of the separated air bubbles is considered to decrease. When the flow reaches the pipe outlet (D), the pressure returns to atmospheric pressure; therefore, the capacity of bubble dissolution decreases, and bubbles are separated. Because the air inlet (A) and tube outlet (D) have the same atmospheric pressure, the volume and mass of the separated air in (A) are equivalent to that in (D). As described above, the calibration apparatus in this research can equalize the volume and mass of the injected air with those of the air at the probe measurement position and is therefore considered suitable for the calibration of high-speed two-phase flow.
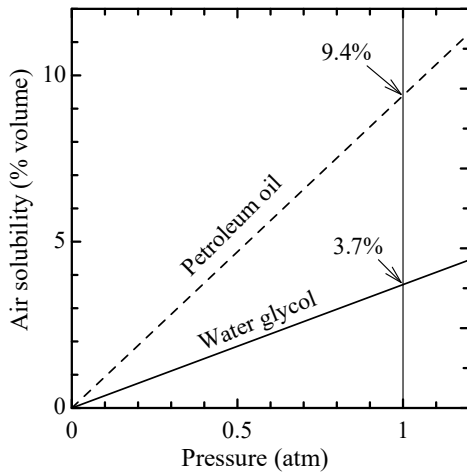
Fig. 3.3-4 Air solubility for oil and water (experimental results) [93]
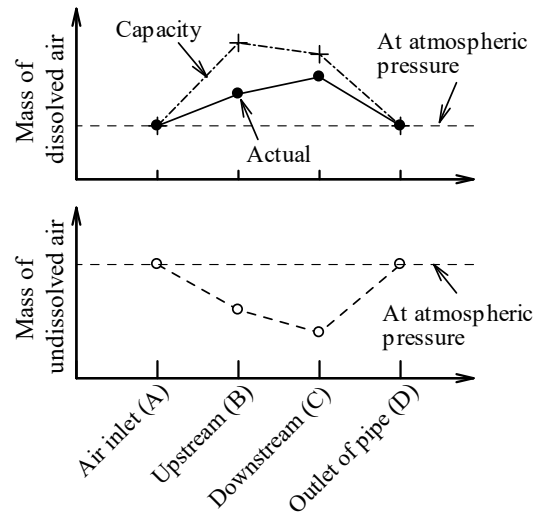
Fig. 3.3-5 Anticipation of air dissolution into oil along the flow passage

(2)   Comparison with General Low-Speed Two-Phase Measurement Apparatus

For comparison, a typical low-speed gas–liquid two-phase flow measurement apparatus [96] is shown in Fig. 3.3-6 (a). This device indicates the rise of bubbles in a vertical pipe, and the apparent two-phase flow velocity is as slow as 0.05 m/s. The bubble dissolution phenomenon expected when this apparatus is applied to a high-speed two-phase flow of air and oil is shown in Fig. 3.3-6 (b). The pressure in the pipe is higher than the atmospheric pressure because the distance from the air inlet ("A" in Fig. 3.3-6 (a)) to the two-phase flow outlet ("D" in Fig. 3.3-6 (a)) is large. Therefore, the air injected from the compressor ("A" in Fig. 3.3-6 (a)) is pressurized and flows into the upstream of the pipe ("B" in Fig. 3.3-6 (a)). Subsequently, the air bubbles are considered to dissolve in oil as they flow along to the downstream of the pipe, and the amount of separated air decreases at the observation position downstream of the pipe ("C" in Fig. 3.3-6 (a)). The air flow rate injected by the compressor differs from the air flow rate separated as bubbles at the observation position ("C" in Fig. 3.3-6 (a)) owing to the influence of the bubbles dissolving, making calibration difficult. An apparatus with a measurement position in the pipe, such as this apparatus, is not suitable for the calibration of high-speed two-phase flow.

(a) Calibration system setup

(b) Air bubble condition when high-speed flow of oil and air is used
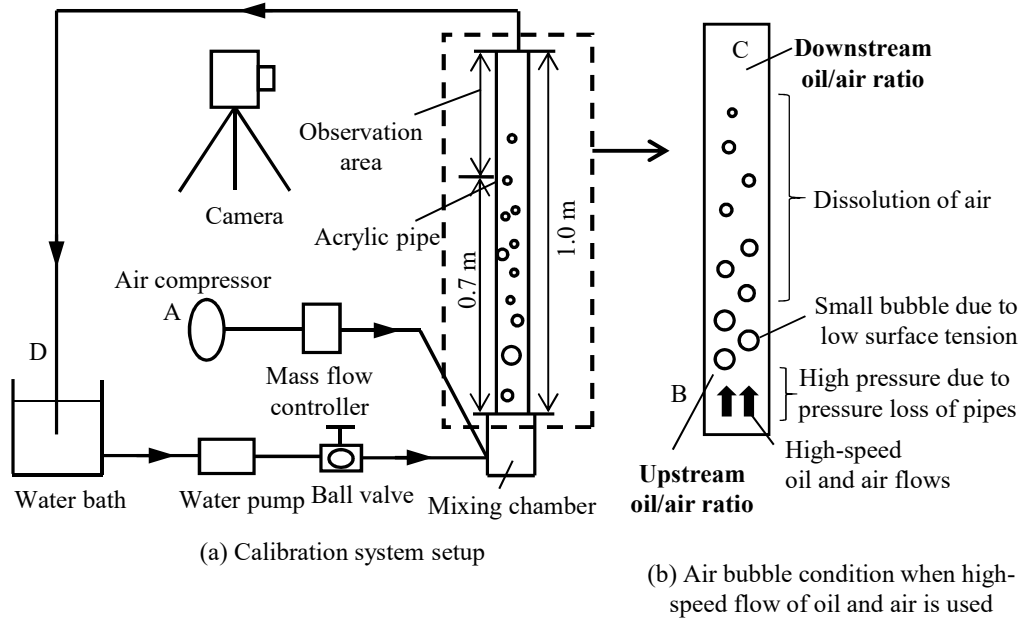
Fig. 3.3-6 Example of a general calibration setup for two-phase flow measurement [96]

3.3.2.2 Calibration Method for Oil Fraction and Mixture Velocity

(1)   Generality of the Calibration Method and Necessity of Validation with Measurements in an Actual Gearbox

In the two-phase flow probe of this research, the measured pressure may be underestimated owing to the reflection of the droplet at the edge of the measurement hole when the droplet size is larger than the measurement hole of the probe [72]. Therefore, the size and velocity of the bubble or droplet should be measured to obtain more general calibration results. To measure the size and velocity of the bubble or droplet, generally, the two-phase flow is photographed by a camera, and the continuous image is processed to measure the size and velocity of the bubble (e.g., [96]). However, such a general measurement method cannot be applied to the high-speed two-phase flow of air and oil that contains minute bubbles and droplets. Therefore, in the calibration of the two-phase flow probe of this research, the area-averaged oil fraction and mixture velocity at the measurement hole are used. Because the size and velocity of bubbles or droplets are not considered, this calibration method may lack generality. In other words, the calibration results are considered to be effective when the sizes of bubbles and droplets in the calibration experiments of the two-phase flow probe are equivalent to those in the gearbox applied with the probe. As it is difficult to confirm this, the results obtained in the gearbox must be validated from other viewpoints. In this research, the oil flow rate in the gear shroud is evaluated using the measurement results of the two-phase flow probe (oil fraction and mixture velocity), and this is validated by comparing the oil-supply flow rate set by the apparatus.

(2)   Outline of the Calibration Method

A flow chart of the calibration is shown in Fig. 3.3-7 .

The isokinetic suction method is used to measure the oil fraction. The measured oil fraction ($\alpha_{oil,mes}$) is corrected by the calibration curve of the oil fraction and becomes the corrected oil fraction ($\alpha_{oil,corr}$).

In the dynamic pressure measurement for the mixture velocity measurement, no suction is performed, and

the stagnation pressure (Δp_{mes}) is measured using the probe as a total-pressure tube. Using Δp_{mes}, and $\alpha_{oil,mes}$ or $\alpha_{oil,corr}$, the measured mixture velocity ($u_{m,mes}$) is calculated.

The "Simple method" and "High-accuracy method" are used to calibrate the mixture velocity. The simple method uses a linear calibration curve obtained using the Lockhart–Martinelli parameter. The high-accuracy method increases the measurement accuracy although the shape of the calibration curve is complicated.
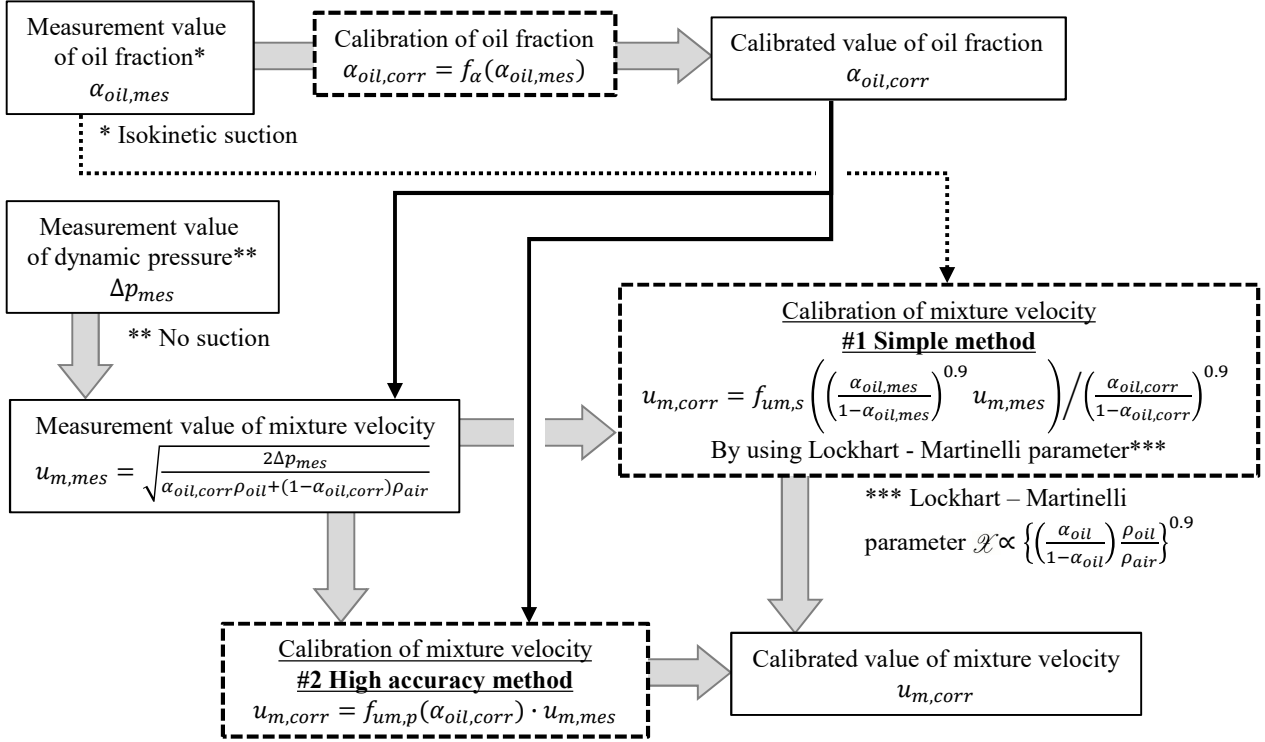
Fig. 3.3-7 Flow chart for the measurement of oil fraction and mixture velocity

(3)   Calibration Method for Oil Fraction

The measured oil fraction ($\alpha_{oil,mes}$) is measured using the calibration apparatus shown in Fig. 3.3-3 . The function f_α between the setting oil fraction ($\alpha_{oil,set}$) and $\alpha_{oil,mes}$ is obtained and used as the calibration function.

$$\alpha_{oil,set} = f_\alpha(\alpha_{oil,mes}), \text{ in the calibration test} \tag{3.5}$$

In the gearbox test, using f_α, the corrected oil fraction ($\alpha_{oil,corr}$) is obtained using ($\alpha_{oil,mes}$).

$$\alpha_{oil,corr} = f_\alpha(\alpha_{oil,mes}), \text{ in the gearbox test} \tag{3.6}$$

(4)   Simple Calibration Method for Mixture Velocity

The measured mixture velocity ($u_{m,mes}$) is calculated using the measured dynamic pressure (Δp_{mes}) and $\alpha_{oil,corr}$ as follows:

$$u_{m,mes} = \sqrt{\frac{2\Delta p_{mes}}{\alpha_{oil,corr}\rho_{oil} + (1 - \alpha_{oil,corr})\rho_{air}}} \tag{3.7}$$

To simplify the calibration curve for the mixture velocity, we introduce a similarity parameter. As the similarity parameter, the Lockhart–Martinelli parameter ($\mathscr{X}$) [97] is used:

$$\mathscr{X} = \left(\frac{\dot{m}_{oil}}{\dot{m}_{air}}\right)^{0.9} \left(\frac{u_{oil}}{u_{air}}\right)^{0.5} \left(\frac{\mu_{oil}}{\mu_{air}}\right)^{0.1} \tag{3.8}$$

In the above equation, an empirical equation for a two-phase flow in which the liquid phase is water, the gas phase is air, and both gases and liquids are turbulent, is applied to a two-phase flow of oil and air. $\dot{m}_{oil}$ and $\dot{m}_{air}$ are the mass flow rates of oil and air, respectively. u_{oil} and u_{air} are the oil and air speeds, respectively. μ_{oil} and μ_{air} are the oil and air viscosities, respectively. If $u_{oil} = u_{air} = u_m$ is used as the definition of the mixture velocity, and if each viscosity is assumed to be the same before and after calibration and therefore the viscosity term is omitted, $\mathscr{X}$ is given by the following equation.

$$\mathscr{X} = \left(\frac{\dot{m}_{oil}}{\dot{m}_{air}}\right)^{0.9} = \left\{\frac{\alpha_{oil}\rho_{oil}u_m A_{pipe}}{(1-\alpha_{oil})\rho_{air}u_m A_{pipe}}\right\} = \left\{\left(\frac{\alpha_{oil}}{1-\alpha_{oil}}\right)\frac{\rho_{oil}}{\rho_{air}}\right\}^{0.9} \tag{3.9}$$

Because ρ_{oil} and ρ_{air} are known values, $(\frac{\alpha_{oil}}{1-\alpha_{oil}})^{0.9}$ is used as the calibration parameter for the mixture velocity.

The function $f_{um,s}$ between "the calibration parameter of the mixture velocity (setting value of $\mathscr{X}$) $\times$ the setting mixture velocity ($u_{m,set}$)" and " the calibration parameter of the mixture velocity (measured value of $\mathscr{X}$) $\times$ the measured mixture velocity ($u_{m,mes}$)" is derived. The function $f_{um,s}$ is the correction function and is expressed as follows:

$$\left(\frac{\alpha_{oil,set}}{1-\alpha_{oil,set}}\right)^{0.9} u_{m,set} = f_{um,s}\left(\left(\frac{\alpha_{oil,mes}}{1-\alpha_{oil,mes}}\right)^{0.9} u_{m,mes}\right), \text{ in the calibration test} \tag{3.10}$$

In the gearbox test, using the calibration function $f_{um,s}$, the corrected mixture velocity ($u_{m,corr}$) is obtained using $u_{m,mes}$.

$$u_{m,corr} = f_{um,s}\left(\left(\frac{\alpha_{oil,mes}}{1-\alpha_{oil,mes}}\right)^{0.9} u_{m,mes}\right) \Big/ \left(\frac{\alpha_{oil,corr}}{1-\alpha_{oil,corr}}\right)^{0.9}, \text{ in the gearbox test} \tag{3.11}$$

(5) High-Accuracy Calibration Method for Mixture Velocity

Generally, the law of similarity for two-phase flows may contain large errors. Therefore, the simple calibration method using the similarity parameter described above is considered to have errors. Therefore, a highly accurate calibration method suitable for actual phenomena in the gearbox should be considered.

In this calibration method, the calibration function ($f_{um,p}$) is obtained considering that the ratio of $u_{m,set}$ and $u_{m,mes}$ is linear for $\alpha_{oil,corr}$ (described in Section 3.6.2 in detail). That is,

$$\frac{u_{m,set}}{u_{m,mes}} = f_{um,p}(\alpha_{oil,corr}), \text{ in the calibration test} \tag{3.12}$$

In the gearbox test, using $f_{um,p}$, $u_{m,corr}$ is obtained using $u_{m,mes}$.

$$u_{m,corr} = u_{m,mes} \cdot f_{um,p}(\alpha_{oil,corr}), \text{ in the gearbox test} \tag{3.13}$$

In contrast, because this method is new and has not been used before, it is necessary to carefully evaluate the validity of the calibration function.

3.3.2.3   Calibration Conditions for Oil Fraction and Mixture Velocity

(1)   Supply Conditions for Two-Phase Flow of Air and Oil

Table 3.3-1 shows the supply conditions of the two-phase flow of air and oil. Assuming the two-phase flow in the gearbox, the oil fraction is set to 0.2%–75%, and the maximum mixture velocity is set to 50 m/s. In the gearbox of this research, the mixture velocity is approximately 50 m/s or less even under the condition of the peripheral speed of 100 m/s (Fig. 3.6-23). Therefore, this maximum flow speed is considered reasonable. The oil type and oil temperature are set to be the same (Table 3.1-8) in the one-axis spur gearbox (GB3) to which this oil fraction and mixture velocity measurements are applied.

Table 3.3-1 Conditions for calibration of a two-phase flow probe

Items	Parameters					
Oil ratio (%)	0.20	5.0	10	25	50	75
Mixture velocity (m/s)	50	25, 50	50	13, 18, 25	6.0, 9.0, 12	4.0, 6.0, 8.0
Oil specification	MIL-PRF-23699, 981 kg/m^3, 26 mm^2/s at 40°C					
Oil inlet temperature	40°C					

(2)   Measurement Conditions for Spatial Distribution of Air and Oil in a Two-Phase Flow Supply Pipe

For the spatial distribution of the oil fraction and mixture velocity in the cross-section of the two-phase flow supply pipe, the distance between the mixing chamber and the two-phase flow supply pipe outlet shown in Fig. 3.3-3 is short; therefore, we expect that the air and oil will be homogenized. In contrast, depending on the measurement conditions, the spatial distribution such as the flow deviation of the oil along the wall (annular flow) cannot be ignored, and the spatial distribution must be measured.

A condition with a large spatial distribution of the two-phase flow is considered to be an annular flow. Figure 3.3-8 shows a map of the flow pattern of a two-phase flow by Mandhane et al. [98]. The measurement conditions in Table 3.3-1 are also plotted. The figure depicts that the flow becomes annular when the oil fraction is 10% or less. The other conditions are close to the dispersion or slug flow, and the spatial distribution is considered to be small. Therefore, the spatial distribution measurement should be performed under the condition that the oil fraction is 10% or less.

The image of the measurement of the spatial distribution is shown in Fig. 3.3-9 . Figure 3.3-9 (a) shows a scenario in which the probe measurement hole is located on the central axis of the supply pipe ($r = 0$), and the location is applied for all calibration conditions. Figure 3.3-9 (b) shows the scenario in which the probe measurement hole is apart from the center axis by 1.5 mm ($r = 1.5$ mm) and is measured only when the spatial distribution is large. In this scenario, the cross-sectional mean value of the oil fraction is obtained by linearly interpolating the radial value of the oil fraction and averaging the area. The area mean value of the mixture velocity is also obtained similarly.
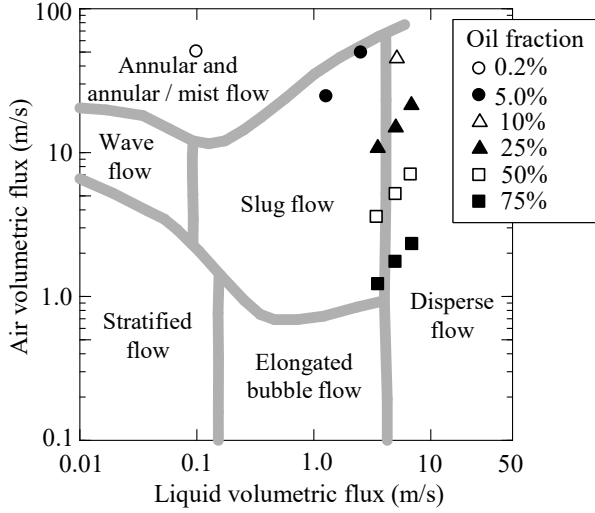
Fig. 3.3-8 Prediction of flow regime by comparison with an experimental flow regime map for the flow of air–water mixture in a horizontal, 2.5 cm diameter pipe at 25 °C and 1 bar [98]
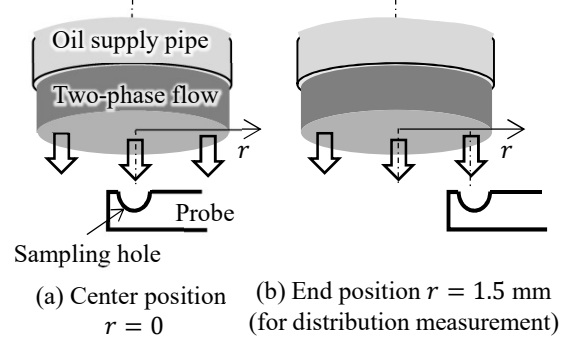
Fig. 3.3-9 Probe settings for measuring flow distribution

3.3.3 Evaluation Methods and Targets of Measurement Error

(1) Repeatability Error for Each Measurement Condition

The measurement error is defined as the standard error of σ in the repetition of $\mathcal{N}_{rep}$ times. The standard error ($E_{\sigma_{rep,\alpha}}$) of σ of the oil fraction and standard error ($E_{\sigma_{rep,um}}$) of σ of the mixture velocity are given by the following equations.

$$E_{\sigma_{rep,\alpha}} = \sigma_{rep,\alpha}/\sqrt{\mathcal{N}_{rep}} = \frac{1}{\sqrt{\mathcal{N}_{rep}}}\sqrt{\frac{1}{\mathcal{N}_{rep}}\sum_{i=1}^{\mathcal{N}_{rep}}\left(\alpha_{oil,i} - \hat{\alpha}_{oil}\right)^2} \tag{3.14}$$

$$E_{\sigma_{rep,um}} = \sigma_{rep,um}/\sqrt{\mathcal{N}_{rep}} = \frac{1}{\sqrt{\mathcal{N}_{rep}}}\sqrt{\frac{1}{\mathcal{N}_{rep}}\sum_{i=1}^{\mathcal{N}_{rep}}\left(u_{m,i} - \hat{u}_m\right)^2} \tag{3.15}$$

To reduce the measurement error for the true value of the oil fraction and mixture velocity to less than or equal to the target error, the target of $E_{\sigma_{rep,\alpha}}$ at each measurement point of the oil fraction should be 1% or less (before calibration), and the target of $E_{\sigma_{rep,um}}$ at each measurement point of the mixture velocity should be 1 m/s or less (before calibration). The minimum number of measurements at each measurement condition should be 3, and the measurement should be repeated until the target repeatability error or less is attained. The ensemble mean value of the measurement results should be the measurement value under the condition.

(2) Measurement Error of Oil Fraction and Mixture Velocity

The measurement error is the relative standard deviation between the measured value and setting value (true value). The relative standard deviation of the oil fraction ($\sigma_{mes,\alpha}/\alpha_{oil,set}$) and the relative standard

deviation of the mixture velocity ($\sigma_{mes,um}/u_{m,set}$) are given in the following equations.

$$\sigma_{mes,\alpha}/\alpha_{oil,set} = \frac{1}{\alpha_{oil,set}}\sqrt{\frac{1}{\mathcal{N}_{mes}}\sum_{i=1}^{\mathcal{N}_{mes}}\left(\alpha_{oil,i} - \alpha_{oil,set}\right)^2} \tag{3.16}$$

$$\sigma_{mes,um}/u_{m,set} = \frac{1}{u_{m,set}}\sqrt{\frac{1}{\mathcal{N}_{mes}}\sum_{i=1}^{\mathcal{N}_{mes}}\left(u_{m,i} - u_{m,set}\right)^2} \tag{3.17}$$

where $\mathcal{N}_{mes}$ is the number of measurement conditions, the subscripts *mes* and *set* indicate the measurement and setting values, respectively. The measurement error target value should be 15% or less, which is empirically practical.

3.4   Visualization of Oil Particles and Measuring Method of their Velocity

For the validation of the numerical simulation method to understand the phenomena of the fluid dynamic loss, a comparison with the visualization result of the oil around the gear is effective. In this section, methods of visualizing oil particles and measuring the velocity of oil particles based on the image analysis of visualized oil particles are presented.

3.4.1   Visualization Method

3.4.1.1   Visualization Method

To visualize the oil around the gear, as mentioned in Section 1.3.3, we must eliminate the influence of oil mist between the light source and visualization object in addition to eliminating the influence of oil mist between the visualization borescope and visualization object. Therefore, we use a method in which the direction of the camera view and the light source are coaxial, and the oil mist around the axis is eliminated using an air purge.

Figure 3.4-1 shows the visualization system, Fig. 3.4-2 shows the structure at the tip of the visualization borescope, and Table 3.4-1 provides the specifications of the visualization system. As shown in Fig. 3.4-1 , a borescope covered by an air purge jacket is axially connected to a high-speed camera. The borescope is also connected to a laser light source. The air purge jacket is connected to an air source.

As shown in Fig. 3.4-2 , the borescope with an outer diameter of 8 mm is installed coaxially in the air purge jacket with an outer diameter of 16 mm. A visualization image is obtained from the high-speed camera through the borescope. Laser light is emitted from the tip through an optical fiber in the borescope. This laser light source is designed with non-coherence; therefore, it does not generate interference fringes. Because the optical fiber has a high transmittance in the wavelength range of the laser light, it prevents burning of the optical fiber owing to energy loss during transmission of the laser light. The strong light power of the laser light enables high-speed imaging of the object. The air purge jacket forms an air tunnel between the borescope and object by removing the oil mist between the borescope and the object to be visualized. The problem of this borescope is that the light source and camera are facing in the same direction; therefore, halation (overexposure due to highlights) of the image may occur. The halation is avoided by using a high-speed camera with a wide dynamic range and low noise characteristics of a charge-coupled device.

High-speed cameras can capture images of 256×256 pixels at a speed of 70000 fps (Table 3.4-1). This image size and the capture speed enable us to clarify local phenomena around gears. For example, a photographing

speed of 70000 fps is a speed that enables a 10000 rpm gear to be captured every 0.86°

The above analysis indicates that this visualization system can elucidate the phenomena of oil particles around the gear.
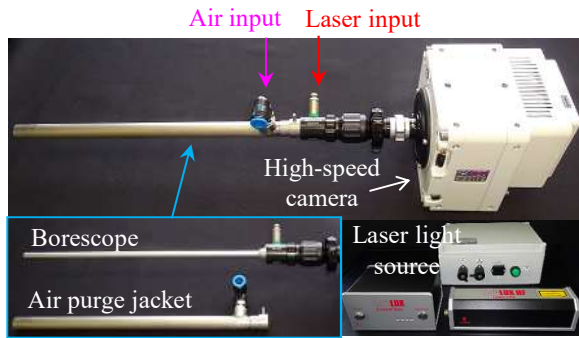
Fig. 3.4-1 Configuration of a flow visualization borescope
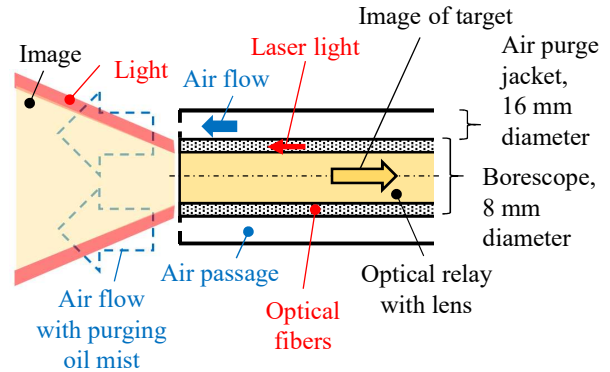
Fig. 3.4-2 Schematic of the internal structure within the visualization borescope

Table 3.4-1 Specifications of the flow visualization borescope

Items	Manufacturer, specifications
Laser light source	Cavitar Ltd (Nobby Tech. Ltd.), CAVILUX^{TM} HF, Low-coherence light, Max. 400 kHz, Output power 280 W (640 nm)
Borescope	Karl Storz Endoscopy Japan K. K., outer diameter of 8 mm, length 300 mm, for laser light source
Air purge jacket	Koyama Garage, Co., Ltd., 16 mm outer diameter with air passage to purge oil mist in front of the borescope
High-speed camera	Vision Research Inc. (Nobby Tech. Ltd.), Phantom$^{®}$ VEO 710L, Max. 70000 frame/sec (256×256 pixels), 2.3 kg

3.4.1.2   Validation of Visualization Results

To validate the visualization results, the oil jet inflow into the gear tooth surface was visualized with gearbox GB1 mentioned in Section 3.1.2.1, and the results were qualitatively compared with the results of previous studies. Because the oil inflow phenomena to the tooth surface is a typical phenomenon in the gearbox of an aeroengine, it is appropriate to for validating the visualization system. The visualization results and explanation of the oil jet inflow phenomena are provided in Section 3.6.3.1.

3.4.2   Image Analysis Method of the Velocity of Oil Particles

3.4.2.1   Image Analysis Method of the Velocity of Oil Particles

DIPP-MOTION V2D (DITECT Co. LTD., Tokyo, Japan) [99] was used as particle velocity analysis software using continuous images of oil particles. The velocity analysis methods are shown in Fig. 3.4-3 . The velocity analysis procedure is described below.

1. The user specifies the particle for which the velocity measurement is to be performed ("①" in Fig. 3.4-3). The specified particle should be preferably clear.

2. The user specifies the range for calculating the correlation of the image ("②" in Fig. 3.4-3).

3. The software automatically detects the particle with the highest correlation with the particle specified in step 1 using the two images that are continuous in time and the correlation range specified in Step 2 ("③" in Fig. 3.4-3).

4. The velocity is automatically calculated using the moving distance obtained from the particle positions in steps 1 and 3 and the time difference of the image ("④" in Fig. 3.4-3).

5. The position of the particles is updated, and steps 3 and 4 are automatically repeated using the image at the subsequent time. The result of the automatic tracking of the particles and time history of the velocity of the particles is output.

6. The automatic tracking result of the particle has to be visually confirmed whether the particle (oil mist particle, etc.) that differs from the user-designated particle is misrecognized as the user-designated particle. If a tracking error occurs, it reverts to the time before the occurrence of the error and begins over from step 2. The influence of oil mist should be reduced and clear images of target particles obtained to avoid the tracking error.

7. The time-averaged value is calculated using the time history of the velocity obtained, and this is used as the velocity of the oil particles.
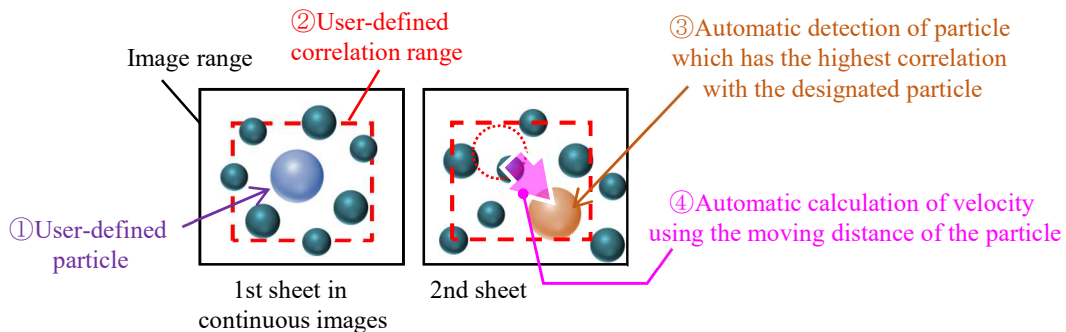
Fig. 3.4-3 Image analysis method for the velocity of an oil particle

3.4.2.2 Validation Method for the Velocity Analysis Results of Oil Particles

To validate the analysis results of the velocity of oil particles, the velocity of oil flowing out from the opening of the shroud in gearbox GB3 (Section 3.1.2.3) was obtained using the image analysis method. The velocity of oil was validated by comparing it with the velocity of oil obtained from the measurement results of the oil fraction and mixture velocity using the method described in Section 3.3. The experimental results and flow phenomena are described in Section 3.6.3.2.

3.4.2.3 Evaluation Method and a Target of Measurement Error

(1) Repeatability Error for each Measurement Condition

The image analysis obtains the velocity of oil particles should be performed five times with different tracking oil particles. The repeatability error is defined as the relative standard error ($E'_{\sigma_{rep,up}}$) of the velocity given

by the following equation:

$$E'_{\sigma_{rep,up}} = \frac{\sigma_{rep,up}/\hat{u}_{par}}{\sqrt{\mathscr{N}_{rep}}} = \frac{1}{\hat{u}_{par}\sqrt{\mathscr{N}_{rep}}}\sqrt{\frac{1}{\mathscr{N}_{rep}}\sum_{i=1}^{\mathscr{N}_{rep}}\left(u_{par,i} - \hat{u}_{par}\right)^2} \tag{3.18}$$

(2)   Measurement Error of the Velocity of Oil Particles

The velocity of oil particles using the image analysis method is compared with oil flow velocity obtained from the measurement results of oil fraction and mixture velocity (density-weighted mean velocity near the inner wall of the shroud, described in Section 3.6.3.2). The target is to obtain an agreement between them within the repetition error range.

3.5   Summary of Evaluation Methods and Targets for Experimental Measurement Errors

On each experimental measurement in this chapter, evaluation methods and targets are summarized for measurement errors in Table 3.5-1 . As repeatability errors, standard "errors" are used to evaluate the dispersion of the ensemble mean values of measurement results. As measurement errors compared with the setting values (true values), standard "deviations" are used to evaluate the essential errors of measurement methods. For the measurement error of velocity of oil particles, the velocity of oil particles using the image analysis method is compared with oil flow velocity obtained using the measurement results of oil fraction and mixture velocity, and the target is to have an agreement between them within the repetition error range.

Table 3.5-1 Summary of definition, evaluation method, and target error in each measurement

Measurements	Objectives	Definition for standard errors	Error evaluation methods	Target errors
Power loss	Repeatability	Variation with respect to mean value $\sigma_{rep,p}=\sqrt{\frac{1}{\mathcal{N}_{rep}}\sum_{i=1}^{\mathcal{N}_{rep}}\left(P_i-\hat{P}\right)^2}$	Standard error of $2\sigma^*$ $2\sigma_{rep,p}/\sqrt{\mathcal{N}_{rep}}$	0.1 kW (Equivalent to torque meter error)
Oil fraction	Repeatability	Variation with respect to mean value $\sigma_{rep,\alpha}=\sqrt{\frac{1}{\mathcal{N}_{rep}}\sum_{i=1}^{\mathcal{N}_{rep}}\left(\alpha_{oil,i}-\hat{\alpha}_{oil}\right)^2}$	Standard error of σ $\sigma_{rep,\alpha}/\sqrt{\mathcal{N}_{rep}}$	1% or less (Without calibration)
	Measurement error with respect to the setting value (true value)	Variation with respect to setting value (true value) $\sigma_{mes,\alpha}=\sqrt{\frac{1}{\mathcal{N}_{mes}}\sum_{i=1}^{\mathcal{N}_{mes}}\left(\alpha_{oil,i}-\alpha_{oil,set}\right)^2}$	Relative standard deviation of σ $\sigma_{mes,\alpha}/\alpha_{oil,set}$	15% or less**
Mixture velocity	Repeatability	Variation with respect to mean value $\sigma_{rep,um}=\sqrt{\frac{1}{\mathcal{N}_{rep}}\sum_{i=1}^{\mathcal{N}_{rep}}\left(u_{m,i}-\hat{u}_m\right)^2}$	Standard error of σ $\sigma_{rep,um}/\sqrt{\mathcal{N}_{rep}}$	1 m/s or less (Without calibration)
	Measurement error with respect to the setting value (true value)	Variation with respect to setting value (true value) $\sigma_{mes,um}=\sqrt{\frac{1}{\mathcal{N}_{mes}}\sum_{i=1}^{\mathcal{N}_{mes}}\left(u_{m,i}-u_{m,set}\right)^2}$	Relative standard deviation of σ $\sigma_{mes,um}/u_{m,set}$	15% or less**
Oil particle velocity	Repeatability	Variation with respect to mean value $\sigma_{rep,up}=\sqrt{\frac{1}{\mathcal{N}_{rep}}\sum_{i=1}^{\mathcal{N}_{rep}}\left(u_{par,i}-\hat{u}_{par}\right)^2}$	Relative standard error of σ $(\sigma_{rep,up}/\hat{u}_{par})/\sqrt{\mathcal{N}_{rep}}$	15% or less**
	Measurement error with respect to oil velocity (derived by oil fraction and mixture velocity)	—	Comparison with measurement of oil velocity	Oil particle velocity agree with oil velocity within the repeatability error

* More strictly than other measurements is because power loss is important data.

** Practical accuracy required in experience

3.6　Validation of Applicability of Experimental Measurement Methods

3.6.1　Validation of High-Accuracy Measurement Method of Fluid Dynamic Loss (In-situ Measurement Method)

3.6.1.1　Validation of the Accuracy of In-situ Measurement of Power Loss

This section describes that power loss can be measured with high accuracy by minimizing the influence of temperature changes in bearings and seals, which are considered to be the cause of measurement errors in conventional measurements.

(1)　Example of High-Accuracy Temperature Control for Bearings and Seals

An example of in-situ power loss measurement based on the method described in Section 3.2.1 is shown in Fig. 3.6-1 . It shows the time history of the rotational speed of the input shaft and bearing temperature. The bearings No. 1 and No. 3 shown in this figure (the locations are shown in Fig. 3.1-1) are the parts with the highest temperatures among the bearings and seals. Preliminary measurements indicate that the temperatures of other parts can be maintained within the target temperature range if the temperatures of these bearings are controlled within the target temperature range.

"A" in Fig. 3.6-1 refers to the moment when the rotational speed is set to 8500 rpm, which is the setting rotational speed. Before this time, the rotational speed is temporarily lowered to decrease the temperature of the bearing and seal (Fig. 3.2-2). Subsequently, after fixing to the setting rotational speed ("A" in Fig. 3.6-1), the time histories of the bearings No. 1 and No. 3 are monitored. The torque is sampled for 3 s at the timing ("D" in Fig. 3.6-1) when it is confirmed that these temperatures have attained ("B" and "C" in Fig. 3.6-1 , respectively) the target temperature ranges (target temperatures $\pm 2°$C).
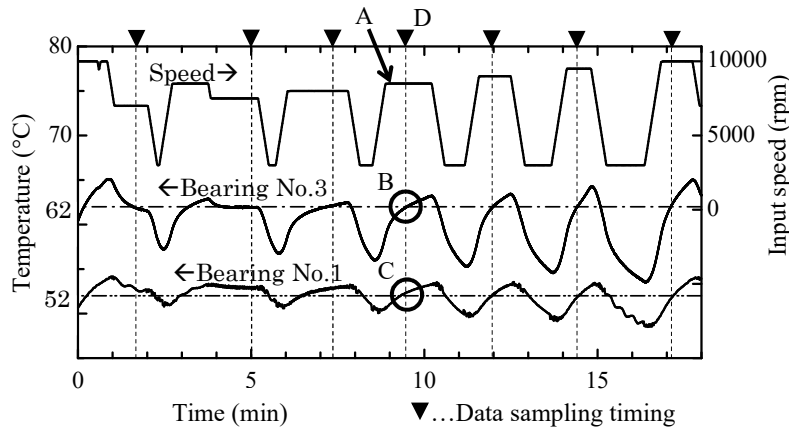
Fig. 3.6-1 Experimental results on the time histories of speed and temperatures

(2)　Results of Power Loss Measurement Error

The probability density of power loss is shown by the rotational speed of the input gear in Fig. 3.6-2 . This probability density is the result of 12 repeated measurements. In the figure, Gaussian distribution is also shown. The Gaussian distribution ($f_{Ga,P}$) of the power loss (P) is given by the following equation.

$$f_{Ga,P} = \frac{1}{\sqrt{2\pi\sigma_P{}^2}} \exp\left\{-\frac{(P-\hat{P})^2}{2\sigma_P{}^2}\right\} \tag{3.19}$$

81

where σ_P is the standard deviation, and $\hat{P}$ is the ensemble mean power loss. We can observe that the error range of the power loss widens as the rotational speed decreases. This is because the power loss decreases as the rotational speed decreases, and the error of the torque meter increases relatively.

Table 3.6-1 shows the standard error of three measurements. The standard error was obtained using Eq. 3.3. The standard error of 2σ of the obtained power loss was within 0.1 kW, which satisfies the target. The error is equivalent to that of the torque meter, which suggests that the influence of the temperature change of the bearing and seal on the measurement error of power loss is small.

The above results indicate that this measurement method can minimize the influence of the temperature change of bearings and seals and can be used to measure power loss with high accuracy.

| (a) 7000 rpm of input gear | (b) 9000 rpm of input gear | (c) 10000 rpm of input gear |
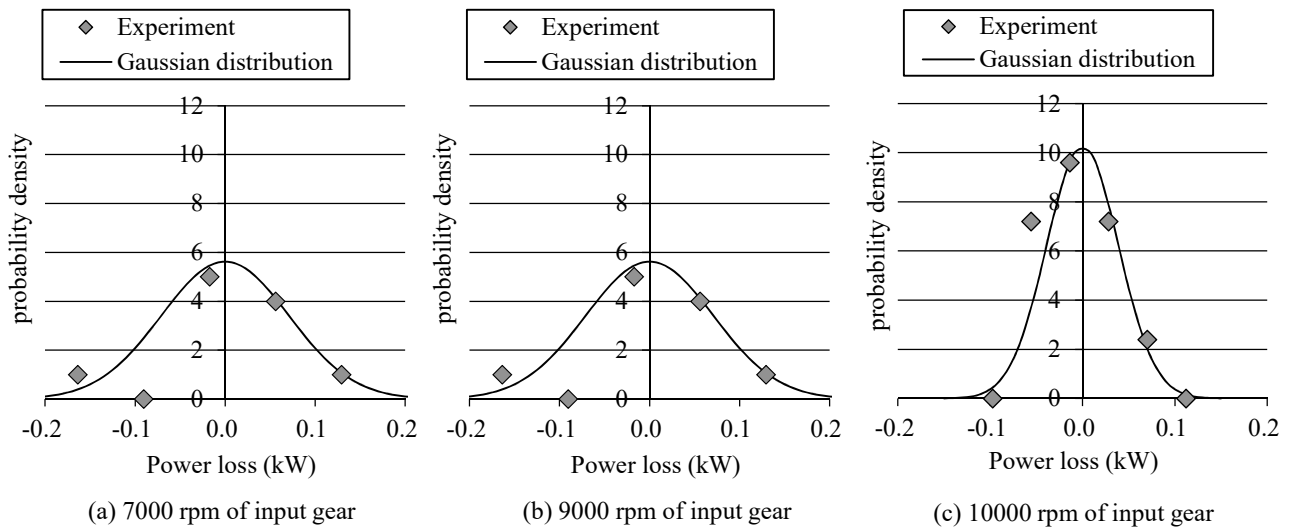
Fig. 3.6-2 Experimental results on the probability density function of the power loss

Table 3.6-1 Experimental results on the standard error of the power loss

Speed of input gear	Standard error of 2σ in 3 times measurement
7000 rpm	0.082 kW
9000 rpm	0.055 kW
10000 rpm	0.044 kW

3.6.1.2   Example of the Process of Separation to Aerodynamic and Oil Dynamic Loss, and the Results of the Separation

Figure 3.6-3 (a) shows an example of the experimental evaluation of the loss with zero oil-supply flow rate, and Fig. 3.6-3 (b) shows an example of the experimental evaluation of the loss with zero oil-supply flow rate and zero air pressure. In Fig. 3.6-3 (a), the loss with zero oil-supply flow rate was obtained by extrapolating the experimental results obtained by changing the oil-supply flow rate at each rotational speed condition. In Fig. 3.6-3 (b), the loss with zero oil-supply flow rate and zero air pressure was obtained by extrapolating with the losses at 1.0 and 0.5 bar.

(a) Evaluation of zero oil-supply loss

(b) Evaluation of zero oil-supply vacuum loss
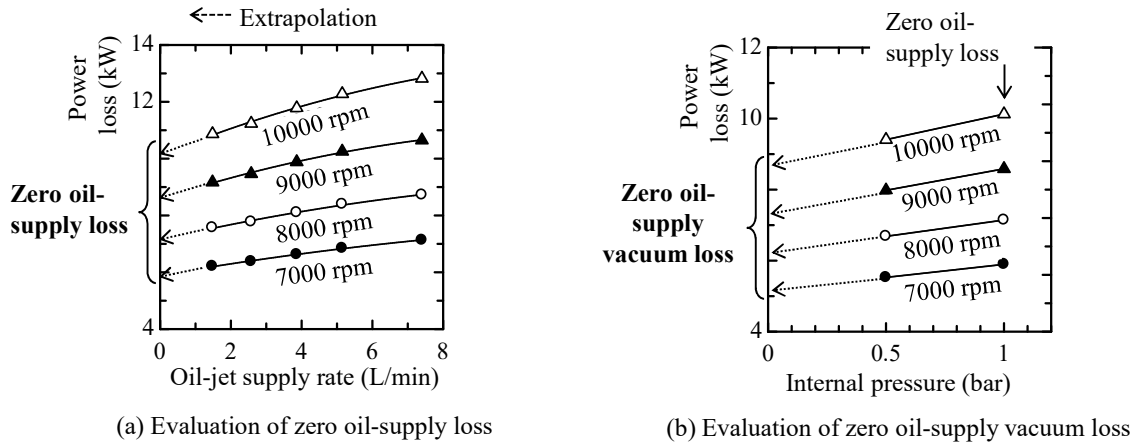
Fig. 3.6-3 Examples of experimental results for zero oil-supply and zero oil-supply vacuum losses, Shroud 2

(a) Power loss with speed changes, Shroud 1, oil supply 7.40 L/min

(b) Power loss with speed changes, Shroud 1, oil supply 3.85 L/min

(c) Power loss with oil supply rate changes, Shroud 1, input speed 10000 rpm

(d) Power loss with speed changes, Shroud 2, oil supply 7.40 L/min

(e) Power loss with speed changes, Shroud 2, oil supply 3.85 L/min

(f) Power loss with oil supply rate changes, Shroud 2, input speed 10000 rpm

Fig. 3.6-4 Experimental results of fluid dynamic, aerodynamic, and oil dynamic losses

In Fig. 3.6-3 (b), only two measurement points were obtained at each rotational speed condition. However, we considered it possible to estimate the loss with zero oil-supply flow rate and the loss with zero air pressure owing to the aerodynamic loss being proportional to the air density, as described in Chapter 2. In contrast, the results should be carefully considered as there may have errors in the extrapolation.

The experimental results of power loss are shown in Fig. 3.6-4 . Figures 3.6-4 (a) to (c) show the results with Shroud 1, and (d) to (f) show the results with Shroud 2. Figures 3.6-4 (a) and (d) show the fluid dynamic, aerodynamic, and oil dynamic losses at an oil-supply flow rate of 7.40 L/min and a rotational speed of 7000–10000 rpm. Figures 3.6-4 (b) and (e) show the losses at an oil-supply flow rate of 3.85 L/min and a rotational speed of 7000–10000 rpm. Figures 3.6-4 (c) and (f) show the losses at an oil-supply flow rate of 1.48–7.40 L/min at a rotational speed of 10000 rpm. Considerations on these power losses are described in Chapter 5.

3.6.2 Validation of the Measurements Method for Oil Fraction and Mixture Velocity

3.6.2.1 Calibration Results for Oil fraction

(1) Calibration Curve and Measurement Accuracy of Oil Fraction

The calibration curve for the oil fraction is shown in Fig. 3.6-5 . The horizontal axis represents the measured value of the oil fraction, and the vertical axis represents the setting value of the oil fraction. As indicated by "A" in the figure, the calibration curve is lower than the line of "measured value = setting value". That is, the measured value is larger than the setting value, resulting in a large amount of oil being sucked. The measured value "B" around the measured value 60% exhibits variations that do not follow the calibration curve.

The calibration results of measurement values using this calibration curve are shown in Fig. 3.6-6 . The details of measurement errors are shown in Table 3.6-2 . The measurement error (standard deviation) was 13.4%, which satisfied the 15% or less target. Therefore, this measurement method is considered to have practical accuracy.
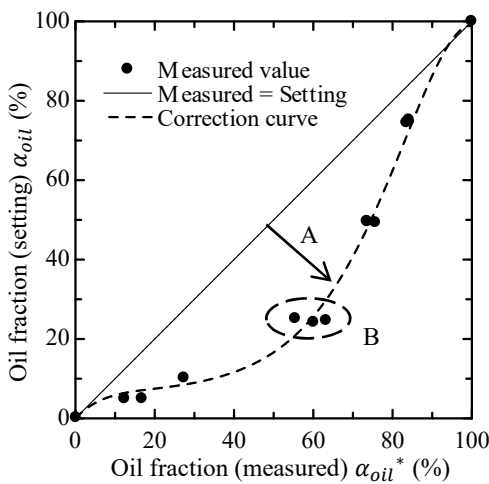
Fig. 3.6-5 Correction curve for the oil fraction measurement
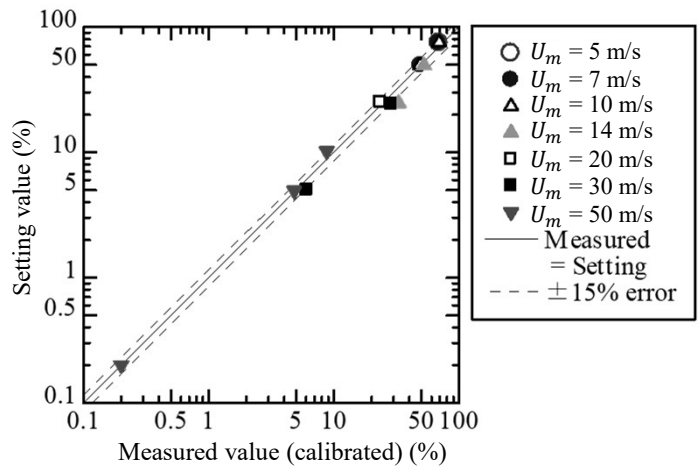
Fig. 3.6-6 Accuracy of the oil fraction measurement

Table 3.6-2 Calibration conditions and errors in the oil fraction measurement

Oil fraction (setting) (%)	Oil fraction (measured) (%)	Error (%)
74.7	69.2	−7.41
74.5	67.9	−8.92
75.2	69.1	−8.10
49.5	48.8	−1.51
49.6	48.6	−2.08
49.3	52.4	6.17
24.7	32.8	33.1
25.2	23.6	−6.35
24.2	28.8	18.8
10.2	8.75	−14.3
4.94	4.82	−2.47
4.99	6.07	21.4
0.20	0.20	−0.50
	Standard deviation	13.4

(2)   Consideration of the Shape of the Calibration Curve for the Oil Fraction

The shape of the calibration curve for the oil fraction (Fig. 3.6-5) is discussed. A comparison of the shape of a typical isokinetic suction probe and that of the probe in this research is shown in Fig. 3.6-7 . Figure 3.6-7 (a) shows a typical isokinetic suction probe with pressure measuring holes on the outer and inner walls of the probe in a direction perpendicular to the flow. With these pressure holes, the static pressures of the external and internal flows can be measured. Isokinetic suction is possible by equalizing the static pressures of the external and internal flows. In contrast, the probe used in this research, shown in Fig. 3.6-7 (b), cannot measure the static pressure outside the probe because the probe wall has no measuring hole. Because the pressure measuring hole (it is also used as a suction hole) is directed against the flow, the total pressure of the flow is measured in this measuring hole.

Figure 3.6-8 shows a reason of the pressure measurement differences between Fig. 3.6-7 (a) (a typical isokinetic suction probe) and Fig. 3.6-7 (b) (the probe in this research). Because the pressure inside the probe is set to atmospheric pressure, the pressure is higher than the pressure of the external flow (static pressure) by the dynamic pressure. Here, as shown in Fig. 3.3-1 (c), the probe suction flow is considered to be slower than the external flow, resulting in non-isotropic suction in which more oil particles are detected. This may be the cause of "A" in Fig. 3.6-5 .

Next, we consider the cause of "B" in Fig. 3.6-5 . Because each point in "B" has a different flow velocity, the dynamic pressure shown in Fig. 3.6-8 may be different in the detection of the pressure at the probe measuring hole in this research. We infer that this causes a change in the intensity of the non-isotropic suction, i.e., the degree to which many oil particles were detected, resulting in a variation in "B".

(a) General isokinetic suction probe   (b) Isokinetic suction probe for a gearbox
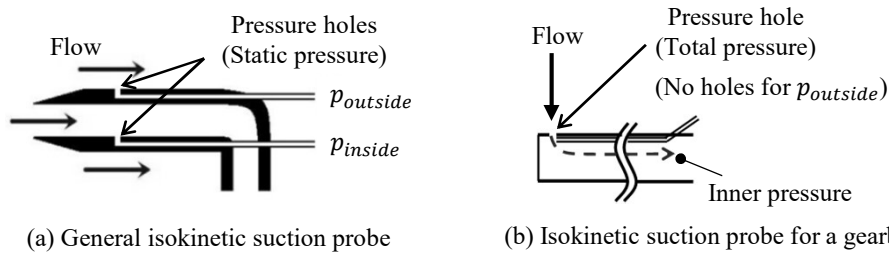
Fig. 3.6-7 Comparison of a general sampling probe and a sampling probe for a gearbox
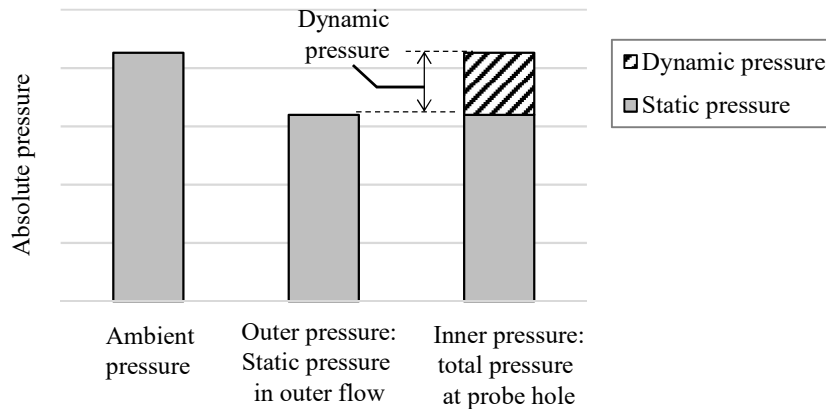
Fig. 3.6-8 Outer and inner pressures anticipated around the sampling probe for a gearbox

3.6.2.2   Calibration Results for Mixture Velocity

(1)   Simple Calibration Curve for Mixture Velocity and Measurement Accuracy

Calibration curves evaluated based on the simplified calibration method for mixture velocity (Section 3.3.2.2 (4)) are shown in Fig. 3.6-9 . The horizontal axis indicates the Lockhart–Martinelli parameter obtained from the measured oil fraction and measured mixture velocity ("measured Lockhart–Martinelli parameter"). The vertical axis indicates the Lockhart–Martinelli parameter obtained from the setting oil fraction and setting mixture velocity. Figure 3.6-9 shows that the calibration curve is near linear. As indicated by "A" in Fig. 3.6-9 , the measured value becomes larger than the setting value when the horizontal axis value is approximately 2 or more. This may be because the measured oil fraction is included in the "measured Lockhart–Martinelli parameter," and due to the phenomenon that more oil particles are detected because the probe suction flow speed is slower than the external flow speed in the oil fraction measurement as described in Section 3.6.2.1.

The results of calibrating the mixture velocity using this calibration curve are shown in Fig. 3.6-10 . The measurement error (standard deviation) was 23%, which did not satisfy the target of 15% or less. This is because the "measured Lockhart–Martinelli parameter" contained two types of measured values (measured oil fraction and measured mixture velocity), which both had measurement errors. Therefore, the accuracy of calibration can be enhanced by developing a calibration method using only the measured mixture velocity as a parameter.
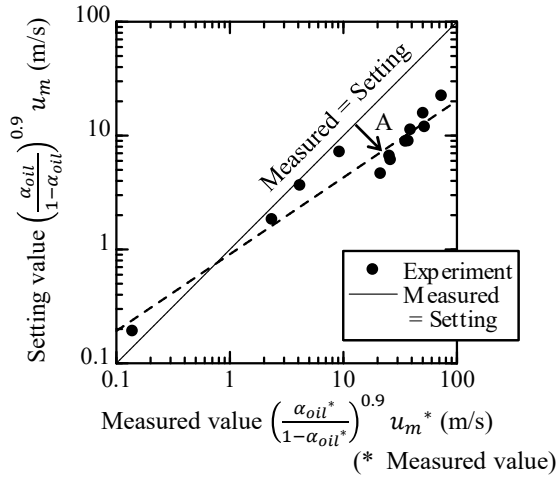
Fig. 3.6-9 Simple correction curve for mixture velocity
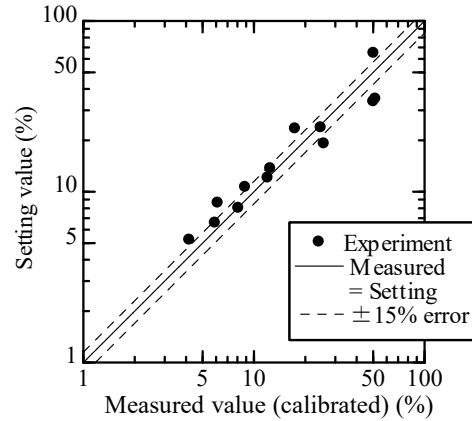
Fig. 3.6-10 Accuracy of the mixture velocity measurements by applying the simple correction curve

(2)   High-Accuracy Calibration Curve and Measurement Accuracy for Mixture Velocity

The characteristics of the measured mixture velocity are shown in Fig. 3.6-11 . The horizontal and vertical axes show the measured and setting mixture velocities, respectively. The oil fraction in the legend indicates the setting values. We observe that the measured mixture velocity is proportional to the setting mixture velocity if the setting oil fraction is the same. Figure 3.6-12 shows a graph with the oil fraction and setting mixture velocity/measured mixture velocity on the horizontal and vertical axes, respectively. The function becomes convex upward in the range in which the oil fraction is less than 25% and convex downward in the range in which the oil fraction is greater than 25%.
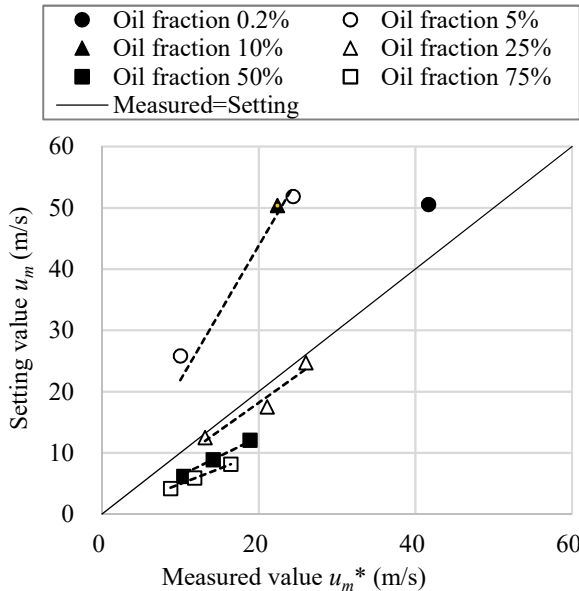
Fig. 3.6-11 Linear correlations between measurement and setting values of the mixture velocity
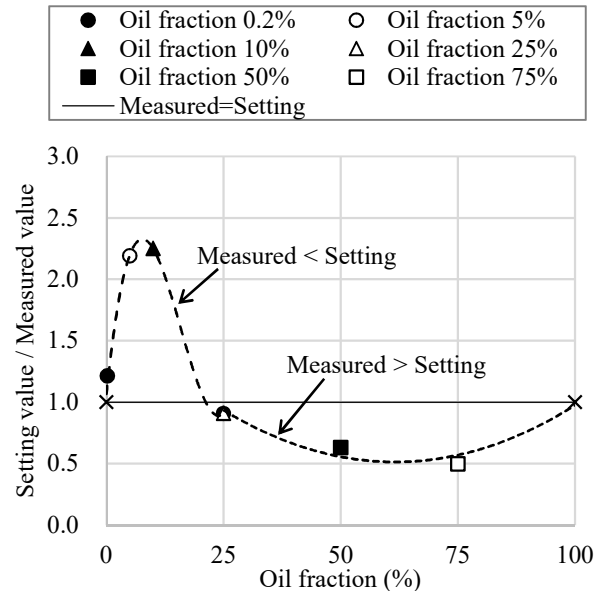
Fig. 3.6-12 High-accuracy correction curve for the mixture velocity

The calibration results of the measured mixture velocity using the function as a "high-accuracy calibration curve" are shown in Fig. 3.6-13 . Measurement errors under each measurement condition are shown

in Table 3.6-3 . The table also shows the accuracy when the simple calibration method is used. As a result of calibrating using the high-accuracy calibration curve, the measurement error (standard deviation) becomes 9.3%, satisfying the target of 15% or less. The improvement in accuracy compared with the simple calibration method is considered to be due to the measured value being used for the oil fraction in the simple calibration curve (Fig. 3.6-9), while the calibrated value is used for the oil fraction in the high-accuracy calibration curve (Fig. 3.6-12), which reduces the error caused by the oil fraction. In the meantime, it is necessary to examine the validity and generality, because the curve of the high-accuracy calibration curve is not a general curve.

Table 3.6-3 Calibration conditions and errors in the mixture velocity measurements
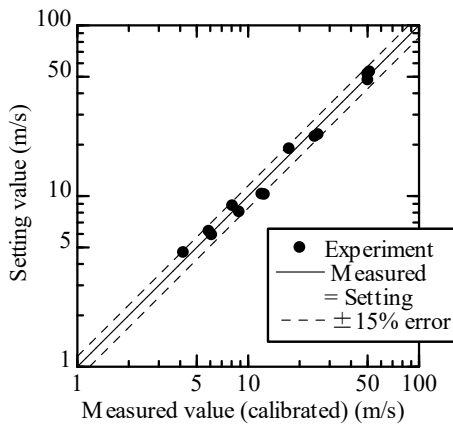
Fig. 3.6-13 Accuracy of the mixture velocity measurements by applying the high-accuracy correction curve

Setting	Measured value (calibrated)			
	Simple method		High-accuracy method	
Mixture velocity	Mixture velocity	Error	Mixture velocity	Error
m/s	m/s	%	m/s	%
4.20	5.21	24.1	4.64	−10.5
5.94	6.56	10.5	6.19	−4.34
8.15	8.00	−1.86	8.73	−7.10
6.16	8.58	39.3	5.88	4.54
8.92	10.61	18.9	8.03	10.0
12.1	12.0	−0.55	10.2	15.7
12.5	13.6	8.89	10.2	18.9
17.5	23.4	33.4	18.8	−7.59
24.7	23.7	−4.26	22.2	10.3
50.4	33.6	−33.2	51.7	−2.64
51.8	34.9	−32.7	53.2	−2.53
25.8	19.1	−26.1	22.8	11.7
50.5	64.7	28.1	47.5	5.95
	Standard deviation	23.4	Standard deviation	9.3

(3) Consideration of the Shape of High-Accuracy Calibration Curve of Mixture velocity
The high-accuracy calibration curve for the mixture velocity shown in Fig. 3.6-12 has a convex upward region and a convex downward region. Therefore, the two types of phenomena may overlap. As phenomena affecting the shape of the calibration curve, the characteristics of the dynamic pressure conversion of a droplet impinging on the probe measuring hole and the velocity slip between gas velocity and liquid velocity are considered. We will attempt to explain the shape of the calibration curve from qualitative studies of the two types of phenomena.

(i) Characteristics of Dynamic Pressure Conversion Coefficient of Droplet Impingement
When measuring the mixture velocity, the inside of the probe is filled with stationary oil to form a total-pressure measuring tube. The momentum conversion coefficient is used as an index of the conversion of the droplet momentum into the dynamic pressure when the droplet collides with the

liquid surface. The momentum conversion coefficient of the droplet impingement varies depending on the condition of collision of the droplet with the liquid surface.

The total pressure (p_{total}), which is the sum of the dynamic pressure induced by airflow and the dynamic pressure induced by droplet impingement, is given by the following equation [72].

$$p_{total} = \frac{1}{2}\rho_{air}u_{air}{}^2 + c\frac{\dot{m}_{oil}u_{oil}}{A_{hole}} \tag{3.20}$$

where ρ_{air} is the air density, u_{air} is the air velocity, c is the momentum transfer coefficient, $\dot{m}_{oil}$ is the mass flow rate of oil, u_{oil} is the oil velocity, and A_{hole} is the cross-sectional area of the probe measuring hole. The first and second terms on the right side of the equation are the dynamic pressures generated by the airflow and by the droplet impingement, respectively. If the droplet is completely stopped on the liquid surface, the momentum transfer coefficient c is 1.

The dynamic pressure generated by the droplet impingement in the second term on the right side ($p_{total,oil}$) is given by the following equation using $\dot{m}_{oil} = \rho_{oil}u_{oil}A_{hole}$ (ρ_{oil} is the oil density).

$$p_{total,oil} = c\frac{\dot{m}_{oil}u_{oil}}{A_{hole}} = \frac{\rho_{oil}u_{oil}A_{hole} \cdot u_{oil}}{A_{hole}} = c\rho_{oil}u_{oil}{}^2 \tag{3.21}$$

Comparing the above equation with Bernoulli's principle, we observe that $c = 0.5$ is obtained when droplets collide continuously, as in an oil flow.

To understand the characteristics of the momentum transfer coefficient, we performed a numerical simulation. The numerical simulation method described in Chapter 4 was used. The applicability of the method to simulate droplet behavior has been verified by conventional studies [100][*1]. The simulation model is shown in Fig. 3.6-14 . The shape of the tip of the two-phase flow probe in this research was modeled to have a cylinder with an outer diameter of 5 mm and a measuring hole of 1 mm. The droplets were impinged perpendicularly to the cross-section of the measuring hole. The inside of the measuring hole was modeled as a short cylinder, and the pressure was output at the bottom of the cylinder. Figure 3.6-15 shows the calculation mesh and boundary conditions. The calculation mesh size was 0.1 mm and the number of calculation cells was 115200. The pressure boundaries were defined around the calculation mesh.

Table 3.6-4 shows the calculation conditions. The droplet size was set to 0.2–0.8 mm, the oil fraction was set to 0.0147–0.857, and the particle velocity was set to 2 m/s. The oil fraction was obtained from the volume fraction of the oil in the cylinder obtained by extending the cross-section of the measuring hole perpendicular to the section at the beginning of the calculation. The droplet velocity was determined to ensure calculation stability.

[*1] The conventional research here is the same as the method of this research except that the calculation accuracy of the gas–liquid interface was improved using the normal vector of the liquid surface. Therefore, the results obtained using the methods in this research are considered to be qualitatively equivalent to those obtained using conventional research methods.
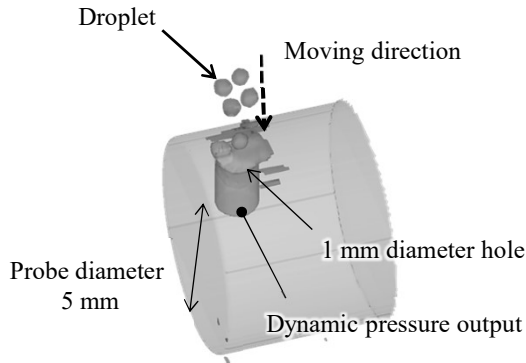
Fig. 3.6-14 Calculation model for droplet impact simulation

(a) Side view   (b) Top view
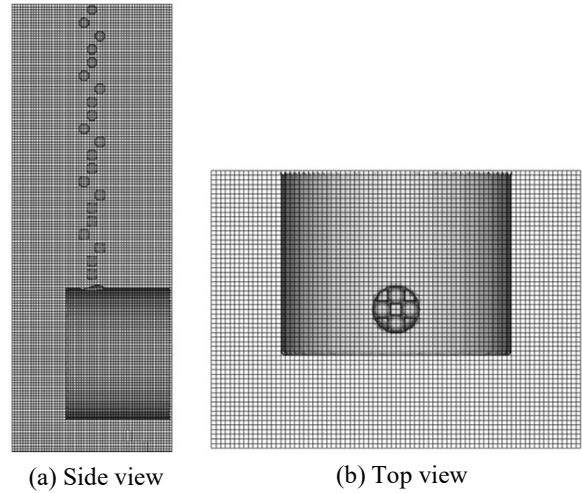
Fig. 3.6-15 Calculation mesh for droplet impact simulation

Table 3.6-4 Calculation conditions for droplet impact simulation

Droplet diameter (mm)	Oil fraction (%)	Droplet velocity (m/s)
0.2	1.47	
0.4	10.3	
0.6	31.2	2 m/s
0.8	57.6	
0.6	85.7	

The results of the simulation of the momentum transfer coefficient are shown in Fig. 3.6-16 . The momentum transfer coefficient $c = 0.5$ was added at oil fractions of 0% (air only) and 100% (oil only), and an approximate curve was obtained by including these additions. The figure shows that the momentum transfer coefficient became maximum at an oil fraction of approximately 30%.

To understand the cause of the tendency of the momentum transfer coefficient, the velocity contours for each calculation condition are shown in Fig. 3.6-17 , and the pressure contours are shown in Fig. 3.6-18 . The results for each oil fraction condition are shown in (a) to (e) in Figs. 3.6-17 and 3.6-18 . In the pressure contours (Fig. 3.6-18), the pressures on the gas–liquid interface were almost the same and it was difficult to consider the difference of the pressure. Therefore, the velocity contours (Fig. 3.6-17) were used for consideration.

At a velocity contour with an oil fraction of 1.47% (Fig. 3.6-17 (a)), a large deformation of the liquid surface was observed accompanying the collision of droplets. The deformation of the liquid surface was considered to be a result of the momentum transfer of a part of the impinging momentum of the liquid surface. Therefore, the pressure generated by momentum transfer at the time of liquid surface collision probably decreased, and the momentum transfer coefficient ("A" in Fig. 3.6-16) decreased below 1.

At a velocity contour with an oil fraction of 31.2% (Fig. 3.6-17 (c)), we observed that the deformation of the liquid surface was small and the liquid stripped off from the wall after colliding with the liquid surface. Because the deformation of the liquid surface was small, the momentum of the droplet was

considered to be almost converted to pressure. Therefore, the momentum transfer coefficient ("B" in Fig. 3.6-16) was considered to be approximately 1.

At a velocity contour with an oil fraction of 85.7% (Fig. 3.6-17 (e)), the deformation of the liquid surface was small, but the momentum remained in the liquid after the collision. Therefore, all the momentum of the droplet was probably not converted to pressure, and the momentum transfer coefficient ("C" in Fig. 3.6-16) was below 1.

The above results indicate that the momentum transfer coefficient decreased owing to the deformation of the liquid surface when the oil fraction was small, and it decreased owing to the remaining momentum in the liquid after collision when the oil fraction was large.
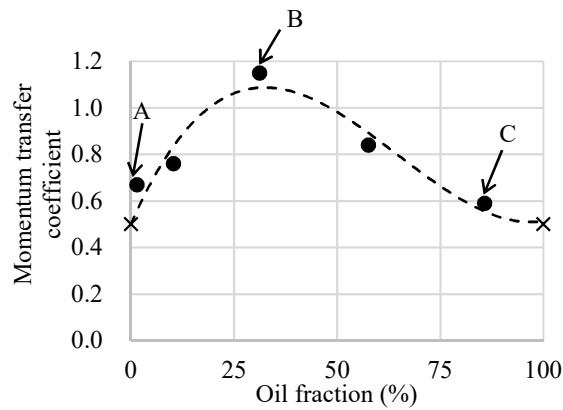
Fig. 3.6-16 Moment transfer coefficients for droplet impact (simulation results)

(a) Oil fraction 1.47%

(b) Oil fraction 10.3%

(c) Oil fraction 31.2%

(d) Oil fraction 57.6%

(e) Oil fraction 85.7%
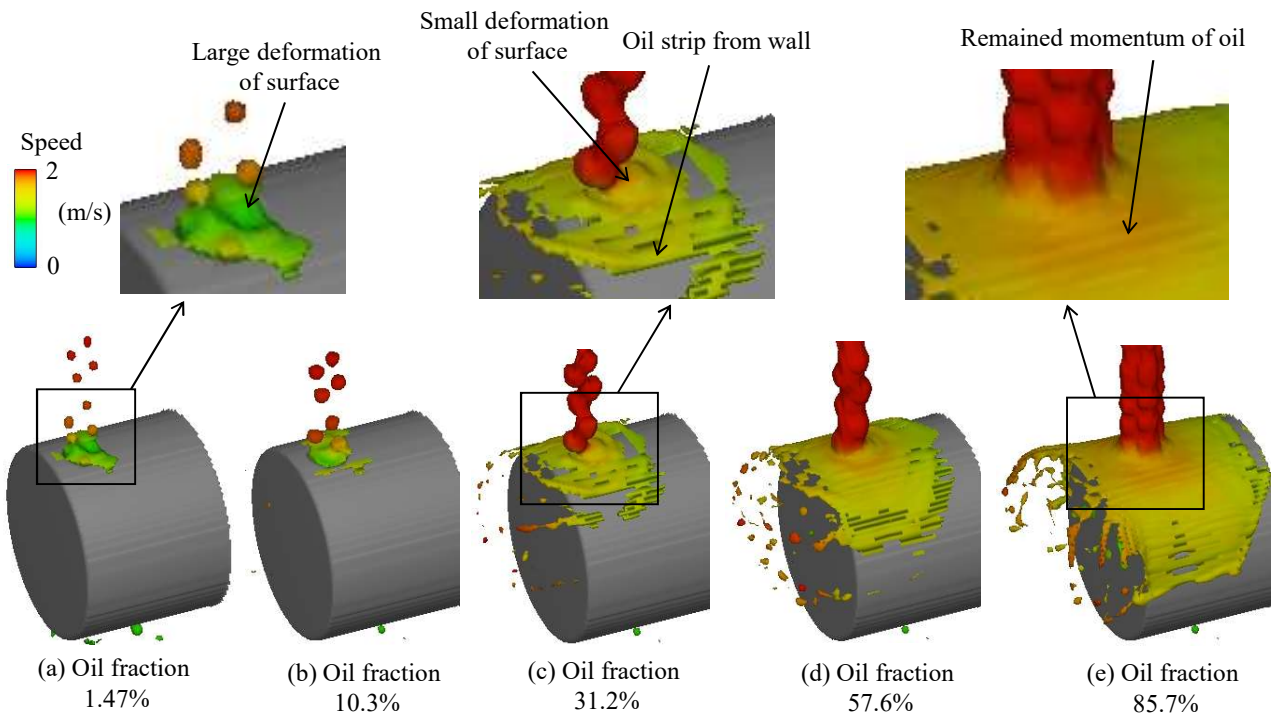
Fig. 3.6-17 Velocity contour on iso-surface of 50% oil in the calculation cell (simulation results)

(a) Oil fraction 1.47% (b) Oil fraction 10.3% (c) Oil fraction 31.2% (d) Oil fraction 57.6% (e) Oil fraction 85.7%
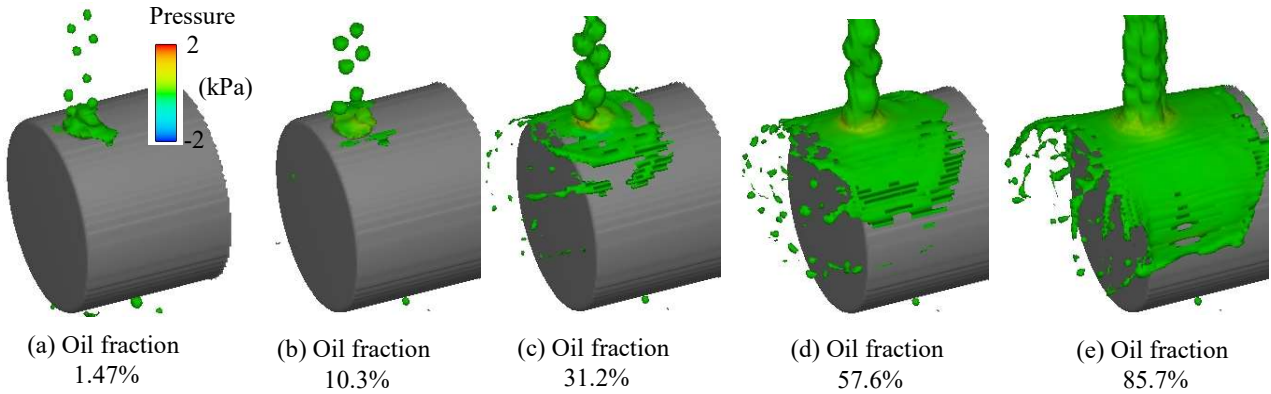
Fig. 3.6-18 Pressure contour on iso-surface of 50% oil in the calculation cell (simulation results)

(ii) Characteristics of Gas–liquid Interface Slip of Velocity

Figure 3.6-19 shows an example of the results of experiments conducted in the past on the velocity difference between the gas and liquid phases (velocity slip) when air and water were used. The horizontal axis is the air/liquid flow rate, and the vertical axis is the air/droplet velocity (gas–liquid velocity ratio), where the Froude number (Fr) is defined by the following equation:

$$\text{Fr} = \frac{v_a{}^2}{g D_e} \tag{3.22}$$

where v_a is the apparent velocity of the liquid, g is the gravitational acceleration, and D_e is the equivalent diameter of the cylindrical pipe. When the air flow rate is large relative to the liquid flow rate, that is, the liquid volume fraction is small, the gas velocity relative to the liquid velocity increases. The slower the apparent velocity of the liquid, the smaller the Froude number and the larger the gas velocity relative to the liquid velocity.
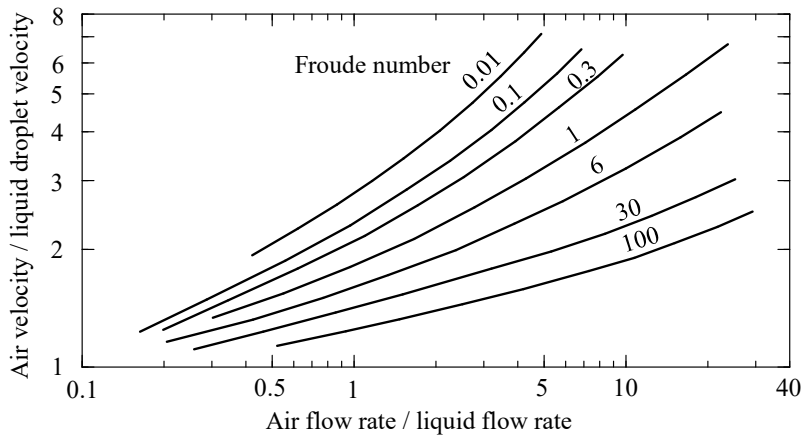
Fig. 3.6-19 Experimental results on velocity slip between air and liquid (water) [101]

(iii) Consideration of the Shape of the Calibration Curve

Using the momentum transfer coefficient of the droplet and the gas–liquid slip velocity, the cause of the shape of the high-accuracy calibration curve of the mixture velocity is considered here. First, the influences of the momentum transfer coefficient of the droplet and the gas–liquid slip velocity are formulated. The setting mixture velocity $(u_{m,set})$/the measured mixture velocity $(u_{m,mes})$ becomes the

following equation using $\rho_{m,corr} \simeq \rho_{m,set}$ (the calibrated density and the setting density are equivalent).

$$\frac{u_{m,set}}{u_{m,mes}} = \sqrt{\frac{\Delta p_{set} / \left(\frac{1}{2}\rho_{m,set}\right)}{\Delta p_{mes} / \left(\frac{1}{2}\rho_{m,corr}\right)}} \simeq \sqrt{\frac{\Delta p_{set}}{\Delta p_{mes}}} \tag{3.23}$$

Here, the definition of mixture velocity in which the flow rates of air and oil are the same ($u_{air} = u_{oil} = u_m$) is used for Δp_{set}. That is,

$$\Delta p_{set} = \frac{1}{2}\alpha_{oil}\rho_{oil}u_{oil}{}^2 + \frac{1}{2}(1-\alpha_{oil})\rho_{air}u_{air}{}^2 = \frac{1}{2}\alpha_{oil}\rho_{oil}u_m{}^2 + \frac{1}{2}(1-\alpha_{oil})\rho_{air}u_m{}^2 \tag{3.24}$$

For Δp_{mes}, consider the phenomena of the momentum transfer of droplets and gas–liquid velocity slip. Eq. 3.21 of dynamic pressure generated when droplets collide with the probe holes is used. Subsequently, the following equation is derived [*2].

$$\Delta p_{mes} = c\,\alpha_{oil}\rho_{oil}u_{oil}{}^2 + \frac{1}{2}(1-\alpha_{oil})\rho_{air}u_{air}{}^2 \tag{3.25}$$

The velocity of the air (u_{air}) is assumed to be equivalent to the mixture velocity ($u_{air} \simeq u_m$). The oil velocity (u_{oil}) is expressed by the following equation using the slip ratio s (= air velocity/droplet velocity).

$$u_{oil} = \frac{u_{air}}{s} \simeq \frac{u_m}{s} \tag{3.26}$$

Substituting these into Eq. 3.25 yields the following expression:

$$\Delta p_{mes} = \left(\frac{2c}{s^2}\right)\frac{1}{2}\alpha_{oil}\rho_{oil}u_m{}^2 + \frac{1}{2}(1-\alpha_{oil})\rho_{air}u_m{}^2 \tag{3.27}$$

Substituting Eqs. 3.24 and 3.27 into Eq. 3.23, the following equation is obtained:

$$\frac{u_{m,set}}{u_{m,mes}} \simeq \sqrt{\frac{\Delta p_{set}}{\Delta p_{mes}}} \simeq \sqrt{\frac{\alpha_{oil}\rho_{oil} + (1-\alpha_{oil})\rho_{air}}{(2c/s^2)\,\alpha_{oil}\rho_{oil} + (1-\alpha_{oil})\rho_{air}}} \tag{3.28}$$

Using the simulation results of the momentum transfer coefficient (c) of the droplet described in (i) above and the gas–liquid velocity slip ratio (s) in (ii), $u_{m,set}/u_{m,mes}$ is calculated using Eq. 3.28. A comparison of the calculation result with the experimental results of this research is shown in Fig. 3.6-20 . The figure shows that the tendency that became convex upward at an oil rate of 20% or less and the tendency that became convex downward at an oil rate of 20% or more qualitatively agreed with the calculation and experimental results. The tendency of the convex upward at the oil fraction less than 20% was primarily affected by s. The tendency of the convex downward at the oil rate above 20% was primarily affected by c. As quantitative differences, we observed that the oil fraction at which the form of the function was switched differed, as indicated by "A" in the figure, and that the setting mixture velocity/measured mixture velocity was underestimated when the oil fraction was large, as indicated by "B". For the cause of "A" in the figure, it is possible that the difference of surface tension and viscosity of oil affected it because the velocity slip ratio diagram of water and air was applied to the velocity slip ratio of oil and air. Regarding the cause of "B" in the figure, the momentum transfer

---

[*2] Equation 3.20 [72] for the sum of the dynamic pressures of airflow and droplet impingement needs an assumption that the oil fraction α_{oil} is sufficiently smaller than 1. In this study, because the assumption does not hold, the effect of α_{oil} was considered.

coefficient of the droplet may have been underestimated because the condition of the velocity lower than the velocity in the actual gearbox was used in the numerical simulation.

The above results indicate that the shape of the mixture velocity calibration curve is due to the tendencies of the velocity slip ratio and momentum transfer coefficient. Because the shape of the mixture velocity calibration curve can be explained phenomenologically, this calibration curve is considered to be valid. In contrast, this calibration curve is not considered to be general because it is affected by oil specifications and flow speed conditions. Therefore, when it is applied to the gearbox, it is necessary to validate the result from another perspective.
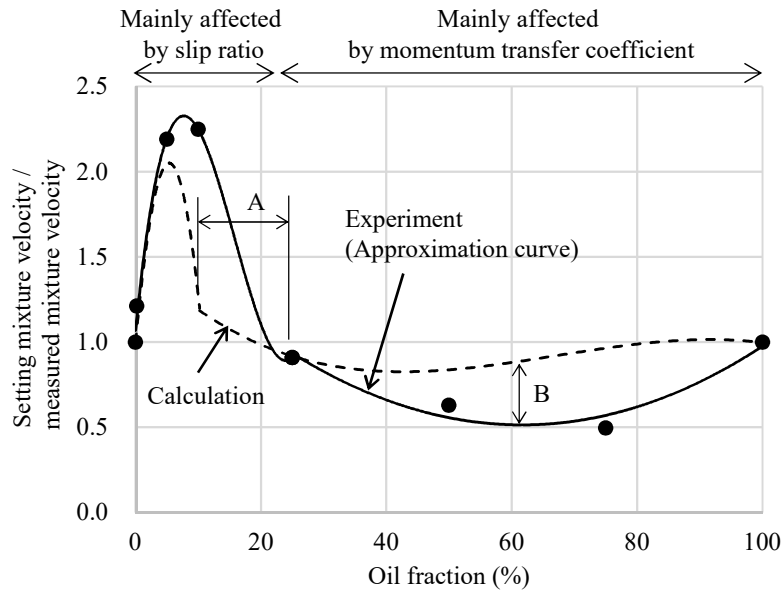
Fig. 3.6-20 Consideration of the correction curve for mixture velocity

3.6.2.3   Measurement Results of Oil fraction and Mixture Velocity around Gears

In this section, the oil fraction calibration method and the high-accuracy mixture velocity calibration method described in Section 3.3.2.2 are applied to the one-axis spur gearbox (GB3, see Section 3.1.2.3) and the results of measurement of the oil fraction and mixture velocity at the gearbox are discussed. To validate the measurement results from a different perspective, we calculated the oil flow rate using the measurement results of the oil fraction and mixture velocity, and we compared it with the oil-supply flow rate.

(1)   Measurement Results of Oil Fraction

The measurement results of the radial distribution of the oil fraction are shown in Fig. 3.6-21 (for the vertical axis in the figure, a linear axis is used in (a) and a logarithmic axis is used in (b)). The oil fraction was high near the wall of the shroud and decreased as the rotational speed increased. The approximate exponential function obtained using the least-squares method is shown in Fig. 3.6-22 .

In the leftmost graph (7000 rpm) in Fig. 3.6-22 (a), the oil fraction distribution was approximated by a single curve. In contrast, the middle graph (8500 rpm) and the right graph (10000 rpm) in Fig. 3.6-22 (a) show that two curves are necessary to approximate the oil fraction distribution. Figure 3.6-22 (b) shows a comparison of the exponents of these approximated curves. For the radial position $r/r_p < 1.15$,

the exponent was almost the same, while for the radial position $r/r_p \geq 1.16$, the exponent varied with the rotational speed. This was considered to be because oil near the shroud wall could not follow the high-speed airflow around the gear at 8500 and 10000 rpm.

(a) Oil fraction distribution with linear scales   (b) Oil fraction distribution with a log scale
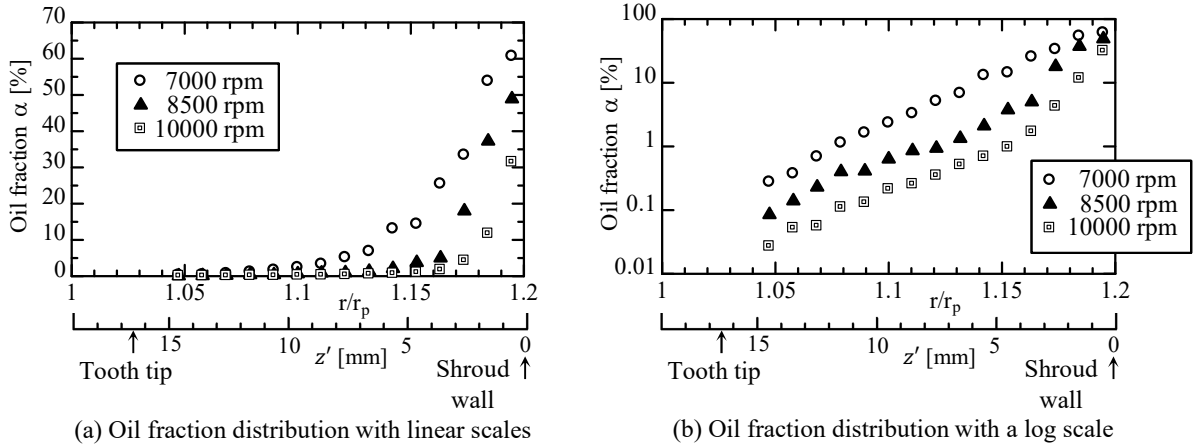
Fig. 3.6-21 Oil fraction distributions measured using a two-phase flow probe

(a) Exponential approximation curves   (b) Comparison of exponents
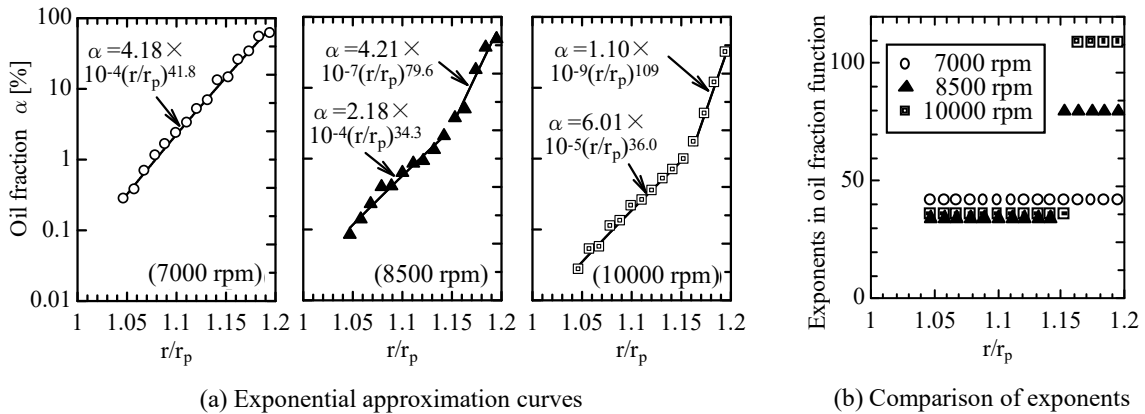
Fig. 3.6-22 Comparisons of exponential approximation curves for measured oil fraction

(2)   Measurement Results of Mixture Velocity and Qualitative Validation of the Measurement Results

Figure 3.6-23 shows the measurement results of the radial distribution of the mixture velocity. For comparison, the results of Massini et al. [33] measuring the velocity distribution of airflow around a spur gear and the results of El Telbany and Relnolds et al. [102] measuring the velocity distribution of turbulent Couette flow are also shown. In the velocity distribution of the turbulent Couette flow, the position of the moving wall was set at the gear tooth tip ($r/r_p = 1.026$, where r is the radial position, r_p is the pitch circle radius), and the position of the stationary wall was set at the shroud inner wall position $r/r_p=1.2$. The turbulent Couette flow is considered to be a "closed channel flow" in which flow is enclosed between the moving and stationary walls. In contrast, the flow when the periphery of the spur gear is not enclosed by a shroud is considered to be "open flow". For the gear in this research, because it was enclosed by a shroud but had an opening in part, it was considered to be a "semi-open channel flow" and the value should

be between the "open flow" and "closed channel flow." Fig. 3.6-23 shows that the velocity distribution around the one-axis spur gear in this research had a value between the open and closed channel flows. Therefore, the measurement result of the mixture velocity around the one-axis spur gear was considered to be qualitatively valid.
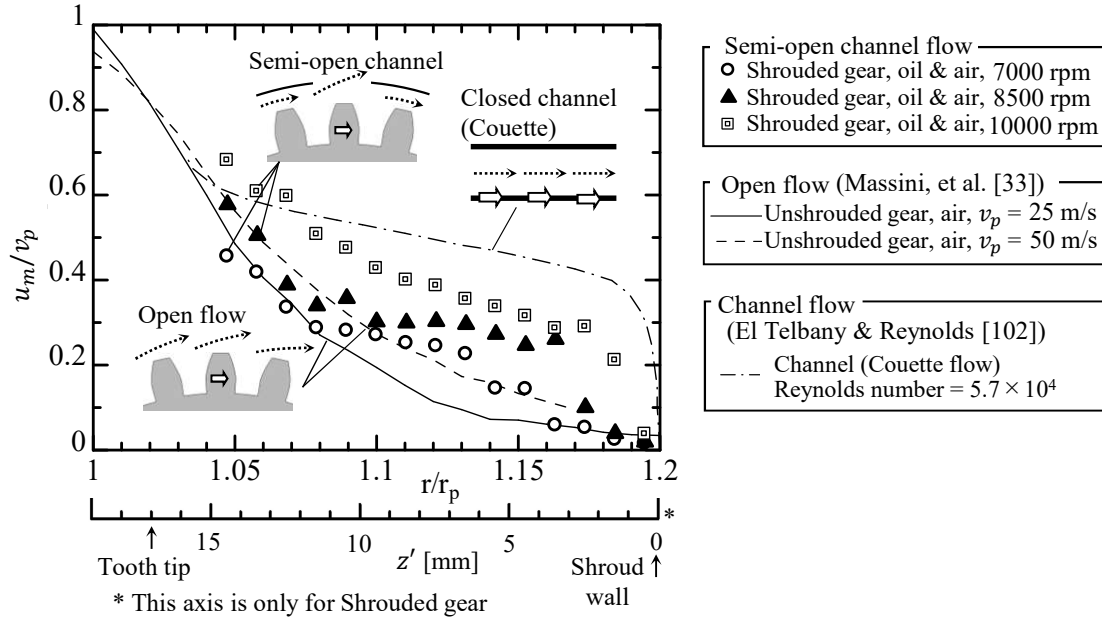
Fig. 3.6-23 Mixture velocity distributions measured using the two-phase flow probe

(3) Measurement Results of Oil Flow Rate and Quantitative Validation of the Measurement Results

To quantitatively validate the measurement results, we calculated the oil flow rate between the gear and shroud using the measurement results of the oil fraction and mixture velocity and compared with it the oil-supply flow rate. The equation for calculating the oil flow rate (Q_{oil}) is

$$Q_{oil} = \sum_{z'=0}^{z_h} \alpha_{oil} u_m W dz' \tag{3.29}$$

where z' is the distance in the gear radial direction with the shroud inner wall position set to zero, z_h is the distance from the shroud inner wall to the gear tooth tip, and W is the width of the shroud inner wall. The definition of the coordinate system is shown in Fig. 3.6-24 .
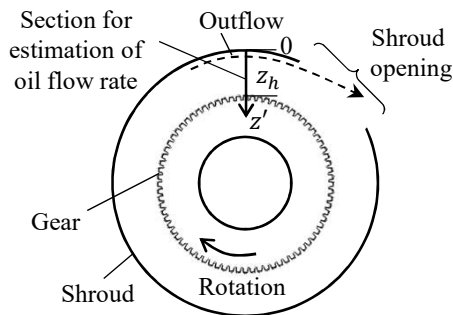
Fig. 3.6-24 Coordinate system

96

Figure 3.6-25 shows the comparison of the oil flow rate evaluated using the above equation with the actual oil-supply flow rate. As the figure shows, the evaluated oil and oil-supply flow rates were approximately the same at 8500 and 10000 rpm. Therefore, the measurement results at 8500 and 10000 rpm were considered to be quantitatively valid.

In contrast, the oil flow rate evaluated at 7000 rpm was 32% higher than the oil-supply flow rate, which was considered to be caused by oil recirculation in the shroud at 7000 rpm. The oil dynamic loss was considered to increase with increasing oil flow rate owing to oil recirculation. Using the theory in Section 2.3, if the oil flow rate is 32% higher, the oil dynamic loss is estimated to increase by 32%.

To confirm this, Fig. 3.6-26 shows the oil fluid dynamic loss. The oil dynamic loss was obtained by subtracting the power loss without oil supply from the power loss with oil supply. The oil dynamic loss was considered to be proportional to the power of 2–3 of the rotational speed based on the theory in Section 2.3. Subsequently, the rotational speed exponent was obtained using the oil dynamic loss at 8500 and 10000 rpm, and the exponent was observed to be 2.4, which was consistent with the theory. When this function with the power loss of the rotational speed exponent was extrapolated to 7000 rpm, the loss at 7000 rpm was observed to be 26% larger as indicated by the arrow in the figure. This was generally consistent with the estimated 32% increase in the oil dynamic loss due to the increase in oil flow rate at 7000 rpm. Therefore, the measurement result seemed to be quantitatively appropriate even at 7000 rpm. The above analysis indicates that the measurement results of the oil fraction and mixture velocity around the gear are quantitatively reasonable.
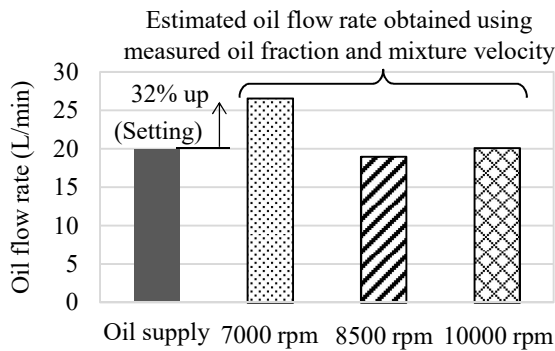
Fig. 3.6-25 Comparison of estimated oil flow rates with respect to the set value of oil supply flow rate
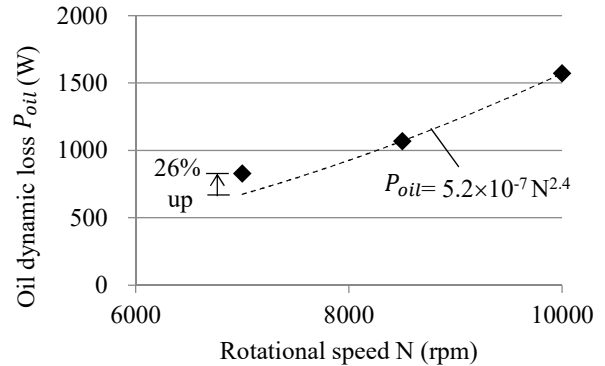
Fig. 3.6-26 Measured oil dynamic loss with respect to rotational speed changes in one-axis spur gearbox (GB3)

(4)   Measurement Result of Oil Velocity (for the Validation of Oil Flow Visualization Method)

The qualitative and quantitative validity of the measurements of oil fraction and mixture velocity are discussed in sections (1) to (3) above. In this section, the measurement result of oil flow velocity using the visualization of the oil flow is evaluated to validate the visualization method. The oil flow velocity is the object of the evaluation because the visualization seemed to capture the oil flow.

As shown in Fig. 3.6-21 , a high oil fraction tended to exist near the shroud wall. To evaluate the existence, we define the distance (z) from the shroud wall where the oil fraction is over a certain range as the oil layer thickness ($\delta_{\alpha_{oil}}$). For example, the distance from the shroud wall where the oil fraction is 10% is defined as the thickness of the oil layer $\delta_{10\%}$. Figure 3.6-27 shows the oil layer thicknesses at 1% oil fraction ($\delta_{1\%}$), 10% oil fraction ($\delta_{10\%}$), and 25% oil fraction ($\delta_{25\%}$). As the rotational speed increased, the thickness of

the oil layer tended to decrease.

Subsequently, to evaluate the velocities in these oil layers, we defined the representative velocities of the oil layers as density-weighted average velocities (u_e) through the following equation (the example of $\delta_{10\%}$ is shown here).

$$u_{e,10\%} = \int_0^{\delta 10\%} \frac{\overline{\rho_m u_m}}{\overline{\rho_m}} dz'$$

(3.30)

Figure 3.6-28 shows the results of u_e. We observe that u_e was considerably slower than the gear peripheral speed. For example, at 8500 rpm, $u_{e,10\%} = 4$ m/s, which was approximately 1/20 of the gear peripheral speed of 85 m/s. Using the results shown in Fig. 3.6-28 , the validation of velocity measurement results using the visualization of oil particles is conducted in Section 3.6.3.2.
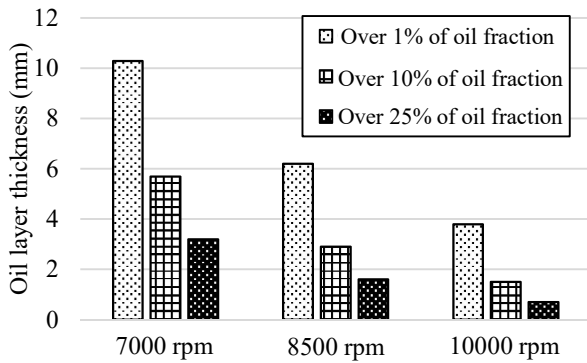
Fig. 3.6-27 Estimated oil layer thickness (experimental results)
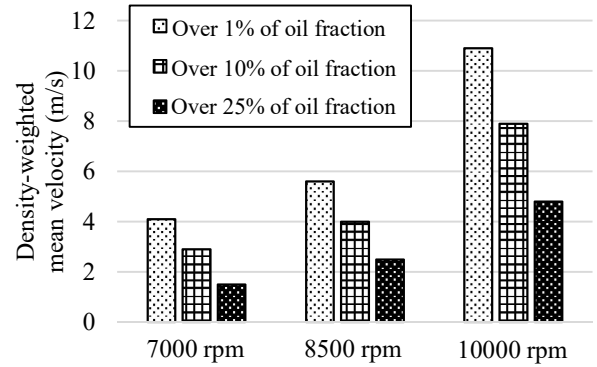
Fig. 3.6-28 Estimated density-weighted mean velocity (experimental results)

3.6.3 Validations of Oil Particles Visualization Method and Oil Particle Velocity Measurement Method

3.6.3.1 Validation of Oil Particle Visualization Method

Images were captured in the one-axis spur gearbox (GB2-1, Section 3.1.2.2) to validate the visualization of oil jet impingement to gear tooth surfaces under the conditions in Table 3.1-6 using the oil particle visualization method (Section 3.4). The airflow rate ejected from the air purge jacket was set to be such that it would not interfere with the flow of oil jets. The results are shown in Fig. 3.6-29 .

Fig. 3.6-29 (a) shows an image of an oil jet impinging near the tip of the gear teeth, and Figs. 3.6-29 (b) and (c) show the images after 0.01 and 0.02 ms, respectively. A schematic of the flow obtained from the image observation is shown in Fig. 3.6-30 . The phenomena are explained using the schematic. The oil jet is divided into "Collision to tooth tip" and "Oil splash" after the collision, and "Oil film" that flows into the tooth surface. The oil that flows into the tooth surface flows toward the bottom of the tooth. "Oil splash" and "Oil film" in Fig. 3.6-30 correspond to "Oil splash" and "Oil film" in Fig. 3.6-29 , respectively.

The phenomenon of oil flowing to the tooth bottom is explained based on the change in oil momentum. For example, in the branch piping, oil flows into the branch with a lower pressure loss. This indicates that the fluid behaves such that the change in momentum is as small as possible. If the oil also behaves to maintain a small change in momentum with respect to the flow of oil on the gear tooth surface, the oil on the tooth surface is

considered to flow to the tooth bottom because the momentum inside in the radial direction (tooth bottom) is smaller than the momentum outside in the radial direction (tooth tip).

(a) 0 s   (b) 0.01 ms   (c) 0.02 ms
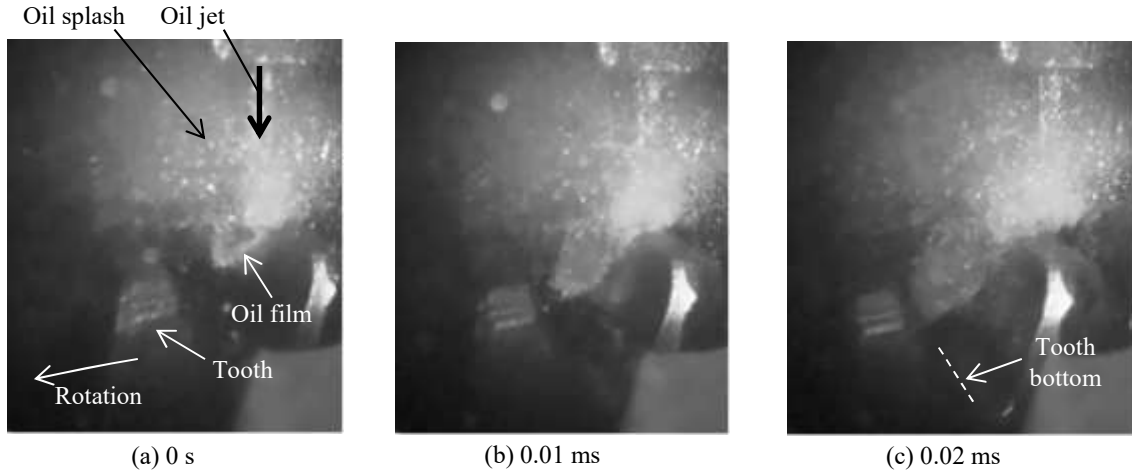
Fig. 3.6-29 Visualization results of the oil jet impingement
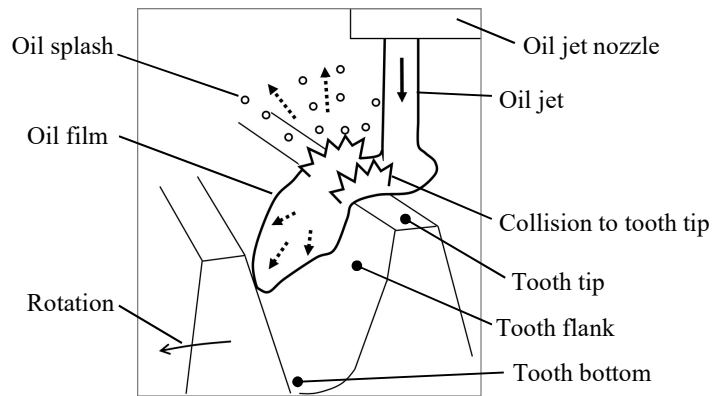
Fig. 3.6-30 Schematic of the oil jet impingement

(a) Oil jet impingement with Volume of Fluid (VOF) Simulation by Fondelli [53]

(b) Oil jet impingement with Smoothed Particle Hydrodynamics (SPH) Simulation by Keller [54]

(c) Oil jet impingement with Lattice Boltzman Method (LBM) by Ambrose [55]
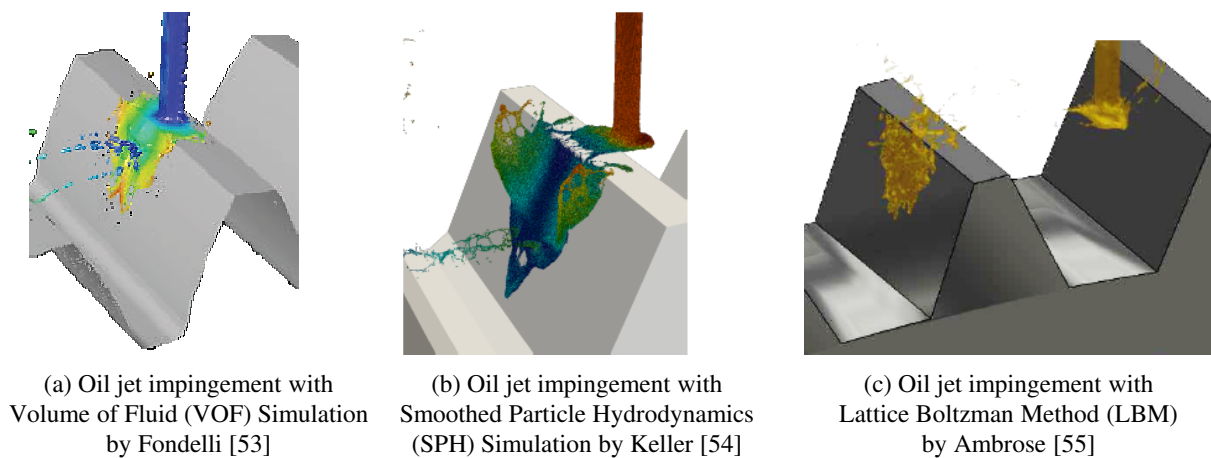
Fig. 3.6-31 Simulation results of an oil jet impingement [53] [54] [55]

Examples of conventional studies are shown in Fig. 3.6-31 , which shows oil flowing into the tooth bottom [53] [54] [55]. The results of these conventional studies were qualitatively consistent with Fig. 3.6-29 of this

research[*3].

From the above results, the results of Fig. 3.6-29 are considered valid. Therefore, we observed that the visualization method of oil particles in this research can remove the influence of oil mist in the gearbox, and it can qualitatively capture the phenomenon of oil flow in an object.

3.6.3.2 Validation of Image Analysis Method for Oil Particle Velocity

In this section, we show that oil flow can be quantitatively evaluated with the velocity measurement method using visualized images of oil particles. For this, we captured photographs under the conditions in Table 3.1-8 using the visualization method of oil particles (Section 3.4) in the one-axis spur gearbox (GB3, Section 3.1.2.3) to validate the image analysis method of the velocity of oil particles. The airflow rate ejected from the air purge jacket was set to a level that did not interfere with the flow of oil jets.

(1) Oil Flow Pattern

Figure 3.6-32 shows the flow from the opening of the shroud. Unsteady flow was observed in images captured from the side ((a) and (b) in the figure). In these images, the radial flow (indicated by the arrow in (a)) and the tangential flow (indicated by the arrow in (b)) overlapped. In the image captured from the upper direction of the opening (c), we observed that the flow was slower at the center of the width of the opening and faster at both ends. The flow patterns of these oil flows are shown in Fig. 3.6-33 .

*…Picture of reverse rotation
(a) Radial flow (side view)

*…Picture of reverse rotation
(b) Tangential flow (side view)

(c) Top view
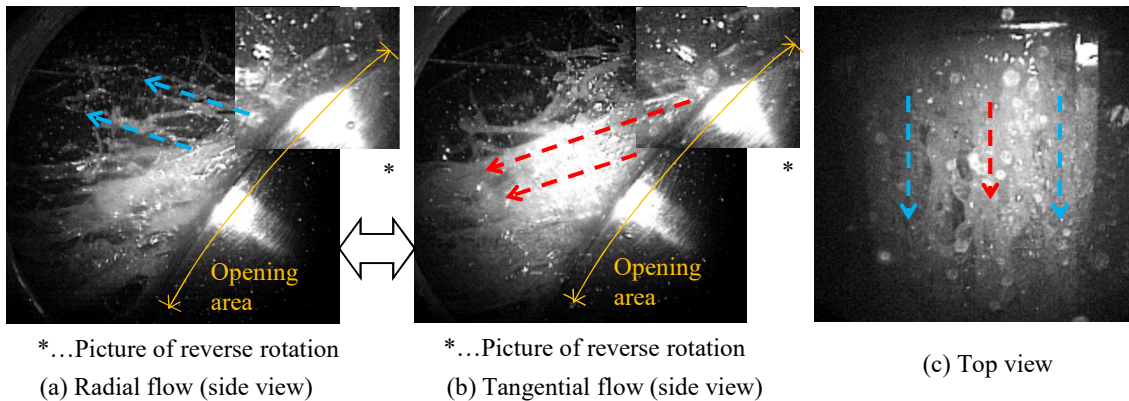
Fig. 3.6-32 Visualizations of oil flow patterns from the shroud opening (7000 rpm)
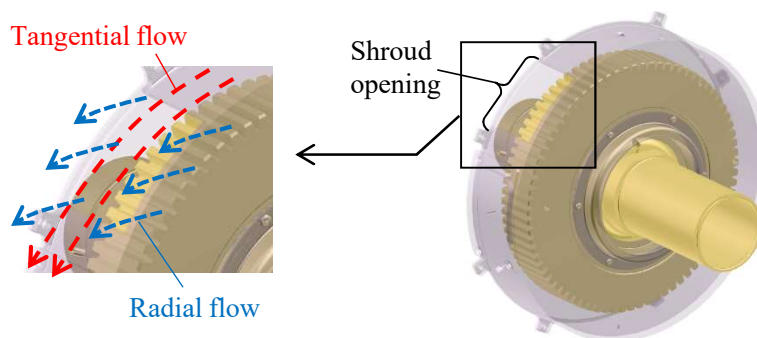
Fig. 3.6-33 Schematic of the oil flow patterns

[*3] Previous studies have shown that each example in Fig. 3.6-31 is calculated based on experimentally validated numerical methods. In contrast, as details of the calculation conditions are not disclosed, qualitative comparisons are conducted here.

(2)   Results of Image Analysis of Oil Flow Velocity

The velocity of oil particles was analyzed from the image of the shroud opening viewed from above using the image analysis method of oil particles described in Section 3.4.2. An example of the points for the image analysis of the movement of oil particles is shown in Fig. 3.6-34 . In (a) in the figure, regarding the oil flow through the shroud opening at 7000 rpm, the analysis start time (0 ms) and the image 2 ms later are shown. The particle was specified at 0 ms to analyze the velocity of the oil particle. Thereafter, the image analysis software automatically followed the oil particle and calculated the velocity from the distance and time of movement. Comparing the position of the oil particle at 0 and 2 ms ("Point" in the figure), we observed that the particle was moving. Similarly, the image processing at the center of the opening at 8500 rpm in (b), at the edge of the opening at 8500 rpm in (c), and at the center of the opening at 10000 rpm in (d) are shown. In every scenario, each position of the oil particle was tracked automatically.

The time histories of the velocity of the oil particles from the results of the automatic tracking of the oil particles are shown in Fig. 3.6-35 . The velocities at the center and edge of the opening are shown at 7000, 8500, and 10000 rpm, respectively. The velocity at the center of the opening was considered to be equal to the velocity of the oil particle from the opening because the velocity at the center of the was almost in the tangential direction (Figs. 3.6-32 and 3.6-33) and because the velocity was captured perpendicular to the tangential direction of the flow of the opening. As Fig. 3.6-35 shows, the velocity fluctuation of the particles at 10000 rpm was large. This velocity fluctuation was a noise caused by the image analysis software erroneously recognizing the oil mist crossing in front of the oil particles. The effect of this noise was reduced by changing the tracked oil particles, measuring five times, and ensemble averaging the obtained time-averaged velocities. For this measurement condition, the error (relative standard error of σ) was 2 to 4%.
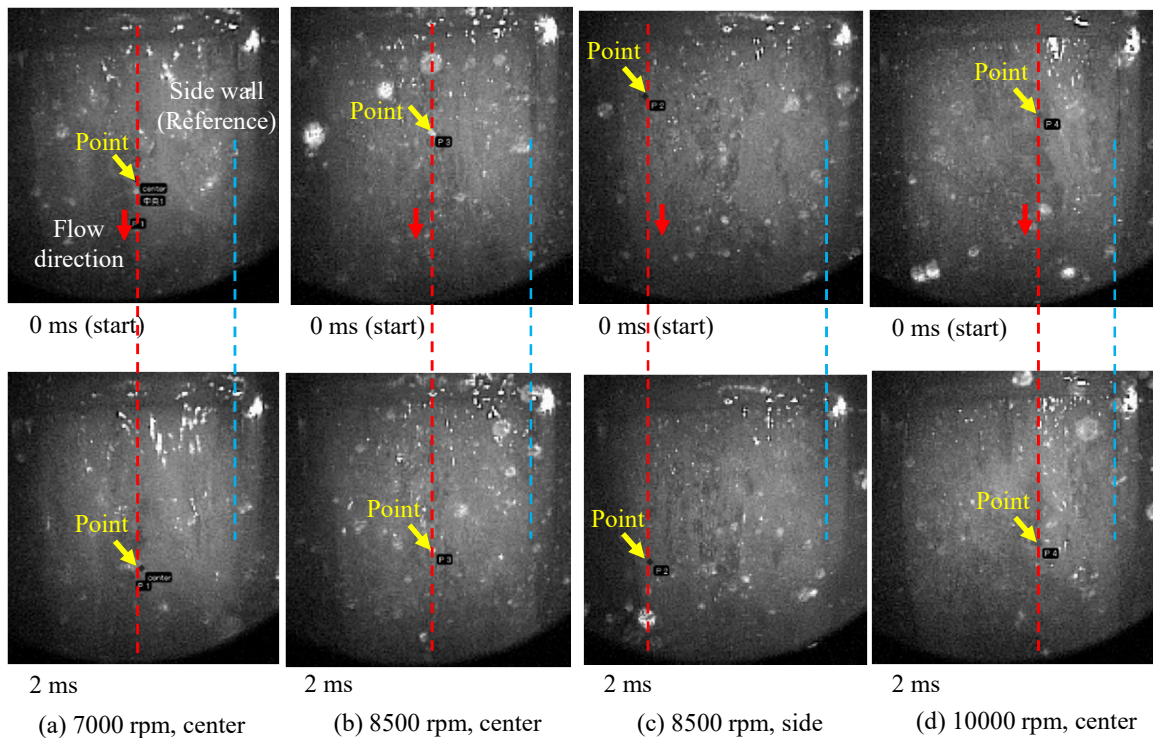
Fig. 3.6-34 Extraction locations for the velocity magnitude of oil particles

The image analysis results of the velocity of oil particles are shown in Fig. 3.6-36 . Compared with the velocity of oil particles at the center of the opening, the velocity at the edge of the opening was slightly larger. We inferred that the flow at the center of the opening was slower because the flow was in contact with the shroud wall for a longer time and decelerated at the wall.
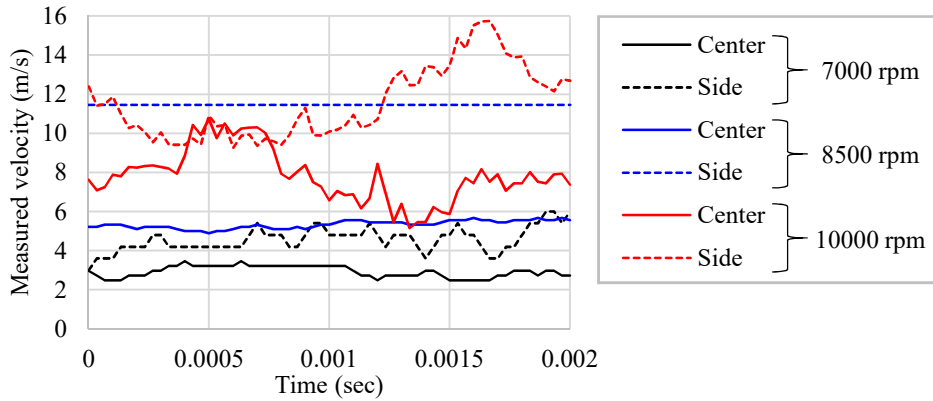
Fig. 3.6-35 Time histories of the measured velocity magnitude of oil particles

| (a) Top view, 7000 rpm | (b) Top view, 8500 rpm | (c) Top view, 10000 rpm |
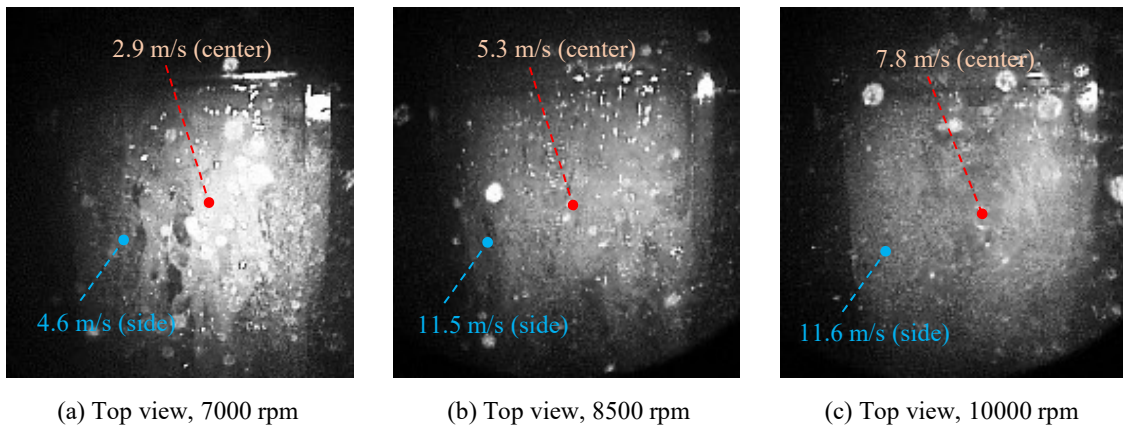
Fig. 3.6-36 Comparisons of measured velocity magnitude at different locations and rotational speeds

(3)   Validation of Results of Image Analysis of Oil Flow Velocity

To validate the image analysis results of the oil flow from the shroud opening, we compared them with the measurement results using the two-phase flow probe. The measurement position of the two-phase flow probe was located 30° upstream from the shroud opening, slightly far from the imaging position (at the shroud opening); however, these positions were close to each other; therefore, the comparison was considered to be effective.

Figure 3.6-37 shows the comparison between the measurement result of the two-phase flow probe and the image analysis result of the oil flow. The results of the two-phase flow probe measurement indicated a density-weighted mean velocity in the region near the shroud wall with an oil fraction of 10% or more. The error of the mean velocity was 16%, which was derived as the root mean square value with the error of oil fraction of 13% and error of velocity of 9%. The error of oil fraction was used because the integral range

of velocity $\delta_{10\%}$ in Eq. 3.30 was determined by the oil fraction. Figure 3.6-37 shows that the results of the two-phase flow probe and oil particle image analysis almost agreed within their error range.

Figure 3.6-38 shows the radial distribution of the oil flow rate per unit width. The position 0 on the left end of the horizontal axis is the inner wall of the shroud and the position on the right end is the gear tooth tip. In the figure, the distance from the shroud wall where the oil rate was 10% (thickness of the oil layer $\delta_{10\%}$) is shown. Figure 3.6-38 shows that $\delta_{10\%}$ corresponded approximately to the maximum oil flow rate. This was considered to be because the mass of oil with a large flow rate strongly reflected light from the flow visualization borescope.

These results indicated that oil flow can be quantitatively evaluated using velocity measurement via the image analysis method of oil particles.
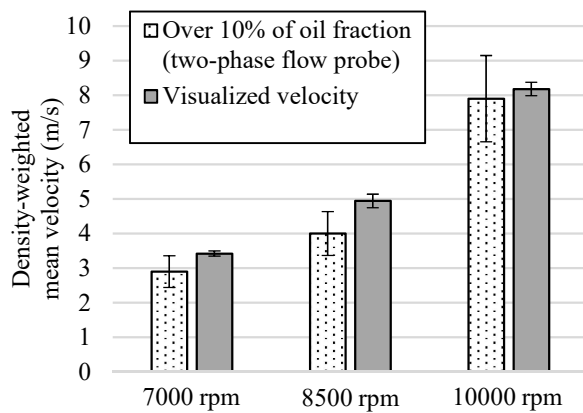
Fig. 3.6-37 Comparisons of the density-weighted mean and visualized velocities (experimental results)
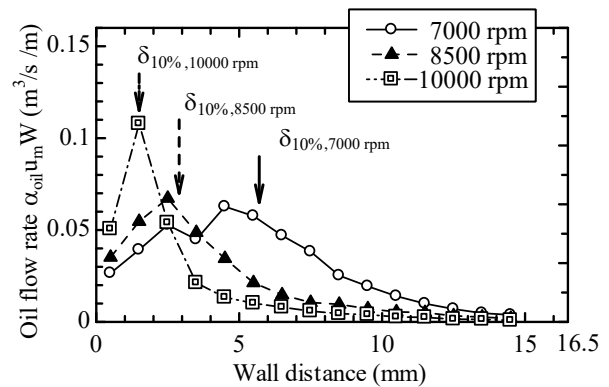
Fig. 3.6-38 Radial distributions of the estimated oil flow rate (experimental results)

3.6.4 Summary of Measurement Errors of Experimental Measurement Methods

A summary of the measurement errors of the experimental measurement methods discussed in this section is shown in Table 3.6-5 . The results of the errors in all the measurement methods satisfy each error target. The above results show that each measurement method can be applied to the gearbox with practical accuracy.

Table 3.6-5 Summary for the results of measurement errors

Measurements	Objectives	Error evaluation methods	Target errors	Results of errors
Power loss	Repeatability	Standard error of 2 σ* $2\sigma_{rep,p}/\sqrt{\mathcal{N}_{rep}}$	0.1 kW (Corresponding to torque meter error)	0.082kW (7000rpm)– 0.044kW (10000rpm)
Oil fraction	Repeatability	Standard error of σ $\sigma_{rep,\alpha}/\sqrt{\mathcal{N}_{rep}}$	1% or less (without calibration)	1% or less (without calibration)
	Measurement error with respect to the setting value (true value)	Relative standard deviation of σ $\sigma_{mes,\alpha}/\alpha_{oil,set}$	15% or less**	13%
Mixture velocity (with high-accuracy calibration method)	Repeatability	Standard error of σ $\sigma_{rep,um}/\sqrt{\mathcal{N}_{rep}}$	1m/s or less (without calibration)	1m/s or less (without calibration)
	Measurement error with respect to the setting value (true value)	Relative standard deviation of σ $\sigma_{mes,um}/u_{m,set}$	15% or less**	9%
Oil particle velocity	Repeatability	Relative standard error of σ $(\sigma_{rep,up}/\hat{u}_{par})/\sqrt{\mathcal{N}_{rep}}$	15% or less**	2–4%
	Measurement error with respect to oil velocity (derived by oil fraction and mixture velocity)	Comparison with measurement of oil velocity	Oil particle velocity agree with oil velocity within the repeatability error	Oil particle velocity agreed with oil velocity within the repeatability error

* More strictly than other measurements is because power loss is important data.

** Practical accuracy required in experience

3.7   Summary of Chapter 3

This chapter describes the following experimental measurement methods of fluid dynamic loss: test gearboxes and measurement conditions for the validation of the fluid dynamic loss and experimental and numerical simulation methods, high-accuracy measurement methods for fluid dynamic loss, the oil fraction and mixture velocity measurement methods, and the visualization method of oil particles and velocity measurement methods of the oil particle. In addition, the validation of the applicability of experimental measurement methods to obtain reliable experimental data to clarify the phenomena of fluid dynamic loss is described. These are summarized below.

3.7.1   Summary of Experimental Measurement Methods

1. To clarify the phenomenon of fluid dynamic loss and validate the numerical simulation method, the input gear shaft was driven by a motor, and the output gear shaft was set to free (no load) in the two-axis helical gearbox. The power loss in the gearbox was measured using a torque meter installed between the motor and input gear. For in-situ measurement of fluid dynamic loss, a vacuum pump that could control internal pressure and a thermocouple to measure the temperature of each bearing and seal were installed.

2. Various gearboxes were used to validate the experimental measurement and numerical simulation methods. These gearboxes enabled measurement of oil jet flow to gear meshing, oil jet flow to the gear tooth surface, oil spray flow to the gear tooth surface, oil flow between gear tooth tip and shroud wall, and velocity of oil particles. These gearboxes were realized by replacing the two-axis helical gearbox with a spur gear or by installing an oil jet nozzle, an oil spray nozzle, and a gear shroud.

3. As a high-accuracy measurement method of fluid dynamic loss, we developed an in-situ measurement method of the friction loss at the contact surface of the gears, bearings, and seals, because the temperature dependence of the friction loss is high. The in-situ measurement of the friction loss is possible by extrapolating the loss of zero oil flow rate and zero air pressure (fluid dynamic loss is zero) by changing the oil-supply flow rate and internal air pressure of the gearbox. Here, the temperatures of the bearings and seals are set to a constant temperature range at set rotational speeds to minimize the change in the friction loss due to temperature.

4. Fluid dynamic loss was calculated by subtracting the friction loss of the gears, bearings, and seals from the total power loss of the gearbox. Aerodynamic loss was calculated by subtracting the friction loss of the gears, bearings, and seals from the loss at zero oil supply rate (the zero oil supply rate loss is evaluated by the extrapolation of the loss obtained by changing the oil supply rate). The oil dynamic loss was calculated by subtracting the aerodynamic and friction losses from the total power loss of the gearbox.

5. As a method to measure the oil fraction and mixture velocity, the isokinetic suction method, which is often used to measure the sampling of soot or dust, was used. To apply this method to two-phase flows of air and oil, we used a test apparatus that considers the influence of bubble dissolution in oil and the calibration method that considers annular flow (deviation to wall) in the calibration pipe.

6. To visualize oil particles in the gearbox, we developed a borescope equipped coaxially with a visualization borescope, a laser light source, and an air purge jacket. The air purge was installed to reduce the influence of oil mist, which is a problem in conventional methods of visualizing the oil flow in the gearbox. For the velocity measurement of oil particles, a method to detect the velocity of particles from the correlation

between two consecutive images was used.

3.7.2 Summary of Validation Results for the Applicability of Experimental Measurement Methods

1. We validated the in-situ measurement method of power loss (high-accuracy temperature control method for bearings and seals) for the high-accuracy measurement of fluid dynamic loss. As a result, we observed that the measurement error was equivalent to the torque diameter error, and the influence of temperature change of bearings and seals could be minimized. Through this, power loss was separated into "aerodynamic loss," "oil dynamic loss," and "friction loss due to the contact of bearings, seals, and gears" with high accuracy.

2. To validate the measurement method of oil fraction and mixture velocity, we verified the accuracy of the correction methods of measured values using calibration curves, and we confirmed the rationality of the shape of the calibration curve.

   (a) The correction of the oil fraction using the calibration curve resulted in a measurement error of 13%, less than the target value of 15%. We also observed that the shape of the calibration curve was due to non-isokinetic suction caused by the shape of the probe.

   (b) As the result of correcting the mixture velocity with the high-accuracy calibration curve, the measurement error was 9%, less than the target value of 15% or less, and we observed that the shape of the calibration curve can be explained by the momentum transfer coefficient at the collision of the droplet with the liquid surface and velocity slip of air and oil.

   (c) The momentum transfer coefficient of the droplet and gas–liquid velocity slip that affect the shape of the calibration curve is considered to be affected by the size and velocity of the droplet. Because these are considered to be different according to gearbox, measurement results should be verified from another perspective when the measuring method of oil fraction and mixture velocity is applied to a gearbox.

3. As a result of the measurement of the oil fraction and mixture velocity between the gear and the shroud, we observed that there was a flow with a high oil fraction and slow speed near the shroud wall. The measurement result was reasonable because the oil flow rate evaluated from the measurement result of the oil fraction and mixture velocity agreed with the oil-supply flow rate.

4. To validate the visualization method of oil flow, the flow of the oil jet to the gear tooth was qualitatively validated, and the velocity of oil outflow from the shroud opening was quantitatively validated.

   (a) As a result of visualization of the oil jet to the gear tooth, the flow of oil impinging on the tooth surface toward the tooth bottom was qualitatively consistent with the results of previous studies.

   (b) The velocity of the oil outflow from the shroud opening was almost the same as the density-weighted mean velocity near the shroud wall, which suggested that the flow visualization can capture the mass of the flow with a large oil flow rate.

The above results validated the applicability of the experimental measurement methods to the gearbox. Therefore, by using obtained experimental results, we prove that the validation of the numerical simulation method and the clarification of the fluid dynamic loss phenomena are possible.

Chapter 4

Numerical Simulation Method of Fluid Dynamic Loss

4.1 Numerical Simulation Method

4.1.1 Numerical Simulation Method for Two-Phase Flow of Air and Oil in a Gear System

4.1.1.1 Overview of Numerical Simulation Method

The most important requirement for ensuring the practicability of a numerical fluid dynamic simulation of a gear system is to ensure numerical stability at the gas–liquid interface and boundary on the gear meshing part, and to simultaneously maintain a practical calculation speed. First, for the calculation mesh at the gas–liquid interface with the highest calculation stability, a rectangular mesh (which is fixed in space) is used. Furthermore, the volume of fluid (VOF) method [103] (which is one of the simplest methods of calculating the gas–liquid interface and offers high stability owing to its simplicity) is used. Using the porosity method [104] to model the boundary condition on the gear meshing part allows both stable and rapid calculations to be realized. In simulations, the commercial software FLOW-3 D Ver. 6.1.3 [105] is used to implement this.

An overview of the modeling of gas–liquid interfaces and object boundaries is shown in Fig. 4.1-1 . The VOF method defines the volume fraction of oil in a calculation cell. The volume fraction α_{oil} of oil is $0 < \alpha_{oil} < 1.0$, and the cell is defined as a gas–liquid interface cell. In the porosity method, if the cell contains an object, the fluid region is defined as the region excluding the object; it is characterized by the fluid volume V_f and the fluid areas A_x, A_y, and A_z (areas of the x-, y-, and z-direction cell surfaces, respectively) at the cell boundary.
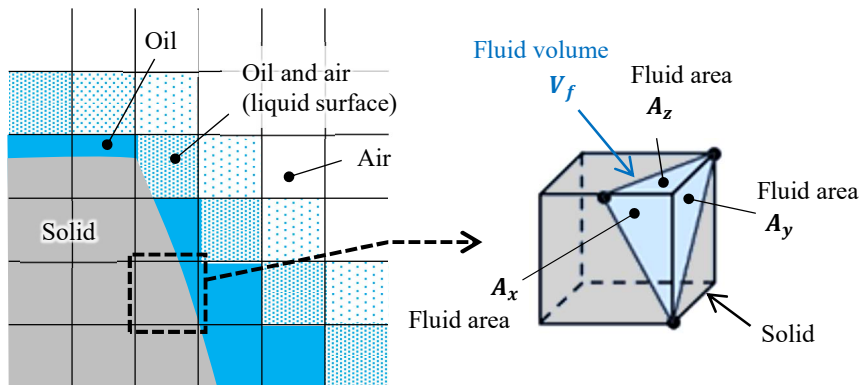
Fig. 4.1-1 VOF method for modeling the gas–liquid surface; porosity method for modeling a solid

The mass and momentum conservation equations use one equation for both oil and air (one-fluid model), in which the pressure and velocity at the gas–liquid interface cell on the air and oil sides match and no velocity slip occurs at the gas–liquid interface. The movement of the object is considered via changes in the volume V_f of the fluid fraction of the cell, as well as changes in the fluid areas A_x, A_y, and A_z of the cell surface. The shear stress at the wall is calculated from the difference between the object and fluid velocities, using a turbulence model.

4.1.1.2 Mass and Momentum Conservation Equations

(1)   Mass Conservation Equation

The mass conservation equation is a general fluid mass conservation equation [106] that takes into account the influence of the object boundary; it is expressed as

$$V_f \frac{\partial \rho}{\partial t} + \frac{\partial}{\partial x}(\rho u A_x) + \frac{\partial}{\partial y}(\rho v A_y) + \frac{\partial}{\partial z}(\rho w A_z) = R_{sor} \tag{4.1}$$

where ρ is the fluid density; t is time; u, v, w are the velocities in the x, y, z directions, respectively; and R_{sor} is the fluid source. The above equation takes into account the fluid volume in the cell V_f and the fluid area at the cell surface A_x, A_y, and A_z. Considering the microcompressibility (propagation of pressure waves) of the fluid, the $\frac{\partial \rho}{\partial t}$ in the first term on the right-hand side can be approximated by the following equation, if $|\delta p/\rho| < 0.1$:

$$\frac{\partial \rho}{\partial t} \simeq \frac{1}{c_a{}^2} \frac{\partial p}{\partial t} \tag{4.2}$$

Here, c_a is the sound velocity of the fluid and p denotes the pressure. The source term R_{sor} on the right-hand side of Eq. 4.1 takes into account the volume source R_{jet} attributable to the oil source at the oil jet impinging position (see Section 4.1.3.2 for details) and the time variation of V_f produced by object movement. That is,

$$R_{sor} = R_{jet} - \rho \frac{\partial V_f}{\partial t} \tag{4.3}$$

Using Eqs. 4.1–4.3, the mass conservation equation is calculated as

$$\frac{V_f}{\rho c_a{}^2} \frac{\partial p}{\partial t} + \frac{\partial u A_x}{\partial x} + \frac{\partial v A_y}{\partial y} + \frac{\partial w A_z}{\partial z} = \frac{R_{jet}}{\rho} - \frac{\partial V_f}{\partial t} \tag{4.4}$$

(2)   Momentum Conservation Equation

The momentum conservation equation is the general momentum conservation equation used for fluids [106]; it takes into account the influence of object boundaries. When the viscous accelerations f_x, f_y, and f_z and oil-jet velocities u_{jet}, v_{jet}, and w_{jet} are used, the equation becomes

$$
\begin{aligned}
\frac{\partial u}{\partial t} + \frac{1}{V_f}\left\{ u A_x \frac{\partial u}{\partial x} + v A_y \frac{\partial u}{\partial y} + w A_z \frac{\partial u}{\partial z} \right\} &= -\frac{1}{\rho}\frac{\partial p}{\partial x} + f_x - \frac{R_{jet}}{\rho V_f}(u - u_{jet}) \\
\frac{\partial v}{\partial t} + \frac{1}{V_f}\left\{ u A_x \frac{\partial v}{\partial x} + v A_y \frac{\partial v}{\partial y} + w A_z \frac{\partial v}{\partial z} \right\} &= -\frac{1}{\rho}\frac{\partial p}{\partial y} + f_y - \frac{R_{jet}}{\rho V_f}(v - v_{jet}) \\
\frac{\partial w}{\partial t} + \frac{1}{V_f}\left\{ u A_x \frac{\partial w}{\partial x} + v A_y \frac{\partial w}{\partial y} + w A_z \frac{\partial w}{\partial z} \right\} &= -\frac{1}{\rho}\frac{\partial p}{\partial z} + f_z - \frac{R_{jet}}{\rho V_f}(w - w_{jet})
\end{aligned}
\tag{4.5}
$$

Then, the viscous accelerations f_x, f_y, and f_z become

$$f_x = \frac{1}{\rho V_f} \left[wsx - \left\{ \frac{\partial}{\partial x}(A_x \tau_{xx}) + \frac{\partial}{\partial y}(A_y \tau_{xy}) + \frac{\partial}{\partial z}(A_z \tau_{xz}) \right\} \right]$$

$$f_y = \frac{1}{\rho V_f} \left[wsy - \left\{ \frac{\partial}{\partial x}(A_x \tau_{xy}) + \frac{\partial}{\partial y}(A_y \tau_{yy}) + \frac{\partial}{\partial z}(A_z \tau_{yz}) \right\} \right] \qquad (4.6)$$

$$f_z = \frac{1}{\rho V_f} \left[wsz - \left\{ \frac{\partial}{\partial x}(A_x \tau_{xz}) + \frac{\partial}{\partial y}(A_y \tau_{yz}) + \frac{\partial}{\partial z}(A_z \tau_{zz}) \right\} \right]$$

where wsx, wsy, and wsz denote the wall shear forces and τ is the flow shear stress. The wall shear forces wsx, wsy, and wsz are taken as relative values, to incorporate the velocity component of the wall surface of the object when it moves. For example, the contribution of the z-direction velocity $WOBS$ to the z-direction wall shear force wsz in the x-direction is

$$wsz = \frac{2\mu(w_{n+1} - WOBS)(1 - A_x)}{\delta x} \qquad (4.7)$$

where w_{n+1} is the speed at the next time step. The shear stress τ of the flow is

$$\tau_{xx} = -2\mu \left\{ \frac{\partial u}{\partial x} - \frac{1}{3} \left(\frac{\partial u}{\partial x} + \frac{\partial v}{\partial y} + \frac{\partial w}{\partial z} \right) \right\}$$

$$\tau_{yy} = -2\mu \left\{ \frac{\partial v}{\partial y} - \frac{1}{3} \left(\frac{\partial u}{\partial x} + \frac{\partial v}{\partial y} + \frac{\partial w}{\partial z} \right) \right\}$$

$$\tau_{zz} = -2\mu \left\{ \frac{\partial w}{\partial z} - \frac{1}{3} \left(\frac{\partial u}{\partial x} + \frac{\partial v}{\partial y} + \frac{\partial w}{\partial z} \right) \right\}$$

$$\tau_{xy} = -\mu \left\{ \frac{\partial v}{\partial x} + \frac{\partial u}{\partial y} \right\} \qquad (4.8)$$

$$\tau_{xz} = -\mu \left\{ \frac{\partial u}{\partial z} + \frac{\partial w}{\partial x} \right\}$$

$$\tau_{yz} = -\mu \left\{ \frac{\partial v}{\partial z} + \frac{\partial w}{\partial y} \right\}$$

Here, viscosity coefficient μ takes into account the influence of turbulence.

4.1.1.3 Numerical Simulation Method for Gas–Liquid Interface

The VOF method [103] is used to simulate the gas–liquid interface. In this method, the volume fraction of oil is defined as the VOF value in the fluid region of the calculation cell. The "Fluid" in the VOF method refers to liquid or oil. For example, the VOF value (designated $\mathcal{F}$) = 1 for 100% oil and 0 for 100% air, and $0 < \mathcal{F} < 1$ in the case of a calculation cell containing a gas–liquid interface; ρ and c in Eq. 4.4 and μ in Eqs. 4.7 and 4.8 denote the weighted averages of $\mathcal{F}$, as follows:

$$\rho = (1 - \mathcal{F})\rho_{air} + \mathcal{F}\rho_{oil} \qquad (4.9)$$

$$c = (1 - \mathcal{F})c_{air} + \mathcal{F}c_{oil} \qquad (4.10)$$

$$\mu = (1 - \mathcal{F})\mu_{air} + \mathcal{F}\mu_{oil} \qquad (4.11)$$

The advection equation for the VOF value $\mathcal{F}$ is given by

$$\frac{\partial \mathcal{F}}{\partial t} + \underbrace{\frac{1}{V_f} \left\{ \frac{\partial}{\partial x} \left(\mathcal{F} A_x u \right) + \frac{\partial}{\partial y} \left(\mathcal{F} A_y v \right) + \frac{\partial}{\partial z} \left(\mathcal{F} A_z w \right) \right\}}_{\text{Advection of } \mathcal{F}}$$
$$+ \underbrace{\frac{1}{V_f} \left\{ \frac{\partial}{\partial x} \left((1-\mathcal{F}) \mathcal{F} C_\alpha A_x u_r \right) + \frac{\partial}{\partial y} \left((1-\mathcal{F}) \mathcal{F} C_\alpha A_y v_r \right) + \frac{\partial}{\partial z} \left((1-\mathcal{F}) \mathcal{F} C_\alpha A_z w_r \right) \right\}}_{\text{Surface compression}} = \mathcal{F}_{jet} - \frac{\partial V_f}{\partial t} \quad (4.12)$$

where u_r, v_r, and w_r are the relative velocities of the gas and liquid, C_α is the sharpening coefficient of the gas–liquid interface, $\mathcal{F}_{jet}$ is the source term of the oil jets, and $-\frac{\partial V_f}{\partial t}$ is a source term produced by the change of V_f attributable to the movement of the object. In Eq. 4.12, the oil and air in the gas–liquid interface cell (i.e., the cells with $0 < \mathcal{F} < 1$) lack information describing the ratio between gas and liquid on each surface of the cell; thus, they are treated as having a uniform density in the cell. Therefore, the term "Advection of $\mathcal{F}$" in Eq. 4.12 fails to take into account the influence of the deviation of gas or liquid in the cell upon the flux at each cell surface. For example, as indicated by the arrows in Fig. 4.1-2 , even when a cell surface of the gas–liquid interface cell is actually 100% air, oil flux is generated in the numerical simulation. This results in numerical diffusion of the gas–liquid interface, which leads to numerical simulation errors.

To suppress the numerical diffusion of the gas–liquid interface, the surface compression method [107] is introduced ("Surface compression" in Eq. 4.12). In this method, a compression speed is added in the direction perpendicular to the gas–liquid interface, as shown in Fig. 4.1-3 . In this paper, because the air and oil velocities at the gas–liquid interface are identical (i.e., no velocity slip), we assume that u_r, v_r, and w_r are equal to u, v, and w, respectively. C_α is set to 1.0. The surface compression term only acts (to compress the thickness) when the gas–liquid interface exhibits a thickness; thus, it is not considered to affect the validity of the numerical simulation results, though it is validated by comparison with experiments.
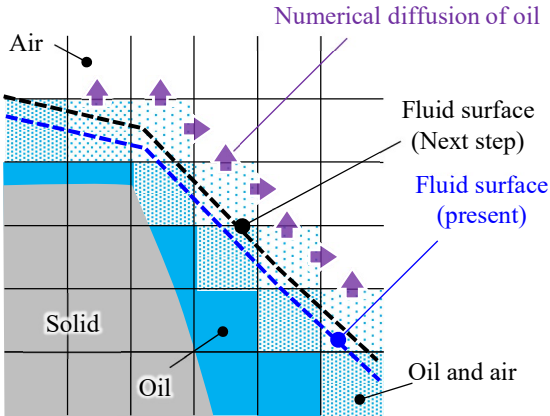
Fig. 4.1-2 Numerical diffusion of liquid surface
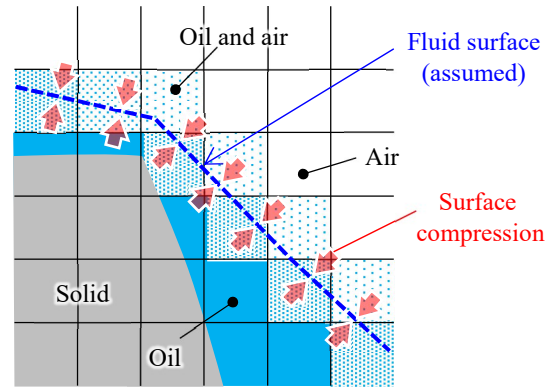
Fig. 4.1-3 Surface compression method for reducing the numerical diffusion of liquid surface [107]

4.1.1.4 Modeling the Wall Boundary Conditions of a Gear

(1) Boundary Condition in the Direction Normal to the Wall Surface

For the boundary condition in the direction normal to the wall surface, a simple immersed boundary condition is used; this imposes a no-penetration condition (i.e., a normal velocity component of zero) upon advection at the wall surface. To achieve this, the velocity derivative is set to zero when the definition

point for the velocity (used for the spatial differentiation of velocity) lies within the object region, as shown in Fig. 4.1-4 . When compared with methods that do not use the differential value of zero, this method is found to be in good agreement with the real flow (e.g., a uniform flow in an inclined channel) [104] [108].
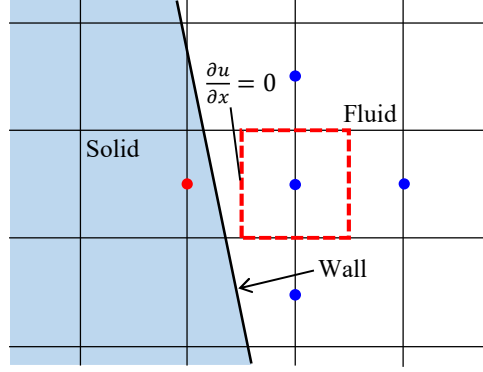
Fig. 4.1-4 Non-penetration condition in the vicinity of wall [105]

(2)   Boundary Conditions Parallel to the Wall

Under these conditions, the Reynolds number near the wall is high; however, the calculation mesh near the wall is rough. Therefore, the wall function [106] and a turbulence model are used. In the calculation cell (including the wall), the velocity distribution is assumed using the wall function, and the turbulence viscosity is calculated from the turbulence model. The turbulence model is described in the next section.

4.1.1.5   Turbulence Model

The large eddy simulation (LES) turbulence model is used as the turbulence model in this study. Compared with the standard k-ϵ turbulence model, the LES method is more numerically stable because it does not require the equations of the turbulence model to be solved. Therefore, it is considered suitable for the simulation of two-phase flows around gears, a task which requires high numerical stability.

The LES turbulence model directly calculates vortices larger than the mesh size and approximates vortices smaller than it. As an approximation method, the Smagorinsky model [109] is used. In this model, the eddy viscosity is defined using the mesh width L and model constant (Smagorinsky constant) c_g via

$$\nu_T = (c_g L)^2 \sqrt{2e_{ij}2e_{ij}} \tag{4.13}$$

where L and the strain rate tensor e_{ij} are

$$L = (\delta x \delta y \delta z)^{\frac{1}{3}} \tag{4.14}$$

$$e_{ij} = \frac{1}{2}\left(\frac{\partial u_i}{\partial x_j} + \frac{\partial u_j}{\partial x_i}\right) \tag{4.15}$$

where δx, δy, and δz are calculation mesh sizes in the x, y, and z directions, respectively; u_i is the velocity in the i direction; and x_i is the coordinate. The Smagorinsky constant c_g is 0.1 for turbulence flow between parallel plates (channel turbulence), 0.15 for mixed layers, and 0.17–0.2 for isotropic turbulence. In this paper, because the turbulence on the wall is important, c_g is set to 0.1 for channel turbulence. The dynamic viscosity μ in Eqs. 4.7 and 4.8 is obtained from the kinematic viscosity ν and eddy viscosity ν_T of the fluid, using

$$\mu = \rho(\nu + \nu_T) \tag{4.16}$$

111

4.1.1.6 Evaluating Fluid Dynamic Loss

The fluid dynamic loss is evaluated by integrating the pressure and shear force on the gear surface.

The fluid dynamic loss P is the sum of the fluid dynamic loss $P_{pressure}$ attributable to pressure and the fluid dynamic loss P_{shear} attributable to shear force:

$$P = P_{pressure} + P_{shear} \tag{4.17}$$

The fluid dynamic loss $P_{pressure}$ attributable to pressure is calculated with the torque $\boldsymbol{T}_{pressure}$ and angular velocity $\boldsymbol{\omega}$. $\boldsymbol{T}_{pressure}$ is obtained by integrating $\boldsymbol{F}_{pressure}$ (caused by pressure) multiplied by the position vector $\boldsymbol{r}$. These are shown in the following equation:

$$P_{pressure} = \boldsymbol{T}_{pressure} \cdot \boldsymbol{\omega} = \sum (\boldsymbol{F}_{pressure} \times \boldsymbol{r}) \cdot \boldsymbol{\omega} \tag{4.18}$$

Similarly, the fluid dynamic loss P_{shear} attributable to shear force is calculated using the torque $\boldsymbol{T}_{shear}$ and angular velocity $\boldsymbol{\omega}$. $\boldsymbol{T}_{shear}$ is obtained by integrating $\boldsymbol{F}_{shear}$ (caused by shear force) multiplied by the position vector $\boldsymbol{r}$. These are shown in

$$P_{shear} = \boldsymbol{T}_{shear} \cdot \boldsymbol{\omega} = \sum (\boldsymbol{F}_{shear} \times \boldsymbol{r}) \cdot \boldsymbol{\omega} \tag{4.19}$$

4.1.2 Modeling Methods for Airflow

4.1.2.1 Modeling Air Leakage Flow from Gear Meshing

Modeling the gear meshing component is important because it affects the leakage flow from the gear mesh. In this section, the difference between the real gear meshing and numerical simulation model, as well as the modeling method that considers this difference, are described.

Figure 4.1-5 (a) shows the gear drive configuration under no-load conditions (no load is specified to minimize friction loss in gears, bearings, and seals), and Fig. 4.1-5 (b) shows the gear drive configuration in the numerical simulation. In the no-load gear drive in Fig. 4.1-5 (a), the motor is connected to the drive gear via a torque meter. The drive gear rotates the driven gear via tooth contact during gear meshing. Nothing is connected to the driven gear. The power loss required for gear rotation is evaluated using the torque and rotational speed, as measured by the torque meter. In the simulated gear drive in Fig. 4.1-5 (b), neither the drive gear nor the driven gear is connected to anything, and each gear is forcibly rotated. The power loss due to the fluid drag is evaluated by integrating the pressure and shear force generated on the gear surface.

The numerical simulation modeling of gear tooth contact and backlash is described in Fig. 4.1-6 . Figure 4.1-6 (a) shows the actual gear meshing. The tooth surface of the drive gear contacts the tooth surface of the driven gear. Backlash is set on the opposite side of the tooth surface to the contact side, to prevent tooth contact when the tooth deforms. Figure 4.1-6 (b) present a simulation model of the condition in Fig. 4.1-6 (a). Because the tooth is modeled using a rectangular mesh with a fixed space and non-boundary fitting, the calculation cell collapses at the contact point of the tooth and under small clearance of the backlash, as shown in "Clogging of calculation cell" in Fig. 4.1-6 (b). The collapse of the cell may produce a calculation instability or unrealistic flow, and it should be improved. Therefore, as shown in Fig. 4.1-6 (c), a gap is left between the teeth. To provide this gap, the peripheral thickness of the teeth is reduced by 20%, and the phase of the teeth is adjusted so that the gaps between the teeth are even.

(a) Gear drive with no load condition in an experiment (b) Individual gear rotations in a simulation
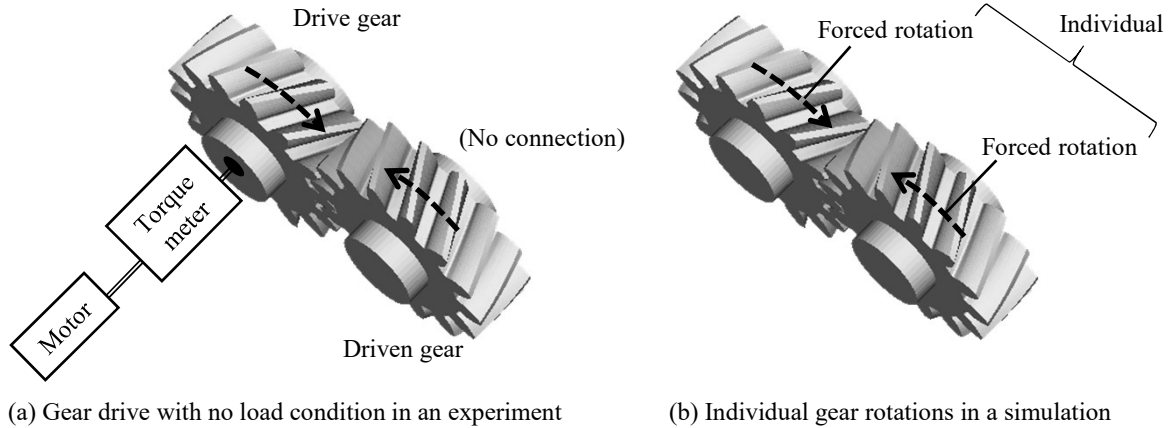
Fig. 4.1-5 A comparison of gear drive in an experiment and gear rotation in a simulation

(a) Real gear meshing (b) Calculation model without modification (c) Calculation model with modification
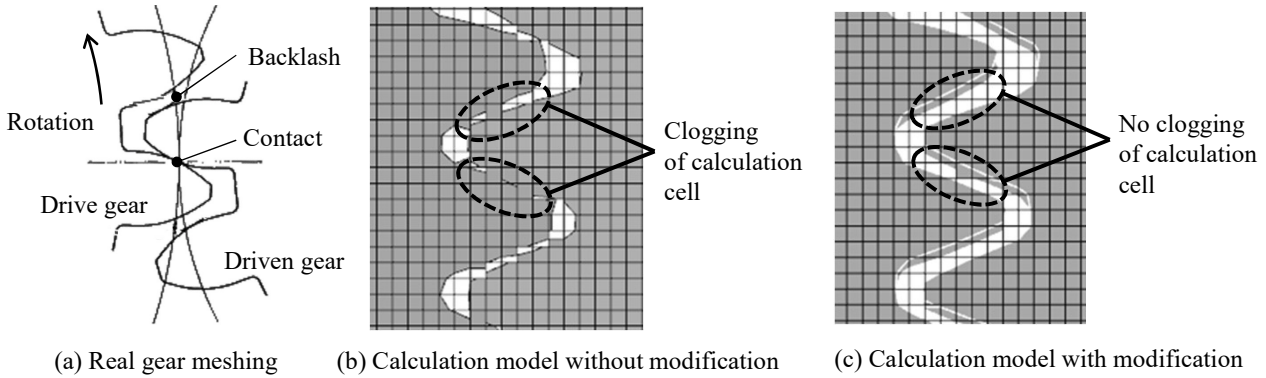
Fig. 4.1-6 A modeling method for gear contact surfaces

Figure 4.1-7 shows the difference in pressure on the contact tooth surface, to illustrate the influence of the difference between the numerical simulation modeling in Fig. 4.1-6 (c) and the actual gear mesh. A schematic diagram of the contact line on the actual gear tooth surface is shown in Fig. 4.1-7 (a1), and an example of the pressure distribution near the contact position under the no-load condition is shown in Fig. 4.1-7 (a2). For the surface pressure distribution, the pressure at the contact surface is calculated under the conditions of Table 1.5-2 using the calculation program developed from previous research [22] (see Appendix B.1.3 for details).

The pressure around the contact surface was set to the typical pressure used in this research, to compare the pressure magnitude with that on the contact surface. Figure 4.1-7 (b1) schematically illustrates the pressure in the numerical simulation; here, no pressure is present at the contact surface, and only the fluid-drag-induced pressure acts on the tooth surface; this is achieved by setting a gap between tooth surfaces, as shown in Fig. 4.1-6 (c). Figure 4.1-7 (b2) presents an example of the pressure distribution in the numerical simulation. This pressure differs from the actual pressure because ① there is no pressure attributable to tooth contact; and ②, the pressure changes because the gap between tooth surfaces differs from the actual gap.

Regarding ①, it is considered that the interferences between the contact surface and other surface can be neglected because the fraction of the tooth surface in contact is as small as ∼0.4%, as shown in Section 1.5. Regarding ②, it is considered that the pressure of the tooth surface changes because the distance between the tooth surfaces differs from the actual distance. This pressure change is considered to affect the results of

this research. This is discussed in our comparison of the numerical simulation and the experimental result, as presented in Section 4.4.1.

(a1) Schematic of real surface pressure
with tooth contact

(b1) Schematic of computational surface pressure
without tooth contact

(a2) Example of real surface pressure with tooth contact
(calculation results using empirical model)

(b2) Example of simulated surface pressure
without tooth contact (anticipated)
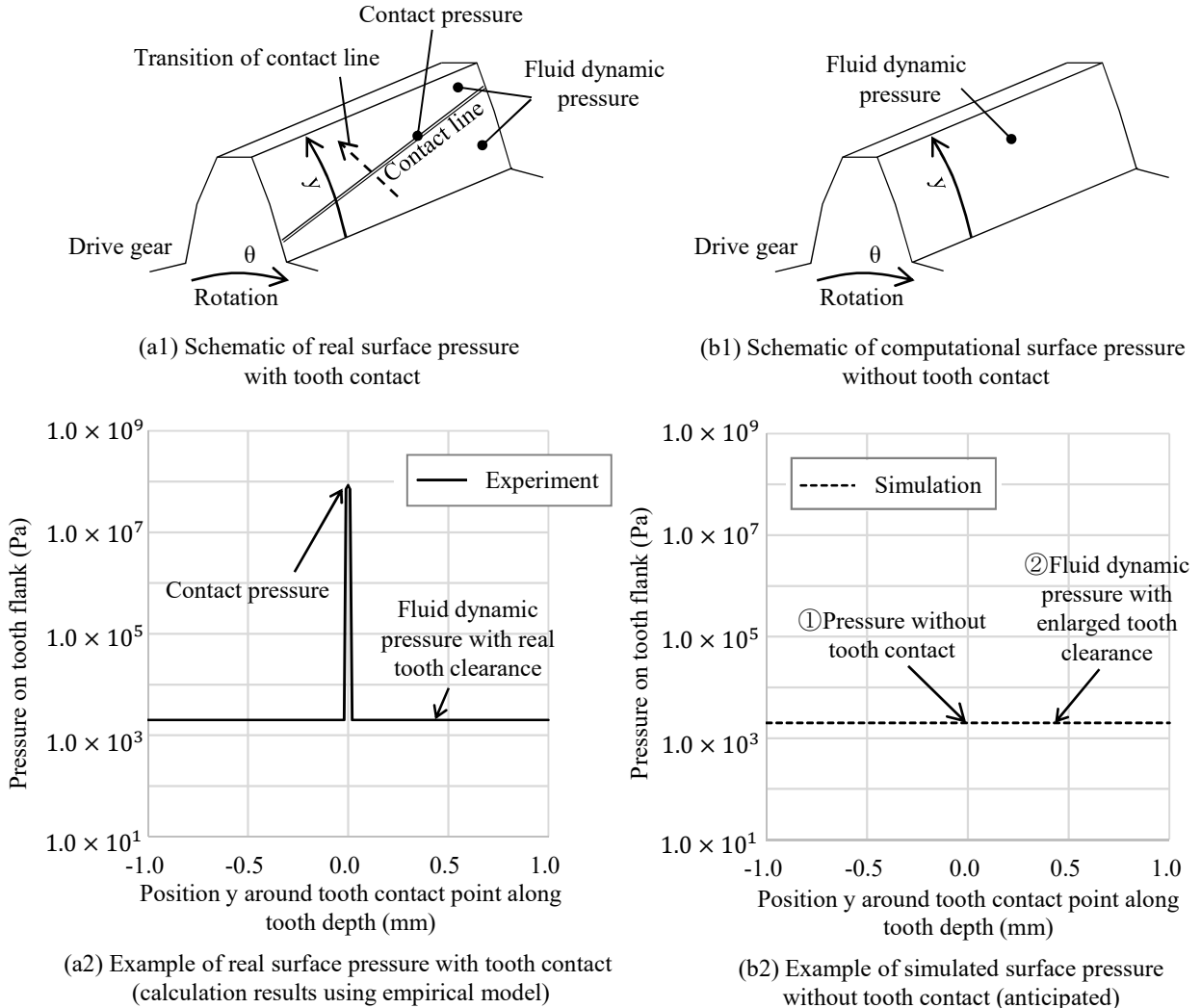
Fig. 4.1-7 Influence of the modeling method on tooth contact

4.1.2.2 Influence of Air Compressibility

The compressibility of air in the gear mesh is discussed in the studies of Delgado et al. [63] and Houjoh et al. [58].

The test gearbox used by Delgado et al. [63] is shown in Fig. 4.1-8 ; here, a spur gear pair with a module of 4, pitch circle diameters of 279 mm (input gear) and 330 mm (output gear), a tooth width of 28 mm, and an input rotational speed of 10000 rpm (pitch peripheral speed 146 m/s) are used. Under these conditions, the out-of-mesh temperature and power loss are compared under gear-to-shroud side clearances of 1 mm and ~30 mm. When this side clearance is 1 mm, a significant temperature increase of ~30 °C (relative to that at a side clearance of 30 mm) is observed. In contrast, the power loss is equivalent. Because the temperature rise occurs when the side clearance is small, it is estimated that the significant out-of-mesh temperature increase is caused by the local adiabatic compression of air in gear meshing.

The gearbox used by Houjoh et al. [58] is shown in Fig. 4.1-9 ; there, a spur gear pair with a module of 4 mm, a pitch diameter of 304 mm (input and output), a tooth width of 100 mm, and an input speed of 4000 rpm (pitch peripheral speed: 64 m/s) was used. Under these conditions, the out-of-mesh air temperature became very large (estimated from the melting of plastic parts installed out-of-mesh at 160 °C or above) when the clearance between the gear and shroud was set to 0.2–0.5 mm. Most likely, this high temperature was also produced by the local adiabatic compression of air in gear meshing.

From the above example, it can be seen that air compressibility in gear meshing arises at a peripheral speed of no less than 60 m/s and a gear-to-shroud axial clearance of no more than 1 mm. In an actual gearbox for an aeroengine, it is common to maintain an axial clearance of no less than several mm, to prevent interference between the gear and components arising through dimensional errors, assembly errors, shaft vibrations, and so on. In other words, air compressibility in gear meshing is insignificant in an actual aeroengine gearbox. Therefore, air can be treated as incompressible in this research.
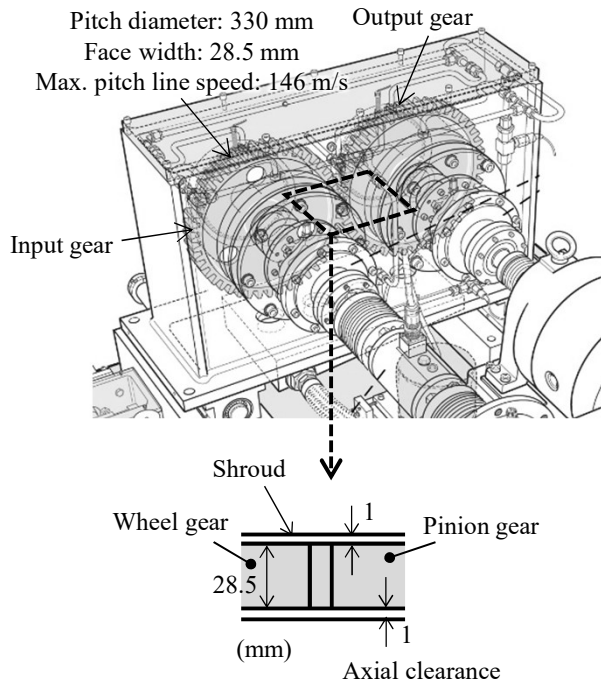
Fig. 4.1-8 A clearance setting between spur gears and a shroud [63]
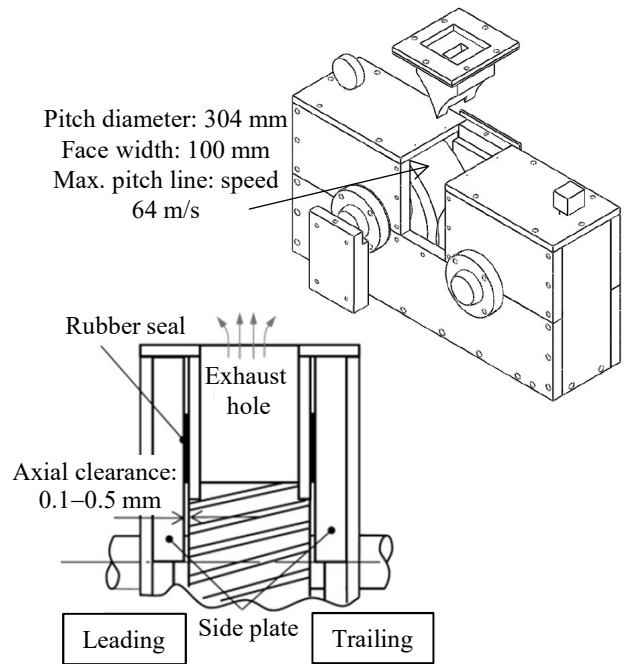
Fig. 4.1-9 A clearance setting between helical gears and a shroud [58]

4.1.3 Modeling Methods for Oil Flow

Because the oil supply flow rate is smaller than the air flow rate produced by the gear rotation, the oil particles are dispersed in the airflow. Simulating the behavior of all oil particles is unrealistic because the calculation time would be excessively large. Therefore, as an oil-flow modeling method that ensures a realistic calculation time, a coarse-graining method for the oil particles and a simple modeling method for the oil jet are shown below. In addition, the flow drag of an object in a two-phase flow differs from that in a single-phase flow, owing to the followability of the oil particles to the airflow. A modeling method for improving the simulation accuracy (by considering the difference of the flow drag) is described.

4.1.3.1 Coarse-Graining Method for Oil Particles

The coarse-graining method is used to speed up calculations in, for example, discrete element method (DEM) simulations of powders (e.g., [110]). To perform coarse-graining in this research, oil particles with a size smaller than the calculation mesh are replaced with particles of the same size as the mesh. A coarse-graining image is shown in Fig. 4.1-10 . Oil particles with a size smaller than the mesh are shown in Fig. 4.1-10 (a); each oil particle has a mass m_i and a velocity $\boldsymbol{U}_i$. Figure 4.1-10 (b) shows coarsened oil particles with a mass m_{sum} and a velocity $\hat{\boldsymbol{U}}$[*1]. For a given calculation mesh, the summed masses of the oil particles in the calculation mesh $\sum_i m_i$ is conserved and equivalent to the mass m_{sum} of the coarsened oil particles. The velocities $\boldsymbol{U}_i$ of the oil particles in the calculation cell are considered to be approximately equivalent. Therefore, the velocity $\hat{\boldsymbol{U}}$ of a coarse-grained oil particle is assumed to be equivalent to the averaged velocity of the oil particles in the calculation cell. That is, the summed momentums of oil particles in the calculation mesh are considered equivalent to the momentum of the coarse-grained oil particle, as shown by

$$\sum_i m_i U_i \simeq m_{sum} \hat{\boldsymbol{U}} \tag{4.20}$$

Because the change in the oil particles' momentum becomes the force on them, the force generated on the gear tooth surface by the coarse-grained oil particles is considered to be equivalent to the sum of the forces generated by the individual oil particles.
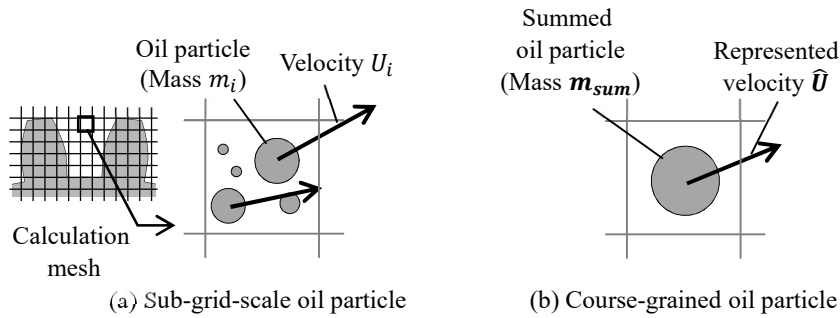
Fig. 4.1-10 Schematic of a coarse-grained oil particle model.

4.1.3.2 Simplified Modeling Method for Oil Jet

Figure 4.1-11 shows a simplified (and therefore faster) modeling method for an oil jet. When the flow around the gear is resolved, the reference dimensions are the gear tooth height or gear tooth width. The gear tooth height commonly used for an aeroengine is ~5–10 mm (equivalent to a module of 2–4), which makes it possible to resolve the flow around the gear tooth using a calculation mesh of the order of 1 mm. Figure 4.1-11 (a) shows an oil jet for a resolution of ~1 mm; this is common for aeroengine gears and is the appropriate mesh size for resolving the flow around the gear tooth. This calculation mesh shows that the resolution of the oil jet is insufficient.

To solve the flow of an oil jet, a calculation mesh with a width of up to 1/3 of the nozzle diameter (i.e., 0.3 mm or less for a nozzle diameter of 1 mm) is required. An example is shown in Fig. 4.1-11 (b). However, it

---

[*1] In the VOF method used in this research, a cell with uniform density (obtained by averaging the density of oil and the density of air) is treated as a single particle in the explanation of the coarse-grained method.

is practically impossible to solve the flow of the entire gearbox using this fine calculation mesh, owing to the enormous calculation time.

Therefore, as shown in Fig. 4.1-11 (c), a simplified modeling method is used to set the source and flow velocity of oil when an oil jet collides with an obstacle. This facilitates simulation in a realistic calculation time whilst simulating the impingement of oil upon an obstacle.

(a) Insufficient resolution for an oil jet in a coarse mesh

(b) Sufficient resolution for an oil jet in a fine mesh

(c) Sufficient resolution for an oil jet in a coarse mesh, applying a simple oil jet model
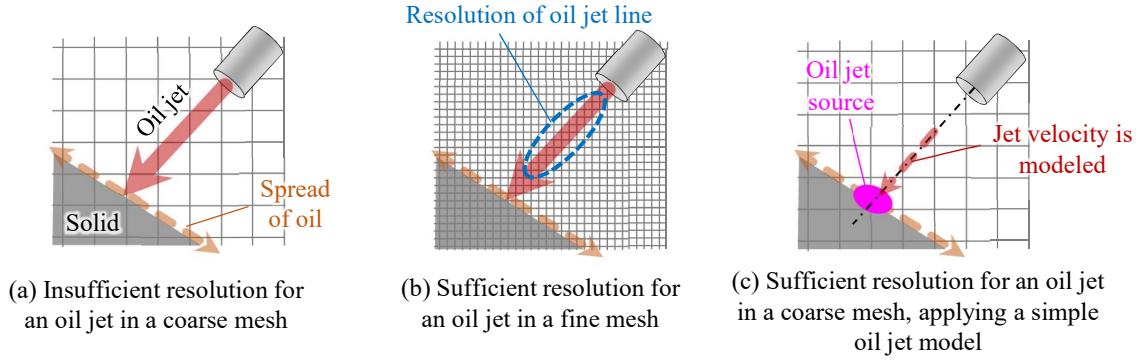
Fig. 4.1-11 Schematics of a simple oil jet model

4.1.3.3 Improving Simulation Accuracy by Considering the Flow Drag Coefficient in Two-Phase Flow

A simulation modeling method using the experimental results of the two-phase flow drag of air and oil on a cylinder is proposed to improve the simulation accuracy.

(1) Flow Drag Phenomena in Two-Phase Flow

The local pressure coefficients $c_{p,cyl,air}$ around the cylinder in an airflow, as well as the local pressure coefficients $c_{p,cyl,m}$ around the cylinder in a two-phase flow of air and oil, are given by

$$c_{p,cyl,air} = \frac{p_{cyl,air} - p_{\infty,air}}{p_{cyl,stag,air} - p_{\infty,air}} \tag{4.21}$$

$$c_{p,cyl,m} = \frac{p_{cyl,m} - p_{\infty,m}}{p_{cyl,stag,m} - p_{\infty,m}} \tag{4.22}$$

where $p_{cyl,air}$ indicates the pressure distribution around the cylinder in the airflow, $p_{\infty,air}$ is the atmospheric pressure, and $p_{cyl,stag,air}$ indicates the stagnation pressure around the cylinder. Similarly, $p_{cyl,m}$ denotes the pressure distribution around the cylinder in a two-phase flow of air and oil, $p_{\infty,m}$ is the atmospheric pressure, and $p_{cyl,stag,m}$ is the stagnation pressure.

For the experimental measurement of local pressure coefficients $c_{p,cyl,m}$ around a cylinder in a two-phase flow of air and oil, the one-axis spur gear box (Section 3.1.2.3) and the measurement apparatus for oil fraction and mixture velocity (Section 3.3.1.2) are used. Pressure measurement around the cylinder was performed by fixing the radial position of the measuring hole at a position 2 mm from the gear tooth tip (14.5 mm from the inner wall of the shroud) and changing the phase of the probe. The rotational speed was set to 10000 rpm (peripheral speed 100 m/s); other conditions (e.g., the oil supply flow rate) were set the same as in Table 3.1-8 . This measurement condition is within the range for which correction using a calibration curve (shown in Section 3.6.2) is not required.

The experimental results for the pressure distribution around the cylinder are shown in Fig. 4.1-12 . In the

figure, the local pressure coefficients $c_{p,cyl,air}$ around the cylinder in airflow [111] are also shown[*2] (where θ is the phase from the stagnation point). A schematic diagram of the two-phase flow phenomena assumed in this result is shown in Fig. 4.1-13 .

As shown in Fig. 4.1-12 , the results in the two-phase flow and airflow are almost identical at $\theta = 0$–35°; however, at $\theta > 35°$, the value in the two-phase flow is smaller than that in the airflow. This is considered to be because the apparent density behind the cylinder decreases owing to the separation of oil particles from the airflow in the two-phase flow, as illustrated in Fig. 4.1-13 . To simulate the separation phenomena of the oil particles, it is necessary to ensure that the calculation mesh around the cylinder is sufficiently fine. On the other hand, to perform two-phase flow simulations in a gearbox within a realistic calculation time, the calculation mesh around objects (e.g., gear teeth) cannot be set too fine. Therefore, it is necessary to consider a method for modeling the drag coefficient of the two-phase flow.
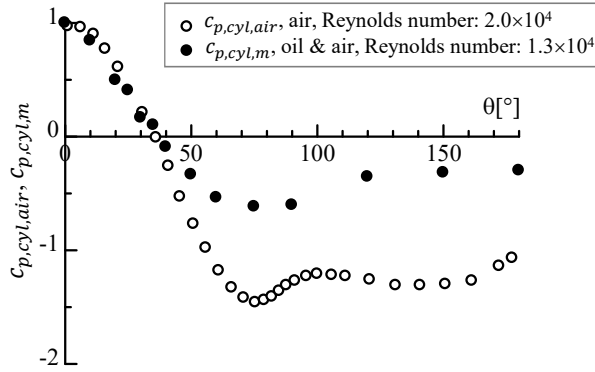
Fig. 4.1-12 Pressure around a cylinder (experimental results)
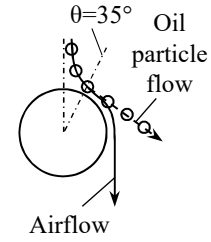
Fig. 4.1-13 Schematic of the two-phase flow of air and oil around a cylinder

(2)　Modeling the Flow Drag in Two-Phase Flow

The equation for the force F_m loaded upon an object in a two-phase flow is as follows:

$$F_m = C_{D,m}\frac{1}{2}\rho_m u^2 \tag{4.23}$$

where $C_{D,m}$ is a two-phase-flow drag coefficient, ρ_m is a two-phase flow apparent density $(= (1-\alpha_{oil})\rho_{air} + \alpha_{oil}\rho_{oil}$, where α_{oil} is the oil fraction), and u is a velocity. Here, the ratio Ψ' between the drag coefficient in a two-phase flow and that in the airflow is expressed as

$$F_m = C_{D,air}\Psi'\frac{1}{2}\rho_m u^2 \tag{4.24}$$

$$\Psi' = \frac{C_{D,m}}{C_{D,air}} \tag{4.25}$$

Ψ' is estimated from the pressure distribution on the cylinder surface (Fig. 4.1-12). Here, regarding the drag coefficient $C_{D,air}$ in the airflow and the drag coefficient $C_{D,m}$ in the two-phase flow, the value

---

[*2] The comparison between this and previous studies is valid because the Reynolds number and the distances between the cylinder tip and measuring hole (divided by the cylinder diameter) are equivalent. (The Reynolds number is 2.0×10^4 in our two-phase flow measurement and 1.3×10^4 in the conventional research [111]. The distance between the cylinder tip and the measuring hole, divided by the cylinder diameter, is 0.2 here and 0.48 in the conventional research [111].)

integrated over θ_0–180° (measured from the stagnation point) is used (the meaning of the integration is described later). The ratio Ψ' is shown in

$$\Psi' = \frac{C_{D,m}}{C_{D,air}} = \frac{\int_{\theta_0}^{\pi} c_{p,m}}{\int_{\theta_0}^{\pi} c_{p,air}} \tag{4.26}$$

Results obtained from the above equation are shown in Fig. 4.1-14 (a). The meaning of integrating away from the stagnation point is explained below.

Figure 4.1-14 (b) shows an anticipated schematic diagram of the flow toward the gear teeth. The gear tooth surface is considered to be inclined by the pressure angle with respect to the flow toward the gear teeth. When this is replaced with a cylinder, the drag coefficient from a position separated from the stagnation point by the pressure angle becomes important. The pressure angle of the gear for which the fluid dynamic loss is experimentally measured is 20°. From Fig. 4.1-14 (a), Ψ' is 0.25 at $\theta_0 = 20°$.

(a) Two-phase flow drag coefficient / air drag coefficient
with respect to the starting angle of pressure integration
(estimated using experimental results)

(b) Relationship between pressure angle
and flow at front tooth (anticipated)
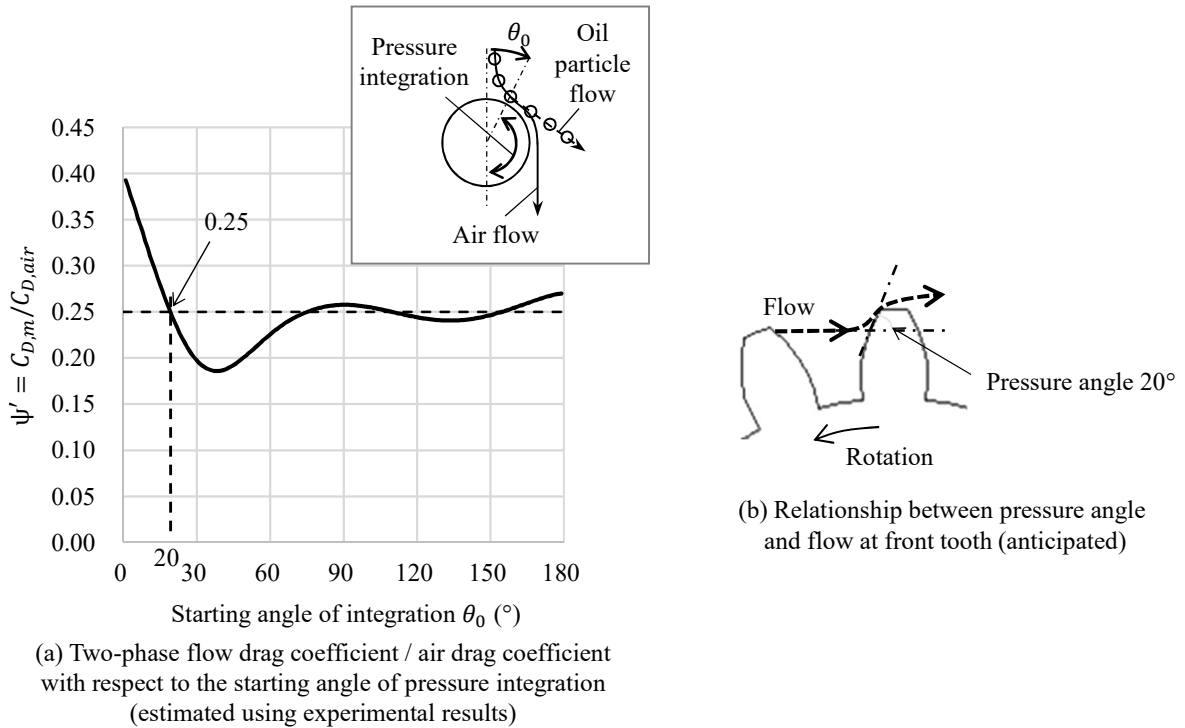
Fig. 4.1-14 Ratio between the two-phase flow and air drag coefficients for accurately modeling the two-phase flow

The flow drag in numerical simulations is considered to be larger than that in actual two-phase flows because the influence of the oil particles' separation from the air flow cannot be considered. Therefore, the accuracy of numerical simulations is improved by setting the oil density according to Ψ' in the simulation model. This is as follows (first, in Eq. 4.24, Ψ' is included in ρ_m):

$$F_m = C_{D,air} \frac{1}{2} (\Psi' \rho_m) u^2 = C_{D,air} \frac{1}{2} \{(1 - \alpha)\Psi' \rho_{air} + \alpha \Psi' \rho_{oil}\} u^2 \tag{4.27}$$

To incorporate the drag coefficient of the two-phase flow in the numerical simulation, the oil density $\rho_{oil,CFD}$ in the numerical simulation must be equal to $\Psi' \rho_{oil}$ (the subscript "CFD" indicates numerical simulation); this is expressed as

$$\rho_{oil,CFD} = \Psi' \rho_{oil} \tag{4.28}$$

On the other hand, when the oil density is changed, the mass flow rate of the oil supply jet changes. The mass flow rate of the oil supply jet affects the oil dynamic loss, as shown in Section 2.3; therefore, it is necessary to maintain it. The mass flow rate of the oil supply jet is maintained by adjusting its volume flow rate. This is expressed as

$$\dot{m}_{oil} = \rho_{oil}Q_{oil} = \Psi'\rho_{oil}\frac{Q_{oil}}{\Psi'} = \rho_{oil,CFD}\frac{Q_{oil}}{\Psi'} \tag{4.29}$$

If the air density is defined as ρ_{air} (based on Eq. 4.27), the mass of air in the gearbox changes, and subsequently the air density cannot be changed. Based on the above, the model considering the drag coefficient in a two-phase flow for numerical simulation is as follows (the subscript "mod" represents a value after correction):

$$F_{m,CFD,mod} = C_{D,air}\frac{1}{2}\left\{(1-\alpha)\rho_{air} + \alpha\rho_{oil,CFD}\right\}u^2 \tag{4.30}$$

$$\rho_{oil,CFD} = \Psi'\rho_{oil} \tag{4.31}$$

$$\text{The volumetric oil supply flow rate} = \frac{Q_{oil}}{\Psi'} \tag{4.32}$$

$$\tag{4.33}$$

In the case of the two-axis helical gearbox used in this research, $\Psi' = 0.25$. Although it is necessary to review the value of Ψ' according to the gearbox, the approach is considered to be effective provided it does not deviate considerably from the gearbox type and the experimental conditions of the research.

(3)   Effect of Modeling the Flow Drag in Two-Phase Flow

The effect of modeling the flow drag coefficient in two-phase flow is clarified by comparison of the cases that do and do not consider it. The flow drag $F_{m,CFD,org}$ when the modeling of the drag coefficient in the two-phase flow is neglected is given by the following equation (subscript "org" denotes the value before correction):

$$F_{m,CFD,org} = C_{D,air}\frac{1}{2}\left\{(1-\alpha)\rho_{air} + \alpha\rho_{oil}\right\}u^2 \tag{4.34}$$

The errors of $F_{m,CFD,mod}$ and $F_{m,CFD,org}$, when compared with F_m, are shown in Fig. 4.1-15 .
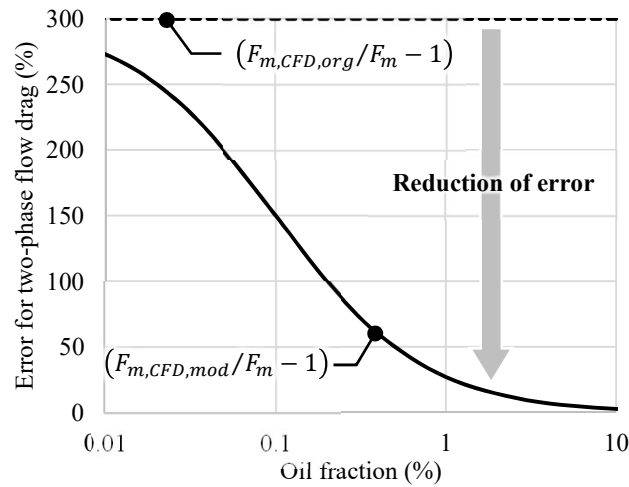
Fig. 4.1-15 Estimated error reduction induced by the difference between two-phase flow drag and single-phase flow drag

The horizontal axis (oil fraction) is set as a practical range within the range of 0.01–10%, according to the measurement results of the oil fraction around the gear (Section 3.6.2.3). It can be seen from the figure that the error is reduced in the model that considers the drag coefficient in the two-phase flow, as opposed to the model that neglects that drag coefficient ("Reduction of error" in the figure). Therefore, it is found that the modeling of the drag coefficient in two-phase flow is effective.

4.1.3.4   Effect of Phase Change of Oil

In general, a phase change of the oil may occur through boiling (attributable to the heat or pressure drop) or the separation of dissolved air (attributable to the pressure drop or shear force).

(1)   The Influence of Boiling Oil Attributable to Heat or Pressure Drop

In general, the boiling point of oil exceeds its flash point. The flash point of oil is 260 °C for the aeroengine gearbox oil (MIL-PRF-23699, etc.). Aeroengine gearboxes are operated at a temperature sufficiently lower (e.g., 160 °C) than this flash point, to prevent early deterioration of the oil. In addition, as shown in Section 4.1.2.2, the local temperature increase attributable to the compressibility of air is not considered to arise.

The temperature change of the saturated vapor pressure is shown in Fig. 4.1-16 . In the figure, the saturated vapor pressure of 160 °C is 650 Pa (0.0065 bar) in the "Synthetic Hydrocarbon", which is close to the oil for the aeroengine gearbox. This is sufficiently low, even if the dynamic air pressure of 0.05 bar at a flow speed of 100 m/s (the typical flow speed around the high-speed gear assumed in this research) is further reduced from the atmospheric pressure of 0.3 bar at the maximum altitude of the aircraft (∼10000 m).

Based on the above, it is highly likely that the boiling of oil is not influenced by the heat or pressure drop.
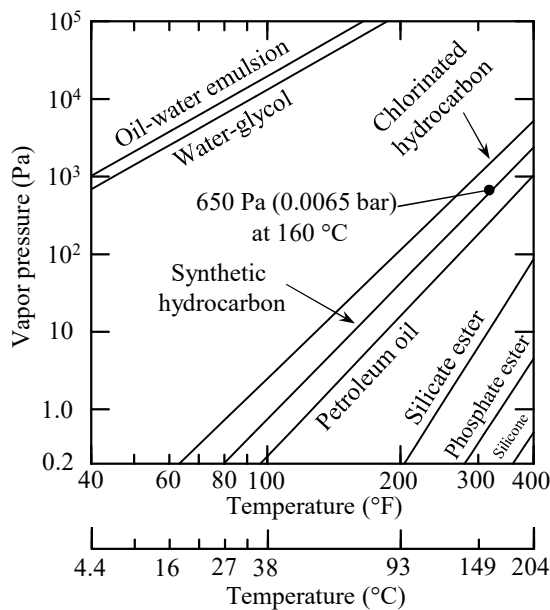
Fig. 4.1-16 Typical vapor pressure values (experimental results) [112]

(2)   Influence of Separation of Dissolved Air by Pressure Drop or Shear Force

As a phase change of oil attributable to the pressure drop or shear force, it is considered that the air dissolved in oil becomes separated. Oil supplied from the oil pump to the gearbox by an oil jet is discharged by a scavenge pump, passed through a cooler, returned to the oil tank, and then resupplied to the gearbox via the oil pump. Generally, air (with a volume of $\sim 8\%$) is dissolved in oil at atmospheric pressure and 20 °C. Furthermore, if air bubbles in the tank cannot be separated sufficiently, when the oil pressure is increased by an oil pump, the quantity of dissolved air bubbles is further increased according to Henry's law [93]. Bubbles dissolved in oil are considered to separate under a decrease in oil pressure after oil jet injection, as well as by the shear force of flow during injection. On the other hand, bubbles separated on the gear surface generally produce cavitation jets. Because no erosion occurs in real gearboxes, it is inferred that no large cavitation arises to affect the flow field.

From the above, it is concluded that the influence of the oil's phase change can be neglected in the gearbox considered here.

4.1.4   Separation Method to Aerodynamic and Oil Dynamic Losses

To numerically separate the fluid dynamic losses of air and oil into the components of air only (aerodynamic loss) and oil only (oil dynamic loss), the aerodynamic loss is calculated separately and subtracted from the fluid dynamic losses of air and oil:

- Fluid dynamic loss of air and oil = fluid dynamic loss obtained from numerical simulations of two-phase flow of air and oil
- Aerodynamic loss = fluid dynamic loss obtained from numerical simulations of airflow only
- Oil dynamic loss = fluid dynamic loss of air and oil, minus the aerodynamic loss

4.2   Simulation Models, Simulation Conditions, and Method of Evaluating Simulation Results

This section describes the evaluation method, simulation models, and simulation conditions used to clarify the fluid dynamic loss phenomena and validate the numerical simulation. Each gearbox is referred to as "GA", "GB1", and so on, to make each type easier to distinguish. Each gearbox has a target phenomenon, which covers not only fluid dynamic loss but also the phenomena of airflow and oil flow, as well as phenomena in the gear meshing and gear peripheral parts.

4.2.1   Evaluating Numerical Results to Clarify the Phenomena of Fluid Dynamic Loss

(1)   Overview of Evaluation Methods for Numerical Results

An outline of the evaluation method used for clarifying the phenomena of fluid dynamic loss is shown in Fig. 4.2-1 . To clarify the phenomena, it is necessary to understand the phenomena that constitute the fluid dynamic loss. In addition, the validation of this theory also helps to clarify the phenomena.

The phenomena that constitute fluid dynamic loss include the flow distribution, pressure distribution, torque distribution, and the influences of shrouds that affect them. The validation of the fluid dynamic

loss theory includes rotational speed characteristics and a dimensionless evaluation. Evaluation methods for clarifying the phenomena of fluid dynamic loss are described below.
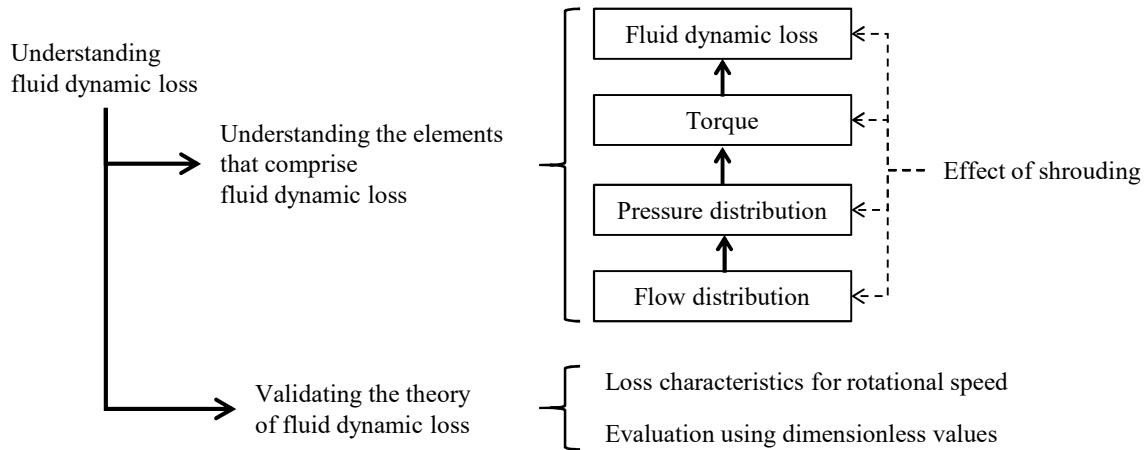
Fig. 4.2-1 Outline for understanding fluid dynamic loss (repost of Fig. 1.6-1)

(2)   Methods for Understanding Phenomena Constituting Aerodynamic Loss

（ⅰ） Airflow Distribution-Based Method

Understanding the characteristics of the airflow distribution from the airflow pattern and the resulting pumping action of the gear.

（ⅱ） Peripheral Distribution of Air Drag Torque Method

The torque produced by the air pressure is compared with that caused by the air shear force, and the validity of considering the torque arising from the air pressure distribution is examined. The peripheral distribution of the air drag torque is evaluated, and the cause of the torque is considered from the pressure distribution information.

（ⅲ） Influence of Shroud on Aerodynamic Loss Method

The effect of the shroud is evaluated by focusing on the range in which the gear moves air, the pumping action of the gear, and the aerodynamic loss.

（ⅳ） Validation of the Theory of Aerodynamic Loss (Rotational Speed Characteristics and Dimensionless Evaluation)

The validity of the aerodynamic loss theory is confirmed by the rotational speed characteristics of the airflow rate around the gear and the rotational speed characteristics of the aerodynamic loss. A dimensionless evaluation of the aerodynamic loss shows that its dimensionless number can capture the loss characteristics.

(3)   Understanding Phenomena Constituting Oil Dynamic Loss

（ⅰ） Oil Flow Distribution

To understand the phenomenon of oil flow in the gear meshing and peripheral parts, and to deepen our understanding of the phenomena, we perform a simplified simulation.

（ⅱ） Peripheral Distribution of Torque due to Oil Flow Drag

The peripheral distribution of oil drag torque is obtained by subtracting the torque distribution in air from that in a two-phase flow of air and oil. Similarly, the oil pressure distribution is obtained by

subtracting the air pressure distribution from the pressure distribution in a two-phase flow of air and oil. The causes of the torque generated by the oil pressure field are discussed.

(ⅲ) Influence of Shroud on Oil Dynamic Loss

We evaluate the influence of the shroud by focusing on the amount of oil around the gear, the oil churning of the gear, and the oil dynamic loss.

(ⅳ) Validating the Theory of Oil Dynamic Loss (Rotational Speed Characteristics and Dimensionless Evaluation)

The validity of the theory of oil dynamic loss is confirmed using the rotational speed characteristics of oil flow rate around the gear and the rotational speed characteristics of the oil dynamic loss. The dimensionless evaluation of the oil dynamic loss shows that the dimensionless number of the loss can capture the loss characteristics.

4.2.2 Two-Axis Helical Gearbox (GA) for Clarifying Phenomena of Fluid Dynamic Loss and Validating the Numerical Simulation

(1) Simulation Model and Simulation Conditions

The simulation model is shown in Fig. 4.2-2 . The shape of the simulation model almost matches that of the actual machine. Two-axis helical gears, a shroud, oil jet nozzles, bearings, and a housing are modeled. Two types of gear shrouds are used, as shown in Fig. 3.1-3 . The side and bottom surfaces are subjected to pressure boundary conditions (atmospheric pressure) to model the effects of an air breather and scavenge port. The remaining boundaries are subjected to no-slip boundary conditions. The simulation region is divided into eight blocks; each block is assigned to a different computer for parallel calculation, as shown in "Block #1" in Fig. 4.2-2 .
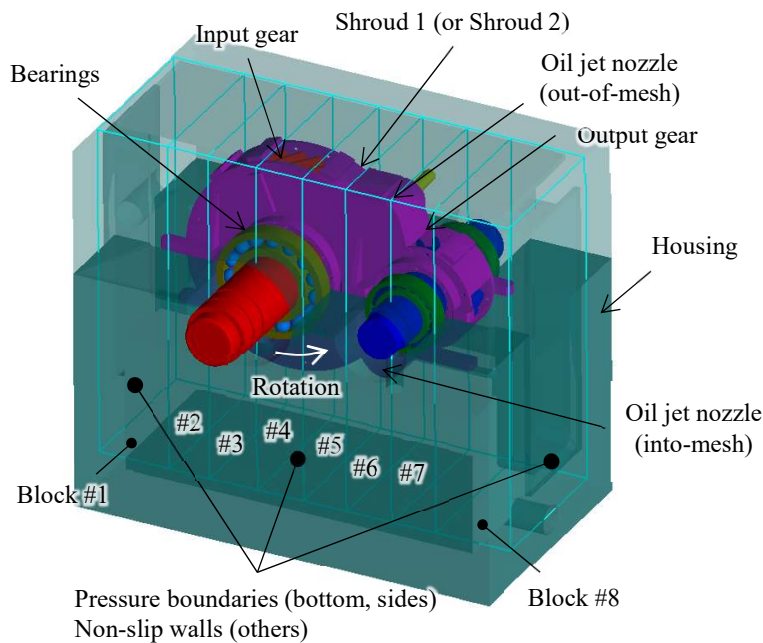
Fig. 4.2-2 Simulation model of the two-axis helical gearbox (GA)

124

The calculation mesh around the gear meshing is shown in Fig. 4.2-3 (a). The calculation mesh size is uniform in all the x, y, and z directions and set to 1.5 mm. The gear tooth along its height is discretized using eight cells of the calculation mesh. As shown in Section 4.1.2.1, a gap is set between the gear tooth surfaces when modeling the gear teeth. The gear tooth thickness is reduced by 20%, and the phase is adjusted such that the gaps between the teeth are uniform. The calculation mesh around the gear periphery is shown in Fig. 4.2-3 (b). The clearance of 5 mm between the gear tooth tip and the inner wall of the shroud is discretized using approximately three cells. The total number of cells in the calculation mesh is 4.18 million.

The oil conditions (oil specifications, oil supply conditions, etc.), air conditions (internal pressure of gearbox, etc.), and rotational speed conditions are shown in Table 4.2-1 . During the simulation, oil and air temperatures are held constant at the scavenging oil temperature of 55 °C in the experiment. This temperature setting considers the rapid temperature increase in gear meshing, as the fluid dynamic loss in gear meshing accounts for more than half of the total fluid dynamic loss when the oil supply flow rate is large (see Section 6.11.5).

(a) Around gear mesh

(b) Around gear periphery
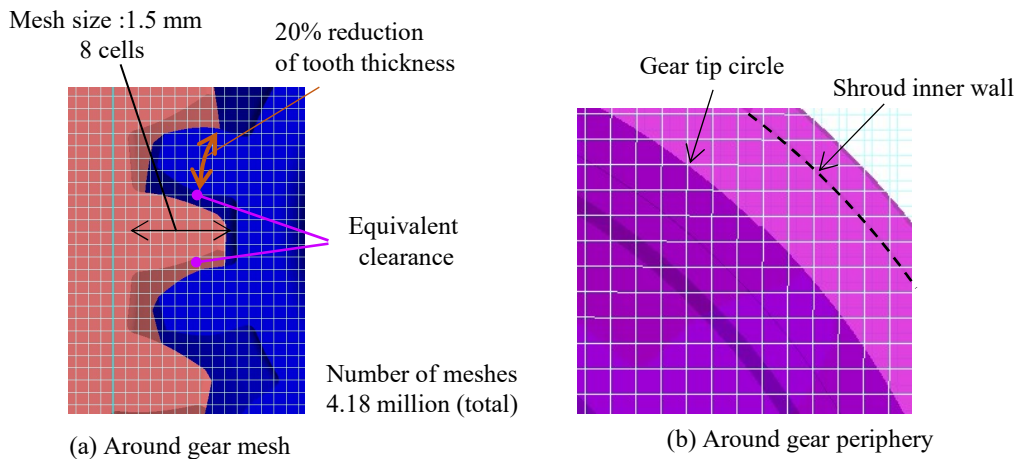
Fig. 4.2-3 Mesh calculation for the two-axis helical gearbox (GA) simulation model

Table 4.2-1 Simulation conditions for the two-axis helical gearbox (GA) model

Items	Conditions
Oil density	971 kg/m^3
Oil kinematic viscosity	15.7 mm^2/s
Oil jet direction	Into-mesh, out-of-mesh
Oil jet supply rate to gears (total)	1.48–7.40 L/min
Air density	1.06 kg/m^3
Air dynamic viscosity	18.7 mm^2/s
Internal pressure	1.0 atm
Input speed	7000–10000 rpm

(2)   Simulation Result Evaluation Method

To validate the numerical simulation of fluid dynamic loss, the numerical simulation results must reproduce the experimental results qualitatively. Thereafter, the qualitative reproducibility of the numerical

simulation results for the fluid dynamic loss of air and oil, the aerodynamic loss, and the oil dynamic loss is evaluated by comparison with the experimental results. The method shown in Section 4.2.1 is used to evaluate the phenomena of fluid dynamic loss.

(3)   Simulation Error Evaluation Method

To contribute to the standardization of low-power-loss designs for high-speed gear systems, it is necessary to clarify quantitative errors. The errors are evaluated as follows.

- The random error $[= (2\sigma/\hat{\bar{P}})/\sqrt{N_{rot}}$, where σ is the standard deviation, ˆdenotes the ensemble averaged value, $\bar{P}$ is the time-averaged power loss in one rotation, and N_{rot} is the number of rotations and is set to 10 because of the fluctuation in time] is evaluated as the relative standard error of 2σ for the averaged value of one rotation.

- The quantitative systematic error is evaluated as the standard deviation of the relative value of the deviation from the experimental value (true value).

4.2.3   Various Gearboxes for Validation of Numerical Simulation Methods

4.2.3.1   Two-Axis Helical Gears (GX1) for Validating Air Pressure in the Tip Clearance under Gear Meshing

(1)   Simulation Model and Conditions

To validate the air pressure at the tip clearance under gear meshing, we use the experimental results of Diab et al. [42] for two-axis helical gears. A simulation model with the same configuration as the experiment is shown in Fig. 4.2-4 (a). The gear shaft is ∼40 mm and considerably smaller than the gear diameter of 312 mm; hence, it is omitted. The surrounding boundary surface is set to the pressure boundary.

(a) Simulation model   (b) Calculation mesh around gear mesh
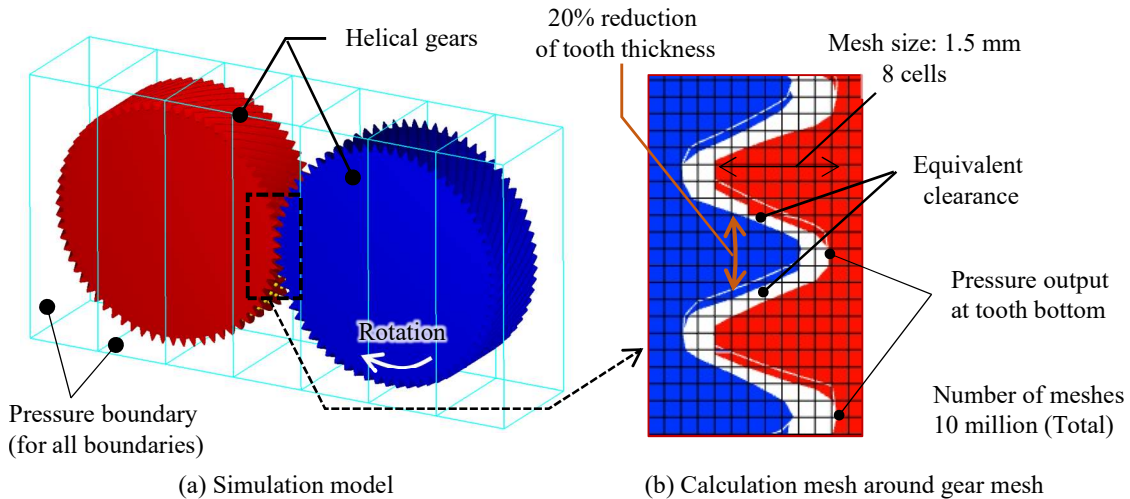
Fig. 4.2-4 Simulation model and calculation mesh for two-axis helical gears (GX1)

Figure 4.2-4 (b) shows the calculation mesh around the gear mesh. When modeling the gear meshing part (as shown in Section 4.1.2.1), to provide a clearance between the gear tooth surfaces, the tooth thickness is reduced by 20%, and the phase is adjusted so that the clearance between the teeth become uniform. As in the experiment, the time history of the pressure at the tooth bottom is evaluated. The calculated mesh size is set to 1.5 mm in the x, y, and z directions. The number of cells for the tooth height is eight.

The number of calculation meshes is 10 million for the whole model. The gear specifications and operating conditions are shown in Table 4.2-2 .

Table 4.2-2 Gear specifications and operation condition for two-axis helical gears (GX1)

Gear type	Helical
Module	4 mm
Number of teeth	66
Helix angle	30°
Pitch diameter	312 mm
Face width	100 mm
Rotational speed	3780 rpm
Peripheral velocity	62 m/s

(2)   Methods for Evaluating Simulation Results and Simulation Error

To validate the air pressure in the tip clearance under gear meshing, the numerical simulation results are compared with the experimental ones. The simulation error is evaluated as follows:

- The relative standard error $(= (\sigma/\hat{\max}(p))/\sqrt{\mathscr{N}_{pos}}$, where $\max(p)$ is the maximum pressure and $\mathscr{N}_{pos}$ is the number of places at the bottom of the tooth) of σ for the maximum pressure at the bottom of the tooth is used as the error of the maximum pressure there. The relative standard error of the minimum pressure is evaluated in the same manner. $\mathscr{N}_{pos}$ is set to eight for both errors.

- The quantitative systematic error is set as the relative value and compared with the experimental value (true value). This is averaged with errors at 35% and 65% positions from the leading side of the helical gear.

4.2.3.2   One-Axis Spur Gear (GX2) for Validation of Aerodynamic Loss in Single Gear

For the aerodynamic loss in a single gear, the loss value and loss reduction effect of the shroud are important. Next, the numerical simulation accuracy is validated using the aerodynamic loss in a single gear under different gear specifications (without the shroud), as well as with the loss reduction rate of three types of shrouds.

(1)   Simulation Model and Conditions

（ⅰ）   Simulation Model and Simulation Conditions for Validating Aerodynamic Loss in A Single Gear

To validate the aerodynamic loss in a single gear, Dawson's experimental results [31] are used. Table 4.2-3 shows the gear specifications; 16 gears with different specifications are used.

An example of a simulation model for the No.1 gear in Table 4.2-3 is shown in Fig. 4.2-5 (a). The gear shaft (25 mm diameter) is fairly small compared with the gear diameter of 300 mm; hence, it was omitted. The surrounding boundaries are set to pressure boundaries. When modeling the gear, the thickness of the teeth is reduced by 20% following the method shown in Section 4.1.2.1. The calculation mesh is shown in Fig. 4.2-5 (b). The calculation mesh size is set to 9 mm. The calculation mesh size is four meshes for the tooth height of the gear. The number of calculation meshes is ~160000. For other gears in Table 4.2-3 , the simulation modeling and calculation mesh are similar, as shown in Fig. 4.2-5 .

Table 4.2-3 Gear specifications for one-axis spur gears (GX2)

Gear No.	Spur or Helical	Root diameter mm	Module mm	Face width mm	Number of teeth −
1	Spur	300	16	187	19
2	Spur	760	24	187	32
3	Spur	514	16	187	32
4	Helical	514	16	187	32
5	Spur	300	8	187	38
6	Spur	760	16	187	48
7	Spur	514	8	187	64
8	Spur	1160	16	187	73
9	Spur	300	3	74	94
10	Spur	760	8	32	95
11	Spur	760	8	70	95
12	Spur	760	8	114	95
13	Spur	760	8	187	95
14	Spur	760	8	267	95
15	Spur	760	8	355	95
16	Spur	760	8	543	95

(a) Simulation model   (b) Calculation mesh
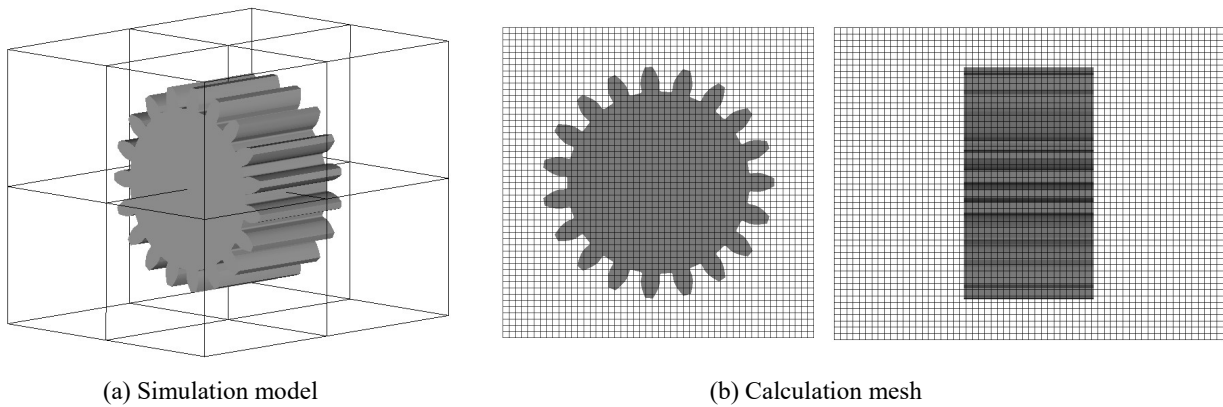
Fig. 4.2-5 Simulation model and calculation mesh for Gear No.1 (one-axis spur gears, GX2)

(ii)   Simulation Model and Conditions for Validating Loss Reduction Rate with Shroud in Aerodynamic Loss for A Single Gear

The effect of reducing the aerodynamic loss by shrouding is validated. Dawson conducted experiments on the effect of seven types of shrouds [31]. Here, the numerical simulation is validated using three types of representative shrouds. The shrouds to be validated are shown in Fig. 4.2-6 . The specifications of the shrouds are shown in Table 4.2-4 . Shroud *d* (shown in Fig. 4.2-6 (a)) features a peripheral wall in the range of 270 °, without side plates. Shroud *f* (shown in Fig. 4.2-6 (b)) is simply Shroud *d* with those added side plates. Shroud *g* (shown in Fig. 4.2-6 (c)) is a shroud with a completely surrounding peripheral wall, though otherwise identical to Shroud *f*. Operating conditions match those in the experiment (rotational speed: 750 rpm; air temperature: 20 °C; 1 atm).

(a) Shroud d (b) Shroud f (c) Shroud g
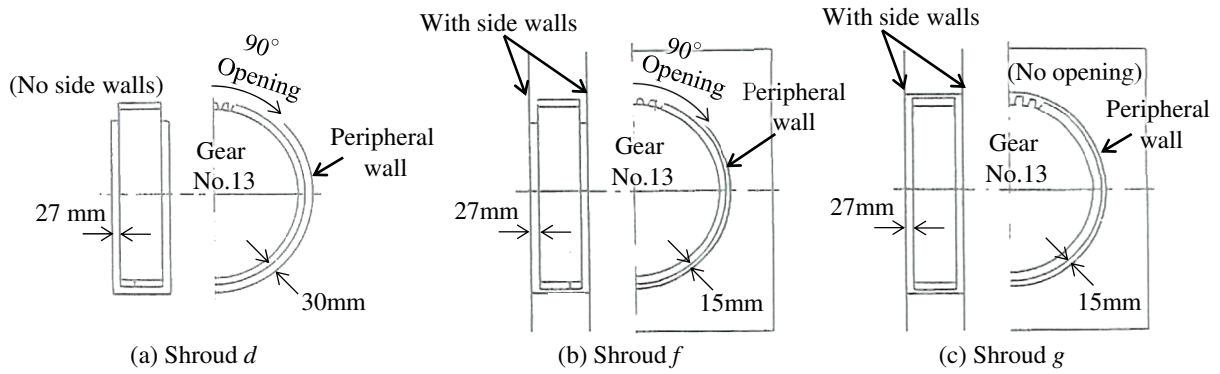
Fig. 4.2-6 Shrouds for Gear No. 13 (one-axis spur gears, GX2)

Table 4.2-4 Shroud specifications for one-axis spur gears (GX2)

Shroud No.	Peripheral wall		Axial wall	
	Opening angle	Clearance	Presence/Absence	Clearance
Unshrouded	Fully open	∞	Absent	∞
Shroud d	90 °	30 mm	Absent	∞
Shroud f	90 °	15 mm	Present	27 mm
Shroud g	No opening	15 mm	Present	27 mm

(a) Simulation model   (b) Calculation mesh
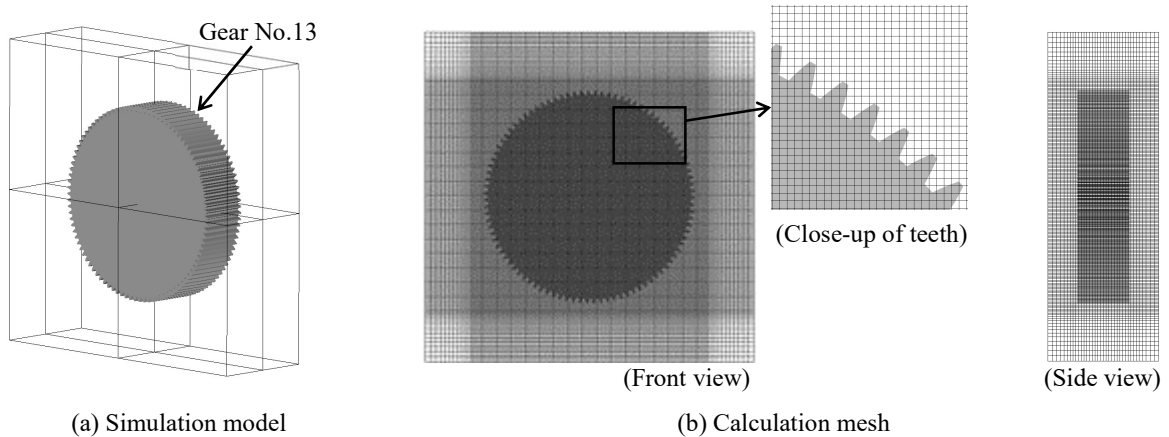
Fig. 4.2-7 Simulation model and calculation mesh for Gear No.13 (one-axis spur gears, GX2)

(a) Simulation model   (b) Calculation mesh
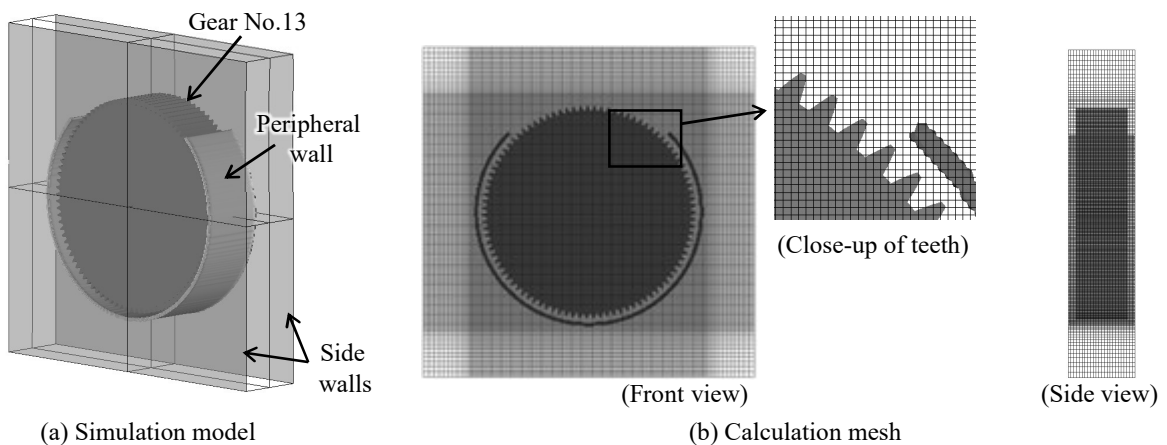
Fig. 4.2-8 Simulation model and calculation mesh for Gear No.13 with Shroud f (one-axis spur gears, GX2)

Figure 4.2-7 shows the simulation model and calculation mesh without shrouds. The surrounding boundaries are set to pressure boundaries. The calculation mesh size around the gear is set to 5 mm in the direction perpendicular to the gear axis, and 10 mm in the direction of that axis. For the gear tooth height, the calculation mesh is roughly set to four. The number of calculation meshes was set to ~2 million. Figure 4.2-8 shows the simulation model and calculation mesh for the gear under Shroud *f*. The surrounding boundaries are set to pressure boundaries. The calculation mesh size around the gear is set to match that in Fig. 4.2-7 (5 mm in the direction perpendicular to the gear axis, and 10 mm in the direction of that axis). The number of calculation meshes is set to ~1.14 million.

(2)   Methods for Evaluating Simulation Results and Simulation Errors

To validate the aerodynamic loss in a single gear, the numerical simulation results are compared with the experimental ones. The aerodynamic loss in a single gear under different gear specifications (without a shroud) and the loss reduction rates for three types of shrouds are evaluated. The simulation error is evaluated as follows.

- A random error attributable to the fluctuation over time is defined as the relative standard error [$= (\sigma/\hat{\bar{P}})/\sqrt{N_{rot}}$] of σ for the mean value of one rotation after reaching the steady state. N_{rot} is set to 3.
- The quantitative systematic error is defined as the relative value of the deviation from the experimental value (true value).

4.2.3.3   Two-Axis Spur Gearbox (GB1) for Validating Oil Jet Flow to Gear Mesh

(1)   Simulation Model and Conditions

The simulation model and calculation mesh are shown in Fig. 4.2-9 (a). The simulation region is set as the surroundings of the gear meshing part, and the boundaries of the surroundings are set as pressure boundaries. The oil jet is injected from the top of the gear mesh; thus, the rotational direction of the input gear is clockwise (gear mesh moves from the top to the bottom) for the into-mesh jet and counterclockwise (gear mesh moves from bottom to top) for the out-of-mesh jet.

(a) Simulation model and calculation mesh   (b) Calculation mesh around gear mesh
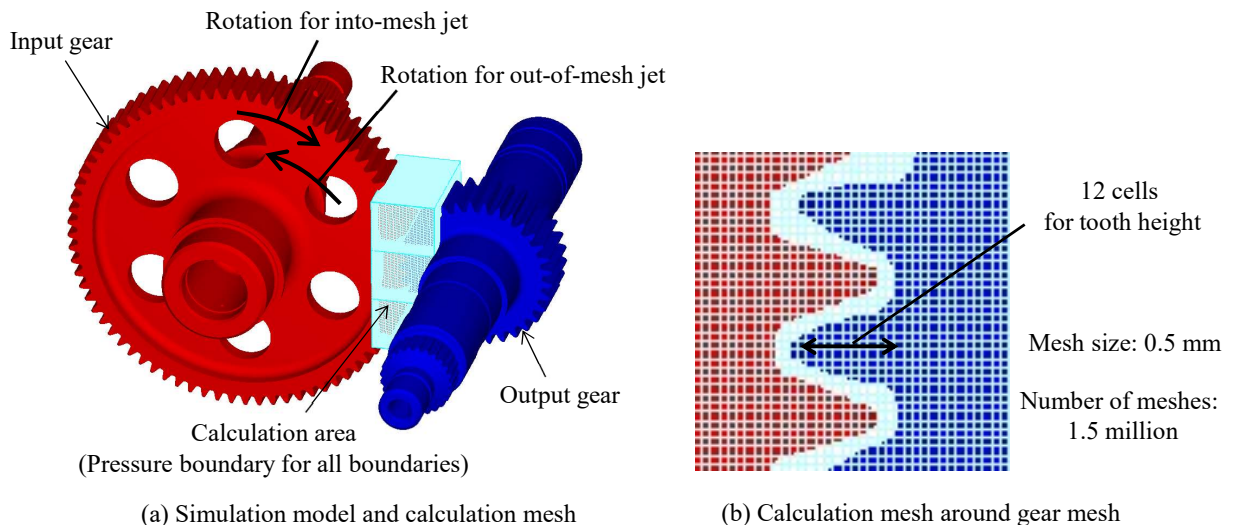
Fig. 4.2-9 Simulation model and calculation mesh for two-axis spur gearbox (GB1)

The calculation mesh around the gear mesh is shown in Fig. 4.2-9 (b). In the gear meshing modeling (as shown in Section 4.1.2.1), to provide a clearance between gear teeth, the tooth thickness is reduced by 20%, and the phase is adjusted such that the clearance between the teeth is equivalent. The calculation mesh size is set to 0.5 mm (12 meshes for the gear tooth height). The number of calculation meshes is 1.5 million. Other simulation conditions are the same as those shown in Table 3.1-4 .

(2)   Method Evaluating Simulation Result

To validate the oil jet flow to the gear mesh, we confirm that the numerical simulation results qualitatively reproduce the experimental ones regarding the inflow of the oil jet to the gear mesh (for the into-mesh jet) and the spread of the oil jet to the gear tooth (for the out-of-mesh jet).

4.2.3.4   One-Axis Spur Gearbox for Validation of Oil Spray Flow to Gear Tooth (GB2-2)

(1)   Simulation Model and Conditions

The simulation model is shown in Fig. 4.2-10 (a). The simulation region contains the entire gear, and the surrounding boundaries are set to pressure boundaries. The oil spray nozzle is directed to the gear center in the radial direction. When modeling the gear shape, the tooth thickness is reduced by 20% to follow the method described in Section 4.1.2.1. The calculation mesh around the oil spray nozzle is shown in Fig. 4.2-10 (b). The calculation mesh size is 0.5 mm (12 meshes for gear tooth height). The number of calculation meshes is 5.6 million.

(a) Simulation model   (b) Calculation mesh
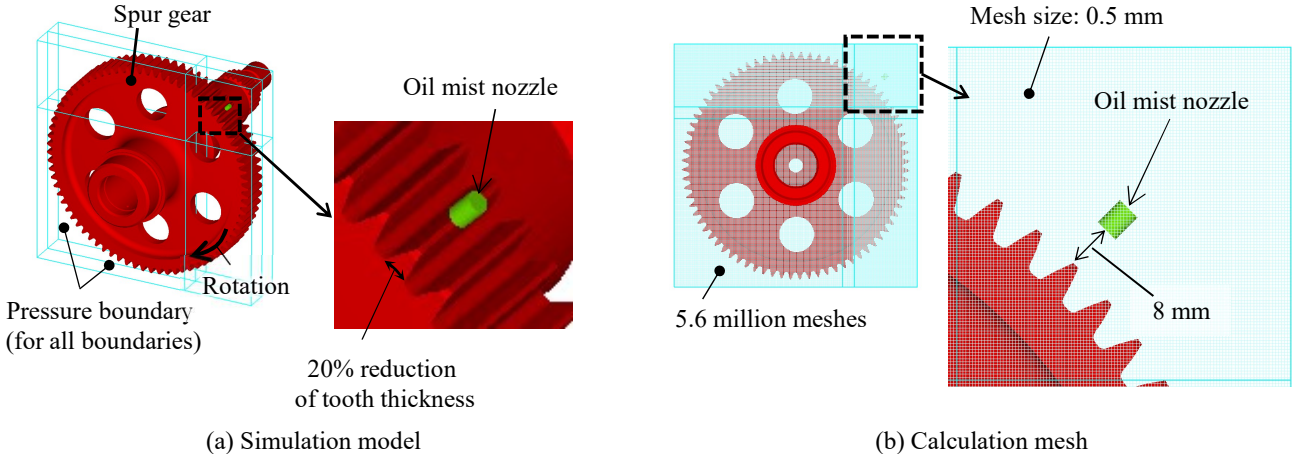
Fig. 4.2-10 Simulation model and calculation mesh for one-axis spur gearbox (GB2-2)

The operating conditions, oil specifications, and temperature match the experimental conditions indicated under "Oil mist nozzle" in Table 3.1-6 , where the numerical simulation model of the oil spray nozzle is set such that the condition at the spray reach position to the gear tooth is equivalent to the experimental condition. The correspondence between the simulation conditions and experimental conditions for the oil spray nozzle is shown in Fig. 4.2-11 .

Figure 4.2-11 (a) shows an experiment using only the spray nozzle. The experiment was conducted using a two-fluid nozzle MMA 10 manufactured by Kyoritsu Gokin Co., Ltd., which has an air passage annularly installed around a liquid tube. The liquid particle velocity on the central axis was measured at distances of 100, 300, 500 mm from the nozzle under the experimental conditions of 10 L/min for air and 0.05 L/min for

liquid[*3] (liquid volume fraction = 0.48%). Using the measured results of these particle velocities and the relationship in which the distance along the central axis of the jet is inversely proportional to the distance from the nozzle [113], the particle velocity at the tooth tip position (25 mm from the nozzle tip) in the one-axis spur gear box (GB 2-2) experiment is estimated as 64 m/s.

When modeling this in a numerical simulation model, it is necessary to remember that the simulation cannot solve the oil particles individually and that the spread of the oil spray in the experiment cannot be reproduced (because the mixing layer between the oil spray and air cannot be resolved). Therefore, the simulation is modeled so that the gas–liquid mixing ratio and flow velocity at the tooth tip position are equivalent to those of the oil spray. The simulation model is shown in Fig. 4.2-11 (b). The liquid volume fraction of the oil spray in the simulation is set to 0.48%, and the velocity is set to 64 m/s along the central axis of the spray at the tooth tip position. Both the liquid fraction and velocity match that in the experiment. The diameter of the oil spray nozzle in the simulation is set to 1.8 mm, to match the total flow rate of the air and oil. To suppress the spread of the spray (in contrast to the experiment) in the simulation, the oil nozzle is set close to the tooth tip (8 mm clearance), as shown in Fig. 4.2-10 (b).

Air flow rate 10 L/min
Liquid flow rate 0.05 L/min
(ethanol 20 %, water 80 %)
Liquid fraction 0.48 %

25mm

A

Center speed 64 m/s (estimated)

(a) Experimental oil mist nozzle (photograph)

Oil jet nozzle

Mixture flow rate 10 L/min
Mixture density 5.9 kg/m^3
(liquid fraction 0.48 %)
Oil jet speed 64 m/s

Jet diameter 1.8 mm

A'

Jet speed ~64 m/s
(estimated/uniform)

(b) Simulated oil jet nozzle
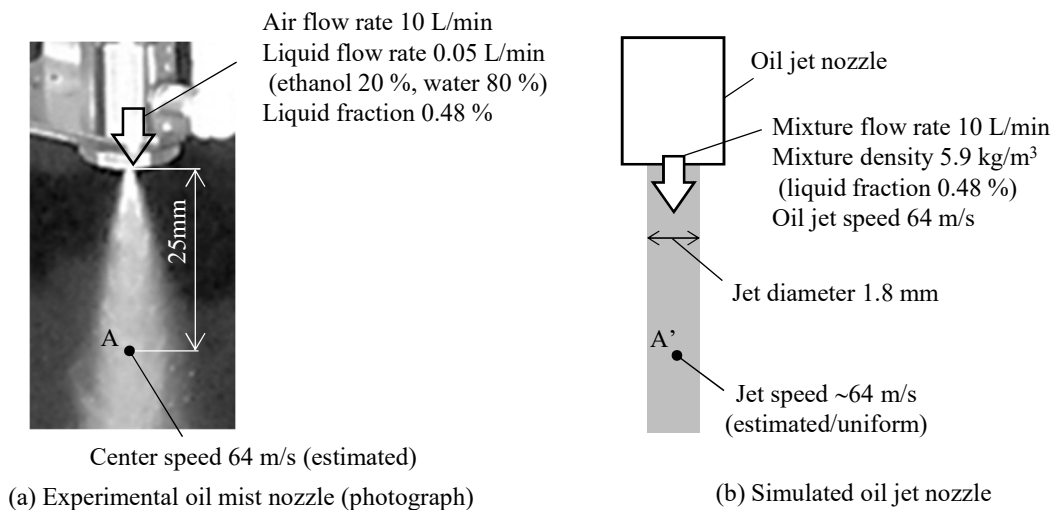
Fig. 4.2-11 Real and simulated oil jet nozzle

(2) Method of Evaluating Simulation Result

To validate the oil spray flow to the gear tooth surface, we confirm that the numerical simulation result qualitatively reproduces the experimental result regarding the inflow of the oil spray to the gear tooth surface.

4.2.3.5 One-Axis Spur Gearbox (GB3) for Validation of Oil Flow between Gear Tooth Tip and Shroud Wall

(1) Simulation Model and Conditions

The simulation model is shown in Fig. 4.2-12 (a). Similarly to the one-axis spar gearbox experiment with a shroud (GB3), a single spar gear is enclosed by a shroud with one opening on the peripheral surface. An oil jet is directed at 16 positions on both gear sides (eight positions on each side) for a total flow rate of 20 L/min (10 L/min on each side). During modeling, the tooth thickness is reduced by 20%, to follow the method shown in Section 4.1.2.1. To incorporate the drag coefficient of two-phase flow (Section 4.1.3.3),

---

[*3] Water mixed with 20% ethanol was used to reduce surface tension.

the oil density in the simulation is multiplied by Ψ' (0.25, ratio of drag coefficient, Eq. 4.28).

The calculation mesh and boundary conditions are shown in Fig. 4.2-12 (b). The simulation range contains the entire gear (including the shroud), and the surroundings are set as a pressure boundary. The calculation mesh size is 1.5 mm (approximately four meshes for tooth height and 11 meshes between the gear tooth tip and shroud inner wall); the number of calculation meshes is 1.9 million.

(a) Simulation model
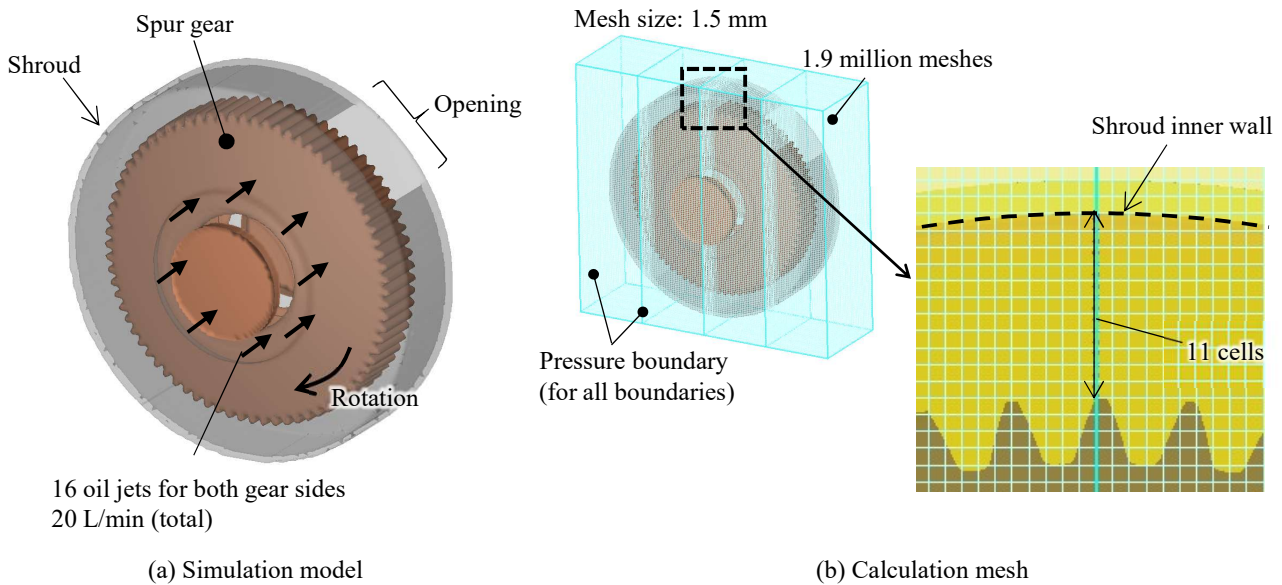
(b) Calculation mesh

Fig. 4.2-12 Simulation model and calculation mesh for one-axis spur gearbox with shrouding (GB3)

(2)   Methods of Evaluating the Simulation Result and Simulation Error

To validate the oil flow between the gear tooth tip and shroud wall, the reproducibility of the experimental result is evaluated with regard to the oil fraction, mixture velocity, and oil flow speed between the gear tooth tip and shroud wall. The oil flow speed is considered to be related to the oil flow rate around the gear.

When the oil fraction in the numerical simulation is compared with the experimental results, it is first multiplied by Ψ' (0.25, Eq. 4.28). As for the mixture velocity, air and oil are measured at the same speed (mixture velocity) as in the experiment, and air and oil are used at the same speed in the gas–liquid interface cell as in the simulation. Therefore, the flow speed in the simulation results can be compared with the mixture velocity in the experiment. The oil flow speed is evaluated using both the experimental and simulation results, using the oil fraction $\times$ mixture velocity.

We evaluate the simulation error as follows:

- The random error attributable to the variation in time is set as the relative standard error ($= (\sigma/\hat{\bar{P}})/\sqrt{N_{rot}}$) of σ for the mean value of one rotation after the steady state. N_{rot} is set to 10.
- The quantitative systematic error is evaluated as the relative value of the deviation from the experimental value (true value).

4.3   Summary of the Evaluation Methods of Numerical Simulation Error

The error evaluation methods used for the numerical simulation are summarized in Table 4.3-1 .

Table 4.3-1 A summary of methods for evaluating simulation error

Fluid	Validation items for numerical simulation and modeling	Gearbox	Experimetal results for comparison	Precision of numerical simulation — Random error due to fluctuation in time	Accuracy of numerical simulation — Quantitative error (systematic error) = deviation from true value (experimental value)
Air and oil	Fluid dynamic loss in two-phase flow of air and oil	Two-axis helical gearbox (GA), 2 shrouds	Aerodynamic loss	Relative standard error of 2σ (with values for last 10 rotations, averaged in each rotation)	Relative standard deviation between experimental and simulation results
			Oil dynamic loss		
			Fluid dynamic loss of air and oil		
Air	Air leak flow from clearance in gear mesh	Two-axis helical gears (GX1)	Time history of pressure at tooth bottom	Relative standard error of σ (with min and max value at 8 tooth bottoms)	Relative error (averaged at 35% width and 65% width from helical leading side)
Air	Aerodynamic loss with single gear	One-axis spur gears (GX2), 16 gears	Aerodynamic loss with different gears	Relative standard error of σ (with values for last 3 rotations, averaged in each rotation)	Relative error between experimental and simulation results
		One-axis spur gears (GX2), 3 shrouds	Aerodynamic loss with different shrouds		
Oil	Inflow of oil jet into gear mesh	Two-axis spur gearbox (GB1)	Visualization of oil distribution	—	—
Oil	Inflow of oil mist onto tooth surface	One-axis spur gearbox (GB2-2)	Visualization of oil distribution	—	—
Oil	Superficial flow velocity of oil near the wall	One-axis spur gearbox (GB3)	Superficial flow velocity of oil	Relative standard error of 2σ (with values for lat 10 rotations, averaged in each rotation)	Relative error between experimental and simulation results

4.4   Validating the Applicability of Numerical Simulation Methods

To clarify the phenomena of fluid dynamic loss, it is necessary to qualitatively reproduce them. In this section, we show that the phenomena can be qualitatively reproduced using the simulation modeling methods for airflow and oil flow, as well as the combined simulation modeling methods for the fluid dynamic loss of air and oil. We also identify the quantitative accuracy for practical applications.

4.4.1   Validation of Modeling Methods for Airflow

4.4.1.1   Validation of Air Pressure in the Tip Clearance of Gear Mesh for Validation of Airflow in Gear Meshing Part

In the gear meshing part, the pressure increases and air is pushed out by the tooth approach and contact; then, the pressure decreases and the air is sucked in by the tooth separation [42]. The qualitative reproduction of these phenomena serves to validate the numerical simulation method of the airflow in the gear meshing part. Then, we compare the experimental results for tooth bottom pressure under gear meshing [42] with the simulation results, using the simulation model and conditions shown in Section 4.2.3.1. When modeling the gear meshing part, it is necessary to ensure a clearance between the gear teeth, to prevent clogging of the calculation cell in the gear meshing part, as described in Section 4.1.2.1. Therefore, because the pressure on the tooth surface in the gear meshing part is considered to differ from the actual pressure, we include this difference.

The pressure distribution on the tooth surface around the gear meshing part is shown in Fig. 4.4-1 . This pressure distribution is the result of averaging at every one pitch of the tooth during one rotation. It can be seen that the pressure increases at the into-mesh side and decreases at the out-of-mesh side.

The pressure distribution with respect to the velocity vector on the central cross section of the tooth width (around the gear meshing) is shown in Fig. 4.4-2 . The pressure contour of the gear meshing part is shown in Fig. 4.4-2 (a). The into-mesh part is enlarged in Fig. 4.4-2 (b), and the out-of-mesh part is enlarged in (c). It can be seen from Fig. 4.4-2 (a) that the pressure increases at the former ("A" in the figure) and decreases at the latter ("B" in the figure). Figure 4.4-2 (b) shows the pressure contour and relative velocity vector at the into-mesh. It can be seen that the air outflow direction opposes the rotational direction ("Discharge of air" in the figure). Figure 4.4-2 (c) shows the pressure contour and relative velocity vector at the out-of-mesh part. It can be seen that air inflow occurs in the direction opposing the rotational direction ("Suction of air" in the figure).
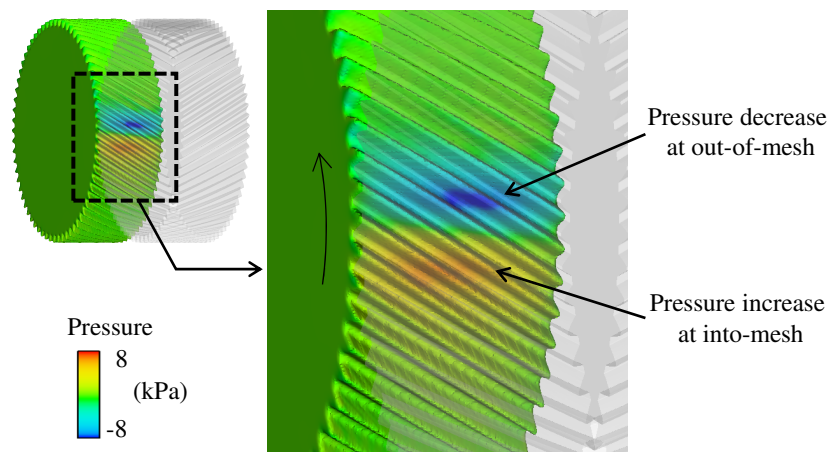
Fig. 4.4-1 Pressure distribution on the gear tooth flank around the gear mesh (simulation results)

(a) Pressure contour around gear mesh   (b) Detail of A (into-mesh)   (c) Detail of B (out-of-mesh)
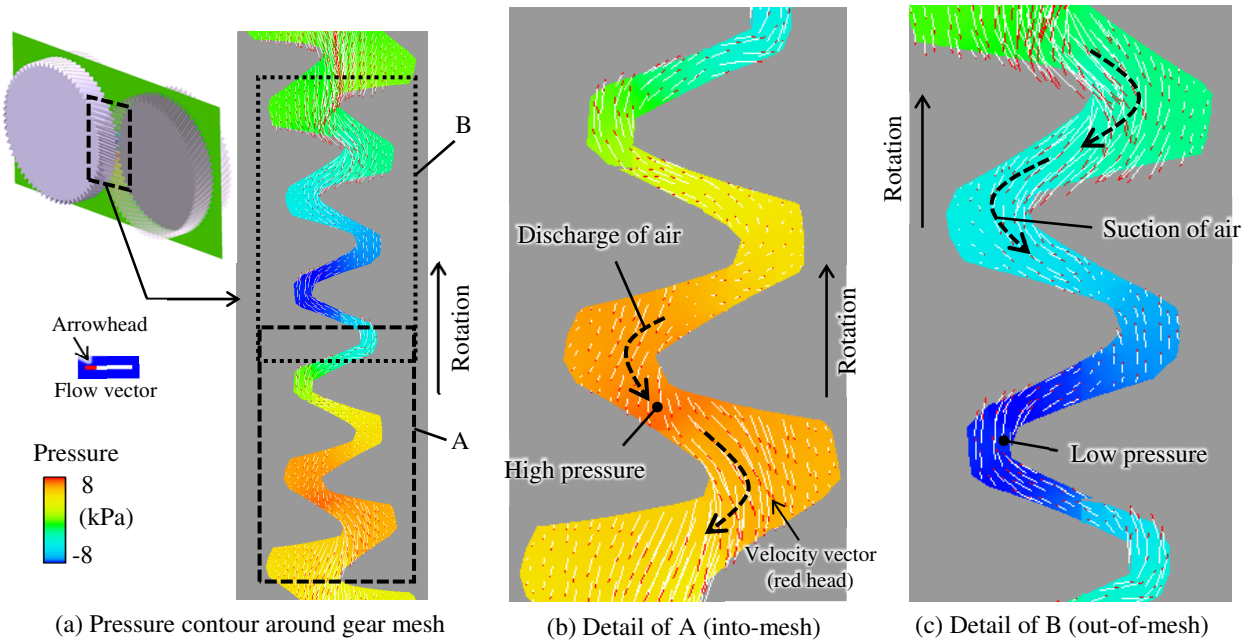
Fig. 4.4-2 Velocity vector around the gear mesh in rotational coordinate system (simulation results)

Fig. 4.4-3 compares the simulation and experimental results for the tooth bottom pressure. Figure 4.4-3 (a) shows the time history of the pressure at a position 35% of the width away from the helical leading side (forward side in the rotational direction), and Fig. 4.4-3 (b) shows the time history of the pressure at a position 65% of the width away from the helical leading side. In each figure, the horizontal axis shows the rotation angle (0 is the meshing center position), and the vertical axis indicates the tooth bottom pressure. Because the pressure change is important, the phase of the horizontal axis in the simulation is adjusted to match the peak of the experiment. The simulation results qualitatively agree with the experimental results.

(a) 35% width from helical leading side   (b) 65% width from helical leading side
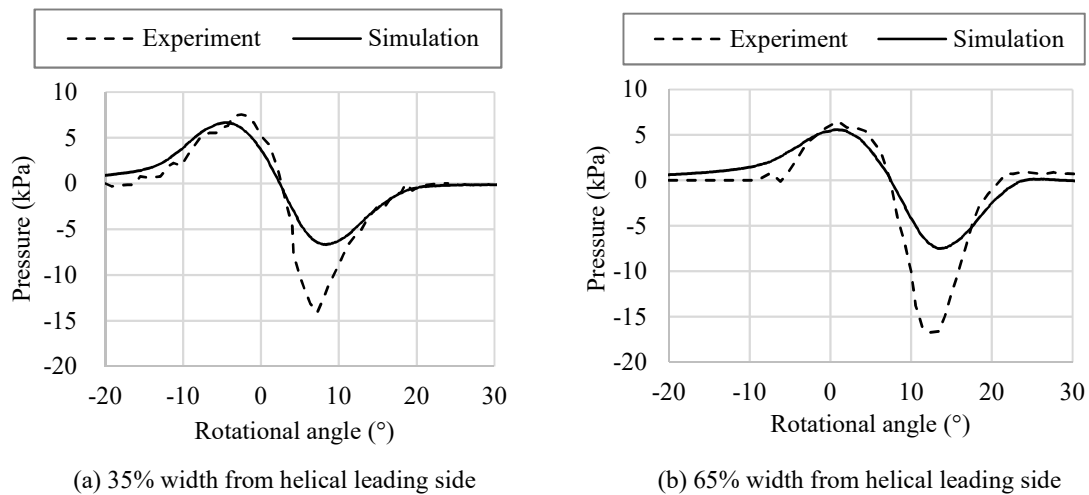
Fig. 4.4-3 Comparisons of experimental and simulation pressures at the tooth bottom (helical gear, $\beta=30°$)

Regarding the random pressure error attributable to the fluctuation over time in the simulation, the relative standard error $(\sigma/\hat{p})/\sqrt{\mathcal{N}_{rep}}$ (where σ is the standard deviation, $\hat{p}$ is the ensemble averaged pressure, and $\mathcal{N}_{rep}$ is the number of repetitions) of σ is 0.3% or less, which is obtained by evaluating the maximum and minimum values

of the time histories at eight positions on the tooth bottom. The quantitative error of the simulation results when compared with the experimental results in terms of pressure becomes -18% for the maximum pressure (absolute) and -50% for the minimum pressure (absolute), as shown in Fig. 4.4-3 .

To examine the influence of the quantitative error, the pressure is integrated from $-20°$ to $20°$, and the results are shown in Fig. 4.4-4 . The integrated pressure is related to the force loaded on the gear. From the figure, the difference between the simulation and experimental results is $\sim20\%$. Although this difference slightly exceeds the practical accuracy of 15%, it is considered feasible to evaluate the force and fluid dynamic loss loaded on the gear of interest in this research.

(a) 35% width from helical leading side   (b) 65% width from helical leading side
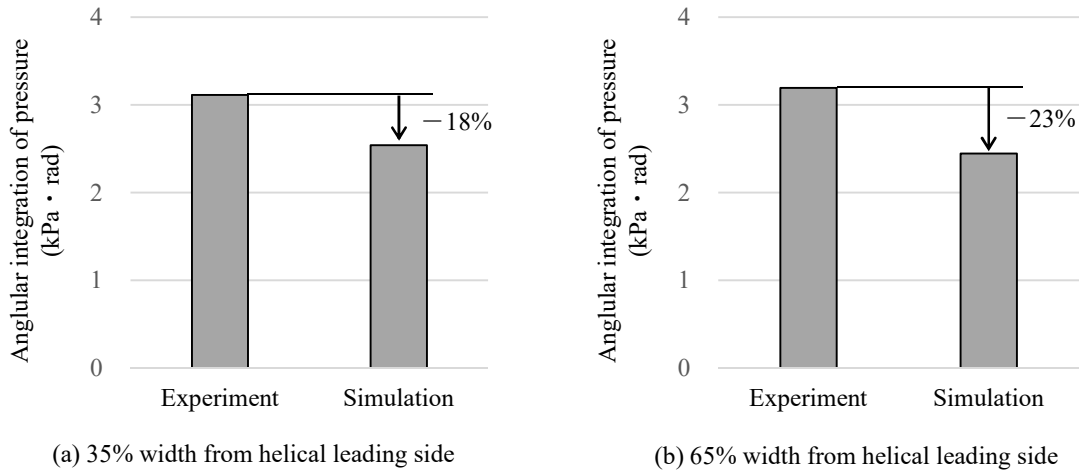
Fig. 4.4-4 Comparisons of angular integration of pressure at tooth bottom

In Fig. 4.4-3 , the simulated maximum value of the bottom pressure roughly agrees with the experimental value; however, the simulated minimum value (absolute value) is smaller than the experimental one. The pressure difference when the clearance between the tooth surfaces is set to exceed the real case is also reported in previous research, which describes the airflow in gear meshing [51].

Figure 4.4-5 (a) shows the reason why the experimental and simulation results almost agree with respect to the maximum value of the tooth bottom pressure. In the into-mesh, the volume between the gear teeth is almost eliminated before the gear teeth make contact. Therefore, the effect of widening the clearance between the teeth in the simulation is reduced.

Figure 4.4-5 (b) illustrates why the simulation result is smaller than the experimental one for the minimum value (absolute value) of the tooth bottom pressure. In the out-of-mesh, the volume between the gear teeth rapidly expands with respect to gear rotation from the minimum volume. In this case, the airflow into the volume between teeth is increased by widening the clearance between the teeth. Therefore, it is considered that the minimum value (absolute value) of the pressure in the simulation is smaller than the experimental value.

From the above, we see that in the simulation, the pressure drop at the gear meshing is estimated to be lower than the actual value. However, the time integral value of the pressure associated with the force on the gears (and the fluid dynamic loss) of interest in this research generally agrees with the experimental result within a range close to the practical error. Therefore, it is considered possible to clarify the airflow at the gear meshing part using the present simulation modeling method.

(a) Influence of tooth contact difference
at into-mesh

(b) Influence of tooth contact difference
at out-of-mesh
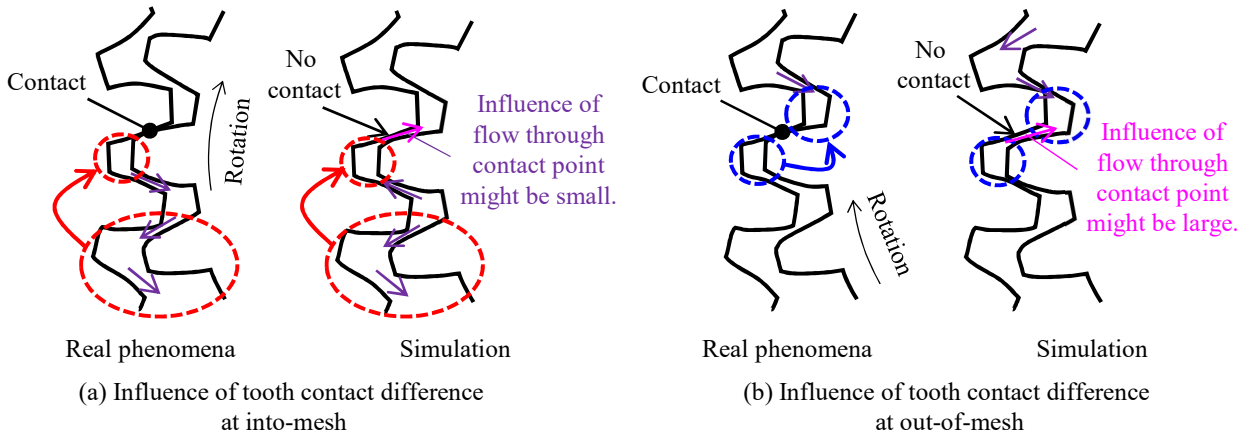
Fig. 4.4-5 Influence of tooth contact differences between real phenomena and simulation results (anticipated)

4.4.1.2 Validation of Aerodynamic Loss of a Single Gear for Validation of Airflow around the Gear

To validate the airflow around the gear, the aerodynamic loss of a single gear is here validated. In addition, the effect of reducing the aerodynamic loss by shrouding is validated. The cause of this reduction effect is described in the clarification and classification of the fluid dynamic loss (Chapter 5). In this section, only the numerical simulation method is validated by comparison with the aerodynamic loss.

(1)   Validation of the Aerodynamic Loss of a Single Gear

As an example of the simulation results, the velocity contour of Gear No.1 is shown in Fig. 4.4-6 (a), and the pressure contour is shown in Fig. 4.4-6 (b). From Fig. 4.4-6 (a), the rotational flow around the gear and the radial flow from the center width of the tooth can be observed. The flow speed is low at the gear wall, which is attributable to a problem in the display (because the speed for displaying the contour inside the gear is set to zero). However, the rotational speed is actually imparted to the gear wall in the calculation. From Fig. 4.4-6 (b), it can be seen that the pressure change around the gear is small.

(a) Velocity contour and vector

(b) Pressure contour and velocity vector
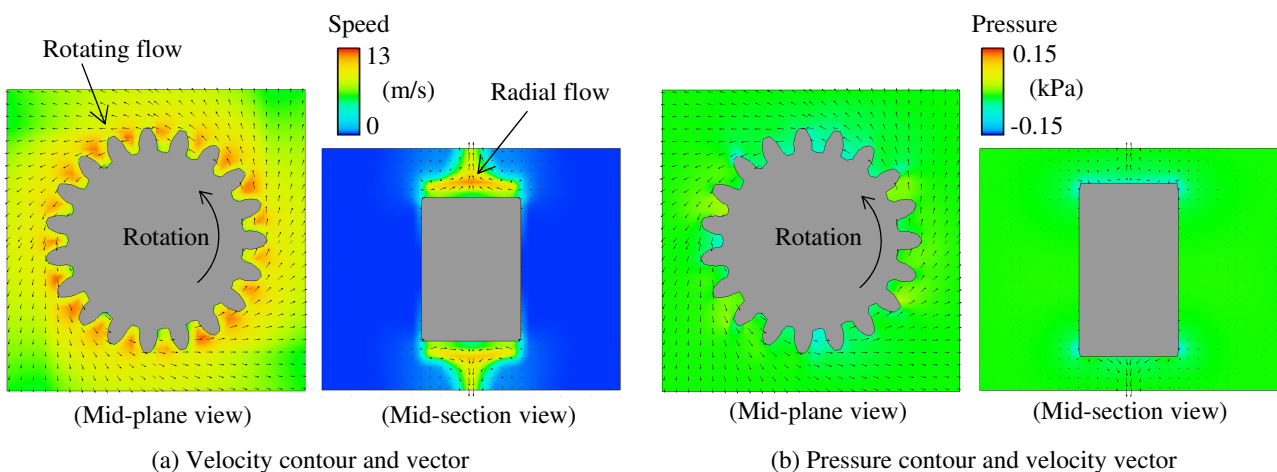
Fig. 4.4-6 Simulation results for Gear No.1

Figure 4.4-7 (a) shows the time history of the aerodynamic loss in Gear No.1. Figure 4.4-7 (b) shows the averaged pressure for each rotation. The mean value of the last three rotations is the aerodynamic

loss of the gear. Using the values of the last three rotations, the relative standard error of σ is calculated, and the error is defined as the time variation error. As a result, the time variation error in the numerical simulation is below 0.8%.

(a) Time history of aerodynamic loss

(b) Aerodynamic loss at every rotation
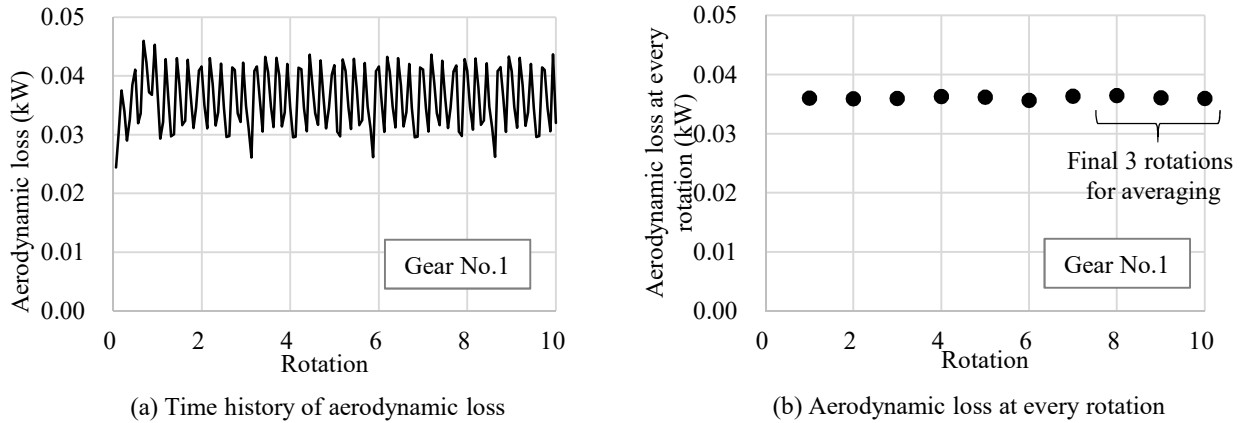
Fig. 4.4-7 Time history of aerodynamic loss for Gear No.1 (simulation results)

Figure 4.4-8 compares the simulation results of aerodynamic loss with the experimental results; it shows the horizontal axis as the measured value and the vertical axis as the numerical simulation value. The experimental measurement error of 20% is shown as an error bar at each point in the figure. A line of ±15% is shown as a practical accuracy. It can be seen that in some cases the error exceeds ±15% even when the experimental measurement error is taken into account. The parameter dependence of this error is examined, and it is found that the most dependent parameter is the number of teeth. This is shown in Fig. 4.4-9 .
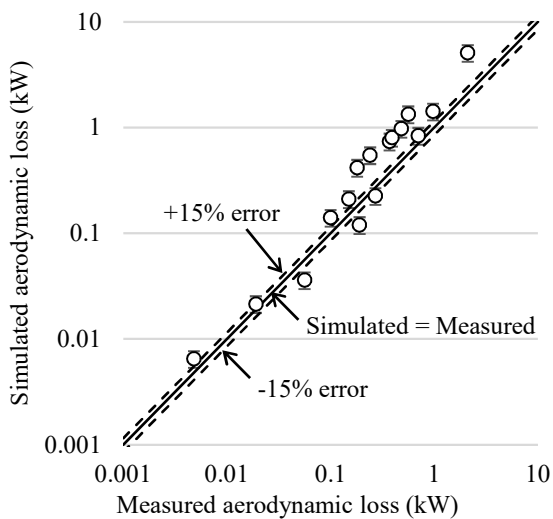
Fig. 4.4-8 Comparison of simulation and experimental results for the aerodynamic losses of different gears
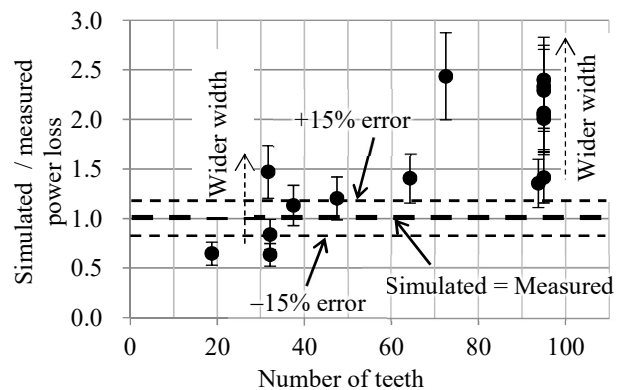
Fig. 4.4-9 Comparison of simulation results (with respect to the number of teeth) for the aerodynamic losses of different gears

The horizontal axis in the figure denotes the number of teeth, and the vertical axis is the numerical simulation value divided by the measurement one. From this figure, it can be seen that the error when the number of teeth is 65 or less is roughly within ±15% (the range including the error bar is within approximately ±15%).

Figure 4.4-10 shows a comparison between the experimental and simulation results under typical conditions with less than 65 teeth. In the figure, the experimental measurement error (±20%) and simulation error (relative standard error of σ: 0.8%) are also shown. From the figure, it is found that the experimental and simulation results generally agree within the error range. For aeroengine gears, the number of teeth is often kept small for downsizing, and the limitation of the simulation with fewer than 65 teeth is considered to be no problem for practical use.

The above results show the aerodynamic loss when the tooth thickness is reduced by 20%. Regarding the difference with and without reduction of tooth thickness, the comparison using Gear No.13 in Table 4.2-3 shows that it is as small as 1%. Therefore, the influence of the 20% tooth thickness reduction is considered negligible.
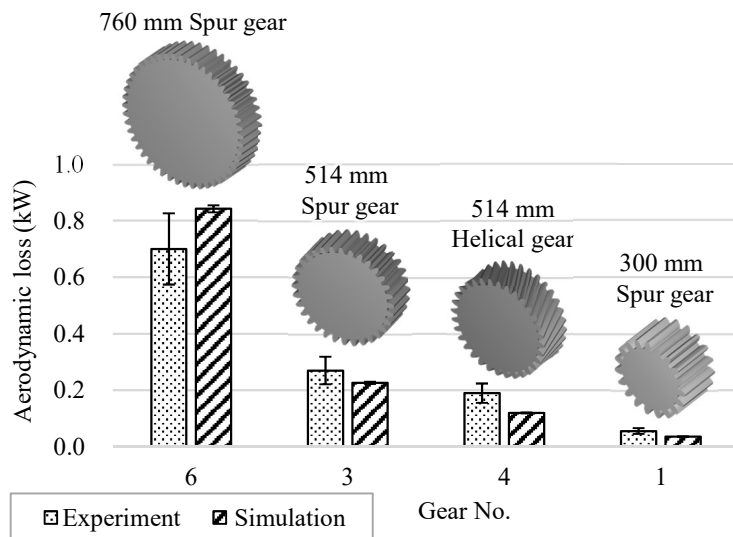
Fig. 4.4-10 A comparison of simulation results for the aerodynamic loss under different gear diameters (the number of teeth is less than 65)

(2)   Validation of the Shrouding Effect for a Single Gear

To validate the effect of the shroud upon a single gear, the reduction rate of the aerodynamic loss via shrouding is used. The experimental results are compared with the simulation results using three typical shrouds from Dawson's shroud experiment [31]. The results are shown in Fig. 4.4-11 . Shroud *d* is a shroud enclosing the peripheral surface of the gear for 270 ° (without side plates). In Shroud *f*, the clearance between the shroud and gear tooth tip is halved (from 30 mm to 15 mm) and side plates are added based on Shroud *d*. Shroud *g* is entirely enclosed (no peripheral opening) though otherwise similar to Shroud *f*. The vertical axis in the figure shows the loss reduction ratio for the aerodynamic loss without a shroud. For the simulated loss reduction ratio, the loss is based on the unshrouded loss in the simulation. For the experimental loss reduction ratio, the loss based on the unshrouded loss in the experiment is used.

In the figure, experimental and simulation errors are shown with error bars, and it is found that the larger the shroud's enclosure range (i.e., the smaller the opening), the lower the loss; furthermore, within the error range, the simulation results agree with the experimental ones. The maximum simulation error is 16% (= |(simulation value/experimental value − 1)| × 100%, for Shroud *f*). This value is approximately equivalent to the practical accuracy of 15%.
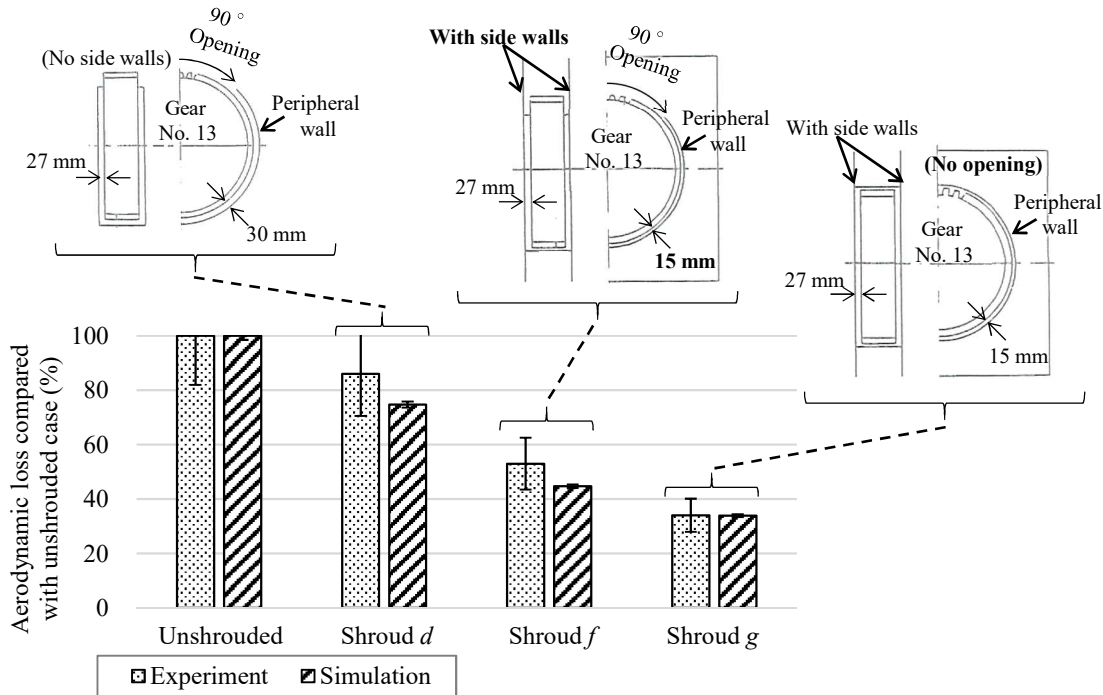
Fig. 4.4-11 A comparison of simulation and experimental results for the aerodynamic loss under different shrouds

Figure 4.4-12 compares the velocity and pressure contours with and without the shroud. The velocity contours without shrouding are shown in Fig. 4.4-12 (a1), and the pressure contours without shrouding are shown in Fig. 4.4-12 (a2). The velocity contours with Shroud *f* are shown in Fig. 4.4-12 (b1). The pressure contours with Shroud *f* are shown in Fig. 4.4-12 (b2). The velocity around the gear without shrouding is increased, as shown in "A1" in Fig. 4.4-12 (a1) of the figure; meanwhile, the velocity outside the shroud for Shroud *f* is decreased, as shown in "A2" in (b1). The change in the pressure at the gear periphery without shrouding is small, as shown in "B1" in Fig. 4.4-12 (a2); meanwhile, the pressure in the shroud for Shroud *f* decreases, as shown in "B2" in (b2). Therefore, it is considered that the installation of the shroud reduces the aerodynamic loss by restricting the increase in the velocity of the peripheral air, owing to the gear rotation, as well as by reducing the pressure around the gear.

From the above results, it is found that the aerodynamic loss in a single gear qualitatively agrees with the experimental results, and that the simulation accuracy is almost quantitatively practical (under the condition that the number of teeth is 65 or less, which is practical for an aeroengine). Therefore, it is considered feasible to clarify the phenomena of airflow around the gear using the numerical simulation method and simulation modeling methods for the airflow.

(Mid-plane view)   (Mid-section view)

(a1) Velocity contour and vector for unshrouded gear

(a2) Pressure contour and velocity vector for unshrouded gear

(b1) Velocity contour and vector for Shroud *f*

(b2) Pressure contour and velocity vector for Shroud *f*
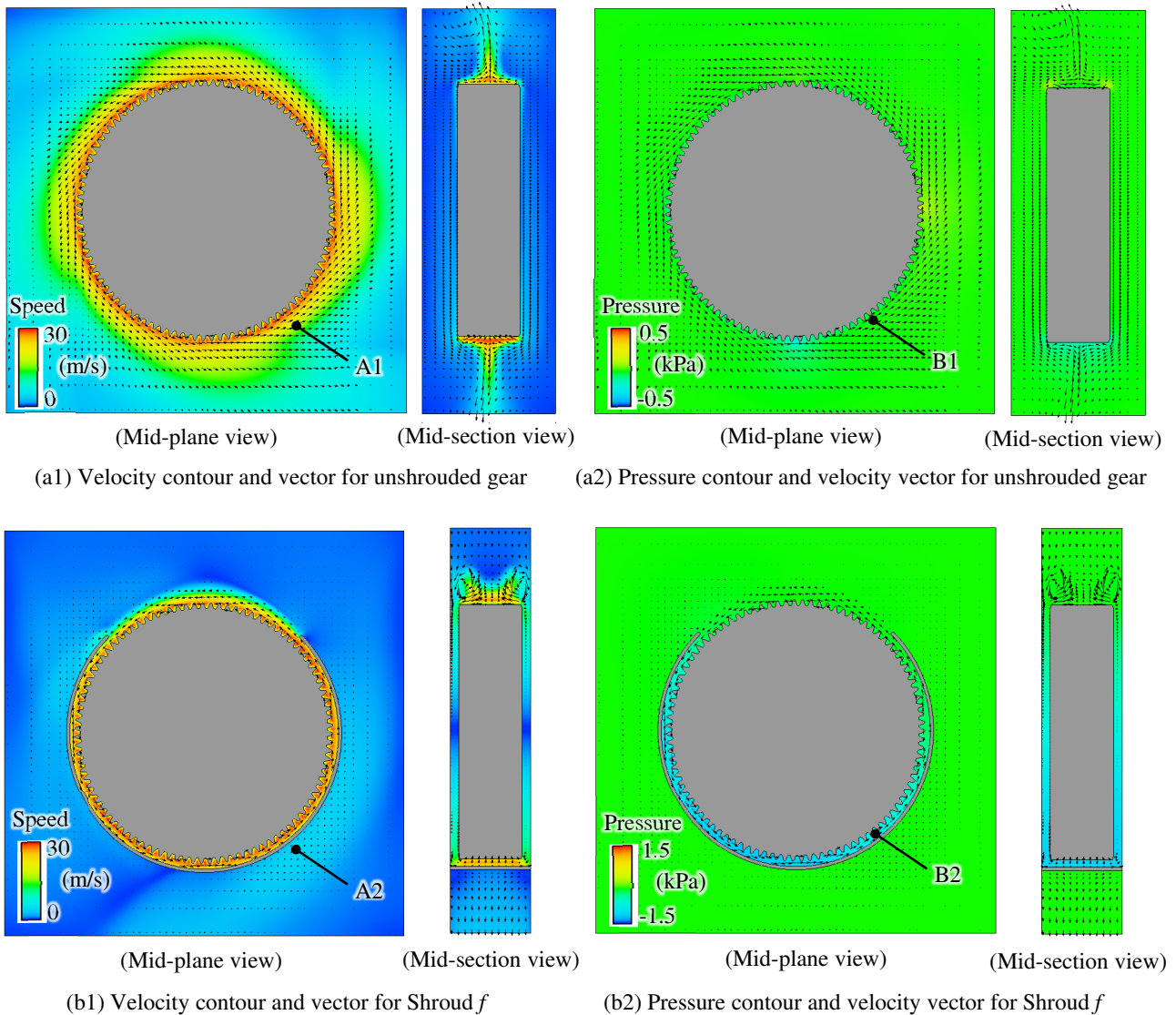
Fig. 4.4-12 Simulation results for Shroud *f*

4.4.2 Validation of Modeling Methods for Oil Flow

4.4.2.1 Validation of Oil Jet Flow into Gear Mesh for Validation of Oil Flow in Gear Meshing Part

Figure 4.4-13 shows a comparison between the results of the visualization experiment and those of the numerical simulations when an oil jet is injected from the into-mesh side. Figure 4.4-13 (a1) in the figure shows the result of the visualization experiment at 500 rpm of the input gear, and (a2) is the result of the simulation. The results of the experiment and simulation are qualitatively consistent with respect to the oil outflow in the side direction from the gear mesh. Figure 4.4-13 (b1) in the figure is the result of the visualization experiment at 4000 rpm of the input gear, and (b2) is the result of the simulation. The results of the experiment and simulation are qualitatively consistent with respect to the lack of oil outflow from the gear mesh when the rotational speed is increased. Thus, the oil outflow from the gear mesh changes according to the rotational speed, regarding whether the oil jet flow rate is larger than the air pumping flow rate of the gear mesh (= volume of tip clearance and backlash × the number of teeth × rotational frequency) or not. This is shown in Fig. 4.4-14 . In the numerical

simulation results, a tooth thickness reduction of 20% and Ψ' (0.25, Eq. 4.28) were taken into consideration. Figures 4.4-13 (a1) and (a2) show the case in which the oil flow rate is equivalent to the air pumping flow rate, and Figs. 4.4-13 (b1) and (b2) show the case in which the oil flow rate is lower than the air pumping flow rate.

| (a1) Experiment; Input: 500 rpm; peripheral velocity: 5 m/s | (a2) Simulation; Input: 500 rpm; peripheral velocity: 5 m/s | (b1) Experiment; Input: 4000 rpm; peripheral velocity: 40 m/s | (b2) Simulation; Input: 4000 rpm; peripheral velocity: 40 m/s |
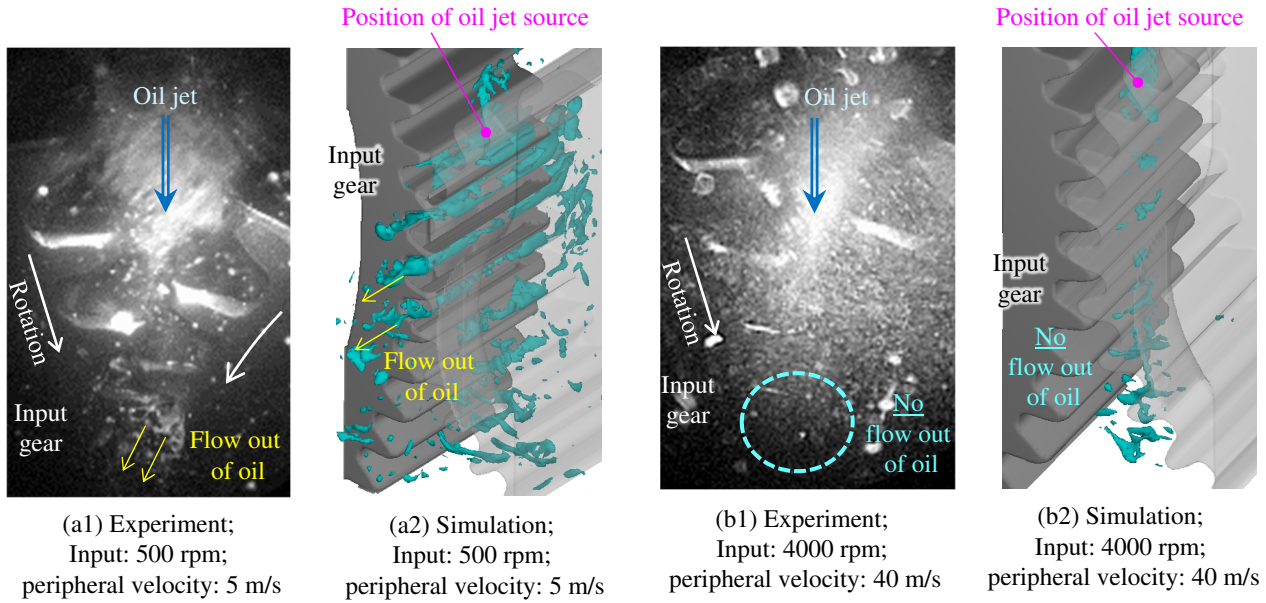
Fig. 4.4-13 Comparisons of simulated and experimentally visualized oil flows (oil jet directed to into-mesh: 3.8 L/min)
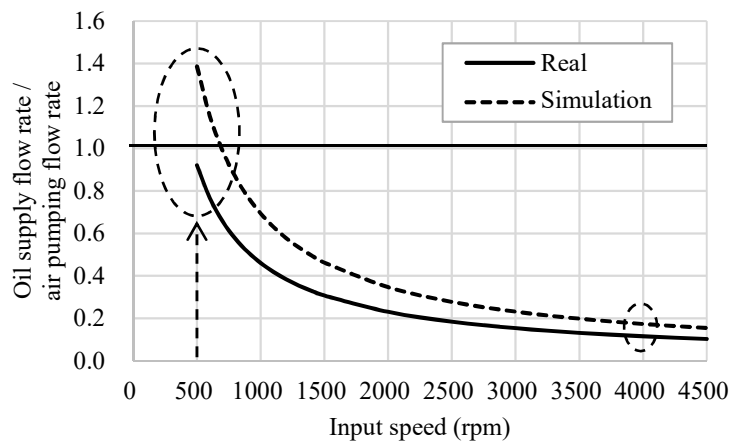
Fig. 4.4-14 Ratio of oil supply flow rate to air pumping flow rate

Figure 4.4-15 presents a comparison between the results of visualization experiments and numerical simulations when an oil jet is injected from the out-of-mesh side. In the figure, (a1) is the result of visualization experiments at 1600 rpm of the input gear, (a2) is a schematic diagram of the flow, and (b) is the numerical simulation result. The experimental and simulation results are qualitatively consistent for the flow of oil into the gear tooth surface.

From the above, the numerical simulation and simulation modeling methods for the oil flow are qualitatively validated for the flow of an oil jet to the gear meshing part.

(a1) Experiment   (a2) Schematic of experiment   (b) Simulation
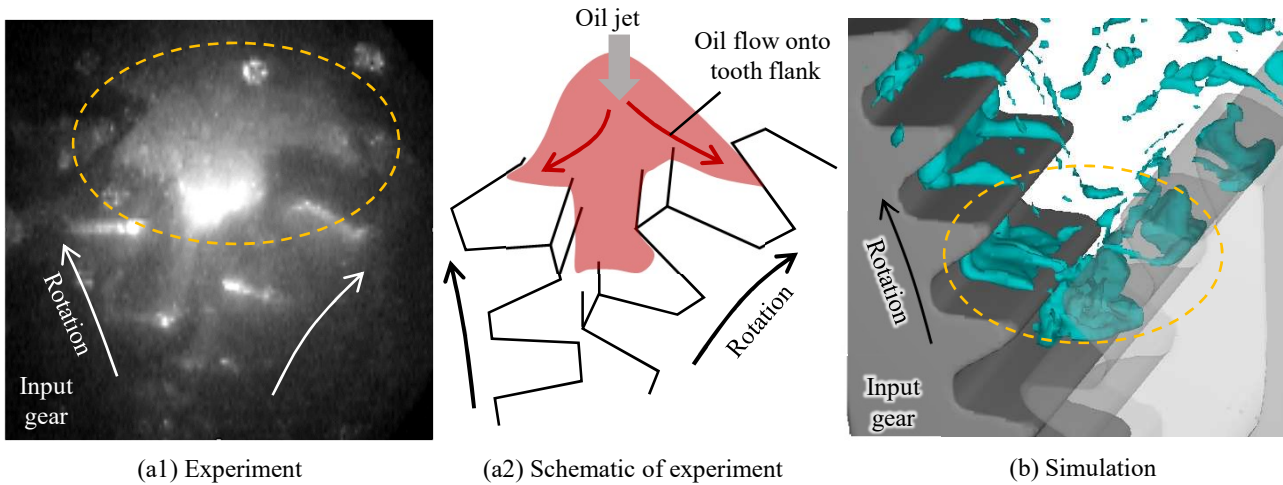
Fig. 4.4-15 Comparison of simulated and experimentally visualized oil flows (oil jet directed to out-of-mesh: 3.8 L/min; input: 1600 rpm; peripheral velocity: 16 m/s)

4.4.2.2   Validation of Oil Inflow to Gear Tooth Surface for Validation of Oil Flow around Gear

Figure 4.4-16 shows a comparison between the results of visualization experiments and numerical simulations when oil mist is sprayed into the gear periphery. Figure 4.4-16 (a1) shows the result of visualization experiments at 2500 rpm of the input gear, and (a2) shows the simulation result. In Figs. 4.4-16 (a1) and (a2), the results of experiments and simulation qualitatively show that oil mist flowed between the gear teeth. It is considered that this oil mist flows in because the gear peripheral speed is slower than the oil mist spray velocity. Figure 4.4-16 (b1) shows the result of visualization experiments at 7500 rpm of the input gear, and (b2) shows the simulation results. In Figs. 4.4-16 (b1) and (b2), the simulation result qualitatively agrees with the experimental results regarding the non-inflow of oil mist between the gear teeth. The reason why no inflow occurred is because the gear peripheral speed exceeds the oil mist spray velocity and subsequently scatters oil mist.

From the above, the numerical simulation and simulation modeling method for oil flow are qualitatively validated for the flow of oil mist into the gear periphery.

(a1) Experiment;
input: 2500 rpm;
peripheral velocity: 25 m/s

(a2) Simulation;
input: 2500 rpm;
peripheral velocity: 25 m/s

(b1) Experiment;
input: 7500 rpm;
peripheral velocity: 75 m/s

(b2) Simulation;
input: 7500 rpm;
peripheral velocity: 75 m/s
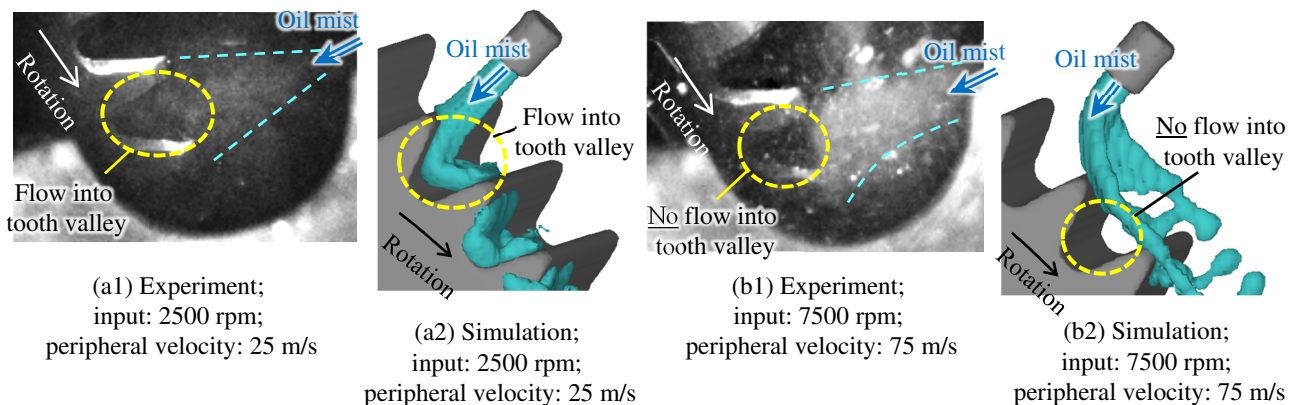
Fig. 4.4-16 Comparison between simulated and experimentally visualized oil flows (oil mist directed to gear periphery)

4.4.2.3 Validation of Oil Flow near Shroud Wall

Because the oil flow near the shroud wall can increase the oil dynamic loss by flowing into the gear tooth, it is necessary to validate the numerical simulation method and simulation modeling method for the oil flow near the shroud wall.

We summarize the phenomena from the simulation results, which are shown in Fig. 4.4-17 . Figure 4.4-17 (a) shows the oil distribution. The oil fraction isosurface of 5% in the calculation cell is shown alongside the velocity contours. The oil outflow from the opening of the peripheral surface of the shroud can be observed. Figure 4.4-17 (b) shows the oil fraction contour on the center cross-section (mid-plane) of the tooth width. Figure 4.4-17 (c) shows the oil fraction contour on the longitudinal center cross section (mid-section). It can be seen that the oil is distributed near the wall surface, as shown in "A" in Fig. 4.4-17 (b) and "B" in (c). Figure 4.4-17 (d) shows the velocity contours. It can be seen that the high speed region remains inside the shroud ("C" in the figure). Figure 4.4-17 (e) shows the pressure contours. It can be seen that the pressure decreases inside the shroud ("D" in the figure).
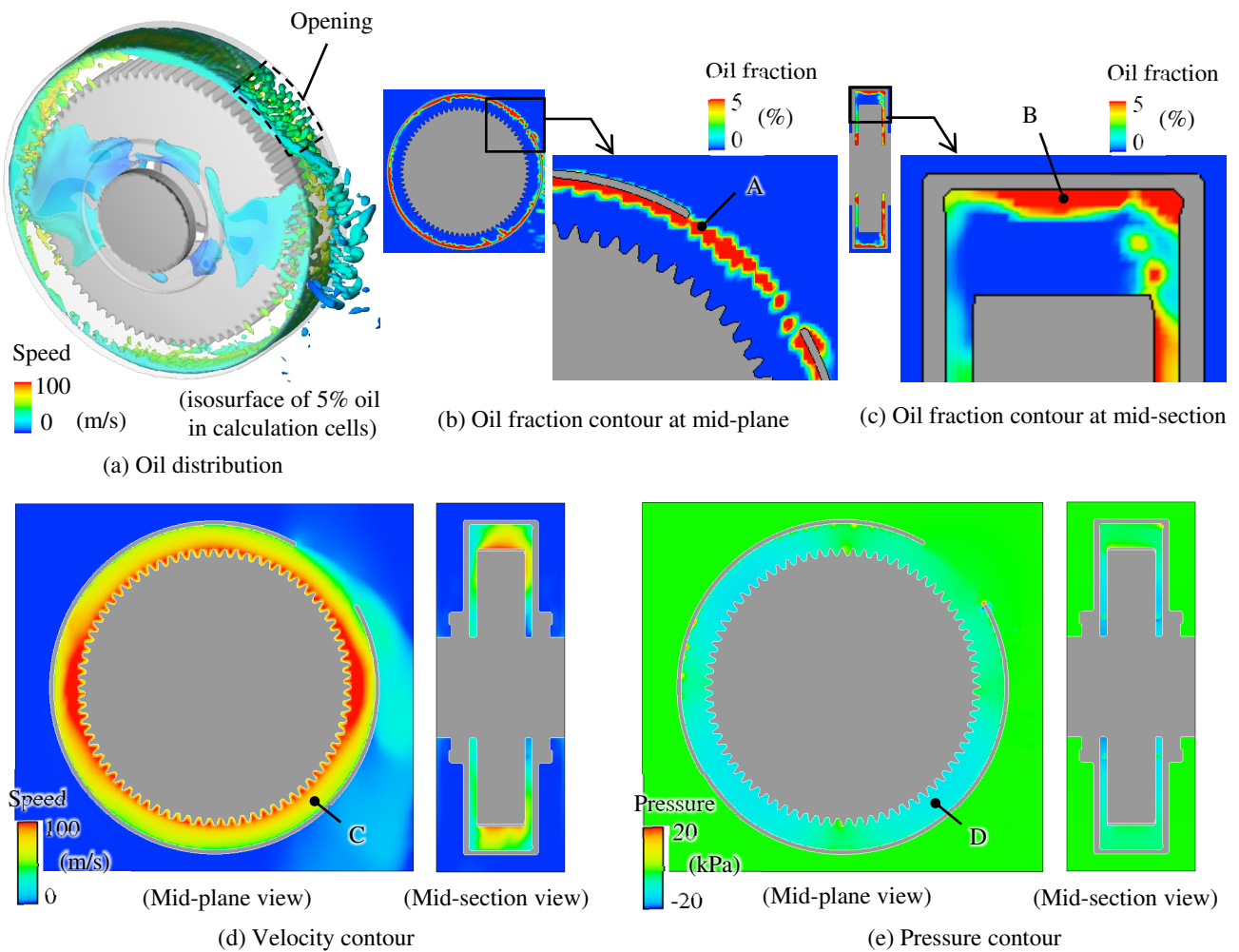
Fig. 4.4-17 Simulation results for one-axis spur gearbox with shrouding (GB3)

145

Next, the simulation and experimental results are compared with respect to the oil fraction, mixture velocity, and oil flow velocity (= oil fraction × mixture velocity). The oil fraction in the simulation is calculated by multiplying the oil fraction within the calculation cell by Ψ' (0.25, in Eq. 4.28). As for the mixture velocity, air and oil are measured as the same velocity (mixture velocity) in the experiment, and the air and oil are set to the same velocity in the gas–liquid interface cell in the simulation. Therefore, the velocity in the simulation result can be directly compared with the mixture velocity in the experiment. The oil flow velocity is evaluated in both the experimental and simulation results by using the oil fraction × mixture velocity. The oil flow velocity is considered to be related to the oil flow rate around the gear, and the oil flow rate relates to the oil dynamic loss, as shown in Section 2.3. Therefore, the oil flow velocity is important.

Figure 4.4-18 compares the simulation results and experimental results in terms of the oil fraction ((a) in the figure), the mixture velocity ((b) in the figure), and the oil flow velocity ((c) in the figure). The radial distribution of the oil fraction (Fig. 4.4-18 (a)) shows that the simulation result is similar to the experimental result in terms of the trend toward a high oil fraction on the wall of the shroud. On the other hand, the simulation result for the absolute value of the oil fraction is lower than the experimental one. The radial distribution of the mixture velocity (Fig. 4.4-18 (b)) shows that the simulation result is similar to the experimental result in terms of the high mixture velocity near the gear tip and the low mixture velocity on the wall of the shroud. On the other hand, the simulation result of the mixture velocity is approximately double that of the experimental results, as indicated by "A1" in the figure. In Fig. 4.4-18 (c), which shows the radial distribution of the oil flow velocity, the simulation and experimental results roughly agree in terms of having a peak value slightly away from the wall and absolute value, as shown by "B1" in the figure.

To understand the cause of the difference between the simulation results and experimental results in Fig. 4.4-18 , we try to explain this difference through the influence of air bubbles mixing into the oil (aeration). It has been reported that the apparent viscosity of oil increases under aeration of oil [114]. This is shown in

$$\mu_{oil,aeration} = \mu_{oil} \left\{ 1 + C(1 - \alpha_{oil}) \right\} \tag{4.35}$$

where $\mu_{oil,aeration}$ is the apparent dynamic viscosity of aerated oil, μ_{oil} is the dynamic viscosity of the oil (without aeration), C is the experimental coefficient, and α_{oil} is the oil fraction. Therefore, assuming aeration as described above, a numerical simulation is performed in which the viscosity of the oil is increased. The results are shown in Fig. 4.4-19 .
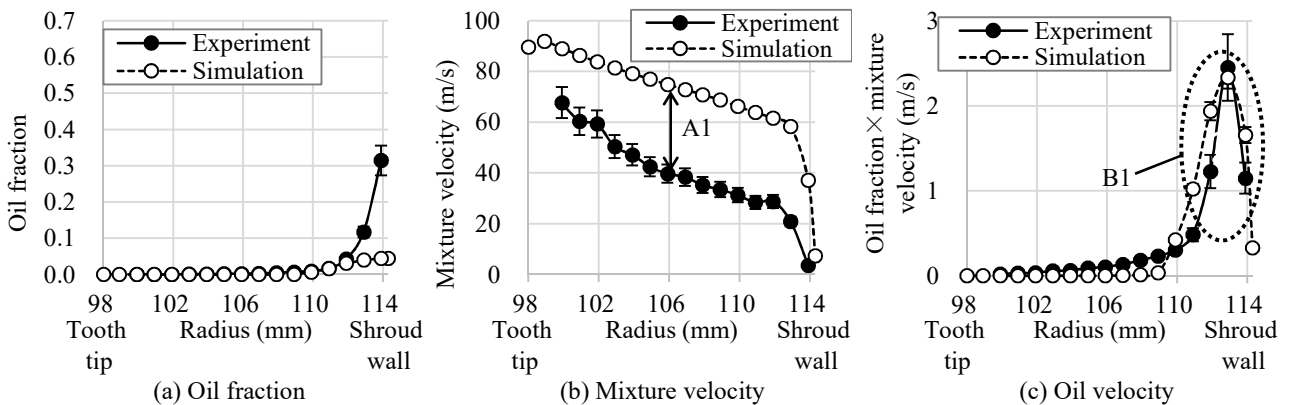
Fig. 4.4-18 Comparison of simulation and experimental results for oil fraction, mixture velocity, and oil velocity

(a) Oil fraction   (b) Mixture velocity   (c) Oil velocity
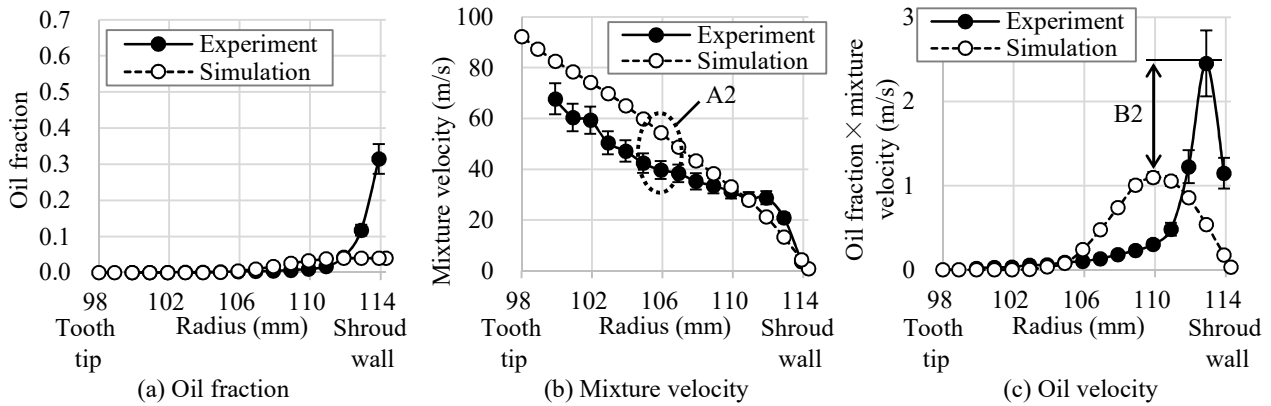
Fig. 4.4-19 Comparison of simulation and experimental results with "aerated" viscosity

By considering the increase in oil viscosity attributable to aeration, the simulation result approached the experimental one near the mid-position between the gear tooth tip and shroud wall surface, as shown in "A2" in Fig. 4.4-19 (b). On the other hand, the simulation result of the oil flow velocity near the wall is smaller than the experimental result, as shown in "B2" in Fig. 4.4-19 . From the above, we see that when aeration is considered (owing to the increase in oil viscosity attributable to aeration), the simulated values near the mid-position between the gear tooth tip and shroud wall tend to correspond to the experimental results; furthermore, when aeration is neglected, the simulated values near the shroud wall tend to correspond to the experimental results.

From these tendencies, it is considered possible that the aeration condition changes between the gear tooth tip and shroud wall. A schematic diagram of the assumed aeration condition is shown in Fig. 4.4-20 . If a large quantity of air is mixed in with the oil particles near the gear tooth tip, bubbles will separate owing to the centrifugal force as they move toward the shroud wall. This may reduce the aeration on the shroud wall. However, the simulated oil fraction near the shroud wall still differs from the experimental result even when the influences of oil aeration are considered (Fig. 4.4-18 (a) and Fig. 4.4-19 (a)). This may be caused by the influences of the oil surface tension and contact angle on the oil's adhesion to the wall.
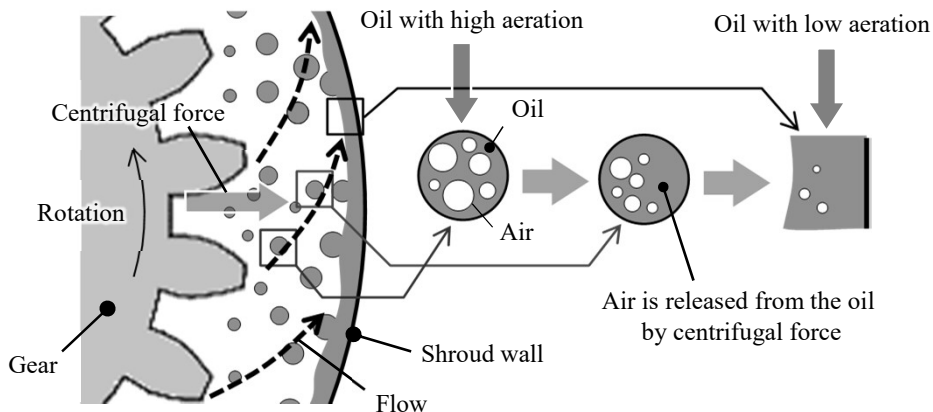
Fig. 4.4-20 Schematic of the anticipated aeration phenomena

Regarding the oil flow velocity, the simulation and experimental results generally agree in Fig. 4.4-18 (c); thus, it is considered that the oil flow velocity is related to the oil flow rate around the gear, and the oil flow rate

relates to the oil dynamic loss (Section 2.3). Therefore, it is considered feasible to clarify the phenomena of the oil flow near the wall of the shroud and the resultant oil dynamic loss by using the numerical simulation method and the oil flow modeling method presented here. The error of the simulation result for the oil flow velocity, when compared with the experimental result, is 5%, as shown in the comparison of peak values in Fig. 4.4-18 (c).

4.4.3 Validation of Simulation Method for Fluid Dynamic Loss

4.4.3.1 Validation of Fluid Dynamic Loss of Air and Oil

In this section, the numerical simulation results of the fluid dynamic loss for air and oil are compared with the experimental results, to validate the simulation methods for the loss. An example of the time history of the fluid dynamic losses of air and oil is shown in Fig. 4.4-21 (a). The result of averaging each rotation of the input gear in this time history is shown in Fig. 4.4-21 (b). The relative standard error $(=(2\sigma/\hat{\bar{P}})/\sqrt{N_{rot}}$, where σ is the standard deviation, $\hat{}$ is the ensemble averaged value, $\bar{P}$ is the averaged value in one rotation, and N_{rot} is the number of rotations) of 2σ (as the time variation error of the numerically simulated loss) is obtained by using the time-averaged loss of each rotation from 21 to 30 rotations after the loss reached an almost steady state, as shown in Fig. 4.4-21 (b).

As a result, the maximum values of this time variation error (the relative standard error of 2σ) are 2.4% for the fluid dynamic loss of air and oil, 1.5% for the aerodynamic loss, and 1.9% for the oil dynamic loss. The measurement errors of the loss are 0.082 kW at 7000 rpm, 0.055 kW at 9000 rpm, and 0.044 kW at 10000 rpm (Table 3.6-1). These numerical simulation errors (time variation errors) and experimental measurement errors are small compared to the loss value, and their graphical representation is omitted below.

(a) Time history of fluid dynamic loss (b) Averaged time history of fluid dynamic loss at each rotation
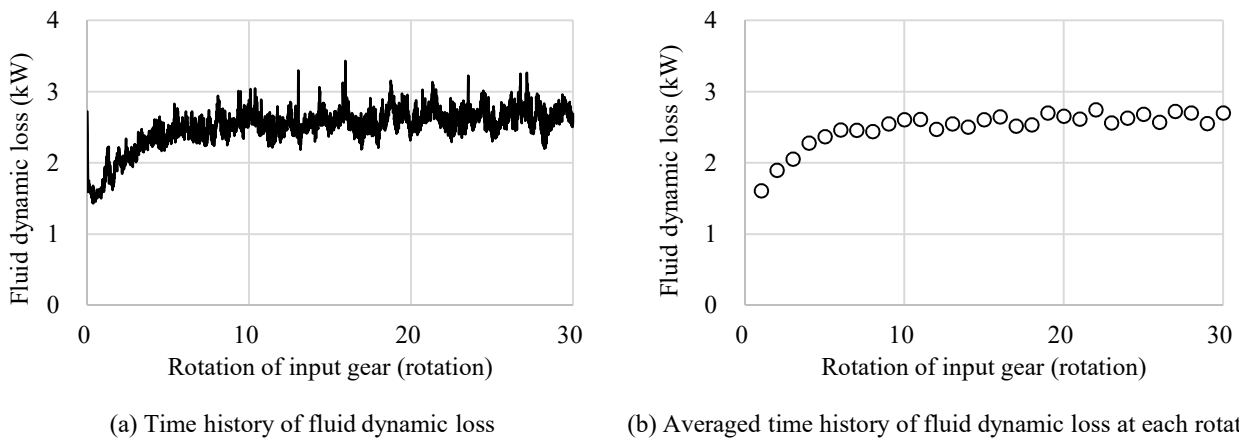
Fig. 4.4-21 Example time history of simulated fluid dynamic loss (oil supply rate: 3.85 L/min; input: 9000 rpm; Shroud 2)

Figure 4.4-22 compares the numerical simulation and experimental results regarding the fluid dynamic loss of air and oil, aerodynamic loss, and oil dynamic loss with respect to rotational speed changes at an oil supply flow rate of 7.40 L/min. Figures 4.4-22 (a1) and (a2) show the fluid dynamic losses of air and oil, (b1) and (b2) show the aerodynamic loss, and (c1) and (c2) show the oil dynamic loss. Figures 4.4-22 (a1), (b1), and (c1) show the losses for Shroud 1, and (a2), (b2), and (c2) show the losses for Shroud 2. The numerical simulations and experimental results are in good agreement.

Figure 4.4-23 compares the numerical simulation and experimental results for the fluid dynamic loss of air and oil, aerodynamic loss, and oil dynamic loss with respect to rotational speed changes at an oil supply flow rate of

3.85 L/min, similar to Fig. 4.4-22 . The numerical simulation and experimental results qualitatively agree.

Figure 4.4-24 compares the numerical simulation and experimental results regarding the fluid dynamic loss of air and oil, aerodynamic loss, and oil dynamic loss with respect to oil supply flow rate changes at a rotational speed of 10000 rpm, similar to Fig. 4.4-22 . The difference is that the horizontal axis shows the oil supply flow rate. The numerical simulation and experimental results qualitatively agree.

From the above qualitative agreements, it is concluded that fluid dynamic loss phenomena can be clarified using the numerical simulation method.

The quantitative error of the numerical simulation is defined as the relative standard deviation, and the error is obtained for the aerodynamic loss, the oil dynamic loss, and the fluid dynamic loss of air and oil using the results of Figs. 4.4-22 , 4.4-23 , and 4.4-24 . The error in the aerodynamic loss is 5%, that in the oil dynamic loss is 14%, and that in the fluid dynamic loss of air and oil is 8%. Because these errors are less than 15% of the practical errors, the quantitative evaluation of each loss is also concluded to be possible.

(a1) Fluid dynamic loss
with respect to input speed
(7.40 L/min, Shroud 1)

(b1) Aerodynamic loss
with respect to input speed
(7.40 L/min, Shroud 1)

(c1) Oil dynamic loss
with respect to input speed
(7.40 L/min, Shroud 1)

(a2) Fluid dynamic loss
with respect to input speed
(7.40 L/min, Shroud 2)

(b2) Aerodynamic loss
with respect to input speed
(7.40 L/min, Shroud 2)

(c2) Oil dynamic loss
with respect to input speed
(7.40 L/min, Shroud 2)

Fig. 4.4-22 Comparison of simulation and experimental results for power loss with respect to input speed changes (oil supply rate: 7.40 L/min; Shroud 1 & Shroud 2)
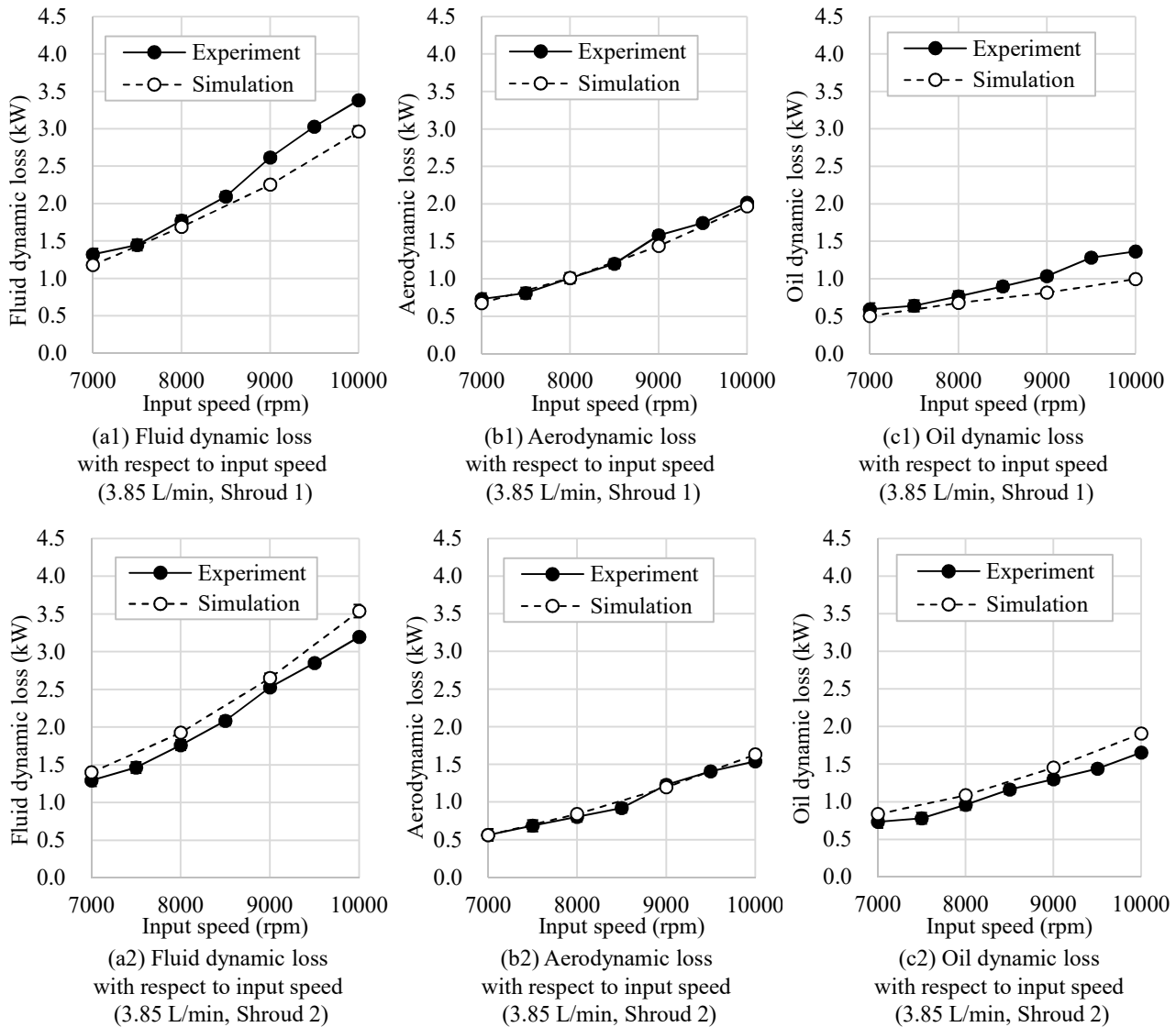
Fig. 4.4-23 Comparison of simulation and experimental results for power loss with respect to input speed changes (oil supply rate: 3.85 L/min; Shroud 1 & Shroud 2)

4.4.3.2 Influence of Air Compressibility

To confirm the influence of air compressibility, a simulation result for air (modeled as a compressible fluid) is shown in Fig. 4.4-25 . When air is modeled as a compressible fluid, the aerodynamic loss is equivalent at 7000 rpm and increases by 3% at 10000 rpm, compared to incompressible air.

The qualitative tendency of the aerodynamic loss is similar when air is modeled as a compressible or incompressible fluid. Therefore, it is concluded that the phenomena of fluid dynamic loss can be clarified using the numerical simulation method with air modeled as an incompressible fluid.

4.4.3.3 Influence of the Size of Calculation Mesh

The influences of the calculation mesh size on the losses with respect to the rotational speed changes are shown in Fig. 4.4-26 . The influences of the calculation mesh size on the losses with respect to the oil supply flow rate
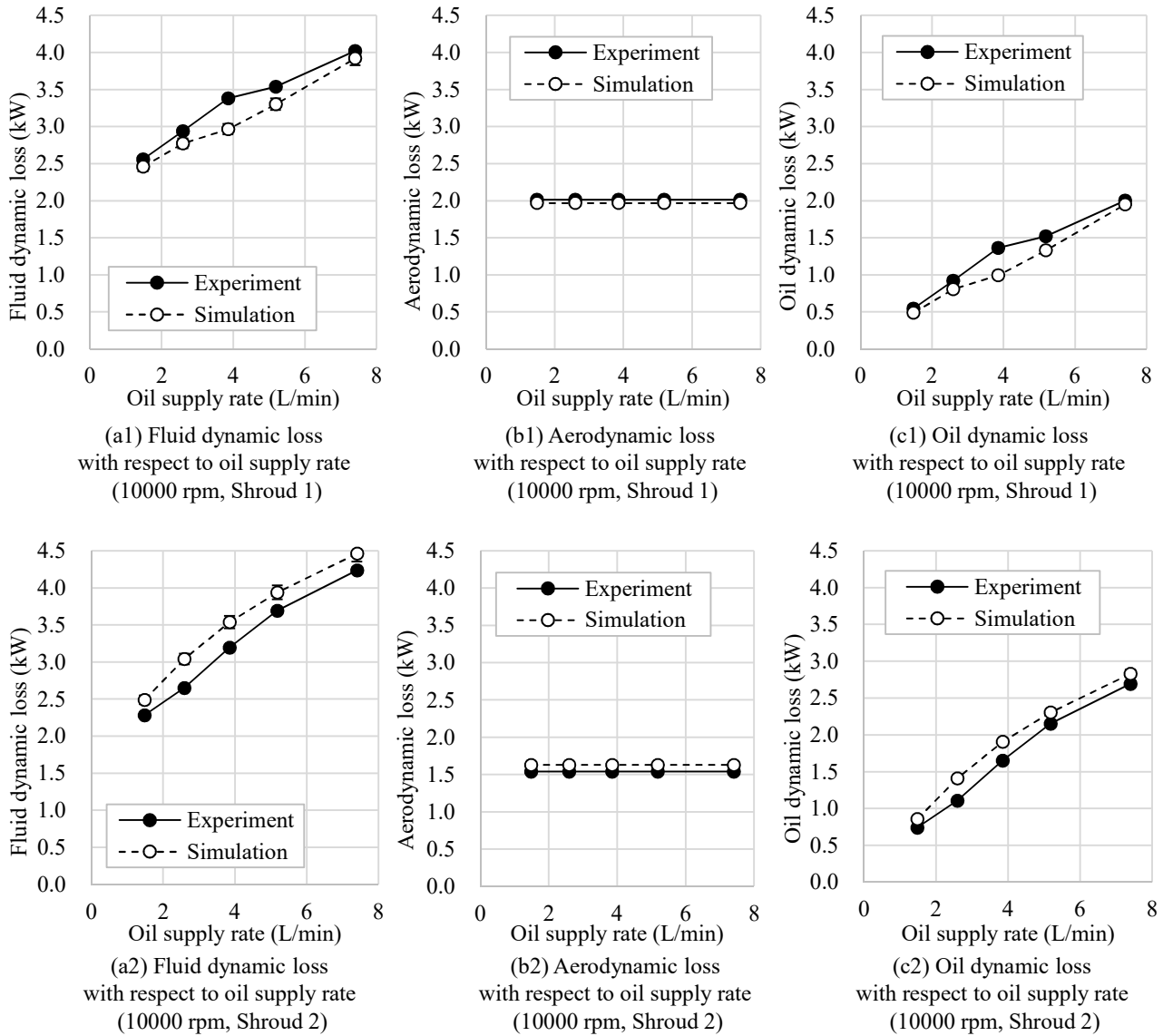
Fig. 4.4-24 Comparison of simulation and experimental results for power loss with respect to oil supply rate changes (input speed: 10000 rpm; Shroud 1 & Shroud 2)

changes are shown in Fig. 4.4-27 . Although the oil dynamic loss differs when the calculation mesh size is varied, the qualitative trend is equivalent. Therefore, the phenomena of fluid dynamic loss can be clarified using the numerical simulation method.

4.4.4 Summary of Numerical Simulation Error

The numerical simulation errors are summarized in Table 4.4-1 . The table shows that they are less than the practical error (± 15%).

The simulation error of the aerodynamic loss for single spur gears is a little outside the practical error. However, the simulation error of the fluid dynamic loss for the two-axis helical gearbox (GA), which is the subject of this research, is less than the practical error, and no problems arise when clarifying the fluid dynamic loss.
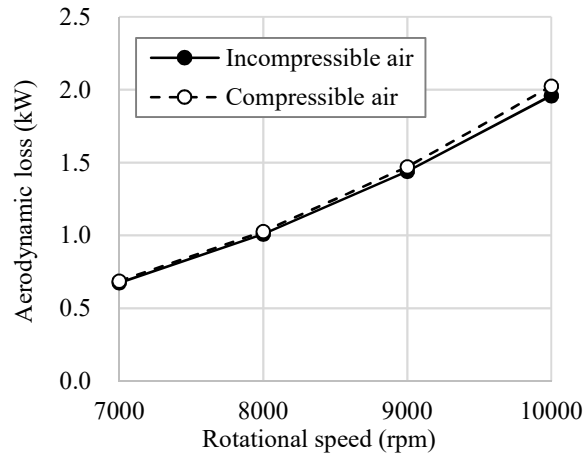
Fig. 4.4-25 Influence of air compressibility on aerodynamic loss (simulation results, Shroud 1)
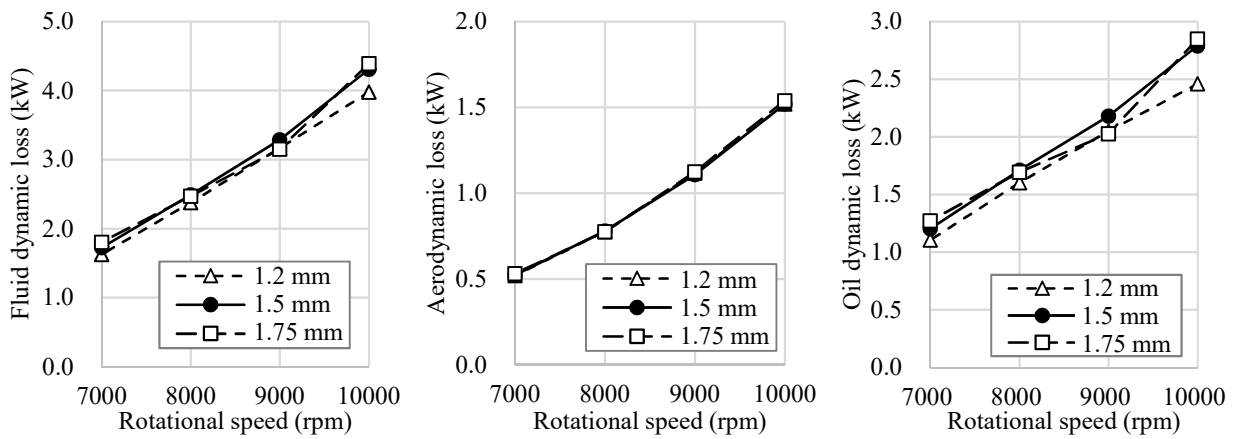
Fig. 4.4-26 Influence of calculation mesh size on power losses for different rotational speeds (simulation results, constant oil supply rate: 7.40 L/min, Shroud 2)
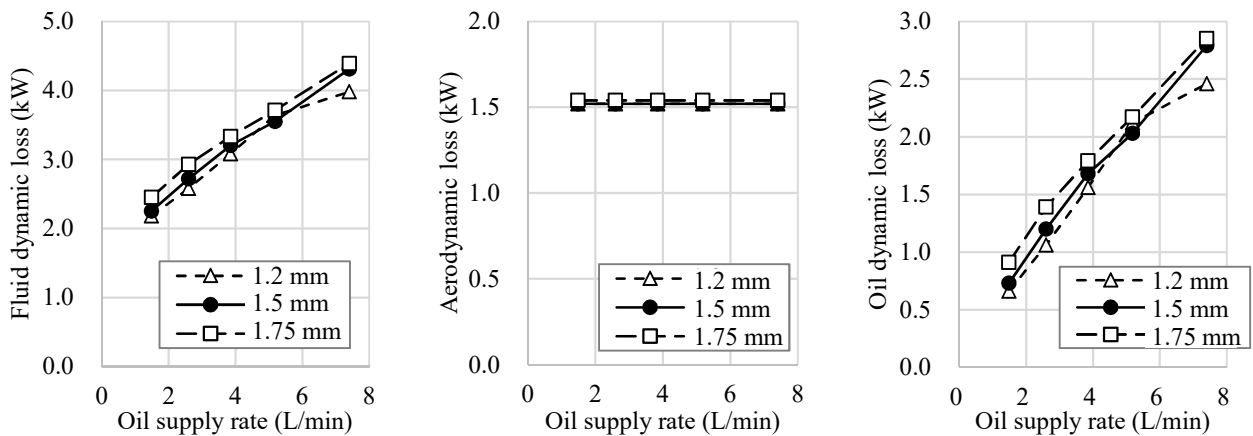
Fig. 4.4-27 Influences of calculation mesh size on power losses for different oil supply rates (simulation results, constant input speed: 10000 rpm, Shroud 2)

Table 4.4-1 Summary of calculation errors in numerical simulations

Fluid	Validation items for numerical simulation and modeling	Gearbox	Experimental results for comparison	Measurement error in experiment	Precision of numerical simulation — Random error due to fluctuation in time	Accuracy of numerical simulation — Qualitative comparison between experiment and simulation	Accuracy of numerical simulation — Quantitative error (systematic error) = deviation from true value (experimental value)
Air and oil	Fluid dynamic loss in two-phase flow of air and oil	Two-axis helical gearbox (GA), two shrouds	Aerodynamic loss	4%*1	1.5%*4	Qualitatively agree	5%*7
			Oil dynamic loss	3%*1	1.9%*4	Qualitatively agree	14%*7
			Fluid dynamic loss of air and oil	2%*1	2.4%*4	Qualitatively agree	8%*7
Air	Air leak flow from clearance in gear mesh	Two-axis helical gears (GX1)	Time history of pressure at tooth bottom	–	0.3% or less*5	Qualitatively agree	18%–23% (Integration of pressure)
Air	Aerodynamic loss with single gear	One-axis spur gears (GX2), 16 gears	Aerodynamic loss with different gears	5%–20%*2	0.8% or less*6	Qualitatively agree	40%(Simulation vs. Experiment) ± 20% (Experiment error) (when number of teeth ≤ 65)
		One-axis spur gears (GX2), three shrouds	Aerodynamic loss with different shrouds	–	–	Qualitatively agree	16% or less *9
Oil	Inflow of oil jet into gear mesh	Two-axis spur gearbox (GB1)	Visualization of oil distribution	–	–	Qualitatively agree	–
Oil	Inflow of oil mist onto tooth surface	One-axis spur gearbox (GB2-2)	Visualization of oil distribution	–	–	Qualitatively agree	–
Oil	Superficial flow velocity of oil near the wall	One-axis spur gearbox (GB3)	Superficial flow velocity of oil	16%*3	6% or less*4	Qualitatively agree	5% (Comparison of peak values) *10

*1 Relative standard error of 2σ, *2 Dawson[31], *3 Root mean squared value of oil ratio error (13%) and mixture velocity error (9%),

*4 Relative standard error of 2σ (with values for last ten rotations, averaged in each rotation)

*5 Relative standard error of σ (with min and max value at eight tooth bottoms)

*6 Relative standard error of σ (with values for last three rotations, averaged in each rotation)

*7 Relative standard deviation between experimental and simulation results, *8 Relative error (averaged at 35% width and 65% width from helical leading side)

*9 Maximum error between Shroud d, Shroud f, and Shroud g, *10 Error at 10000 rpm

4.5   Summary of Chapter 4

In this chapter, a numerical simulation method for fluid dynamic loss, as well as simulation conditions for clarifying it and validating the numerical simulation method were described. In addition, to use the numerical simulation methods to clarify the phenomena of fluid dynamic loss, we examined whether the numerical simulation results can qualitatively reproduce the experimental results. The findings are summarized below.

4.5.1   Summary of Numerical Simulation Methods

1. To ensure both numerical stability and calculation speed at gas–liquid interfaces (which are important for ensuring the practicality of numerical fluid simulations of gear systems), we used a rectangular mesh for calculation, the VOF method for calculating gas–liquid interfaces, and the porosity method for modeling object boundaries.

   The porosity method (used to model a moving object (e.g., a gear with a rectangular mesh fixed in space)) defines the volume of air and oil in the cell and the area of air and oil at the cell surface (excluding the region of the object), where the calculation cell contains the object. The object movement is considered in terms of the volume changes of the air and oil regions in the cell, as well as the change of the air and oil areas of the cell surface.

   To suppress the numerical diffusion of the liquid fraction in the cell under the VOF method, we applied a compression speed in the direction perpendicular to the interface (surface compression method).

   Mass conservation and momentum conservation equations were compiled into one common equation (one fluid model) for both oil and air. In this case, the pressure and flow velocity in the gas–liquid interface cell were the same on the air and oil sides, and no velocity slip occurred at the gas–liquid interface.

   The shear stress at the wall was calculated from the difference between the object and fluid velocities and from the turbulence model. The LES method was used for turbulence, to ensure numerical stability.

2. As a simulation modeling method for airflow, to ensure numerical stability, the gear tooth thickness was reduced and clearance was provided between the gear teeth. Because the gear contact surface was in Hertzian contact and the contacts were placed in a narrow linear area (owing to the high rigidity of the gear material), the impact of excluding the contact area was limited. On the other hand, increasing the distance between the contact surfaces influenced the whole tooth surface; hence, experimental validation was required.

3. As simulation modeling methods for oil flow, this research shows that the momentum change of oil can be modeled without individually solving oil particles, by coarse-graining the oil particles, applying a simple modeling method of the oil jet (to reduce the number of calculation meshes), and implementing a method for improving simulation accuracy that considers the case in which the drag coefficient in a two-phase flow is lower than that in the single phase flow.

4. As a method for separating the fluid dynamic loss, we suggested that the aerodynamic loss could be obtained by the simulation of air alone, and the oil dynamic loss could be obtained by subtracting the aerodynamic loss from the fluid dynamic loss of air and oil.

4.5.2   Summary of Validation Results for the Applicability of Numerical Simulation Methods

1. To validate the airflow in the gear meshing part, the air pressure in the tip clearance thereof was validated. As a result, it was found that the numerical simulation could reproduce the pressure increase in the into-mesh part and the pressure decrease in the out-of-mesh part.

2. To validate the airflow around the gear peripheral part, we validated the aerodynamic loss of a single gear. It was found that the numerical simulation can qualitatively reproduce the aerodynamic loss of a single gear, as well as the loss reduction rate caused by shrouding.

3. To validate the oil flow in the gear meshing part, the oil jet flow to the gear meshing part from into-mesh or out-of-mesh was validated. It was found that the numerical simulations could qualitatively reproduce the visualization results of the oil jet flow.

4. To validate the oil flow around the gear peripheral part, the oil spray flow to the gear tooth under different peripheral speeds of the gear was validated. As a result, and it was found that the numerical simulations could qualitatively reproduce the visualization results of the oil spray flow.

5. To validate the oil flow near the shroud wall, the oil fraction, mixture velocity, and oil flow velocity between the gear tooth tip and shroud wall were validated. It was found that the numerical simulation could reproduce the experimental results, because the oil fraction was large near the shroud wall, the flow velocity near the tooth tip was high, the flow velocity tended to decrease as it approached the wall, and the peak value of oil flow velocity tended to be slightly further away from the shroud wall.

6. The simulation results for the fluid dynamic loss (of air and oil), aerodynamic loss, and oil dynamic loss were found to reflect the experimental results.

7. As described above, because the numerical simulation results were qualitatively consistent with the experimental results in all simulations, the numerical simulation method could be applied to clarify the phenomena of fluid dynamic loss. In addition, the quantitative accuracy almost satisfied the practical accuracy (15% or less) in the validation for the air pressure in the gear mesh, the validation of the aerodynamic loss for a single gear, the validation of the oil flow velocity near the shroud wall, and the validation of the fluid dynamic loss. Therefore, a quantitative evaluation using the numerical simulation method is considered possible.

Chapter 5

Clarification and Classification of Fluid Dynamic Loss Phenomena

In this chapter, we first explain the phenomena of fluid dynamic loss by considering the results of numerical simulations, and thereafter, we classify the fluid dynamic losses.

5.1 Clarification of the Phenomenon of Aerodynamic Loss

5.1.1 Airflow Fields

Figure 5.1-1 depicts the configurations of the gears and peripheral parts, and the division of the gear areas used to clarify the aerodynamic loss phenomenon. The configurations of the gears and peripheral parts are shown in Fig. 5.1-1 (a). Oil jets are ejected from the top and bottom of a helical gear pair toward its gear meshing part, where the input gear (large gear) and output gear (small gear) interlock with each other. The meshing point of the gears moves from the bottom to the top; the lower side of the meshing part is defined as the "into-mesh" side, and the upper side is defined as the "out-of-mesh" side. The helical gear consists of a leading side (front side in the rotational direction) and trailing side (the side that follows the front side in the rotational direction). The gears are enclosed by a shroud with openings.

(a) Configurations of gears   (b) Gear meshing and gear peripheral parts
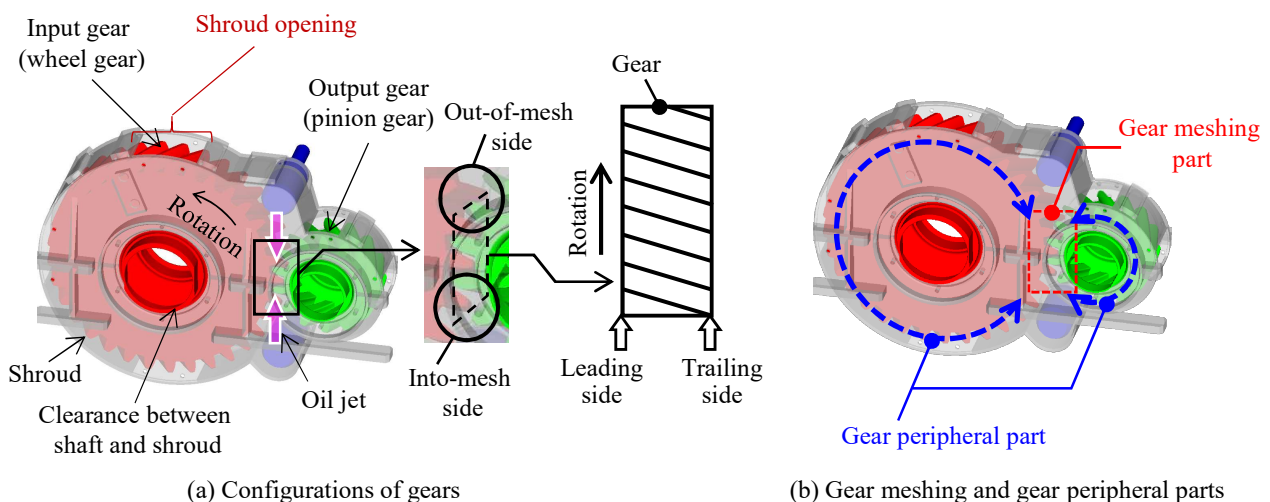
Fig. 5.1-1 Gear and shroud configurations; definitions of the gear parts

In loss classification, the gear part is divided into gear meshing and gear peripheral parts, as depicted in Fig. 5.1-1 (b). The aerodynamic loss phenomena in each part were examined, and the same parts were used to clarify the phenomena of the oil dynamic loss; these parts are the same as described in Chapter 2.

(1)   Airflow Pattern and Gear Pumping Work

The airflow pattern around the gear and the pumping work of the gear are depicted in Fig. 5.1-2 . After air is sucked from the clearance between the gear shaft and the shroud, it flows radially inside the shroud (① in Fig. 5.1-2) and flows out from the shroud opening (② in Fig. 5.1-2). In this case, the power required for gear rotation (the power is the aerodynamic loss, which is obtained from the integral of the pressure and shear force on the gear surface) is 2 kW. In contrast, the airflow work performed by the gear (pumping work) was calculated from the product of the pressure difference and volumetric flow rate of the air sucked by the gear rotation. The result was 8 W, and the pumping efficiency compared to the input power was 0.4%.

In an experiment by Houjoh et al. [58], the power loss was reduced when the pressure in the gearbox was lowered by an external vacuum pump, but the loss increased when the pressure in the gearbox was lowered by using the gear's own pumping work. As depicted in Fig. 5.1-2 , because the pumping efficiency was significantly lower (0.4%), the power required for the pumping work of the gear was larger than the power reduction owing to the internal pressure reduction in the gearbox. Therefore, the utilization of the pumping work of the gear is considered to be difficult, whereas the significant reduction of power loss is found to be effective.

Speed
100
(m/s)
0

②Outflow from peripheral openings

①Inflow from clearance between shaft and shroud

Pumping work 8 W

Estimated using volumetric flow rate × pressure through the clearance between shaft and shroud

Rotating power 2 kW

Efficiency 0.4%

Time-averaged velocity field of air, Shroud 1, 10000 rpm
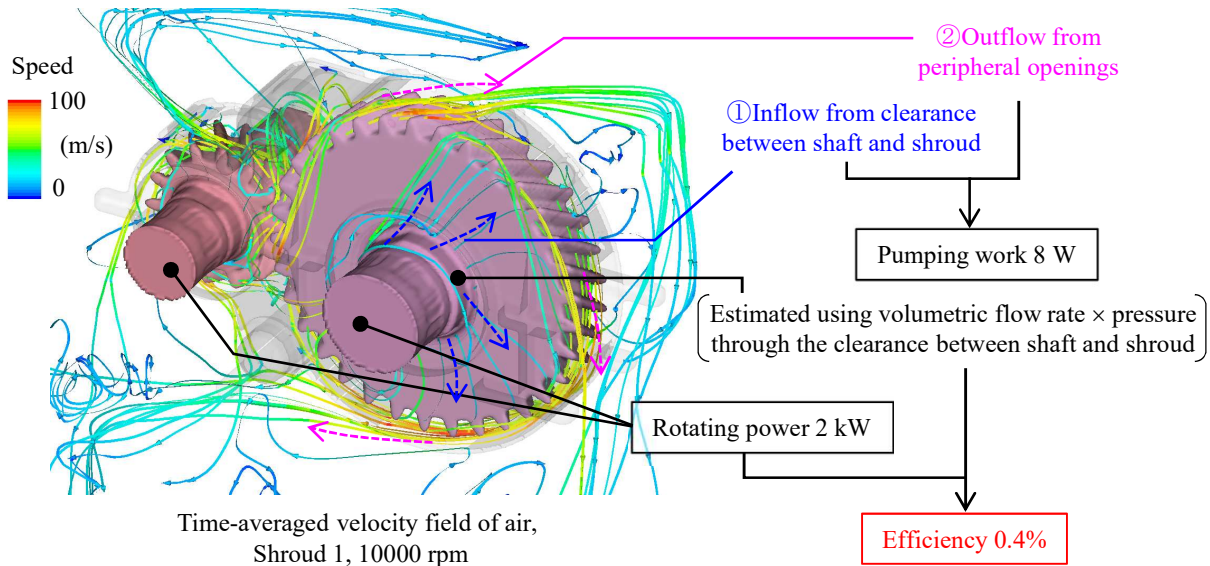
Fig. 5.1-2 Airflow streamline and air pumping work via gear rotation (simulation results)

(2)   Characteristics of Airflow in Gear Meshing and Gear Peripheral Parts

The characteristics of airflow are depicted in Fig. 5.1-3 . (a) depicts the streamline at the gear meshing part; (b) depicts the pressure contour at the cross-section of the gear meshing part; (c) depicts the gear surface pressure of the gear peripheral part and the streamline on the gear fixing coordinate system.

From the streamline depicted in Fig. 5.1-3 (a), we can see that the air is pushed out at the into-mesh side ("A" in the figure), flow beside the gear meshing part ("B" in the figure), and is sucked in at the out-of-mesh side ("C" in the figure).

157

From the pressure contour at the cross-section of the gear meshing part depicted in Fig. 5.1-3 (b), we can see that the air pressure increases owing to the pushing out of air at the into-mesh side and decreases owing to the suction of air at the out-of-mesh side. In the gear meshing part, it was also found that there is a slight gap, such as tip clearance (clearance between the tooth peak of a gear and the tooth bottom of another gear) and backlash, and that the air in the gap flows following the rotation of the gear ("D" in the figure).

From the streamline on the gear fixed coordinate system in Fig. 5.1-3 (c), it was found that air is sucked from the leading side of the helical gear, flows while swirling along the tooth flank line, and then flows out from the trailing side. The pressure distribution on the gear surface indicated that the pressure increased at the tooth front surface in the rotational direction and decreased at the tooth rear surface in the rotational direction. The force loaded on the tooth is considered to be generated by the pressure difference between the front and rear surfaces in the rotational direction.

(a) Streamline around gear mesh   (b) Pressure distribution and velocity vector around gear mesh

(c) Pressure distribution on gear surface and streamline of relative velocity
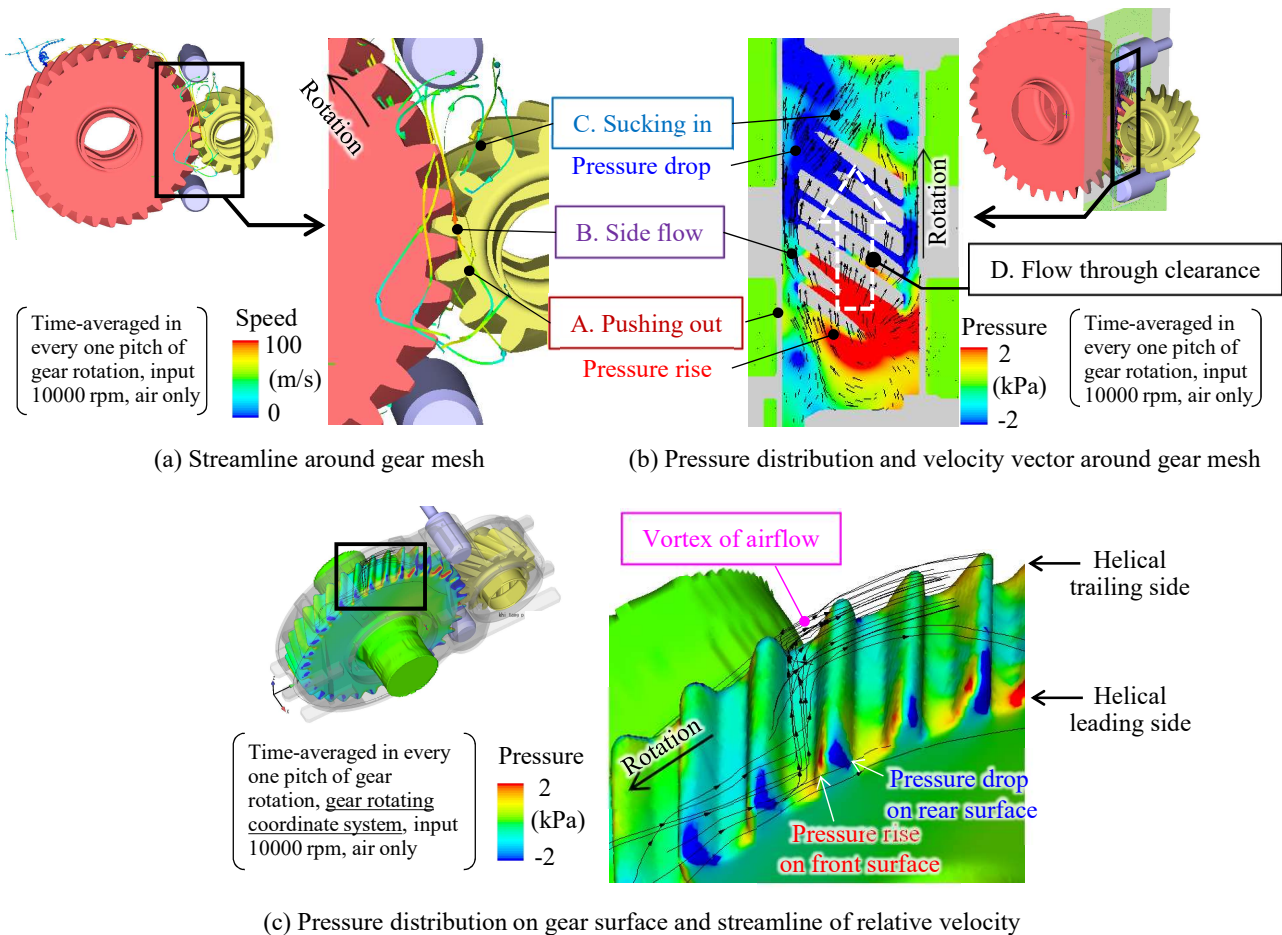
Fig. 5.1-3 Characteristics of airflow around the gears (simulation results)

5.1.2 Consideration of the Gear Peripheral Distribution of Air Drag Torque

(1) Comparison of the Order of Magnitude between the Pressure-Induced and Shear Force-Induced Torques

The power loss caused by the fluid dynamic force loaded on the gear is depicted in Fig. 5.1-4 . The rotational speed changes of the aerodynamic losses owing to pressure and shear force are depicted in Fig. 5.1-4 (a); the fraction of the loss caused by the pressure and shear force in the aerodynamic loss is depicted in Fig. 5.1-4 (b).

The aerodynamic loss owing to pressure was obtained by integrating the pressure on the gear surface, as listed in Eq. 4.18. Similarly the one owing to the shear force was obtained by integrating the shear force on the gear surface, as listed in Eq. 4.19.

Figure 5.1-4 (a), (b) shows that a significant amount of the aerodynamic losses are due to pressure. The aerodynamic losses caused by both the pressure and shear force tend to increase with increasing rotational speed. The fraction of pressure-induced loss was large owing to the protruding shape of the gear teeth, and were susceptible to the dynamic pressure of the airflow. In the oil flow, the pressure-induced loss is considered to tend to be dominant, similar to that in the airflow.

Therefore, the pressure field should be considered to clarify the main causes of torque and fluid dynamic loss generated by the flow.

(a) Power loss induced by pressure or shear force*

* Time-averaged, Shroud 1, air only

(b) Fractions of power loss induced by pressure or shear force at 10000 rpm*
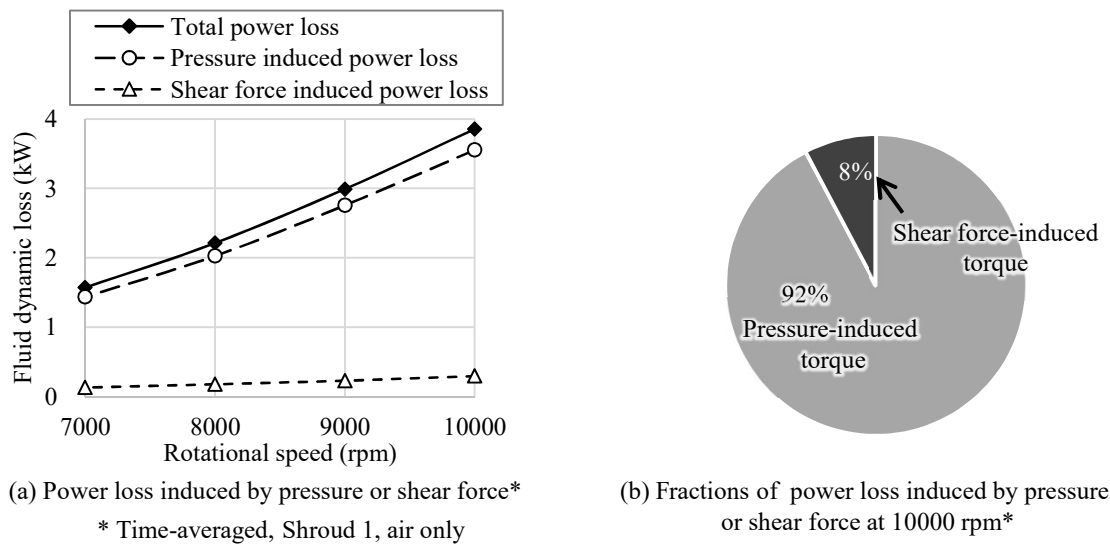
Fig. 5.1-4 Torque component decomposition to pressure-induced torque or shear force-induced torque (simulation results)

(2)   Consideration of Torque Distribution from Air Pressure Field

The torque distribution, pressure distribution, and velocity vector around the gears are depicted in Fig. 5.1-5 . Figure 5.1-5 (a1) depicts the pressure distribution of air around the input gear. Figure 5.1-5 (a2) depicts the peripheral distribution of the input gear torque. Figure 5.1-5 (a3) is the superposition of (a1) and (a2). Similarly, (b1) depicts the pressure distribution of air around the output gear, (b2) depicts the peripheral distribution of the output gear torque, and (b3) is the superposition of (b1) and (b2).

At first, we considered the torque and pressure distributions around the input gear. A peak of torque ("A1" in Fig. 5.1-5 (a3)) was observed at the into-mesh side. This is because the pressure in the forward surface of the tooth increases with increasing pressure as it approaches the meshing part, and as a result, the pressure difference between the forward and backward surfaces of the tooth increases. A negative torque ("B" in Fig. 5.1-5 (a3)) was observed at the center of the gear mesh. This is because when the tooth is located at the center of the gear mesh, the pressure on the forward surface in the rotational direction (out-of-mesh side) is low, and the pressure on the backward surface in the rotational direction (into-mesh side) is high, so that the tooth receives a force rotating in the rotational direction from the pressure difference between the forward and backward surfaces of the tooth. A peak torque ("A2" in Fig. 5.1-5 (a3)) was

observed at the out-of-mesh side. This is due to the increased pressure difference between the forward and backward surfaces of the tooth as a result of the pressure increase as the tooth moves away from the gear mesh to out-of-mesh.

(a1) Pressure distribution around input gear*

(a2) Torque distribution around input gear**

(b1) Pressure distribution around output gear*

(b2) Torque distribution around output gear**

D1. Torque increase near obstacle

A2. Larger torque around out-of-mesh

B. Negative torque at the center of meshing

A1. Larger torque around into-mesh

C. Equivalent torque around gear periphery

D2. Torque increase near obstacle (edge of shroud opening)

Oil-jet nozzle position

Direction of view

Arrowhead

Flow vector

D2. Torque increase near obstacle (edge of shroud opening)

(a3) Torque, pressure, and velocity vector (Input gear)

(b3) Torque, pressure, and velocity vector (Output gear)

* Time-averaged in every one pitch of gear rotation
** Time-averaged

Fig. 5.1-5 Understanding of the airflow phenomena via torque and pressure distributions (simulation results, Shroud 1, input 10000 rpm)

An equivalent torque is generated in the gear periphery ("C" in Fig. 5.1-5 (a3)). A part of the gear is enlarged at the upper left of (a3) in the figure. From this figure, it can be observed that the pressure on the forward side of the tooth in the rotational direction is high, and the pressure on the backward side is low. This pressure trend is similar to the pressure on the forward and backward sides of the gear tooth in Fig. 5.1-3 (c). Because the torque of the gear periphery is caused by the vortex generated between the teeth, and the strength of the vortex is assumed to be caused by the peripheral speed and shape of the teeth (which is similar in gear periphery), the torque of the gear periphery is considered to be equivalent. An increase in torque can be observed near the oil jet nozzle, where the clearance between the gear and shroud becomes narrow ("D1" in Fig. 5.1-5 (a3)). The torque increases at the edge of the shroud opening ("D2" in Fig. 5.1-5 (a3)). Therefore, it was proven that the oil jet nozzle and shroud shape became obstacles to the flow, and the torque increased around them.

In Fig. 5.1-5 (b3), the tendency of torque and pressure distribution around the output gear is similar to that around the input gear [the torque increased with increasing pressure at the into-mesh side ("A1" in

160

Fig. 5.1-5 (b3)), the negative torque at the center of the gear mesh ("B" in Fig. 5.1-5 (b3)), the torque increased with decreasing pressure at the out-of-mesh side ("A2" in Fig. 5.1-5 (b3)), and the torque increased near the obstacles ("D2" in Fig. 5.1-5 (b3))].

From the above, it is possible to understand the cause of the torque generation from the tendency of the pressure distribution.

5.1.3 Effect of Shroud on Aerodynamic Loss

Although it has been proven that aerodynamic loss can be reduced by enclosing the gear with a shroud [31], the mechanism of the loss reduction has not been clarified yet. Therefore, the mechanism of loss reduction by shrouding is clarified by considering the phenomena and the difference in loss between two types of shrouds.

(1)   Effect of Reducing the Range in which the Gears Causes High-Velocity Airflow

A comparison of airflow patterns between Shroud 1 and Shroud 2 is depicted in Fig. 5.1-6 . The flow patterns in Shroud 1 are depicted in (al) and (a2). The flow patterns in Shroud 2 are depicted in (b1) and (b2). (a1) and (b1) in the figure are observed from the helical leading side (the front side in which the teeth move in the rotational direction). (a2) and (b2) in the figure are observed from the helical trailing side. To draw the streamline, the streamline source was placed at a peripherally uniform angle in the clearance between the gear shaft and shroud. The number of streamline sources was the same for Shroud 1 and Shroud 2.

In total, it can be seen that the leakage of airflow from Shroud 1 to the outside (Fig. 5.1-6 (a1), (a2)) is larger than that from Shroud 2 (Fig. 5.1-6 (b1), (b2)). This leakage of air causes outside air flow from the shroud. In the absence of any shrouds, it was inferred that the airflow was greater than that of Shroud 1. The airflow leakage from the shroud opening is compared here. Regarding the streamline on the gear side, there are few streamlines on the side of Shroud 1 indicated by "A1" in Fig. 5.1-6 (a2), whereas there are several streamlines on the side of Shroud 2 indicated by "A2" in Fig. 5.1-6 (b2). The reason for fewer streamlines on the side of Shroud 1 in "A1" in Fig. 5.1-6 (a2) is the outflow from the shroud opening indicated by "B1" in the figure. On the other hand, in "A2" in Fig. 5.1-6 (b2), the streamlines are dispersed because there is no shroud opening nearby.

The outflow from the shroud opening of Shroud 1 was observed. It can be seen that the outflow from the shroud openings significantly disturbs the air in the gearbox in "B1" and "B1*" (near from out-of-mesh) in Fig. 5.1-6 (a1), (a2), whereas in "C1," "C1*", "D1" and "D1*" in Fig. 5.1-6 (a1), (a2), the air turbulence in the gearbox caused by the outflow from the shroud openings is less than that in "B1" and "B1*".

The outflow from the shroud opening of Shroud 2 was observed. As indicated by "C2" and "C2*" in Fig. 5.1-6 (b1), (b2), there is little air disturbance in the gearbox due to the outflow from the shroud opening. From the above results, it was found that in Shroud 1, the outflow from the shroud opening close to the out-of-mesh significantly disturbs the air in the gearbox as shown in "B1" and "B1*" in Fig. 5.1-6 (a1), (a2). In Shroud 2, the air turbulence in the gearbox was relatively small because there were no such openings.

To consider the difference in flow fields depending on the presence or absence of a shroud opening, Shroud 1 and Shroud 2 were compared with respect to the flow velocity distribution near the shroud opening, as depicted in Fig. 5.1-7 . Each figure depicts the contours and vectors of velocity (relative velocity) in a

gear-fixed coordinate system.

(a1) Helical leading side, Shroud 1

(a2) Helical trailing side, Shroud 1

(b1) Helical leading side, Shroud 2

(b2) Helical trailing side, Shroud 2
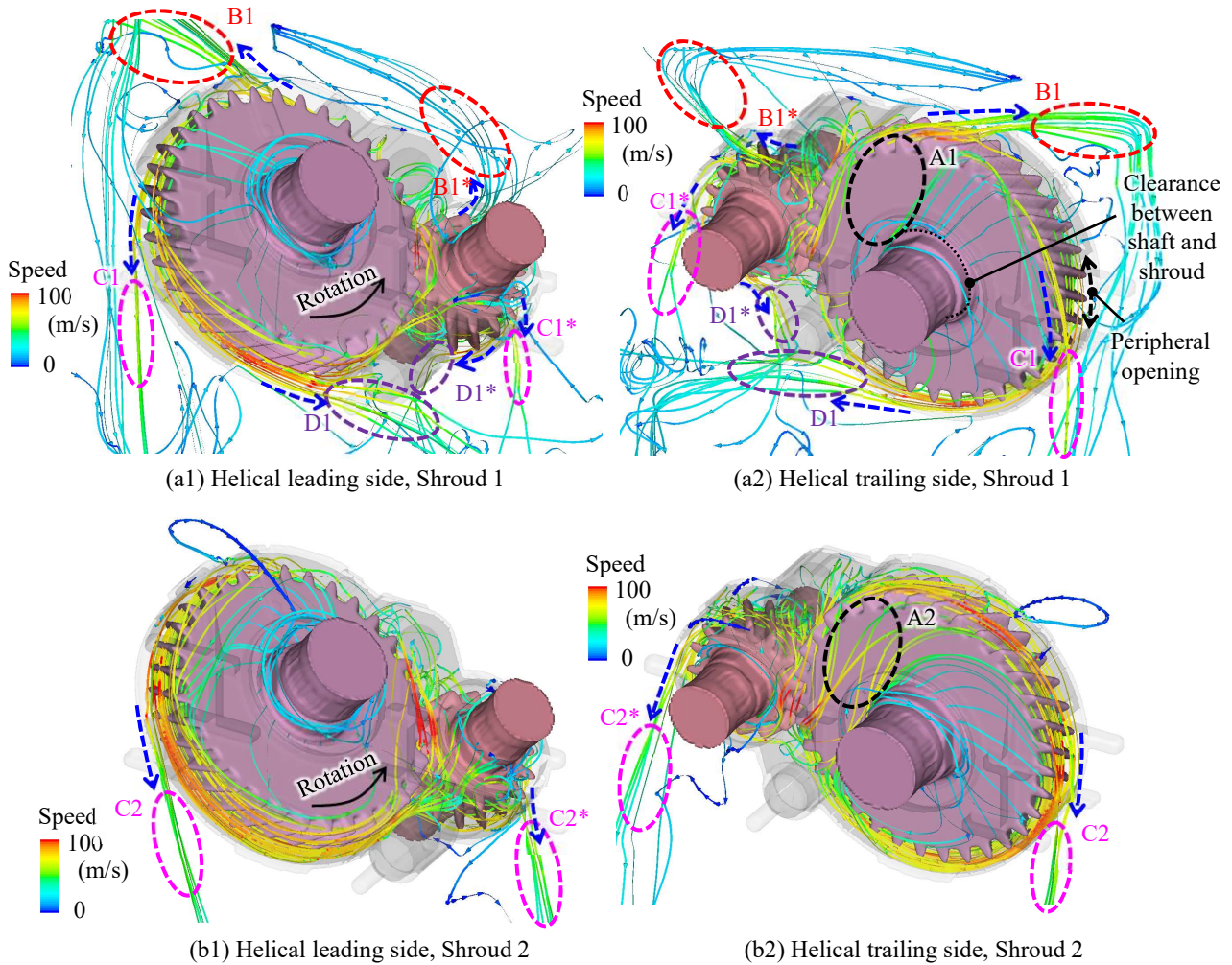
Fig. 5.1-6 Comparisons of Shroud 1 and Shroud 2 on the streamline of airflow (simulation results)

(a) Relative speed distribution and vector* on Shroud 1

(b) Relative speed distribution and vector* on Shroud 2
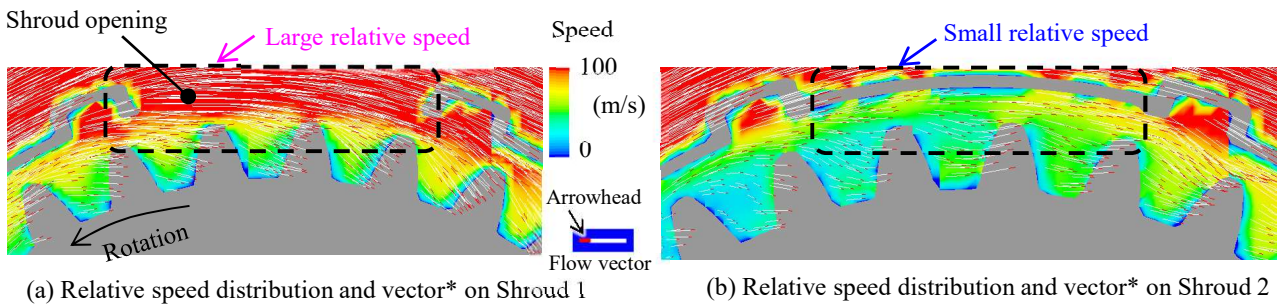
* Time-averaged in every one pitch of gear rotation, rotating coordinate system

Fig. 5.1-7 Comparison of Shroud 1 and Shroud 2 on relative speed in gear peripheral part (simulation results)

In the velocity distribution of Shroud 1 as depicted in Fig. 5.1-7 (a), it can be seen that the airflow is decelerated owing to the shroud opening (the velocity is high when viewed from the gear). On the other hand, in the velocity distribution of Shroud 2 as depicted in Fig. 5.1-7 (b), it can be seen that the airflow is not decelerated owing to the absence of the shroud opening, and the velocity is approximately the same as

that of the gear velocity (the velocity is low when viewed from the gear). The higher the relative velocity, the greater the fluid force applied to the gear teeth. Therefore, enclosing the gear in the shroud separates the fluid around the gear from the fluid outside the shroud, thereby reducing the fluid force applied to the gear.

(2)   Effect of Reducing the Pumping Work of the Gear

The pumping work was evaluated based on the pressure and flow rate at the clearance between the gear and the shaft. As an evaluation result of the pumping work of the gear, Fig. 5.1-8 (a) depicts the volumetric flow rate of the air passing through the sampling surface; Fig. 5.1-8 (b) depicts the pressure rise (pressure at the shroud opening (atmospheric pressure) − average pressure on the sampling surface); Fig. 5.1-8 (c) depicts the pumping work calculated from (a) and (b). In each figure, the results of Shroud 1 and Shroud 2 are shown separately on the helical leading and helical trailing sides.

For both Shroud 1 and Shroud 2, the values on the helical leading side exceeded those on the helical trailing side. In the flow around the helical gear, the radial flow generated by the rotational centrifugal force of the flow caused by the gear teeth (Fig. 5.1-2) overlaps the flow generated from the helical leading side to the helical trailing side by the teeth having an inclination angle with respect to the rotational direction (Fig. 5.1-3 (c)). As a result, the volumetric flow rate, pressure rise, and pumping work on the helical leading side exceeded the values on the helical trailing side.

From (a) to (c) depicted in Fig. 5.1-8 , the volumetric flow rate, pressure rise, and pump work of Shroud 2 were lower than those of Shroud 1. This is because the peripheral opening of Shroud 2 is smaller than that of Shroud 1, and the air drag decreases. Based on this analogy, the pumping work of the gear can be reduced by enclosing the gear with a shroud.

(a) Volumetric flow rate   (b) Averaged pressure   (c) Pumping work
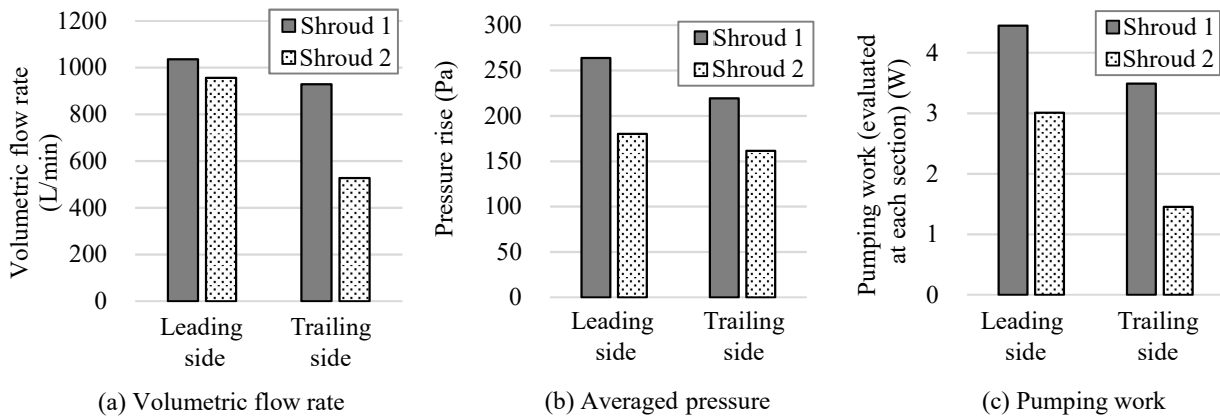
Fig. 5.1-8 Comparison of Shroud 1 and Shroud 2 on gear pumping work (simulation results)

(3)   Effect of Aerodynamic Loss Reduction

Regarding the effect of the shroud on the reduction of gear torque, the peripheral distribution of torque of Shroud 2 was compared with that of Shroud 1, as depicted in Fig. 5.1-9 . Fig. 5.1-9 (a) depicts the gear meshing part, and Fig. 5.1-9 (b) depicts the peripheral part of the input gear. The pressure contours and velocity vectors of Shroud 2 are shown in each figure.

According to Fig. 5.1-9 (a), the torque of Shroud 2 was smaller than that of Shroud 1 on both the into-mesh and out-of-mesh sides. In addition, the torque of Shroud 2 became smaller than that of Shroud

163

1 around the peripheral part of the gear, as shown in Fig. 5.1-9 (b). These results are attributed to the reduction in the pumping work of the gear described in (2).

Thereafter, we demonstrated the reduction effect of the shroud on the aerodynamic loss and clarified the relationship between the shroud and pumping efficiency of the gear. Figure 5.1-10 (a) compares the aerodynamic losses of Shroud 1 and Shroud 2, and Fig. 5.1-10 (b) shows the comparison of the pumping efficiency. The pumping efficiency depicted in Fig. 5.1-10 (b) was obtained by dividing the pumping work depicted in Fig. 5.1-8 (c) by the aerodynamic loss depicted in Fig. 5.1-10 (a).

(a) Torque distribution*(Shroud 1, Shroud 2) and pressure distribution**(Shroud 2) around gear meshing

(b) Torque distribution*(Shroud 1, Shroud 2) and pressure distribution**(Shroud 2) around gear periphery

* Time-averaged, ** Time-averaged in every one pitch of gear rotation
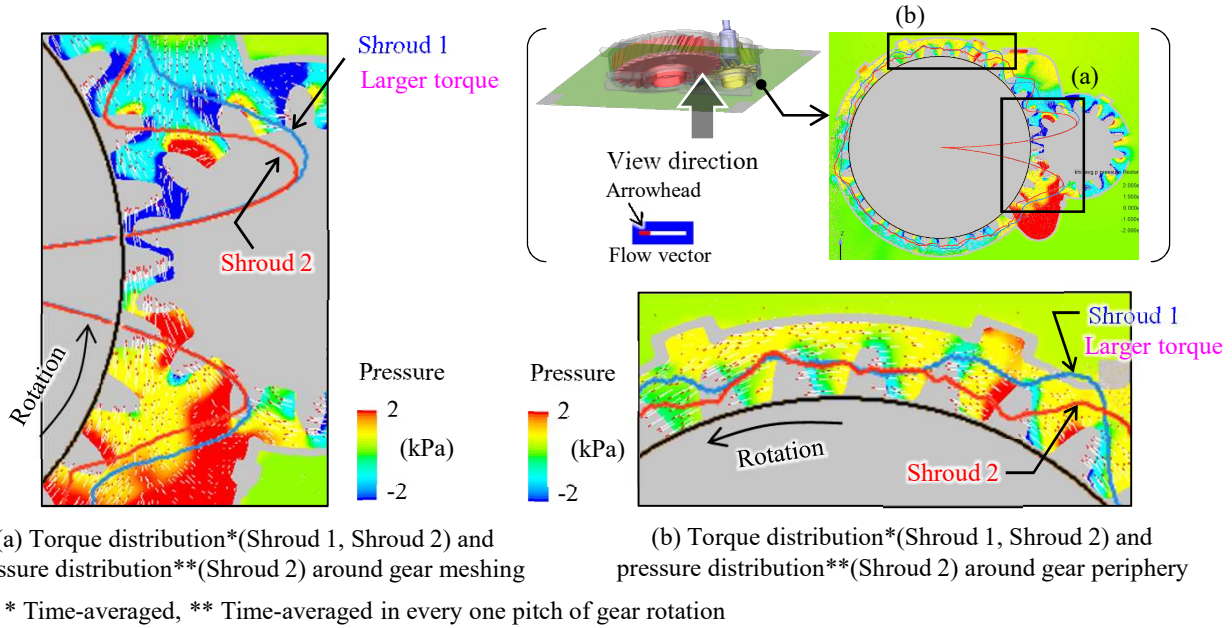
Fig. 5.1-9 Comparison of Shroud 1 and Shroud 2 on torque distribution and pressure contour (simulation results)

(a) Aerodynamic loss (Experimental results)

(b) Pumping efficiency
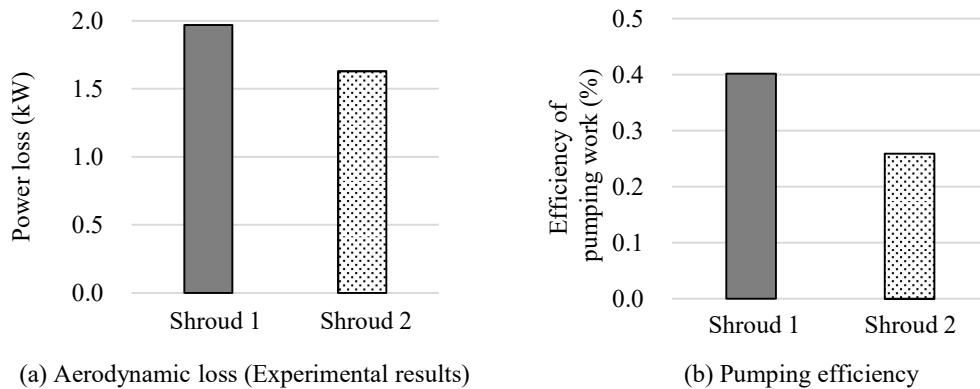
Fig. 5.1-10 Comparison of Shroud 1 and Shroud 2 on aerodynamic loss and pumping efficiency (simulation results)

Figure 5.1-10 (a) shows that the aerodynamic loss of Shroud 2 is lower than that of Shroud 1, and Fig. 5.1-10 (b) shows that the pumping efficiency of Shroud 2 is lower than that of Shroud 1. Therefore, although the pumping efficiency decreases as the number of shroud openings is reduced (the total opening area is smaller), as in Shroud 2, the aerodynamic loss decreases owing to the decrease in the pumping work. Thus, it is estimated that the effect of enclosing the gear with the shroud is to reduce the aerodynamic loss and further reduce the loss by reducing the total opening area.

5.1.4 Rotational Speed Characteristics and Dimensionless Evaluation of Aerodynamic Loss

(1)   Rotational Speed Characteristics of Aerodynamic Loss

In this section, the theory of aerodynamic loss is validated and the characteristics of the loss are clarified via a dimensionless evaluation.

To validate the theory of aerodynamic loss (Section 2.2), the rotational speed characteristics of the aerodynamic loss are depicted in Fig. 5.1-11 . Figure 5.1-11 (a) depicts a sampling section of the air flow rate caused by gear rotation. The sampling section was installed at the meshing part of the gear as the air generated by the input and output gears passes through it. Figure 5.1-11 (b) shows the air flow rate passing through the sampling section with respect to the rotational speed changes. The air flow rate was proportional to the rotational speed in both Shroud 1 and Shroud 2. Figure 5.1-11 (c) shows the aerodynamic loss with respect to the rotational speed changes. Only the longitudinal axis was set as a logarithmic display. For both Shroud 1 and Shroud 2, the losses were proportional to the third power of the rotational speed.

The gear-driven air flow rate was proportional to the rotational speed as depicted in Fig. 5.1-11 (b), and the aerodynamic loss was proportional to the third power of rotational speed as depicted in Fig. 5.1-11 (c). These facts were consistent with the theory of aerodynamic loss given in Section 2.2. The validity of the theory of aerodynamic loss was thus confirmed.

(a) Sections for Sampling airflow rate around gears

(b) Airflow rate around gears with rotational speed changes

(c) Aero dynamic loss with rotational speed changes
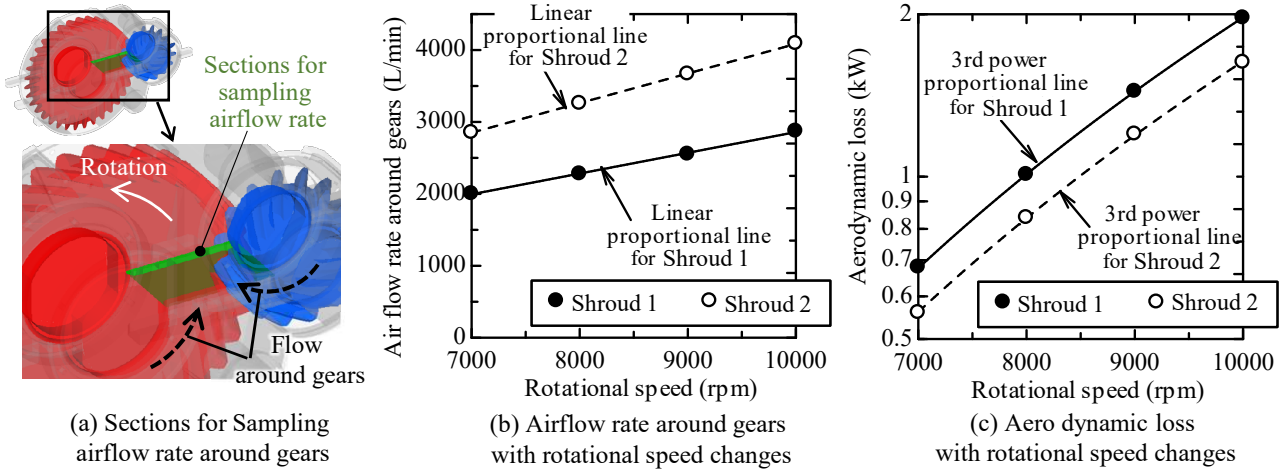
Fig. 5.1-11 Characteristics of airflow rate and aerodynamic loss on rotational speed (simulation results)

(2)   Dimensionless Evaluation of Aerodynamic Loss

To understand the characteristics of aerodynamic loss, the loss was made dimensionless. Figure 5.1-12 shows a schematic of the parameters related to the aerodynamic force applied to the gear tooth surface, which is the pressure applied to the tooth surface multiplied by the applied area. The force applied to the tooth surface is considered to be related to the dynamic pressure of the airflow $\frac{1}{2}\rho_{air}v_p{}^2$, and the pressure applied area is related to the tooth area $hB/\cos\beta$. Therefore, the power loss due to the force loaded on the gear tooth surface P_{air} is given by the following equation by considering that the fluid force is F_{air}:

$$P_{air} = F_{air}r_p\omega = F_{air}v_p \propto \frac{1}{2}\rho_{air}v_p{}^3\frac{hB}{\cos\beta} \tag{5.1}$$

Here, shroud coefficient λ, which represents the loss reduction effect of covering the gear with a shroud, and the number of gears n_G (= 1 for a single gear and = 2 for a gear pair) were introduced to compare the loss of a single gear. The dimensionless aerodynamic loss $\tilde{P}_{air}$ is defined as follows:

$$\tilde{P}_{air} = \frac{P_{air}}{\lambda \frac{1}{2} \rho_{air} v_p^3 \frac{hB}{\cos \beta} n_G} \tag{5.2}$$

An additional dimensionless number associated with this dimensionless number $\tilde{P}_{air}$ is considered. As an example of the dimensionless number of airflow drag of an object, the airflow drag force of a prism can be characterized as a function of the aspect ratio of the prism (e.g., [115]). Based on this, the gear aspect ratio (= tooth width / gear diameter= B/D_p) was used as a dimensionless number.

The dimensionless evaluation was conducted using the non-dimensional aerodynamic loss $\tilde{P}_{air}$ and the gear aspect ratio B/D_p for the experimental results of the two-axis helical gearbox and Dawson's single spur gears [31]. The results are depicted in Fig. 5.1-13 . For the two-axis helical gearbox, the gear aspect ratio was set to the tooth width / averaged pitch diameter. The shroud coefficient was obtained from the empirical equations given in Section 6.4. Both the experimental results of the two-axis helical gearbox of this study and the experimental results of Dawson's single-spur gears show a similar tendency. $\tilde{P}_{air}$ tends to increase under the condition of a small gear aspect ratio (larger gear diameter and smaller tooth width). This is because a smaller gear aspect ratio increases the aerodynamic loss on the sides of the gear.

The approximate curve obtained from the data depicted in Fig. 5.1-13 is expressed in the following equation:

$$\tilde{P}_{air} = 3.522 \left(\frac{B}{D_p} \right)^{-0.436} \tag{5.3}$$

The approximation curve illustrated in Fig. 5.1-13 represents the data. Therefore, we can easily estimate the aerodynamic loss from the gear dimensions, shroud dimensions and operating conditions by using this approximation curve (see Appendix A.5).
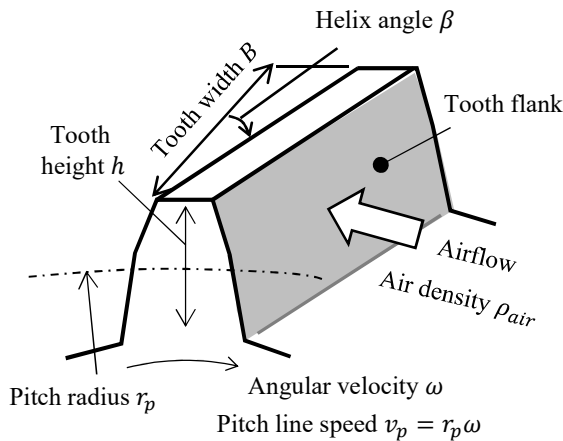
Fig. 5.1-12 Parameters for air drag on gear tooth
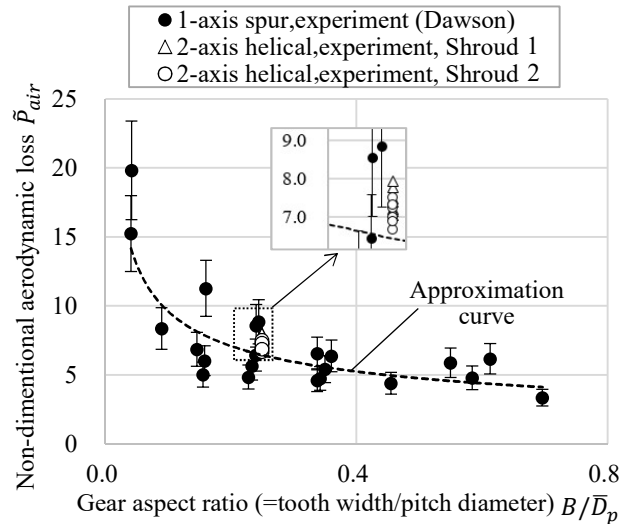
Fig. 5.1-13 Non-dimensional aerodynamic loss with respect to gear aspect ratio changes

5.1.5 Summary of the Clarification of Aerodynamic Loss

1. The rotating gear has a pumping effect that sucks the air around the shaft and discharges it in the peripheral direction of the gear, further resulting in aerodynamic losses. The efficiency of the pumping effect against the required power for gear rotation is extremely low (less than 1 %).

2. Around the meshing part of the gear, air is pushed out at the into-mesh side, which later on passes through the side of the gear mesh, and is sucked in on the out-of-mesh side. The pressure increases when the air is pushed out at the into-mesh side and decreases when the air is sucked in at the out-of-mesh side. The torque increases at the into-mesh and out-of-mesh sides owing to the pressure variations. At the center of the gear mesh, a negative torque is generated by the high pressure at the into-mesh side and the low pressure at the out-of-mesh side.

3. In the peripheral part of the gear (other than the meshing part of the gear), owing to the vortex generated in the valley of the tooth of the gear, the pressure on the forward side of the tooth in the rotational direction is high and the pressure on the rear side of the tooth is low, which results in the torque generation. The torque in the peripheral part of the gear is almost equivalent in the peripheral direction; however, it tends to increase slightly in the vicinity of obstacles.

4. The effect of the gear shroud on the aerodynamic loss is that the shroud separates the fluid around the gear from the fluid outside the shroud, further reducing the pumping work of the gear and aerodynamic loss. In addition, reducing the number of openings in the shroud (reducing the total opening area) enhances the loss reduction effect of the shroud.

5. The air flow rate generated by the gear rotation is proportional to the rotational speed, and the aerodynamic loss is proportional to the third power of the rotational speed. These proportional characteristics are consistent with this theory.

6. A similar tendency was obtained when the aerodynamic loss was arranged using the dimensionless number of the aerodynamic loss (considering the dynamic pressure of airflow on the gear tooth surface, pressure applied area, and shroud coefficient) and the gear aspect ratio.

5.2 Clarification of the Oil Dynamic Loss Phenomena

5.2.1 Oil Flow Fields

In this section, the oil flow that causes oil dynamic loss is identified.

(1) Characteristics of Oil Flow

The characteristics of oil flow around the gear are depicted in Fig. 5.2-1 . The oil distribution, as observed from the helical leading side, is depicted on the left side of Fig. 5.2-1 (a), and the oil distribution as observed from the helical trailing side is depicted on the right side of the figure. The acceleration phenomena of oil at the meshing part of the gear are shown in Fig. 5.2-1 (b), the oil flow dividing at the out-of-mesh side is shown in (c), the oil flow adhering to the gear tooth surface is shown in (d), the oil flow from the gear side into the gear tooth surface is shown in (e), from the oil flow from the shroud opening and oil remaining in the shroud are shown in (f).

As depicted in Fig. 5.2-1 (a), the amount of oil on the gear side of the helical leading side is larger than

167

that of the helical trailing side. The reason for this difference is shown in Fig. 5.2-2 . The oil jet nozzle is a cantilever structure inserted halfway into the shroud from the helical trailing side, and a clearance is provided between the tip of the nozzle and shroud. This cantilever structure of an oil jet nozzle is generally adopted for aeroengine gears because it is easy to install the nozzle and manage the dimensions of the nozzle holes.
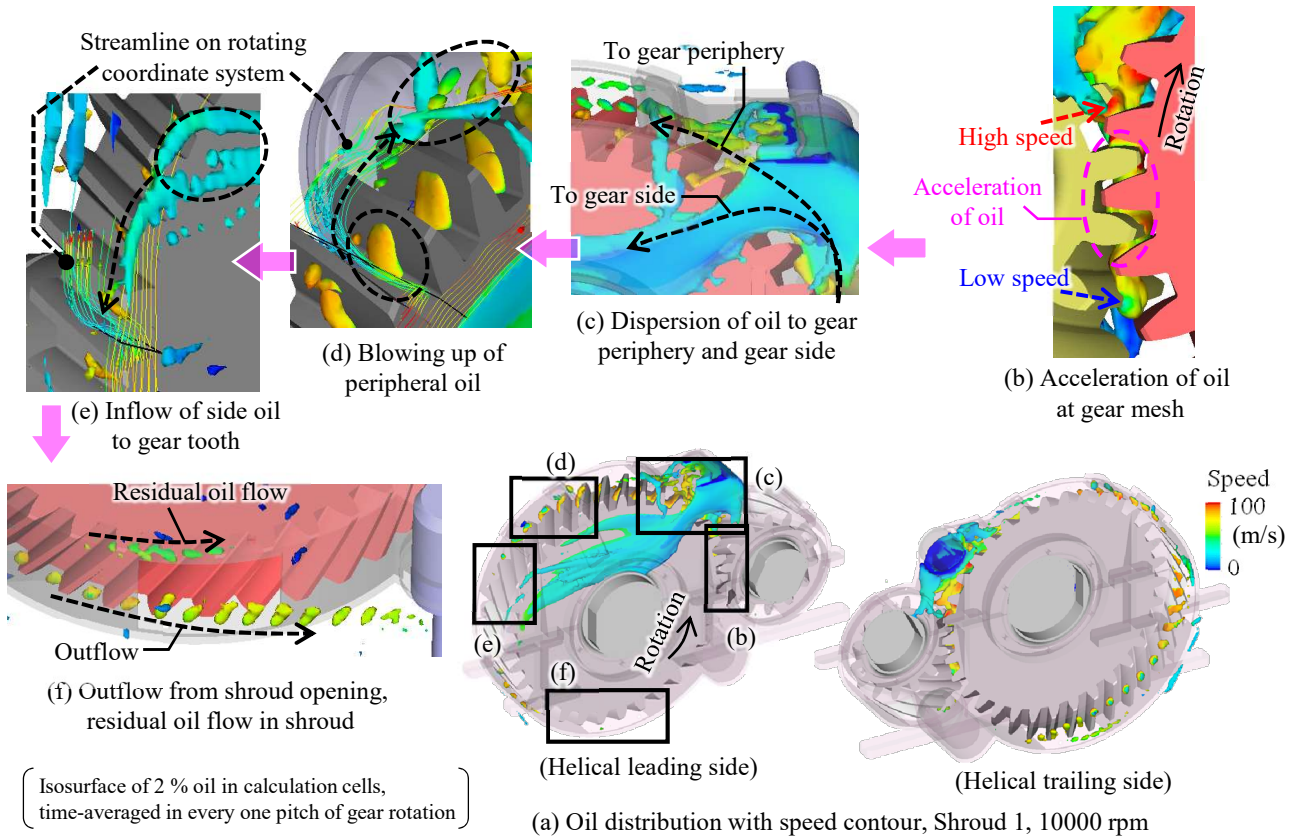
Fig. 5.2-1 Characteristics of oil flow around gears (simulation results)
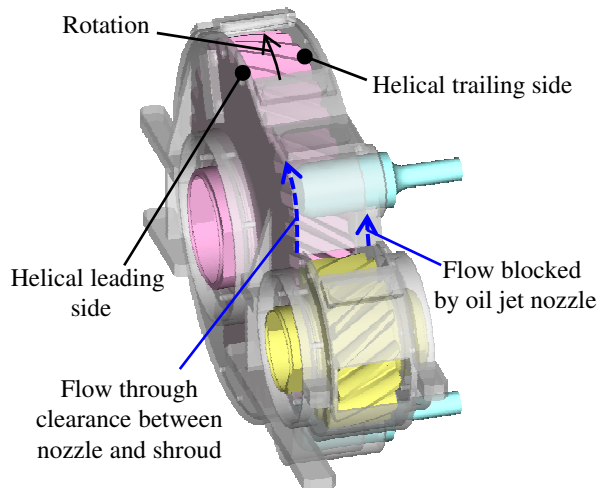
Fig. 5.2-2 Schematic of asymmetrical oil flow around the oil jet nozzle

As indicated by the blue arrow in Fig. 5.2-2 , the flow from the out-of-mesh side near the helical leading side can pass through the clearance between the nozzle and shroud. In contrast, the flow from the out-of-mesh side near the helical trailing side is blocked by the nozzle. Therefore, it is assumed that the oil flow on the helical leading side as depicted in Fig. 5.2-1 (a) is because of the clearance between the nozzle and shroud.

The flow of (b) to (f) in Fig. 5.2-1 is described in detail later.

(2)   Oil Dynamic Loss Phenomena owing to Oil Jet Acceleration at the Gear Meshing Part

The acceleration of oil at the meshing part of the gear (Fig. 5.2-1 (b)) consists of the "acceleration of oil supplied to the meshing part of the gear" and "acceleration of oil when the residual oil in the shroud reflows into meshing part of the gear". At first, the "acceleration of oil supplied to the meshing part of the gear" of the former is considered.

The oil-jet acceleration loss is defined as the power loss caused when the supplied oil particles are accelerated at the meshing part of the gear. The theoretical equation for the oil-jet acceleration loss P_{jac} is as follows:

$$P_{jac} = \rho_{oil} Q_s v_p^2 \cos \beta \tag{5.4}$$

where ρ_{oil} is the oil density, Q_s is the volumetric oil supply flow rate, v_p is the pitch circle speed, and β is the helix angle of the helical gear.

The oil-jet acceleration loss expressed by this theoretical equation was confirmed via numerical simulation. The numerical simulation model is illustrated in Fig. 5.2-3 (a). The simulation was conducted in two dimensions with a gear and a cylinder set close to the gear. The gear meshing condition was not used to minimize the additional loss owing to oil deformation during oil acceleration, as described later. Oil was injected from the nozzle in the tangential direction of the gear pitch circle. The gear rotation was set in clockwise direction, and the cylinder rotation was set in counterclockwise direction when oil was injected to the into-mesh side. Conversely, the gear rotation was set in counterclockwise direction, and the cylinder rotation was set in clockwise direction when the oil was injected into the out-of-mesh side. The simulation range was limited to areas including the area around the oil jet nozzle and the area where the gear and cylinder came close to each other. The calculation mesh is illustrated in Fig. 5.2-3 (b). The mesh size was set to 0.125 mm, and 16 cells were set to resolve the nozzle width. The simulation conditions are listed in Table 5.2-1 . The calculation parameters were set in the direction of the oil jet nozzle (the into-mesh side or the out-of-mesh side), gear rotational speed (= cylinder rotational speed), oil supply flow rate, and oil-jet speed. As a numerical simulation method based on the one described in Section 4.1.1, only the oil flow was solved here.

Figure 5.2-4 depicts the simulation results of the oil distribution during the acceleration of oil under typical conditions. Figure 5.2-4 (a) shows the simulation result of the velocity contour under the conditions simulating the into-mesh jet. As shown by "Acceleration of oil" in Fig. 5.2-4 (a), it can be seen that the oil is accelerated via teeth rotation. Figure 5.2-4 (b) shows the simulation result under the condition where the jet speed is increased compared to the condition depicted in Fig. 5.2-4 (a). Compared to the oil flowing into the tooth valley of the gear indicated by "Oil flow in the tooth valley" as depicted in Fig. 5.2-4 (a), it can be seen that there is no oil flowing into the tooth valley of the gear indicated by "No oil" in Fig. 5.2-4 (b). Figure 5.2-4 (c) shows the simulation results under the condition of simulating the

out-of-mesh jet. As shown by "Acceleration of the oil" in Fig.5.2-4 (c), the oil can be accelerated by the rotation of the teeth. In addition, as shown by "Oil flowed into tooth valley" in Fig. 5.2-4 (c), oil can be seen to flow into the tooth valley of the gear.
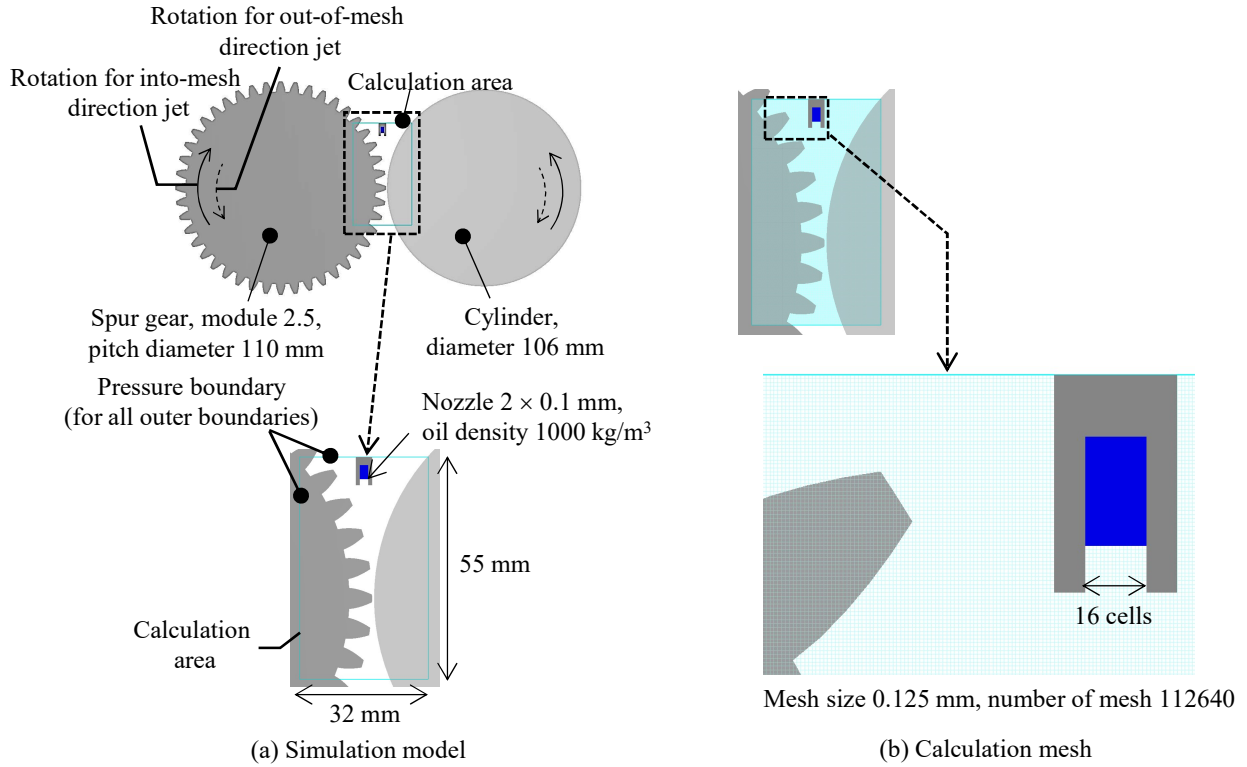
Fig. 5.2-3 Simulation model and calculation mesh for the validation of oil-jet acceleration loss

Table 5.2-1 Calculation conditions for the validation of oil-jet acceleration loss

Oil jet direction	Rotational speed (rpm)	Peripheral speed (m/s)	Oil supply rate (L/min)	Oil jet speed (m/s)
Into-mesh	7000–10000	40–58	0.12	10
	10000	58		10–30
			0.06–0.27	10
Out-of-mesh	7000–10000	40–58	0.12	10
	10000	58		10–30

The simulation results for the oil jet acceleration loss are shown in Fig. 5.2-5 . In Fig. 5.2-5 , (a) shows the simulation result with respect to rotational speed changes under the conditions simulating the into-mesh jet, (b) shows the simulation result with respect to jet speed changes under the conditions simulating the into-mesh jet, and (c) shows the simulation result with respect to oil flow rate changes under the conditions simulating the into-mesh jet. Fig. 5.2-5 (d) shows the simulation results with respect to rotational speed changes under the condition simulating the out-of-mesh jet, and Fig. 5.2-5 (e) shows the simulation results with respect to jet speed changes under the condition simulating the out-of-mesh jet. "A," "B," and "C" depicted in Fig. 5.2-5 correspond to "Condition A," "Condition B," and "Condition C" of Fig. 5.2-4 , respectively.

(Displayed with over 50 % oil in calculation cells)
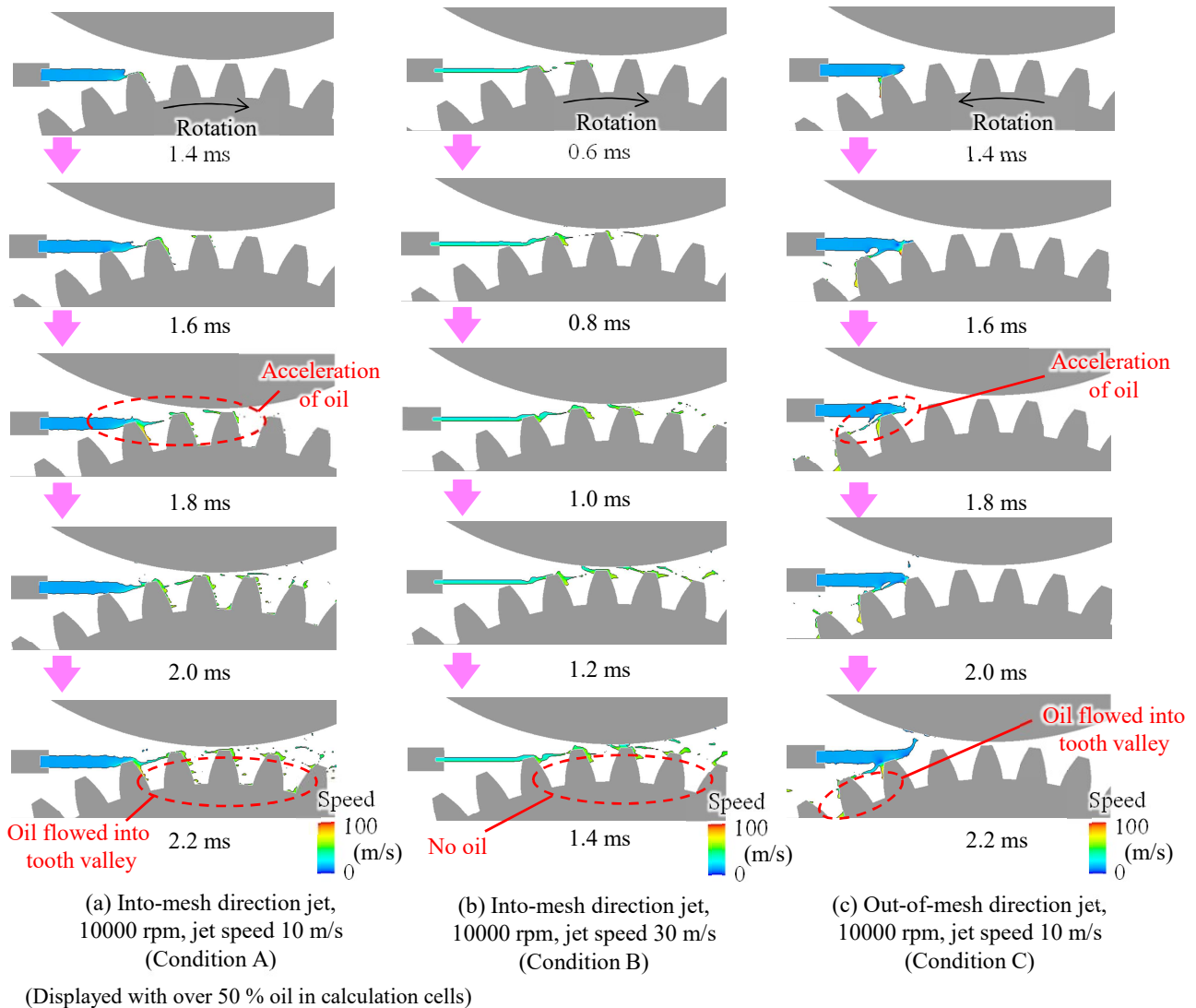
Fig. 5.2-4 Comparison of oil flow during oil jet acceleration (simulation results)

In "A" of Fig. 5.2-5 (a), the numerical simulation results exceeded the theoretical calculation results. This is because the loss caused by the oil flowing into the gear tooth valley, as depicted in Fig. 5.2-4 (a), was added to the loss caused by the oil acceleration.

On the other hand, in "B" of Fig. 5.2-5 (b), the numerical simulation results were lower than the theoretical calculation results. This is because there was no inflow of oil into the gear tooth valley, as shown in Fig. 5.2-4 (b), and the oil was scattered from the tip of the gear tooth, which resulted in insufficient oil acceleration.

In "C" of Fig. 5.2-5 (d), the numerical simulation results exceeded the theoretical calculation results. This is because the loss caused by the oil flowing into the gear tooth valley, as shown in Fig. 5.2-4 (c), was added to the loss caused by the oil acceleration.

From the abovementioned results, it is found that although there are loss differences owing to the oil flow, the oil injected by the oil jet nozzle to the into-mesh or out-of-mesh sides is accelerated by gear meshing, and the loss by the acceleration can be estimated by the theoretical equation.

171

(a) Oil dynamic loss for into-mesh
direction jet with rotational speed changes

(b) Oil dynamic loss for into-mesh
direction jet with oil jet speed changes

(c) Oil dynamic loss for into-mesh
direction jet with oil supply rate changes

(d) Oil dynamic loss for out-of-mesh
direction jet with rotational speed changes

(e) Oil dynamic loss for out-of-mesh
direction jet with oil jet speed changes

Fig. 5.2-5 Comparisons of the theory and the numerical simulation on oil dynamic loss

(3)   Oil Dynamic Loss Phenomena due to Oil Reacceleration at the Gear Meshing Part

The oil acceleration at the gear meshing part of the two-axis helical gearbox (Fig. 5.2-1 (b)) is discussed again. The oil acceleration at the meshing part of the gear is considered as the "acceleration of oil supplied to the meshing part of the gear" as shown in Fig. 5.2-4 and "acceleration of oil when residual oil in the shroud reflows into the gear meshing part". In this part, the "acceleration of oil when residual oil in the shroud reflows into the gear meshing part" of the latter is considered.

When the oil is accelerated by gear rotation, the momentum of the oil is considered to increase, as shown in the theory of oil dynamic loss (Section 2.3). Therefore, we compared the momenta before and after the acceleration at the meshing part of the gear. The results are shown in Fig. 5.2-6 .

Figure 5.2-6 (a) shows the momentum flowing into the meshing part of the gear. from the input gear side. This momentum was obtained from the oil density × volumetric flow rate of the oil passing through the sampling section ("A" in the figure) × cross-sectional averaged flow speed. Figure 5.2-6 (b) shows the momentum flowing into the meshing part of the gear from the output gear side (this was obtained from "B" depicted in the figure as the sampling section). Figure 5.2-6 (c) shows the comparison between the total momentum flowing into the meshing part of the gear (the sum of (a) and (b) in the figure) and the momentum at the meshing part of the gear (the momentum is calculated by subtracting the momentum due to oil-jet acceleration from the momentum obtained from "C" depicted as the sampling section in the

figure).

Fig. 5.2-6 (c) shows the increase in the momentum between after meshing ("Section C" in the figure) and before meshing ("Section A+B" in the figure). This increase in momentum is considered to cause an increase in power loss. Therefore, when residual oil in the shroud flows into the meshing part of the gear, the power loss due to re-acceleration of oil is considered to occur.

* Fluid density × volumetric oil flow rate × average speed
** Fluid density × (volumetric oil flow rate – volumetric oil-supply rate to into-mesh) × average speed
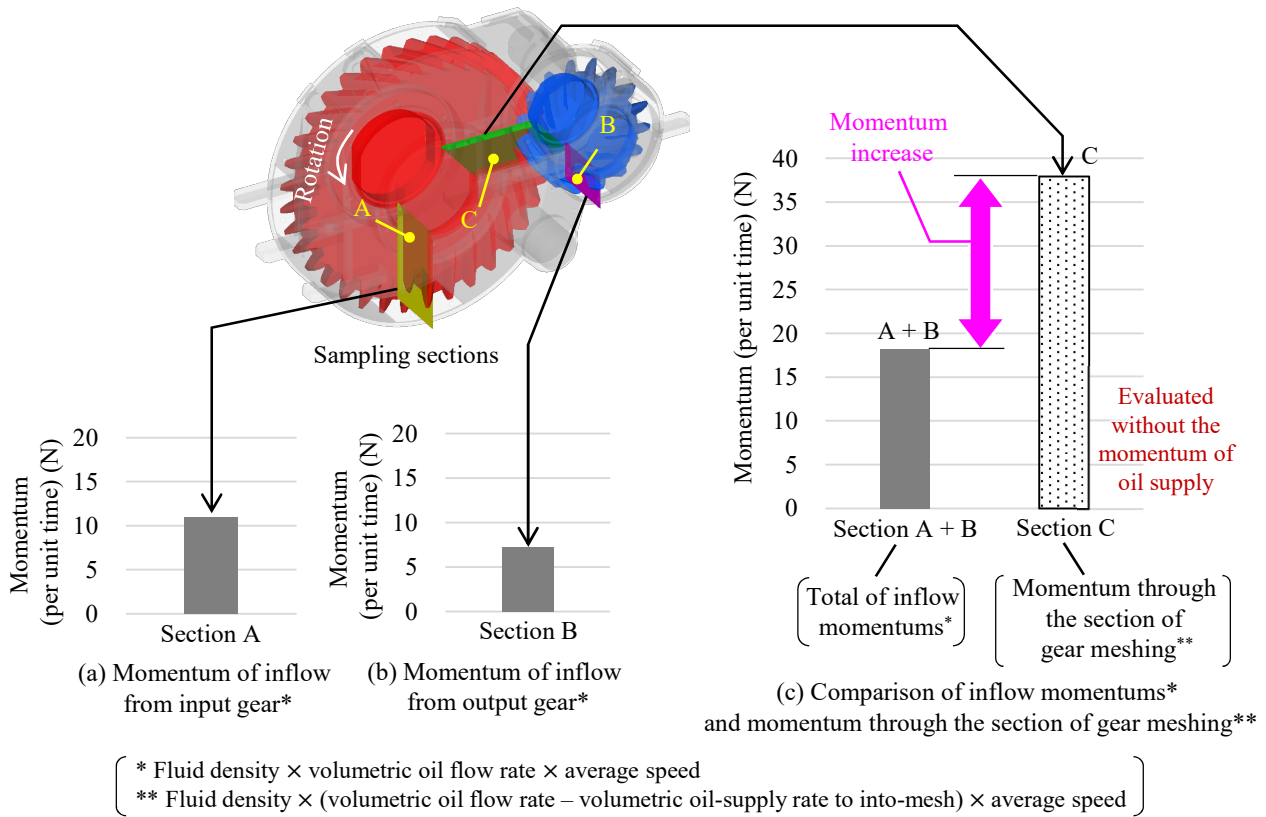
Fig. 5.2-6 Comparison of inflow momentums and momentum through the gear mesh (simulation results, Shroud 2, 10000 rpm)

(4) Oil Churning Phenomenon in the Peripheral Part of the Gear

Figure 5.2-7 shows the oil churning phenomenon. The oil distribution and streamlines flowing from the gear side to the gear tooth are depicted on the left side of Fig. 5.2-7 (a), and the oil contour on the gear surface is shown on the right side of Fig. 5.2-7 (a). The oil distribution and streamlines that flow from the gear tooth are shown on the left side of Fig. 5.2-7 (b), and the oil contour on the gear surface is shown on the right side of Fig. 5.2-7 (b). Figure 5.2-7 (c) shows the total oil volume on the gear surface with respect to the changes in the oil supply rate.

As shown in Fig. 5.2-7 (a), according to the oil flowing along the airflow from the side of the gear ("Inflow of side oil to gear tooth" in the figure), oil adheres to the gear surface and the amount of oil increases ("Adhesion of oil" in the figure). As shown in Fig. 5.2-7 (b), the oil flows from the gear tooth as the airflow spins ("Blowing up peripheral oil" in the figure), causing the oil to separate from the gear surface and reducing the amount of oil ("Separation of oil" in the figure). From the above results, it was determined that oil flows by airflow, causing oil adhesion on the gear surface or oil separating from the gear surface. From Fig. 5.2-7 (c), it can be observed that the amount of oil on the gear surface increases as the oil

supply flow rate increases, and that the slope of the increase becomes mild at a large flow rate ("Mild slope on large flow rate" in the figure). It is presumed that this is because the centrifugal force increases with the amount of oil on the gear surface, making it easier for the oil to separate from the gear.
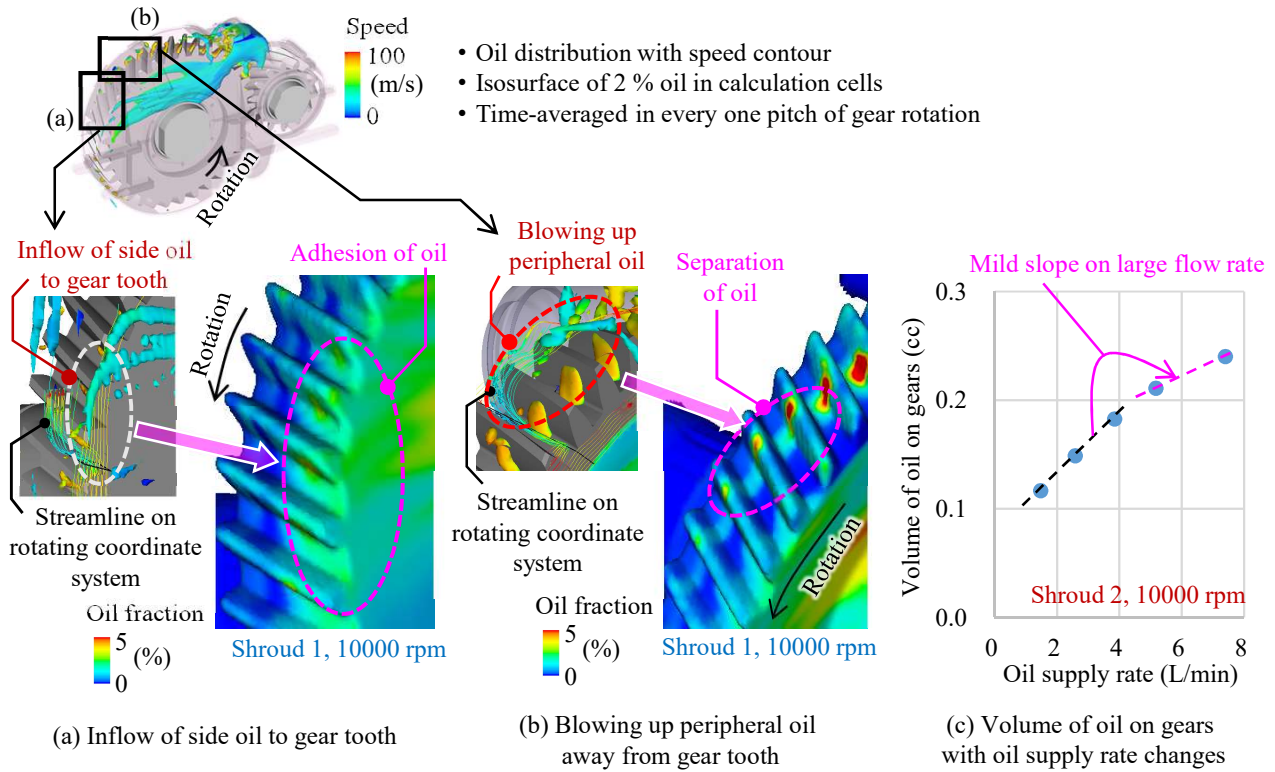
Fig. 5.2-7 Characteristics of oil churning phenomenon (simulation results)

5.2.2   Consideration of the Gear Peripheral Distribution of Oil Drag Torque

The relationship between the gear torque and pressure field was considered. Because most of the gear torque is caused by pressure (Fig. 5.1-4), it is possible to consider the causes of torque generation by understanding the pressure field.

The torque distribution, pressure distribution, and velocity vector due to the oil around the gears are depicted in Fig. 5.2-8 . Figure depicted on the left side of Fig. 5.2-8 (a) shows the pressure distribution of the two-phase flow of air and oil, and the one on the right side shows the pressure distribution of air. Both figures were obtained by averaging the time intervals of each gear pitch. The pressure distribution of the oil was obtained by subtracting the pressure distribution of the air depicted on the right side of Fig. 5.2-8 (a) from the pressure distribution of the two-phase flow of the air and the oil depicted on the left side of Fig. 5.2-8 (a). The pressure distribution of oil is shown in Fig. 5.2-8 (b). To make the deviation of the oil easier to distinguish, the contour was displayed when the oil fraction in the calculation cell was 0.5% or more. For the gear meshing part, the center section of the tooth width was used, as shown in the upper right of Fig. 5.2-8 . This is because the center section of the tooth width can detect the acceleration phenomena of the supplied oil because the oil supply jet is injected toward the center of the gear width. In the other section, a section on the helical leading side of the gear was used. This is because the helical leading side is not easily affected by the secondary flow owing to the vortex

174

between the gear teeth, and it is easy to clarify the characteristics of the phenomena. Figure 5.2-8 (c) shows the peripheral distribution of torque around the input gear. Figure 5.2-8 (d) shows the superposition of the pressure distribution in Fig. 5.2-8 (b) and the torque distribution in Fig. 5.2-8 (c). Figure 5.2-8 (d) was used to discuss the phenomena.

The relationship between the pressure and torque at the gear meshing part is indicated by "A" in Fig. 5.2-8 (d). "Pressure increase" in the figure is observed in the oil before and after the gear meshing. Pressure increase is due to the pumping work of the gear, and it is considered that torque by the pumping work increased ("High torque" in the figure) there.

(a) Pressure distributions around input gear

(b) Oil pressure distribution*

(c) Torque distribution of oil**
(derived by subtracting "air torque" from "air and oil torques")

* Displayed over 0.5% oil in calculation cells, time-averaged in every one pitch of gear rotation
** Time-averaged

(d) Oil pressure distribution* and torque distribution** around input gear
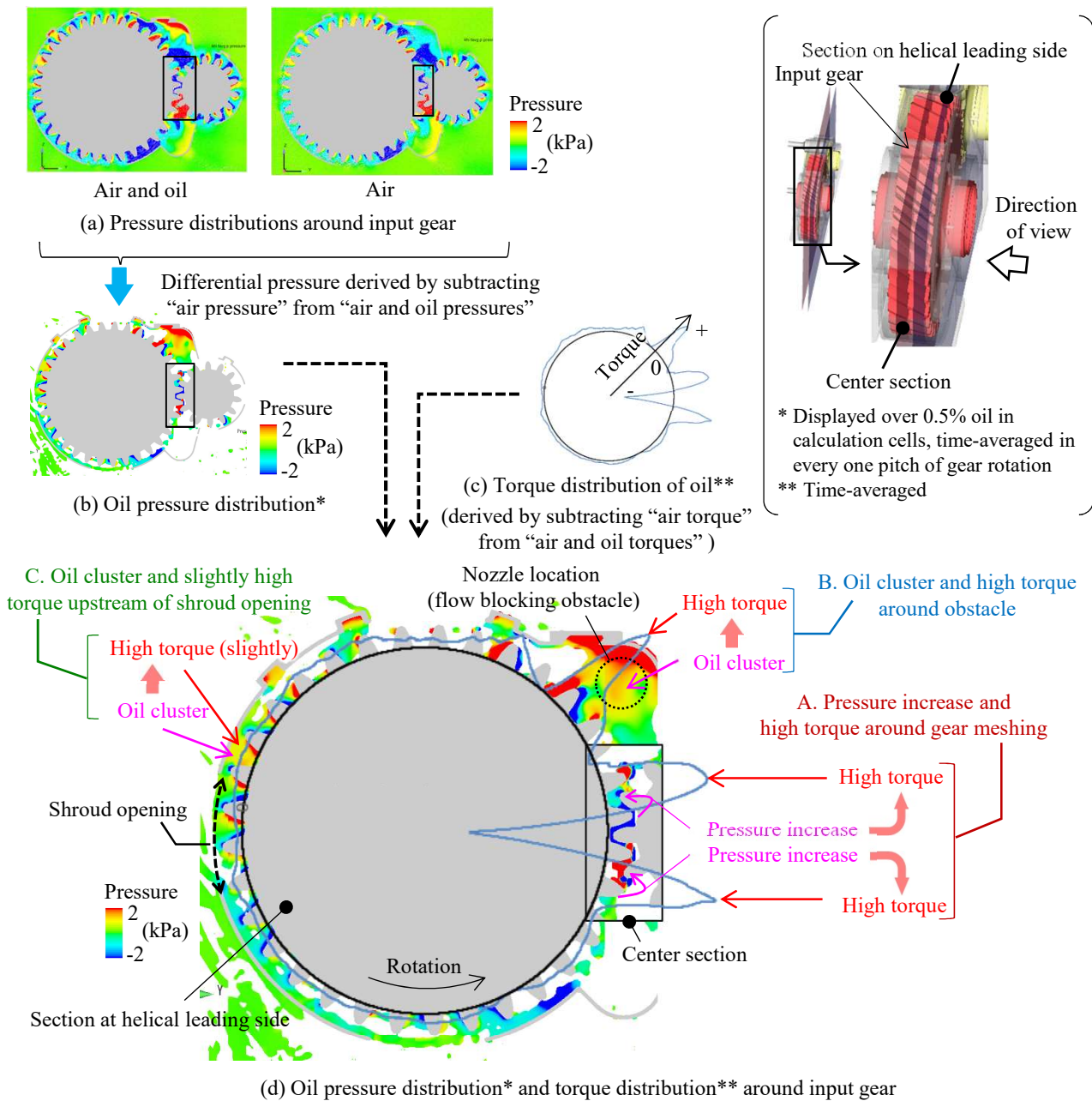
Fig. 5.2-8 Understanding of the oil flow phenomenon by torque and pressure distributions (simulation results, Shroud 1, input 10000 rpm)

In the phenomena near the oil jet nozzle indicated by "B" in Fig. 5.2-8 (d), there is an oil cluster near the oil jet nozzle, where the torque increases ("High torque" in the figure). This oil cluster is considered to be caused by the drag of the oil jet nozzle and shroud wall when the oil passes through the clearance between the tip of the oil jet nozzle and shroud wall (shown in Fig. 5.2-2).

On the upstream side of the opening of the shroud, which is indicated by "C" in Fig. 5.2-8 (d), oil accumulation ("oil cluster" in the figure) and torque increase ("High torque" in the figure) can be seen. In the vicinity of the shroud opening, the relative velocity of the airflow around the gear is large, and the airflow decelerates, as shown in Fig. 5.1-7 . In the peripheral part of the gear, the oil flows along the airflow, as shown in Fig. 5.2-1 (d) and (e). Therefore, it is probable that the oil accumulation upstream of the opening of the shroud in "C" of Fig. 5.2-8 (d) is due to the deceleration of the airflow near the opening of the shroud. The increase in the torque is highly attributed to stagnation of the oil.

5.2.3 Effect of Shroud on Oil Dynamic Loss

Because of the effects of shroud on aerodynamic loss, as described in Section 5.1.3, by covering the gear with a shroud, the fluid around the gear and fluid outside the shroud are isolated, and therefore aerodynamic loss is reduced. In this section, the effect of the shroud on the oil dynamic loss is estimated by comparing Shroud 1 and Shroud 2.

(1) Increase in the Amount of Oil Around the Gear

A comparison of the oil distribution in the shroud between Shroud 1 and Shroud 2 is shown in Fig. 5.2-9 . Figure 5.2-9 (a) shows the oil distribution in Shroud 1 (each gear has three peripheral openings) and Fig. 5.2-9 (b) shows the oil distribution in Shroud 2 (each gear has one peripheral opening). Comparing (a) and (b) in Fig. 5.2-9 , it can be seen that Shroud 2 has more oil than Shroud 1.

(a) Oil distribution around input gear*, Shroud 1   (b) Oil distribution around input gear*, Shroud 2
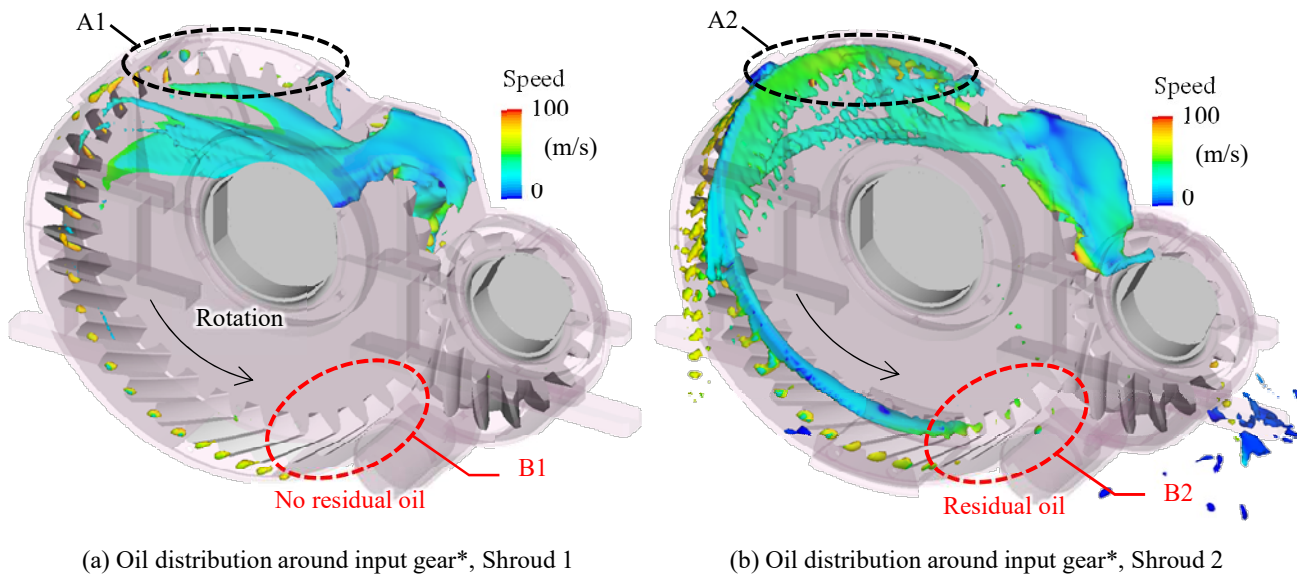
* Isosurface of 2 % oil in calculation cells, time-averaged in every one pitch of gear rotaion, input 10000 rpm

Fig. 5.2-9 Comparison of residual oil in shroud (simulation results)

"A1" (an opening of Shroud 1) in Fig. 5.2-9 (a) is compared with "A2" (no opening of Shroud 2 at the position) in Fig. 5.2-9 (b). In "A2" in Fig. 5.2-9 (b), it can be seen that no oil is discharged because there is no shroud opening, and therefore oil remains inside the shroud. "B1" near the into-mesh in Fig. 5.2-9 (a) is compared with "B2" in the same position in Fig. 5.2-9 (b). Residual oil is found in "B2" of Fig. 5.2-9 (b). This residual oil flowed into the gear-meshing part.

From the above, it was found that when the number of shroud openings was small (the total opening area was small), the amount of oil remaining inside the shroud increased, and the amount of oil flowing into the gear mesh part increased.

(2)   Increase in the Oil Churning of the Gear

The influence of the difference in the shroud opening on the gear torque is depicted in Fig. 5.2-10 . The figure on the left side of Fig. 5.2-10 (a) shows the pressure distribution of the two-phase flow of air and oil in Shroud 2 and the one on the right side shows the pressure distribution of air. The pressure distribution of oil obtained by subtracting the pressure distribution of air from that of the two-phase flow of air and oil is depicted in Fig. 5.2-10 (b). To make the deviation of the oil easier to distinguish, the contour was displayed when the oil fraction in the calculation cell was 0.5% or more. For the meshing part of the gear, the center section of the tooth width was used, as depicted in the upper right of the figure. In the other section, a section on the helical leading side of the gear was used. The peripheral distribution of the torque around the input gear in Shroud 2 is depicted in Fig. 5.2-10 (c).

Figure 5.2-10 (d) shows the superposition of the pressure distribution of oil around the input gear and the peripheral distribution of torque in Shroud 1 (same as Fig. 5.2-8 (d)). Figure 5.2-10 (e) shows the superposition of the pressure distribution in Fig. 5.2-10 (b) and the torque distribution in Fig. 5.2-10 (c) for Shroud 2. For comparison, the peripheral distribution of torque in Shroud 1 is also shown in the figure. Focusing on the difference in torque between Shroud 1 and Shroud 2 in the vicinity of the gear meshing part, as indicated by "A" in Fig. 5.2-10 (e). The torque of Shroud 2 was higher than that of Shroud 1. This is considered to be due to the fact that the number of shroud openings in Shroud 2 is small, which causes oil to reflow into the gear meshing part ("B2" in Fig. 5.2-9), and the oil is accelerated by the gear meshing part.

Focusing on the difference between the torques of Shroud 1 and Shroud 2 at the peripheral part of the gear, as shown in "B" of Fig. 5.2-10 (e). The torque of Shroud 2 was larger than that of Shroud 1. This is considered to be due to the increase in the amount of oil around the gear owing to the smaller number of shroud openings in Shroud 2 ("A2" in Fig. 5.2-9).

From the above results, it was found that when the number of shroud openings was small (the total opening area was small), oil reflowed into the meshing part of the gear and increased the torque there, and the amount of oil increased around the peripheral part of the gear, which increased the torque there.

(3)   Increase in Oil Dynamic Loss

The effect of the difference in the shroud opening on the dynamic loss of oil is shown in Fig. 5.2-11 .

Figure 5.2-11 shows that the oil dynamic loss in Shroud 2 was larger than that in Shroud 1. This is because, from Fig. 5.2-9 and Fig. 5.2-10 , when the number of shroud openings is small (the total opening area is small), the loss increases owing to the inflow of oil into the gear meshing part and the acceleration of the oil. In addition, the loss increases owing to the increase in the amount of oil in the peripheral part

of the gear and the acceleration of the oil.

From the above, it can be considered that the oil dynamic loss increases as the number of openings of the shroud decreases (the total opening area is smaller). However, the aerodynamic loss decreased as the number of openings of the shroud decreased (Section 5.3). This is the opposite tendency of the oil dynamic loss. Therefore, it is considered that there is an optimal shroud shape that reduces the aerodynamic loss while suppressing the increase in the oil dynamic loss.

(a) Pressure distributions around input gear (Shroud 2)

Deferential pressure derived by subtracting "air pressure" from "air and oil pressures"

(b) Oil pressure distribution* (Shroud 2)

(c) Torque distribution of oil**
(Shroud 2, derived by subtracting "air torque" from "air and oil torques")

* Displayed over 0.5% oil in calculation cells, time-averaged in every one pitch of gear rotation
** Time-averaged

(d) Oil pressure distribution* and torque distribution** around input gear (Shroud 1)

(e) Oil pressure distribution around input gear* (Shroud 2), torque around input gear** (Shroud 1, Shroud 2)

Fig. 5.2-10 Understanding of the shroud effect by the difference of torque and pressure distributions between Shroud 1 and Shroud 2 (simulation results, input 10000 rpm)
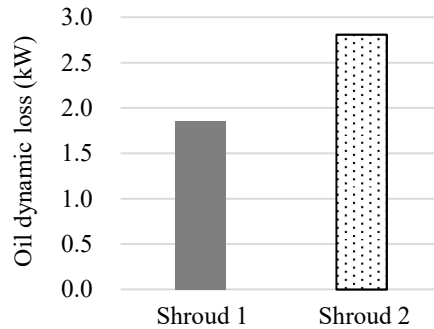
Fig. 5.2-11 Oil dynamic loss increase in Shroud 2 compared to that in Shroud 1 (simulation results, input 10000 rpm)

5.2.4 Characteristics of Oil Dynamic Loss with respect to Rotational Speed Changes, Oil Supply Flow Rate Changes, and the Dimensionless Evaluation

(1) Characteristics of Oil Dynamic Loss with respect to Rotational Speed Changes

In the oil dynamic loss phenomenon, as described in the theory of oil dynamic loss (Section 2.3), both "a phenomenon in which the oil flow rate accelerated by the gear rotation is constant and the oil dynamic loss is proportional to the square of the rotational speed" and "a phenomenon in which the oil flow rate accelerated by the gear rotation is proportional to the rotational speed and the oil dynamic loss is proportional to the third power of the rotational speed" exist. In both cases, the rotational speed exponent of the oil dynamic loss was obtained by adding two to the rotational speed exponent of the oil flow rate. Therefore, if the actual phenomena follow the theory, the rotational speed exponent of the oil flow rate at which the gear accelerates is from zero to one, and adding two to the rotational speed exponent of the oil flow rate yields the rotational speed exponent of the oil dynamic loss. For example, if the rotational speed exponent of the oil flow rate is 0.6, then that of the oil dynamic loss should be 2.6.

The characteristics of the oil dynamic loss with respect to rotational speed and oil supply flow rate changes are shown in Fig. 5.2-12 .

(a) Sampling sections for oil flow rate

(b) Oil flow rate with rotational speed changes

(c) Oil dynamic loss with rotational speed changes
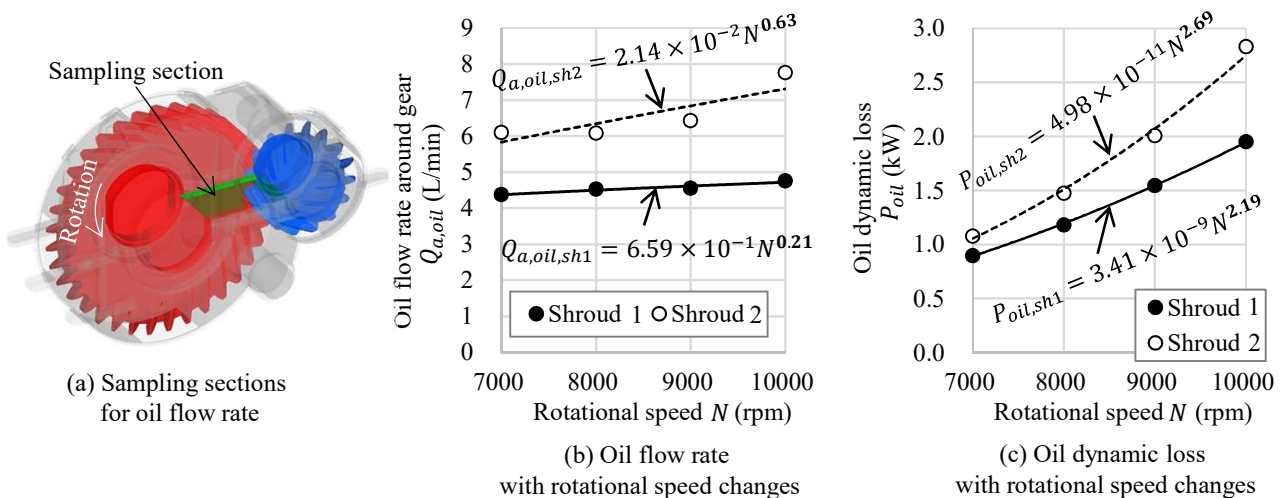
Fig. 5.2-12 Characteristics of oil flow rate and oil dynamic loss (simulation results, Shroud 2)

Figure 5.2-12 (a) shows a sampling section of the oil flow rate around the gear. The oil flow rate in this section represents the characteristics of the oil flow rate around the gear because it is a section in which the

supplied oil and residual oil in the shroud flow. Figure 5.2-12 (b) shows the oil flow rate with respect to rotational speed changes, and Fig. 5.2-12 (c) shows the oil dynamic loss with respect to rotational speed changes.

For Shroud 1, the rotational speed exponent of the oil flow rate is 0.21, as depicted in Fig. 5.2-12 (b), and falls in the range of 0–1, as predicted by the theory. The value 2.21 obtained by adding two to this exponent becomes approximately equal to the rotational speed exponent 2.19 of the oil dynamic loss of Shroud 1 shown in Fig. 5.2-12 (c). For Shroud 2, the rotational speed exponent of the oil flow rate is 0.63, as shown in Fig. 5.2-12 (b), and falls in the range of 0–1, as predicted by the theory. The value 2.63 obtained by adding two to this exponent becomes approximately equal to the rotational speed exponent 2.69 of the oil dynamic loss of Shroud 2 shown in Fig. 5.2-12 (c).

From the above, the validity of the theory was confirmed for the oil flow rate around the gear and the oil dynamic loss caused by gear rotation.

(2)　Characteristics of Oil Dynamic Loss with respect to Oil Supply Rate Changes

The oil dynamic loss with changes in the oil supply rate is shown in Fig. 5.2-13 . The amount of oil on the gear surface (Fig. 5.2-7 (c)) is also shown in the figure. From Fig. 5.2-13 , it can be seen that the oil dynamic loss increases as the oil supply rate increases and that the increase in loss becomes mild at a large oil supply rate. This trend is similar to that of the amount of oil on the gear surface shown in Fig. 5.2-13 . This is because the amount of oil on the gear surface is related to the ambient fluid density around the gear, which affects the oil dynamic loss.
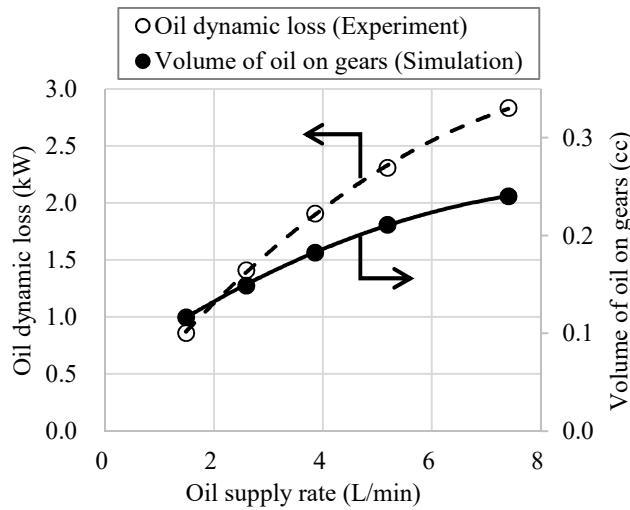
Fig. 5.2-13 Analogy between experimental oil dynamic loss and the simulated volume of oil on gears regarding oil supply rate (Shroud 2, Input 10000 rpm)

(3)　Dimensionless Evaluation of Oil Dynamic Loss

To make the oil dynamic loss dimensionless, we consider the major phenomena and representative parameters. The dynamic loss of oil in the gear meshing part is the sum of the acceleration loss of the supplied oil (oil-jet acceleration loss) and loss due to the acceleration of the residual oil in the shroud that reflows into the gear meshing part (oil reacceleration loss). The oil-jet acceleration loss is calculated by $\rho_{oil} Q_s v_p{}^2 \cos\beta$ from the theory of oil dynamic loss (Section 2.3) (where ρ_{oil} is the oil density, Q_s is the oil supply flow

rate, v_p is the pitch circle speed, and β is the helix angle). The oil reacceleration loss is considered to be a function of the oil-jet acceleration loss as this loss is related to the amount of oil remaining in the shroud, which is related to the oil supply flow rate.

Regarding the effect of the shroud, the smaller the shroud coefficient, the lesser the leakage of airflow from the shroud, and smaller the oil discharge accompanying the airflow. In addition, when the opening of the shroud is small, it is presumed that oil quickly accumulates inside it. Therefore, the smaller the shroud coefficient, the larger the oil reacceleration loss. Assuming that the oil dynamic loss, including the oil-jet acceleration loss and oil reacceleration loss, is a function of the oil-jet acceleration loss and inversely proportional to the shroud coefficient (considering the accelerated accumulation of oil when the shroud opening is small), the dimensionless number $\tilde{P}_{oil}$ of the oil dynamic loss is defined by the following equation:

$$\tilde{P}_{oil} = \frac{P_{oil}}{\rho_{oil} Q_s v_p{}^2 \cos\beta / \lambda} \tag{5.5}$$

$\tilde{P}_{oil}$ is herein called the "oil supply acceleration ratio."

Thereafter, we considered a dimensionless number related to the oil supply acceleration ratio, $\tilde{P}_{oil}$. Because the oil dynamic loss is related to the oil supply flow rate, we considered the dimensionless number for the oil supply flow rate. The dimensionless oil supply flow rate $\tilde{Q}_s$ is expressed as the ratio of the oil supply flow rate to the oil churning flow rate of the gear, using the following equation:

$$\tilde{Q}_s = \frac{Q_s}{v_p B M_g} \tag{5.6}$$

The denominator in the above equation is proportional to the peripheral speed of the gear $v_p \times$ gear tooth area ($\propto BM_g$, where B is the tooth width, and M_g is the gear module), which is considered to be proportional to the oil churning flow rate of the gear.

The evaluation was performed using the above oil supply acceleration ratio (non-dimensional oil dynamic loss) and non-dimensional oil supply flow rate. The results of the above-mentioned non-dimensionalization using the experimental results in the two-axis helical gearbox in this study are shown in Fig. 5.2-14 .
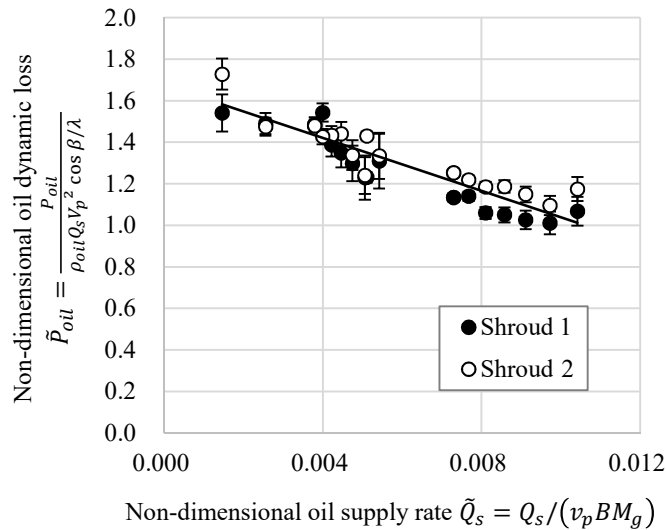
Fig. 5.2-14 Non-dimensional characteristics of the oil dynamic loss (experimental results including calculated shroud coefficient)

For the shroud coefficient, we used the values obtained from the empirical equations in Section 6.2 (to be described later). In Fig. 5.2-14 , the results for Shroud 1 and Shroud 2 exhibit a constant tendency. The approximate curve obtained from the points in the figure is given by the following equation:

$$\tilde{P}_{oil} = -63.59\,\tilde{Q}_s + 1.674 \tag{5.7}$$

In both Shroud 1 and Shroud 2, the lower the oil supply flow rate, the larger the oil supply acceleration ratio (non-dimensional oil dynamic loss); this is likely because, the smaller the oil supply flow rate, the smaller the fraction of oil in the two-phase flow of air and oil, and easier it is for the oil to flow according to the airflow (easier to accelerate).

The above results reveal that the characteristics of the oil dynamic loss can be clarified by the dimensionless oil dynamic loss (oil supply acceleration ratio) and dimensionless oil supply flow rate. By using the approximate curve (Eq. 5.7), the oil dynamic loss can be easily estimated from the gear dimensions, shroud dimensions, operating conditions, and oil supply conditions (see Appendix A.5).

5.2.5   Summary of the Clarification of Oil Dynamic Loss

1. The oil flow pattern included the acceleration of oil at the gear meshing part, division of oil flow in the out-of-mesh side, blow up of oil adhering to the gear tooth surface, inflow of oil on the gear side to the gear tooth surface, outflow of oil from the shroud opening, and residual oil in the shroud.

2. The oil injected by the oil jet nozzle to the into-mesh side or the out-of-mesh side is accelerated in the gear meshing part, and the power loss due to the acceleration can be estimated using the theoretical equation.

3. When the residual oil in the shroud reflows into the gear meshing part, power loss due to oil acceleration occurs.

4. There is an increase in the pressure at the into-mesh and out-of-mesh sides, where torque increases. When passing near an obstacle, such as an oil jet nozzle, oil stagnates and torque increases. The airflow decelerates near the opening of the shroud, and the oil stagnates upstream of the opening, thereby increasing the torque.

5. When the number of openings of the shroud (the small total opening area) is less, it causes oil to flow into the gear meshing part, and the torque and the oil dynamic loss increase at the part, which causes a large amount of oil around the gear peripheral part and the torque and the oil dynamic loss increase at the part. However, the aerodynamic loss, contrary to the oil dynamic loss, decreases with decrease in the number of shroud openings (the total opening area). Therefore, it is considered that there is an optimal shape for the shroud that reduces the aerodynamic loss while suppressing the increase in oil dynamic loss.
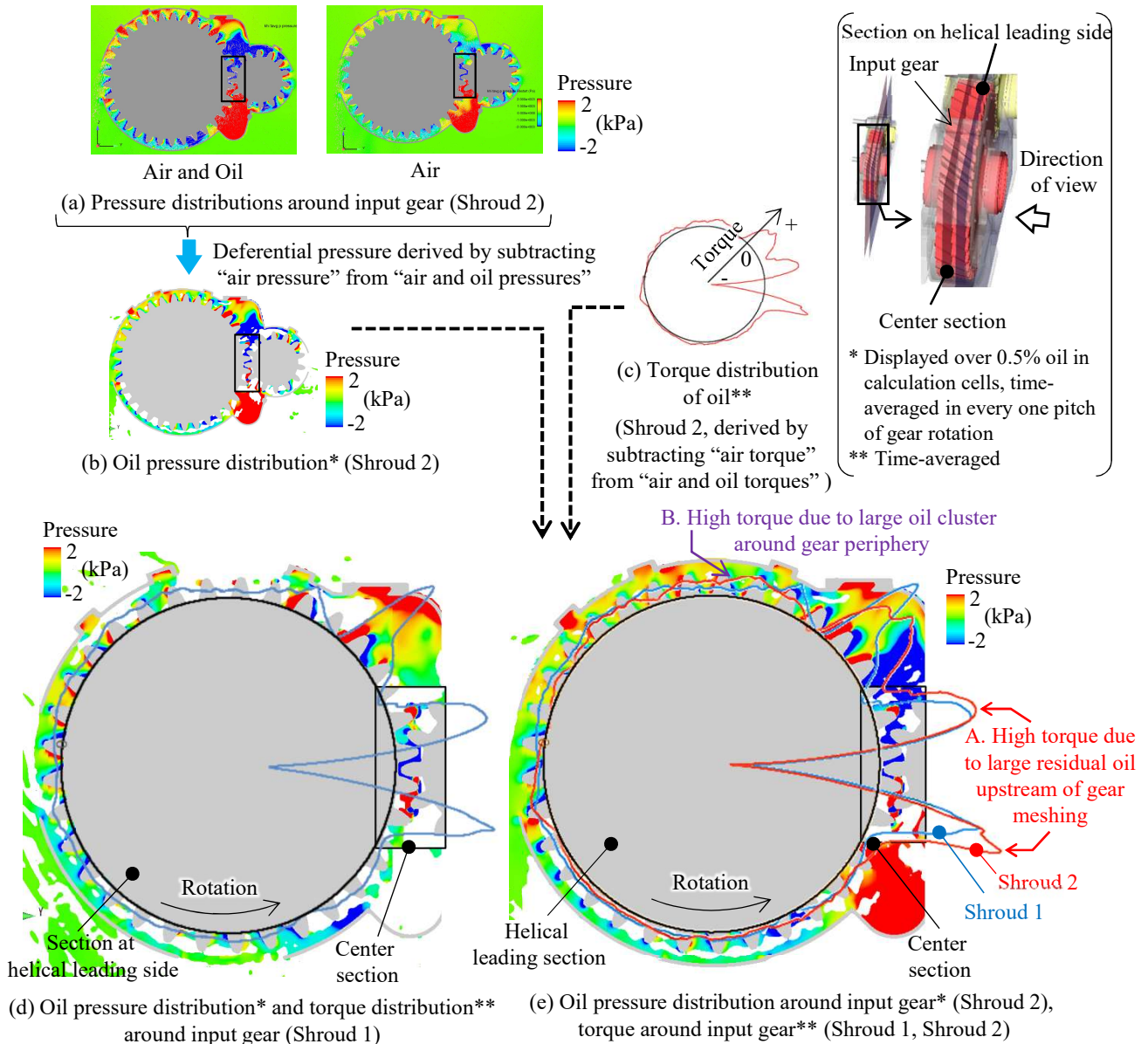
6. In the theory of oil dynamic loss, the rotational speed exponent of the oil flow rate at which the gear acceleration ranges from 0–1, the rotational speed exponent of the oil fluid dynamic loss ranges from 2–3, and the rotational speed exponent of the oil dynamic loss is obtained by adding two to the rotational speed exponent of the oil flow rate. The numerical simulation results showed that the exponents from the theory were valid.

7. The tendency of the amount of oil on the gear surface with respect to the oil supply flow rate changes is similar to that of the oil dynamic loss with respect to the oil supply flow rate changes. The rate of change at a high oil supply flow rate was smaller than that at a low oil supply flow rate.

8. Non-dimensionalization using the oil supply acceleration ratio (the oil dynamic loss divided by "the theoretical equation of the oil-jet acceleration loss / shroud coefficient") and the dimensionless oil supply flow rate (oil supply flow rate divided by "oil churning flow rate by gear tooth") makes it possible to understand

the characteristics of the oil dynamic loss.

5.3 Classification of Fluid Dynamic Loss

5.3.1 Classification of Aerodynamic Loss

The classification results of aerodynamic loss based on the knowledge obtained in the clarification of the aerodynamic loss phenomena (Section 5.1) are depicted in Fig. 5.3-1 .

The loss caused at the gear meshing part is divided into the "air side-flow loss" shown in Fig. 5.3-1 (a) and the "air pumping loss" shown in Fig. 5.3-1 (b). The loss generated around the peripheral part of the gear is defined as the "air vortex loss, " as shown in Fig. 5.3-1 (c).

At the gear meshing part, as shown in Fig. 5.3-1 (a), air is pushed out at the into-mesh side, and after passing through the sides of the gear mesh, air is sucked in at the out-of-mesh side. Because of the flow pattern of this flow passing through the sides of the gear mesh, the airflow is referred to as the "air side-flow loss".

As another flow at the gear meshing part, flow passing through the tip clearance and backlash, as shown in Fig. 5.3-1 (b), occurs. From the analogy of the oil-jet acceleration loss, it is assumed that the air is accelerated in the tip clearance and backlash, and the loss due to this acceleration is referred to as the "air pumping loss," which is different from the air side-flow loss that passes through the sides of the gear mesh.

In the peripheral part of the gear, air vortices are generated in the gear tooth valleys, as depicted in Fig. 5.3-1 (c). The loss owing to these vortices is referred to as "air vortex loss".
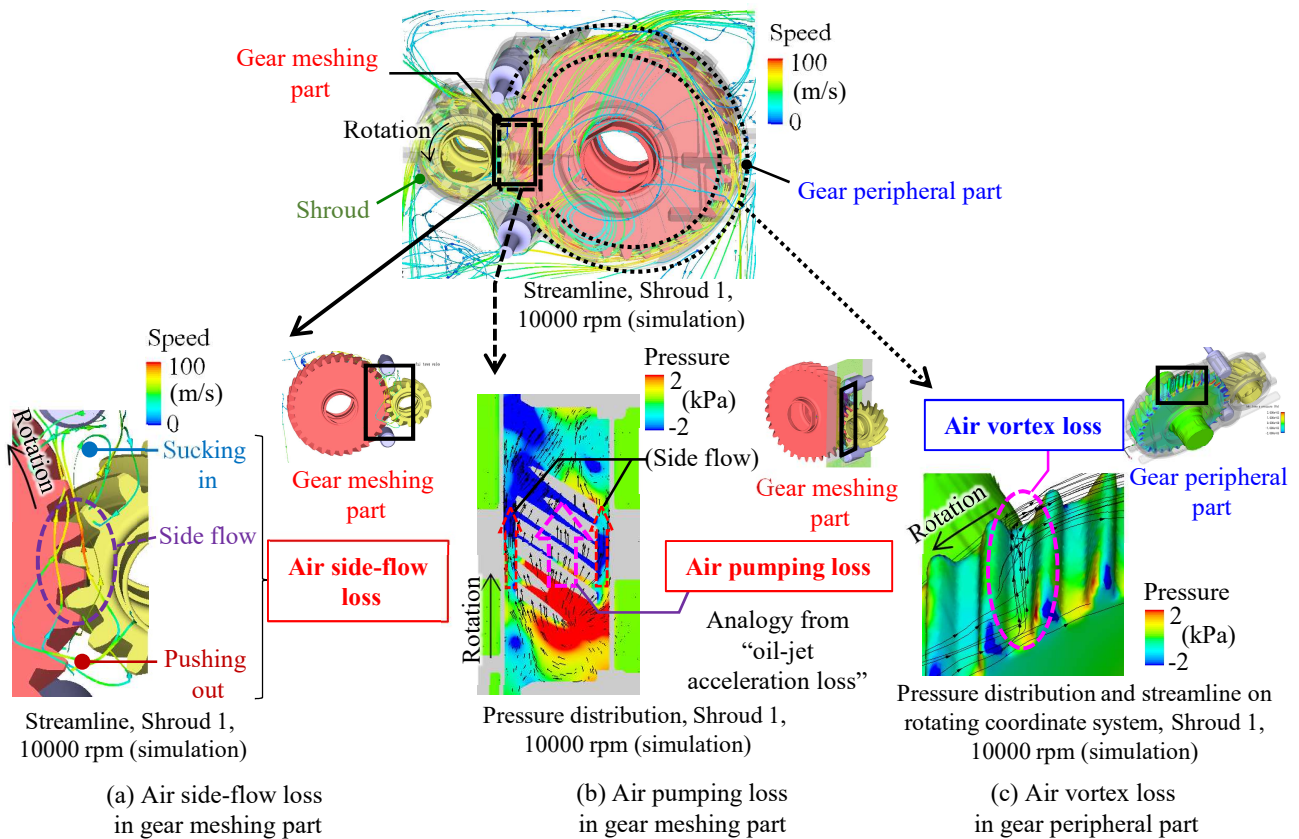
Fig. 5.3-1 Classification of aerodynamic loss

5.3.2   Classification of Oil Dynamic Loss

The classification results of the oil dynamic loss based on the knowledge obtained from the clarification of the phenomena of oil dynamic loss (Section 5.2) are shown in Fig. 5.3-2 .

The loss caused at the meshing part of the gear is divided into the "oil-jet acceleration loss" shown in Fig. 5.3-2 (a) and the "oil reacceleration loss" as shown in Fig. 5.3-2 (b). The loss generated around the peripheral part of the gear is defined as the "oil churning loss, " as shown in Fig. 5.3-2 (c).

In the gear meshing part, the oil is accelerated, as shown in the lower-left side of Fig. 5.3-2 . This oil consists of the oil supplied to the gear meshing part by the oil jet nozzle, and the oil reflows into the meshing part. Therefore, the loss generated when the supplied oil is accelerated through the gear meshing part is referred to the "oil-jet acceleration loss" (Fig. 5.3-2 (a)) and the loss generated when the oil re-flows into the gear meshing part and is accelerated is referred to the "oil reacceleration loss" (Fig. 5.3-2 (b)).

In the peripheral part of the gear, as shown in Fig. 5.3-2 (c), oil is entrained in the air vortex generated in the gear tooth valley. The loss caused by the oil entrainment of the air vortex is referred to "oil churning loss".
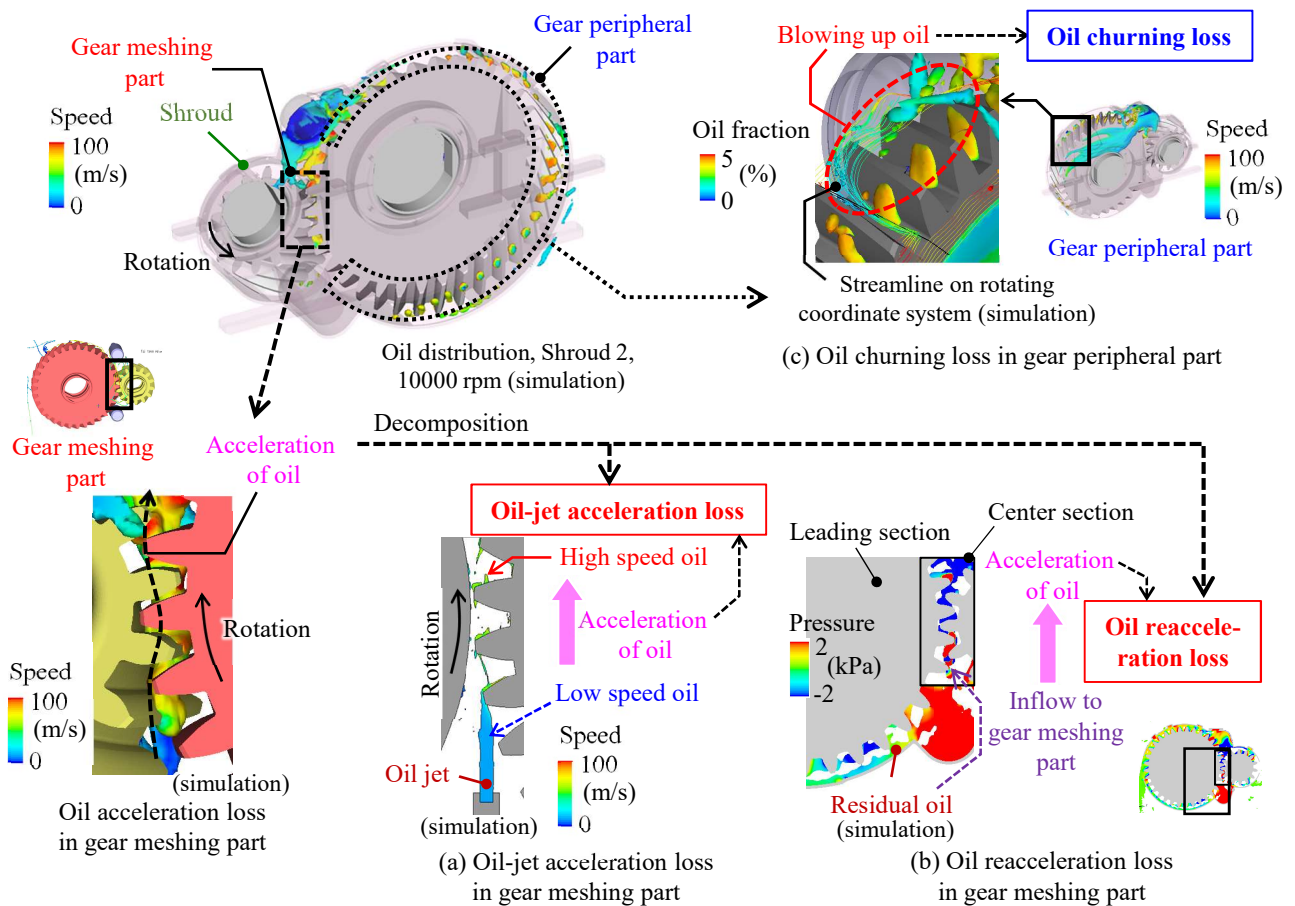
Fig. 5.3-2 Classification of oil dynamic loss

5.4   Summary of Chapter 5

In this chapter, based on the numerical simulation results, we clarify and classify the phenomena of fluid dynamic loss. The results are summarized as follows.

5.4.1   Summary of the Clarification of Fluid Dynamic Loss

1. The findings obtained regarding the aerodynamic loss are as follows:
   (a) Air is sucked from around the gear shaft and discharged in the peripheral direction of the gear, and the pumping efficiency owing to the gear rotation is low.
   (b) Torque is generated in the meshing part of the gear by the action of pushing out and sucking in of air, whereas it is generated in the peripheral part of the gear by the air vortex generated in the gear tooth valley.
   (c) Shrouding the gears reduces the torque by suppressing the flow in the peripheral parts of the gear.
   (d) The rotational speed exponent to which the airflow rate generated by the gear rotation is proportional is one, and the rotational speed exponent to which the aerodynamic loss is proportional is three, which is consistent with theory.
   (e) The characteristics of aerodynamic loss can be clarified by the dimensionless number of aerodynamic losses using the dynamic pressure of the airflow loaded on the gear tooth surface and the gear aspect ratio (dimensionless number).
2. The findings obtained regarding the oil dynamic loss are as follows:
   (a) The oil acceleration phenomena in the gear meshing part, blowing up of oil adhering to the gear tooth surface, inflow of oil into the tooth surface in the peripheral part of the gear, and outflow from the shroud opening and residual oil in the shroud are found to be related to torque.
   (b) The oil acceleration phenomenon in the meshing part of the gear includes the acceleration of the oil supplied to that part and the acceleration of the oil reflowing into the gear meshing part, which increases torque. The loss from the acceleration of the oil supplied to the gear meshing part agrees with the loss obtained from the theoretical equation.
   (c) When oil flows near an obstacle such as an oil jet nozzle, it accumulates, and the oil flowing into the tooth surface increases, further increasing the torque.
   (d) A smaller number of openings in the shroud (small total opening area) causes oil to re-inflow to the gear meshing part and increases the amount of oil around the gear peripheral part, which increases the torque and oil dynamic loss.
   (e) The rotational speed exponent of the oil flow rate churned by the gear rotation and the rotational speed exponent of the oil dynamic loss are consistent with theory.
   (f) The characteristics of the oil dynamic loss can be clarified by the dimensionless number of the oil dynamic loss using the theoretical equation of the oil-jet acceleration loss, shroud coefficient, and dimensionless number of the oil supply flow rate, using the flow rate at which the tooth surface churns.
3. Enclosing the gear in a shroud reduces the aerodynamic loss but increases the oil dynamic loss. Therefore, an optimal shroud shape that reduces aerodynamic loss while suppressing the increase in oil dynamic loss should be considered.

5.4.2   Summary of the Classification of Fluid Dynamic Loss

A summary of the classification of fluid dynamic losses is presented in Table 5.4-1 and described below.

1. The results of the classification of the aerodynamic loss are as follows:
   (a) Torque is generated at the meshing part of the gear through the action of pushing out and sucking in of air; this flow passes through the sides of the gear mesh. Therefore, this flow is termed "air side-flow loss." The air side-flow loss is generated by the pressure rise owing to the pushing out of air at the into-mesh side and pressure drop owing to the sucking in of air at the out-of-mesh side.
   (b) Other losses in the gear meshing part are considered to be losses due to airflow passing through the clearances, such as the tip clearance and backlash. These are termed "air pumping losses" by analogy with the oil-jet acceleration loss.
   (c) Because torque is generated at the peripheral part of the gear by the air vortex generated in the gear tooth valley, the loss owing to this vortex is referred to as the "air vortex loss."
2. The results of the classification of the oil dynamic loss are as follows:
   (a) Among the torques generated by the oil acceleration phenomena in the gear meshing part, the loss in the acceleration of the oil supplied to the gear meshing part is termed as the "oil-jet acceleration loss."
   (b) Among the torques generated by the oil acceleration phenomena in the gear meshing part, the loss of accelerating oil re-flowing into the gear meshing part is termed the "oil reacceleration loss."
   (c) Torque is generated by the blowing up of oil adhering to the gear tooth surface and the inflow of oil into the gear tooth surface around the peripheral part of the gear. The blowing up of oil and inflow of oil are generated via oil churning by air vortices in the tooth valley, and the loss due to this phenomenon is termed as "oil churning loss."

Table 5.4-1 Summary of the classification of fluid dynamic loss

Air /Oil	Gear area		Classification	Cause of power loss
	Meshing	Periphery		
Air	✓		Air side-flow loss	Pressure rise at into-mesh due to pushing air out to gear sides, and pressure drop at out-of-mesh due to sucking air from gear sides
	✓		Air pumping loss	Air pumping through gear tip clearance and backlash
		✓	Air vortex loss	Pressure difference between the front and rear surfaces of teeth due to air vortices in tooth valleys
Oil	✓		Oil-jet acceleration loss	Oil acceleration in gear meshing (supplied oil)
	✓		Oil reacceleration loss	Oil acceleration in gear meshing (re-inflowed oil)
		✓	Oil churning loss	Oil churned by air vortices generated in tooth valleys

Chapter 6

Fluid Dynamic Loss Model

6.1 Overview of the Fluid Dynamic Loss Model

From the classification of the fluid dynamic loss based on the clarification of the phenomena described in the previous chapter, the fluid dynamic loss P_{fluid}, includes the aerodynamic loss P_{air} and the oil dynamic loss P_{oil}.

$$P_{fluid} = P_{air} + P_{oil} \tag{6.1}$$

The aerodynamic loss P_{air} consists of the air side-flow loss P_s, the air pumping loss P_{pump}, and the air vortex loss P_v.

$$P_{air} = P_s + P_{pump} + P_v \tag{6.2}$$

The oil dynamic loss P_{oil} consists of the oil-jet acceleration loss P_{jac}, the oil reacceleration loss P_{rac}, and the oil churning loss P_{ch}.

$$P_{oil} = P_{jac} + P_{rac} + P_{ch} \tag{6.3}$$

6.1.1 Figures and Tables to Overview the Loss Model

The facts and assumptions used in the air side-flow loss model are shown in Fig. 6.1-1 . In Fig. 6.1-1 , the facts and proof of the phenomena shown in the clarification and classification of the phenomena in Chapter 5 are shown. In addition, the assumptions and analogy required to construct the loss model are also shown.

Similarly, Fig. 6.1-2 shows the air pumping loss model, Fig. 6.1-3 shows the air vortex loss model, Fig. 6.1-4 shows the oil-jet acceleration loss model, Fig. 6.1-5 shows the oil reacceleration loss model, and Fig. 6.1-6 shows the oil churning loss model.

An outline of the aerodynamic loss model is shown in Table 6.1-1 , an outline of the oil dynamic loss model is shown in Table 6.1-2 , and an outline of the modeling of the shroud effects is shown in Table 6.1-3 .

In Tables 6.1-1 and 6.1-2 , which outline the fluid dynamic loss model of air or oil, from the left column, "Classification," (classified loss elements) "Location," (location that loss occurs) "Concept of power loss," "Mass flow rate due to gear rotation," "Force on gear," "Torque (moment) due to gear rotation," and "Fluid dynamic loss" are shown. The product of the pressure loaded on the gear tooth surface and the area on which the pressure is applied becomes the force loaded on the gear, which is divided by the peripheral speed of the gear, and the mass flow rate at which the gear rotates can be obtained. The rotational torque of the gear is the product of the force loaded on the gear and rotational radius. The fluid dynamic loss is the product of the torque and angular

velocity, or the product of the force loaded on the gear and the peripheral speed of the gear. The highlights (yellow parts) in each figure indicate the most important equations in the model of each loss element.

An overview of the modeling of the shroud effect in Tables 6.1-3 shows the effect of shrouding on the aerodynamic loss ("Effect of shrouding for air vortex loss" in the table) and the effect of shrouding on the oil dynamic loss ("Effect of shrouding for oil reacceleration loss" and "Effect of shrouding for oil churning loss" in the table).

An outline of the coefficients in the aerodynamic loss model is shown in Table 6.1-4 , an outline of the coefficients in the oil dynamic loss model is shown in Table 6.1-5 , and an outline of the shroud coefficients is shown in Table 6.1-6 . For the equations in which the coefficients in the loss model are used, refer to the highlights (yellow parts) in the table of the outline for the fluid dynamic loss model (Table 6.1-1 for aerodynamic loss or Table 6.1-2 for oil dynamic loss).

The values of the coefficients are listed in Tables 6.1-7 and 6.1-8 . These values correspond to the "Range of values of the coefficients" shown in the right column of the outline of the coefficients (Tables 6.1-4 , 6.1-5 , and 6.1-6).

The facts and assumptions used in each fluid dynamic loss model, the outlines of the fluid dynamic loss, the outlines of the coefficients in the loss model, and the tables of the coefficient values are described in Section 6.1. The fluid dynamic loss model is then described in detail in Section 6.2.
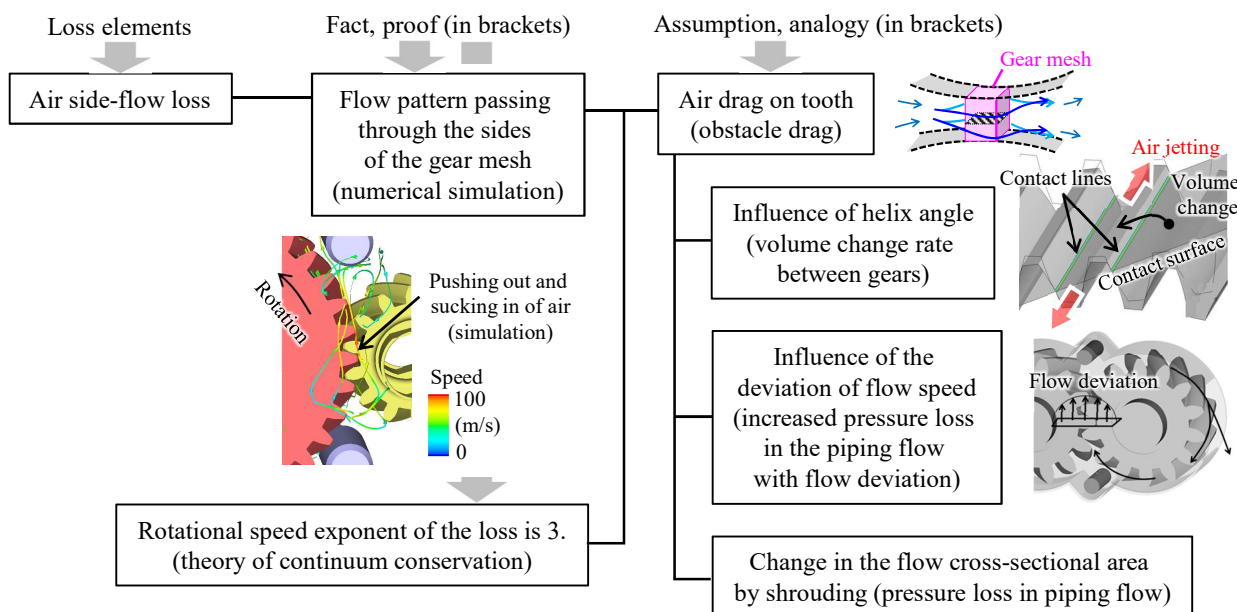
Fig. 6.1-1 Facts and assumptions used in the air side-flow loss model
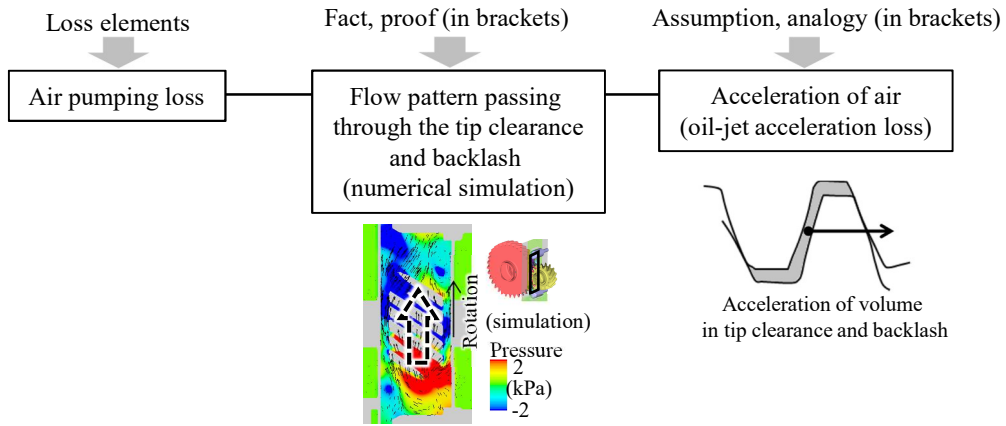
Fig. 6.1-2 Facts and assumptions used in the air pumping loss model
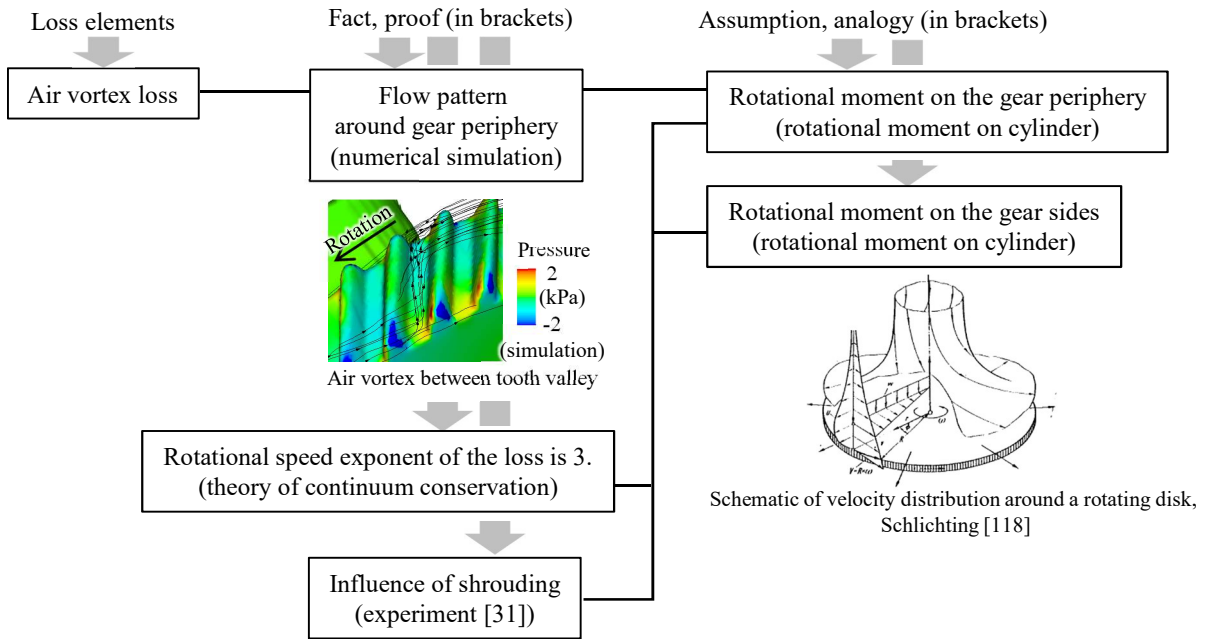
Fig. 6.1-3 Facts and assumptions used in the air vortex loss model
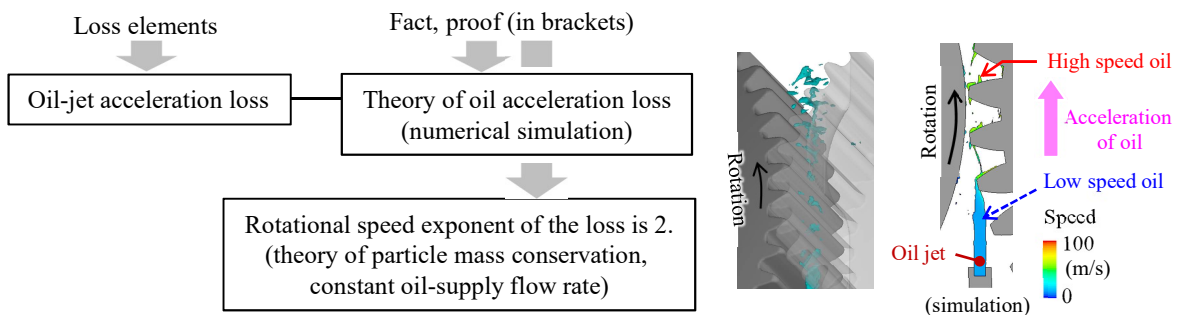
Fig. 6.1-4 Facts and assumptions used in the oil-jet acceleration loss model

189
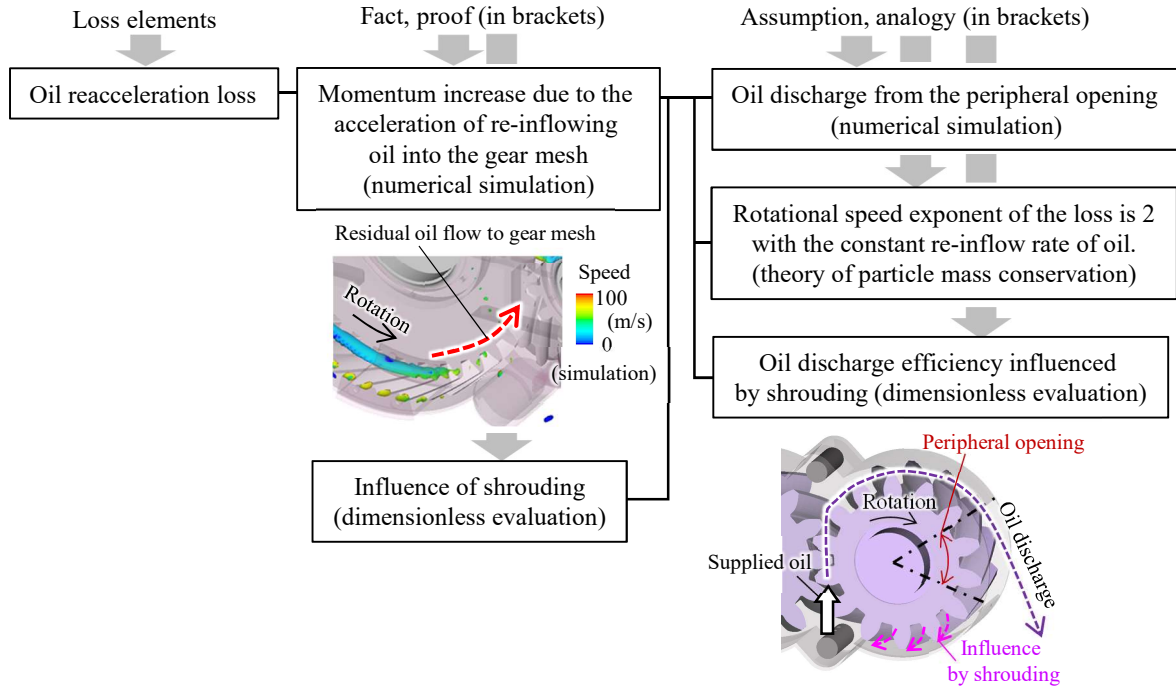
Fig. 6.1-5 Facts and assumptions used in the oil reacceleration loss model
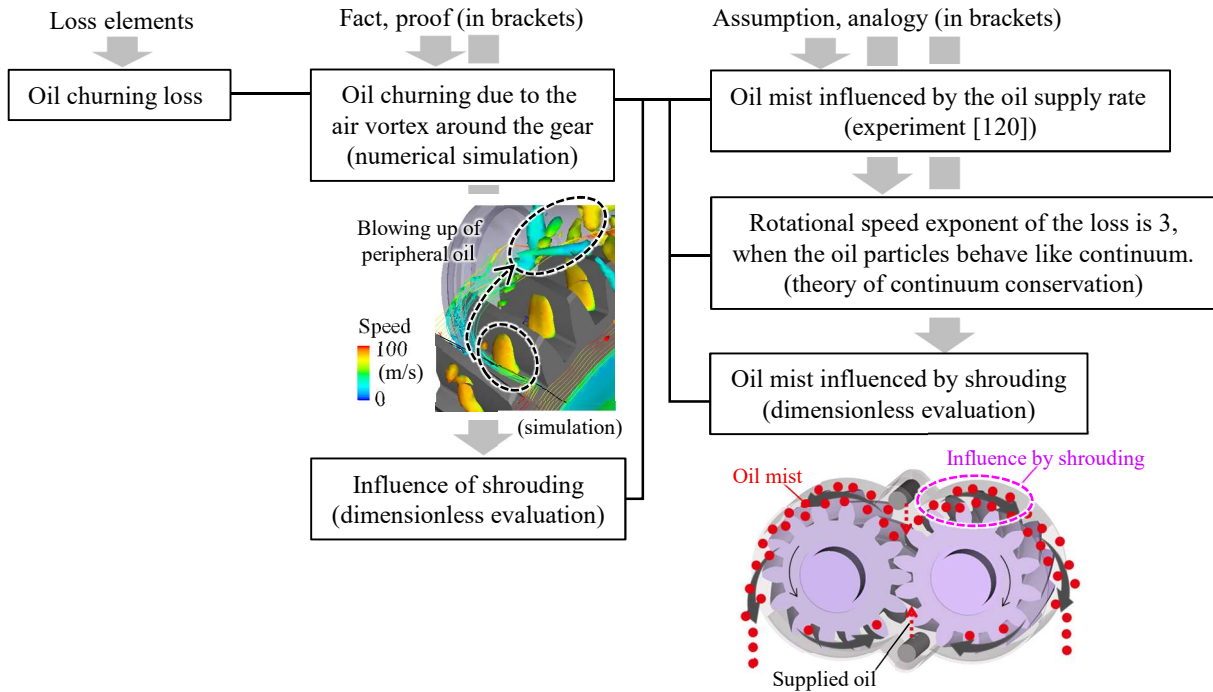
Fig. 6.1-6 Facts and assumptions used in the oil churning loss model

Table 6.1-1 Summary of the aerodynamic loss model
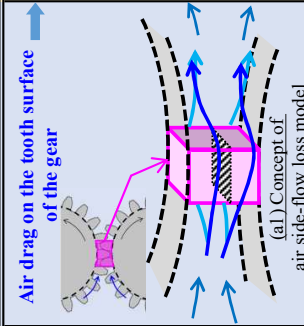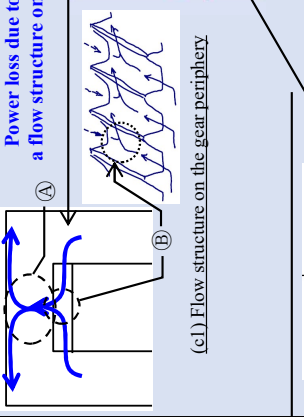
Classification	Location	Mass flow rate due to gear rotation	Force on gear	Torque (moment) due to gear rotation	Fluid dynamic loss
	Equation	$\dot{m} = \rho A/v = F/v$	$F = pA = \dot{m}v$	$T = Fr$	$P = T\omega = Fv$
	Exponent of power loss for peripheral speed / Concept of power loss	Proportional to peripheral speed	Proportional to the square of peripheral speed	Proportional to the square of peripheral speed	Proportional to the cube of peripheral speed
	Unit	kg/s	N	Nm	W

Air side-flow loss (Subscript "s") — Around gear meshing

- Mass flow rate: $\dot{m}_s = C_{D,s}\dfrac{1}{2}\rho_{air}Bhv_p$
- Force on gear: $F_s = C_{D,s}\dfrac{1}{2}\rho_{air}Bhv_p^2$ — **Air drag of gear teeth**
- Torque: $T_{s,*} = C_{D,s}\dfrac{1}{4}\rho_{air}Bhv_p^2 r_{p,*}$
- Fluid dynamic loss: $P_s = C_{D,s}\dfrac{1}{2}\rho_{air}Bhv_p^3$

$C_{D,s}$: **Air drag coefficient**

Effective parameters
① **Helix angle**
Air jetting intensity during gear meshing
② Number of shroud openings
Increase in loss coefficient due to the deviation of flow speed

Key parameters: Air drag coefficient, Air density, Tooth area, Speed³

Air drag on the tooth surface of the gear

(a1) Concept of air side-flow model

(a2) Air jetting during gear meshing

Air pumping loss (Subscript "pump") — Around gear meshing

- Mass flow rate: $\dot{m}_{pump} = \rho_{air}Q_{pump} \propto \rho_{air}v_p$ — **Air mass flow rate due to the air acceleration at the tooth tip clearance and backlash**
- Force on gear: $F_{pump} = \rho_{air}Q_{pump}v_p \cos\beta \propto \rho_{air}v_p^2 \cos\beta$ — **Force that accelerates the air at the tooth tip clearance and backlash**
- Torque: $T_{pump,*} = \dfrac{1}{2}\rho_{air}Q_{pump}v_p r_{p,*}\cos\beta \propto \dfrac{1}{2}\rho_{air}v_p^2 r_{p,*}\cos\beta$
- Fluid dynamic loss: $P_{pump} = \rho_{air}Q_{pump}v_p^2 \cos\beta \propto \rho_{air}v_p^3 \cos\beta$ (Loss is negligibly small.)

Force that accelerates the air in tooth tip clearance and backlash

(b) Concept of air pumping loss model

Air vortex loss (Subscript "v")

Gear periphery

Power loss due to the formation of a flow structure on the gear periphery

Proportional to λ

- Torque: $T_{v,peri,*} = C_{M,peri,*}\dfrac{1}{2}\rho_{air}\pi B r_{f,*}^2 v_f^2 \lambda_* \varepsilon_{\theta,*}$ — **Torque due to the formation of a flow structure on the gear periphery**
- Fluid dynamic loss: $P_{v,peri,*} = C_{M,peri,*}\dfrac{1}{2}\rho_{air}\pi B r_{f,*}^3 v_f^3 \lambda_* \varepsilon_{\theta,*} \propto \dfrac{\rho_{air}}{\cdots}B^{0.75}M_g^{1.15}v_f^{2.9}\lambda_*$

$C_{M,peri,*}$: **Rotational moment coefficient on gear periphery**

Effective parameters
① **Ratio of module to gear radius:** The flow structure is influenced by air discharge flow from gear. ⑧
② **Rotational Reynolds number:** The flow structure is influenced by the boundary layer on gear periphery. Ⓐ

Key parameters: Air density, Tooth area (equivalent), Speed²·⁹, Shroud coefficient

Shroud coefficient λ_* — Proportional to λ

(c1) Flow structure on the gear periphery

Ⓐ Ⓑ Air flow / Rotation

(c) Schematic of the flow around the gears

Gear sides

Power loss due to the formation of a flow structure on the gear side

- Torque: $T_{v,sides,*} = C_{M,sides,*}\dfrac{1}{2}\rho_{air}r_{f,*}^3 v_f^2 \lambda \varepsilon_{\theta,*}$ — **Torque due to the formation of a flow structure on the gear sides**
- Fluid dynamic loss: $P_{v,sides,*} = C_{M,sides,*}\dfrac{1}{2}\rho_{air}r_{f,*}^2 v_f^3 \lambda_* \varepsilon_{\theta,*}$

$C_{M,sides,*}$: **Rotational moment coefficient on gear sides**

Effective parameters
Rotational Reynolds number: The flow structure is influenced by the boundary layer on gear sides.

(Key parameters for the gear periphery should be used to represent the vortex loss because the loss at the gear periphery is larger than that at the gear sides.) Ⓒ

(c2) Flow structure on the gear sides Ⓒ

Table 6.1-2 Summary of the oil dynamic loss model
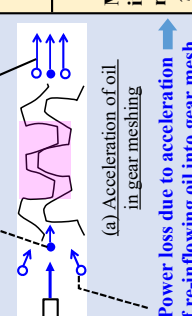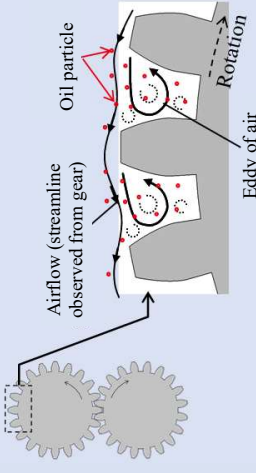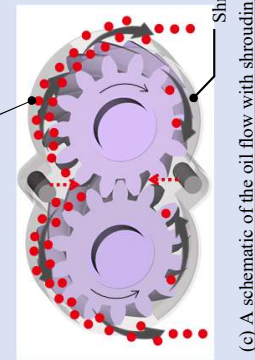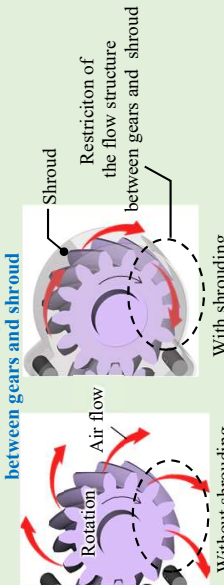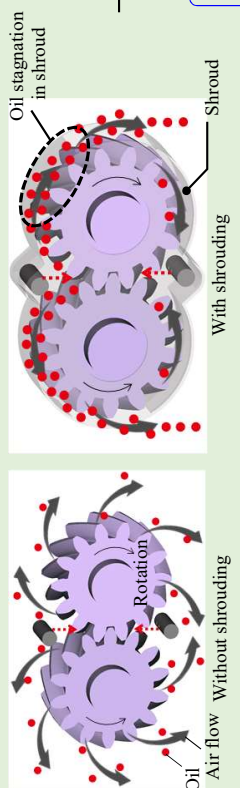
Classification	Location	Concept of power loss	Mass flow rate due to gear rotation	Force on gear	Torque (moment) due to gear rotation	Fluid dynamic loss
		Equation	$\dot{m} = pA/v = F/v$	$F = pA = \dot{m}v$	$T = Fr$	$P = T\omega = Fv$
		Exponent of power loss for peripheral speed	Constant	Proportional to peripheral speed	Proportional to peripheral speed	Proportional to the square of peripheral speed
		Unit	kg/s	N	Nm	W
Oil-jet acceleration loss (Subscript "jac")	Around gear meshing	Power loss due to oil-jet acceleration in gear meshing — Acceleration of oil in gear meshing (a) Acceleration of oil in gear meshing	Mass flow rate of oil supply $\dot{m}_{jac} = \rho_{oil}Q_S$	Acceleration of supplied oil $F_{jac} = \rho_{oil}Q_S v_p \cos\beta$	$T_{jac,*} = \frac{1}{2}\rho_{oil}Q_S v_p r_{p,*}\cos\beta$	$P_{jac} = \rho_{oil}Q_S v_p^{2}\cos\beta$ Volumetric flow rate of supplied oil — Speed². Key parametes
Oil reacceleration loss (Subscript "rac")	Around gear meshing	Power loss due to acceleration of re-inflowing oil into gear mesh	Mass flow rate of re-inflowing oil into gear mesh $\dot{m}_{rac} = \chi_{re}\rho_{oil}Q_S$	Acceleration of re-inflowing oil into gear mesh $F_{rac} = \chi_{re}\rho_{oil}Q_S v_p \cos\beta$	$T_{rac,*} = \frac{1}{2}\chi_{re}\rho_{oil}Q_S v_p r_{p,*}\cos\beta$	$P_{rac} = \chi_{re}\rho_{oil}Q_S v_p^{2}\cos\beta$ Oil reacceleration coefficient — Volumetric flow rate of supplied oil — Speed². Key parametes
Oil churning loss (Subscript "ch")	Gear periphery and gear sides	Power loss due to oil entrainment in the air vortex around the gear				Power loss due to churning of oil mist around gears (except for loss due to air) $P_{ch} = \sum_{*=in,out}(\Phi - 1)_{*}P_{v,*}$ Oil mist coefficient — Air vortex loss. Key parametes

χ_{re} : Oil reacceleration coefficient $= Q_{re}/Q_S$ (Ratio of oil re-inflow rate to oil supply rate)

Effective parameters
① Peripheral opening angle $\Delta\theta_{op}$: Oil discharge improves with an increase in the opening angle.
② Shroud coefficient λ : The separation of oil from the gear improves with an increase in the clearance between the gears and the shroud.

$\Phi - 1$: Oil mist coefficient, apparent increase in the fluid density due to the oil mist (excluding air density)

Effective parameters
① Volumetric flow rate of supplied oil Q_S
The amount of oil around the gears may increase as the oil supply increases.
② Shroud coefficient λ
The separation of oil from the gears improves by increasing the clearance between the gears and the shroud.

Inversely proportional to λ for χ_{re}

Inversely proportional to the square of λ for $\Phi - 1$

Shroud coefficient λ_{*}

(a) Acceleration of oil in gear meshing

(b) Oil entrainment into air vortex around gear

Airflow (streamline observed from gear)
Oil particle
Eddy of air
Rotation

(c) A schematic of the oil flow with shrouding

Shroud

Table 6.1-3 Summary of the modeling of shroud effect

Power loss elements	Modeling concepts of shroud effect
Effects of shrouding for air vortex loss	**Loss reduction by restricting the flow structure between gears and shroud** (a) Effects of shrouding on the aerodynamic flow structures **Air vortex loss is proportional to shroud coefficient λ** **λ* : Shroud coefficient restricts the flow structure on the gear periphery and sides** * A special coefficient that influences multiple losses (air vortex loss, oil reacceleration loss, and oil churning loss) and has an optimum value. **Effective parameters** ① **Ratio of radial clearance C_{rr} to gear diameter D_p** It influences the development of Ⓐ and Ⓑ in Table 6.1-1 (c1) ② **Ratio of axial clearance C_{rx} to gear width B** It influences the development of Ⓒ in Table 6.1-1 (c2) ③ **Peripheral opening angle $\Delta\theta_{op}$** It influences the development of Ⓑ in Table 6.1-1 (c1)
Effects of shrouding for oil reacceleration loss	**Power loss increase due to oil stagnation in shroud** (b) Comparisons of oil stagnation around gears **Oil reacceleration loss is inversely proportional to λ** (Oil reacceleration coefficient χ_{re} is inversely proportional to λ)
Effects of shrouding for oil churning loss	**Oil churning loss is inversely proportional to λ** (Oil mist coefficient Φ-1 is inversely proportional to the square of λ, and air vortex loss is proportional to λ)

Optimal range exists for shroud coefficient λ

A:area, B:tooth width, β:helix angle, $C_{D,S}$:air drag coefficient, $C_{M,sides}$:momento coefficient on gear sides,
$C_{M,peri}$:moment coefficient on gear periphery, C_{rr}:radial clearance, C_{rx}:axial clearance, D_p:pitch diameter,
ε_θ:peripheral ratio of gear periphery, F:force, h:tooth height, λ:shroud coefficient, $\dot{m}$:mass flow rate, ω:angular velocity, P:power loss, p:pressure,
Φ − 1:oil mist coefficient, Q:volumetric flow rate, r_f:radius of tooth bottom, ρ_{air}:air density, ρ_{oil}:oil density, r_p:pitch radius, T:torque,
$\Delta\theta_{op}$:peripheral opening angle, v_p:pitch line speed, v_f:peripheral speed on tooth bottom, χ_{re}:oil reacceleration coefficient

: Newly suggested in this research
: Reformulation of a previous research

Table 6.1-4 Features and ranges of the coefficients in the aerodynamic loss model

Power loss model	Progress in this research		Previous research and issues	How to determine the coefficients	Range of values of the coefficients	Remarks for applying the loss model
	Theory, model	Coefficients				
Air side-flow loss model	Created a new aerodynamic drag model	Defined a new aerodynamic drag coefficient	**Diab [42]** A method of calculating fluid dynamic loss by numerically solving the governing equations of fluid dynamics by setting a calculation mesh at the meshing part of a gear. Issues: Numerical analysis is required.	**Two-axis helical gearbox in this research (GA)** A helical gear pair and two types of shroud	**1.3** (Shroud 2)–**2.1** (Shroud 1) * See following tables for details	Unprecedented for the aerodynamic drag model and the aerodynamic drag coefficient. Therefore, it needs to be validated with various gears.
Air pumping loss model	Applied the theoretical equation for oil-jet acceleration loss	—	—	—	—	—
Air vortex loss model	Applied the equations using the rotational moment coefficients for cylinders and disks	Reformulated to rotational moment coefficients for cylinders and disks	**Dawson [31]** An empirical equation was proposed based on experiments using 22 types of gears and four types of disks. The effect of a shroud was shown experimentally. Issues: The physical features of the coefficient in the experimental equation was not shown. The empirical equation did not take into account the effect of helix angle and air viscosity. **Diab [40]** An empirical equation was proposed based on experiments using four types of gears. Issues: The applicability of the equation was limited (Massini [33]), because the influence of flange (shaft) in the equation was not validated.	**Experiments by Dawson [31]** The empirical equation is reformulated to ①An equation with a rotational moment coefficient on gear periphery ②An equation with a rotational moment coefficient on gear sides	①Rotational moment coefficient on gear periphery: **0.01** (diameter 1160 mm, width 187 mm, module 2 mm)–**0.5** (diameter 300 mm, width 187 mm, module 16 mm) ②Rotational moment coefficient on gear sides: **0.02** (diameter 1160 mm)–**0.07** (diameter 300 mm) * See following tables for details	**Consideration of the influence of the helix angle:** The influence of the helix angle on the air vortex loss is ignored in this study. This is because both increasing effect and decreasing effect were reported with helical gears (Voeltzel [41] and Dawson [31]). Further data are needed. **Consideration of the influence of air viscosity:** Air viscosity relating shear force-induced power loss should be modeled in order to improve the accuracy of the model.

Table 6.1-5 Features and ranges of the coefficients in the oil dynamic loss model

: Newly suggested in this research
: Revalidation of a previous research

Power loss model	Progress in this research		Previous research and issues	How to determine the coefficients	Range of values of the coefficients	Remarks for applying the loss model
	Theory, model	Coefficients				
Oil-jet acceleration loss model	Validated the theoretical equations	—	—	—	—	—
Oil reacceleration loss model	Using oil acceleration loss excluding oil-jet acceleration loss	Developed equations to evaluate the coefficient (oil reacceleration coefficient) from gears and a shroud	**Ariura [36], Matsumoto [46]** The theoretical equation of power loss due to the acceleration of oil was validated by experiments using helical gears. Issues: Empirical coefficients were introduced for large gears; however, no method was proposed to predict the coefficients with shrouding.	**Two-axis helical gearbox in this research (GA)** A helical gear pair and two types of shrouds	**0.2** (Shroud 1)–**1.0** (Shroud 2) * See following tables for details	Unprecedented for the prediction method of the oil reacceleration coefficient. Therefore, it needs to be validated with various gears.
Oil churning loss model	Using a model that only considers the effects of oil mist	Developed equations to evaluate the coefficient (oil mist coefficient) from the gear, shroud shape, and operating conditions	**Dawson [31], Matsumoto [46], Anderson [47]** Oil churning loss was defined as aerodynamic loss multiplied by fluid density around the gear. Issues: No method was proposed to predict the fluid density around the gear.	**Two-axis helical gearbox in this research (GA)** A helical gear pair and two types of shrouds	**0.2** (Shroud 1, 10000 rpm, 1.48 L/min)–**1.1** (Shroud 2, 70000 rpm, 3.85 L/min) * See following tables for details	Unprecedented for the prediction method of the oil mist coefficient. Therefore, it needs to be validated with various gears.

Table 6.1-6 Features and ranges of the shroud coefficients in the modeling of the shroud

: Newly suggested in this research
: Reformulation of a previous research

Power loss model	Progress in this research		Previous research and issues	How to determine the coefficients	Range of values of the coefficients	Remarks for applying the loss model
	Theory, model	Coefficients				
Effect of shrouding for air vortex loss	Using a model for the effect of shrouding (shroud coefficient) in the air vortex loss model	A new empirical equation is proposed using the experimental results of Dawson [31].	**Dawson [31]** The effects of seven shrouds were tested. Issues: No method was proposed to predict the effect of the shrouds.	**Experiments by Dawson [31]** Seven types of shrouds for a gear	**0.34** (completely enclosed)–**1.0** (no shroud) * See following tables for details	Unprecedented for the empirical equations of the shroud coefficients. Therefore, it needs to be validated with various shrouds and gears.
Effect of shrouding for oil reacceleration loss and oil churning loss	Created new models for the modeling of shroud effect in the oil reacceleration loss and the oil churning loss models	New coefficients using the shroud coefficient are proposed for the modeling of the shroud effect.	**Johnson [28]** Experiments with six shrouds of a bevel gear showed the optimum value of the size of the shroud opening. Issues: No method was proposed to predict the optimal size of the shroud opening.	**Two-axis helical gearbox in this research (GA)** A helical gear pair and two types of shrouds	**1.72** (Shroud 1)–**2.08** (Shroud 2) *Effect for the loss	Unprecedented for the models and the coefficients. Therefore, it needs to be validated with various shrouds and gears.

Table 6.1-7 Details of the coefficient values for the two-axis helical gearbox (GA)

Air drag coefficient, oil reacceleration coefficient, oil mist coefficient, and shroud coefficient

No.	Gearbox No.	Speed (rpm)	Oil supply rate (L/min)	Shroud (–)	Air drag coefficient (–)	Oil reacceleration coefficient (–)	Oil mist coefficient (–)	Shroud coefficient (–)
1	GA	7000	7.40	Shroud 1	2.1	0.22	0.66	0.58
2		10000	7.40				0.54	
3		7000	3.85				0.59	
4		10000	3.85				0.57	
5		10000	1.48				0.24	
6		7000	7.40	Shroud 2	1.3	0.98	0.90	0.48
7		10000	7.40				0.84	
8		7000	3.85				1.06	
9		10000	3.85				0.95	
10		10000	1.48				0.58	
				Minimum value	1.3	0.22	0.24	0.48
				Maximum value	2.1	0.98	1.06	0.58

Moment coefficients

No.	Gearbox No.	Input gear or Output gear	Root diameter (mm)	Face width (mm)	Tooth module (mm)	Number of teeth (–)	Rotational speed (rpm)	Reynolds number (–)	Face width / root radius (–)	Module / root radius (–)	Moment coefficient on periphery (–)	Moment coefficient on sides (–)
1	GA	Input gear	179	34	5	33	7000	3.75×10^5	0.38	0.056	0.267	0.023
2							10000	5.35×10^5			0.258	0.019
3		Output gear	69			14	7000	5.52×10^4	0.99	0.146	0.767	0.066
4							10000	7.89×10^4			0.740	0.054
										Minimum value	0.258	0.019
										Maximum value	0.767	0.066

Table 6.1-8 Details of the coefficient values for gears used in Dawson [31]

Moment coefficients

No.	Gear No. (in validation with simulation)	Disc, Spur gear or helical gear	Root diameter	Face width	Tooth module	Number of teeth	Rotational speed	Reynolds number	Face width / root radius	Module / root radius	Moment coefficient on periphery	Moment coefficient on sides
–	–		mm	mm	mm	–	rpm	–	–	–	–	–
1	–	Disc		–	–	–			–	–	–	–
2	9	Spur gear	300	74	3.2	94			0.49	0.021	0.093	0.072
3	–	Spur gear		187	2	150		1.17×10^5	1.25	0.013	0.043	
4	5	Spur gear			8	38				0.053	0.212	
5	1	Spur gear			16	19				0.107	0.469	
6	–	Disc		–	–	–			–	–	–	
7	–	Spur gear	514	187	2	257			0.73	0.008	0.024	0.040
8	7	Spur gear			8	64		3.43×10^5		0.031	0.117	
9	3	Spur gear			16	32				0.062	0.260	
10	4	Helical gear					750					
11	–	Disc		–	–	–			–	–	–	
12	–	Spur gear	760	32	2	380			0.08	0.005	0.024	0.026
13	10	Spur gear			8	95				0.021	0.118	
14	11	Spur gear		70					0.18		0.097	
15	12	Spur gear		114				7.50×10^5	0.30		0.086	
16	–	Spur gear		187	2	380			0.49	0.005	0.015	
17	13	Spur gear			8	95				0.021	0.076	
18	6	Spur gear			16	48				0.042	0.169	
19	2	Spur gear			24	32				0.063	0.269	
20	14	Spur gear		267	8	95			0.70	0.021	0.070	
21	15	Spur gear		355					0.93		0.065	
22	16	Spur gear		543					1.43		0.058	
23	–	Disc		–	–	–			–	–	–	
24	–	Spur gear	1160	187	2	580			0.32	0.003	0.010	0.016
25	–	Spur gear			8	145		1.75×10^6		0.014	0.048	
26	8	Spur gear			16	73				0.028	0.106	
										Minimum value	0.010	0.016
										Maximum value	0.469	0.072

6.1.2 Overview of the Air Side-Flow Loss Model

(1)   Facts and Assumptions Used in the Air Side-Flow Loss Model (Fig. 6.1-1)

The classification of the air side-flow loss is based on the fact that air is pushed out at the into-mesh part, passes through the sides of the gear mesh, and is then sucked in at the out-of-mesh part, as shown in the numerical simulation results (Fig. 5.1-3 (a)). In addition, from the theory of momentum conservation in the continuum, it is also found that the air side-flow loss is proportional to the third power of the peripheral speed (the mass flow rate of air at which the gear accelerates in the peripheral direction is proportional to the peripheral speed, and the force loaded on the gear tooth surface is proportional to the square of the peripheral speed).

To model the losses caused by this flow, the gear meshing part was assumed to be an obstacle to the flow, and the airflow resistance of the tooth surface was used. In the airflow resistance of the tooth surface, the helix angle, velocity deviation in the cross-section of the sides of the gear meshing part, and change in the flow section near the gear meshing part were considered. The helix angle is related to the rate of volume change during gear meshing. The influence of the velocity deviation at the cross-section of the sides of the gear meshing part is analogously inferred from the increase in the pressure loss of the flow in the pipe with velocity deviation. The influence of the change in the flow section near the gear meshing part is inferred from the pressure loss of the flow in the piping, where the flow section changes.

(2)   Concepts, Representative Equations, and Coefficients for the Air Side-Flow Loss Model

In the air side-flow loss model, the gear meshing part was modeled as a flow drag element, as shown in Table 6.1-1 (a1). The force loaded on the gear tooth surface by the flow is assumed to be due to air drag on the gear tooth surface (highlighted in Table 6.1-1).

Table 6.1-1 lists the parameters that affect the air drag coefficient, $C_{D,s}$, which are important for the flow drag of the gear meshing part. The air drag coefficient $C_{D,s}$ is mainly affected by the helix angle of the helical gear and the number of shroud openings.

The influence of the helix angle of the helical gear is presented in Table 6.1-1 (a2). When the gears are in contact, the volume between the teeth changes, and air jetting occurs on the gear side. The helical angle of the helical gear affects the strength of the air jet. For example, in the meshing of a spur gear pair, the entire width of the tooth comes in contact simultaneously; thus, the air in the tooth valley is pushed out all at once to the sides, and the accompanying airflow becomes stronger.

Another influential parameter is the number of openings in the shroud. In the shroud opening, flow velocity deviation occurs in the flow in the shroud because the flow is divided into that flowing out of the opening and that remaining in the shroud. The flow velocity deviation reaches the gear meshing part, which is believed to increase the flow drag in the gear meshing part. The number of shroud openings is used as an influential parameter because, as the number of shroud openings increases, the flow drag in the gear meshing part is considered to increase owing to the increase in the flow velocity deviation. In addition, the change in the flow section near the gear meshing part owing to the presence of the shroud is considered the flow resistance.

(3)   Characteristics and Range of Coefficient Values in the Air Side-Flow Loss Model

Table 6.1-4   shows the characteristics and range of values of the air drag coefficient $C_{D,s}$, which is a

representative coefficient of the air side-flow loss model.

Diab et al. [42] set a calculation grid at the gear meshing part, and the inflow and outflow of air at the gear meshing part were solved numerically. However, a simple loss equation cannot be obtained because the flow at the gear meshing part is numerically solved.

In this research, we introduced the concept of the air drag of the gear tooth surface, as described in (1) above, and set the air drag coefficient. However, there is no precedent for the introduction of the concept of air drag into the modeling of the gear meshing part; thus, it is necessary to validate it with various gears and expand its applicability.

The range of values of the air drag coefficient obtained from the two-axis helical gearbox in this study is from 1.3 to 2.1. The conditions for each value are listed in Table 6.1-7 .

6.1.3   Overview of the Air Pumping Loss Model

(1)   Facts and Assumptions Used in the Air Pumping Loss Model (Fig. 6.1-2)

The classification of air pumping losses is based on the fact that the flow passes through the tip clearance and backlash between the gears, as shown in the numerical simulation results (Fig. 5.1-3 (b)).

To model the losses caused by this flow, the acceleration of air at the tip clearance and backlash were assumed from the analogy of the oil-jet acceleration loss. Assuming that the volume of air at the tip clearance and backlash is the minimum volume when the gear teeth are closest to each other, a constant volume is specified. Therefore, the mass flow rate to be accelerated was proportional to the peripheral speed. Consequently, the torque and force loaded on the gear are proportional to the square of the peripheral speed, and the air pumping loss is proportional to the cube of the peripheral speed.

(2)   Concepts, Representative Equations, and Coefficients for the Air Pumping Loss Model

For the air pumping loss model, consider the acceleration of air at the tip clearance and the backlash between the gears, as shown in Table 6.1-1 (b). The acceleration of air is assumed to be calculated by a theoretical equation, like the oil-jet acceleration loss.

6.1.4   Overview of the Air Vortex Loss Model

(1)   Facts and Assumptions Used in the Air Vortex Loss Model (Fig. 6.1-3)

The classification of the air vortex loss is based on the fact that vortices occur in the gear teeth valleys, as shown in the results of the numerical simulation (Fig. 5.1-3 (c)). The theory of momentum conservation in the continuum also indicates that the air vortex loss is proportional to the cube of the peripheral speed (the mass flow rate of air at which the gear accelerates in the peripheral direction is proportional to the peripheral speed, and the force loaded on the gear tooth surface is proportional to the square of the peripheral speed). The reduction in air vortex loss by shrouding was clarified in the experimental results of a previous study [31].

To model the losses caused by the air vortices, we applied the idea of a rotational moment, which is commonly used in flow resistance with a rotating cylinder (the idea of the rotational moment is applied separately on the peripheral and side surfaces of the gear). This is because the gear is analogous to a cylinder with a rough surface on the peripheral surface. The shroud is assumed to reduce both the

rotational moment on the gear peripheral surface and the rotational moment on the gear sides.

(2)　Concepts, Representative Equations, and Coefficients for the Air Vortex Loss Model

In the air vortex loss model, the torque associated with the formation of the flow structure on the gear peripheral surface and the torque associated with the formation of the flow structure on the gear side surfaces were considered. The flow structure on the peripheral surface of the gear is shown schematically in Table 6.1-1 (c1). The flow structure on the gear-side surfaces is shown schematically in Table 6.1-1 (c2).

（ⅰ）　Loss Model at the Gear Peripheral Surface

Regarding the structure of flow on the gear peripheral surface, consider the structure of the flow near the shroud peripheral surface (Ⓐ in Table 6.1-1 (c1)) and the radial jetting flow from the gear (Ⓑ in Table 6.1-1 (c1)). In relation to the torque generated by the formation of these structures, the rotational moment coefficient $C_{M,peri}$ of a cylindrical surface is defined based on an analogy with the general rotational torque of a cylinder (the highlight in Table 6.1-1).

The parameters that mainly affect $C_{M,peri}$, of the gear peripheral surface are considered to be the ratio of the gear module to the gear radius and the rotational Reynolds number (= angular velocity × rotational radius^2 / kinematic viscosity), as shown in Table 6.1-1 .

$C_{M,peri}$ is thought to be affected by the ratio of the gear module to the gear radius, because it is thought to affect the strength of the jetting flow (Ⓑ in Table 6.1-1 (c1)) from the gear. The value of $C_{M,peri}$ is affected by the rotational Reynolds number because it is thought to affect the development of the boundary layer (Ⓐ in Table 6.1-1 (c1)) on the peripheral surface of the shroud.

The shroud coefficients included in the equations for the gear torque and air vortex loss on the gear peripheral surface can be used to model the effect of the shroud on suppressing the flow structure (Table 6.1-1 (c)) on the gear peripheral surface, as described in Section 6.1.8.

（ⅱ）　Loss Model at the Gear Sides

The flow structure on the sides of the gear is considered to be the same as that on the rotating disk shown in Table 6.1-1 (c2), and the coefficient of rotational moment on the sides, $C_{M,sides}$, is defined using the equation of rotational torque of the disk, as well as the flow on the rotating disk (highlighted in Table 6.1-1).

As shown in Table 6.1-1 , the parameter that mainly affects the coefficient of rotational moment of the gear sides, $C_{M,sides}$, is considered to be the rotational Reynolds number, because the boundary layer (Ⓒ in Table 6.1-1 (c2)) on the gear sides is considered to depend on the rotational Reynolds number. The shroud coefficient in the equations for the gear torque and air vortex loss at the sides of the gear can be used to model the effect of the shroud on suppressing the flow structure (Table 6.1-1 (c)) at the sides of the gear. This is described in Section 6.1.8.

The angle range coefficient ϵ_θ (= angle range of the gear peripheral part / 2π) of the peripheral part of the gear included in the equations of torque and fluid dynamic loss is defined as the fraction of the gear peripheral part excluding the meshing part.

(3)　Characteristics and Range of the Coefficient Values in the Air Vortex Loss Model

The characteristics and range of values of the rotational moment coefficient, which is a typical coefficient of the air vortex loss model, are listed in Table 6.1-4 . Dawson [31] constructed an empirical equation for aerodynamic loss from experiments using 22 types of gears and four types of disks. Furthermore, he

experimentally demonstrated the effects of the shrouds. The problems he found included the following: the characteristics of the coefficients of the empirical equation were not shown, and the effect of the helix angle of the helical gear was not considered. Diab et al. [40] constructed an empirical equation for aerodynamic loss from the experimental results using four types of gears. However, the applicability of this equation is limited because the effect of the flange (shaft) in the experimental equation has not been validated [33].

In this study, we utilized the experimental results of Dawson [31] with a larger number of gears. The results were re-evaluated by introducing the concept of general rotational moment coefficients. The coefficient of the rotational moment is divided into the rotational moment coefficient of the gear peripheral surface and rotational moment coefficient of the gear side surfaces.

On the influence of the helix angle, comprex experimental results on the influence of the helix angle exist, in which the aerodynamic loss of the helical gear becomes larger and smaller than that of a spur gear [41]. Therefore, the influence of the helical angle was ignored for simplicity in the air vortex loss model. On the influence of the air viscosity, we ignored the effects of air viscosity, because the influence of the shear force of air is small (Fig. 5.1-4). However, the shear force of air should be considered in future studies to improve the accuracy of the experimental equation.

The coefficients of the rotational moment were based on Dawson's experimental results [31]. The rotational moment coefficient $C_{M,peri}$ of the peripheral surface is in the range from 0.01 (gear diameter 1160 mm, tooth width 187 mm, and module 2 mm) to 0.5 (gear diameter 300 mm, tooth width 187 mm, and module 16 mm). The rotational moment coefficient of the side surfaces, $C_{M,sides}$, is in the range from 0.02 (1160 mm in gear diameter) to 0.07 (300 mm in gear diameter). The conditions for each value are listed in Table 6.1-8 .

6.1.5   Overview of the Oil-Jet Acceleration Loss Model

(1)   Facts and Assumptions Used in the Oil-Jet Acceleration Loss Model (Fig. 6.1-4)
The classification of oil-jet acceleration loss is based on the fact that the acceleration of the oil supplied to the gear meshing part and the associated losses can be evaluated by a theoretical equation, as shown in the numerical simulation results (Figs. 5.2-4 and 5.2-5). It was also confirmed from the momentum conservation theory of mass particles that the oil-jet acceleration loss is proportional to the square of the peripheral speed (the oil mass flow rate at which the gear accelerates in the peripheral direction is constant (= oil supply flow rate), and the force loaded on the gear tooth surface is proportional to the peripheral speed). Because the oil supply acceleration occurs at the tip clearance and backlash, we assume that it is not affected by the shroud.

(2)   Concept and Equation for the Oil-jet Acceleration Loss Model
In the oil-jet acceleration loss model, the forces generated by the acceleration of the oil at the tip clearance and backlash between gears are considered, as shown in Table 6.1-2 (a). This oil is defined as the supplied oil jetted to the gear meshing part in this case, and the oil supply flow rate is constant regardless of the peripheral speed of the gear. The force loaded on the gear tooth surface by the acceleration of the oil is obtained from the theoretical equation based on the momentum change of the oil (highlighted in Table 6.1-2).

6.1.6   Overview of the Oil Reacceleration Loss Model

(1)   Facts and Assumptions Used in the Oil Reacceleration Loss Model (Fig. 6.1-5)

The classification of oil reacceleration loss is based on the fact that the momentum of oil re-inflowing into the gear meshing part increases around the gear mesh, as shown in the numerical simulation results (Fig. 5.2-6). In addition, the increase in the oil dynamic loss by shrouding is included in Eq. 5.5, a dimensionless equation of the oil dynamic loss, as "the inverse of the shroud coefficient," and its validity is shown in Fig. 5.2-14 . The inverse of the shroud coefficient assumes accelerated oil stagnation in the shroud when the shroud opening is small (the shroud coefficient is small).

To model the loss caused by oil reacceleration, we focused on oil discharge from the shroud opening (Fig. 5.2-1 (f)). Using the theory of momentum conservation of mass particles and the assumption of a constant oil reacceleration flow rate, the oil reacceleration loss becomes proportional to the square of the peripheral speed (the oil mass flow rate at which the gear accelerates in the peripheral direction is constant (= oil reacceleration flow rate), and the force loaded on the gear tooth surface is proportional to the peripheral speed).

Regarding the influence of the shroud, in the nondimensionalization of the oil dynamic loss (Fig. 5.2-14), the oil dynamic loss includes the oil-jet acceleration, oil reacceleration, and oil churning losses. Because the oil-jet acceleration loss is not considered to be affected by the shroud, as described above, it is considered that the shroud affects either or both the oil reacceleration and oil churning losses. Here, we assume that the shroud affects both the oil reacceleration and the oil churning losses, and consider the "inverse of the shroud coefficient," which influences the discharge of oil from the shroud opening.

(2)   Concepts, Representative Equations, and Coefficients for the Oil reacceleration loss Model

The oil reacceleration loss model considers the acceleration of oil flowing into the gear meshing part as well as the oil-jet acceleration loss. The oil is supposed to re-flow into the gear meshing part, and the oil flow rate is assumed to be constant regardless of the peripheral speed of the gear. Here, the oil reacceleration coefficient χ_{re} is introduced as the ratio of the flow rate of the oil reflowing into the gear meshing part to the oil supply flow rate. The force loaded on the gear tooth surface by the acceleration of oil is obtained from the theoretical equation based on the change in oil momentum (highlighted in Table 6.1-2).

The parameters affecting the oil reacceleration coefficient χ_{re} are listed in Table 6.1-2 . The oil reacceleration coefficient χ_{re} was mainly affected by the opening angle on the peripheral surface of the shroud and the shroud coefficient.

The opening angle on the peripheral surface of the shroud is affected because the larger the opening of the shroud, the more oil is discharged from the opening of the shroud, and the less oil reflows into the gear meshing part.

The shroud coefficient is affected because, for example, when the clearance between the gear and shroud is large, the amount of oil reflowing into the gear meshing part is reduced because oil is easy to separate from the gear. This is described in Section 6.1.8.

(3)   Characteristics and Range of Coefficient Values in the Oil reacceleration loss Model

The characteristics and range of values of the oil reacceleration coefficient χ_{re}, which is a representative coefficient in the oil reacceleration loss model, are listed in Table 6.1-5 .

In conventional studies, Ariura et al. [36] and Matsumoto et al. [46] validated the theoretical equation of loss due to oil acceleration from the experimental results of helical gears. As a problem, in the case of large gears, an empirical coefficient was introduced to adjust the theoretical equation to the experimental results; however, a method for predicting the coefficient with shrouding has not been developed.

In this study, the coefficient is defined as the oil reacceleration coefficient, as shown in (1), and a new prediction method is proposed. The problem with this method is that because there is no precedent for the prediction method, it must be validated with various gears, and its applicability must be expanded.

The range of values of the oil reacceleration coefficient is from 0.2 to 1.0 as obtained from the two-axis helical gearbox in this study. The conditions for each value are listed in Tables 6.1-7 .

6.1.7 Overview of the Oil Churning Loss Model

(1) Facts and Assumptions Used in the Oil Churning Loss Model (Fig. 6.1-6)

The classification of oil churning loss is based on the fact that oil is churned by an air vortex at the gear periphery, as shown in the numerical simulation results (Fig. 5.2-7). In addition, the increase in the oil churning loss by shrouding is included in Eq. 5.5, which is a dimensionless equation, of oil dynamic loss as "the inverse of the shroud coefficient," and its validity is shown in Fig. 5.2-14 .

To model the loss caused by oil churning, we focus on the oil mist around the gear. We assume that the amount of oil mist around the gear is related to the amount of oil on the gear surface, as shown in Figs. 5.2-7 (a) and (b). The amount of oil on the gear surface is a function of the oil supply flow rate, as shown in Fig. 5.2-7 (c). Therefore, the amount of oil mist around the gear is assumed to be a function of the oil supply flow rate. Furthermore, assuming that the oil mist behaves as a continuum, using the momentum conservation theory of continuum, the oil churning loss is proportional to the cube of the peripheral speed (the oil mass flow rate at which the gear accelerates peripherally is proportional to the peripheral speed, and the force loaded on the gear tooth surface is proportional to the square of the peripheral speed). As for the influence of the shroud, it is assumed that the shroud affects both the oil reacceleration loss and the oil churning loss, as in the oil reacceleration loss model, and the "inverse of the shroud coefficient" is taken into account for the amount of oil mist.

(2) Concepts, Representative Equations, and Coefficients for the Oil Churning Loss Model

In the oil churning loss model, the power loss due to the churning of the oil mist around the gear is considered, as shown in Table 6.1-2 (b). The oil mist enters the air vortex and is churned, thus apparently increasing the air density. Therefore, the ratio of the increase in power loss due to the churning of air containing oil mist to the air vortex loss is defined as Φ. In this case, the ratio of the increase in power loss due to oil mist is $\Phi - 1$, which is defined as the oil mist coefficient (highlighted in Table 6.1-2).

The parameters affecting the oil mist coefficient $\Phi - 1$ are listed in Table 6.1-2 . The oil mist coefficient $\Phi - 1$ is mainly affected by the oil supply flow rate and the shroud coefficient.

The oil mist coefficient $\Phi - 1$ is affected by the oil supply flow rate because the quantity of oil around the gear increases when the oil supply flow rate is high.

The oil mist coefficient $\Phi - 1$ is affected by the shroud coefficient because, for example, when the clearance between the gear and shroud is large, the amount of oil around the gear is reduced because oil easily separates from the gear. This is described in Section 6.1.8.

(3)   Characteristics of the Coefficients and Range of Values in the Oil Churning Loss Model

The characteristics and ranges of the values of the oil mist coefficient $\Phi - 1$ in the oil churning loss model are shown in Table 6.1-5 .

In previous studies (e.g., [31] [46] [47]), the oil churning loss was calculated by multiplying the aerodynamic loss by the magnification of the density of the ambient fluid around the gear. The prediction equation for the density of ambient fluid is a problem that has not yet been studied.

In this study, we propose a novel equation to predict the oil mist coefficient by dividing the density of the atmospheric fluid into the surrounding oil density and air density, and introducing the oil mist coefficient into the surrounding oil density. The problem with this method is that because there is no precedent for the prediction method of the oil mist coefficient, it must be validated with various gears, and its applicability must be expanded.

The range of oil mist coefficient values is from 0.2 to 1.1, which was obtained from the two-axis helical gearbox in this research. The conditions for each value are listed in Tables 6.1-7 .

6.1.8   Overview of the Modeling of Shroud Effects

(1)   Concepts and Representative Coefficients for Modeling the Shroud Effect

(i)   Modeling the Effect of the Shroud on the Aerodynamic loss

A schematic of the shroud effect on aerodynamic loss is presented in Table 6.1-3 (a). As described in the outline of the air vortex loss model (Section 6.1.4), the shroud can effectively reduce the air vortex loss by suppressing the flow structure on the gear sides and gear peripheral surfaces.

The shroud coefficient λ is defined as the effect of suppressing the flow structure of air. The parameters affecting the shroud coefficient λ are listed in Table 6.1-3 . The shroud coefficient λ is mainly affected by the radial clearances between the gear and shroud, axial clearances between the gear and shroud, and peripheral opening angles.

The shroud coefficient is affected by the radial clearance because, for example, when the radial clearance is increased, the flow structure on the shroud peripheral surface (Ⓐ in Table 6.1-1 (c1)) and radial jetting flow from the gear (Ⓑ in Table 6.1-1(c1)) are considered to have developed.

The shroud coefficient is affected by the axial clearance because, for example, when the axial clearance increases, a flow structure develops on the sides of the gear (Ⓒ in Table 6.1-1 (c2)).

The shroud coefficient is affected by the peripheral opening angle because, for example, when the peripheral opening angle increases, a flow develops from the gear (Ⓑ in Table 6.1-1 (c1)).

(ii)   Modeling the Effect of the Shroud on the Oil dynamic loss

A schematic of the effect of the shroud on the oil dynamic loss is presented in Table 6.1-3 (b). As described in the overview of the oil reacceleration loss model (Section 6.1.6), oil accumulates in the shroud and increases the oil reacceleration loss. Similarly, as described in the overview of the oil churning loss model (Section 6.1.7), the shroud also increases the oil churning loss. In other words, the shroud increases the oil dynamic loss as opposed to reducing the aerodynamic loss. Therefore, we use the inverse of the shroud coefficient to consider the shroud in the oil dynamic loss model.

The effect of the shroud on the oil reacceleration loss model is included in the oil reacceleration coefficient χ_{re}, and the effect of the shroud on the oil churning loss model is included in the oil mist coefficient $\Phi - 1$.

(2)　Characteristics of the Shroud Coefficient

（ⅰ）　Characteristics of the Shroud Coefficient for the Aerodynamic Loss

The characteristics and ranges of values of the shroud coefficients for the air vortex loss are shown in the upper part of Tables 6.1-6 .

Dawson [31] conducted a systematic study that included the effect of clearances between a gear and shroud and opening angles on the aerodynamic loss. In the experiment, the effect of reducing the aerodynamic loss in eight types of shrouds was shown. However, an empirical equation for the effect of shrouds was not suggested.

In a different study, empirical equations for predicting the effect of shroud on aerodynamic loss (shroud coefficient) were constructed using Dawson's experimental results [31]. The empirical equations have no precedent; thus, it is necessary to validate them with various gears and shrouds, and to expand their applicability.

According to Dawson's experiment [31], the value of the shroud coefficient ranges from 0.34 to 1.0. The conditions for each value are shown in Fig. 6.4-4 in Section 6.4.6.

（ⅱ）　Characteristics of the Shroud Coefficient for the Oil Dynamic Loss

The characteristics and ranges of values of the shroud coefficients for the oil reacceleration loss and oil churning loss are shown in the lower part of Tables 6.1-6 .

In a conventional study, Johnson et al. experimentally demonstrated the optimal value of the shroud opening angle using six types of bevel gear shrouds [28]. However, they did not present an empirical equation for predicting the effect of the shroud on the oil dynamic loss, including the optimal value of the shroud opening angle.

In this study, we propose a new prediction equation for the effect of shroud on the oil reacceleration loss and oil churning loss. One problem is that there is no precedent for this prediction equation; thus, it is necessary to validate it with various gears and shrouds to expand its applicability.

As shown in (1) and (ii) above, the inverse of the shroud coefficient is used as a coefficient to represent the effect of the shroud on the oil reacceleration loss and oil churning loss. The values of the inverse of the shroud coefficient range from 1.72 (= 1/0.58, Shroud 1) to 2.08 (= 1/0.48, Shroud 2) as obtained for the two-axis helical gearbox in this study.

(3)　Range of Optimal Shroud Coefficient Values

The shroud reduces the aerodynamic loss by suppressing the flow structure on the peripheral and side surfaces of the gear, as shown in Table 6.1-3 　(a). In contrast, the shroud causes oil to stagnate and increases the oil reacceleration loss and oil churning loss, as shown in Table 6.1-3 　(b). Thus, the shroud reduces the aerodynamic loss, but increases the oil dynamic loss. Therefore, the shroud is considered to have an optimal shape.

The results of the investigation of the optimal value of the shroud coefficient using the two-axis helical gearbox are presented in Section 7.6.

6.2 Air Side-Flow Loss Model

6.2.1 Phenomena Focused on the Air Side-Flow Loss Model

The air side-flow loss model focuses on the flow caused by the volume change between the teeth during gear meshing, as shown in Fig. 6.2-1 . The sequence of the flow pattern is thought to be as follows: combining of the flows around the gears (1. Combining flow), the axial pushing out of the flow when the tooth crest of the gear enters the tooth valley of the other gear (2. Pushing out), the side-flow in which the pushed flow passes the sides of the gear mesh (3. Side flow), the sucking in of the flow when the gear tooth crest is separated from the tooth valley of the other gear (4. Sucking in), and the dividing of the flow to the periphery of the gears (5. Dividing flow). The fluid dynamic loss associated with these flows is defined as the "air side-flow loss" based on the characteristics of airflow through the side of gear mesh, and its modeling is described as follows.
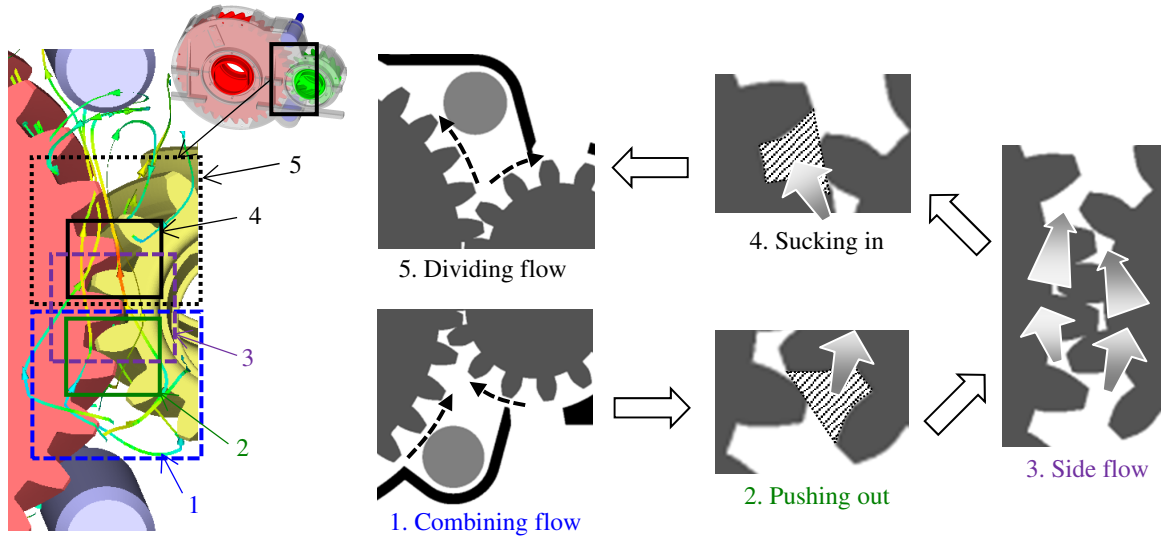
Fig. 6.2-1 Schematics of airflow due to the change in the inter-tooth volume at gear meshing (air side-flow loss model)

6.2.2 Air Drag Coefficient

6.2.2.1 Definition of Air Drag Coefficient, Modeling Concepts of Each Coefficient Constituting the Air Drag Coefficient

(i) Definition of Air Drag Coefficient

The pressure p_s loaded on the surface of the gear tooth by the airflow during gear meshing (Fig. 6.2-1) is expressed by the following equation using the air drag coefficient $C_{D,s}$, the air density ρ_{air}, and the pitch circle speed v_p.

$$p_s = C_{D,s} \frac{1}{2} \rho_{air} v_p{}^2 \tag{6.4}$$

In this study, the air drag coefficient $C_{D,s}$ is defined as follows.

$$C_{D,s} = \zeta_s Z_v Z_\beta \tag{6.5}$$

In the above equation, ζ_s is the gear meshing pressure loss coefficient, Z_v is the velocity coefficient, and Z_β is the helical angle coefficient.

(ii)   Modeling Concept of Gear Meshing Pressure Loss Coefficient

The concept of modeling the gear meshing pressure loss coefficient ζ_s is shown in Fig. 6.2-2 . In this model, the pressure loss associated with gear meshing is replaced by the pressure loss in the "orifice model" and the pressure loss in the "sudden expansion tube" or "sudden contraction tube".

The concept of the orifice model is shown in Fig. 6.2-2 (a). In the left of Fig. 6.2-2 (a), the condition before gear meshing is indicated as "A", the condition in which the gear is fully meshed is indicated as "C", and the intermediate condition is indicated as "B". The air is gradually pushed out to the side of the gear mesh by the time it changes from "A" to "B" to "C". Therefore, "B" is assumed to be the average condition of "A" and "C", which can represent the pushing out characteristics of air to the side of the gear mesh. The orifice model is shown on the right of Fig. 6.2-2 (a). On the right of Fig. 6.2-2 (a), consider an orifice with an opening ratio of "area of a gear tooth valley / total area of a peak and a valley of a gear tooth" as a model equivalent to "B".

(a) Modeling of gear meshing to "Orifice model"

(b) Modeling of flow area change to "expansion or contraction model"

c) Modeling of the influence of shroud opening-induced velocity deviation
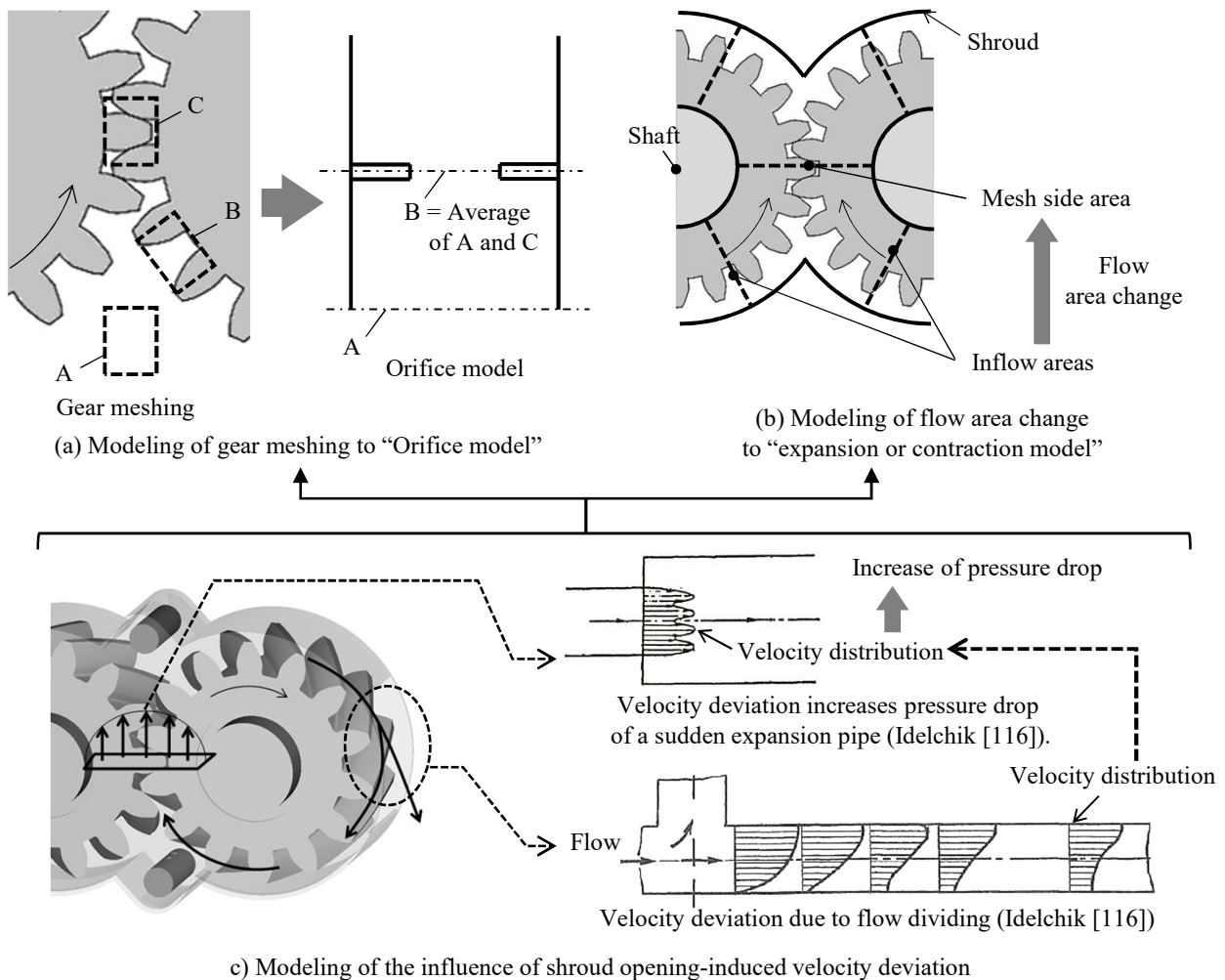
Fig. 6.2-2 Concept for the "pressure loss coefficient of orifice ζ_s" with modeling gear meshing to "orifice model" and "expansion or contraction model" (air side-flow loss model)

Figure 6.2-2 (b) shows the concept of modeling the airflow entrained according to the gear rotation before and during gear meshing. The model uses a pipeline which expands or contracts the area change around the gear before and during gear meshing. The modeling region is from the cross-sectional area upstream of gear mesh ("Inflow areas" in Fig. 6.2-2 (b)) to the cross-sectional area beside the gear mesh ("Mesh side area" in Fig. 6.2-2 (b)). In this region, if the cross-sectional area of the flow path is expanded, it is modeled with a sudden expansion tube, and if the cross-sectional area decreases, it is modeled with a sudden contraction tube. The above mentioned modeling is for the into-mesh, to which the modeling method for the out-of-mesh is similar.

Figure 6.2-2 (c) shows the influence of the velocity deviation in gear meshing on the pressure loss coefficient and the image of the velocity deviation caused by shroud opening. It is generally known that the pressure loss increases when there is a velocity deviation (if the flow velocity contains fast and slow parts in the cross section perpendicular to the flow). In the shroud opening, flow is considered to be divided into the flow flowing out from the shroud opening and the flow remaining in the shroud. Therefore, flow velocity deviation occurs as shown in "Velocity deviation due to flow dividing" in Fig. 6.2-2 (c) [116]. When this flow velocity deviation reaches the gear meshing, the pressure loss coefficient at the gear meshing part increases, for example, the flow velocity deviation of the sudden expansion tube increases the pressure loss coefficient [116].

Details of the orifice model, the sudden expansion tube or sudden contraction tube model, and the model of the increase in the pressure loss coefficient due to the velocity deviation are described in Section 6.2.2.2.

(iii)   Modeling Concepts for Velocity Coefficient

The velocity coefficient Z_v is related to the representative speed at the gear meshing part. The details of modeling the velocity coefficient Z_v is shown in Fig. 6.2-3 .

For Fig. 6.2-3 (a), (b) is rotated by half a pitch, (c) is rotated by another half pitch, and (d) is rotated by another half pitch. "E" and "F" in Fig. 6.2-3 refer to the same tooth and move with rotation. "G" in Fig. 6.2-3 indicates a fixed point in space on the pitch circle.

In "G" in Fig. 6.2-3 , at the fixed point in space on the pitch circle, panels (a) to (d) show that peaks and valleys of the gear pass alternately. When the velocity in the object (gear) is set to zero, the average velocity of "G" in Fig. 6.2-3 is considered to be smaller than the pitch circle speed. This is considered in terms of the velocity coefficient Z_v. The details of the modeling are described in Section 6.2.2.3.

(a) "Open" at point G   (b) "Close" at point G   (c) "Open" at point G   (d) "Close" at point G
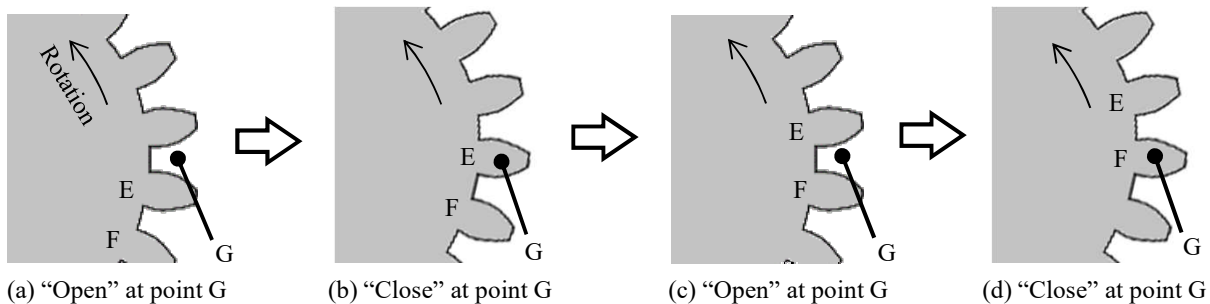
Fig. 6.2-3 The concept for "velocity coefficient Z_v" by focusing on alternating passing of gear teeth and valleys at a fixed point (air side-flow loss model)

(iv)   Modeling Concept of Helix Angle Coefficient

The concept of modeling the helix angle coefficient Z_β is shown in Fig. 6.2-4 . The volume change between the teeth in a spur gear part is shown in Fig. 6.2-4 (a), and that in a helical gear part is shown in Fig. 6.2-4 (b). The contact surface in Fig. 6.2-4 (a) and (b) is spatially fixed, and the gear teeth come in contact on this contact surface.

In the spur gear part, contact among the teeth is made in the whole width of the tooth. Therefore, as shown in "Rapid volume change" of Fig. 6.2-4 (a), the volume between the teeth rapidly changes, and the air between the teeth is pushed out rapidly in the axial direction to generate a jet stream ("Strong air jetting" in Fig. 6.2-4 (a)). In contrast, in the helical gear, tooth contact occurs in a part of the tooth width. As shown in "Mild volume change" in Fig. 6.2-4 (b), the volume change between the teeth is slower than that in a spur gear. Therefore, the air flow is possibly pushed out more slowly ("Mild air jetting" in Fig. 6.2-4 (b)). This difference in the strength of pushing out of air is considered in terms of the helix angle coefficient Z_β. The modeling is described in detail in Section 6.2.2.4.

(a) Spur gear   (b) Helical gear
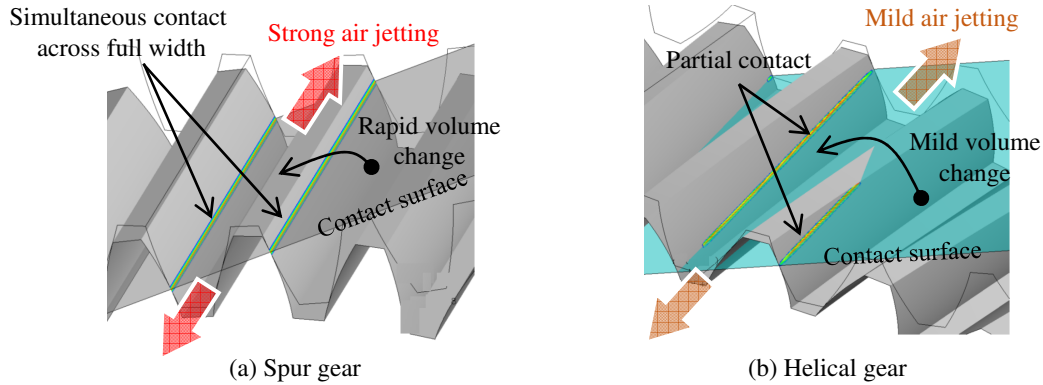
Fig. 6.2-4 The concept of "helix angle coefficient Z_β" with a focus on the difference in the volume change rate at the gear meshing between spur gears and helical gears (air side-flow loss model)

6.2.2.2   Gear Meshing Pressure Loss Coefficient

(i)   Configuration of Gear Meshing Pressure Loss Coefficient

The orifice pressure loss coefficient that models the volume change between teeth is ζ_A, the pressure loss coefficients due to the change in the airflow carried along the gear rotation before and after the gear mesh are ζ_{B1} and ζ_{B2}, respectively, and the ratio of the increase in the pressure drop coefficient due to the flow velocity deviation in the gear meshing part is M_A, M_{B1}, and M_{B2}. The gear meshing pressure loss coefficient ζ_s is defined by the following equation.

$$\zeta_s = \zeta_A M_A + \max\left(\zeta_{B1} M_{B1}, \zeta_{B2} M_{B2}\right) \tag{6.6}$$

(ii)   Orifice Pressure Loss Coefficient ζ_A, Modeling the Volume Change between Gear Teeth

The pressure loss coefficient ζ_A due to the volume change between the teeth is estimated from the pressure loss coefficient of the orifice shown in Fig. 6.2-5 . The orifice opening ratio (= orifice hole cross-sectional area / main pipe cross-sectional area) is required to obtain the pressure loss coefficient of the orifice.

As shown in Fig. 6.2-2 , the cross-sectional area of flow before gear meshing ("A" in Fig. 6.2-2) is the cross-sectional area of the main pipe, and the midway of the cross-sectional area between the cross-sectional area at the time of gear meshing and the cross-sectional area before gear meshing ("B" in Fig. 6.2-2) is the cross-sectional area of the orifice hole. The cross-sectional area of the main pipe is the sum of the cross-sectional area of the tooth peak (area of the axially projected cross-section) and the cross-sectional area of the valley. Assuming that the cross-sectional area of the orifice hole is the cross-sectional area of the valley and that the cross-sectional area of the peak and the cross-sectional area of the valley are equivalent, the opening ratio of the orifice (= the cross-sectional area of the valley / the sum of the cross-sectional areas of the peak and the valley) is 0.5.

From the experimental results of the orifice (Fig. 6.2-5), the pressure loss coefficient of the orifice is 4.0 for an opening ratio of 0.5. Therefore, ζ_A is given as follows.

$$\zeta_A = 4.0 \tag{6.7}$$
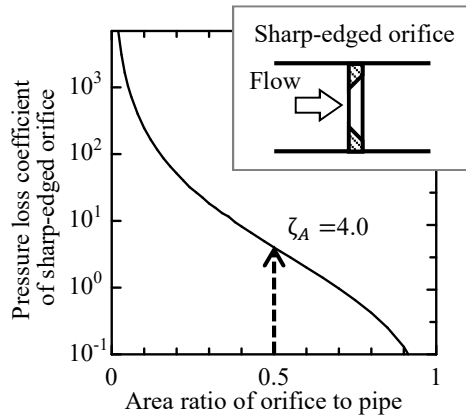
Fig. 6.2-5 The experimental pressure loss coefficient in orifice ζ_A [116] (air side-flow loss model)

(iii) Pressure Loss Coefficient ζ_{B1}, ζ_{B2} due to Changes in Airflow Accompanying to the Rotation of the Gear Teeth before and after Gear Meshing

Figure 6.2-6 shows the modeling of the pressure loss coefficients ζ_{B1} and ζ_{B2} due to changes in the airflow accompanying the rotation of the gear teeth.

Figure 6.2-6 (a) shows a cross section for estimating the pressure loss coefficient. As cross sections of the airflow, consider "Section A" and "Section B" upstream of the gear meshing and "Section C" at the gear meshing, as shown in Fig 6.2-6 (a).

The cross-sectional area A through which the airflow passes in Section A and Section B is selected based on the following two methods.

The first is the method of considering only the radial clearance (① in Fig. 6.2-6 (a), subscript "B1"). The other is the method of considering both the radial clearance and the axial clearance (② in Fig. 6.2-6 (a), subscript "B2"). The cross-sectional areas $A_{B1,in}$ and $A_{B1,out}$ at ① in Fig. 6.2-6 (a) are shown in the hatched part in Fig. 6.2-6 (a)①, and the cross-sectional areas $A_{B2,in}$ and $A_{B2,out}$ at ② are shown in

the hatched part in Fig. 6.2-6 (a)②. These are shown by the following equations.

$$A_{B1,in} = A_{B1,out} = (C_{rr} + h)(B + 2C_{rx}) \tag{6.8}$$

$$A_{B2,in} = A_{B1,in} + \frac{1}{2}(D_{f,in} - D_{a,in})C_{rx} \times 2 \tag{6.9}$$

$$A_{B2,out} = A_{B1,out} + \frac{1}{2}(D_{f,out} - D_{a,out})C_{rx} \times 2 \tag{6.10}$$

where the subscript *in* is the input gear, the subscript *out* is the output gear, C_{rr} is the radial clearance, C_{rx} is the axial clearance, h is the tooth height, B is the tooth width, D_f is the tooth root diameter, and D_a is the shaft diameter.

The cross sectional area A_{B0} at the gear meshing part is obtained by the method shown in ③ in Fig. 6.2-6 (a). The cross sectional area A_{B0} in ③ in Fig. 6.2-6 (a) is taken as the hatched part in Fig. 6.2-6 (a)③ and is given by the following equation.

$$A_{B0} = 2C_{rx}(L_a - D_{a,in}/2 - D_{a,out}/2) + B(L_a - D_{f,in}/2 - D_{f,out}/2) \tag{6.11}$$

where L_a is the distance between the input and output axes.

As shown in Fig. 6.2-6 (b), ζ_{B1} is taken as the loss coefficient when the cross sectional area of flow changes from $A_{B1,in} + A_{B1,out} \rightarrow A_{B0} \rightarrow A_{B1,in} + A_{B1,out}$ (it corresponds to ① → ③ → ① in Fig. 6.2-6 (a)). As shown in Fig. 6.2-6 (c), ζ_{B2} is taken as the loss coefficient when the cross sectional area of the flow changes as follows $A_{B2,in} + A_{B2,out} \rightarrow A_{B0} \rightarrow A_{B2,in} + A_{B2,out}$ (corresponding to ② → ③ → ② in Fig. 6.2-6 (a)).

The pressure loss coefficient due to the change in the cross-sectional area of these flows is determined by the combination of the sudden expansion tube shown in Fig. 6.2-6 (d) (cross-sectional area ratio of the horizontal axis in Fig. 6.2-6 (d) = outlet cross-sectional area / inlet cross-sectional area) and the sudden contraction tube shown in Fig. 6.2-6 (e) (cross-sectional area ratio of the horizontal axis in Fig. 6.2-6 (e) = outlet cross-sectional area / inlet cross-sectional area). Whether to use the pressure loss coefficient of the sudden expansion tube or that of the sudden contraction tube is determined by the relationship between the magnitudes of $A_{B1,in} + A_{B1,out}$ (or $A_{B2,in} + A_{B2,out}$) and A_{B0}. For example, when $A_{B1,in} + A_{B1,out} < A_{B0}$, the pressure loss coefficient of the sudden expansion tube shown in Fig. 6.2-6 (d) is used for the pressure loss coefficient from the into-mesh to the gear mesh, and the pressure loss coefficient of the sudden contraction tube shown in Fig. 6.2-6 (e) is used for the pressure loss coefficient from the gear mesh to the out-of-mesh. The pressure loss coefficient in Fig. 6.2-6 (d) is given as $\zeta_{B,expansion}$, and the pressure loss coefficient in Fig. 6.2-6 (e) is given as $\zeta_{B,contraction}$. Approximate equations for these pressure loss coefficients are shown below with the area ratio denoted as R_A.

$$\zeta_{B,expansion} = 0.9905{R_A}^2 - 1.9918R_A + 1.0 \tag{6.12}$$

$$\zeta_{B,contraction} = -1.3376{R_A}^4 + 2.1397{R_A}^3 - 1.2292{R_A}^2 - 0.5711R_A + 1.0 \tag{6.13}$$

The above equations are obtained from Idelchik's experimental data [116].
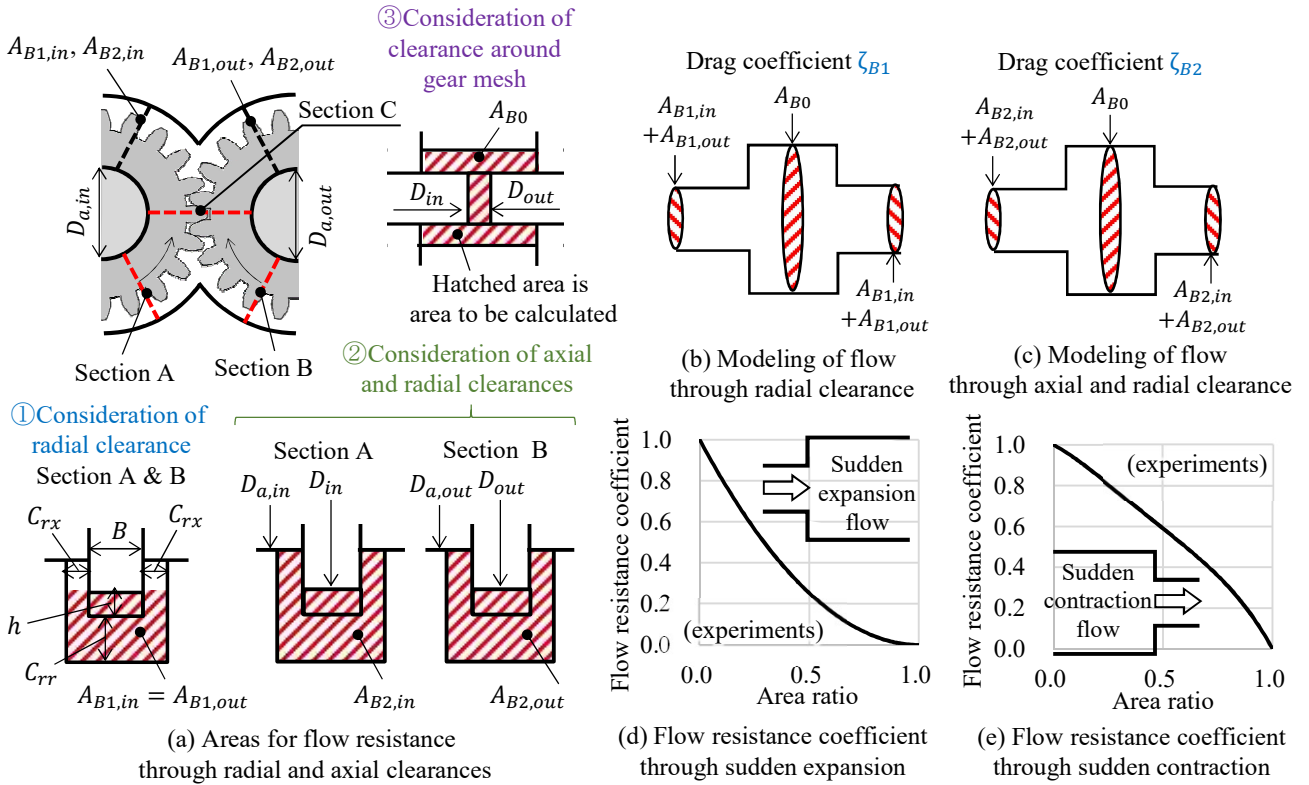
Fig. 6.2-6 Modeling of the airflow entrained into the gear meshing part (air side-flow loss model)

(iv)   Ratios of Increase M_A, M_{B1}, M_{B2} in Pressure Loss Coefficient due to Velocity Deviation at Gear Meshing Part

We estimated the ratio of the increase in M_A, M_{B1}, and M_{B2} of the pressure loss coefficient due to the flow velocity deviation at the gear meshing part from the pressure loss coefficient of the flow with the flow velocity deviation in the sudden expansion tube. Figure 6.2-7 shows the influence of the velocity deviation on the pressure loss coefficient.

Figure 6.2-7 (a) shows the experimental results [116] of the pressure loss coefficient when a flow velocity deviation occurs upstream of the sudden expansion tube. In Fig. 6.2-7 , $\bar{v}$ shows the upstream average flow velocity, and δv shows the deviation of the flow velocity with respect to the average flow velocity. $\delta v / \bar{v}$ is the relative flow velocity deviation. The pressure loss coefficient ζ_M increases as the relative flow velocity deviation $\delta v / \bar{v}$ increases.

Here, the "pressure loss coefficient increase ratio M" is defined as the "pressure loss coefficient ζ_M with a flow velocity deviation" / "pressure loss coefficient $\zeta_{M, \delta v / \bar{v}=0}$ without flow velocity deviation", as shown in Fig. 6.2-7 (b). The horizontal axis in Fig. 6.2-7 (b) is the ratio of the cross-sectional areas of the upstream and downstream flows.

The following equation shows the approximate equation of the pressure loss coefficient increase ratio obtained using the least squares approximation with the data in Fig. 6.2-7 (b).

$$M_* = \zeta_M / \zeta_{M, \delta v / \bar{v}=0} = \exp \left\{ \left(2.555 (A_0/A_2)^4 - 1.964 (A_0/A_2)^3 + 2.051 (A_0/A_2)^2 \right. \right.$$
$$\left. \left. +0.695 (A_0/A_2) + 1.02 \right) (\delta v / \bar{v}) \right\} \tag{6.14}$$

The symbol "$*$" on the left side of the above equation is "$B1$", "$B2$", or "A", and the area ratios A_0/A_2

are as follows:

$$A_0/A_2 = \begin{cases} \min(A_{B1}/A_{B0}, A_{B0}/A_{B1}) & \text{(for } M_{B1}) \\ \min(A_{B2}/A_{B0}, A_{B0}/A_{B2}) & \text{(for } M_{B2}) \\ \frac{1}{2}\{\min(A_{B1}/A_{B0}, A_{B0}/A_{B1}) + \min(A_{B2}/A_{B0}, A_{B0}/A_{B2})\} & \text{(for } M_A) \end{cases} \quad (6.15)$$

(a) Flow resistance coefficient through sudden expansion with velocity deviation

(b) Amplitude of flow resistance coefficient through sudden expansion with velocity deviation (estimated with (a))
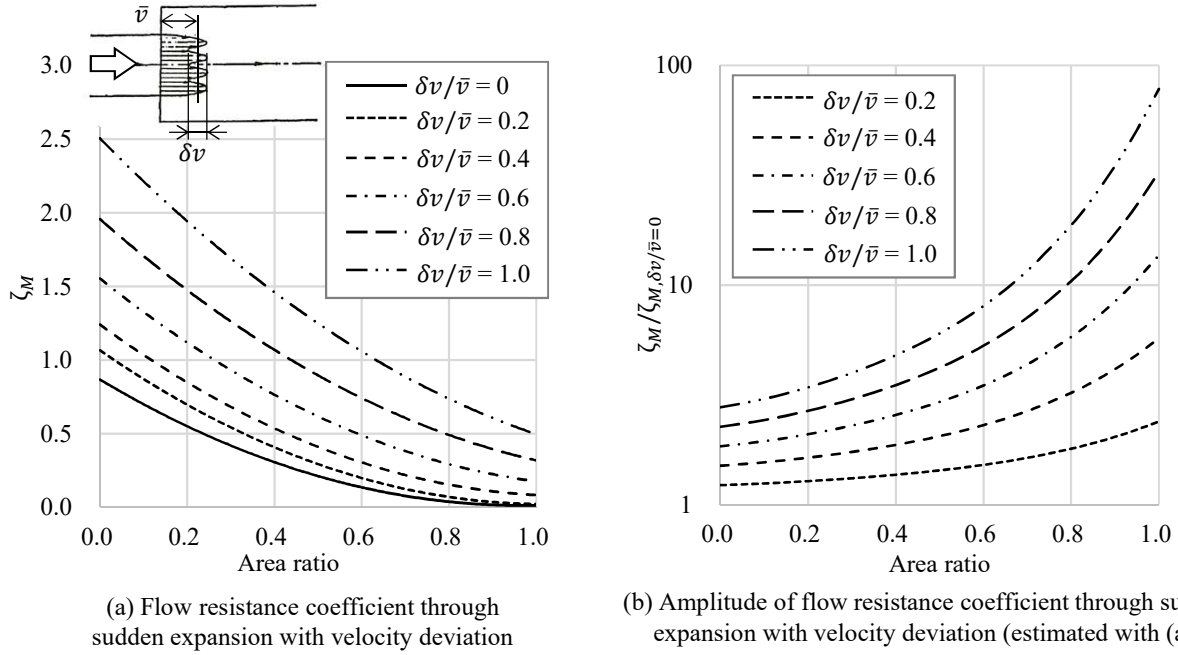
Fig. 6.2-7 Experimental effects of the flow velocity deviation on the pressure drop coefficient (air side-flow loss model)

We now relate the flow velocity deviation ratio $\delta v/\bar{v}$ to the shroud shape. Figure 6.2-8 shows the results of the numerical simulation on the correspondence between the flow velocity deviation and the shroud shape. Each point in the figure was obtained by the flow velocity deviation ratio (= (root-mean-square velocity − mean flow velocity) / mean flow velocity) using the root-mean-square value of the flow velocity distribution at the gear meshing section, as shown in the upper part of Fig. 6.2-8.

Figure 6.2-8 (a) shows the relationship between the number of the shroud openings n_{op} (per gear) and the flow velocity deviation. The two-axis helical gearbox (GA) in this study and the shroud shapes of Shroud 1 and Shroud 2 were used. Figure 6.2-8 (a) shows that the flow velocity deviation is large for Shroud 1 with three openings and small for Shroud 2 with one opening.

Figure 6.2-8 (b) shows the relationship between the shroud opening ratio (ratio of the total opening angle per gear to the total periphery) and the velocity deviation. We used the two-axis helical gearbox (GA) with shroud shapes with a different opening angle based on Shroud 2. Figure 6.2-8 (b) shows that the larger the opening angle, the larger the velocity deviation.

Figures 6.2-8 (a) and (b) show that when the number of the openings is n_{op}, the ratio of the openings is R_{op} ($= \frac{1}{2\pi}\{(\Delta\theta_{\sum op,in} + \Delta\theta_{\sum op,out})/2\}$); $\Delta\theta_{\sum op}$ is the peripheral opening angle of the shroud (total per gear), and the subscript "*in*" is the input gear and "*out*" is the output gear. The following approximate equation is obtained:

$$\delta v/\bar{v} = 8.618 \times 10^{-2} R_{op}{}^{0.3356} n_{op}{}^{1.413} \quad (6.16)$$

213

The above equation shows that the exponent of the number of the openings n_{op} is larger than the exponent of the ratio of the openings R_{op}. Therefore, the number of the openings n_{op} is the parameter that mainly affects the increase ratio in the pressure loss coefficient due to the velocity deviation.

Thus, it is possible to determine the gear meshing pressure loss coefficient ζ_s from Eq. 6.6.

(a) Approximation curve of velocity deviation ratio with the number of openings changes*

(b) Approximation curve of velocity deviation ratio with opening ratio changes*

* Simulation results
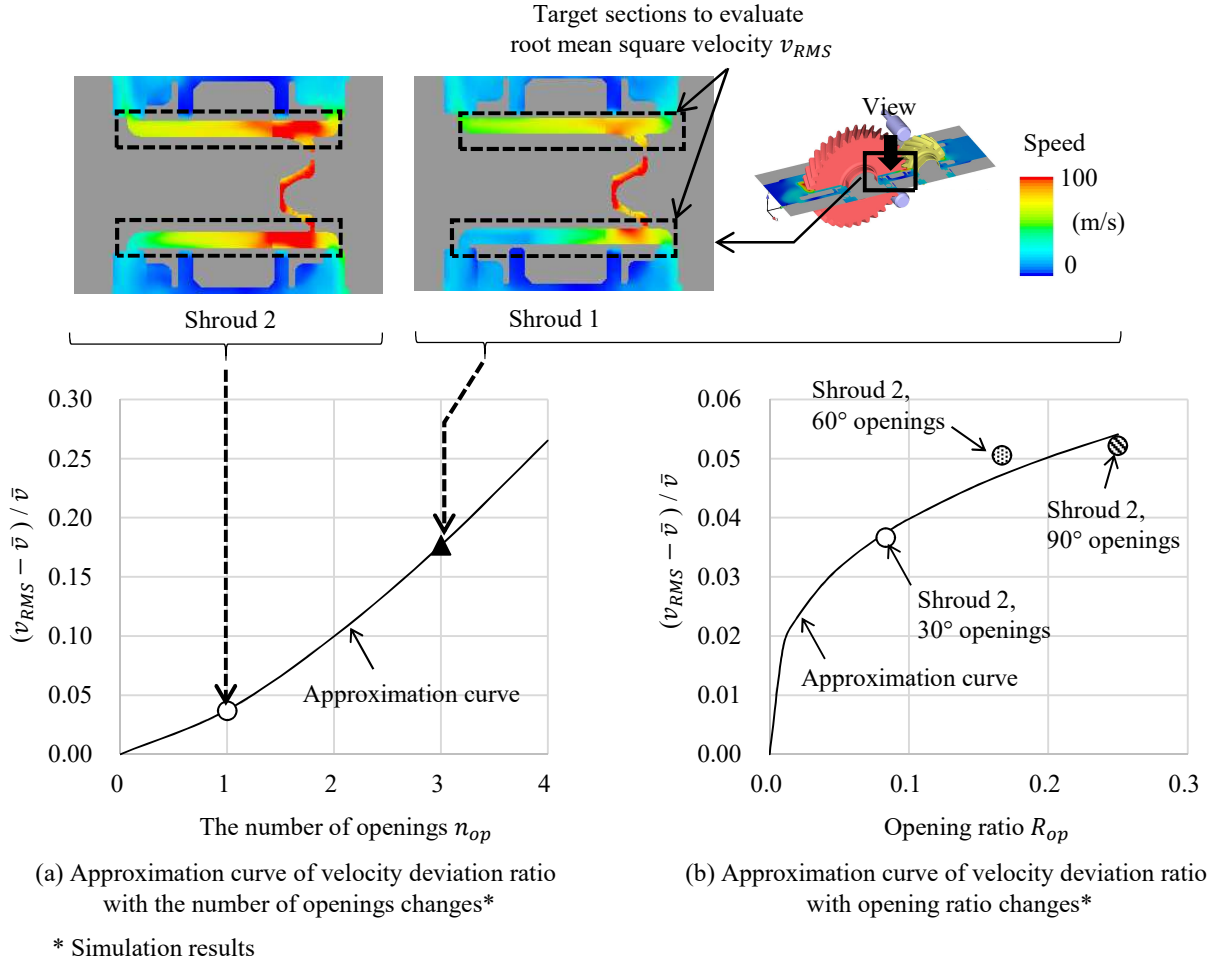
Fig. 6.2-8 Relationships between the flow velocity deviations and shroud openings evaluated using simulation results (air side-flow loss model)

6.2.2.3 Velocity Coefficient Z_v

As shown in Fig. 6.2-3 , at a fixed point in space on a pitch circle ("G" in the figure), gear peaks and valleys pass alternately. We model the case in which gear valleys pass through, whereas the airflow passes at the peripheral speed. When gear peaks pass through, the airflow velocity is assumed to be zero because it is in the gear structure. If the lengths of tooth peaks and tooth valleys on the pitch circle are the same, the average flow velocity at the point G is 1/2 of the peripheral speed. In addition, because the pressure applied to the gear tooth surface (Eq. 6.4) is proportional to the square of the flow velocity, the velocity coefficient Z_v is set using the following equation.

$$Z_v = (1/2)^2 = 0.25 \tag{6.17}$$

6.2.2.4 Helix Angle Coefficient Z_β

Figure 6.2-9 (a) shows the results of an analysis of the effect of the helix angle on the aerodynamic loss in the gear meshing part [44]. The analysis results were obtained by solving the fluid conservation equation by dividing the space around the gear meshing part into calculation cells. In the analysis, this loss includes the air side-flow loss and the air pumping loss. In contrast, the air pumping loss is negligibly small as described in Section 6.11.3; thus, the aerodynamic loss in Fig. 6.2-9 (a) can be regarded as equivalent to the air side-flow loss.

Figures 6.2-9 (b) show the magnification of the air side-flow loss at helix angles $\beta = 15°$ and $\beta = 0°$ based on the loss at $\beta = 30°$ in Fig. 6.2-9 (a). The loss at $\beta = 30°$ is used as a base loss because the helix angle of the two-axis helical gearbox (GA) used to validate the fluid dynamic loss model in this research is 30 °. Figure 6.2-9 (b) shows that the magnification increases as the helix angle β decreases (as it approaches the spur gear) because, as shown in Fig. 6.2-4 , the whole width of the gear teeth in the spur gear comes into contact at one time, causing air in the tooth valley to be rapidly pushed out to the axial direction.

Figure 6.2-9 (c) shows the helix angle coefficient Z_β with the changes in the helical angle β. The values at each point in Fig. 6.2-9 (c) are those at the peripheral speed of 18 m/s or higher, which are roughly constant in the magnification of loss in Fig. 6.2-9 (b). The values of "A", "B", and "C" in Fig. 6.2-9 (c) correspond to "A", "B", and "C" in Fig. 6.2-9 (b), respectively. An approximate equation for the helix angle coefficient Z_β is given as follows.

$$Z_\beta = \max(-6.403\beta^2 + 2.787, 0) \tag{6.18}$$

The unit of β is radian, and if the value of Z_β is less than zero, the value of Z_β is set to zero. In this approximation equation, the value is extrapolated when $\beta > 30°$, which is considered to reduce the reliability of the value. However, gears with a Helix angle of 30° or more are not generally used.

(a) Influence of the helix angle on the aerodynamic loss around the gear meshing (numerical simulation, Talbot [44])

(b) Amplitude of aerodynamic loss based on β=30° (estimated with (a))

(c) Coefficient Z_β on the influence of helix angle (estimated with (b))
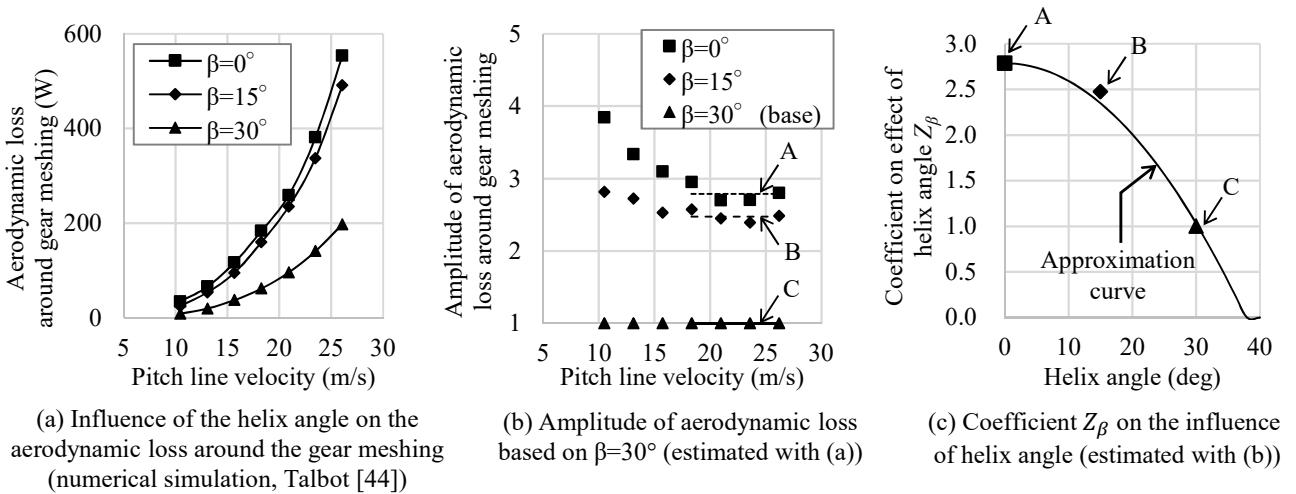
Fig. 6.2-9 Modeling of the influence of the helix angle (air side-flow loss model)

6.2.2.5 Influences of Shrouding on Gear Meshing Pressure Loss Coefficient

The effects of shrouding are included in the pressure loss coefficients ζ_{B1} and ζ_{B2} due to the change in the airflow accompanied with the rotation of gear teeth before and after gear meshing and are included in the increase ratios of pressure loss coefficients M_A, M_{B1}, and M_{B2} due to the flow velocity deviation at the gear meshing.

These parameters are included in the gear meshing pressure loss coefficient ζ_s. The other coefficients are modeled to not be affected by shrouding.

6.2.3 Force Loaded on the Gear, Mass Flow Rate that the Gear Drives, Gear Rotational Torque, and Air Side-Flow Loss

From the air side-flow pressure loss p_s, we obtain the force $F_{s,in}$ loaded on the input gear tooth surface and the force $F_{s,out}$ loaded on the output gear tooth surface. $F_{s,in}$ and $F_{s,out}$ are calculated by the following equation, assuming that the air side-flow pressure loss p_s is evenly distributed on the input gear and the output gear.

$$F_{s,in} = F_{s,out} = p_s Bh/2 = C_{D,s}\frac{1}{4}\rho_{air}Bhv_p{}^2 \tag{6.19}$$

$$F_s = F_{s,in} + F_{s,out} = p_s Bh = C_{D,s}\frac{1}{2}\rho_{air}Bhv_p{}^2 \tag{6.20}$$

The mass flow rate $\dot{m}_s$ of the air driven by the gear rotation is obtained by dividing the total of forces loaded on the gears, F_s, by the peripheral speed v_p.

$$\dot{m}_s = (F_{s,in} + F_{s,out})/v_p = C_{D,s}\frac{1}{2}\rho_{air}Bhv_p \tag{6.21}$$

The rotational torque $T_{s,in}$ of the input gear is obtained as a product of the force $F_{s,in}$ loaded on the input gear and the rotational radius $r_{p,in}$. Similarly, the rotational torque $T_{s,out}$ of the output gear is obtained as a product of the force $F_{s,out}$ loaded on the output gear and the rotational radius $r_{p,out}$. These are shown as follows:

$$T_{s,in} = F_{s,in}r_{p,in} = C_{D,s}\frac{1}{4}\rho_{air}Bhv_p{}^2 r_{p,in}$$
$$T_{s,out} = F_{s,out}r_{p,out} = C_{D,s}\frac{1}{4}\rho_{air}Bhv_p{}^2 r_{p,out} \tag{6.22}$$

The air side-flow loss $P_{s,in}$ of the input gear is obtained as a product of the rotational torque $T_{s,in}$ of the input gear and the angular velocity ω_{in}. Similarly, the air side-flow loss $P_{s,out}$ of the output gear is obtained as a product of the rotational torque $T_{s,out}$ of the output gear and the angular velocity ω_{out}.

$$P_{s,in} = T_{s,in}\omega_{in} = C_{D,s}\frac{1}{4}\rho_{air}Bhv_p{}^2 r_{p,in}\omega_{in} = C_{D,s}\frac{1}{4}\rho_{air}Bhv_p{}^3$$
$$P_{s,out} = T_{s,out}\omega_{out} = C_{D,s}\frac{1}{4}\rho_{air}Bhv_p{}^2 r_{p,out}\omega_{out} = C_{D,s}\frac{1}{4}\rho_{air}Bhv_p{}^3 \tag{6.23}$$

where the following relationships exist: $v_p = r_{p,in}\omega_{in} = r_{p,out}\omega_{out}$. The air side-flow loss P_s can be calculated by the following equation.

$$P_s = P_{s,in} + P_{s,out} = C_{D,s}\frac{1}{2}\rho_{air}Bhv_p{}^3 \tag{6.24}$$

6.2.4 Key Parameters of the Air Side-Flow Loss Model

The key parameters of the air side-flow loss model are the air drag coefficient $C_{D,s}$, the (third power of) peripheral velocity $v_p{}^3$, the tooth area ($\propto Bh$), and the air density ρ_{air}, as shown in Eq. 6.24.

The key parameters that mainly affect the air drag coefficient $C_{D,s}$ are the helix angle β (Eq. 6.18), which is related to the strength of pushing out air during gear meshing, and the number of openings of the shroud n_{op} (Eqs. 6.14 and 6.16), which is related to the increase in the loss coefficient due to the flow velocity deviation.

6.3 Air Pumping Loss Model

6.3.1 Phenomena Focused on the Air Pumping Loss Model

Figure 5.3-1 showed the classification of the aerodynamic loss in the gear meshing part. The figure shows that in the gear meshing part, there is a flow passing through the sides of gear mesh and a flow in the tip clearance and backlash in the gear mesh. The loss due to the flow through the sides of the gear mesh is regarded as air side-flow loss, and the loss due to the flow in the tip clearance and backlash in the gear mesh is considered air pumping loss. In the air pumping loss model, we focused on the flow in the tip clearance and backlash in the gear mesh.

The air pumping loss is considered to be a loss caused by the acceleration of the air in the gear meshing part, based on an analogy with the oil-jet acceleration loss, which is the loss caused by the acceleration of oil supplied to the gear mesh. The oil-jet acceleration loss is described in Section 6.5.

6.3.2 Mass Flow Rate by Air Pumping

To evaluate the mass flow rate of air pumping, the tip clearance and backlash in the gear meshing part is shown in Fig. 6.3-1 .

The mass flow rate $\dot{m}_{pump}$ pumped from the gear meshing part is calculated using the following equation using the volume flow rate Q_{pump} and the air density ρ_{air} [46].

$$\dot{m}_{pump} = \rho_{air} Q_{pump} = \rho_{air} \left\{ 2M_g j + 0.5(S_{in} + j + S_{out})(C_{h,in} + C_{h,out}) \right\} B z_{in} \frac{\omega_{in}}{2\pi} \tag{6.25}$$

where M_g is the gear module, j is the backlash, S_{in} and S_{out} are the tooth tip lengths, C_{in} and C_{out} are the tip clearances, B is the tooth width, z_{in} is the number of teeth of the input gear, and ω_{in} is the rotation angular velocity of the input gear. Because $S_{in} + j + S_{out} \propto M_g$, and $M_g z_{in} = D_{p,in}$ (D_p is the pitch circle diameter), $\dot{m}_{pump} \propto D_{p,in}\omega_{in} \propto v_p$ (v_p is the pitch circle speed).
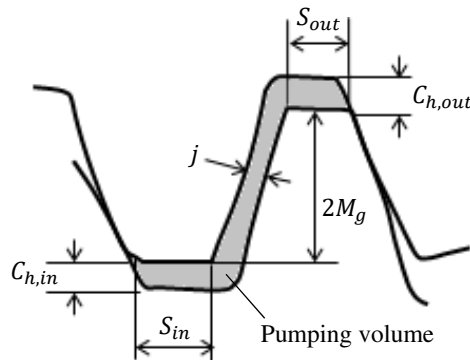
Fig. 6.3-1 Inter-tooth pumping volume for modeling aerodynamic loss (air pumping loss model)

6.3.3 Force Loaded on the Gear, Gear Rotational Torque, and Air Pumping Loss

$F_{pump,in}$ loaded on the input gear tooth surface and $F_{pump,out}$ loaded on the output gear tooth surface are given by the following equation, assuming that F_{pump} generated by accelerating the air pumping mass flow rate

$\dot{m}_{pump}$ to the gear peripheral speed is equally divided between the input and output gears.

$$F_{pump,in} = F_{pump,out} = \frac{1}{2}\rho_{air}Q_{pump}v_p\cos\beta \tag{6.26}$$

$$F_{pump} = F_{pump,in} + F_{pump,out} = \rho_{air}Q_{pump}v_p\cos\beta \tag{6.27}$$

The helix angle β of the tooth in the above equation was introduced as the acceleration of air in the direction perpendicular to the tooth of the helical gear.

The rotational torque $T_{pump,in}$ of the input gear is obtained as a product of the force $F_{pump,in}$ loaded on the input gear and the rotational radius $r_{p,in}$. Similarly, the rotational torque $T_{pump,out}$ of the output gear is obtained as a product of the force $F_{pump,out}$ loaded on the output gear and the rotational radius $r_{p,out}$. These are shown below.

$$T_{pump,in} = F_{pump,in}r_{p,in} = \frac{1}{2}\rho_{air}Q_{pump}v_p r_{p,in}\cos\beta$$
$$T_{pump,out} = F_{pump,out}r_{p,out} = \frac{1}{2}\rho_{air}Q_{pump}v_p r_{p,out}\cos\beta \tag{6.28}$$

The air pumping loss $P_{pump,in}$ of the input gear is obtained as a product of the rotational torque $T_{pump,in}$ of the input gear and the angular velocity ω_{in}. Similarly, the air pumping loss $P_{pump,out}$ of the output gear is obtained as a product of the rotational torque $T_{pump,out}$ of the output gear and the angular velocity ω_{out}. These are shown in the following equation ($v_p = r_{p,in}\omega_{in} = r_{p,out}\omega_{out}$):

$$P_{pump,in} = T_{pump,in}\omega_{in} = \frac{1}{2}\rho_{air}Q_{pump}v_p r_{p,in}\cos\beta\omega_{in} = \frac{1}{2}\rho_{air}Q_{pump}v_p{}^2\cos\beta$$
$$P_{pump,out} = T_{pump,out}\omega_{out} = \frac{1}{2}\rho_{air}Q_{pump}v_p r_{p,out}\cos\beta\omega_{out} = \frac{1}{2}\rho_{air}Q_{pump}v_p{}^2\cos\beta \tag{6.29}$$

$$P_{pump} = P_{pump,in} + P_{pump,out} = \rho_{air}Q_{pump}v_p{}^2\cos\beta \tag{6.30}$$

Because $Q_{pump} \propto v_p$ from Eq. 6.25, $P_{pump} \propto v_p{}^3$. The air pumping loss can be calculated from the above equation.

6.3.4 Key Parameters of the Air Pumping Loss Model

The key parameters of the air pumping loss model are the (third power of) peripheral velocity $v_p{}^3$, air density ρ_{air}, and tip clearance and backlash from Eqs. 6.25 and 6.30, respectively.

6.4 Air Vortex Loss Model

6.4.1 Phenomena Focused on the Air Vortex Loss Model

Regarding the airflow pattern in the gear periphery, as shown in Fig. 5.3-1 , a flow exists in which air is sucked in from around the gear shaft, flows on the gear sides, and is then discharged to the peripheral direction of the gear. In addition, classification of the aerodynamic loss in Fig. 5.3-1 shows the air vortex between the gear teeth.

On the air vortex loss model, we focus on the structure of the flow, such as the air vortex generated on the gear peripheral surface and the side surfaces. A schematic diagram of the flow structure generated on the gear peripheral surface is shown in Table 6.1-1 (c1) and that on the gear side surfaces is shown in Table 6.1-1 (c2).

6.4.2 Rotational Torque and Air Vortex Loss Associated with the Formation of Flow Structure on the Peripheral Surface and Sides of the Gear

For the torque $T_{v,peri,*}$ associated with the formation of the flow structure on the gear peripheral surface, we use the general equation $T_{peri} = C_{M,peri}\frac{1}{2}\rho\omega^2 r^4\pi h$ [117] for the torque of the rotating drum, where the torque is evaluated separately for the input and output gears, and "$*$" stands for "in" (input gear) or "out" (output gear). T_{peri} is the rotational torque on the peripheral surface, $C_{M,peri}$ is the rotational moment coefficient on the peripheral surface, ρ is the fluid density, ω is the rotational angular velocity, r is the cylinder radius, and h is the tooth height. $T_{v,peri,*}$ is given by the following equation:

$$T_{v,peri,in} = C_{M,peri,in}\frac{1}{2}\rho_{air}\pi B r_{f,in}{}^2 v_f{}^2\lambda_{in}\epsilon_{\theta,in}$$
$$T_{v,peri,out} = C_{M,peri,out}\frac{1}{2}\rho_{air}\pi B r_{f,out}{}^2 v_f{}^2\lambda_{out}\epsilon_{\theta,out}$$

(6.31)

where subscript v is the air vortex loss, B is the tooth width, $r_{f,*}$ is the radius of the tooth bottom circle, λ_* is the shroud coefficient, and $\epsilon_{\theta,*}$ is the angular fraction of the gear peripheral part. The shroud coefficient is described in Section 6.4.6, and the angular fraction of the gear peripheral part is described in Section 6.4.7.

The power loss $P_{v,peri,*}$ ($* = in, out$) due to the rotational torque of the peripheral surface of the gear is calculated as a product of the rotational torque $T_{v,peri,*}$ of the gear peripheral surface and the angular velocity ω_* ($r_{f,in}\omega_{in} = r_{f,out}\omega_{out} = v_f$).

$$P_{v,peri,in} = C_{M,peri,in}\frac{1}{2}\rho_{air}\pi B r_{f,in}v_f{}^3\lambda_{in}\epsilon_{\theta,in}$$
$$P_{v,peri,out} = C_{M,peri,out}\frac{1}{2}\rho_{air}\pi B r_{f,out}v_f{}^3\lambda_{out}\epsilon_{\theta,out}$$

(6.32)

For the torque $T_{v,sides,*}$ associated with the formation of the flow structure on the side surfaces of the gear, the general equation $T_{sides} = C_{M,sides}\frac{1}{2}\rho\omega^2 r^5$ [118] for the torque of the rotating disk is used, where $T_{v,sides}$ represents the rotational torque on the side surfaces, and $C_{M,sides}$ represents the rotational moment coefficient on the side surfaces. $T_{v,sides,*}$ is expressed using the following equation:

$$T_{v,sides,in} = C_{M,sides,in}\frac{1}{2}\rho_{air}r_{f,in}{}^3 v_f{}^2\lambda_{in}\epsilon_{\theta,in}$$
$$T_{v,sides,out} = C_{M,sides,out}\frac{1}{2}\rho_{air}r_{f,out}{}^3 v_f{}^2\lambda_{out}\epsilon_{\theta,out}$$

(6.33)

The power loss $P_{v,sides,*}(* = in, out)$ due to the rotational torque on the sides of the gear is obtained as a product of the rotational torque $T_{v,sides,*}$ on the sides of the gear and the angular velocity ω_*.

$$P_{v,sides,in} = C_{M,sides,in}\frac{1}{2}\rho_{air}r_{f,in}{}^2 v_f{}^3\lambda_{in}\epsilon_{\theta,in}$$
$$P_{v,sides,out} = C_{M,sides,out}\frac{1}{2}\rho_{air}r_{f,out}{}^2 v_f{}^3\lambda_{out}\epsilon_{\theta,out}$$

(6.34)

The air vortex loss is the sum of the power loss due to the rotational torque on the peripheral surface of the gear and the power loss due to the rotational torque on the side surfaces of the gear as follows:

$$P_v = \sum_{*=in,out} P_{v,peri,*} + \sum_{*=in,out} P_{v,sides,*}$$

(6.35)

6.4.3 Rotational Moment Coefficient on the Peripheral Surface and Sides of the Gear

The rotational moment coefficient on the peripheral surface of the gear and the rotational moment coefficient on the side surfaces of the gear are important parameters that represent the characteristics of the flow structure that causes rotational torque. An empirical equation for the coefficient of rotational moment is obtained with reference to Dawson's empirical equation [31] (Eq. 1.1) for the aerodynamic loss in a single spur gear. Dawson equated the loss on the gear side surface with the loss on a single disk and constructed an equation for the aerodynamic loss in the peripheral surface and side surfaces of the gear. In this study, these equations are converted into the form of the coefficient of rotational moment.

(i) Rotational Moment Coefficient at the Gear Peripheral Surface
An empirical equation for the rotational moment coefficient on the gear peripheral surface obtained by converting Dawson's empirical equation [31] is given as follows:

$$
\begin{aligned}
C_{M,peri,in} &= 20.90 \, \mathrm{Re}_{in}^{-0.1} \left(\frac{B}{r_{f,in}} \right)^{-0.25} \left(\frac{M_g}{r_{f,in}} \right)^{1.15} \\
C_{M,peri,out} &= 20.90 \, \mathrm{Re}_{out}^{-0.1} \left(\frac{B}{r_{f,out}} \right)^{-0.25} \left(\frac{M_g}{r_{f,out}} \right)^{1.15}
\end{aligned}
\tag{6.36}
$$

where Re_{in} and Re_{out} are the rotational Reynolds number of the input gear and the rotational Reynolds number of the output gear, respectively, and are defined by the following equations.

$$
\begin{aligned}
\mathrm{Re}_{in} &= \frac{\omega_{in} r_{f,in}^2}{\nu_{air}} = \frac{r_{f,in} v_f}{\nu_{air}} \\
\mathrm{Re}_{out} &= \frac{\omega_{out} r_{f,out}^2}{\nu_{air}} = \frac{r_{f,out} v_f}{\nu_{air}}
\end{aligned}
\tag{6.37}
$$

(ii) Rotational Moment Coefficient at the Gear Side Surfaces
An empirical formula for the rotational moment coefficient at the sides of gear obtained by converting Dawson's empirical formula [31] is shown as follows:

$$
\begin{aligned}
C_{M,sides,in} &= 44.10 \, \mathrm{Re}_{in}^{-0.55} \left(1 - \frac{D_a}{D_f} \right) \\
C_{M,sides,out} &= 44.10 \, \mathrm{Re}_{out}^{-0.55} \left(1 - \frac{D_a}{D_f} \right)
\end{aligned}
\tag{6.38}
$$

where D_f is the diameter of the bottom circle of the tooth, and D_a is the diameter of the shaft. The term "$1 - D_a/D_f$" in the equation represents the reduction in the pumping work on the sides of the gear due to the presence of the shaft. The formulation of the function was determined by comparison with the experimental results of the two-axis helical gearbox in this research.

(iii) Validation of the Equation for the Rotational Moment Coefficient
To confirm the validity of Eq. 6.36 for the rotational moment coefficient on the gear peripheral surface and Eq. 6.38 for the rotational moment coefficient on the gear side surfaces, Fig. 6.4-1 shows a comparison between the experimental results [31] and the calculation results[*1]. In Fig. 6.4-1 , the measurement error

---

[*1] The shroud coefficient (Section 6.4.6) and the angular fraction of the gear peripheral part (Section 6.4.7) were both set to 1

is indicated by error bars, and ± 15% of the practical error is indicated by broken lines. The figure shows that the calculation results of air vortex loss are approximately within the practical error range, considering the range of measurement error, and it was found that Eqs. 6.36 and 6.38 are valid.

(a) Gear periphery

(b) Gear sides
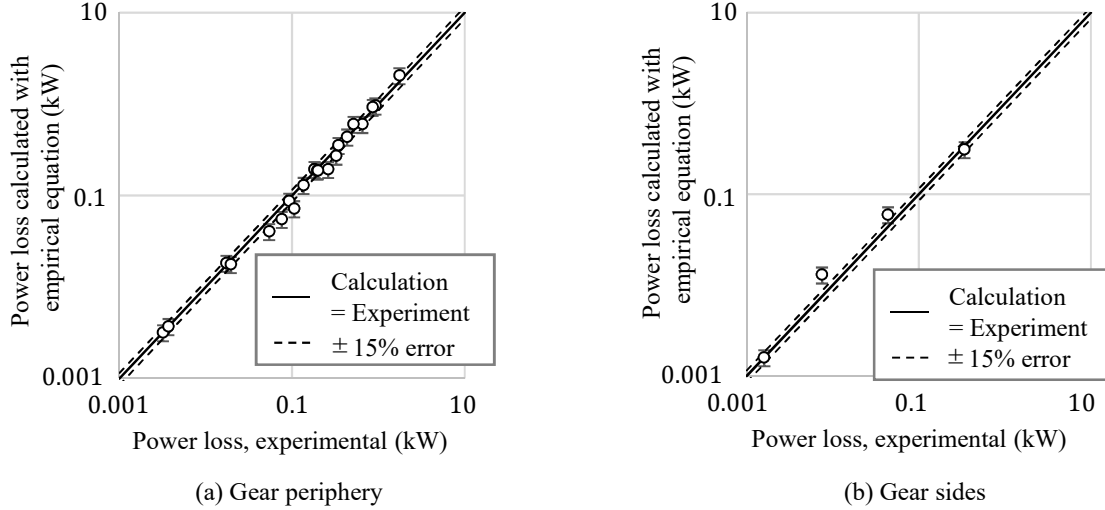
Fig. 6.4-1 Validation of the empirical equations of air vortex loss on the gear periphery and sides (air vortex loss model)

6.4.4 Characteristics of the Rotational Moment Coefficient on the Gear Peripheral Surface

In Fig. 6.4-2 (a), the rotational moment coefficient $C_{M,peri}$ on the gear peripheral surface with the changes in Reynolds number is compared with the experimental result of Furukawa et al. [119] on the moment coefficient of a cylinder.

Fig. 6.4-2 (a) shows the experimental result of the coefficient of rotational moment on the gear peripheral surface with different modules extracted from the experimental result of Dawson [31], excluding the aerodynamic loss on the sides of the gear. Figure 6.4-2 (a) shows the experimental result of Furukawa et al. on the moment coefficient of a cylinder and "a cylinder with rivets".

The dimensionless sizes of a cylinder and a riveted cylinder are compared with dimensionless sizes of the corresponding gear in Fig. 6.4-2 (b). In Eq. 6.36 of the rotational moment coefficient of the peripheral surface if the gear, the exponent 1.15 for module M_g is larger in the magnitude than the exponent -0.25 for the tooth width B. Therefore, considering the module as a parameter that mainly affects the rotational moment coefficient, we focus on the parameters corresponding to the module considered as h_R/r_d (in the case of the riveted cylinder) and h/r_f (in the case of the gear).

The gear close to h_R/r_d of the riveted cylinder is "③ Gear module 16" from Fig. 6.4-2 (b) (gray cell in the table of Fig. 6.4-2 (b)). However, the riveted cylinder is surrounded by shrouds, whereas the gears of ③ do not have a shroud. Therefore, the shroud coefficient corresponding to the relative clearance C_{rr}/r_d of the riveted cylinder is corrected using 0.27 obtained from the equation of the shroud coefficient shown in Section 6.4.6. The gear with the correction with the shroud coefficient is shown in "④ Gear module 16" in Fig. 6.4-2 (a).

---

according to the experimental conditions. The effect of the diameter of the shaft was ignored because it was as small as 2–8% of the gear diameter.

Parameter	Cylinder	Riveted cylinder	①Gear, module 2	②Gear, module 8	③Gear, module 16
B/r_d	0.12	0.064	-	-	-
B/r_f	-	-	0.73	0.73	0.73
h_R/r_d	0	0.16	-	-	-
h/r_f	-	-	0.017	0.070	0.14
C_{rr}/r_d	0.02	0.02	-	-	-
C_{rr}/r_f	-	-	∞	∞	∞

(a) Rotational moment coefficients $C_{M,peri}$ on gear periphery vs. rotational Reynolds number

Riveted cylinder parameters

Gear parameters
h: tooth height, r_f: tooth bottom radius, λ: shroud coefficient, B: width, C_{rr}: clearance between gear tip and shroud

$L_R/d_R=1.116$

(b) Comparisons of a gear and a riveted cylinder

Fig. 6.4-2 Experimental rotational moment coefficients on gear periphery vs. rotational Reynolds number (air vortex loss model)

The comparison of the riveted cylinder and the "④ Gear module 16" shows that the coefficient of rotational moment of the gear is larger than that of the riveted cylinder; furthermore, the slope of the rotational moment coefficient with respect to the Reynolds number changes is more mild than that of the riveted cylinder.

The rotational moment coefficient of the "④ Gear module 16" is larger than that of the riveted cylinder because the air drag of the gear is larger than that of the riveted cylinder because the gear is angularly shaped.

On the reason that the slope of the rotational moment coefficient with respect to the Reynolds number changes of "④ Gear module 16" is more mild than that of the riveted cylinder, we consider it based on the air vortex in the tooth valley. The air vortex in the gear tooth valley is a flow that is characteristically generated in the peripheral surface of the gear, as shown in Fig. 5.1-3 (c). The slope of the rotational moment coefficient with respect to the Reynolds number changes of the gear is mild because the size of the air vortex depends on the size of the gear tooth valley, and the size of the gear tooth valley is not affected by the Reynolds number.

6.4.5   Characteristics of the Rotational Moment Coefficient on the Sides of the Gear

The rotational moment coefficient on the sides of the gear $C_{M,sides}$ with respect to the Reynolds number changes is compared with the rotational moment coefficient of a disk [118], as shown in Fig. 6.4-3 (a). The rotational moment coefficient of the gear in Fig. 6.4-3 (a) is calculated using Eq. 6.38.

The experimental results of the disk shown in Fig. 6.4-3 (a) indicate that the moment coefficient increases as the axial non-dimensional velocity $v_\infty/\omega R$ (v_∞ is axial air velocity toward the disk, and R is the disk radius) of air toward the disk increases. This could be because the air pumping work (the work of air sucking in from the axis center and air flowing out to the periphery) of the disk as shown in Fig. 6.4-3 (b) increases as the axial air velocity increases.

(a) Rotational moment coefficient $C_{M,sides}$
on gear sides vs. rotational Reynolds number

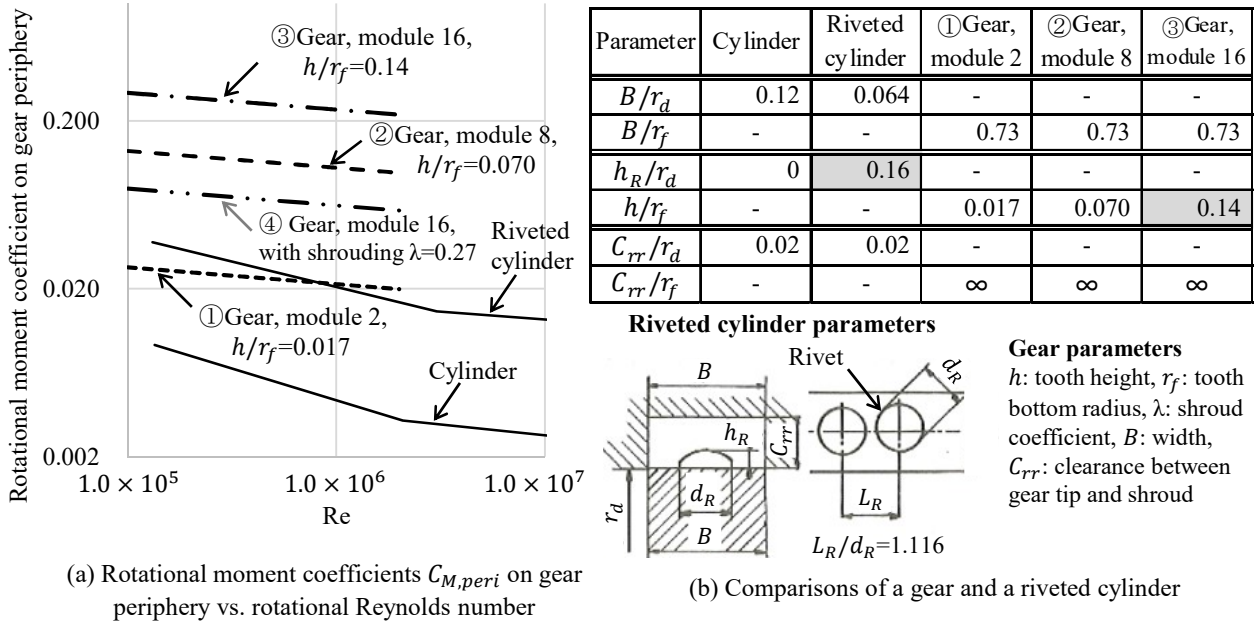(b) Schematic of velocity distribution around
a rotating disk (Schlichting [118])
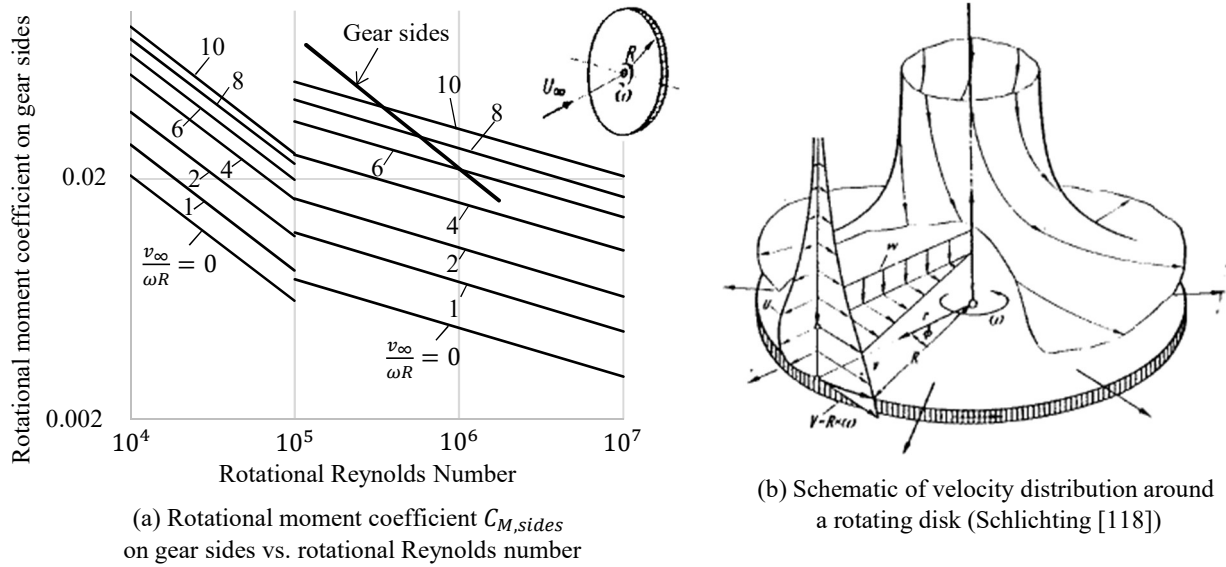
Fig. 6.4-3 Experimental rotational moment coefficients on gear sides vs. rotational Reynolds number (air vortex loss model)

The rotational moment coefficient on the sides of the gear tends to rapidly reduce with increasing Reynolds number in comparison with the rotational moment coefficient of the disk with constant axial flow velocity. This is because, for example, when the rotational speed of the gear increases, the efficiency of the pumping work of the gear decreases by an increase of the flow drag.

6.4.6   Modeling of Shroud Effect (Development of Empirical Equation for Shroud Coefficient)

By enclosing the gear with a shroud, the flow structure on the gear peripheral surface ((c1) in Table 6.1-1)) and the flow structure on the gear side surfaces can be suppressed ((c2) in Table 6.1-1). The shroud coefficient is defined as the loss reduction ratio for the aerodynamic loss without a shroud and is an important index for suppressing the flow structure. The experimental results of the shroud coefficient by Dawson [31] are shown in Fig. 6.4-4 .

In Fig. 6.4-4 , "a" is without a shroud and is a base for aerodynamic loss (it is set to 100%), "b" is similar to "a" but with a rough side plate of 1.2 m × 1.2 m spaced 27 mm from each side of the gear, "c" is similar to "b" but with the four outer faces also enclosed with rough surfaces, "d " is similar to "a" but with the rough cylindrical shroud enclosing 270 ° of the gear and spaced 30 mm from gear tooth tips, "e" is similar to "b" and "d " combined, "f " is similar to "e" but is a smooth cylindrical shroud enclosing 270 ° of the gear and spaced 15 mm from gear tooth tips, "g" is similar to "f" but is a smooth shroud totally enclosing the gear and spaced 15 mm from tooth tips, and "h" is similar to "b" but the ends of teeth are shrouded by a stationary "washer" spaced 8 mm off the ends of the teeth. Figure 6.4-4 shows the loss reduction ratio for each shroud shape.
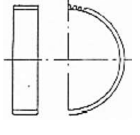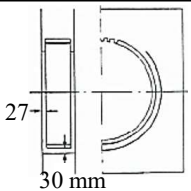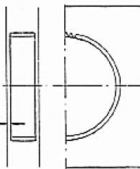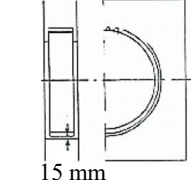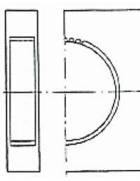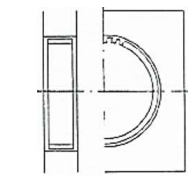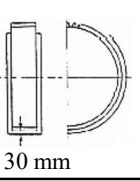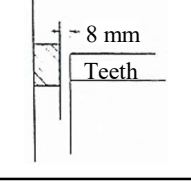
	Description	Aerodynamic power loss (a gear in free space is 100%)		Description	Aerodynamic power loss (a gear in free space is 100%)
a	760 mm root diameter, 187 mm facewidth, 8 mm module gear running in free space.	100	e	"b" and "d" combined (27—, 30 mm)	57
b	As "a" but with a rough side plate 1.2 mm square spaced 27 mm from each side of gear. (27—)	81	f	As "e" but smooth cylindrical shroud enclosed 270° of gear and spaced 15 mm from gear tooth tips. (15 mm)	53
c	As "b" but with the four outer faces also enclosed with rough surfaces.	66	g	As "f" but smooth shroud totally enclosing gear and spaced 15 mm from tooth tips.	34
d	As "a" but with rough cylindrical shroud enclosed 270° of gear and spaced 30 mm from gear tooth tips. (30 mm)	86	h	As "b" but ends of teeth shrouded by a stationary 'washer' spaced 8 mm off the ends of the teeth. (8 mm, Teeth)	79

Fig. 6.4-4 Experimental results of the aerodynamic loss reduction by shrouding [31]

In Dawson's experimental results of the shroud coefficient [31], no empirical equation of the shroud coefficient is presented. Therefore, in this study, an empirical equation is developed to generalize the experimental results.

The shroud coefficient λ is defined by the following equation, which divides the shroud coefficient of the gear peripheral surface into $\lambda_{\theta r}$ and the shroud coefficient of the gear side surfaces into λ_x.

$$\lambda = \kappa \lambda_{\theta r} + (1 - \kappa)\lambda_x \tag{6.39}$$

where κ represents the fraction of air vortex loss on the gear peripheral surface.

The radial relative clearance R_r, peripheral opening ratio R_θ, axial relative clearance R_x, and side wall coefficient R_{w_eff} (coefficients related to the presence or absence of side walls) are set as dimensionless numbers of the shroud shape. R_r, R_θ, R_x, and R_{w_eff} are given as follows:

$$R_r = \frac{2C_{rr}}{D_p} \tag{6.40}$$

$$R_\theta = \frac{\sum_i \Delta\theta_{op,i}}{2\pi} \tag{6.41}$$

$$R_x = \frac{2C_{rx}}{B} \tag{6.42}$$

$$R_{w\_eff} = \begin{cases} \text{the width of peripheral wall of the shroud}/B & \text{(without side walls of the shroud)} \\ \infty & \text{(with side walls of the shroud)} \end{cases} \tag{6.43}$$

where $\sum_i \Delta\theta_{op,i}$ is the total peripheral opening angle of the shroud (per gear).

We assume that $\lambda_{\theta r}$ and λ_x can be approximated by an exponential function. The detailed form of the approximate equations was set to agree with the experimental results. The approximate equations are shown below:

$$\lambda_{\theta r} = a_w{}^{-b_w R_{w\_eff}}(1 - \lambda'_{\theta r}) + \lambda'_{\theta r} \tag{6.44}$$

$$\lambda'_{\theta r} = (\lambda_r - 1)(1 - R_\theta)^{n_\theta} + 1 \tag{6.45}$$

$$\lambda_r = (1 - a_r{}^{-b_r R_r})^{n_r} \tag{6.46}$$

$$\lambda_x = (1 - a_x{}^{-b_x R_x})^{n_x} \tag{6.47}$$

where a_w, a_r, and a_x are coefficients and b_w, n_θ, b_r, n_r, b_x, and n_x are exponents, which are determined using the least squares method.

A comparison of the calculated shroud coefficients with the experimental results is shown in Fig. 6.4-5 . The values of the coefficients used in the experimental equations are shown in Table 6.4-1 . The experimental equations (Eqs. 6.39–6.47) and coefficients (Table 6.4-1) for the shroud coefficients were valid because the calculated and experimental results agreed well.

According to Eqs. 6.39–6.47, the parameters that mainly affect the shroud coefficient λ are the ratio of the radial clearance C_{rr} between the gear and the shroud and the gear diameter D_p, the ratio of the axial clearance C_{rx} to the tooth width B, and the peripheral opening angle $\Delta\theta_{op}$.

Fig. 6.4-5 Validation of the empirical equations for the shroud coefficient
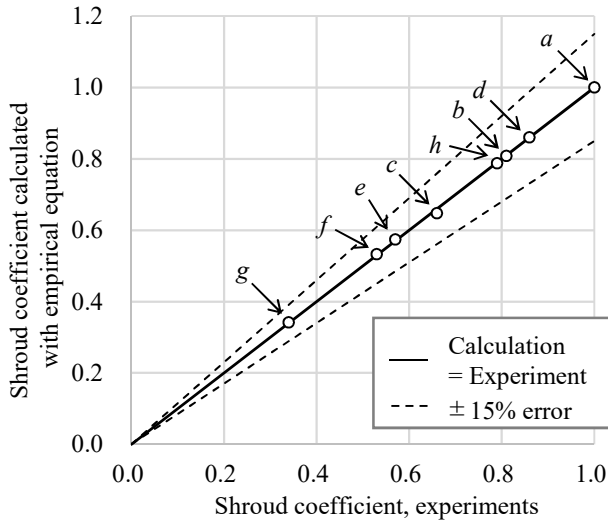
Table 6.4-1 Values of the coefficient in the empirical equations for the shroud coefficient

Parameter	Value
κ	0.7875
a_w	3.5295
b_w	0.5627
n_θ	1.8365
a_r	53.3096
b_r	0.3186
n_r	0.2942
a_x	12.8704
b_x	2.6370
n_x	15.3235

6.4.7   Angle Range Coefficient of Gear Peripheral Part

The angle range coefficient ϵ_θ of the gear peripheral part indicates the ratio of the peripheral angle of the gear peripheral part to the entire periphery to which the air vortex loss model is applied. A schematic diagram is shown in Fig. 6.4-6 .

Two points where the input gear tip circle and the output gear tip circle intersect are determined, and these points are set as the starting and ending points, respectively. The range not including the gear meshing part as indicated by the arrows in the figure is defined as the range where the air vortex loss model applies. $\epsilon_{\theta,in}$ and

$\epsilon_{\theta,out}$ are shown below.

$$\epsilon_{\theta,in} = \frac{1}{2\pi} \times 2\cos^{-1}\left\{\frac{L_a{}^2 + (D_{t,in}/2)^2 - (D_{t,out}/2)^2}{2L_a(D_{t,in}/2)}\right\} \tag{6.48}$$

$$\epsilon_{\theta,out} = \frac{1}{2\pi} \times 2\cos^{-1}\left\{\frac{L_a{}^2 + (D_{t,out}/2)^2 - (D_{t,in}/2)^2}{2L_a(D_{t,out}/2)}\right\} \tag{6.49}$$

where D_t is the diameter of the tooth tip circle.
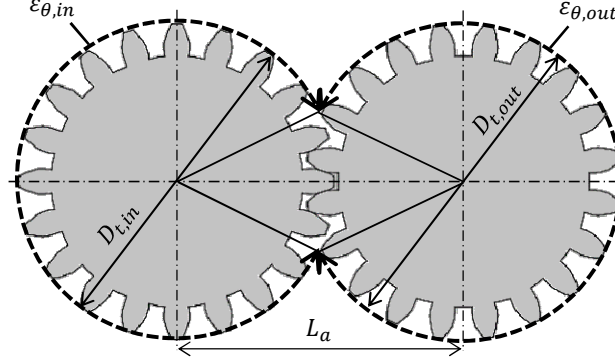
Fig. 6.4-6 The range of angle to which the air vortex loss model applies

6.4.8   Key Parameters of the Air Vortex Loss Model

In the air vortex loss equation, i.e., Eq. 6.35, the loss on the gear peripheral surface $P_{v,peri,*}$ is considered to be larger than the loss on the gear side surfaces $P_{v,sides,*}$ due to the peaks and valleys of the gear teeth. Therefore, we consider the main parameters of loss $P_{v,peri,*}$ on the gear peripheral surface.

Extracting the main parameters from $P_{v,peri,*}$ (Eq. 6.32) gives the following:

$$P_{v,peri,*} \propto C_{M,peri,*}\rho_{air}Br_{f,*}v_f{}^3\lambda \tag{6.50}$$

Here, we extract the main parameters of the rotational moment coefficients $C_{M,peri,*}$ of the gear peripheral surface and consider the main parameters of $P_{v,peri,*}$ together with the above equations. Extracting the main parameters from the equations of $C_{M,peri,*}$ (Eq. 6.36) and rotational Reynolds number (Eq. 6.37) gives the following equation:

$$C_{M,peri,*} \propto (r_{f,*}v_f)^{-0.1}B^{-0.25}M_g{}^{1.15}r_{f,*}{}^{-0.9} \propto r_{f,*}{}^{-1}v_f{}^{-0.1}B^{-0.25}M_g{}^{1.15} \tag{6.51}$$

From Eqs. 6.50 and 6.51,

$$P_{v,peri,*} \propto \rho_{air}B^{0.75}M_g{}^{1.15}v_f{}^{2.9}\lambda \tag{6.52}$$

we get that $B^{0.75}M_g{}^{1.15}$ is correlated with tooth area Bh ($\because h \propto M_g$). As a result, the main parameters of $P_{v,peri,*}$ are shroud coefficient λ, (2.9th power of) peripheral speed $v_f{}^{2.9}$, tooth area Bh, and air density ρ_{air}. The parameters that mainly affect λ are the ratio of the radial clearance C_{rr} to the pitch circle diameter D_p, the ratio of the axial clearance C_{rx} to the tooth width B, and the peripheral opening angle $\Delta\theta_{op}$.

6.5 Oil-Jet Acceleration Loss Model

6.5.1 Phenomena Focused on the Oil-Jet Acceleration Loss Model

Figures 5.2-4 and 5.2-5 validating the acceleration phenomenon of the oil supplied to the gear meshing part showed that oil is accelerated to the gear peripheral speed and that the loss due to acceleration can be theoretically predicted. In the oil-jet acceleration loss model, we focus on the acceleration phenomena of the oil supplied to the gear meshing part.

6.5.2 Mass Flow Rate at which the Gear Accelerates and the Force Loaded on the Gear by the Acceleration

The mass flow rate $\dot{m}_{jac}$ at which the gear accelerates is given by the following equation, where ρ_{oil} is the density of the oil and Q_s is the supply flow rate of the oil (total of the into-mesh and out-of-mesh jets).

$$\dot{m}_{jac} = \rho_{oil} Q_s \tag{6.53}$$

The force F_{jac} loaded on the gear when the gear accelerates the supplied oil is generated by the rotation of gear teeth accelerating the mass flow rate $\dot{m}_{jac}$ from the jet speed v_{jet} to the gear peripheral speed v_p in the direction perpendicular to the surface of the tooth. This is shown in the following equation.

$$F_{jac} = \rho_{oil}\frac{Q_s}{2}(v_p - v_{jet})\cos\beta + \rho_{oil}\frac{Q_s}{2}(v_p + v_{jet})\cos\beta = \rho_{oil}Q_s v_p \cos\beta \tag{6.54}$$

Here, $v_p - v_{jet}$ is the speed increase of the oil jet from the into-mesh side to the gear meshing, and $v_p + v_{jet}$ is the speed increase of the oil jet from the out-of-mesh side to the gear meshing. In these speed increases, a speed difference is generated by the oil jet speed v_{jet}. When the oil jet is injected from the into-mesh side and the out-of-mesh side at the same jet speed, these speed differences are canceled. Here, β is the helix angle of the helical gear teeth.

6.5.3 Gear Rotational Torque, Oil-Jet Acceleration Loss

Assuming that the force loaded on the gear is equally divided between the input and output gears, the gear rotational torque is given by the following equation.

$$T_{jac,in} = \frac{1}{2}\rho_{oil}Q_s v_p r_{p,in}\cos\beta$$
$$T_{jac,out} = \frac{1}{2}\rho_{oil}Q_s v_p r_{p,out}\cos\beta \tag{6.55}$$

The oil-jet acceleration loss P_{jac} is given by the following equation:

$$P_{jac} = F_{jac}v_p = \sum_{*=in,out} T_{jac,*}\omega_* = \rho_{oil}Q_s v_p{}^2 \cos\beta \tag{6.56}$$

6.5.4 Key Parameters of the Oil-Jet Acceleration Loss Model

Equation 6.56 shows that the main parameters of the oil-jet acceleration loss are the oil supply flow rate Q_s and the (second power of) peripheral speed $v_p{}^2$.

6.6   Oil Reacceleration Loss Model

6.6.1   Phenomena Focused on the Oil reacceleration loss Model

Figure 5.2-1 (f) showed that the supplied oil is accelerated at the gear meshing part, and then, part of the oil re-flows into the gear meshing part. Figure 5.2-6 shows that the oil re-flowing into the gear meshing part is re-accelerated at the gear meshing part. In the oil reacceleration loss model, we focus on the process of accelerating the oil that reflows into the gear meshing part.

6.6.2   Mass Flow Rate of Oil at which Gear Accelerates, Force due to Oil Re-acceleration, Gear Rotational Torque, and Oil reacceleration loss

In the oil reacceleration loss model, the oil re-inflow rate to the gear meshing part is defined based on the oil-jet acceleration loss model, and the loss due to the oil acceleration is considered.

The ratio of the oil re-inflow rate to the oil supply flow rate is defined as the oil reacceleration coefficient χ_{re} as follows:

$$\chi_{re} = Q_{re}/Q_s \tag{6.57}$$

The mass flow rate churned by the gear is given as

$$\dot{m}_{rac} = \chi_{re}\rho_{oil}Q_s \tag{6.58}$$

The force loaded on the gear is given by the following equation, assuming that it is similar to Eq. 6.54.

$$F_{rac} = \chi_{re}\rho_{oil}Q_s v_p \cos\beta \tag{6.59}$$

Assuming that the force loaded on the gear is equally divided between the input and output gears, the gear rotational torque is given by the following equation:

$$
\begin{aligned}
T_{rac,in} &= \frac{1}{2}\chi_{re}\rho_{oil}Q_s v_p r_{p,in}\cos\beta \\
T_{rac,out} &= \frac{1}{2}\chi_{re}\rho_{oil}Q_s v_p r_{p,out}\cos\beta
\end{aligned}
\tag{6.60}
$$

The oil reacceleration loss P_{rac} is given by the following equation:

$$P_{rac} = F_{rac}v_p = \sum_{*=in,out} T_{rac,*}\omega_* = \chi_{re}\rho_{oil}Q_s v_p{}^2\cos\beta \tag{6.61}$$

6.6.3   Oil Reacceleration Coefficient

The oil reacceleration coefficient χ_{re} is related to the oil discharge from the shroud openings. Figure 6.6-1 shows the modeling of the oil discharge from the shroud openings.

Figure 6.6-1 (a) shows a schematic diagram of oil supply, oil discharge from the shroud openings, and oil reflow into the gear meshing part. The oil supplied at the oil supply flow rate Q_s moves in the peripheral direction with gear rotation, and a part of the oil is discharged from the shroud openings. Here, the flow rate of the oil that is not discharged from the opening of the input gear shroud but re-flows into the gear meshing part is denoted as $Q_{re,in}$. Similarly, the flow rate of the oil that is not discharged from the opening of the output gear shroud but

re-flows into the gear meshing part is denoted as $Q_{re,out}$. In the next gear rotation, the reflowed oil in addition to the supplied oil flows into the gear meshing. To obtain the steady oil re-inflow rate, the recurrence equation of the oil supply flow rate and the oil reflow rate must be solved. In the following paragraphs, after first modeling the oil discharge from the shroud openings, we have developed recurrence equations for calculating the oil re-inflow rate, and the oil re-inflow rate is calculated.

(a) Schematic of oil supply, oil discharge from shroud openings, and re-inflow to gear meshing region

(b) Modeling of oil discharge rate and oil re-inflow rate (per gear)
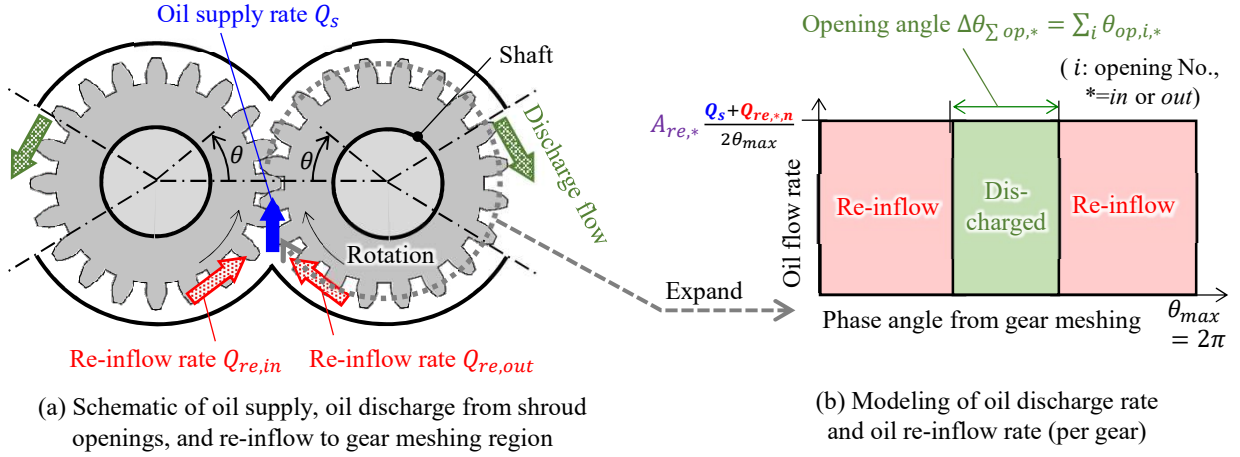
Fig. 6.6-1 Modeling of the oil discharge from the shroud openings (oil reacceleration loss model)

Modeling of the ratio of oil discharged from the shroud openings is shown in Fig. 6.6-1 (b). For simplicity, the oil re-inflow for each gear is considered. The horizontal axis indicates the phase taken from the gear meshing along the rotational direction for one gear. The shroud opening angle is set to $\Delta\theta_{op,*}$. If multiple openings exist, $\Delta\theta_{op,*}$ is set to the sum of the opening angles of each (excluding the gear meshing part) as shown by the following equation:

$$\Delta\theta_{\sum op,*} = \sum_i \theta_{op,i,*} \tag{6.62}$$

For example, if there are three openings, and the width of each is $\pi/6$ ($=30°$), then $\Delta\theta_{\sum op,*} = \pi/2$ ($=90°$).

The vertical axis indicates the flow rate per unit angle. $Q_{re,*,n}$ indicates the oil re-inflow rate to the gear meshing part, and n corresponds to the gear rotation in the recurrence equation of the oil re-inflow rate. $A_{re,*}$ is used to consider the influence of the clearance between the gear and the shroud. This is defined as the "re-inflow reduction coefficient" because it reduces the oil re-inflow rate. The contours of $A_{re,*}$ are shown in Fig. 6.6-2 .

For the re-inflow reduction coefficient $A_{re,*}$, two types of phenomena were modeled. As the first type of phenomenon, for example, when the clearance between the gear and the shroud becomes wider, the turbulence in the vicinity of the shroud wall decreases, making it easier for the oil to be discharged from the opening. To easily model this phenomenon, as shown by the horizontal axis in Fig. 6.6-2 , when the gear enclosure is narrow (Shroud c with shroud coefficient $\lambda = 0.34$ from Dawson's Experiment [31]), the oil re-inflow rate is large ($A_{re,*} = 1.0$). In contrast, when the gear enclosure is large (Shroud g with $\lambda = 0.66$ from Dawson's Experiment [31]), the oil re-inflow rate is 0 ($A_{re,*} = 0.0$). By modeling, $A_{re,*}$ is inversely proportional to the shroud coefficient λ in the range of $\lambda = 0.34$–0.66. As the second type of phenomenon, for example, when the shroud opening is extremely small, oil discharge becomes difficult. It is similar to the case when the pressure loss coefficient of the flow to the branch pipe increases [116]. For simple modeling, we used a function in which $A_{re,*}$ increases in a range in which the shroud opening angle width is less than 30 °.
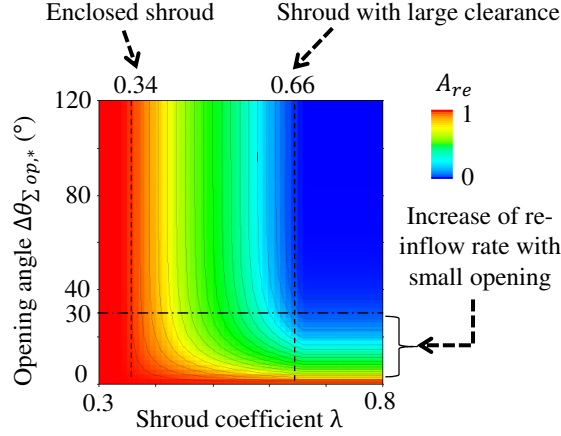
Fig. 6.6-2 Defined contour of the value of "re-inflow reduction coefficient A_{re}" (oil reacceleration loss model)

The equation for $A_{re,*}$ constructed based on the above ideas is shown as follows:

$$
\begin{aligned}
A_{re,*} = & \max\left\{0, \min\left(1.0, \frac{0.66 - \lambda_*}{0.66 - 0.34}\right)\right\} \\
& + \left[1.0 - \max\left\{0, \min\left(1.0, \frac{0.66 - \lambda_*}{0.66 - 0.34}\right)\right\} \times \exp\left(-\frac{0.52\Delta\theta_{\sum op,*}}{2\pi}\right)\right]
\end{aligned}
\tag{6.63}
$$

For the purpose of simplification, the peripheral distribution of the re-inflow rate into the gear meshing part ($Q_s + Q_{re,*,n}$ by combining the oil supply flow rate and the oil re-inflow rate) is assumed to be divided equally between the input and output gears and is assumed to be evenly distributed over the entire gear periphery, as shown in Fig. 6.6-1 (b). Then, the flow rate per unit angle becomes $A_{re,*}(Q_s + Q_{re,*,n})/(2\theta_{max})$. The oil discharge from the opening is the ratio of the total value of the opening angles $\Delta\theta_{\sum op,*}$ to the entire periphery. We assume that the rest of the oil in the shroud will re-flow into the gear meshing part. Therefore, the recurrence equation for the oil reacceleration flow rate is given as follows (the oil re-inflow flow rate is calculated for each gear for simplicity) :

$$
\begin{aligned}
Q_{re,*,n+1} &= A_{re,*}\frac{Q_s + Q_{re,*,n}}{2\theta_{max}}\left(\theta_{max} - \Delta\theta_{\sum op,*}\right) \\
&= A_{re,*}\frac{\theta_{max} - \Delta\theta_{\sum op,*}}{2\theta_{max}}(Q_s + Q_{re,*,n}) = C_{re,*}(Q_s + Q_{re,*,n})
\end{aligned}
\tag{6.64}
$$

$$
C_{re,*} = A_{re,*}\frac{\theta_{max} - \Delta\theta_{\sum op,*}}{2\theta_{max}}
\tag{6.65}
$$

We then solve the recurrence equation Eq. 6.64 of the oil re-inflow rate, which gives the following equation:

$$
Q_{re,*} = \frac{C_{re,*}}{1 - C_{re,*}}Q_s
\tag{6.66}
$$

The total flow rate Q_{re} of the oil re-inflow rate from the input gear periphery and oil re-inflow rate from the output gear periphery and oil reacceleration coefficient χ_{re} are given by the following equations:

$$
Q_{re} = Q_{re,in} + Q_{re,out} = \left(\frac{C_{re,in}}{1 - C_{re,in}} + \frac{C_{re,out}}{1 - C_{re,out}}\right)Q_s
\tag{6.67}
$$

$$
\chi_{re} = Q_{re}/Q_s = \frac{C_{re,in}}{1 - C_{re,in}} + \frac{C_{re,out}}{1 - C_{re,out}}
\tag{6.68}
$$

6.6.4   Modeling of Shroud Effects

The effect of the shroud in the oil reacceleration loss model is modeled as the sum of the shroud opening angles $\Delta\theta_{\sum op,*}$ and as the shroud coefficient λ (included in the re-inflow reduction coefficient $A_{re,*}$) in the equation of the oil reacceleration coefficient χ_{re} of Eqs. 6.65 and 6.68.

From Eqs. 6.65 and 6.66, the oil reacceleration coefficient χ_{re} decreases as the shroud coefficient λ or the sum of the shroud opening angle $\Delta\theta_{\sum op,*}$ increases. If coefficient $C_{re,*}$ is sufficiently smaller than 1, χ_{re} is inversely proportional to $A_{re,*}$ and the shroud coefficient λ.

6.6.5   Key Parameters of the Oil Reacceleration Loss Model

The key parameters of the oil reacceleration loss are the oil reacceleration coefficient χ_{re}, the oil supply flow rate Q_s, and the (second power of) peripheral speed $v_p{}^2$, as shown in Eq. 6.61. The main parameters of the oil reacceleration coefficient χ_{re} are the peripheral opening angle $\Delta\theta_{op,*}$ and shroud coefficient λ.

6.7   Oil Churning Loss Model

6.7.1   Phenomena Focused on the Oil Churning Loss Model

In the oil churning loss model, the oil dynamic loss caused by oil being drawn in (Fig. 5.2-7 (a)) and blowing up (Fig. 5.2-7 (b)) by the airflow around the gear is considered. In addition, for the amount of oil adhering to the gear surface (Fig. 5.2-7 (c)) with the changes in the oil supply flow rate, we found that the amount of oil adhering to the gear surface increases with an increase in the oil supply flow rate and that the rate of increase on the large oil supply flow rate is lower than that on the small oil supply flow rate. This change in the rate of increase in the amount of oil adhering to the gear surface is considered in the oil churning loss model.

6.7.2   Oil Churning Loss

We assume that the apparent density of air increases due to oil entrapment in the airflow. If the ratio of the apparent fluid density around the gear to the air density is Φ_* and the air vortex loss is $P_{v,*}$, the oil churning loss P_{ch} is given by the following equation:

$$\begin{aligned} P_{v,*} + P_{ch,*} &= \Phi_* P_{v,*} \\ P_{ch,*} &= (\Phi - 1)_* P_{v,*} \end{aligned} \tag{6.69}$$

$$P_{ch} = \sum_{*=in,out} (\Phi - 1)_* P_{v,*} \tag{6.70}$$

The ratio "$\Phi - 1$" of the oil churning loss to the air vortex loss of the above equation is called the oil mist coefficient, and the prediction equation is given as follows.

6.7.3 Oil Mist Coefficient

6.7.3.1 Overview of Oil Mist Coefficient

Considering that oil mist coefficient and the amount of oil around the gear are correlated, an estimation method of the amount of oil around the gear is developed.

We found that the amount of oil on the gear surface increases as the oil supply flow rate increases, and that the rate of increase on the large oil supply flow rate is lower than that on the small oil supply flow rate (Fig. 5.2-7 (c)). Therefore, the function constituting the oil mist coefficient is divided into a small flow rate function $f_{A,*}$ when the oil supply flow rate is small, and a large flow rate function $f_{B,*}$ when the oil supply flow rate is large.

The equation of the oil mist coefficient is given as follows using the small flow rate function $f_{A,*}$, the large flow rate function $f_{B,*}$, the transition function H_* between the small flow rate function and the large flow rate function, and the shroud influence coefficient $(0.405/\lambda_*)^2$ (Details of $f_{A,*}$ are described in Section 6.7.3.2, details of $f_{B,*}$ are described in Section 6.7.3.3, details of H_* are described in Section 6.7.3.4, and details of $(0.405/\lambda_*)^2$ are described in Section 6.7.3.5).

$$(\Phi - 1)_* = \{(1 - H_*)f_{A,*} + H_* f_{B,*}\} \left(\frac{0.405}{\lambda_*}\right)^2 \tag{6.71}$$

The oil churning loss is calculated from Eq. 6.70 using the oil mist coefficient $(\Phi - 1)_*$ in the above equation and the air vortex loss $P_{v,*}$.

6.7.3.2 A Small Flow Rate Function in the Case where the Oil Supply Flow Rate is Small

The small flow rate function $f_{A,*}$ is constructed by applying the experimental results of the one-axis spur gearbox (GB3) to the two-axis helical gearbox (GA).

The experimental results show that the oil churning loss P_{ch} of the one-axis spur gearbox (GB3) is 1.57 kW. The air vortex loss P_v was 0.323 kW from the numerical simulation results. Using these, the oil mist coefficient $\Phi - 1$ in the one-axis spur gearbox (GB3) becomes the following:

$$\Phi - 1_{\text{one-axis spur}} = \frac{1.57}{0.323} = 4.86 \tag{6.72}$$

In the application of the one-axis spur gearbox (GB3) to the two-axis helical gearbox (GA), the difference between the one-axis spur gearbox and the two-axis helical gearbox is modeled. The modeling image is shown in Fig. 6.7-1 . As the difference between the one-axis spur gearbox and the two-axis helical gearbox, the difference between the shroud openings ("Ⓐ" in Fig. 6.7-1) and that between the oil supply flow rates ("Ⓑ" in Fig. 6.7-1) are focused on.

With respect to the difference in the shroud openings ("Ⓐ" in Fig. 6.7-1), Fig. 5.1-6 shows that the flow from the shroud opening close to the out-of-mesh side of the gear meshing part considerably disturbs the air in the gearbox. That is, the airflow near the opening close to the out-of-mesh side has large turbulence, and this turbulence of air diffuses the oil; it is thought to be lower than the amount of oil discharged from the shroud opening.
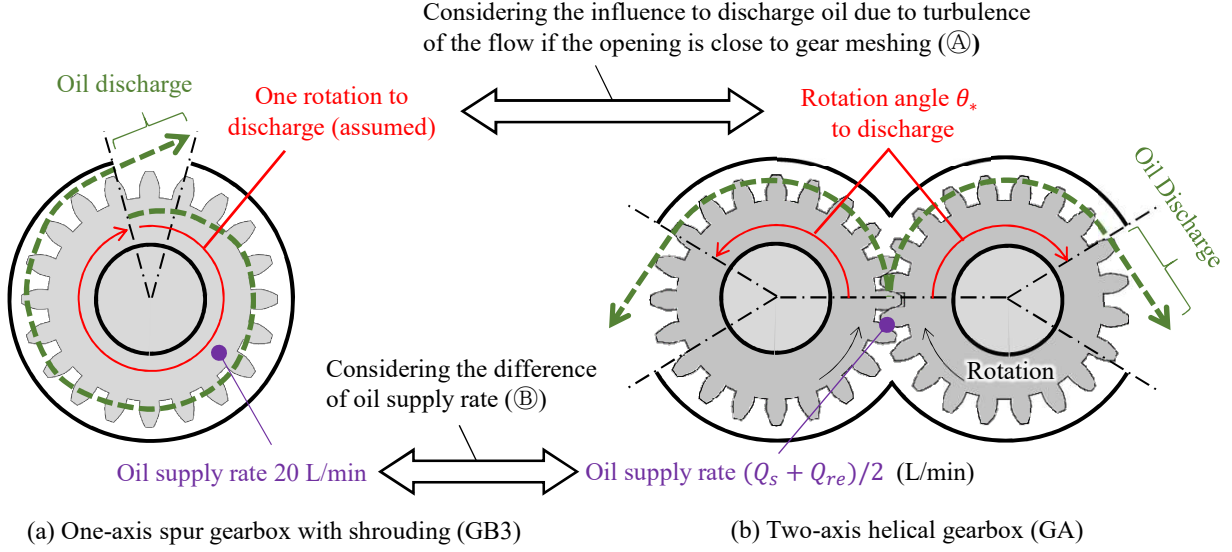
Fig. 6.7-1 "Small flow function $f_{A,*}$" in oil mist coefficient $\Phi - 1$ obtained by the conversion of the experimental result in one-axis spur gearbox to that in the two-axis helical gearbox

We model the reduction in the oil discharging ability of the shroud opening close to the out-of-mesh side of the gear meshing part by the ratio of the phase from the gear meshing to the opening against whole periphery. For the two-axis helical gearbox, the phase from the gear meshing to the opening is the average value of the input and output gears. For the one-axis spur gear box, because the opening is located at only one place and the oil is supplied on the inner peripheral side of the gear, we assume that the oil flows at one rotation from oil supply to discharge, and the phase of the opening is set to 360 $^\circ$ ($= 2\pi$).

The conversion coefficient of the shroud opening position from the one-axis spur gearbox to the two-axis helical gearbox is $E_{ff\_ch,*}$, and the phase from the gear meshing to each opening of the shroud is $\theta_{*,i}$; the number of openings is $n_{op,*}$. Then, $E_{ff\_ch,*}$ is given by the following equation.

$$E_{ff\_ch,*} = \frac{1}{n_{op,*}} \sum_{i=1}^{n_{op,*}} \frac{\theta_{*,i}}{2\pi}, \ \ (* = in, out) \tag{6.73}$$

Next, consider the difference in the oil supply flow rate ("$\textcircled{B}$" in Fig. 6.7-1). The oil supply flow rate of the one-axis spur gearbox is 20 L/min, and that of the two-axis helical gearbox is $(Q_s + Q_{re})/2$ (per gear). Therefore, the conversion coefficient of the oil supply flow rate is assumed to be the flow rate ratio $\{(Q_s + Q_{re})/2\}/20$.

From the above, the small flow rate function $f_{A,*}$ of the oil mist coefficient $\Phi - 1$ is given by the following equation[*2].

$$f_{A,*} = 4.86 \frac{1}{E_{ff\_ch,*}} \frac{(Q_s + Q_{re})/2}{20} = \alpha_{ch,*}(Q_s + Q_{re}) = \alpha_{ch,*}Q', \ \ (* = in, out)$$
$$\alpha_{ch,*} = \frac{0.122}{E_{ff\_ch,*}}, \ Q' = Q_s + Q_{re} \tag{6.74}$$

The conversion coefficient of the shroud opening position $E_{ff\_ch,*}$ is incorporated as an inverse number in the above equation because the closer the shroud opening is to the gear meshing part, the smaller the $E_{ff\_ch,*}$ and the larger the oil mist coefficient.

[*2] $f_{A,*}$ is a dimensionless number. Because the unit of Q' is m^3/s (SI unit), coefficients $\alpha_{ch,*}$ have units of s/m^3.

6.7.3.3   A Large Flow Rate Function in the Case where the Oil Supply Flow Rate is Large

The large flow rate function $f_{B,*}$ is constructed by applying the experimental results of the previous research to the two-axis helical gearbox (GA).

Because the oil mist coefficient is considered to be associated with the amount of oil on the gear surface, the measurement result of the oil film thickness of the oil attached to the gear when oil is sprayed on the gear (Terajima et al. [120]) is used. This is shown in Fig. 6.7-2 . The gear specifications and experimental conditions are shown in Table 6.7-1 .

The left of Fig. 6.7-2 (a) shows a photograph of the spray observed from the lateral direction of the gear, and the right shows a photograph seen from the axial direction. The diameter of the spray at the gear position is estimated to be ∼55 mm from the photograph. Because the spray diameter is larger than the tooth width of 20 mm, only a part of the sprayed oil reaches the gear surface. The spray area normal to the gear axial direction is estimated to be 50 mm × 20 mm, as shown on the right of Fig. 6.7-2 (a).

Figure 6.7-2 (b) shows the experimental results of the oil film thickness on the gear surface as the spray flow rate changes. The oil film thickness was measured using the laser-induced fluorescence (LIF) method. Each point in the figure shows the oil film thickness at 2000 s after spraying, when the oil film thickness reached almost steady state in the experiment.

(a) Visualization of an oil spray to gears   (b) Experimental results of oil film thickness
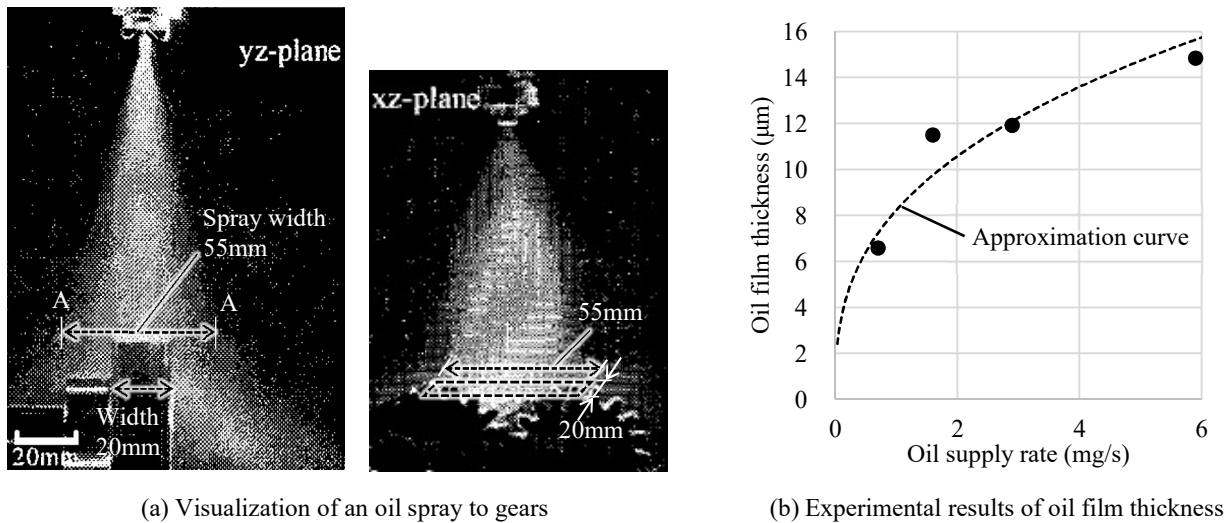
Fig. 6.7-2 Experimental results of an oil spray to gears [120]

Table 6.7-1 Gear specifications and test conditions for an oil spray to gears

Items	Parameter	Value
Gear	Module	2.5
	Number of teeth	20
	Pitch circle diameter	50 mm
	Face width	20 mm
	Rotational speed	484 rpm
Oil spray	Direction	Into-mesh
	Mass flow rate	0.7–5.9 mg/s

The flow rate of oil impinging on the gear surface is estimated from Fig. 6.7-2 . Figure 6.7-3 (a) shows the ratio of the oil spray reaching the gear surface when the radial flow rate distribution of oil is assumed to be a Gaussian distribution. In the range of the width of 20 mm (= tooth width) indicated in gray in Fig. 6.7-3 (a), the area ratio to the whole becomes 0.415. Therefore, we estimate that 41.5% of the oil spray flow rate has reached the gears. Figure 6.7-3 (b) shows the estimated real supply rate on gears for the oil film thickness on the gear surface with changes in the spray flow rate. Using the experimental results in Fig. 6.7-2 (b), the spray flow rate on the horizontal axis was multiplied by 41.5%.

(a) Estimated volume fraction of oil spray rate reaching to the gears

(b) Estimated oil spray rate reaching the gears
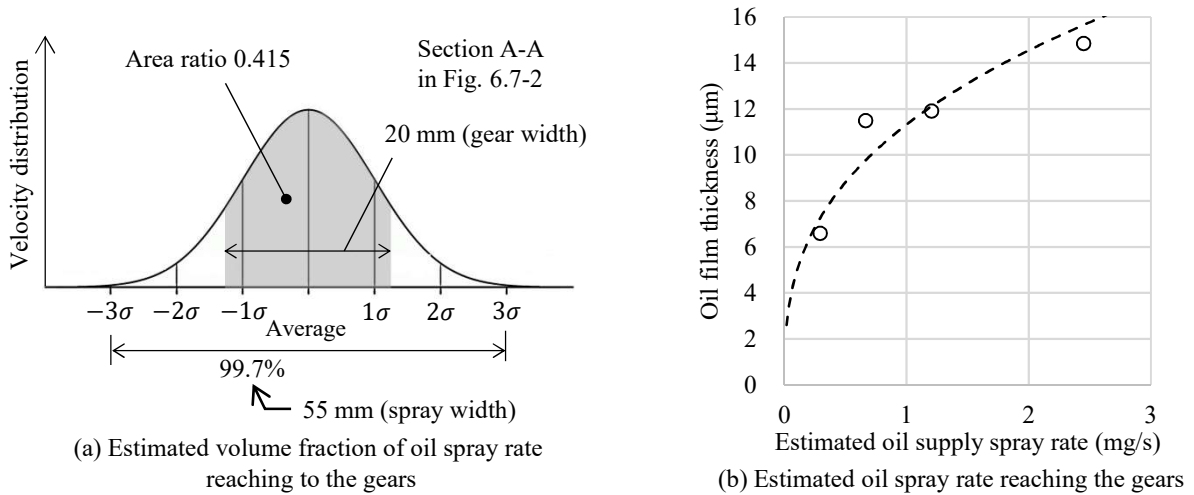
Fig. 6.7-3 An estimation of the actual oil spray rate reaching the gears

Fig. 6.7-4 "Large flow function $f_{B,*}$" obtained by converting the measured oil film thickness to the oil mist coefficient

Construction of the large flow rate function $f_{B,*}$ of the oil mist coefficient $\Phi - 1$ using the experimental results of the oil film thickness shown in Fig. 6.7-4 . The horizontal axis of Fig. 6.7-4 is defined as the non-dimensional

oil supply flow rate (see Section 5.2.4), and the definition is divided into the case of oil spray and the case of oil jet of the two-axis helical gearbox. It is given by the following equation:

$$\text{Non-dimensional oil supply flow rate} = \begin{cases} \dfrac{Q_s}{v_p B M_g} \times \dfrac{\text{sprayed area}}{\text{oil jetted area}} & \text{(for oil spray)} \\ \dfrac{Q_s}{v_p B M_g} & \text{(for oil jet)} \end{cases} \tag{6.75}$$

where Q_s is the oil supply flow rate, v_p is the pitch circle speed, B is the tooth width, and M_g is the gear module.

In Eq. 6.75, the oil supply flow rate to the two gears is used for both the oil spray and oil jet cases. In "sprayed area/oil jetted area" of Eq. 6.75, the difference in the areas of the oil reaching the gear between the oil spray and oil jet cases is considered as the area ratio.

When results of the oil spray experiment by Terajima et al. [120] are shown, the spray area is set to 50 mm × 20 mm, as shown on the right of Fig. 6.7-2 (a). The point indicated by the hollow circle in Fig. 6.7-4 indicates the experimental results of the oil film thickness and refers to the vertical axis on the right. The change in the oil film thickness when the value on the horizontal axis is 0.004 or less is different from the change in oil film thickness when it is 0.004 or more. When the value on the horizontal axis is 0.004 or less, it is referenced as a small flow rate. When it is 0.004 or more, it is referenced as a large flow rate. The approximate equation of the oil film thickness at a large flow rate is given by the following equation:

$$\text{Oil film thickness (large flow rate)} = 34.02 \left(\frac{Q_s}{v_p B M_g} \right)^{0.2} \tag{6.76}$$

This is shown by the broken line in Fig. 6.7-4 ("Modeling ①" in Fig. 6.7-4).

Because Eq. 6.76 is an equation of the oil film thickness, it must be converted to the oil mist coefficient $\Phi - 1$. Therefore, Fig. 6.7-4 shows the small flow function $f_{A,*}$ (which is the convert functi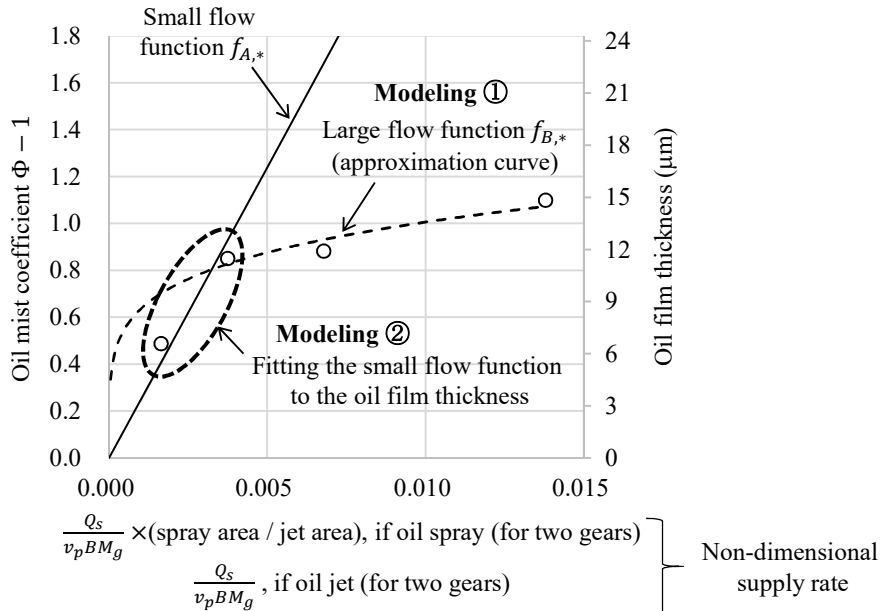on of the experimental result of the one-axis spur gearbox into the two-axis helical gearbox) as a straight line. The vertical axis of the small flow function $f_{A,*}$ is the oil mist coefficient $\Phi - 1$ and refers to the left vertical axis. At this time, the left vertical axis is adjusted to match the experimental result of the oil film thickness on the small flow rate (the horizontal axis is 0.004 or less), as shown for "Modeling ②" in Fig. 6.7-4 . Using a conversion equation from the right to left axis, the empirical Eq. 6.76 for the oil film thickness on the large flow rate can be converted to the oil mist coefficient $\Phi - 1$.

The conversion coefficient $E_{ff\_ch,*}$ must be considered for the opening position when converting the empirical equation Eq. 6.76 for the oil film thickness at the large flow rate to the oil mist coefficient $\Phi - 1$. This is because $f_{A,*}$ becomes smaller when $E_{ff\_ch,*}$ increases (when the opening position is located more downstream from the gear meshing part). Considering this, the conversion coefficient of the oil film thickness at large flow rate to the oil mist coefficient becomes "$0.1111 - 0.07407 E_{ff\_ch,*}$".

Based on the above, the large flow rate function $f_{B,*}$ is expressed as follows[*3].

$$f_{B,*} = 34.02 \left(\frac{Q_s + Q_{re}}{v_p B M_g} \right)^{0.2} (0.1111 - 0.07407 E_{ff\_ch,*}) = \beta_{ch,*} Q'^{\,0.2}, \quad (* = in, out)$$

$$\beta_{ch,*} = \frac{34.02}{(v_p B M_g)^{0.2}} (0.1111 - 0.07407 E_{ff\_ch,*}) \tag{6.77}$$

$$Q' = Q_s + Q_{re}$$

Q_{re} in the above equation was introduced to consider the effect of the oil reacceleration flow rate.

[*3] $f_{B,*}$ is a dimensionless number. Because the unit of Q' is m³/s, the coefficients $\beta_{ch,*}$ have units of $(\text{s/m}^3)^{0.2}$.

6.7.3.4 Transition Function from Small Flow Function to Large Flow Function

We set a function H that switches from the small flow function $f_{A,*}$ to the large flow function $f_{B,*}$ within a specific flow range, considering the possibility of regions in which the small flow functions $f_{A,*}$ and large flow function $f_{B,*}$ are intermingled, such as a transition from laminar flow to turbulent flow.

The transition function H is given by the following equation, where Q_{cr}' is the flow rate at the intersection of the small flow rate function $f_{A,*}$ and the large flow rate function $f_{B,*}$. $\gamma_{ch} = 3.0$ was determined through a comparison between the experimental results of oil churning loss and the calculation results by using the loss model. The graph of H is shown in Fig. 6.7-5 [*4].

$$H_* = \max\left[0, \min\left\{1.0, \frac{Q' - Q_{cr,*}'}{Q_{cr,*}'(\gamma_{ch} - 1)}\right\}\right]$$

$$Q' = Q_s + Q_{re}, \ Q_{cr,*}' = \left(\frac{\beta_{ch,*}}{\alpha_{ch,*}}\right)^{1.25}, \ \gamma_{ch} = 3.0$$

(6.78)
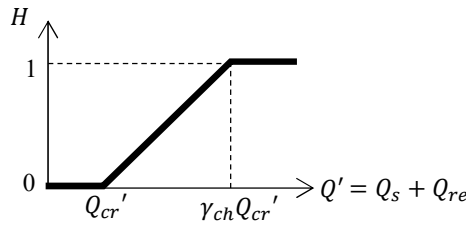
Fig. 6.7-5 "Transition function H" to model the transition from "small flow function $f_{A,*}$" to "large flow function $f_{B,*}$"

6.7.3.5 Modeling the Shroud Effect

An effect of the shroud, for example, is the case in which the clearance between the gear and the shroud is widened (when the shroud coefficient λ increases). In this case, the volume of air between the gear and the shroud increases whereas the oil supply flow rate remains constant; thus, the apparent density between the gear and the shroud and the oil churning loss P_{ch} are likely to decrease. On the basis of the above and the non-dimensional equation 5.5 of oil dynamic loss, we assume that the oil churning loss P_{ch} is inversely proportional to the shroud coefficient λ.

The oil churning loss P_{ch} is the "oil mist coefficient $\Phi - 1$" × the air vortex loss P_v, as shown in Eq. 6.70. The air vortex loss P_v is proportional to the shroud coefficient λ, as shown in Eq. 6.52. Therefore, for the oil churning loss P_{ch} to be inversely proportional to the shroud coefficient λ, the oil mist coefficient $\Phi - 1$ must be inversely proportional to the "square" of the shroud coefficient λ.

In addition, a proportional coefficient must be introduced. In this case, referring to the conversion in which the experimental results of the one-axis spur gearbox (GB3) were converted to the two-axis helical gearbox in the small flow function $f_{A,*}$, the same conversion is to be made for this proportional constant. The shroud coefficient of the one-axis spur gearbox is 0.405 using the calculation equation of the shroud coefficient shown in Section

---

[*4] H is a dimensionless number. The unit of Q' is m^3/s. The unit of $Q_{cr,*}'$ is m^3/s because the unit of $\alpha_{ch,*}$ is s/m^3 and the unit of $\beta_{ch,*}$ is (s/m^3)$^{0.2}$. γ_{ch} is a dimensionless number.

6.4.6. Using this as the proportional coefficient, and using the shroud coefficient λ of the two-axis helical gearbox, the coefficient for the shroud effect is "$(0.405/\lambda)^2$".

6.7.4 Key Parameters of the Oil Churning Loss Model

According to Eq. 6.70, the key parameters of the oil churning loss model are the oil mist coefficient $(\Phi - 1)_*$ and air vortex loss $P_{v,*}$. The parameters that affect the oil mist coefficient $(\Phi - 1)_*$ are the oil supply flow rate Q_s and the shroud coefficient λ_* from Eqs. 6.71, 6.74, and 6.77.

6.8 How to Experimentally Implement Fluid Dynamic Loss Classification

We have described the process of separating the experimental measurements of fluid dynamic loss into "aerodynamic loss" and "oil dynamic loss" in Section 3.2.2. This section describes how to further classify these losses into loss elements.

6.8.1 Experimental Classification Method for Aerodynamic Loss

The experimental results of the aerodynamic loss are classified into "air side-flow loss", "air pumping loss", and "air vortex loss". Theoretical values are used for the air pumping loss, and experimental values are used for the air vortex loss. The air side-flow loss is the remaining loss. These are shown below.

The air pumping losses $P_{pump,cal}$ (where "cal" represents the calculated value) can be calculated using theoretical equations, as detailed in Section 6.2.

The air vortex loss experimental values $P_{v,exp}$ (where "exp" represents the experimental values) are obtained by measuring the aerodynamic losses $P_{air,in,exp}$ of the input gear alone, and the aerodynamic losses $P_{air,out,exp}$ of the output gear alone, as shown below.

$$P_{v,exp} = P_{air,in,exp}\epsilon_{\theta,in} + P_{air,out,exp}\epsilon_{\theta,out} \tag{6.79}$$

where ϵ_θ is the angle range coefficient and is calculated using Eqs. 6.48 and 6.49.

The air side-flow loss $P_{s,exp}$ is obtained by subtracting the measured air vortex loss and the calculated air pumping loss from the measured aerodynamic loss $P_{air,exp}$, as shown in the following equation.

$$P_{s,exp} = P_{air,exp} - P_{v,exp} - P_{pump,cal} \tag{6.80}$$

From the above, the aerodynamic loss can be experimentally classified into loss elements.

6.8.2 Experimental Classification Method for Oil Dynamic Loss

The classification method is shown in Fig. 6.8-1 . The oil dynamic loss is classified into "oil-jet acceleration loss", "oil reacceleration loss", and "oil churning loss". We use theoretical values for the oil-jet acceleration loss. The remaining loss is separated using the characteristics in which the oil reacceleration loss is proportional to the square of the rotational speed (Eq. 6.61) and the characteristics in which the oil churning loss is proportional to the cube of the rotational speed (Eqs. 6.32, 6.34, 6.35, and 6.70). These are shown as follows:
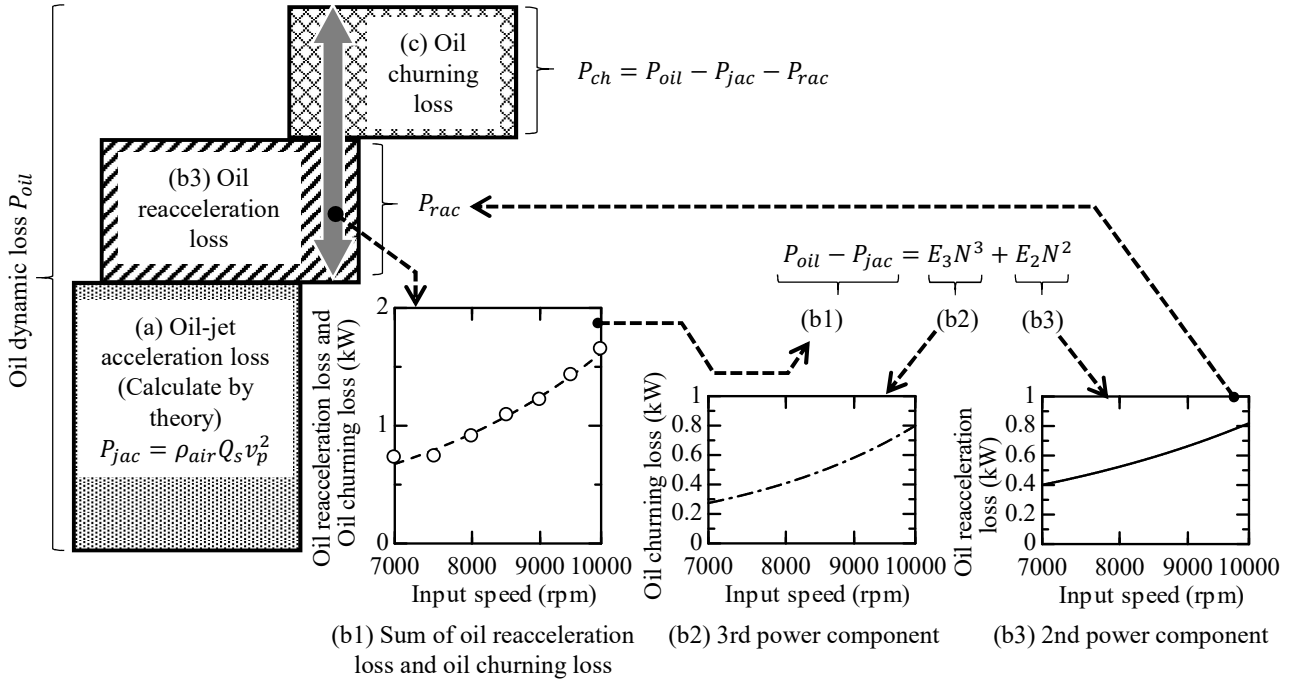
Fig. 6.8-1 An experimental separation method for the oil dynamic loss

We calculate the oil-jet acceleration loss $P_{jac,cal}$ using the theoretical equation, Eq. 6.56 (Fig. 6.8-1 (a)).

When the oil-jet acceleration loss $P_{jac,cal}$ is subtracted from the measured oil dynamic loss $P_{oil,exp}$, the oil reacceleration loss $P_{rac,exp}$ and the oil churning loss $P_{ch,exp}$ remain (Fig. 6.8-1 (b1)).

$$P_{oil,exp} - P_{jac,cal} = P_{rac,exp} + P_{ch,exp} \tag{6.81}$$

The remaining losses (the right term of above equation) are separated into a component proportional to the square of the rotational speed and a component proportional to the cube of the rotational speed, which are the oil reacceleration loss and the oil churning loss, respectively, as shown in the following equation (where N is the rotational speed).

$$P_{oil,exp} - P_{jac,cal} = E_3 N^3 + E_2 N^2 \tag{6.82}$$

where E_3 and E_2 are coefficients and are determined by the least-squares method. Figure 6.8-1 (b2) shows the cubic proportional component $E_3 N^3$ in Fig. 6.8-1 (b1), and Fig. 6.8-1 (b3) shows the square proportional component $E_2 N^2$ in Fig. 6.8-1 (b1). $E_2 N^2$ corresponds to the oil reacceleration loss. That is,

$$P_{rac,exp} = E_2 N^2 \tag{6.83}$$

To match the total loss of the loss elements to the oil dynamic loss, the oil churning loss is determined by subtracting the oil-jet acceleration loss and the oil reacceleration loss from the oil dynamic loss (Fig. 6.8-1 (c)).

$$P_{ch,exp} = P_{oil,exp} - P_{jac,cal} - P_{rac,exp} \tag{6.84}$$

From the above, the oil dynamic loss can be experimentally classified into loss elements.

6.9 How to Numerically Implement Fluid Dynamic Loss Classification

The method of separating the numerical simulation value of fluid dynamic loss into "aerodynamic loss" and "oil dynamic loss" is described in Section 4.1.4. This study describes a method of further classifying the losses into loss elements.

6.9.1 Numerical Classification Method for Aerodynamic Loss

The numerical simulation values of the aerodynamic loss are classified into "air side-flow loss", "air pumping loss", and "air vortex loss". The numerical classification method of the aerodynamic loss is the same as the experimental classification method (Section 6.8.1), except that the air vortex loss is obtained by numerical simulation. That is, the theoretical value is used for air pumping loss, the numerical simulation value is used for the air vortex loss, and the air side-flow loss is the remaining loss. These are shown below.

The air pumping losses $P_{pump,cal}$ (where "cal" represents the calculated value) can be calculated using theoretical equations, as shown in Section 6.2.

Numerical simulation models for the air vortex loss are shown in Fig. 6.9-1 . The two-axis helical gearbox (GA) is used as an example. The simulation model of the input gear is shown in Fig. 6.9-1 (a). The input gear is simulated as a single gear, and the shroud opening at the gear meshing part is closed by adding a shroud in the peripheral direction. This is to minimize the effect of the gear meshing part. The simulation model of the output gear is shown in Fig. 6.9-1 (b). The output gear is simulated as a single gear, and the shroud opening at the gear meshing part is closed.

(a) Modeling of isolated input gear with shrouding   (b) Modeling of isolated output gear with shrouding
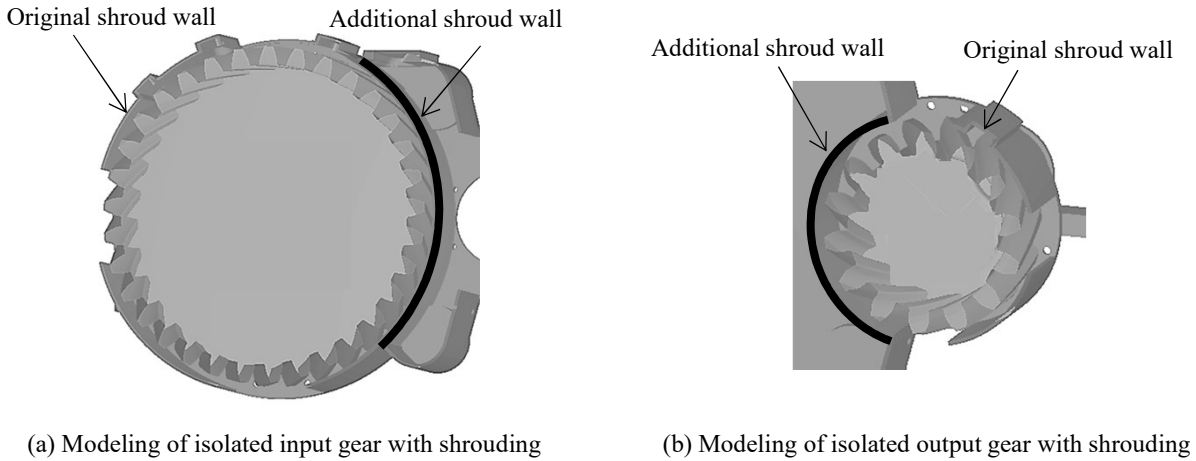
Fig. 6.9-1 Numerical simulation models to evaluate the air vortex loss

Using the air vortex loss $P_{air,in,CFD}$ of the input gear and the air vortex loss $P_{air,in,CFD}$ of the output gear obtained by numerical simulations, the numerical value of the air vortex loss $P_{v,CFD}$ can be calculated using the following equation:

$$P_{v,CFD} = P_{air,in,CFD} \ \epsilon_{\theta,in} + P_{air,out,CFD} \ \epsilon_{\theta,out} \tag{6.85}$$

where ϵ_θ is the angle range coefficient and is calculated by Eqs. 6.48 and 6.49.

The air side-flow loss $P_{s,CFD}$ is obtained by subtracting the simulated air vortex loss $P_{v,CFD}$ and the calculated

air pumping loss $P_{pump,cal}$ from the simulated aerodynamic loss $P_{air,CFD}$, as shown in the following equation:

$$P_{s,CFD} = P_{air,CFD} - P_{v,CFD} - P_{pump,cal} \tag{6.86}$$

Based on the above, the aerodynamic loss can be numerically classified into loss elements.

6.9.2 Numerical Classification Method for Oil Dynamic Loss

The oil dynamic loss is classified into "oil-jet acceleration loss", "oil reacceleration loss", and "oil churning loss". The theoretical value is used for the oil-jet acceleration loss. The oil mist coefficient is evaluated from the numerical simulation result to calculate the oil churning loss. The remaining loss is the oil reacceleration loss. These losses are shown below.

The oil-jet acceleration loss $P_{jac,cal}$ is calculated by the theoretical equation, i.e., Eq. 6.56.

The numerical simulation value $P_{ch,CFD,*}$ of the oil churning loss is calculated from the following equation using the numerical simulation values $P_{v,CFD*}$ of the air vortex loss and the oil mist coefficient $(\Phi - 1)_*$.

$$P_{ch,CFD,*} = (\Phi - 1)_* P_{v,CFD*} \tag{6.87}$$

The oil mist coefficient $(\Phi - 1)_*$ must be evaluated from the numerical simulation results. The larger the number of oil particles around the gear, the larger the ambient density around the gear, and the larger the oil mist coefficient. Therefore, the atmospheric density is assumed to be ρ_m, which is evaluated using the results of the numerical simulation. ρ_m is shown below.

$$\rho_{m,*} = \alpha_{oil,*}\rho_{oil} + (1 - \alpha_{oil,*})\rho_{air} \tag{6.88}$$

The relationship between the ambient density ρ_m and the oil mist coefficient $(\Phi - 1)_*$ is shown below.

$$(\Phi - 1)_* = \frac{\rho_{m,*}}{\rho_{air}} - 1 \tag{6.89}$$

The atmospheric density is considered to be different between the gear meshing part and the gear peripheral part. Therefore, the atmospheric density ρ_m is evaluated in the gear meshing part and the gear peripheral part separately. The evaluation section (sampling section) of the atmospheric density at the gear meshing part is shown in Fig. 6.9-2 (a). The evaluation sections (sampling sections) of the atmospheric density at the gear peripheral part are shown in Fig. 6.9-2 (b).

For the gear meshing part, we focus on the cross section (Fig. 6.9-2 (a)) of the gear meshing part. This section does not include the tip clearance and the backlash of the gear meshing. This makes it possible to eliminate the fluid dynamic loss (oil-jet acceleration loss and oil reacceleration loss) due to oil acceleration at the tip clearance and backlash.

The total flow rate of air and oil passing through the section beside the gear meshing part is $Q_{msides,m}$, and the flow rate of oil is $Q_{msides,oil}$ ("$msides$" indicates the sides of the gear mesh). The ambient density $\rho_{m,msides}$ beside the gear meshing can be evaluated by using the ratio of these flow rates.

$$\rho_{m,msides} = \frac{Q_{msides,oil}}{Q_{msides,m}}\rho_{oil} \tag{6.90}$$

(a) A sampling section for flow rate of air and oil
through the sides of the gear mesh

(b) Schematics of a sampling surface
for oil volume on the gear
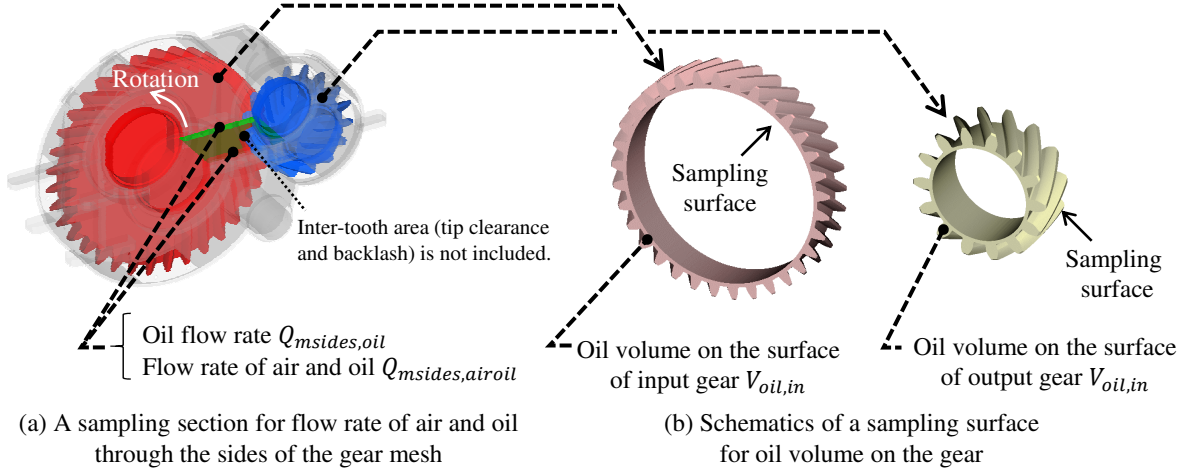
Fig. 6.9-2 Sampling surfaces for evaluating oil mist coefficient

The atmospheric density of the oil near the gear surface is considered to be important in the gear peripheral part. Therefore, using the amount of oil calculated with the gear surface cells, we assume that this is replaced at every rotation of the gear. The oil flow rate $Q_{surface,oil,*}$ in the cells on the gear surface is given by the following equation ("*surface*" denotes gear surface).

$$Q_{surface,oil,*} = V_{oil,*} \times N_* \tag{6.91}$$

where $V_{oil,*}$ is the total oil volume of the gear surface cells. N_* is the rotational speed. $V_{oil,*}$ is evaluated from the results of the numerical simulation.

The flow rate of air and oil around the gear is set to be the same as the flow rate $Q_{msides,m}$ using the gear meshing part. The atmospheric density $\rho_{m,peri,*}$ in the gear peripheral part is evaluated using the following equation:

$$\rho_{m,peri,*} = \frac{Q_{surface,oil,*}}{Q_{msides,m}} \rho_{oil} \tag{6.92}$$

The above can be used to evaluate the ambient density $\rho_{m,msides}$ besides the gear meshing, and the ambient density $\rho_{m,peri,*}$ at the gear peripheral part.

The ambient density $\rho_{m,*}$ representing value in the gear meshing part and the gear peripheral part for each gear is obtained as follows. If $\rho_{m,*}$ is the average value of $\rho_{m,msides}$ and $\rho_{m,peri,*}$, $\rho_{m,*}$ is obtained using following equation:

$$\rho_{m,*} = \frac{1}{2}(\rho_{m,msides} + \rho_{m,peri,*}) \tag{6.93}$$

Using the evaluation equation Eq. 6.93 of the atmospheric density $\rho_{m,*}$, and using the relational equation Eq. 6.89 between the atmospheric density $\rho_{m,*}$ and the oil mist coefficient $(\Phi - 1)_*$, the oil mist coefficient $(\Phi - 1)_*$ and the oil churning loss $P_{ch,CFD,*}$ can be obtained. The oil churning loss $P_{ch,CFD}$ can be obtained by summing the oil churning loss $P_{ch,CFD,in}$ of the input gear and the oil churning loss $P_{ch,CFD,out}$ of the output gear.

$$P_{ch,CFD} = P_{ch,CFD,in} + P_{ch,CFD,out} \tag{6.94}$$

The oil reacceleration loss $P_{rac,CFD}$ can be obtained by subtracting the calculated oil-jet acceleration loss $P_{jac,cal}$ and the above oil churning loss $P_{ch,CFD}$ from the simulated oil dynamic loss $P_{oil,CFD}$.

$$P_{rac,CFD} = P_{oil,CFD} - P_{jac,cal} - P_{ch,CFD} \tag{6.95}$$

Based on the above, oil dynamic loss can be numerically classified into loss elements.

6.10   Method for Evaluating Loss Element from Numerical Simulation Results such as Pressure and Oil Distributions

To allow easy understanding of the phenomena of fluid dynamic loss elements, we aimed to evaluate the loss elements using the pressure and oil distributions obtained from the numerical simulation results.

(1)   Method for Evaluating Element of Aerodynamic Loss

Methods for evaluating the simulation results to understand the loss elements of aerodynamic loss are shown in Fig. 6.10-1 .

An example of a streamline with a speed contour is shown in Fig. 6.10-1 (a). This gives an overview of the flow field.

Figure 6.10-1 (b) shows an example of the pressure distribution at the gear surface at the gear meshing part to understand the air side-flow loss. We consider that the differential pressure between the pressure rise at the into-mesh side and the pressure drop at the out-of-mesh side is related to the air side-flow loss.

(a) Streamline with velocity contour

(b) Pressure distribution on gear surface around gear mesh to evaluate air side-flow loss

(c) Pressure distribution on gear surface around gear periphery to evaluate air vortex loss

Fig. 6.10-1 An example of the evaluation methods of a simulation result to understand aerodynamic loss (Shroud 2, input 10000 rpm, oil supply rate 7.40 L/min)

Figure 6.10-1 (c) shows an example of the gear surface pressure distribution in the gear peripheral part to understand the air vortex loss. The pressure difference between the pressure rise in the forward surface and the pressure drop in the backward surface in the direction of tooth rotation is considered to be related to the air vortex loss.

When we change the parameters, the air pressure difference at the gear meshing part and the air pressure difference on the tooth surface at the gear peripheral part shown above change. This is considered to be related to the change in the fluid dynamic loss element. This helps understand the phenomena of the aerodynamic loss.

(2)   Method for Evaluating Element of Oil Dynamic Loss

Methods for evaluating simulation results to understand the loss elements of oil dynamic loss are shown in Fig. 6.10-2 .

The oil distribution with speed contours is shown in Fig. 6.10-2 (a). This provides an overview of the oil distribution.

Figure 6.10-2 (b1) shows an example of the gear surface pressure distribution at the gear meshing part which will help understand the oil reacceleration loss. This pressure distribution is obtained by subtracting the simulation result with air from the simulation result with air and oil. It shows the pressure by oil only. Therefore, the pressure difference between the pressure rise at the into-mesh side and the pressure drop at the out-of-mesh side is considered to be related to the oil reacceleration loss.

Figure 6.10-2 (b2) shows an example of the contour of the oil fraction on the gear surface of the gear meshing part to understand the oil reacceleration coefficient χ_{re} (a parameter of the oil reacceleration loss model). We consider that the amount of oil in the gear meshing part is related to the oil reacceleration coefficient χ_{re}.

Figure 6.10-2 (c1) shows an example of the gear surface pressure distribution at the gear peripheral part to understand the oil churning loss. This pressure distribution is also obtained by subtracting the simulation result with air from the simulation result with air and oil. Therefore, we consider that the pressure difference between the pressure rise on the forward surface and the pressure drop on the backward surface in the direction of tooth rotation is related to the oil churning loss.

Figure 6.10-2 (c2) shows the contour of the oil fraction on the gear surface in the gear peripheral part to understand the oil mist coefficient $\Phi - 1$. The amount of oil around the gear is considered to be related to the oil mist coefficient $\Phi - 1$.

When the parameters are changed, we consider that the oil pressure difference at the gear meshing part and the amount of oil on the tooth surface change, and the oil pressure difference on the tooth surface around the gear periphery and the amount of oil on the tooth surface change. This change is considered to be related to the changes in the fluid dynamic loss element and the changes in the parameter of the loss model, which can help understand the phenomena of the oil dynamic loss.
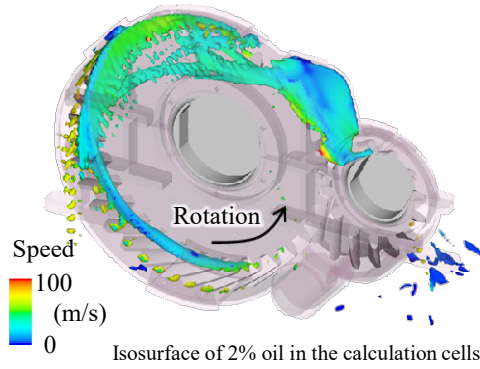
(a) Oil distribution with velocity contour
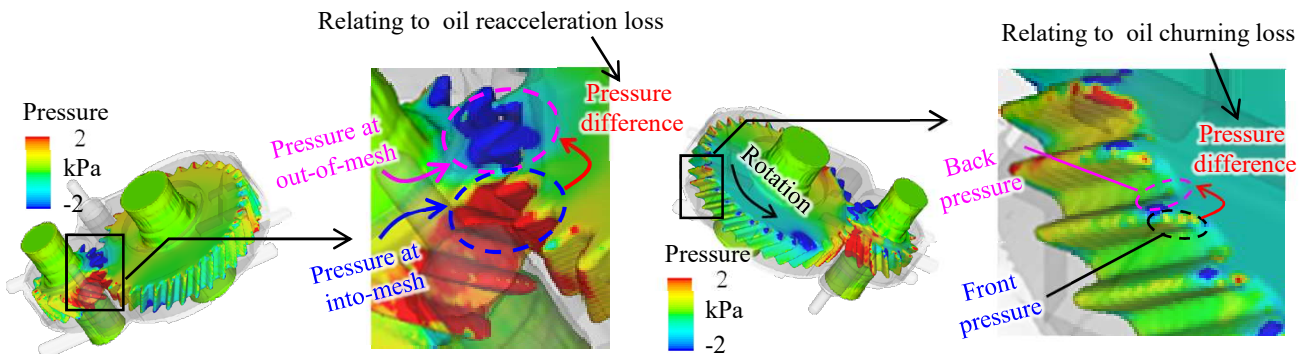
(b1) Pressure distribution on gear surface around gear mesh to evaluate oil reacceleration loss *

(c1) Pressure distribution on gear surface around gear periphery to evaluate oil churning loss *

* Subtracted the simulation result of air from that of air and oil
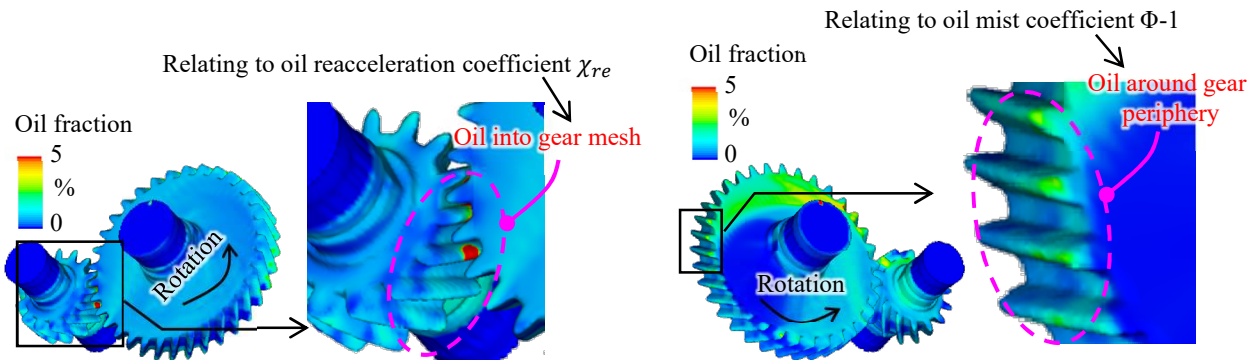
(b2) Oil fraction contour on gear surface around gear mesh to evaluate oil reacceleration coefficient χ_{re}

(c2) Oil fraction contour on gear surface around gear periphery to evaluate oil mist coefficient Φ-1
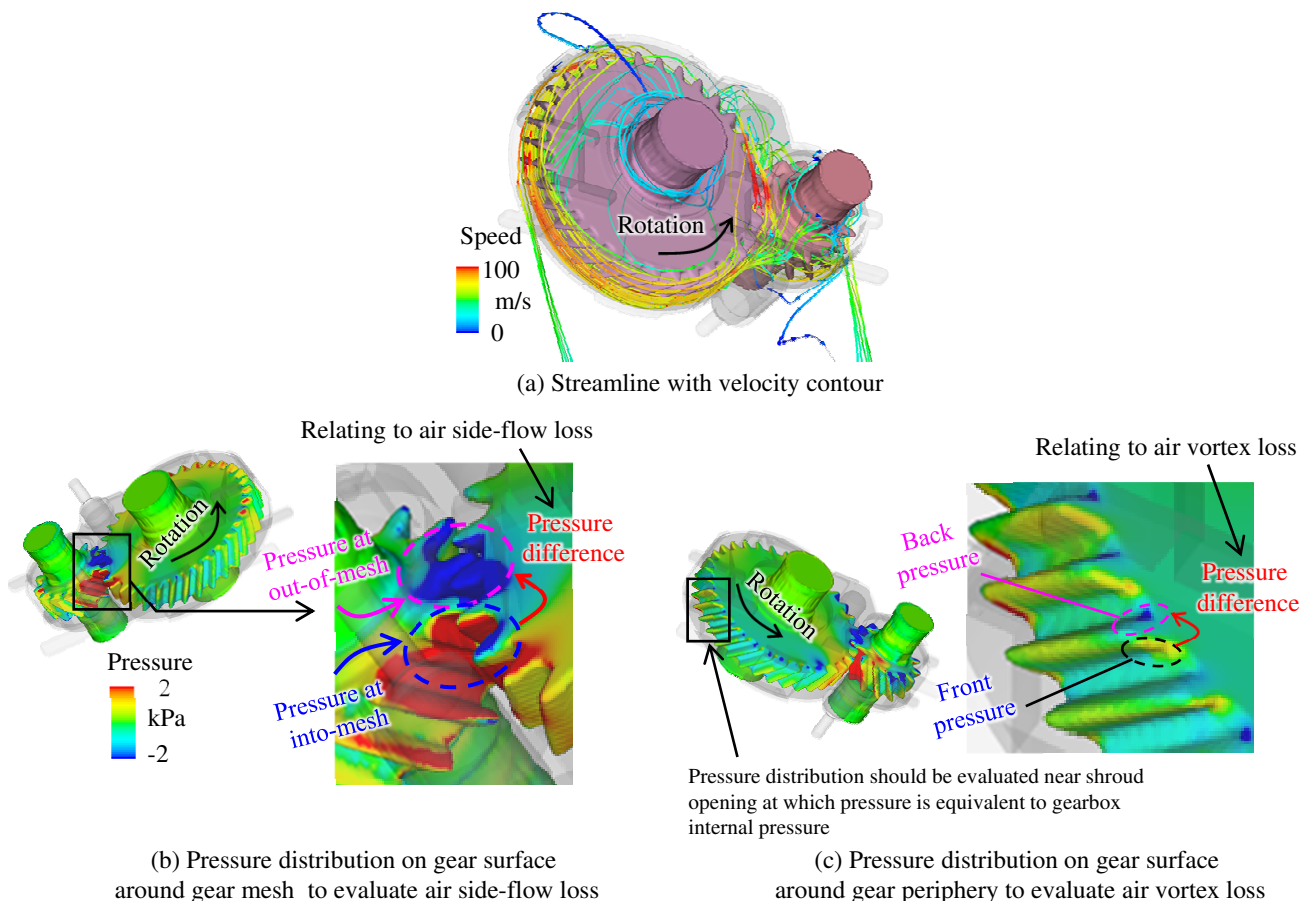
Fig. 6.10-2 An example of the evaluation methods of a simulation result to understand oil dynamic loss (Shroud 2, input 10000 rpm, oil supply rate 7.40 L/min)

6.11 Validation of Fluid Dynamic Loss Model and Validation of Numerical Classification Method of Fluid Dynamic Loss

6.11.1 Overview of Validation

To consider the fluid dynamic loss elements in detail, the loss model calculation results and the numerical simulation results must qualitatively agree with the experimental results at the loss element level.

For the fluid dynamic loss model, the models described in Sections 6.1 to 6.7 are used. For the numerical classification method of the fluid dynamic loss, the method shown in Section 6.9 is used. To obtain the experimental results to validate the results of the loss model calculation and the numerical simulation, the method to classify fluid dynamic loss experimentally (Section 6.8) is used.

A list of validations given in this section is shown in Table 6.11-1 . The validation of the fluid dynamic loss is described in Section 6.11.2, the validation of aerodynamic loss is described in Section 6.11.3, and the validation of the oil dynamic loss is described in Section 6.11.4.

In the validations of the fluid dynamic loss (Section 6.11.2), we used these patterns: ① the oil supply flow rate condition was set constant to 3.85 or 7.40 L/min, and the rotational speed was set to 7000 to 10000 rpm, and ② the rotational speed was constant to 10000 rpm, and the oil supply flow rate was 1.48 to 7.40 L/min.

The validation of the aerodynamic loss (Section 6.11.3) was performed under the condition that the rotational speed condition is 7000 to 10000 rpm.

In the validations of the oil dynamic loss (Section 6.11.4), we used the following patterns: ① the oil supply flow rate condition was set to 3.85 or 7.40 L/min constant, and the rotational speed was set to 7000 to 10000 rpm, and ② the rotational speed was constant to 10000 rpm, and the oil supply flow rate was 1.48 to 7.40 L/min.

Shroud 1 or Shroud 2 was used for all validations.

Table 6.11-1 Calculation conditions to validate the fluid dynamic loss model and the numerical classification method

Section	Validation of fluid dynamic loss			Parameter to change	Module (mm)	Pitch diameter (mm)		Width (mm)	Oil supply rate (L/min)	Operating speed (rpm)	Shroud
	Air & oil	Air	Oil			Wheel	Pinion				
6.11.2	✓			Rotational speed	5	191	81	34	3.85, 7.40	7000–10000	Shroud 1, Shroud 2
	✓			Oil supply rate					1.48–7.40	10000	Shroud 1, Shroud 2
6.11.3		✓		Rotational speed					0	7000–10000	Shroud 1, Shroud 2
6.11.4			✓	Rotational speed					3.85, 7.40	7000–10000	Shroud 1, Shroud 2
			✓	Oil supply rate					1.48–7.40	10000	Shroud 1, Shroud 2

6.11.2 Validation of Loss Model and Numerical Classification Method for Fluid Dynamic Loss

The results of the validation of the loss model and the numerical simulation on the fluid dynamic loss of air and oil are shown in Fig. 6.11-1 .

Figure 6.11-1 (a1) and (a2) show losses with the changes in rotational speed at the oil supply flow rate of 7.40 L/min. Figure 6.11-1 (b1) and (b2) show losses with the changes in rotational speed at the oil supply flow rate of 3.85 L/min. Figure 6.11-1 (c1) and (c2) show the losses with the changes in the oil supply rate. Figure 6.11-1 (a1), (b1), and (c1) show the results of Shroud 1 and Fig. 6.11-1 (a2), (b2), and (c2) show the results of Shroud 2.

(a1) Oil flow rate 7.40 L/min, Shroud 1   (b1) Oil flow rate 3.85 L/min, Shroud 1 (c1) Rotational speed 10000 rpm, Shroud 1

(a2) Oil flow rate 7.40 L/min, Shroud 2   (b2) Oil flow rate 3.85 L/min, Shroud 2 (c2) Rotational speed 10000 rpm, Shroud 2
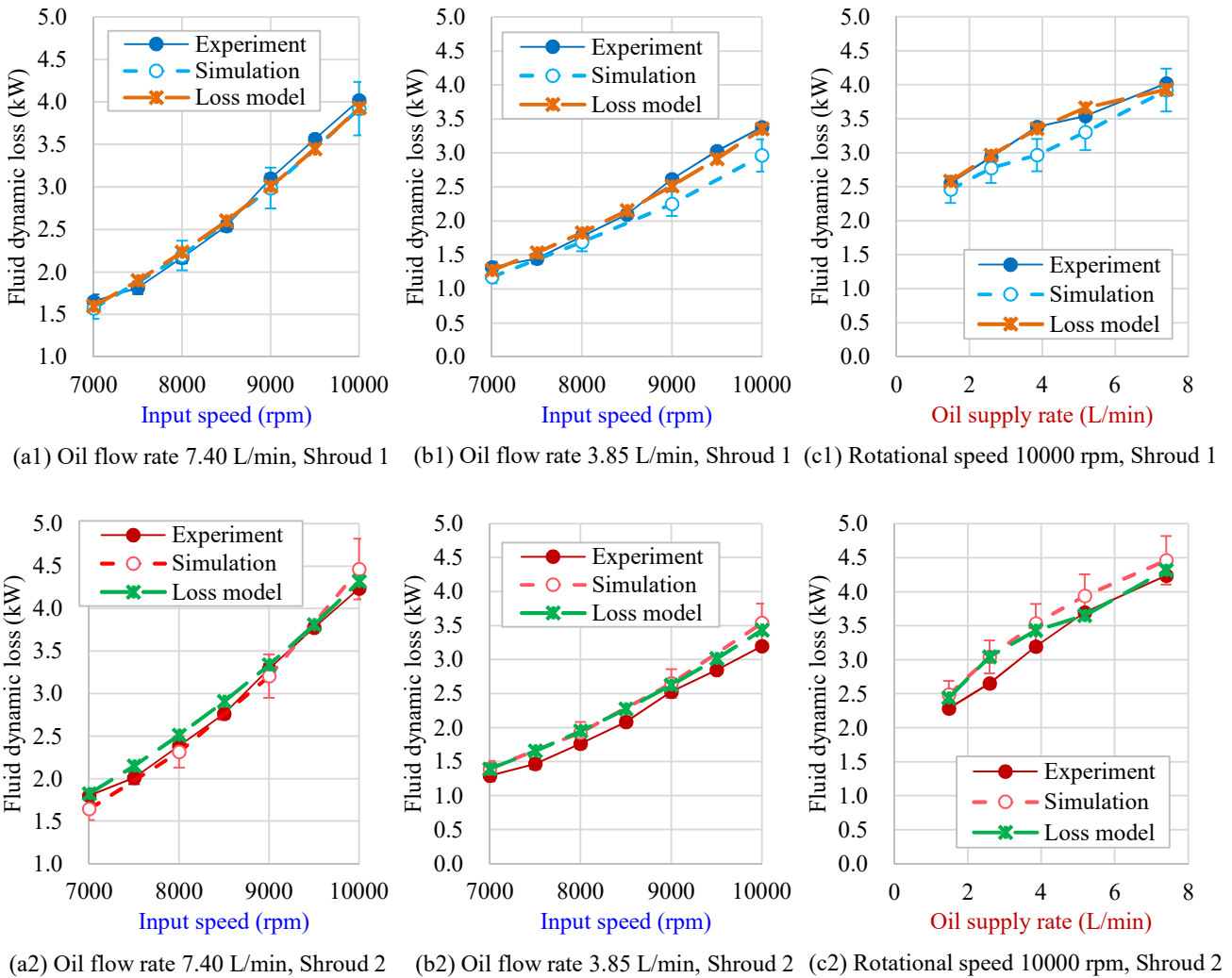
Fig. 6.11-1 Validation results on the fluid dynamic loss with respect to input speed changes, oil supply rate changes, and different shrouds

In the experimental results shown in Fig. 6.11-1 , the measurement error (maximum ±0.08 kW (from Table 3.6-5) as a standard error of 2σ) is indicated as error bars. In the numerical simulation results in Fig. 6.11-1 , the simulation error (±8% for the fluid dynamic loss of air and oil, ±5% for the aerodynamic loss, ±14% for the oil dynamic loss (from Table 4.4-1) as the difference between the experimental results and the simulation

results) is indicated using error bars.

In each panel of Fig. 6.11-1 , the trend of the loss model calculation results and the trend of the numerical simulation results agree with the trend of the experimental results. Therefore, the fluid dynamic loss of air and oil can be considered using the loss model calculation results and numerical simulation results.

6.11.3   Validation of Loss Model and Numerical Classification Method for Aerodynamic Loss

The results of the validation of the loss model and numerical simulation on the aerodynamic loss are shown in Fig. 6.11-2 . Figures 6.11-2 (a1) and (a2) show the aerodynamic loss, which can be classified into the air side-flow loss, the air pumping loss, and the air vortex loss.

Figures 6.11-2 (b1) and (b2) show the air side-flow loss, Figs. 6.11-2 (c1) and (c2) show the air pumping loss, and Figs. 6.11-2 (d1) and (d2) show the air vortex loss. Figures 6.11-2 (a1), (b1), (c1), and (d1) show losses at Shroud 1, and Figs. 6.11-2 (a2), (b2), (c2), and (d2) show losses at Shroud 2. Here, our experimental results of the air vortex loss in Figs. 6.11-2 (d1) and (d2) are substituted by the numerical results. We consider that the numerical simulation results can be substituted for it because we believe that the numerical simulation method had practical accuracy because of the validation of the aerodynamic loss with the single gears described in Section 4.4.1.2.

In each panel in Fig. 6.11-2 , the trend of the loss model calculation results and the trend of the numerical simulation results agrees with the trend of the experimental results. Therefore, it is possible to consider the aerodynamic loss using the loss model calculation results and numerical simulation results. In addition, the air pumping loss was found to be negligibly small enough. This is probably due to the small mass flow rate due to the small tip clearance and backlash volumes[*5].

6.11.4   Validation of Loss Model and Numerical Classification Method for Oil Dynamic Loss

First, Fig. 6.11-3 shows the oil dynamic loss with respect to the rotational speed changes at a constant oil supply flow rate of 7.40 L/min. Figures 6.11-3 (a1) and (a2) show the oil dynamic loss. The oil dynamic loss is classified into the oil-jet acceleration loss, oil reacceleration loss, and oil churning loss. Figures 6.11-3 (b1) and (b2) show the oil-jet acceleration loss, Figs. 6.11-3 (c1) and (c2) show the oil reacceleration loss, and Figs. 6.11-3 (d1) and (d2) show the oil churning loss. Figures 6.11-3 (a1), (b1), (c1), and (d1) indicate the losses at Shroud 1, and Figs. 6.11-3 (a2), (b2), (c2), and (d2) indicate the losses at Shroud 2. Because the oil-jet acceleration loss (Figs. 6.11-3 (b1) and (b2)) is a theoretical calculation result which is common in both the loss model, the numerical simulation, and the experiment, these three results agree. In each figure in Fig. 6.11-3 , the trend of the loss model calculation results and the trend of the numerical simulation results roughly agree with the trend of the experimental results.

Next, Fig. 6.11-4 shows the oil dynamic loss with respect to the rotational speed changes at a constant oil supply flow rate of 3.85 L/min (52% of the oil supply flow rate of 7.40 L/min), similar to Fig. 6.11-3 . In each panel of Fig. 6.11-4 , the trend of the loss model calculation results and the trend of the numerical simulation results roughly agree with the trend of the experimental results.

[*5] The mass flow rate of air is 2.8 g/s (161 L/min) and the air pumping loss is 0.02 kW at 10000 rpm with the two-axis helical gearbox.
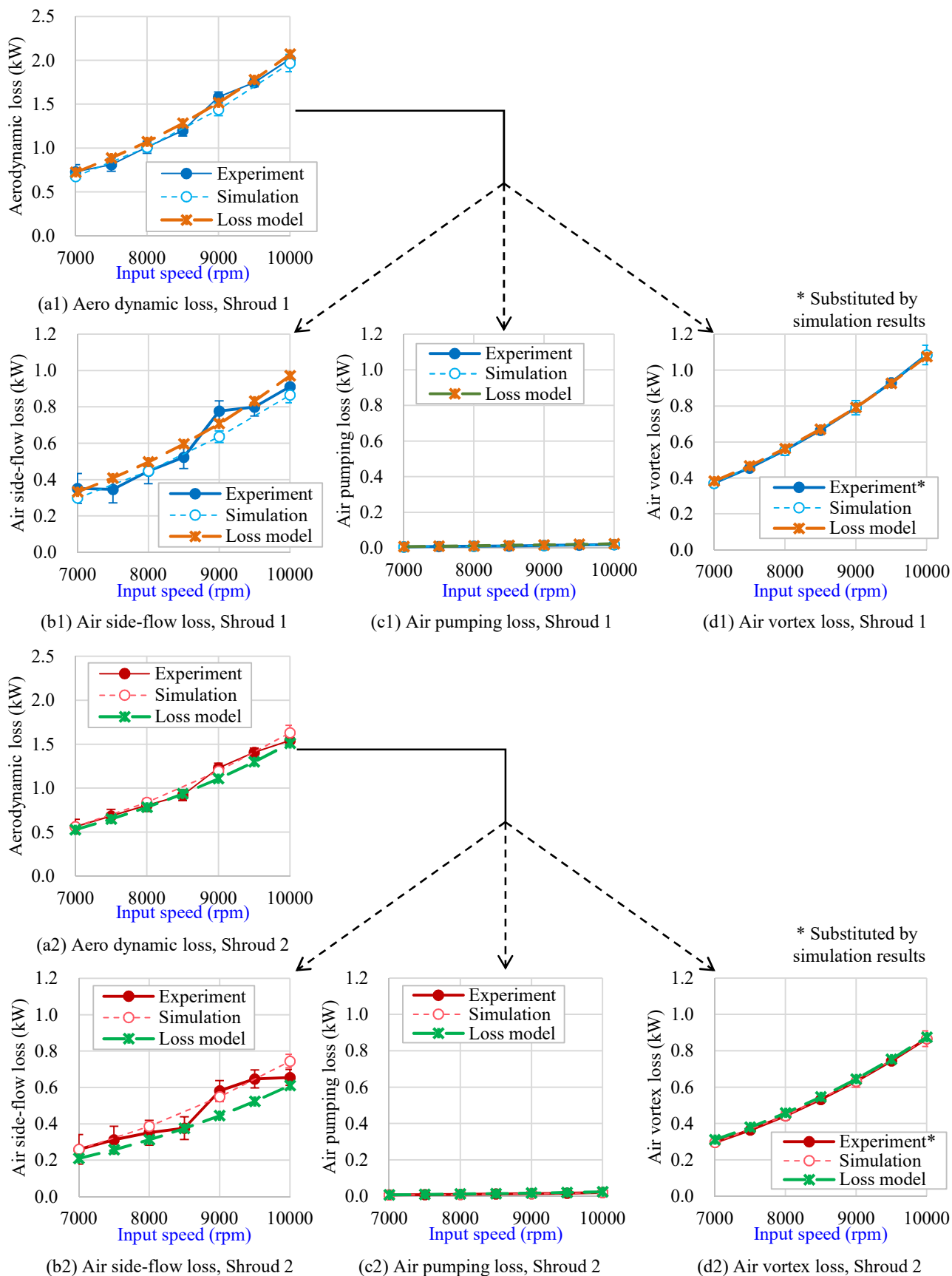
Fig. 6.11-2 Validation results on aerodynamic loss with respect to input speed changes and different shrouds
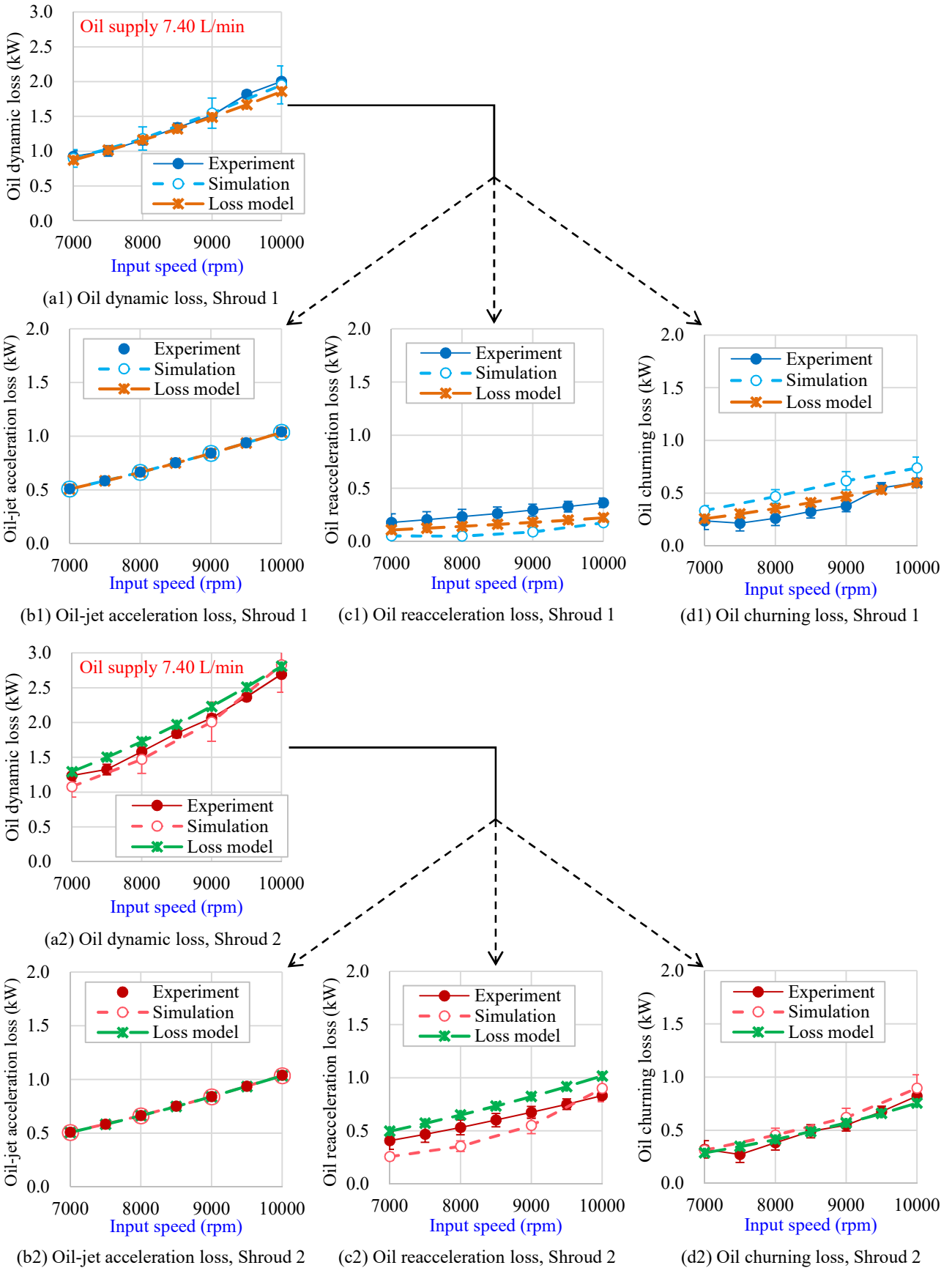
Fig. 6.11-3 Validation results of the oil dynamic loss with respect to input speed changes and different shrouds (oil supply rate 7.40 L/min)

(a1) Oil dynamic loss, Shroud 1

(b1) Oil-jet acceleration loss, Shroud 1

(c1) Oil reacceleration loss, Shroud 1

(d1) Oil churning loss, Shroud 1

(a2) Oil dynamic loss, Shroud 2

(b2) Oil-jet acceleration loss, Shroud 2

(c2) Oil reacceleration loss, Shroud 2

(d2) Oil churning loss, Shroud 2
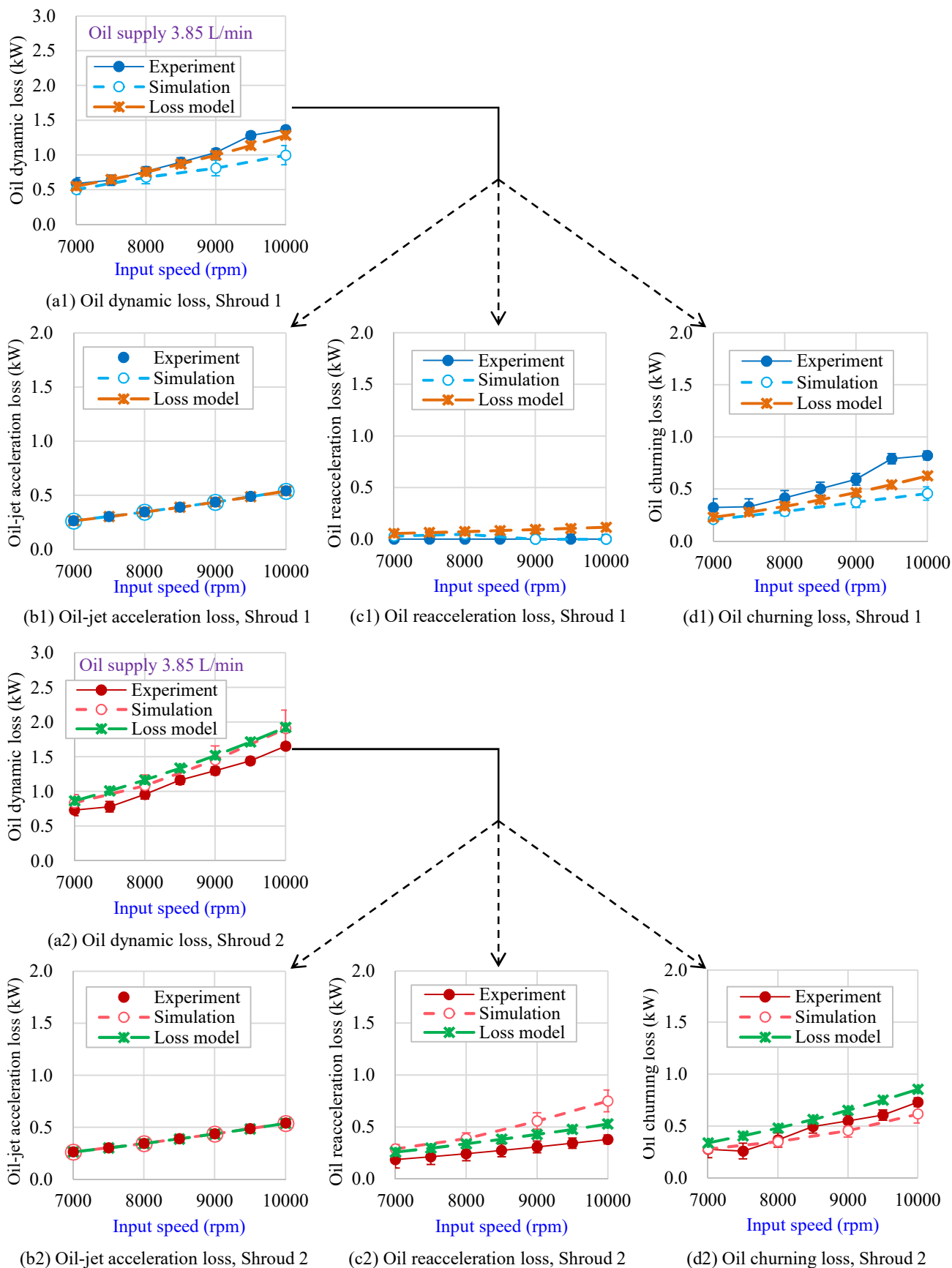
Fig. 6.11-4 Validation results of the oil dynamic loss with respect to input speed changes and different shrouds (oil supply rate 3.85 L/min)

251

(a1) Oil dynamic loss, Shroud 1

(b1) Oil-jet acceleration loss, Shroud 1

(c1) Oil reacceleration loss, Shroud 1

(d1) Oil churning loss, Shroud 1

(a2) Oil dynamic loss, Shroud 2

(b2) Oil-jet acceleration loss, Shroud 2

(c2) Oil reacceleration loss, Shroud 2

(d2) Oil churning loss, Shroud 2

Fig. 6.11-5 Validation results of the oil dynamic loss with respect to oil supply rate changes and different shrouds

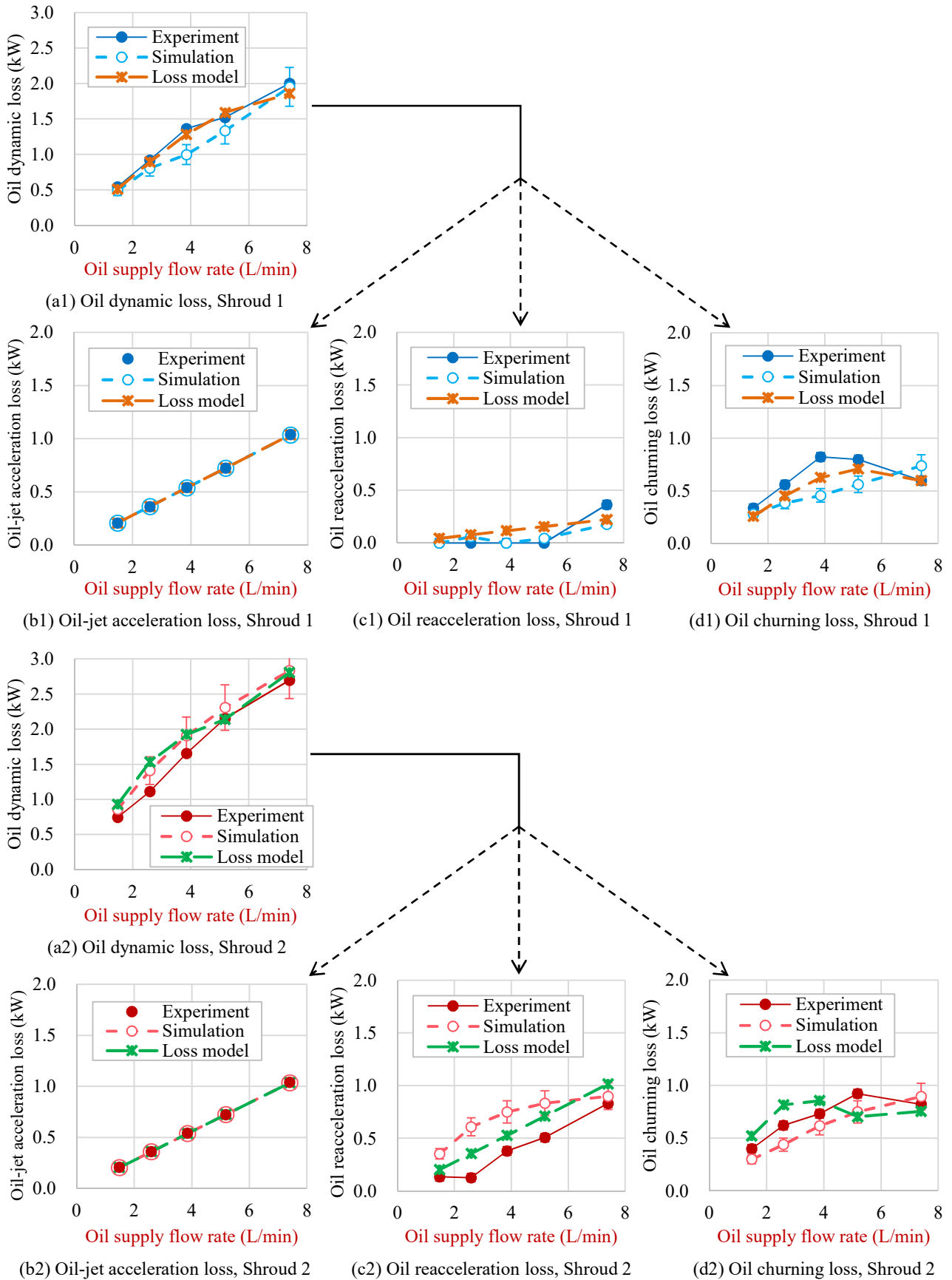Next, Fig. 6.11-5 shows oil dynamic loss with respect to the oil supply flow rate changes at a constant rotational speed of 10000 rpm, similar to Fig. 6.11-3 (The difference is that the horizontal axis is the oil supply rate). In each panel of Fig. 6.11-5 , the trend of the loss model calculation results roughly agrees with the trend of the experimental results. Regarding the simulation results, the trends with the minimum flow rate (1.48 L/min) and the maximum flow rate (7.40 L/min) agree with the experimental results. In contrast, although the oil churning loss simulation results at the midstream flow rate around 4 L/min simply increase with respect to the oil supply flow rate, the experimental results differ in that the midstream flow rate has a maximum value. The difference between the simulation results and the experimental results at the midstream flow rate is discussed using the loss model because the loss model calculation results and the experimental results agree.

In the oil churning loss model, a phenomenon in which the oil film thickness linearly increases with respect to the flow rate on the small flow rate and a phenomenon in which the rate of increase of the oil film thickness decreases on the large flow rate are modeled, and the weighted function is derived so that these phenomena are switched at a constant width of the flow rate. The region affected by the weighted function is considered to be the transition region between the phenomenon at the small flow rate and the phenomenon at the large flow rate. The loss has a maximum value in the loss model because of the weighted function. It is considered that these phenomena cannot be reproduced in the numerical simulation.

The above discussion indicates that it is possible to use the loss model because the calculated results of the oil dynamic loss model qualitatively agreed with the experimental results. The numerical simulation except for the midstream condition of oil churning loss can be used because the numerical simulation results qualitatively agreed with the experimental results except for the midstream condition.

6.11.5 Breakdown of Fluid Dynamic Loss and Trends with respect to Rotational Speed Changes

Figure 6.11-6 shows the experimental results for the fraction of fluid dynamic loss at Shroud 1 with an oil flow rate of 7.4 L/min. From the figure, the fraction of elements of fluid dynamic loss under the condition can be observed. In addition, the fraction change in the loss with respect to rotational speed changes is considered using the proportional exponent of each loss element mentioned in this chapter. See Appendix D for additional data.

Figure 6.11-6 (a) shows the fraction of fluid dynamic loss at a input speed of 10000 rpm. The ratio of the aerodynamic loss to the oil dynamic loss was approximately fifty-fifty. Figure 6.11-6 (b) shows the aerodynamic and oil dynamic losses with respect to rotational speed changes. The fraction of aerodynamic loss increased as the rotational speed increased, because the proportional exponent of the oil dynamic loss was 2 to 3, while that of the aerodynamic loss was 3. Figure 6.11-6 (c) shows the elements of aerodynamic loss with respect to rotational speed changes. The fraction of the air side-flow loss to air vortex loss was approximately equal. The fraction of these losses did not change as the rotational speed changes, because the proportional exponents of the air side-flow and air vortex losses were both 3. Figure 6.11-6 (d) shows the element of oil dynamic loss with respect to rotational speed changes. The oil-jet acceleration loss accounted for approximately half of the total. The fraction of oil churning loss increased as the rotational speed increased, because the proportional exponents of oil-jet acceleration and oil reacceleration losses were 2, while that of oil churning loss was 3. Figure 6.11-6 (e) shows the losses in the gear meshing and peripheral parts of the gear. The fraction of loss in the gear meshing part exceeded 50%, because the fraction of oil-jet acceleration loss was large. The fraction of loss in the gear peripheral part increased as the rotational speed increased, because the proportional exponent of loss in the gear

meshing part was 2 to 3, while that of loss in the gear peripheral part was 3.

These results indicate that the aerodynamic and oil dynamic losses were approximately fifty-fifty, while the fraction of elements with a proportional exponent of 3 (aerodynamic loss (air side-flow loss and air vortex loss), oil churning loss, and loss in the gear peripheral part) increased as the rotational speed increased.
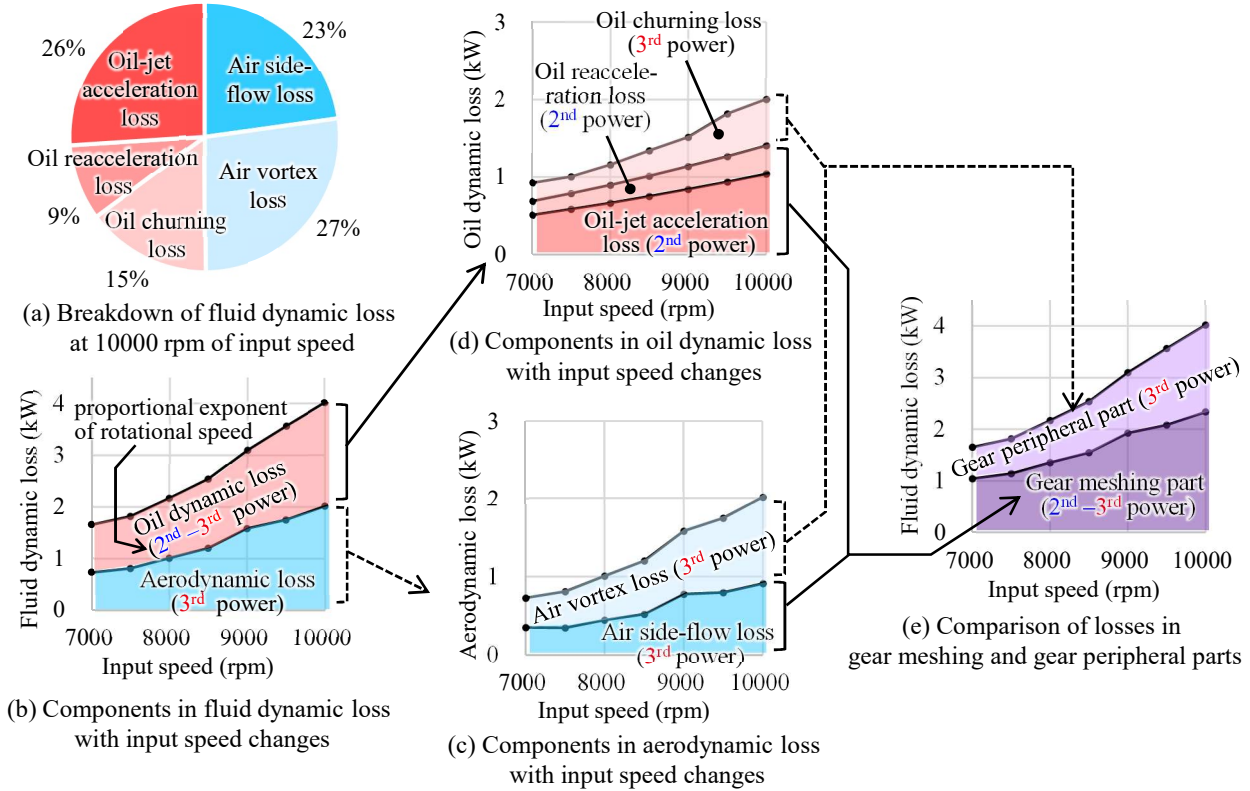

Fig. 6.11-6 Breakdown of fluid dynamic loss (experimental results, Shroud 1, oil flow rate 7.4 L/min)

6.11.6　Error of Fluid Dynamic Loss Model

Figure 6.11-7 shows the error of the fluid dynamic loss model in comparison with the experimental results for the two-axis helical gearbox.
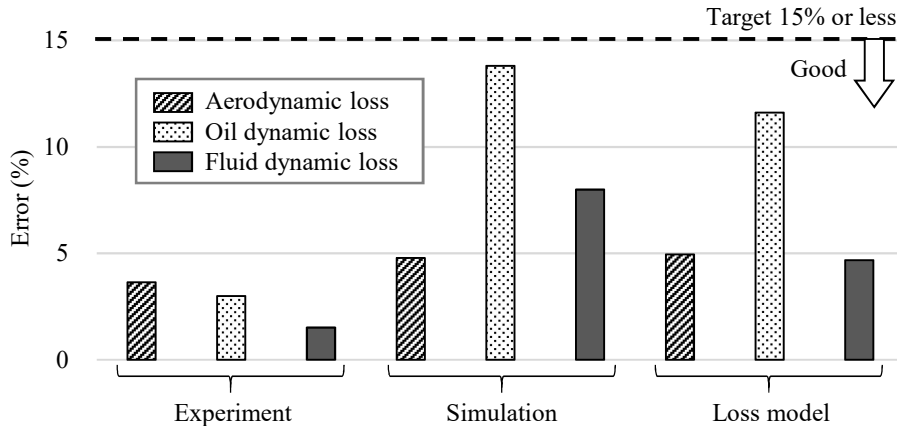

Fig. 6.11-7 Experimental error, numerical simulation error, and loss model error

In Fig. 6.11-7 , the losses that are important for practical use are targeted. In addition to the loss model error, the experimental measurement error and the numerical simulation error are also shown.

For the experimental measurement error, the relative standard deviation was calculated using a relative standard error of 2σ under each condition as the statistical universe (see Sections 3.5 and 3.6.4 for details). For the numerical simulation and loss models, the relative standard deviation was calculated using the difference from the experiment under each condition as the statistical universe (see Sections 4.3 and 4.4.4 for details of the numerical simulation error).

From Fig. 6.11-6, it was found that the experimental measurement error, the numerical simulation error, and the loss model error were empirically practical error of 15% or less for the two-axis helical gearbox.

6.12   Summary of Chapter 6

In this chapter, we proposed a fluid dynamic loss model and experimental and numerical classification methods for fluid dynamic loss elements using the clarification and classification results of fluid dynamic loss described in the previous chapter. We validated the loss model and the numerical classification method by comparing the experimental classification results with the fluid dynamic loss model calculation results and the numerical simulation loss classification results. The results are summarized as follows:

1. The fluid dynamic loss model was constructed by generalizing the characteristics of the velocity distribution and oil distribution obtained through the classification of the fluid dynamic loss and by generalizing the conventional researches.

   (a) The air side-flow loss is modeled as a loss due to the air drag of gear teeth. The key parameters are the air drag coefficient, air density, tooth area, and peripheral speed[3]. The air drag coefficient is affected by the helix angle of the teeth and the number of shroud openings. The coefficient is in the range of 1.4–2.1 under the condition of the two-axis helical gear box in this study.

   (b) The air pumping loss is modeled as a loss because of the acceleration of the air at the tip clearance and the backlash. This loss is negligible because the mass flow rate of the air accelerated in the tip clearance and the backlash is small.

   (c) The air vortex loss is modeled by dividing it into loss at the gear peripheral surface and loss at the gear side surfaces.

       i. The air vortex loss on the gear peripheral surface is defined as the loss due to the torque associated with the formation of a flow structure on the gear peripheral surface. The rotational moment coefficient on the gear peripheral surface is defined in the same way as the rotational moment coefficient of a cylinder. The rotational moment coefficient is affected by the ratio of the gear module to the gear radius and the rotational Reynolds number. This coefficient is in the range of 0.01 to 0.5 under conditions of a previous study conducted on a single gear.

       ii. The air vortex loss at the sides of the gear is the loss due to torque associated with the formation of the flow structure at the sides of the gear. The rotational moment coefficient on the side surfaces of the gear is defined in the same way as the rotational moment coefficient of a disk. The rotational moment coefficient is affected by the rotational Reynolds number and is in the range of 0.02 to 0.07 under the conditions of a previous study conducted on a single disk.

       iii. The shroud reduces the flow structure on the gear peripheral surface and the flow structure on the gear side surfaces and reduces the fluid dynamic loss. The loss reduction ratio by shrouding is

defined as the shroud coefficient, which is affected by the relative radial clearance (ratio of radial clearance to gear diameter), the relative axial clearance (ratio of axial clearance to tooth width), and the peripheral opening angle. The coefficient is in the range of 0.34 to 1.0 under the conditions of a previous study conducted with a gear.

    iv. As the main parameters of the air vortex loss, we consider the loss on the gear peripheral surface because the loss on the gear peripheral surface is greater than the loss on the gear side surfaces due to the gear tooth peak and the valleys. When the equation of the moment coefficient on the peripheral surface is decompressed and arranged, the key parameters of loss on the gear peripheral surface are air density, tooth area, peripheral speed$^{2.9}$, and shroud coefficient.

(d) The oil-jet acceleration loss is modeled as the loss in which the supplied oil is accelerated to the gear peripheral speed. The key parameters are the oil supply flow rate and the peripheral speed^2.

(e) The oil reacceleration loss is modeled as the loss in which the mass flow rate of the oil re-flowing into the gear meshing part is accelerated to the gear peripheral speed. The key parameters are the oil reacceleration coefficient (= re-inflow rate/oil supply flow rate), oil supply flow rate, and peripheral speed^2. The oil reacceleration coefficient is affected by the peripheral opening angle and the shroud coefficient, which is in the range of 0.2 to 1.0 under the condition of the two-axis helical gearbox in this study. The more the gear is enclosed by the shroud (the smaller the shroud coefficient), the more oil remains inside the shroud. To consider this factor in the oil reacceleration loss model, the oil reacceleration loss is inversely proportional to the shroud coefficient.

(f) The oil churning loss is modeled by multiplying the air vortex loss by a magnification (oil mist coefficient) as a loss due to the churning of the oil mist around the gear. The key parameters are the oil mist coefficient and air vortex loss. The oil mist coefficient is affected by the oil supply flow rate and the shroud coefficient. The oil mist coefficient is in the range of 0.2 to 1.1 under the condition of the two-axis helical gearbox in this study. The oil churning loss is inversely proportional to the shroud coefficient to consider the effect of oil accumulating in the shroud as the gear is more enclosed.

(g) Because the air vortex loss is proportional to the shroud coefficient, and the oil reacceleration loss and the oil churning loss are inversely proportional to the shroud coefficient, it is considered that there exists an optimum value for the shroud coefficient.

2. As a method for classifying the fluid dynamic losses experimentally, a method for classifying aerodynamic loss using the theoretical equation and the experimental result with a single gear is proposed, and a method for classifying the oil dynamic loss using the theoretical equation and the difference in the rotational speed exponent of the loss is proposed.

3. As a method for classifying the fluid dynamic losses numerically, a method for classifying aerodynamic loss using a theoretical equation and numerical analysis results of a single gear is proposed, and a method for classifying the oil dynamic loss using a theoretical equation and flow rates of air and oil around the gear is proposed.

4. For the loss element of fluid dynamic loss, the loss model calculation results and the numerical simulation results qualitatively agree with the experimental results. Therefore, the loss model and the numerical simulation can be used to consider the tendency of the loss.

5. The fraction of elements with the proportional exponent of 3 (aerodynamic loss (air side-flow loss and air vortex loss), oil churning loss, and the loss in the gear peripheral part) increases as the rotational speed increases.

Chapter 7

Influence and Optimization of Design Parameters in Gearbox

In this chapter, the influences of the gearbox design parameters on the fluid dynamic losses are described while the phenomena are clarified, and the effects of parameter optimization on the fluid dynamic loss reduction are shown.

7.1 Design Parameters

The design parameters relating to fluid dynamic loss are shown in Fig. 7.1-1. The gear diameter, tooth width, gear module, helix angle, and gear aspect ratio (tooth width / gear diameter) are listed as gear design parameters. The shroud design parameters include the radial clearance, axial clearance, peripheral opening angle, peripheral opening phase, and the number of peripheral openings. The gear shaft design parameters include the rotational speed and the transmitted power. The oil jet design parameters include the oil flow rate, oil jet speed, and oil density. The breather design parameters include the internal pressure (or air density).

The influence of these design parameters on the fluid dynamic loss is discussed in this chapter, and the gear aspect ratio and shroud coefficient are taken as typical parameters and optimized.
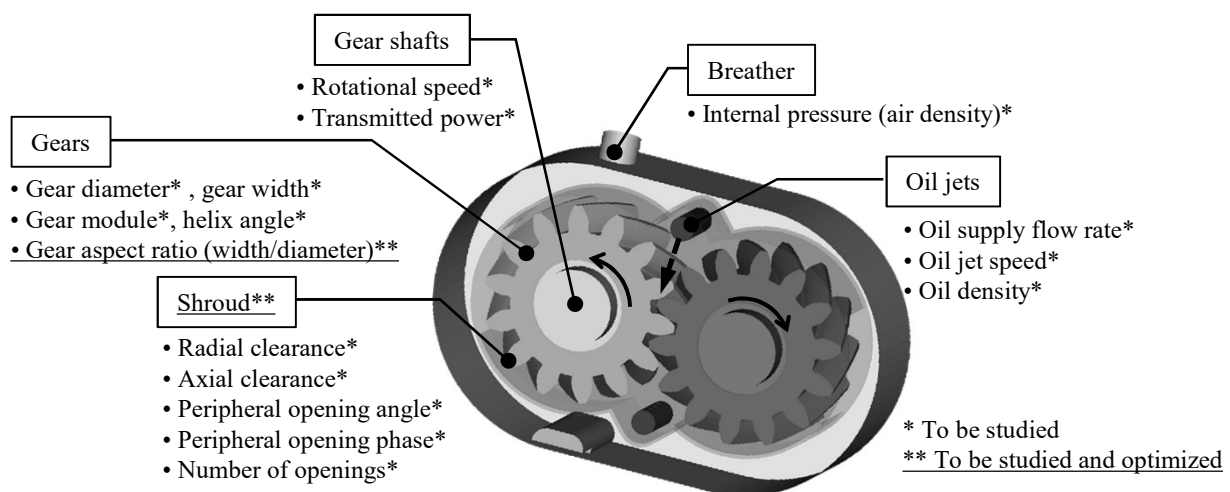
Fig. 7.1-1 Summary of design parameters (which influence the fluid dynamic loss)

7.2   Method of Study

(1)   Method for Studying Fluid Dynamic Loss

For the low-power-loss design of the gearbox, the fluid dynamic loss model (Chapter 6) is used for the calculation of the fluid dynamic loss, and the influence of the design parameters shown in Fig. 7.1-1 is studied based on a two-axis helical gearbox (Section 3.1.1). The range of parameters in this chapter is beyond those examined in Section 6.11, therefore the results should be treated carefully.

From among the design parameters, the influences of the gear aspect ratio and the shroud parameter (peripheral opening angle), which are the targets for optimization were validated using numerical simulations to ensure the reliability of the results (see Appendix C).

(2)   Method for Studying Gear Friction Loss

In the optimization of the gear aspect ratio, the gear friction loss must be considered because the gear friction loss changes in addition to the fluid dynamic loss.

The calculation method of the gear friction loss (power loss at the gear contact surface) can be divided into a simple calculation method using a time-averaged equation for the friction coefficient at the contact surface, and a detailed calculation method for calculating the friction coefficient in consideration of unsteady contact conditions, which are shown in Appendix B. The detailed calculation method was used in this chapter.

7.3   Conditions of Study

Table 7.3-1 shows the base conditions in these study. The "M3" gear in Table 7.3-1 is the gear with module 3. The "M5-1" gear has the same pitch diameter as the M3 gear and but with module changed to 5.

The "M5-2" gear is a gear in which the rated rotational speed of the M5-1 gear is lowered (The rated rotational speed was set to 0.7 times that of the M5-1 gear. To keep the pressure of the tooth surface constant, the tooth width was set to 1/0.7 times). The gears based on the study of each design parameter are shown in "Objectives" in Table 7.3-1 . In the optimization of the gear aspect ratio and the shroud coefficient, the difference between the oil supply temperature and the oil discharge temperature was kept constant on the assumption of an application to the actual gearbox design. This is based on the consideration that the oil supply flow rate can be reduced when the power loss is reduced.

Figure 7.3-1 shows typical gears used for studying the gear aspect ratio[1]. Figure 7.3-1 (a) shows the M3 gear (gear aspect ratio of 0.25). Figure 7.3-1 (b) shows a modified M3 gear for which the tooth width $\times$ gear diameter[2] is the same as that of the M3 gear and the gear aspect ratio is changed to 1.12.

Figure 7.3-2 shows the M5-1 gear, which is used as the base model for the study of the shroud parameters[1]. The gear is surrounded by a shroud and has two openings on the peripheral surface.

---

[1] These models are also numerical simulation models used for an additional validation in Appendix C.

Table 7.3-1 Base conditions for considering the influence and optimization of the design parameters

	Parameter		M3	M5-1	M5-2
Objectives	Influence of gear diameter, aspect ratio		✓		
	Influence of gear width, module, helix angle			✓	
	Influence of shroud parameters			✓	
	Influence of operating parameters			✓	
	Optimization of gear aspect ratio				✓*
	Optimization of shroud			✓*	
	Optimization of gear aspect ratio and shroud		✓*		✓*
Gear parameters	Module (mm)		3.0	5.0	
	Pressure angle (°)		20		
	Gear ratio		2.4		
	Number of teeth	Input gear	55	33	
		Output gear	23	14	
	Pitch diameter (mm)	Input gear	191		
		Output gear	80		
	Face width (mm)		34		49
Shroud parameters	Radial clearance (mm)		5.0		
	Axial clearance (mm)		5.0		
	Opening angle (°)		30		
	Opening phase (°)		180		
	Number of openings (per gear)		1		
Operating conditions	Transmitted power (kW)		570		
	Rotational speed (rpm)	Input gear	10000	7000	
		Output gear	23913	16739	
	Oil supply flow rate (L/min)		7.40*		
	Oil jet speed (m/s)		20**		
	Air density (kg/m^3)		1.062		
	Oil density (kg/m^3)		971		

* Adjusted to keep a 30 °C temperature difference between the supplied oil and the scavenged oil
  for optimization of the gear aspect ratio and/or shroud

** Proportional to the oil supply flow rate under different conditions of the oil supply flow rate

(a) M3 gear with gear aspect ratio 0.25

(b) Gear with gear aspect ratio reduced to 1.12 based on M3 gear
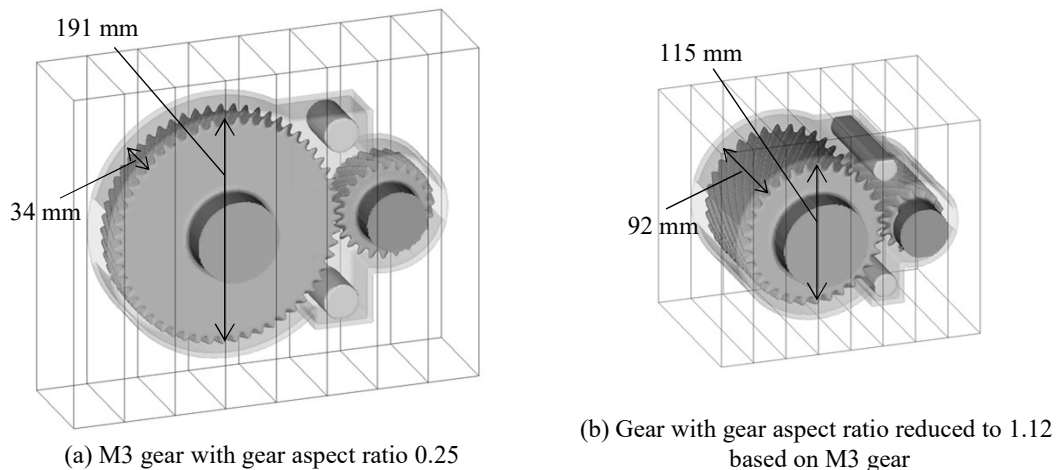
Fig. 7.3-1 Models for studying the influence of changes in the gear aspect ratio

(a) Radial clearance   (b) Axial clearance   (c) Peripheral opening angle and phase
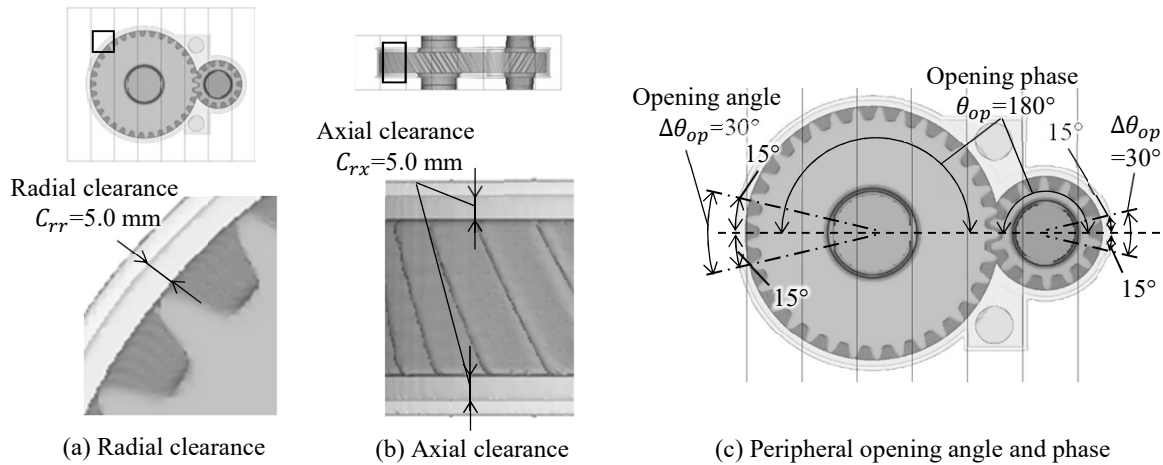
Fig. 7.3-2 Models for studying the influence of the shroud parameters (M5-1 gear)

7.4 Influence of Design Parameters

7.4.1 Influence of Design Parameters

(1) Influence of Gear Parameters

The influence of the gear parameters on the fluid dynamic loss is shown in Fig. 7.4-1 . Figure 7.4-1 (a) shows the result for an oil supply flow rate of 1.48 L/min, and (b) shows the result for an oil supply flow rate of 7.40 L/min. The vertical axis is the ratio of the fluid dynamic loss to the base condition, and the horizontal axis is the ratio of the change in each parameter to the base condition. The inverse of the gear aspect ratio is used to compare the trend with those of other parameters.

Figures 7.4-1 (a) and (b) show that a reduction in the gear diameter is the most effective way of reducing the fluid dynamic loss, and that a reduction in the tooth width or gear module and an increase in the gear aspect ratio (= tooth width / gear diameter) are equivalent. Reductions in the gear diameter, tooth width, and gear module reduce the rated load (surface pressure strength). If the rated load changes, it is necessary to redesign the gear specifications. Increasing the helix angle reduces the fluid dynamic loss, but because the thrust force changes, peripheral parts such as bearings must be redesigned.

In contrast, by keeping the "tooth width × gear diameter^2" constant, the surface pressure strength (important for high-speed gears) of the tooth surface can be kept constant, and the rated load can also be kept constant (gear weight can also be kept constant). Therefore, if the tooth width ×gear diameter^2 is constant, a gear aspect ratio with a specific low fluid dynamic loss can be selected. In Section 7.4.2, the change in the fluid dynamic loss phenomenon with a change in the gear aspect ratio is considered using the loss model. In Section 7.5, the gear aspect ratio is optimized.

(2) Influence of Operating Conditions

The influence of the operating conditions on the fluid dynamic loss is shown in Fig. 7.4-2 . Figure 7.4-2 (a) shows the result for an oil supply flow rate of 1.48 L/min, and (b) shows the result for an oil supply flow rate of 7.40 L/min. The vertical axis shows the ratio of the fluid dynamic loss to the base condition, and the horizontal axis shows the ratio of the change in each parameter to the base condition.

(a) Oil supply flow rate 1.48 L/min

(b) Oil supply flow rate 7.40 L/min
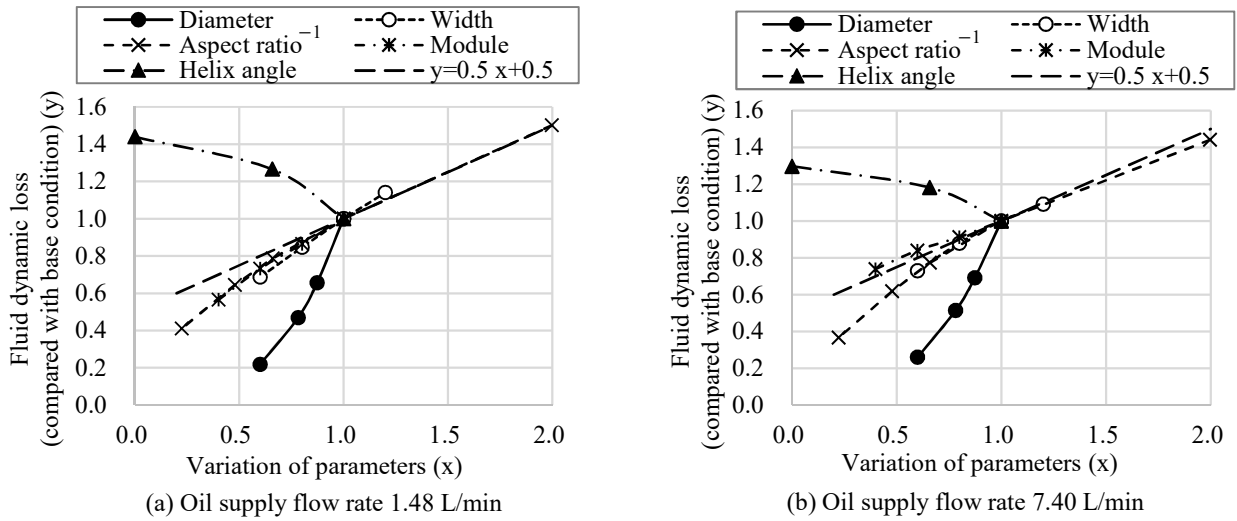
Fig. 7.4-1 Influence of gear parameter on the fluid dynamic loss (obtained using loss models)

(a) Oil supply flow rate 1.48 L/min

(b) Oil supply flow rate 7.40 L/min
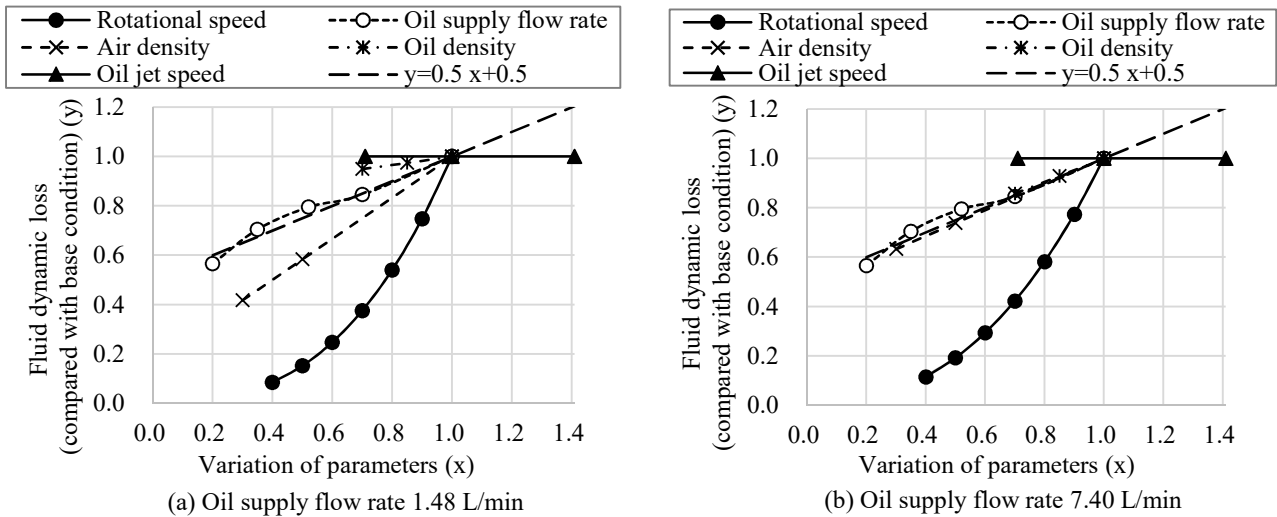
Fig. 7.4-2 Influence of operation parameter on the fluid dynamic loss (obtained using loss models)

(a) Oil supply flow rate 1.48 L/min

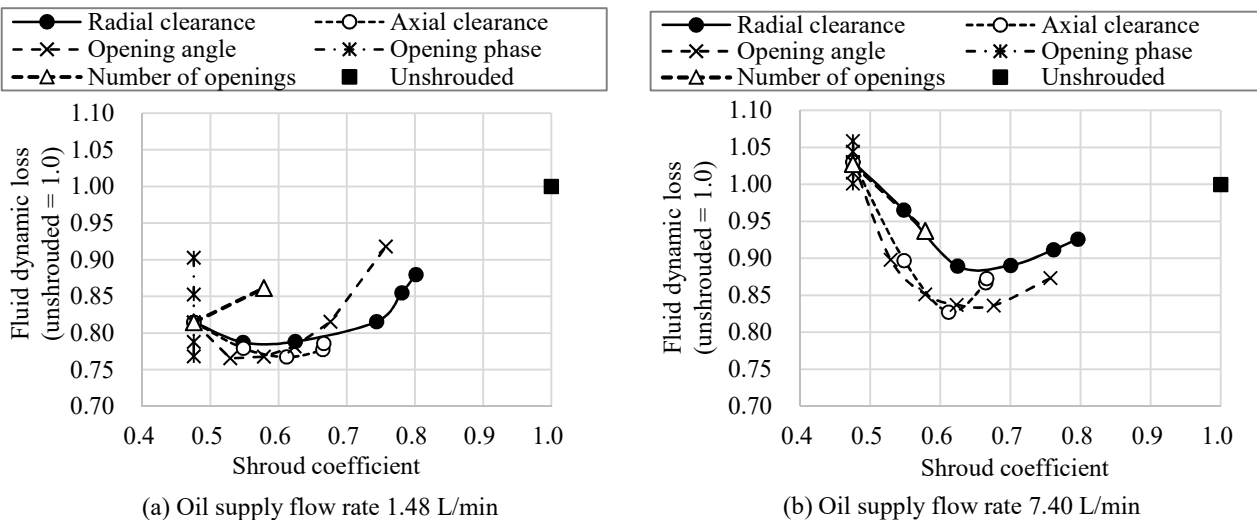(b) Oil supply flow rate 7.40 L/min

Fig. 7.4-3 Influence of shroud parameter on the fluid dynamic loss (obtained using loss models)

From Fig. 7.4-2 (a), the influence of the rotational speed is the largest, followed by air density, oil supply flow rate, and oil density. The influence of the oil jet velocity cannot be observed. In Fig. 7.4-2 (b), the influence of the air density is smaller and the influence of the oil density is larger than in Fig. 7.4-2 (a), which is considered to be because the ratio of the oil dynamic loss to the fluid dynamic loss increased with an increase in the oil supply flow rate.

(3) Influence of Shroud Parameters

The influence of the shroud parameters on the fluid dynamic loss is shown in Fig. 7.4-3 . Figure 7.4-3 (a) shows the result for an oil supply flow rate of 1.48 L/min, and (b) shows the result for an oil supply flow rate of 7.40 L/min. The vertical axis is the ratio of the fluid dynamic loss to the base condition (when the shroud coefficient is 1.0), and the horizontal axis is the shroud coefficient.

Figures 7.4-3 (a) and (b) show that the fluid dynamic loss can be reduced by adjusting each parameter of the shroud. This is related to the fact that installing a shroud reduces the aerodynamic loss while increasing the oil dynamic loss, as shown in Chapter 5. In Section 7.4.3, changes in the fluid dynamic loss phenomenon when the shroud coefficient is changed are considered using the loss model, and the shroud coefficient is optimized in Section 7.6.

7.4.2 Consideration of the Influence of Gear Aspect Ratio on Fluid Dynamic Loss

(1) Trend of Fluid Dynamic Loss

Figure 7.4-4 (a) shows a breakdown of the fluid dynamic loss, (b) shows a breakdown of the aerodynamic loss, and (c) shows a breakdown of the oil dynamic loss. It can be seen that each element of loss is reduced by increasing the gear aspect ratio.

Figure 7.4-5 shows an analysis of the changes in the elements of the fluid dynamic loss. The influence of changes in the gear aspect ratio on the fluid dynamic loss is shown in Fig. 7.4-5 (a). The fluid dynamic loss at a gear aspect ratio of 0.13 as indicated by the arrow in Fig. 7.4-5 (a) is 100%, which can be decomposed into the aerodynamic loss and the oil dynamic loss, resulting in an aerodynamic loss of 33% (leftmost bar graph in Fig. 7.4-5 (b)) and an oil dynamic loss of 67% (leftmost bar graph in Fig. 7.4-5 (c)). A waterfall diagram for a comparison of the gear aspect ratios of 0.13 and 1.12 in terms of the aerodynamic loss is shown in Fig. 7.4-5 (b). As a result of the decrease in 4 points in the air side-flow loss and 19 points in the air vortex loss, the loss is 9% for a gear aspect ratio of 1.12. Here, the air pumping loss was ignored because it was sufficiently small.

Figure 7.4-5 (c) shows a waterfall diagram comparing the gear aspect ratios of 0.13 and 1.12 in terms of the oil dynamic loss. The total of the oil-jet acceleration loss and the oil reacceleration loss decreased by 38 points, and the oil churning loss decreased by 14 points. As a result, the loss was 16% for a gear aspect ratio of 1.12. The aerodynamic loss for a gear aspect ratio of 1.12 was 9% (rightmost bar graph in Fig. 7.4-5 (b)) and the oil dynamic loss for a gear aspect ratio of 1.12 was 16% (rightmost bar graph in Fig. 7.4-5 (c)), which adds up to 25%. This is the fluid dynamic loss at a gear aspect ratio of 1.12 shown by the arrow in Fig. 7.4-5 (d).

The relative changes in the elements of the fluid dynamic loss in Figs. 7.4-5 (b) and (c) are shown in Figs. 7.4-5 (e1)–(e4), and it can be seen from Figs. 7.4-5 (e1)–(e4) that each element of the fluid dynamic loss decreased.

(a) Fluid dynamic loss   (b) Aerodynamic loss   (c) Oil dynamic loss

* Averaged value of input gear and output gear   ** The air pump loss is small enough to be ignored.
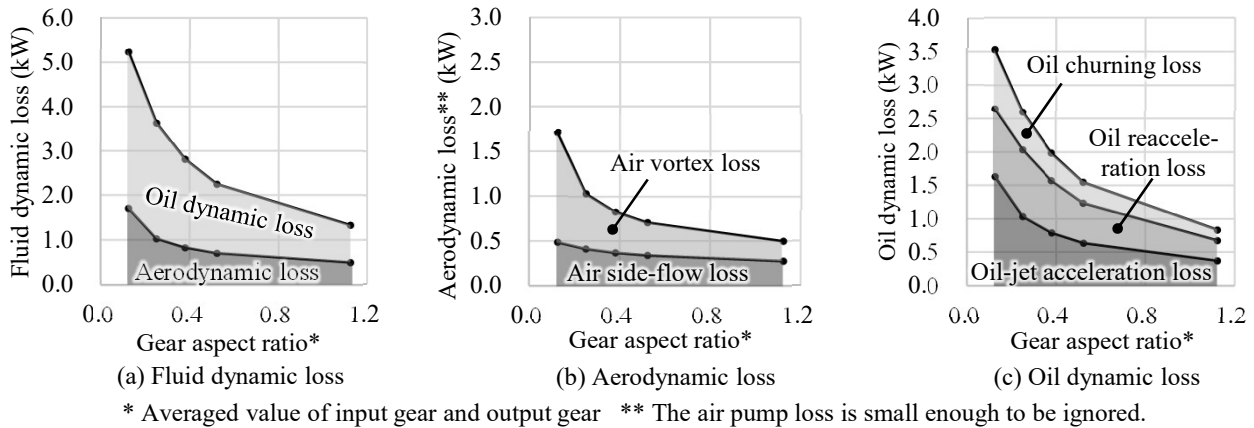
Fig. 7.4-4 Variation in fluid dynamic loss with respect to gear aspect ratio changes (obtained using loss models)

(2)   Consideration with Regard to Parameters of Loss Model

To understand the cause of the relative changes in the elements of the fluid dynamic loss, Fig. 7.4-6 shows the change in each parameter of the loss model according to the gear aspect ratio. The vertical axis of each figure shows the logarithmic values normalized for a gear aspect ratio of 0.13.

In the parameter change of the air side-flow loss shown in Fig. 7.4-6 (a), the peripheral speed[3] decreases and the tooth area increases with an increase in the gear aspect ratio. It is considered that the decrease in the loss for the gear aspect ratio of 1.12 in Fig. 7.4-5 (e1) is due to a larger decrease in the peripheral speed[3] rather than an increase in the tooth area.

For the parameter change of the air vortex loss shown in Fig. 7.4-6 (b), as in (a), the peripheral speed[2.9] decreases and the tooth area increases with an increase in the gear aspect ratio. It is considered that the decrease in the loss for the gear aspect ratio of 1.12 in Fig. 7.4-5 (e2) is due to a larger decrease in the peripheral speed[2.9] rather than an increase in the tooth area. It is considered that the reason why the loss decrease rate of the air vortex loss is larger than that of the air side-flow loss is because the area of the gear sides decreases with an increase in the gear aspect ratio and the loss decreases accordingly.

As shown in Fig. 7.4-6 (c), the parameter changes of the oil-jet acceleration loss and the oil reacceleration loss reduced the peripheral speed[2]. Therefore, the reduction in the loss for a gear aspect ratio of 1.12 shown in Fig. 7.4-5 (e3) was caused by a reduction in the peripheral speed[2]. The reduction rate of the loss in this case was equivalent to the reduction rate of the air vortex loss (Fig. 7.4-6 (b)), and it is considered that this was because the exponent of the peripheral speed was smaller than that of the air vortex loss, but that the increase in tooth area had no influence.

For the parameter change of the oil churning loss shown in Fig. 7.4-6 (d), the air vortex loss decreased, and the loss reduction rate of the oil churning loss (Fig. 7.4-5 (e4)) was the same as that of the air vortex loss (Fig. 7.4-5 (e2)), probably because the oil mist coefficient was hardly changed and only the influence on the air vortex loss was affected.

(a) Fluid dynamic loss,
gear aspect ratio 0.13

(b) Changes in aerodynamic loss

(c) Changes in oil dynamic loss

(d) Fluid dynamic loss,
gear aspect ratio 1.12

(e1) Changes in
air side-flow loss

(e2) Changes in
air vortex loss

(e3) Changes in the sum of
oil-jet acceleration loss
and oil reacceleration loss

(e4) Changes in
oil churning loss
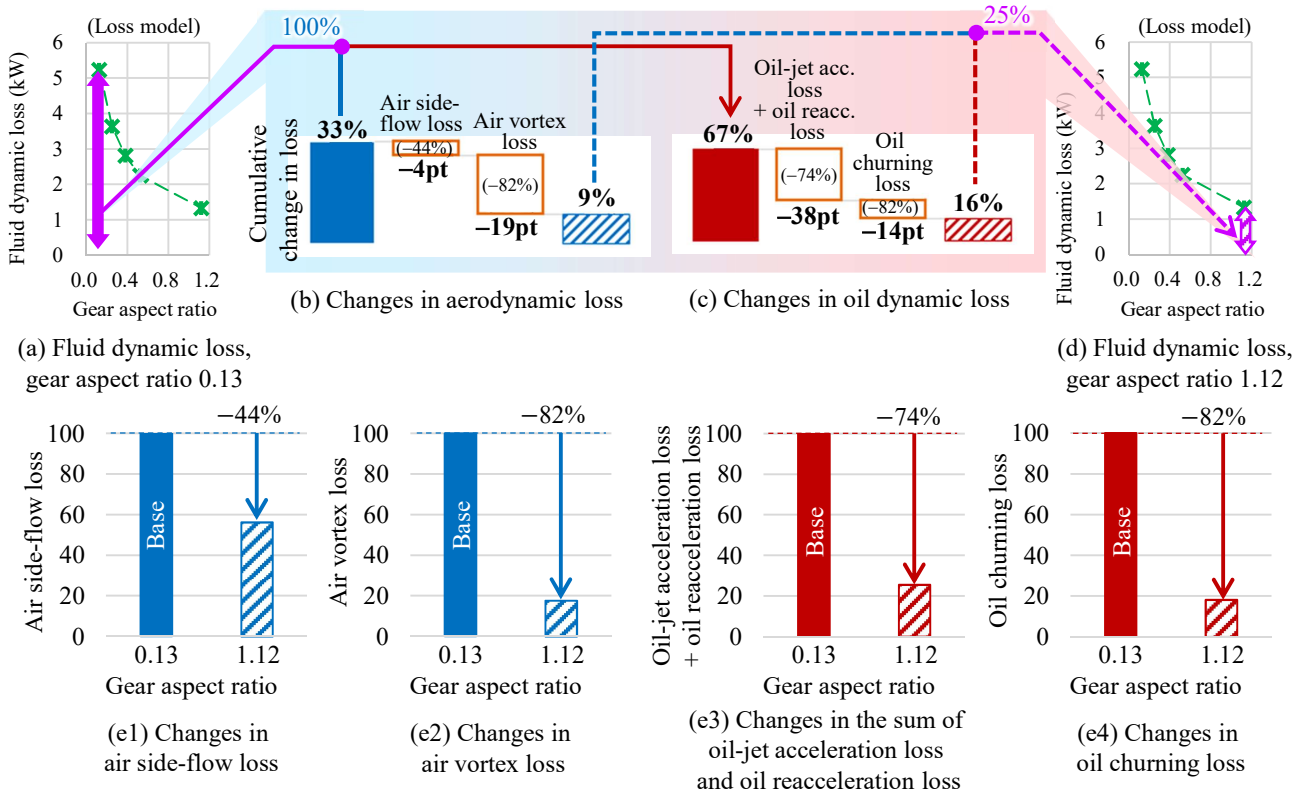
Fig. 7.4-5 Analysis of the decrease in loss due to a decrease in the gear aspect ratio (obtained using loss models)

(a) Parameters of air side-flow loss model

(b) Parameters of air vortex loss model

(c) Parameters of oil-jet acceleration loss model
and oil reacceleration loss model

(d) Parameters of oil churning loss model
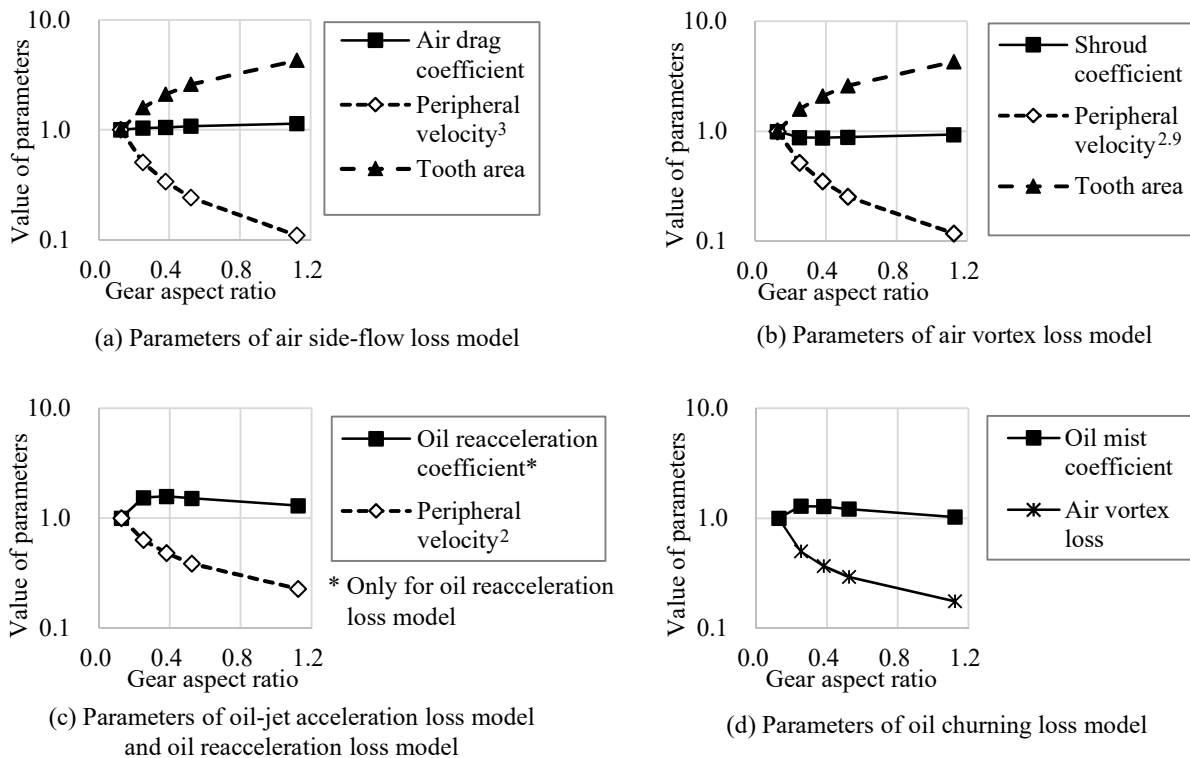
Fig. 7.4-6 Changes in the parameters of the loss model with respect to gear aspect ratio changes

(3)   Results from Numerical Simulations

The change in fluid dynamic loss is discussed based on the numerical simulation results. Figure 7.4-7 shows the results of the numerical simulation at a gear aspect ratio of 0.13. Figure 7.4-7 (a) shows the streamline, (b1) shows the contour of the air pressure, (b2) shows an enlarged view of the gear meshing part of (b1), and (b3) shows an enlarged view of the gear peripheral part. Figure 7.4-7 (c) shows the oil distribution (contour of 2% of the oil in the calculation cell). Figure 7.4-7 (d1) shows the oil pressure (result of subtracting the air pressure from the air and oil pressures), (d2) shows an enlarged view of the gear meshing part of (d1), and (d3) shows an enlarged view of the gear peripheral part. Figure 7.4-7 (e1) shows the oil contour on the gear surface, (e2) shows an enlarged view of the gear meshing part, and (e3) shows an enlarged view of the gear peripheral part. Figure 7.4-8 shows the result of the numerical simulation for a gear aspect ratio of 1.12 in the same manner as Fig. 7.4-7 . In Fig. 7.4-8 , a comparison with Fig. 7.4-7 is shown.

The differential pressure (Figs. 7.4-8 (b2), (b3), (d2), (d3)) at a gear aspect ratio of 1.12 is respectively lower than the differential pressure (Figs. 7.4-7 (b2), (b3), (d2), (d3)) at a gear aspect ratio of 0.13, which corresponds with the decrease in the fluid dynamic loss elements (Figs. 7.4-5 (el)–(e4)). Therefore, it is revealed that the decrease in the fluid dynamic loss elements appears as a decrease in the differential pressure.

The oil on the gear surface at a gear aspect ratio of 1.12 (Figs. 7.4-8 (e2) and (e3)) is more dispersed than the oil on the gear surface at a gear aspect ratio of 0.13 (Figs. 7.4-7 (e2) and (e3)), but there was no significant change in the amount of oil, corresponding to no significant change in the oil reacceleration coefficient (Fig. 7.4-6 (c)) or the oil mist coefficient (Fig. 7.4-6 (d)).

These results indicate that increasing the gear aspect ratio reduces the fluid dynamic loss, but that increasing the tooth area suppresses the reduction in the loss. Moreover, the reduction in the fluid dynamic loss appears in the form of a reduction in the differential pressure between the gear meshing and the gear peripheral parts.

(a) Air streamline* (b1) Air pressure** (c) Oil distribution** (d1) Oil pressure** (e1) Oil on gears**

(b2) Air pressure around meshing (b3) Air pressure around periphery (d2) Oil pressure around meshing (d3) Oil pressure around periphery (e2) Oil on gears around meshing (e3) Oil on gears around periphery

* Time-averaged , ** Time-averaged at every gear pitch
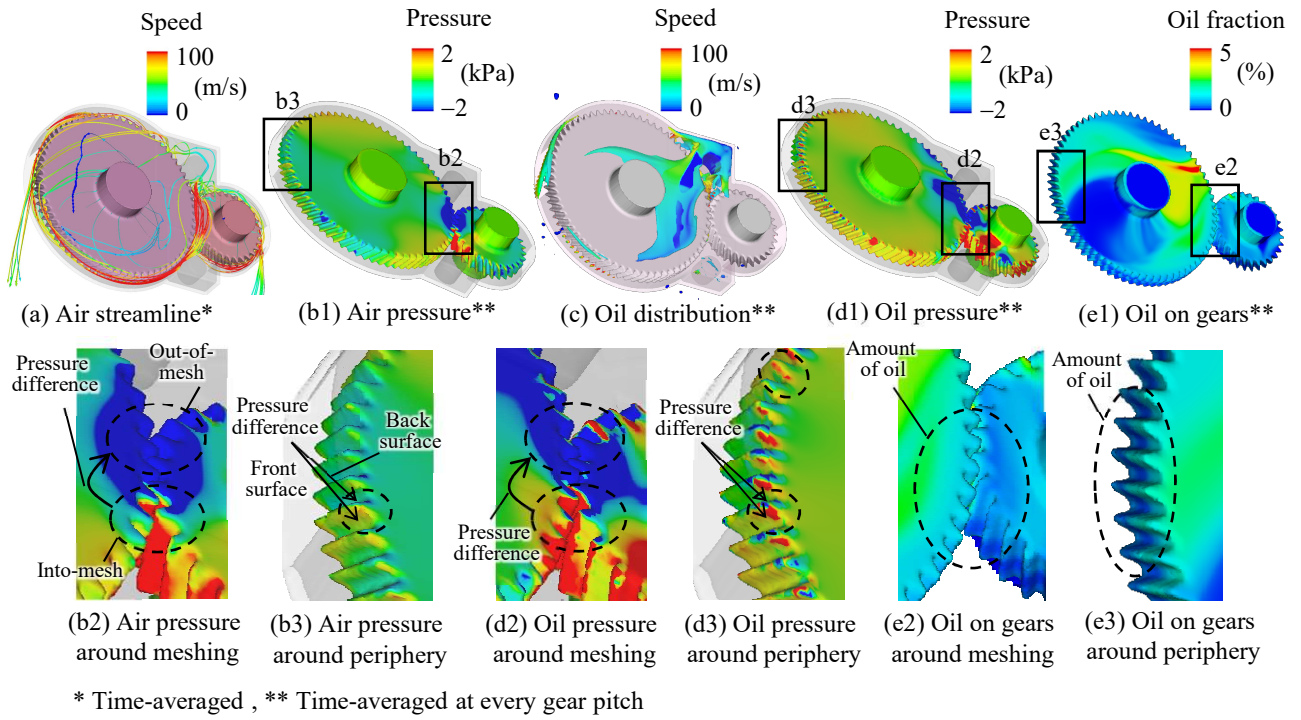
Fig. 7.4-7 Results of the numerical simulation for a gear aspect ratio of 0.13

(a) Air streamline* (b1) Air pressure** (c) Oil distribution** (d1) Oil pressure** (e1) Oil on gears**

(b2) Air pressure around meshing (b3) Air pressure around periphery (d2) Oil pressure around meshing (d3) Oil pressure around periphery (e2) Oil on gears around meshing (e3) Oil on gears around periphery

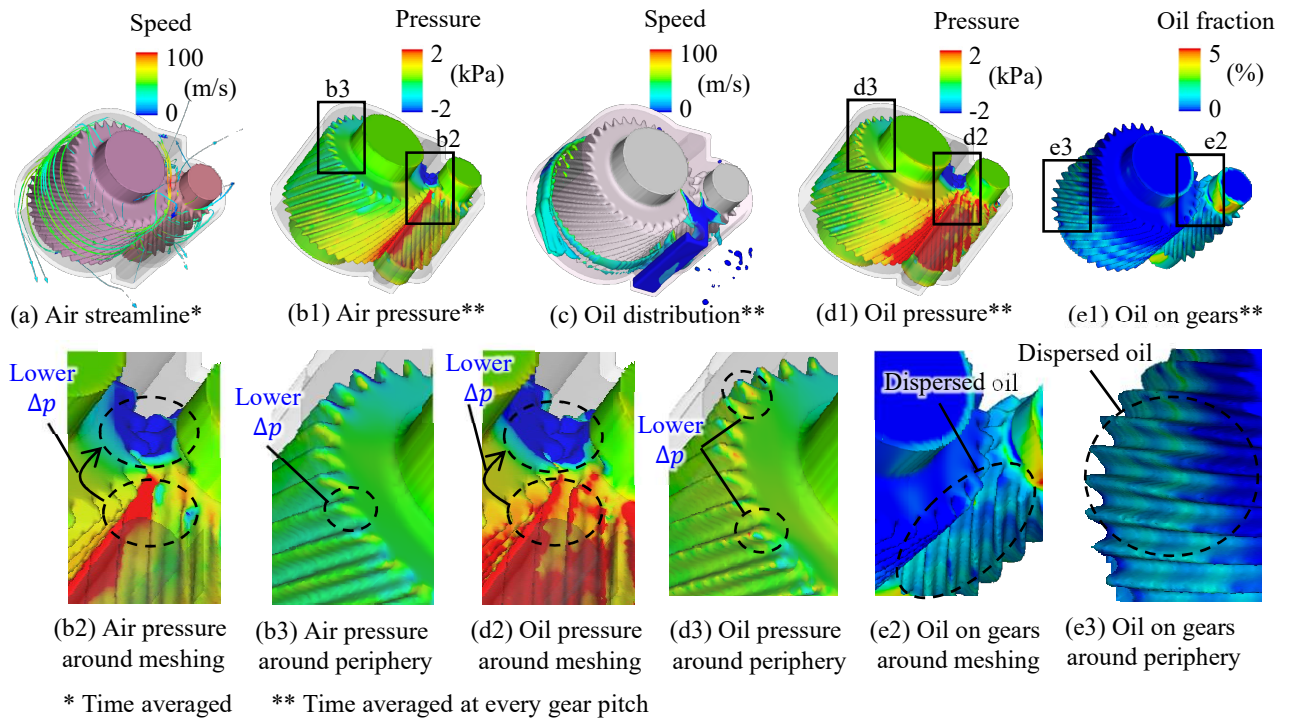* Time averaged   ** Time averaged at every gear pitch

Fig. 7.4-8 Results of the numerical simulation for a gear aspect ratio of 1.12 compared with those for a gear aspect ratio of 0.13

7.4.3 Consideration of the Influence of Shrouding on Fluid Dynamic Loss

(1) Trend of Fluid Dynamic Loss

Figure 7.4-9 (a) shows a breakdown of the fluid dynamic loss, (b) shows a breakdown of the aerodynamic loss, and (c) shows a breakdown of the oil dynamic loss. From Fig. 7.4-9 (a), it is found that the fluid dynamic loss becomes minimal around a shroud coefficient of 0.63. This is because when the shroud coefficient increases, the air vortex loss tends to increase (Fig. 7.4-9 (b)), while the oil reacceleration loss and oil churning loss tend to decrease (Fig. 7.4-9 (c)).

Figure 7.4-10 shows an analysis of the changes in the fluid dynamic loss components at shroud coefficients of 0.48 (peripheral opening angle of 30°, large loss condition) and 0.58 (peripheral opening angle of 90°, low loss condition), and Figs. 7.4-10 (e1)–(e4) show the relative changes in the fluid dynamic loss components in Figs. 7.4-10 (b) and (c). The comparison method for the fluid dynamic loss components is the same as in Fig. 7.4-5 . Figures 7.4-10 (e1)–(e4) show that the aerodynamic loss increases and the oil dynamic loss decreases as the shroud coefficient increases.

(a) Fluid dynamic loss　　　　(b) Aerodynamic loss　　　　(c) Oil dynamic loss

* Averaged value of input gear and output gear　　** The air pump loss is small enough to be ignored.
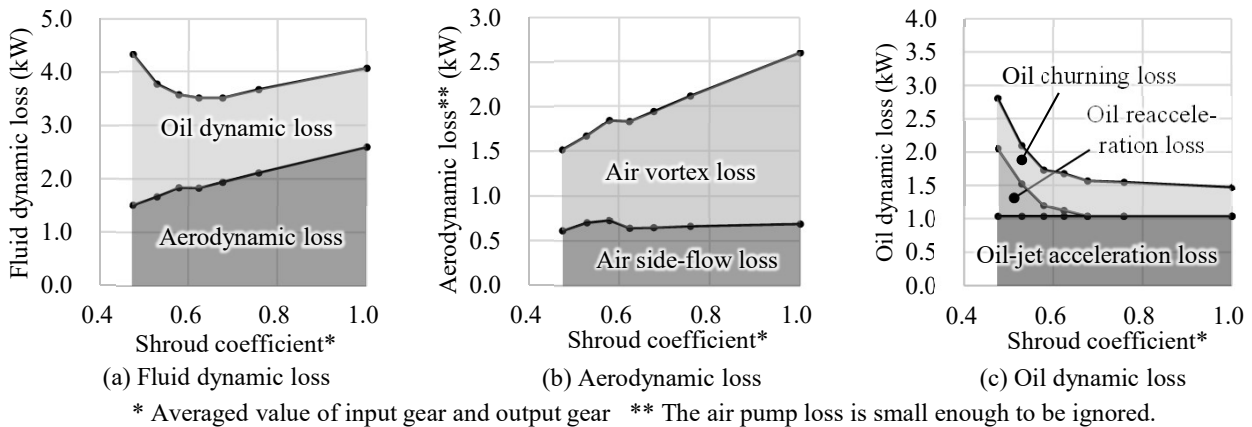
Fig. 7.4-9 Variation in fluid dynamic loss according to shroud coefficient changes (obtained using loss models with respect to radial clearance changes)

(2) Consideration with Regard to Parameters of Loss Model

To understand the cause of the relative change in the fluid dynamic loss components, Fig. 7.4-11 shows the change of each parameter in the loss model according to the gear aspect ratio (only parameters which changed are shown). The vertical axis of each figure shows the normalized value using a value for the shroud coefficient of 0.48.

Figure 7.4-11 (a) shows that the parameter change of the air side-flow loss (change in the air drag coefficient) is small. As a result, it is considered that the change in the air side-flow loss became small, as shown in Fig. 7.4-10 (e1). From the parameter change of the air vortex loss shown in Fig. 7.4-11 (b), it can be seen that the increase in the air vortex loss (Fig. 7.4-10 (e2)) is due to an increase in the shroud coefficient. From the parameter change of the oil reacceleration loss shown in Fig. 7.4-11 (c), it can be seen that the decrease in the oil reacceleration loss (Fig. 7.4-10 (e3)) is caused by a decrease in the oil reacceleration coefficient (because the oil-jet acceleration loss does not change). For the parameter change of the oil churning loss shown in Fig. 7.4-11 (d), as the shroud coefficient increases, the oil mist coefficient decreases and the air vortex loss increases. Therefore, it is considered that the decrease in the oil churning loss (Fig. 7.4-10 (e4)) was caused by the decrease in the oil mist coefficient exceeding the increase in the

air vortex loss.

(a) Fluid dynamic loss,
Shroud coefficient 0.48

(b) Changes in aerodynamic loss

(c) Changes in oil dynamic loss

(d) Fluid dynamic loss,
shroud coefficient 0.58

(e1) Changes in
air side-flow loss

(e2) Changes in
air vortex loss

(e3) Changes in the sum of
oil-jet acceleration loss
and oil reacceleration loss

(e4) Changes in
oil churning loss
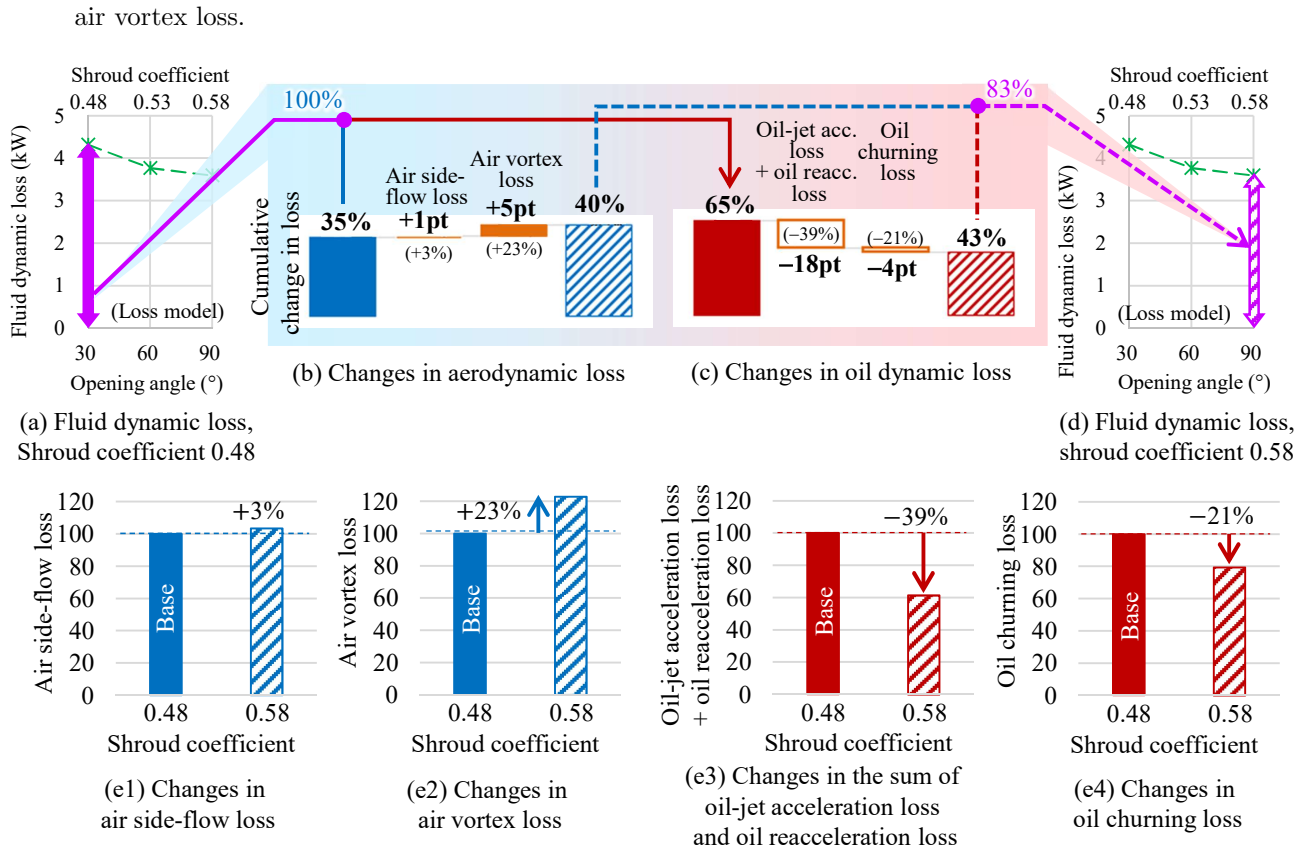
Fig. 7.4-10 Analysis of the decrease in loss due to a decrease in the shroud coefficient (obtained using loss models)

(a) Parameters of air side-flow loss model

(b) Parameters of air vortex loss model

(c) Parameters of oil-jet acceleration loss model
and oil reacceleration loss model

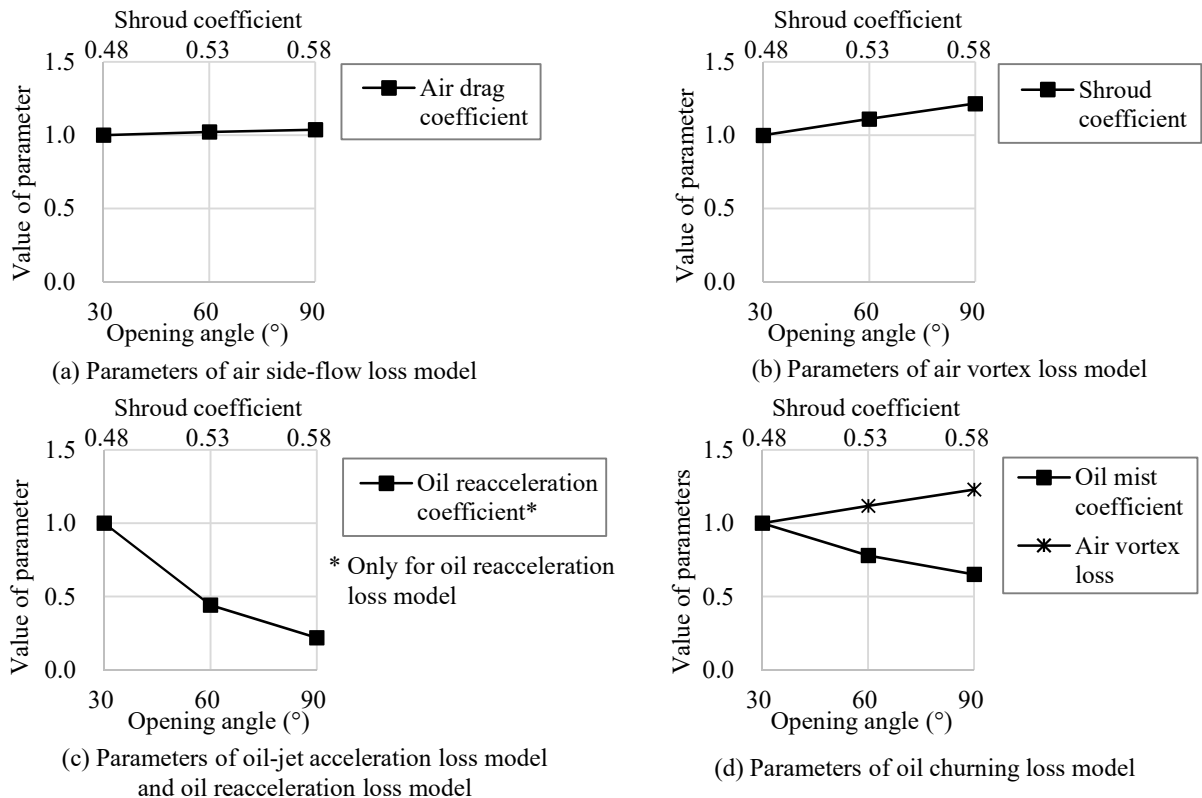(d) Parameters of oil churning loss model

Fig. 7.4-11 Changes in the parameters of the loss model according to shroud coefficient changes

(3)   Results from Numerical Simulations

The change in fluid dynamic loss is discussed based on the numerical simulation results. The results of the numerical simulation for a shroud coefficient of 0.48 are shown in Fig. 7.4-12 , and the results of the numerical simulation for a shroud coefficient of 0.58 are shown in Fig. 7.4-13 . The display method of the pressure distribution and the oil distribution is the same as in Fig. 7.4-7 .

The differential pressure in the gear meshing part at a shroud coefficient of 0.58 (Fig. 7.4-13 (b2)) is equivalent to the differential pressure at a shroud coefficient of 0.48 (Fig. 7.4-12 (b2)), which corresponds to an equivalent air side-flow loss (Fig. 7.4-10 (e1)). The differential pressure in the gear peripheral part is higher for a shroud coefficient of 0.58 (Fig. 7.4-13 (b3)) than for a shroud coefficient of 0.48 (Fig. 7.4-12 (b3)), which corresponds to an increase in the air vortex loss (Fig. 7.4-10 (e2)).

The differential pressure in the gear meshing part (Fig. 7.4-13 (d2)) or the differential pressure in the gear peripheral part (Fig. 7.4-13 (d3)) for a shroud coefficient of 0.58 are lower than the differential pressure for a shroud coefficient of 0.48 (Fig. 7.4-12 or Fig. 7.4-12 (d3)), corresponding to a decrease in the total of the oil-jet acceleration loss and the oil reacceleration loss (Fig. 7.4-10 (e3)) and a decrease in the oil churning loss (Fig. 7.4-10 (e4)), respectively. That is, it was found that the change in the elements of the fluid dynamic loss appeared as a differential pressure.

The oil on the gear surface at a shroud coefficient of 0.58 (Fig. 7.4-13 (e2) and (e3)) decreased compared with the oil on the gear surface at a shroud coefficient of 0.48 (Fig. 7.4-12 (e2) and (e3)), corresponding to a decrease in the oil reacceleration coefficient (Fig. 7.4-11 (c)) and the oil mist coefficient (Fig. 7.4-11 (d)), respectively. That is, it was found that the change in the oil reacceleration coefficient and the change in the oil mist coefficient appeared as the amount of oil on the gear surface.

From the above results, it was found that the main cause for the change in the fluid dynamic loss was an increase in the air vortex loss due to an increase in the shroud coefficient and a decrease in the oil reacceleration loss due to a decrease in the oil reacceleration coefficient. It was found that the change in the fluid dynamic loss appeared due to the differential pressure of the gear meshing part and the gear peripheral part, and that the change in the oil reacceleration coefficient and the oil mist coefficient appeared due to a change in the quantity of oil in the gear meshing part and the gear peripheral part, respectively.

(a) Air streamline* (b1) Air pressure** (c) Oil distribution** (d1) Oil pressure** (e1) Oil on gears**

(b2) Air pressure around meshing (b3) Air pressure around periphery (d2) Oil pressure around meshing (d3) Oil pressure around periphery (e2) Oil on gears around meshing (e3) Oil on gears around periphery

* Time-averaged , ** Time-averaged at every gear pitch
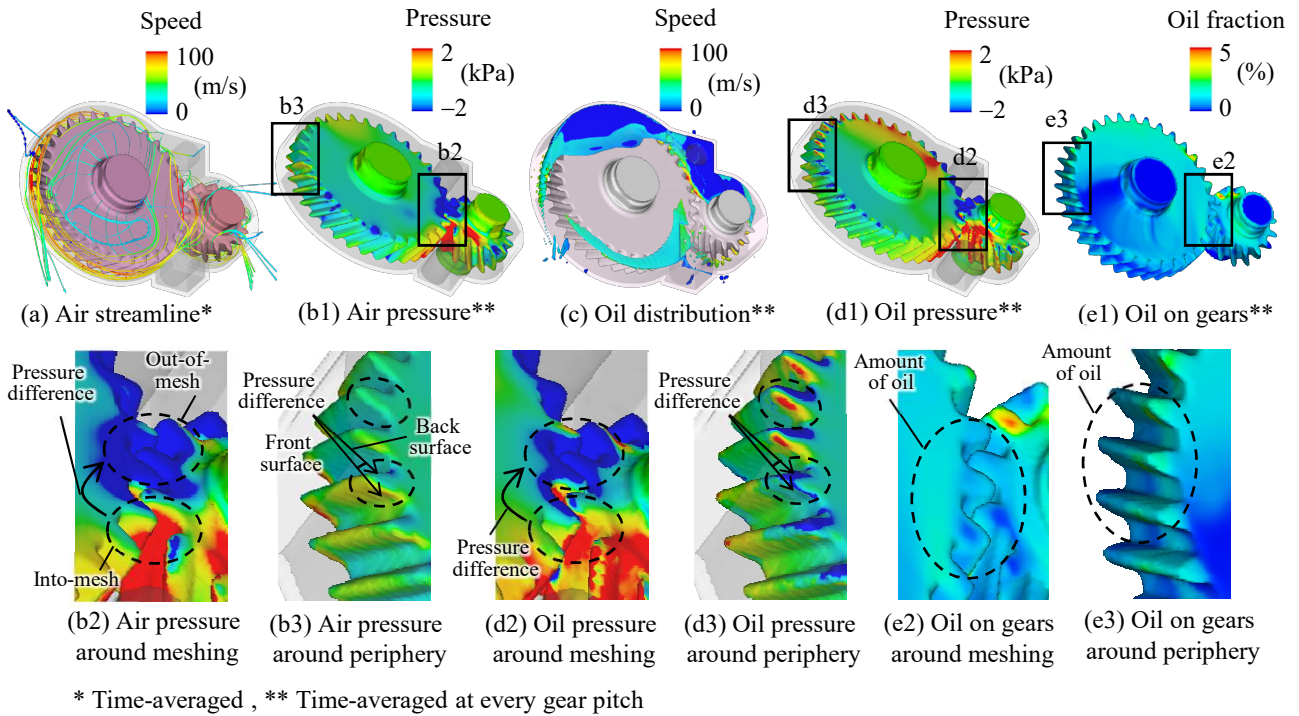
Fig. 7.4-12 Results of the numerical simulation for a shroud opening angle of 30° (shroud coefficient of 0.48)

(a) Air streamline* (b1) Air pressure** (c) Oil distribution** (d1) Oil pressure** (e1) Oil on gears**

(b2) Air pressure around meshing (b3) Air pressure around periphery (d2) Oil pressure around meshing (d3) Oil pressure around periphery (e2) Oil on gears around meshing (e3) Oil on gears around periphery

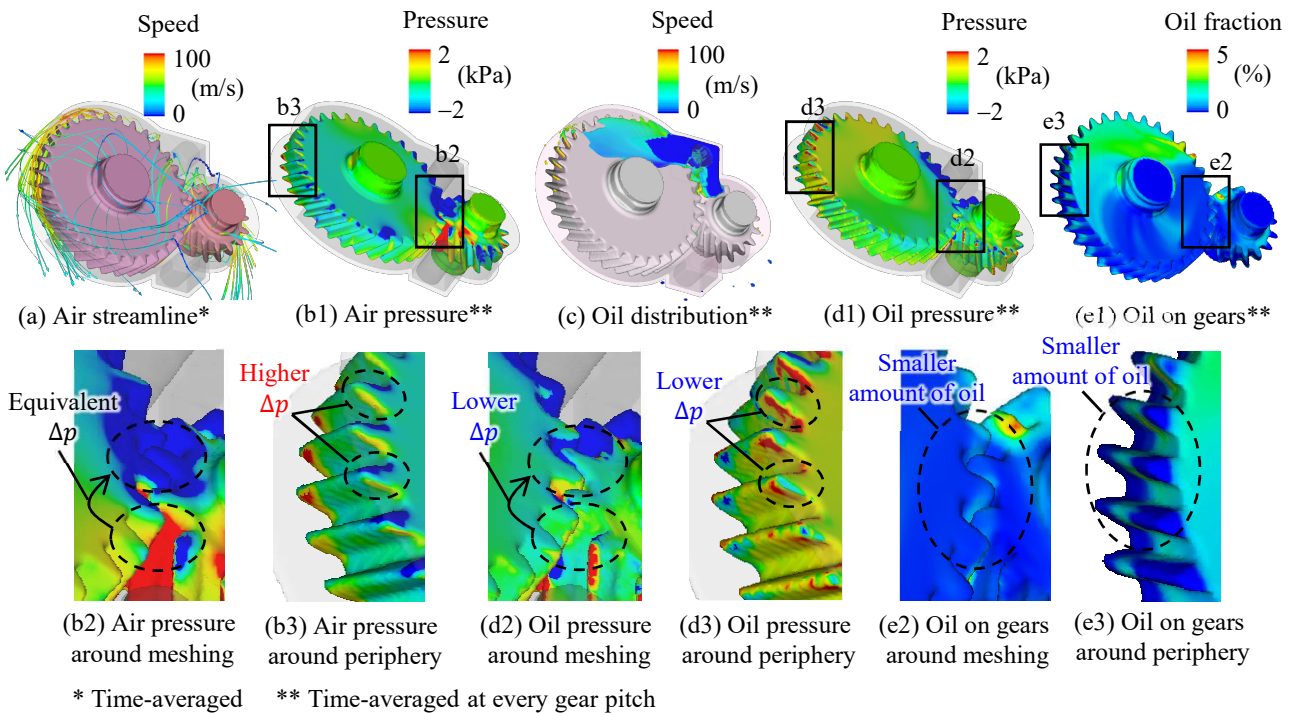* Time-averaged   ** Time-averaged at every gear pitch

Fig. 7.4-13 Results of the numerical simulation for a shroud opening angle of 90° (shroud coefficient of 0.58) compared with those for a shroud opening angle of 30° (shroud coefficient of 0.48)

7.5   Optimization of Gear Aspect Ratio

To determine the optimal gear-aspect ratio, it is necessary to consider not only the fluid dynamic loss but also the gear friction loss. Figure 7.5-1 shows the change in the fluid dynamic loss, the gear friction loss, and the efficiency as the gear aspect ratio changes. It can be seen that the gear friction loss increases monotonically and that the fluid dynamic loss decreases monotonically as the gear aspect ratio increases. Because the trends of these losses are opposite, it can be seen that there is an optimal gear aspect ratio ("A" in Fig. 7.5-1).

The optimal gear aspect ratio is considered to change with changes in the gear friction loss and fluid dynamic loss. Figure 7.5-2 (a) shows the losses and efficiency when the transmitted power is set to 1/2. It can be seen that the optimal gear aspect ratio increases as the gear friction loss decreases (from "A" in Fig. 7.5-1 to "B" in Fig. 7.5-2 (a)). Figure 7.5-2 (b) shows the losses and efficiency when the air pressure is set to 1/3. It can be seen that the optimal gear aspect ratio decreases as the fluid dynamic loss decreases (from "A" in Fig. 7.5-1 to "C" in Fig. 7.5-2 (b)).
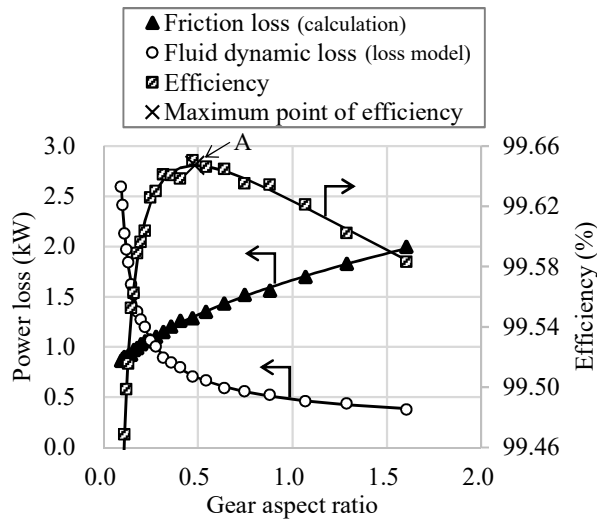

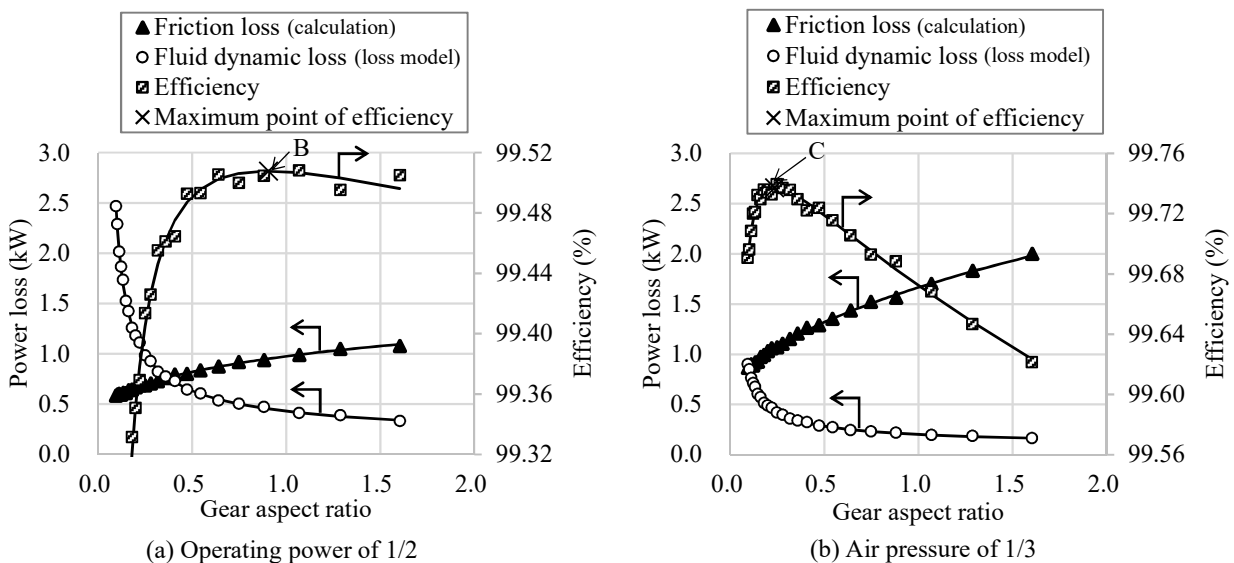Fig. 7.5-1 Optimization result of gear aspect ratio

(a) Operating power of 1/2

(b) Air pressure of 1/3

Fig. 7.5-2 Influence of transmitted power and air pressure on the optimal gear aspect ratio

271

7.6   Optimization of Shroud

Because the shroud shape has no influence on the gear design, it can be optimized for reducing the fluid dynamic loss. The optimal value of the shroud coefficient is determined from the characteristic that the aerodynamic loss increases and the oil dynamic loss decreases as the shroud coefficient increases (Figs. 7.4-9 (b) and (c)). The optimal value of the shroud coefficient is shown in Fig. 7.6-1 . Typical parameters affecting the shroud coefficient are the rotational speed, transmitted power, and air pressure. The vertical axis shows the optimal shroud coefficient, and the horizontal axis shows the rate of change of each parameter with respect to the base condition. From Fig. 7.6-1 , it can be seen that the optimal shroud coefficient is in the range of approximately 0.6–0.7.

When the transmitted power is increased, the fraction of the oil dynamic loss increases as the oil supply flow rate is increased (in consideration of a real design, a constant temperature difference between the oil supply and the scavenged oil was set as a condition). It is considered that the optimal shroud coefficient increased because increasing the shroud coefficient is effective in reducing the oil dynamic loss.

When the air pressure is increased, the fraction of the aerodynamic loss increases with increasing air density. Because it is effective to lower the shroud coefficient in order to reduce the aerodynamic loss, it is considered that the optimal shroud coefficient was lower.

When the rotational speed is increased, the aerodynamic loss increases in proportion to the power of 3 of the rotational speed, and the oil dynamic loss increases in proportion to the power of 2–3 of the rotational speed (from Chapters 2 and 5). With an increase in the fluid dynamic loss, the oil supply flow rate increases in order to keep the temperature difference between the supplied and the scavenged oil constant. When the rotational speed is low, the fraction of the aerodynamic loss is considered to increase, because the effect of the oil supply flow rate is small. Therefore, the optimal shroud coefficient decreases with an increasing rotational speed so as to suppress the aerodynamic loss. In contrast, when the rotational speed is high, it is considered that the fraction of the oil dynamic loss increases with an increase in the oil supply flow rate. Therefore, the optimal shroud coefficient increases as the rotational speed increases, so as to suppress the oil dynamic loss.

As described above, the increase and decrease in the optimal shroud coefficient are considered to be due to the fractions of the aerodynamic loss and oil dynamic loss.
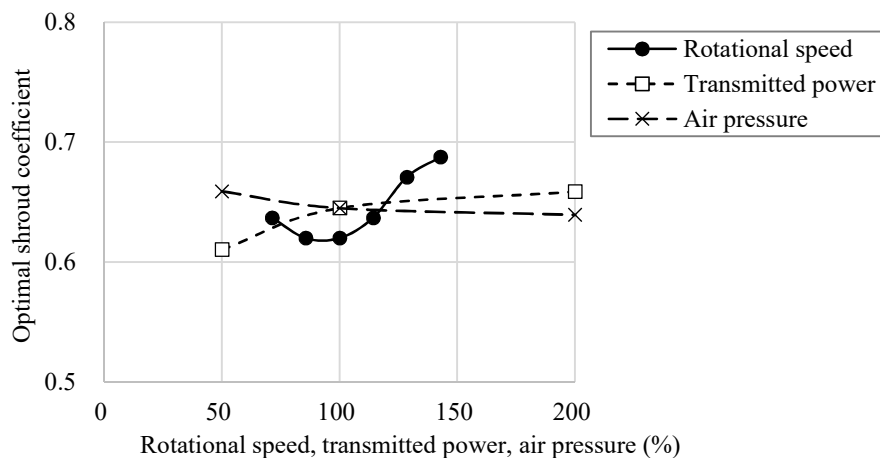
Fig. 7.6-1 Influence of rotational speed, transmitted power, and air pressure on the optimal shroud coefficient (obtained using loss models)

7.7   Effect of the Optimization of Gear Aspect Ratio and Shroud

An example of the effect of the gear aspect ratio and shroud optimizations is shown in Fig. 7.7-1 . Figure 7.7-1 (a) shows an example of the effect of the gear aspect ratio and shroud optimizations at a rated speed of 7000 rpm and (b) at a rated speed of 10000 rpm. The horizontal axis indicates the gear aspect ratio and peripheral speed, and the vertical axis indicates the efficiency. In Figs. 7.7-1 (a) and (b), "A" indicates the initial design point (assumed as the realistic condition), "B" indicates the design point for an optimized gear aspect ratio, and "C" indicates the design point for an optimized shroud.
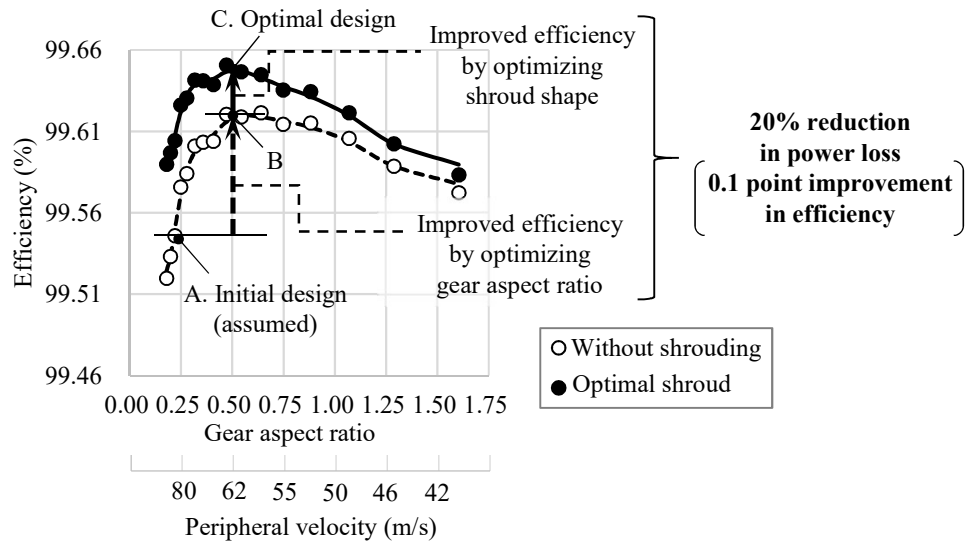
(a) Improved efficiency by optimizing gear aspect ratio and shroud shape at a rated speed of 7000 rpm
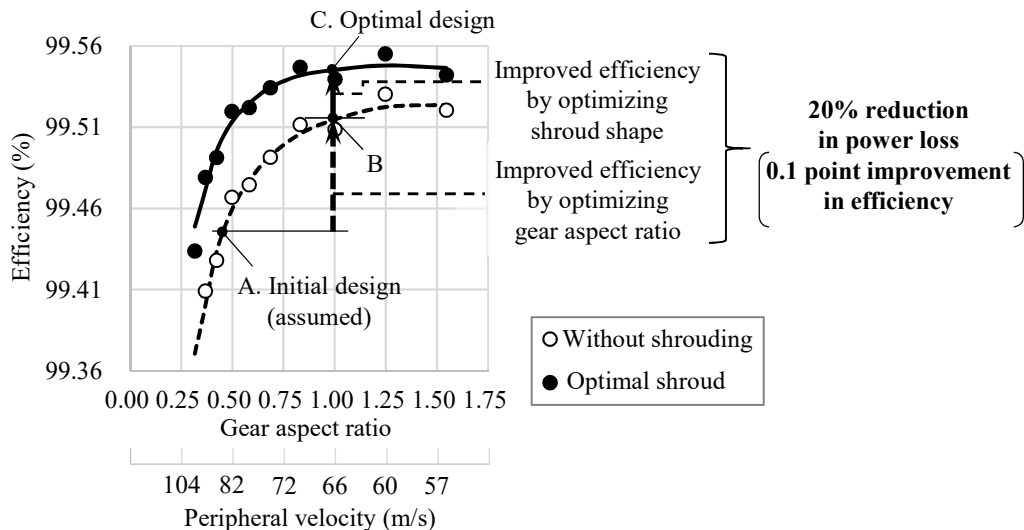
(b) Improved efficiency by optimizing gear aspect ratio and shroud shape at a rated speed of 10000 rpm

Fig. 7.7-1 Impact of the optimizations of the gear aspect ratio and shroud coefficient (obtained using loss models)

273

In the example of the rated speed of 7000 rpm (Fig. 7.7-1 (a)), the gear aspect ratio of 0.2 (peripheral speed of approximately 80 m/s, "A" in the figure) of the initial design was increased to 0.5 (peripheral speed of approximately 60 m/s, "B" in the figure), and by optimizing the shroud, the loss was reduced by approximately 20% (efficiency increased by approximately 0.1 points, "C" in the figure). Similarly, a loss reduction of approximately 20% (approximately 0.1 point increase in efficiency) was achieved for the rated speed of 10000 rpm (Fig. 7.7-1 (b)).

These examples of loss reduction are proof that a 20% reduction in power loss, as assumed in the introduction to Chapter 1, is realistic. The approximately 0.1 point improvement in efficiency shown here is only valid for the transmission efficiency of the gear system. It is considered that a reduction in the size and weight of the lubricating system, including the oil pump, oil tank, and oil cooler, would further improve the overall efficiency of the airframe. For example, when this improvement in efficiency is converted into the effect of geared engines, it can contribute to a 0.3% improvement in engine efficiency, as described in Chapter 1. It is also considered that the reduction in power loss can contribute to the feasibility of geared engines through the feasibility of an oil cooler.

7.8   Summary of Chapter 7

In this chapter, the influence of the gearbox design parameters on the fluid dynamic loss were detailed using a fluid dynamic loss model. The gear aspect ratio and shroud coefficient were selected as parameters that can be optimized to reduce the fluid dynamic loss, and their influence on the fluid dynamic loss was considered. The trends of the optimal values and the effects of improving the engine efficiency were studied. The results are summarized below.

1. When a reduction in the fluid dynamic loss is carried out by changing the gear parameters, a reduction in the gear diameter is most effective. Reductions in the tooth width and gear module or an increase in the gear aspect ratio (= tooth width/gear diameter) are equivalent. When the rated load and gear weight are fixed (tooth width $\times$ gear diameter^2 is constant) and the gear aspect ratio is changed, increasing the gear aspect ratio reduces each element of the fluid dynamic loss, but increasing the tooth area suppresses this decrease in loss. The optimal value of the gear aspect ratio is obtained by considering the opposite tendencies of the fluid dynamic loss and the gear friction loss.

2. When the reduction in the fluid dynamic loss is carried out through a shroud installation, an optimum value exists for the shroud coefficient, because the tendency of the aerodynamic loss and the tendency of the oil dynamic loss are opposite according to changes in the shroud coefficient. The main factors for the change in the fluid dynamic loss are changes in the shroud coefficient and in the oil reacceleration coefficient. In the case of the two-axis helical gearbox presented in this study, the minimum value for the fluid dynamic loss was obtained for a shroud coefficient of approximately 0.6–0.7.

3. When the gear aspect ratio is changed or the shroud coefficient is changed, a change in the fluid dynamic loss tendency appears as a change in the differential pressure at the gear meshing part or the gear peripheral part. A change in the oil reacceleration coefficient and oil mist coefficient (parameters of the oil dynamic loss) appears as a change in the amount of oil at the gear meshing part and the gear periphery, respectively.

4. It was found that the engine efficiency can be significantly improved by optimizing the gear aspect ratio and the shroud.

Chapter 8

Contribution to Standardization of Low-Power-Loss Design

In this chapter, we propose a standardization for low-power-loss designs for high-speed gear systems and describe the contributions of this research to such standardization, with reference to the standardization of existing gear strength designs.

8.1   Proposal for Standardization of Low-Power-Loss Design

The standardization of the low-power-loss design for high-speed gear systems is shown in Fig. 8.1-1 .

(1)   Requirements for Standardization of Design

To consider the requirements for the standardization of low-power-loss designs for high-speed gear systems, reference is made to already established standardizations of gear strength designs. Figure 8.1-1 (a) shows the standardization of the gear strength design. An outline of the existing gear strength design standards is described below.

- Based on a clarification of gear failure phenomena, the phenomena are classified into tooth surface fatigue, tooth surface scuffing, and tooth root bending failure ("Classification of gear damage" in Fig. 8.1-1 (a)).

- As an example of a standard experimental measurement method, the Forschungsstelle für Zahnräder und Getriebebau (FZG) gear standard experimental method has been established ("Standard experimental methods" in Fig. 8.1-1 (a)).

- A strength design standard has been established based on an analysis and classification of gear failure phenomena and experimental data using standard experimental methods ("Development of strength design standard" in Fig. 8.1-1 (a)). For example, the American Gear Manufacturers Association (AGMA) 218.01 provides design criteria for the tooth surface strength and tooth bending strength, and AGMA 217.01 provides design criteria for tooth surface scuffing.

- The established design standards are updated based on results from applications to actual gearbox developments ("Update of strength design standard" in Fig. 8.1-1 (a)). For example, AGMA 2001-D04 is an update of the design standards for the tooth surface strength and tooth bending strength. It specifies a method for evaluating the tooth surface strength and tooth bending strength, and indicates the factors affecting gear life (and calculation methods therefor). AGMA 925-A03 is an update of the

standards for tooth surface scuffing, and describes the effects of oil lubrication on tooth surface damage such as tooth surface scuffing and abrasion.

As described above and shown in Fig. 8.1-1 (a), it can be seen that clarification and classification of phenomena, development of standard experimental measurement methods, development of design standards, and update of design standards are necessary for design standardization.

(2)   Proposal for Standardization of Low-Power-Loss Design

The standardization of the low-power-loss design for high-speed gear systems is shown in Fig. 8.1-1 (b). As the power loss of a high-speed gear system can be classified into the fluid dynamic loss and gear friction loss, a standardization of the low-power-loss design is considered for each.

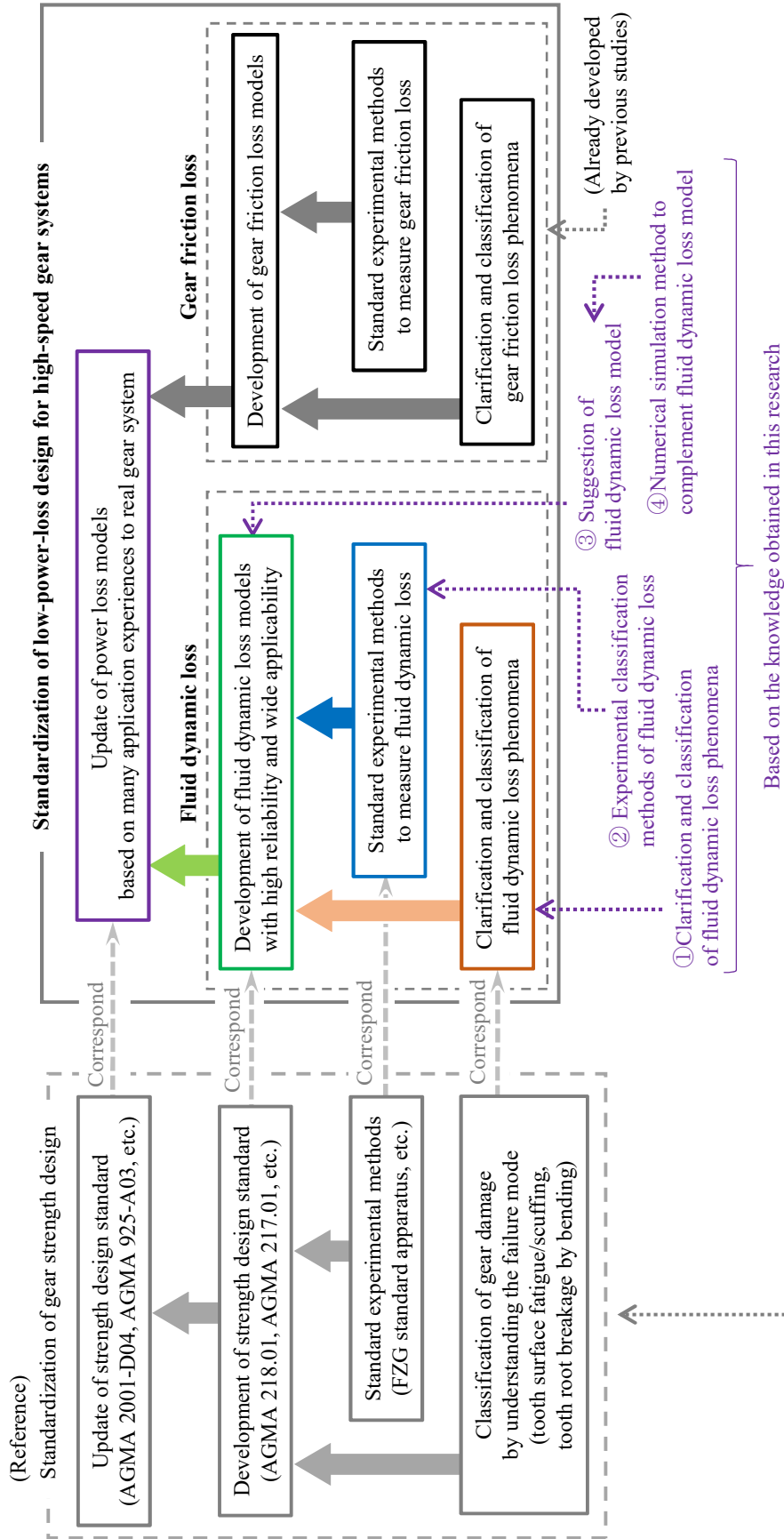Standardization of Low-Power-Loss Design for Fluid Dynamic Loss

- The classification is necessary to be made based on a clarification of the fluid dynamic loss phenomena ("Clarification and classification of fluid dynamic loss phenomena" in Fig. 8.1-1 (b)). This corresponds to a clarification and classification of the phenomena concerning the standardization of the gear strength design ("Classification of gear damage" in Fig. 8.1-1 (a)).

- A standard experimental measurement method is necessary to be established for measuring the fluid dynamic loss ("Standard experimental methods to measure fluid dynamic loss" in Fig. 8.1-1 (b)). This corresponds to the standard experimental measurement method applied in the standardization of the gear strength design ("Standard experimental methods" in Fig. 8.1-1 (a)).

- A fluid dynamic loss model is necessary to be developed based on the clarification and classification of the fluid dynamic loss phenomena, and on experimental data obtained using standard experimental methods ("Development of fluid dynamic loss models" in Fig. 8.1-1 (b)). This corresponds to the design criteria in the standardization of the gear strength design ("Development of strength design standard" in Fig. 8.1-1 (a)).

  In contrast to the standard for the gear-strength design, it is difficult to set a standard for the fluid dynamic loss according to the various gearbox design conditions. Thus, it is necessary to use a fluid dynamic loss model; this model must be adaptable to various gearbox design conditions, and have the same reliability as the gear-strength design.

- The developed fluid dynamic loss model must be updated based on the results from application to actual gearbox development ("Update of power loss models" in Fig. 8.1-1 (b)). This corresponds to the update of strength design standard applied in the standardization of the gear strength design ("Update of strength design standard" in Fig. 8.1-1 (a)).

Standardization of Low-Power-Loss Design for Gear Friction Loss

- The standardization for the low-power-loss design of the gear friction loss has been generally established by conventional research (e.g., [22], [23]) as shown in Fig. 8.1-1 (b), e.g., "Clarification and classification of gear friction loss phenomena," "Standard experimental methods to measure gear friction loss," and "Development of gear friction loss models."

Fig. 8.1-1 Contributions to the standardization of low-power-loss designs for high-speed gear systems

(a) Standardization of gear strength design
(a sample of standardization of design methods)

(b) Suggestion of the standardization of low-power-loss design for high-speed gear systems
and contributions to the standardization based on the knowledge obtained in this research

As the standardization of the gear friction loss has been generally established by conventional research, it is considered that the standardization of the low-power-loss design will be possible by advancing the standardization of the low-power-loss design for the fluid dynamic loss.

8.2 Contribution to Standardization of Low-Power-Loss Design

The following shows the contribution of the results of this research to the standardization of low-power-loss design.

(1)   Contribution to Clarification and Classification of Fluid Dynamic Loss

Regarding the clarification and classification of the phenomena of fluid dynamic losses, in Chapter 5, the phenomena were clarified according to flow fields, pressure fields, oil distributions, and torque distributions, and the fluid dynamic losses were classified into loss elements such as the "air side-flow loss," "air pumping loss," "air vortex loss," "oil-jet acceleration loss," "oil reacceleration loss," and "oil churning loss."

This loss classification was applied through the fluid dynamic loss model, an experimental classification method for the loss, and a numerical classification method for the loss (Chapter 6), in consideration of the studies and optimizations on the influences of the design parameters of the gearbox (Chapter 7). The effectiveness of the classification was confirmed.

The results from the clarification and classification of the fluid dynamic loss phenomena can contribute to the same in the standardization of the low-power-loss design for the fluid dynamic loss ("①" in Fig. 8.1-1 (b)).

(2)   Contribution to Standard Experimental Measurement Methods for Fluid Dynamic Loss

Regarding experimental measurement methods for the fluid dynamic loss, this study proposes a measurement method for the friction losses on gears and bearings and an experimental classification method for the fluid dynamic loss, as necessary for experimental measurements of the elements of the fluid dynamic loss (Chapter 3).

This experimental measurement method was applied to clarify and classify fluid dynamic loss phenomena (Chapter 5) through validation of the applicability of the numerical simulation method (Chapter 4), and the effectiveness of the measurement method was confirmed.

The results from this experimental measurement method for the fluid dynamic loss can contribute to the standardization of experimental measurement methods for the standardization of the low-power-loss design for the fluid dynamic loss ("②" in Fig. 8.1-1 (b)).

(3)   Contribution to Development of Fluid Dynamic Loss Model with Applicability and Reliability
（ⅰ）Proposal of Fluid Dynamic Loss Model

Regarding the development of the fluid dynamic loss model in the standardization, a fluid dynamic loss model was proposed in this research (Chapter 6).

This fluid dynamic loss model was applied to the studies and optimizations on the influences of the design parameters of the gearbox (Chapter 7). The effectiveness of the model was confirmed.

The results from this fluid dynamic loss model can contribute to the development of a fluid dynamic loss model with applicability and reliability in the standardization of the low-power-loss design of a fluid

dynamic loss ("③" in Fig. 8.1-1 (b)).

(ii) Complement of Fluid Dynamic Loss Model by Numerical Simulation Method

To develop a fluid dynamic loss model, it is necessary to complement the fluid dynamic loss model with a numerical simulation method, as the difficulty of the experimental measurements is high. Therefore, we proposed a numerical simulation method in this research (Chapter 4).

The applicability of this numerical simulation method to the gearbox was validated by comparing with experimental measurements (Chapter 4), and was applied to the clarification and classification of fluid dynamic loss phenomena (Chapter 5) and development of fluid dynamic loss model (Chapter 6). In the study on the influences of the design parameters of the gearbox, it was used for the validation of the fluid dynamic loss model (Appendix C).

In this way, the numerical simulation method of this research complements the experimental measurement method ("④" in Fig. 8.1-1 (b)).

Based on the above, it is considered that the bases of the clarification and classification of phenomena of fluid dynamic loss, standard experimental measurement method of fluid dynamic loss, and development of fluid dynamic loss model for the standardization of the low-power-loss design for high-speed gear systems have been established in this research.

8.3   Summary of Chapter 8

To standardize low-power-loss designs for high-speed gear systems, the "Clarification and classification of phenomena," "Standard experimental measurement methods," "Fluid dynamic loss model with applicability and reliability," and "Update of loss models based on application results" are required by analogy with already established standardizations of gear strength designs.

In this research, regarding the fluid dynamic loss, we proposed the "Clarification and classification of phenomena," "Standard experimental measurement method," and "Fluid dynamic loss model," and confirmed their effectiveness. That is, this research is considered to have constructed the basis for the standardization of the low-power-loss design of a high speed gear system.

By applying the results from this study to various gearboxes, it is expected that a fluid dynamic loss model with wide applicability and high reliability will be established, and that updates of loss models based on application results will be possible in the future. This will enable rational design based on phenomena for aeroengine transmission gears (e.g., those with a peripheral speed exceeding 50 m/s).

Chapter 9

Conclusions

9.1   Conclusions

Based on the importance of reducing fluid dynamic losses in high-speed gear systems, the purpose of the research was set to "Clarification and classification of fluid dynamic loss phenomena in two-phase flow of air and oil, which contributes to the standardization of low-power-loss designs for high-speed gear systems." Therefore, the subjects were "clarification and classification of phenomena based on the understanding of the location and cause of fluid dynamic loss" and "construction of a fluid dynamic loss model that contributes to low-power-loss design." In addition, we constructed an "experimental measurement method" and "numerical simulation method," which are necessary to solve these problems, and demonstrated their applicability to gear systems. To show that the above results form the basis for standardization of low-power-loss design, the "effectiveness of low-power-loss design and contribution to standardization of low-power-loss design" was demonstrated.

In this study, phenomena were observed at the gear contact surface in the minimal area of the tooth surface (i.e., the contact line with the Hertz contact width), and it was shown that the region around the gear could be divided into "phenomena at the gear contact surface" and "phenomena in the region around the gear except for the gear contact surface." The fluid dynamic loss considered in this research was the loss caused by "the phenomena in the region around the gear except for the gear contact surface."

First, "1. Experimental measurement method and its applicability" and "2. Numerical simulation method and its applicability" are described. Then, based on the facts of these methods and theories, "3. Clarification and classification of phenomena based on the understanding of the location and cause of fluid dynamic loss" is described. In addition, "4. Constructing fluid dynamic loss models" using assumptions of phenomena and facts is described. Finally, "5. Effectiveness of low-power-loss design and contribution to standardization of low-power-loss design" is described.

1. Experimental Measurement Method and its Applicability

   (a) To validate the numerical simulation of fluid dynamic loss, we used a two-axis helical gearbox with a maximum peripheral speed of 100 m/s, which has specifications equivalent to those of real aeroengine gears. To improve the measurement accuracy of the fluid dynamic loss, in-situ measurements were conducted for the friction losses of the gears, bearings, and seals, by controlling the internal pressure of the gearbox and adjusting the bearing and seal temperatures. Consequently, the measurement error of the friction loss was sufficiently reduced (the measurement error could be reduced to be equivalent to the measurement error of the torque meter).

(b) To validate the simulation results for the oil flow, we used a measurement method for the oil fraction and mixture velocity and an oil flow visualization method. To measure the oil fraction and mixture velocity, we applied the isokinetic suction method, which was applied to dust measurements and two-phase air and oil flows, and its practical accuracy was confirmed. In the oil flow visualization method, we measured the velocities of the oil particles using an air purge mechanism to eliminate the effects of oil mist and a borescope equipped with a light source. The visualization results were consistent with the measurement results for the oil fraction and mixture velocity, and the visualization method was confirmed to be valid.

2. Numerical Simulation Method and its Applicability

   (a) Numerical Simulation Method for Fluid Dynamic Loss and Experimental Validation

      i. As a numerical simulation method for clarifying the phenomena of fluid dynamic loss, a rectangular grid system was used for the grid calculations, and the volume-of-fluid method was used as the calculation method for the gas–liquid interface. The porosity method was used to model object boundaries. The mass conservation and momentum conservation equations were set as equations common to the oil and air (one-fluid model), and a condition of no velocity slip was used at the gas–liquid interface. The object movement was modeled in terms of changes in the fluid volume (air and oil) in the cell and in the fluid area of the cell surface. The shear stress at the wall surface was calculated from the difference between the object velocity, fluid velocity, and turbulent flow models. The large eddy simulation method was used for the turbulent flow model owing to its numerical stability. The fluid dynamic loss is obtained by integrating the pressure and shear forces on the gear tooth surface.

      ii. Regarding the fluid dynamic loss of air and oil, aerodynamic loss, and oil dynamic loss, the trends of the simulation and experimental results agreed within a practical error of $\pm 15\%$. Therefore, the numerical simulation results can be applied to clarify the phenomena of fluid dynamic losses.

   (b) Modeling Method of Numerical Simulation for Airflow and Experimental Validation

      i. As a modeling method for airflow simulation, to ensure numerical stability, a clearance was provided for the tooth surface in the contact surface between the actual gears.

      ii. The air pressure in the tip clearance at the gear meshing was validated to determine the airflow in the gear meshing part. Consequently, the numerical simulation reproduced the pressure increase trend in the into-mesh and the pressure decrease in the out-of-mesh. However, the magnitude of the pressure decrease in the out-of-mesh case was decreased by the influence of the clearance provided between the gear tooth surfaces. This difference was approximately within a practical error of $\pm 15\%$ when evaluated in terms of the force loaded on the gear. Therefore, it was concluded that the difference did not affect the applicability of the numerical simulation.

      iii. To validate the airflow around the gear, with the exception of the gear meshing part, the aerodynamic losses in the single gears were validated. As a result, the numerical simulation could reproduce the aerodynamic loss in single gears with the number of teeth within 65 and the trend of the loss reduction rate via shrouding.

      iv. Because the trend of the numerical simulation of the airflow agreed with that of the experimental result, it was proven that the numerical simulation result could be applied to the clarification of fluid dynamic loss phenomena.

(c) Modeling Method of Numerical Simulation for Oil Flow and Experimental Validation

    i. As modeling methods for oil flow simulation, this study employed a coarse graining concept in which the momentum transfer of the oil in a calculation grid was modeled by an approach based on the coarse graining of oil particles, a simple modeling method for an oil jet to reduce the number of calculation grids, and a method for improving the simulation accuracy by considering a phenomenon in which the flow drag coefficient in a two-phase flow is lower than that in a single-phase flow.

    ii. The flow of the oil jet into the gear meshing part was validate regarding the oil flow in the gear meshing part. The simulation results reproduced the trend of the experimental results for visualizing the oil outflow from the gear mesh at a low rotational speed, and the entrainment of the oil jet into the gear mesh at a high rotational speed.

    iii. The oil spray flow to the gear tooth surface was validated regarding the oil flow around the gear. The simulation results reproduced the trends of the experimental results for visualizing the spray reaching the gear valley at a low rotational speed and failed to reach it at a high rotational speed.

    iv. To validate the oil flow near the shroud wall, the oil fraction, mixture velocity, and oil flow velocity between the gear tooth tip and shroud wall were validated. The simulation results reproduced the experimental results concerning the trend of the oil fraction near the shroud wall (i.e., large), the trend of the flow velocity near the tooth tip (i.e., high), the decreasing trend of the mixture velocity as it approached the shroud wall, and the trend of the oil velocity (oil fraction × mixture velocity) to show a peak value slightly away from the shroud wall.

    v. As the trends of the numerical simulation for the oil flow agreed with those of the experimental results, it was proven that the numerical simulation results could be applied to clarify fluid dynamic loss phenomena.

3. Clarification and Classification of Phenomena Based on the Understanding of the Location and Cause of Fluid Dynamic Loss

    (a) Classification by Location of Fluid Dynamic Loss and Fluid Type

        i. The location where fluid dynamic loss occurs is divided into the "gear meshing part" and "gear peripheral part." This is because the results of the numerical simulation show that the flow around the gear mesh is affected by rapid changes in volume between gears during gear engagement and disengagement, whereas the flow around the gear periphery is affected by the air vortices generated in the valleys between the gear teeth.

        ii. Fluid dynamic losses are divided into those due to air and those due to oil. This is because the airflow is based on the momentum conservation theory of the continuum, whereas the oil flow is based on the momentum conservation theory of the mass particles and continuum.

        iii. From the above, the fluid dynamic loss is divided as "aerodynamic loss in the gear meshing part," "aerodynamic loss in the gear peripheral part," "oil dynamic loss in the gear meshing part," and "oil dynamic loss in the gear peripheral part." Each feature is described in (b) – (e), respectively.

    (b) Aerodynamic Loss in the Gear Meshing Part

        i. The airflow in the gear meshing part is divided into "airflow that is pushed out when the gear is engaged, passes the side of the gear mesh, and is sucked in when the gear is disengaged" and "airflow that passes through the tip clearance and backlash of the gear." These results were

obtained from the numerical simulation results for the airflow pattern. The former is defined as "air side-flow loss" because it passes through the sides of gear mesh, and the latter is defined as "air pumping loss" because air is pumped by the gear through the tip clearance and backlash.

ii. The peripheral speed exponent of the air side-flow loss was derived from the continuum theory, in which the air side flow is simplified to accelerate airflow in the peripheral direction with gear rotation while avoiding the gear meshing part (because of the small volume of the tip clearance and backlash, the gear meshing part becomes an obstacle for the airflow). The results show that the mass flow rate of the air accelerated by gear rotation is proportional to the gear peripheral speed, the force loaded on the gear teeth is proportional to the square of the peripheral speed, and the air side-flow loss is proportional to the cube of the peripheral speed. The proportional exponents were validated using numerical simulation results. In addition, the compressibility of air is negligible because the peripheral speed proportional exponent does not exceed three in conventional research with a peripheral speed exceeding 150 m/s, and the rapid temperature rise due to adiabatic compression in the gear meshing does not occur in the clearance between the gear and shroud equivalent to the actual gearbox.

iii. By analogy with the theory of oil-jet acceleration loss, the air mass flow rate accelerated by the gear rotation in the volume between the gear tip clearance and backlash is proportional to the gear peripheral speed, the force loaded on the gear teeth is proportional to the square of the peripheral speed, and the air pumping loss is proportional to the cube of the peripheral speed. However, the air pumping loss was found to be negligible owing to the small mass flow rate of the accelerated air.

iv. If a gear shroud (gear enclosure) is installed, the numerical simulation results of the root-mean-square flow-speed at the cross section of the gear mesh reveal that the flow-speed deviation around the gear mesh is affected by the shroud shape (the number or angle of the opening). From the analogy with the flow resistance of general piping, this flow-speed deviation is thought to increase the flow resistance at the gear meshing part and increase the air side-flow loss.

(c) Aerodynamic Loss in the Gear Peripheral Part

i. From the numerical simulation results of the airflow pattern, it was understood that the characteristic of the airflow around the gear is "vortex generated in the tooth valley of the gear." This was defined as "air vortex loss" based on the characteristics of the flow.

ii. The peripheral speed proportional exponent of the air vortex loss is obtained from continuum theory, assuming that the air around the gear receives peripheral acceleration from the gear. It was found that the mass flow rate of air accelerated by the gear was proportional to the gear peripheral speed, the force loaded on the gear was proportional to the square of the peripheral speed, and the air vortex loss was proportional to the cube of the peripheral speed.

iii. Numerical simulation results indicate that the flow around the gear is suppressed by the shroud when the gear is covered by the shroud. The aerodynamic loss reduction rate due to the suppression of this flow is defined as the shroud coefficient from the experimental results of conventional research on isolated gears. The applicability of the shroud coefficient to the air vortex loss in a two-axis helical gearbox was confirmed using a dimensionless number incorporating the shroud coefficient.

(d) Oil Dynamic Loss in the Gear Meshing Part

    i. The oil flow pattern and the increase in the momentum of the oil in the gear meshing were ascertained in the numerical simulation such that the oil flow in the gear meshing part is classified into two phenomena: "the phenomenon in which the oil supplied into the gear meshing is accelerated to the gear peripheral speed" and "the phenomenon in which the oil re-enters the gear meshing and is reaccelerated." The former was defined as "oil-jet acceleration loss" from the characteristics of the acceleration phenomenon of oil supplied into the gear mesh, and the latter as "oil reacceleration loss" based on the characteristics of the acceleration phenomenon of oil re-entering the gear mesh.

    ii. The peripheral speed proportional exponent of the oil jet acceleration loss was obtained from the theoretical equation of conservation of momentum when the gear accelerated the mass particles and the mass flow rate of the supplied oil into the gear mesh was constant. It was found that the force loaded on the gear is proportional to the peripheral speed, and the oil jet acceleration loss is proportional to the square of the peripheral speed (the peripheral speed exponent of the oil reacceleration loss is the same as that of the oil jet acceleration loss when the reaccelerated flow rate is assumed to be proportional to the oil supply flow rate).

    iii. When the peripheral opening of the gear shroud is small, the amount of oil remaining in the shroud and the re-entry rate of oil into the gear mesh increase are observed from the numerical simulation result of the oil flow pattern. Without the shroud opening, it is thought that the oil cannot be discharged, and the oil accelerates stagnation, which accelerates the oil reacceleration loss. The effect of this accelerated increase in the oil dynamic loss (including the oil reacceleration loss) was considered as the inverse of the shroud coefficient, and its validity was confirmed by a dimensionless number. The oil-jet acceleration loss was not affected by the shroud because it occurred at the tip clearance and backlash between the gears. Therefore, the shroud only affects the oil reacceleration loss.

(e) Oil Dynamic Loss in the Gear Peripheral Part

    i. From the flow pattern of the airflow and the distribution of the oil, it was understood that the oil flow around the gear periphery is "the flow in which the air vortex generated in the gear tooth valley churns the oil." This was defined as "oil churning loss" from the characteristics of the flow.

    ii. The peripheral speed proportional exponent of the oil churning loss was obtained from continuum theory, assuming that the oil particles were entrained into the air vortex and the apparent fluid density increased. It was found that the mass flow rate of the oil accelerated by the gear was proportional to the gear peripheral speed, the force loaded on the gear was proportional to the square of the peripheral speed, and the oil churning loss was proportional to the third power of the peripheral speed.

    iii. In the case of installing a gear shroud, the phenomenon of the increasing amount of oil remaining around the gear inside the shroud was understood from the result of the numerical simulation of the oil flow pattern. When the shroud opening is small, it is considered that oil discharge becomes difficult and oil accelerates stagnation, which accelerates oil churning loss. The influence of this accelerating stagnation phenomenon on the oil dynamic loss (including oil churning loss) was considered as the inverse of the shroud coefficient, and its validity was confirmed by a dimensionless number.

4. Constructing Fluid Dynamic Loss Models

   (a) Air Side-Flow Loss Model (Modeling a Part of the Aerodynamic Loss in the Gear Meshing Part)

   i. The air side-flow loss was defined as a "loss due to flow being pushed out at the into-mesh part of the gear mesh, passing beside the gear mesh, and sucked in at the out-of-mesh part of the gear mesh" in a "aerodynamic loss in the gear meshing part" according to the clarification of the phenomenon. The air side-flow loss is presumed to be the loss due to the airflow resistance of the gear teeth and was modeled using the aerodynamic drag coefficient.

   ii. The main parameters influencing the aerodynamic drag coefficient were the helix angle related to the strength of air pushed out at the into-mesh of the gear, and the number of shroud openings related to the flow-speed deviation of the channel across the sides of the gear mesh (which increases the pressure loss of flow in the channel). In modeling the shroud effect, the effect of the shroud shape (such as the number of shroud openings) was considered. The main parameters of the air side-flow loss model were the aerodynamic drag coefficient, air density, tooth area and peripheral speed[3]. The air side-flow loss model was shown to be valid within the experimental conditions by experimental validation.

   (b) Air Pumping Loss Model (Modeling a Part of the Aerodynamic Loss in the Gear Meshing Part)

   i. The air pumping loss was defined as a "loss due to the flow passing through the tip clearance and backlash of the gear" in a "aerodynamic loss in the gear meshing part" according to the clarification of the phenomenon. The air pumping loss is modeled as the loss owing to the acceleration of air at the tip clearance and backlash from the analogy of the oil-jet acceleration loss.

   ii. This loss was negligible because of the small mass flow rate of air accelerated by the tip clearance and backlash.

   (c) Air Vortex Loss Model (Modeling Aerodynamic Loss in the Gear Peripheral Part)

   i. The air vortex loss was defined as "the aerodynamic loss around the gear periphery" due to "vortices generated in the tooth valley of the gear" according to the clarification of the phenomenon. In the air vortex loss model, the gear was regarded as a rotating cylinder, and the loss experimental equation of the conventional research was rearranged using the equations "rotational moment coefficient on the peripheral surface" and "rotational moment coefficient on the side surfaces," which are commonly used in conventional research.

   ii. The rotational moment coefficient on the peripheral surface in the air vortex loss model was found to be significantly affected by the ratio of the gear module to the radius (corresponding to the surface roughness of the peripheral surface) from a rearrangement of the experimental results of previous studies. However, the effect of the rotational Reynolds number was small, probably because the size of the vortex depended on the size of the tooth valley. The rotational moment coefficient on the side surfaces was found to be significantly influenced by the rotational Reynolds number from a rearrangement of the experimental results of previous studies. It is presumed that this is because the loss owing to turbulence increases with an increase in the rotational Reynolds number, and the air pumping efficiency decreases. The rate of reduction of the air vortex loss by shrouding was defined as the shroud coefficient, as in previous studies. This loss reduction corresponds to the suppression of the flow around the gear according to the clarification of the phenomenon. The shroud coefficient is presumed to be affected by the radial and axial clearances between the gear and shroud, and the peripheral opening angle of the shroud, because the volume

between the gear and shroud is related to the flow strength. The main parameters of the air vortex loss model were air density, tooth area, peripheral speed[2.9], and shroud coefficient (from the loss equation on the peripheral surface of the gear with large loss). The air vortex loss model was shown to be valid within the experimental conditions by experimental validation.

(d) Oil-jet Acceleration Loss Model (Modeling a Part of the Oil dynamic Loss in the Gear Meshing Part)

    i. The oil-jet acceleration loss was defined as "the loss when oil supplied into the gear mesh is accelerated to the gear peripheral speed" in the "oil dynamic loss in the gear meshing part" according to the clarification of the phenomenon.

    ii. The oil-jet acceleration loss was calculated from the theoretical equation for the conservation of momentum of mass particles. The acceleration of the target oil is unaffected by the shroud because it occurs at the tip clearance and backlash of the gear. The main parameters of the oil-jet acceleration loss model were the oil supply flow rate and peripheral speed[2]. The oil jet acceleration loss model was validated using numerical simulation results.

(e) Oil Reacceleration Loss Model (Modeling a Part of the Oil dynamic Loss in the Gear Meshing Part)

    i. The oil reacceleration loss is defined as "a loss that occurs when oil that has reflowed into the gear mesh is accelerated by the gear" in "oil dynamic loss in the gear mesh part" according to the clarification of the phenomenon. The oil reacceleration loss was modeled based on the oil-jet acceleration loss (which can be calculated using the theoretical equation), assuming that the mass flow rate of the oil re-entering the gear mesh is proportional to the oil supply flow rate, and the re-entered oil is accelerated to the gear peripheral speed.

    ii. In the oil reacceleration loss model, the ratio of the oil reinflow rate to the oil supply flow rate (oil reinflow rate/oil supply flow rate) was defined as the "oil reacceleration coefficient." It was presumed that the oil reacceleration coefficient was affected by the peripheral opening angle (the larger the angle, the better the oil drainage) and the shroud coefficient (the wider the clearance between the gear and shroud, the less affected by turbulence around the gear, and the better the oil drainage). It is confirmed that the influence of the gear shroud on the oil reacceleration loss can be considered as the inverse of the shroud coefficient by the evaluation using dimensionless numbers. The inverse was assumed to be the accelerated oil stagnation when the shroud opening was small. The main parameters of the oil reacceleration loss model were the oil reacceleration coefficient, oil supply flow rate, and peripheral speed[2]. The oil reacceleration loss model (including the influence of the shroud) was shown to be valid within the experimental conditions by experimental validation.

(f) Oil Churning Loss Model (Modeling the Oil dynamic Loss in the Gear Peripheral Part)

    i. The oil churning loss was defined as "oil dynamic loss around the gear periphery," which is a loss caused by "a flow in which an air vortex generated in the tooth valley involve oil particles" according to the clarification of the phenomenon. The oil churning loss model was modeled as an increase in the apparent air density owing to the dispersion of oil particles in the air.

    ii. In the oil churning loss model, the loss was modeled by multiplying the air vortex loss by a magnification factor (oil mist coefficient). It was presumed that the oil mist coefficient was affected by the amount of oil around the gear, which is related to the oil supply flow rate (the higher the oil flow rate, the larger the amount of oil around the gear) and the shroud coefficient (the wider the clearance between the gear and shroud, the easier it is for oil to leave the gear). It is confirmed that the influence of the gear shroud on the oil churning loss can be considered as the inverse of

the shroud coefficient by the evaluation using dimensionless numbers. The inverse was assumed to be the accelerated oil stagnation when the shroud opening was small. The main parameters of the oil churning loss model are the oil mist coefficient and air vortex loss. The oil churning loss model was shown to be valid within the experimental conditions by experimental validation.

5. Effectiveness of Low-Power-Loss Design and Contribution to Standardization of Low-Power-Loss Design

   (a) To demonstrate the effectiveness of the low-power-loss design, the fluid dynamic loss is reduced by changing the gear parameters. As a result, it was revealed that reducing the gear diameter is the most effective method, reducing the tooth width and gear module, and increasing the gear aspect ratio (tooth width / gear diameter) are equivalent. When the gear aspect ratio is changed for a rated load and gear weight constant (surface pressure load and gear weight are proportional to tooth width $\times$ gear diameter^2), the optimal value of the gear aspect ratio can be obtained by considering the opposite tendencies of fluid dynamic and gear friction losses.

   (b) When the fluid dynamic loss is reduced by installing a shroud, the optimal value of the shroud coefficient can be obtained by considering the opposite tendencies of aerodynamic and oil dynamic losses. In the case of the two-axis helical gearbox in this study, the optimal shroud coefficient with minimum fluid dynamic loss was 0.6–0.7.

   (c) The optimization of the gear aspect ratio and shroud can significantly reduce the fluid dynamic loss and contribute to the improvement of the fuel efficiency of the aircraft engine.

   (d) To standardize low-power-loss designs for high-speed gear systems, the "clarification and classification of phenomena," "standard experimental measurement methods," "fluid dynamic loss model with applicability and reliability," and "update of loss models based on application results" must be determined by analogy to already established standardizations for gear strength designs. In this research, we proposed the "clarification and classification of phenomena," "a standard experimental measurement method," and "a fluid dynamic loss model" and demonstrated their effectiveness. In other words, this study is considered to have constructed a basis for the standardization of the low-power-loss design of a high-speed gear system.

9.2 Summary of Key Points for Clarification of Phenomena and Low-Power-Loss Design

The answers to the key points regarding clarification of the phenomena of fluid dynamic loss and to the key points of the low-power-loss design as described in Chapter 1 (i.e., those raising the problems in this research, Section 1.4.2) are summarized below. To facilitate understanding of the phenomenon, we first present an image of the elements of fluid dynamic loss, and then describe the key points for clarification and low-power-loss design.

9.2.1 Image of the Phenomena of Fluid Dynamic Loss Elements

An image of the fluid dynamic loss phenomenon obtained in this study is shown in Fig. 9.2-1 . The gear meshing and gear peripheral parts are shown on the upper left of Fig. 9.2-1 . The flow patterns of the airflow and oil flow are shown in the upper right of Fig. 9.2-1 . The air and oil flow phenomena in the gear meshing part are shown in the middle left of Fig. 9.2-1 . The airflow in the gear meshing area is divided into two flows, as shown in the lower left of Fig. 9.2-1 : "the flow in which air is pushed out laterally at the into-mesh part, passing through the sides of gear mesh, and sucked in at the out-of-mesh part," and "the flow through the tip clearance and backlash of the gear." The loss caused by the flow at the sides of the gear mesh was defined as "air side-flow loss," and the loss caused by the flow through the tip clearance and the backlash was defined as "air pumping loss." The oil flow in the gear meshing part is divided into two flows, as shown in the lower right in Fig. 9.2-1 : "the flow in which the oil supplied to the gear meshing part is accelerated," and "the flow in which the oil reflowing into the gear meshing part is accelerated." The loss associated with the acceleration of the oil supplied to the gear meshing part was defined as the "oil-jet acceleration loss," and the loss associated with the reacceleration of oil was defined as the "oil reacceleration loss." The air and oil flow phenomena at the gear periphery are shown in the middle right of Fig. 9.2-1 . The loss associated with airflow around the gear periphery was defined as "air vortex loss" and the loss associated with oil flow around the gear periphery as "oil churning loss."

9.2.2 Summary of Key Points for Clarification of Phenomena and Low-Power-Loss Design

Figure 9.2-2 shows the key points for the clarification of the phenomena of fluid dynamic loss and the key points of the low-power-loss design as obtained in this research.

1. Classification of Fluid Dynamic Loss Based on Clarification of Loss for Understanding Fluid Dynamic Loss Phenomena ("A1" in Fig. 9.2-2)
   - Aerodynamic loss is classified into air side-flow loss, air pumping loss, and air vortex loss.
   - Air side-flow loss and air pumping loss occur at the gear meshing part.
   - Air vortex loss occurs at the gear peripheral part.
   - Oil dynamic loss is classified into oil-jet acceleration loss, oil reacceleration loss, and oil churning loss.
   - Oil-jet acceleration loss and oil reacceleration loss are losses generated at the gear meshing part.
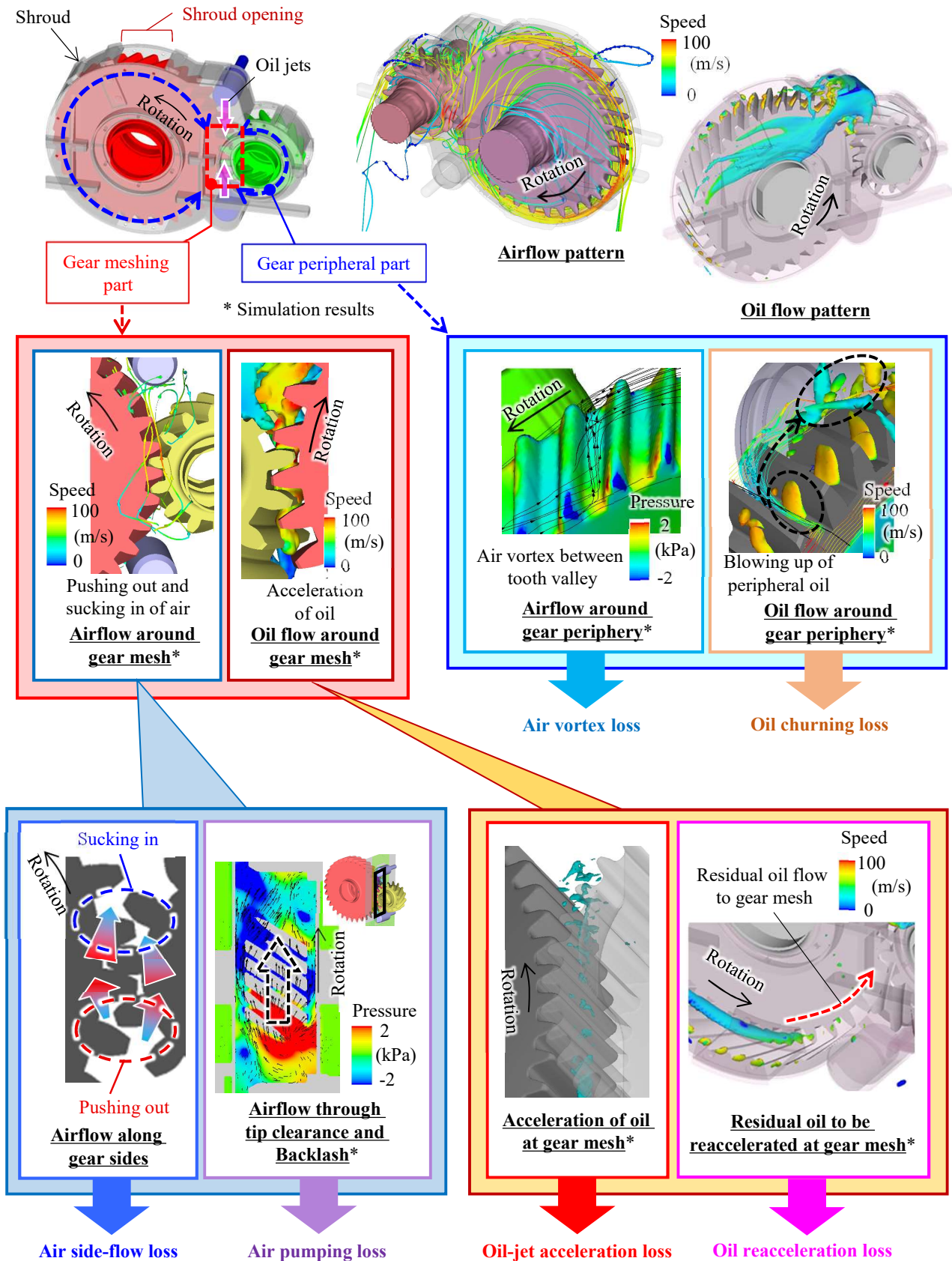   - Oil churning loss occurs at the gear peripheral part.

Fig. 9.2-1 Images of fluid dynamic loss elements

2. Development of Fluid Dynamic Loss Model for Understanding Fluid Dynamic Loss Phenomena and Understanding of Main Parameters of Loss ("A2" in Fig. 9.2-2)

   - The main parameters of the air side-flow loss are air drag coefficient, peripheral speed[3], tooth area, and air density.
   - The air pumping loss is sufficiently small to be negligible.
   - The main parameters of the air vortex loss are the shroud coefficient, peripheral speed[2.9], tooth area, and air density.
   - The main parameters of the oil-jet acceleration loss are the peripheral speed[2] and the oil supply flow rate.
   - The main parameters of the oil reacceleration loss are the oil reacceleration coefficient, peripheral speed[2], and oil supply flow rate.
   - The main parameters of oil churning loss are the oil mist coefficient and air vortex loss.

3. Optimization of Gear Aspect Ratio for Low-Power-Loss Design ("A3" in Fig. 9.2-2)

   - In optimizing the gear aspect ratio, the relationship between the tooth surface strength and weight of the gear is approximately proportional to the tooth width $\times$ gear diameter^2.
   - When the gear aspect ratio is increased while the tooth width $\times$ gear diameter^2 remains constant, the gear friction loss increases, mainly owing to the increase in the area of the gear tooth surface, and the fluid dynamic loss decreases, mainly owing to the decrease in the gear peripheral speed. As these trends are opposite, there is an optimum value for the gear aspect ratio. The optimal value is affected by air pressure, transmitted power, and rotational speed.

4. Optimization of Shroud Shape for Low-Power-Loss Design ("A4" in Fig. 9.2-2)

   - Shroud shape can be optimized relatively freely because it is lightweight (i.e., uses light materials) and easy to install.
   - Reducing the shroud coefficient reduces aerodynamic loss by suppressing the vortex structure of air while increasing the oil dynamic loss by deteriorating the discharge ability of the oil. Therefore, an optimal value exists for the shroud coefficient. The optimal shroud coefficient for the two-axis helical gearbox obtained in this study is approximately 0.6–0.7.
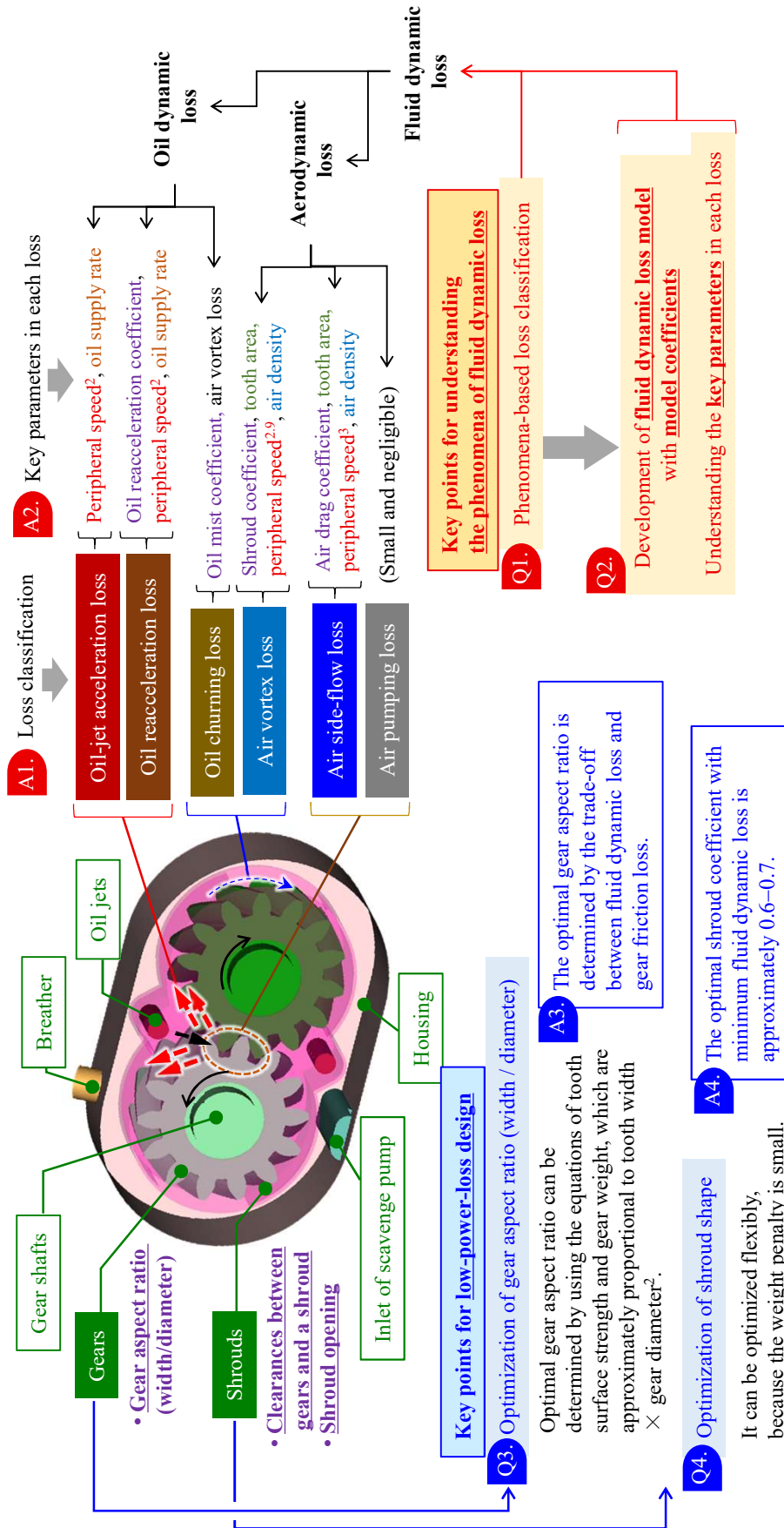
Fluid dynamic loss

Oil dynamic loss

Aerodynamic loss

A1. Loss classification

A2. Key parameters in each loss

Loss	Key parameters
Oil-jet acceleration loss	Peripheral speed^2, oil supply rate
Oil reacceleration loss	Oil reacceleration coefficient, peripheral speed^2, oil supply rate
Oil churning loss	Oil mist coefficient, air vortex loss
Air vortex loss	Shroud coefficient, tooth area, peripheral speed$^{2.9}$, air density
Air side-flow loss	Air drag coefficient, tooth area, peripheral speed^3, air density
Air pumping loss	(Small and negligible)

Q1. **Key points for understanding the phenomena of fluid dynamic loss**
— Phenomena-based loss classification

Q2. Development of **fluid dynamic loss model with model coefficients**
— Understanding the **key parameters in each loss**

Oil jets

Breather

Gear shafts

Gears
- **Gear aspect ratio (width/diameter)**

Shrouds
- **Clearances between gears and a shroud**
- **Shroud opening**

Housing

Inlet of scavenge pump

Key points for low-power-loss design

Q3. Optimization of gear aspect ratio (width / diameter)

Optimal gear aspect ratio can be determined by using the equations of tooth surface strength and gear weight, which are approximately proportional to tooth width × gear diameter^2.

A3. The optimal gear aspect ratio is determined by the trade-off between fluid dynamic loss and gear friction loss.

Q4. Optimization of shroud shape

It can be optimized flexibly, because the weight penalty is small.

A4. The optimal shroud coefficient with minimum fluid dynamic loss is approximately 0.6–0.7.

Fig. 9.2-2 Overview of fluid dynamic loss phenomena and key points for low-power-loss design

9.3 Effective Range of This Research

The effectivity ranges for the numerical simulation method and loss model proposed in this research are limited to those that have been experimentally validated. The two-axis helical gearbox used to validate the fluid dynamic loss in this study is shown in Fig. 9.3-1 . The gear specifications, shroud parameters, and operating conditions are presented in Table 9.3-1 . A dimensionless evaluation of the experimental conditions is presented in Fig. 9.3-2 . The horizontal axis was set to the rotational Reynolds number (dimensionless number of the rotational speed), and the vertical axis was set to the dimensionless oil supply flow rate.
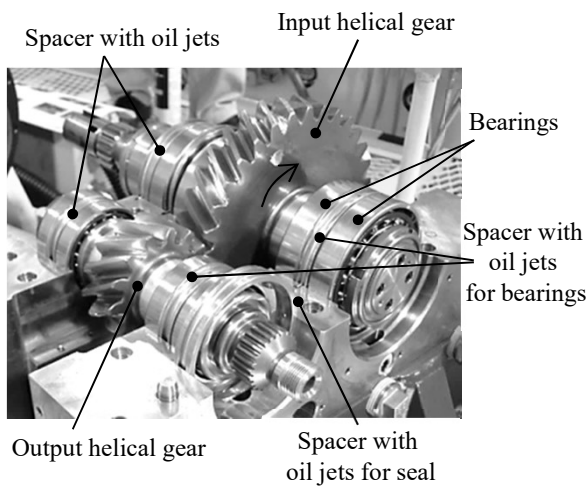
Fig. 9.3-1 Two-axis helical gearbox used in this research (repost of Fig. 3.1-2)
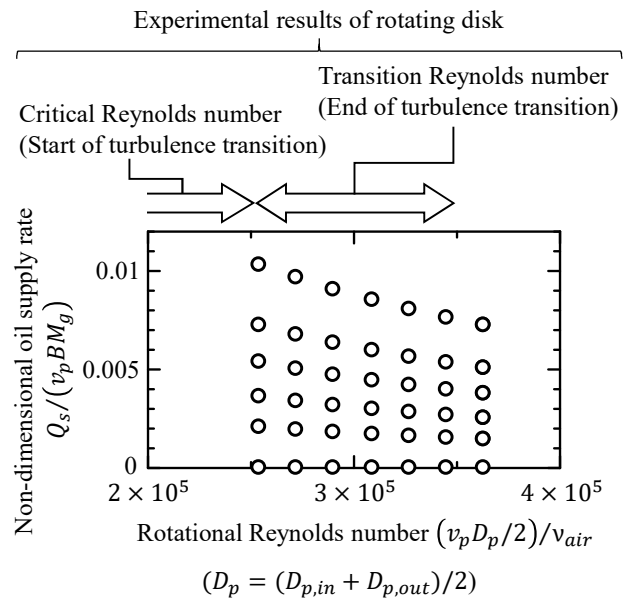
Fig. 9.3-2 Rotational Reynolds number with respect to non-dimensional oil-supply rate changes (experimental results)

Table 9.3-1 Effective range validated by comparison with experiments

Gear type	A pair of single helical gears with shrouding
Gear specifications	Gear ratio 0.4 Input diameter 191 mm, output diameter 81 mm Module 5 mm, face width 34 mm
Shroud parameters	Shroud 1: peripheral opening six ports, 30° each Shroud 2: peripheral opening two ports, 30° each Clearance 5 mm (axial & radial)
Operation conditions	7000–10000 rpm of input gear 70–100 m/s* (pitch line velocity), no load
Oil supply conditions	Two oil-jets (into-mesh and out-of-mesh) 0–7.4 L/min** Mil-PRF-23699 (Mobil Jet Ⅱ)
Internal pressure	1.0 atm, 0.5 atm

* Rotational Reynolds number $v_p(D_p/2)/\nu_{air} = 2.5 \times 10^5$–$3.6 \times 10^5$

** Nondimensional oil-supply rate $Q_s/(v_p BM_g) = 0$–1.0×10^{-2}

In Fig. 9.3-2 , the critical Reynolds number (the starting Reynolds number for the turbulent transition, 4.5×10^4–2.32×10^5) and transition Reynolds number (end Reynolds number for the turbulent transition, 2.65×10^5–3.5×10^5) [126] are shown for a rotating disk. Considering that the conditions used in this research are roughly in the range of the transition Reynolds number and that the gear more easily transitions to turbulence than the disk owing to its convexity, the experimental conditions used in this research are considered to be within the range of the turbulent flow. It is considered that the numerical simulation results validated in the range of Table 9.3-1 give a practically reasonable result (within a practical error of $\pm 15\%$), as long as the conditions are within the experimentally validated range.

9.4   Future Perspectives

9.4.1   Contribution to Standardization of Low-Power-Loss Design for Other Gear Types

As a future perspective, it is considered that the standardization for low-power-loss design will be extended from the helical gear pair targeted in this research to other gear types. The trend of the fluid dynamic loss may differ depending on the gear type. A schematic diagram of the differences in the trends of the fluid dynamic loss when the knowledge of the fluid dynamic loss obtained in this study is applied to other gear types is shown in Fig. 9.4-1 .

Figure 9.4-1 (a) shows the helical gear pair on which the trend of fluid dynamic loss is based. The locations where the fluid dynamic loss occurs are the gear meshing and peripheral parts. In the case of a helical gear pair, there is one gear meshing part, and the gear peripheral parts are located around it. A spur gear pair is similar to a helical gear pair.

Figure 9.4-1 (b) shows a schematic of the trend of the fluid dynamic loss for a bevel gear pair. Similar to a helical gear pair, a bevel gear pair has one gear meshing part and two gear peripheral parts around it. In contrast, the bevel gear pair is considered to have a larger pumping work (i.e., the suction of air from the inner diameter side and air discharge to the outer diameter side, similar to an impeller) for the gear at the gear periphery than a helical gear pair. Therefore, the fluid dynamic loss generated at the peripheral part of the gear is considered to increase.

Figure 9.4-1 (c) shows a schematic diagram of the trend of fluid dynamic loss in a spur gear train. A spur gear train is a gear train with multiple parallel axes. In the spur gear train, the number of gear meshes increases, thereby increasing the fluid dynamic loss at the gear meshing parts.

Figure 9.4-1 (d) shows a schematic diagram of the fluid dynamic loss trend of a planetary gear system. A planetary gear system consists of a sun gear in the center, multiple gears meshing with the sun gear (planetary gears), and a ring gear inscribed with multiple gears. In the planetary gear system, the fluid dynamic loss generated at the gear meshing part increases owing to multiple gear meshing. In addition, the fluid dynamic loss generated at the gear peripheral part increases because the directions of the tooth movements are opposite on the tooth surfaces where the planetary gears are close to each other.

The trends of the fluid dynamic loss elements in the gear types shown above are summarized in Table 9.4-1 . When the fluid dynamic loss generated in the gear meshing part increases, as shown in Fig. 9.2-2 , the air side-flow, oil-jet acceleration, and oil reacceleration losses increase (the air pumping loss is negligible because it is sufficiently small). When the fluid dynamic loss generated in the peripheral part of the gear increases, the air vortex and oil churning losses increase.

By applying the knowledge of fluid dynamic losses obtained in this research, the details of the features shown in Fig. and Table 9.4-1 can be identified, thereby contributing to the standardization of the low-power-loss design for these gears.
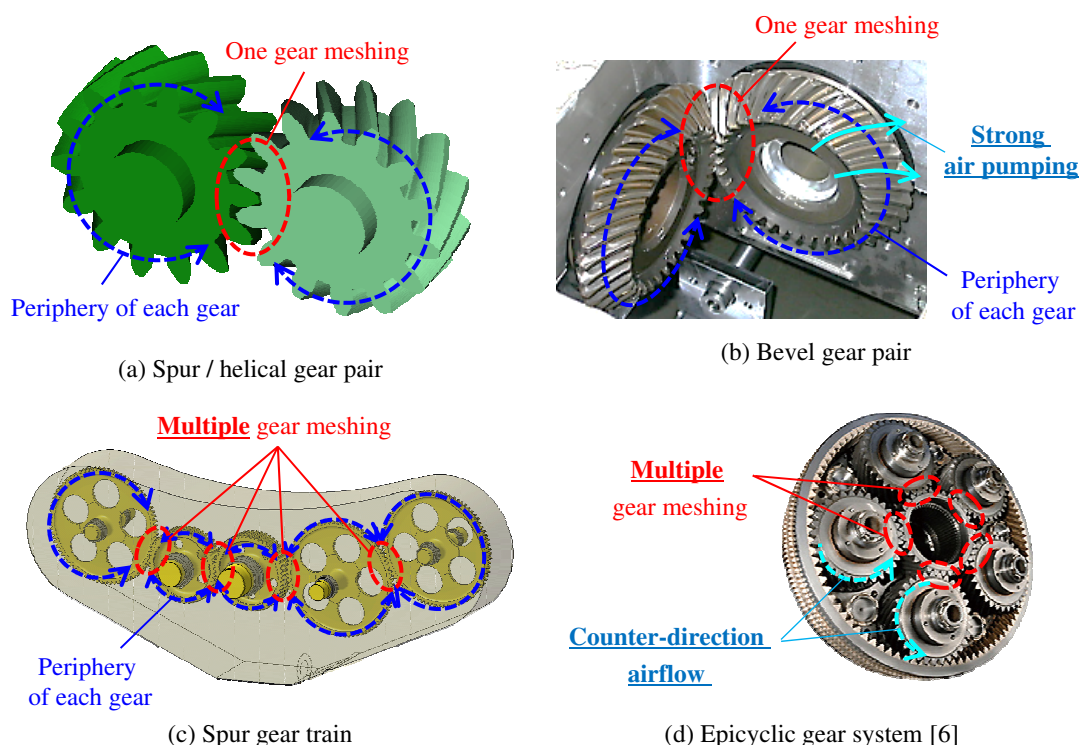

(a) Spur / helical gear pair

(b) Bevel gear pair

(c) Spur gear train

(d) Epicyclic gear system [6]

Fig. 9.4-1 Schematics for applying the knowledge of the fluid dynamic loss to other gear systems

Table 9.4-1 Anticipated trends in elements of fluid dynamic loss for various gear systems

(⇑ Loss may increase.)

Loss→ Gear type↓	Aerodynamic loss*		Oil dynamic loss		
	Air side-flow loss	Air vortex loss	Oil-jet acceleration loss	Oil reacceleration loss	Oil churning loss
Spur/helical gear pair	(Base)	(Base)	(Base)	(Base)	(Base)
Bevel gear pair		⇑			⇑
Spur gear train	⇑		⇑	⇑	
Epicyclic gear system	⇑	⇑	⇑	⇑	⇑

* Air pumping loss is negligible.

9.4.2 Possibility of Contributions to Gear Systems of Future Aeroengines

(1) Possible Contributions to Future Engines Equipped with Fan Drive Gear System

Future engines may include improvements in the engine efficiency equipped with the current fan drive gear system for small- and medium-sized aircraft [8] [127], and the expansion of the applications of the fan drive gear system to engines for medium and large aircraft [128]. The improvement in the engine efficiency for small- and medium-sized aircraft includes increasing the fan diameter and/or increasing the turbine speed, and changing the fan to an open rotor. In both the cases, the efficiency was improved by increasing the bypass ratio. To increase the fan diameter and/or turbine speed, it is necessary to increase the speed reduction ratio of the gear system (turbine speed/fan speed). To increase the reduction ratio,

it is effective to change from the star-type epicyclic gear system (fixing the carrier of the planetary gears and driving the fan with the ring gear) used in the current geared turbofan to a planetary-type epicyclic gear system (fixing the ring gear and driving the fan with a planetary carrier) [8]. In the case of an open rotor fan, a planetary gear system is installed between the front and rear propellers, and the sun gear, which receives the turbine driving force, drives the front fan connected to the planetary carrier and the rear fan connected to the ring gear. In this case, the gear system deceleration ratio also increases [127]. Therefore, to improve the efficiency of engines equipped with a fan drive gear system, the reduction ratio of the gear system is increased. In general, the transmission efficiency decreases as the reduction ratio increases. Therefore, standardization of the low-power-loss design proposed in this study is considered effective. Additionally, with the expansion of the applications of the fan drive gear system to engines for medium and large aircraft, the transmitted power of the gear system increases [128]. The power loss increased as the transmitted power increased. Therefore, standardization of the low-power-loss design proposed in this study is considered effective.

(2)   Possible Contributions to Future Engines Equipped with an Accessory Gearbox Applicable for Large-Capacity Power Generation

In current engines, an accessory gearbox is powered by a high-pressure turbine shaft to drive the power generators and other auxiliary equipment. However, the increasing electrification of the airframe requires large-capacity power generation, and the extraction of power from the high-pressure turbine shaft approaches its limits. If excessive power is extracted from the high-pressure turbine shaft, the rotation of the shaft may become unstable, particularly under idle conditions. To solve this problem, it is conceivable to extract power from the low-pressure turbine shaft of an engine. However, the range of the rotational speed of the low-pressure turbine shaft is wider than that of the high-pressure turbine shaft (e.g., the rotation range of the low-pressure turbine shaft is approximately 5:1 and that of the high-pressure turbine shaft is approximately 2:1 [129]). If the rotational speed of the generator (power generation frequency) varies over a wide range, it becomes difficult to design an electrical system. Therefore, a gear system equipped with a mechanism for converting rotational speed, such as a clutch or transmission mechanism, is required to maintain the rotational speed of the generator within a realistic range. The ideas for the speed conversion gear system include a mechanism for connecting a generator connected to a high-pressure turbine shaft to a generator connected to a low-pressure turbine shaft via a transmission mechanism [129], and a mechanism for driving a generator from each shaft of the engine via a speed reducer [130]. In both cases, increasing the efficiency of the gear system is important, as the power loss increases with the addition of gear systems. Therefore, standardization of the low-power-loss design proposed in this study is considered an effective approach.

References

[1] Wikipedia, "Boeing 787 Dreamliner, " `https://en.wikipedia.org/wiki/Boeing_787_Dreamliner`

[2] Wikimedia Commons, "Rolls-Royce RB211, " `https://commons.wikimedia.org/wiki/Category:Rolls-Royce_RB211`

[3] Rolls-Royce, 1992, *The Jet Engine*, Rolls-Royce plc., translated by Jpn. Aeronaut. Engr. Assoc.

[4] Weiss, T., Hirt, M., 2002, "Efficiency Improvements for High Speed Gears of the 100MW Class, " VDI-Berichte NR. 1665, pp. 1161–1174.

[5] Peltry-Johnson, T. T., Kahraman, A., Anderson, N. E., and Chase, D. R., 2008, "An Experimental Investigation of Spur Gear Efficiency, " J. Mech. Des., **130**(6), pp. 062601-1–062601-10.

[6] Ogata, H., 2018, "Regional Jet Engines PW1500G and PW1900G, " Kawasaki Tech. Rev., **179**, pp. 75–78.

[7] Riegler, C., Bichlmaier, C., 2007, "The Geared Turbofan Technology — Opportunities Challenges and Readiness Status, " 1st CEAS European Air and Space Conference, CEAS-2007-054, Berlin, Germany, Sep. 10–13.

[8] McCune, M. E., 1993, "Initial Test Resutls of 40000 Horsepower Fan Drive Gear System for Advanced Ducted Propulsion Systems, " AIAA 93-2146.

[9] Benzakein, M. J., 2014, "A Look at Technologies for Commercial Aircreft in the Years 2035–2050, " Propulsion and Power Research, **3**(4), pp. 165–174.

[10] Madonna, V., Giangrande, P., and Galea, M., 2018, "Electrical Power Generation in Aircraft: Review, Challenges, and Opportunities, " IEEE Trans. Transportation Electrification, **4**(3), pp. 646–659.

[11] Japanese Aero Engines Corporation, 2009, "Strategic Technology Development (Engine Gear System Technology for Aircraft) ," Ministry of Economy, Trade and Industry, 1st Policy and Project Evaluation on Aircraft-Related Technology, `https://www.meti.go.jp/policy/tech_evaluation/c00/C0000000H21/091207_airplane_1st/airplane_1st.html`

[12] Wikipedia, "Pratt & Whitney R-1830 Twin Wasp, " `https://en.wikipedia.org/wiki/Pratt_%26_Whitney_R-1830_Twin_Wasp`

[13] Wikipedia, "Sakae (Engine), " `https://ja.wikipedia.org/wiki/%E6%A0%84_(%E3%82%A8%E3%83%B3%E3%82%B8%E3%83%B3)`

[14] Wikipedia, "Pratt & Whitney Canada PT6, " `https://en.wikipedia.org/wiki/Pratt_%26_Whitney_Canada_PT6`

[15] Wikipedia, "Allison T56 variants, " `https://en.wikipedia.org/wiki/Allison_T56_variants`

[16] Wikipedia, "Constant Speed Drive, " `https://en.wikipedia.org/wiki/Constant_speed_drive`

[17] Makris, K., "Generator Constant Speed Drive System — Description/Operation," `https://www.k-makris.gr/csd/`

[18] Goi, T., and Tanaka, H., 2007, "Traction Drive CVT Technologies for Aircraft Equipment, " ASME Paper

No. DETC2007-34116.

[19] Kilmain, C. J., and Murray, R., 1995, "V-22 Drive System Description and Design Technologies, " American Helicopter Soc. 51st Annual Forum, Fort Worth, Texas, May 9–11.

[20] Hamstra, J. W., and McCallum, B. N., 2010, "Tactical Aircraft Aerodynamic Integration, " *Encyclopedia of Aerospace Engineering*, John Wiley & Sons, Hoboken, New Jersey.

[21] Atuk, B., and Majchrowicz, 2019, "Dr. Paul Bevilaqua: The Brilliant Mind Behind the F-35B Lightning II, " AIAA 2019-0120.

[22] Anderson, N. E., and Loewenthal, S. H., 1980, "Spur-Gear-System Efficiency at Part and Full Load, " Cleveland, Ohio, Report No. NASA TP-1622.

[23] Li, S. and Kahraman, A., 2010, "A Transient Mixed Elastohydrodynamic Lubrication Model for Spur Gear Pairs, " J. Tribol. **132**(1), pp. 011501-1–011501-9.

[24] Czichos, H., 1978, *Tribology — A Systems Approach to the Science and Technology of Friction, Lubrication and Wear*, Elsevier, Amsterdam, Netherlands.

[25] Krantz, T. L., 2005, "The Influence of Roughness on Gear Surface Fatigue, " Cleveland, Ohio, Report No. NASA TM-2005-213958.

[26] Akazawa, M., Tejima, J., Narita, T., 1980, "Full Scale Test of High Speed High Powered Gear Unit — Herical Gears of 25000 PS at 200mps PLV, " Intl. Power Transmissions Gearing Conf., San Francisco, California, Aug. 18–21.

[27] Anderson, N. E., Loewenthal, S. H., and Black J. D., 1984, "An Analytical Method to Predict Efficiency of Aircraft Gearboxes, " AIAA-84-1500.

[28] Johnson, G., Chandra, B., Foord, C., and Simmons, K., 2009, "Windage Power Losses from Spiral Bevel Gears with Varying Oil Flows and Shroud Configurations, " J. Turbomach. **131**(4), pp. 041019-1–041019-7.

[29] Massini, D., Fondelli, T., Facchini, B., Tarchi, L., and Leonardi, F., 2018, "Windage Losses of A Meshing Gear Pair Measured at Different Working Conditions, " ASME Paper No. GT2018-76823.

[30] Winfree, D. D., 2013, "Reducing Gear Windage Losses from High Speed Gears and Applying These Principles to Actual Running Hardware, " ASME Paper No. DETC2013-13039.

[31] Dawson, P. H., 1984, "Windage Loss in Larger High-Speed Gears, " Proc. Inst. Mech. Eng., **198A**(1), pp. 51–59.

[32] Delgado, I. R., Hurrell, M. J., 2017, "Experimental Investigation of Shrouding on Meshed Spur Gear Windage Power Loss, " Cleveland, Ohio, Report No. NASA GRC-E-DAA-TN42435.

[33] Massini, D., Fondelli, T., Andreini, A., Facchini, B., Tarchi, L., and Leonardi, F., 2018, "Experimental and Numerical Investigation on Windage Power Losses in High Speed Gears, " J. Eng. Gas Turbines Power, **140**(8), pp. 082508-1–082508-11.

[34] Townsend, D. P., 1985, "Lubrication and Cooling for High Speed Gears, " Cleveland, Ohio, Report No. NASA TM-87096.

[35] Massini,D., Fondelli, T., Facchini, B., Tarchi, L., Leonardi, F., 2017, "Experimental Investigation on Power Losses due to Oil Jet Lubrication in High Speed Gearing Systems, " ASME Paper No. GT2017-64703.

[36] Ariura, Y., Ueno, T., Sunaga, T., and Sunamoto, S., 1973, "The Lubricant Churning Loss in Spur Gear Systems, " Trans. JSME, **16**(95), pp. 881–892.

[37] Houjoh, H., Ohshima, S., Matsumura, S., Yumia, Y., and Itoh, K., 2003, "Pressure Measurement of Ambient Air in the Root Space of Helical Gears for the Purpose of Understanding Fluid Flow to Improve Lubrication Efficiency, " ASME Paper No. DETC2003/PTG-48117.

[38] LePrince, G., Changenet, C., Ville, F., Velex, P., Dufau, C., and Jarnias, F., 2011, "Influence of Aerated Lubricants on Gear Churning Losses — An Engineering Model, " Tribol. Trans., **54**(6), pp. 929–938.

[39] Neurouth, A., Changenet, C., Ville, F., Octure, M., and Tinguy, E., 2017, "Experimental Investigations to Use Splash Lubrication for High-Speed Gears, " J. Tribol. **139**(6), pp. 061104-1–061104-7.

[40] Diab, Y., Ville, F., Changenet, C., and Velex, P., 2003, "Windage Losses in High Speed Gears — Preliminary Experimental and Theoretical Results, " ASME Paper No. DETC2003/PTG-48115.

[41] Voeltzel, N., Marchesse, Y., Changenet, C., Ville, F., and Velex, P., 2016, "On the Influence of Helix Angle and Face Width on Gear Windage Losses, " Proc. Inst. Mech. Eng., **230C**(7,8), pp. 1101–1112.

[42] Diab, Y., Ville, F., Houjoh, H., Sainsot, P., and Velex, P., 2005, "Experimental and Numerical Investigations on the Air-Pumping Phenomenon in High-Speed Spur and Helical Gears, " Proc. Inst. Mech. Eng., **219C**(8), pp. 785–800.

[43] Seetharaman, S. and Kahraman, A., 2010, "A Windage Power Loss Model for Spur Gear Pairs, " Tribol. Trans., **53**(4), pp. 473–484.

[44] Talbot, D., Kahraman, A., and Seetharaman, S., 2014, "A Helical Gear Pair Pocketing Power Loss Model, " J. Tribol. **136**(2), pp. 021105-01–021105-11.

[45] Erkilic, E., Talbot, D., and Kahraman, A., 2015, "A Model to Predict Pocketing Power Losses in Spiral Bevel Gears, " ASME Paper No. DETC2015-47344.

[46] Matsumoto, S., Asanabe, S., Takano, K., and Yamamoto, M., 1985, "Evaluation Method of Power Loss in High-Speed Gears, " Proc. Jpn. Soc. Lubrication Engrs. Intl. Tribol. Conf., Tokyo, Japan, Jul. 8–10, pp. 1165–1170.

[47] Anderson, N. E. and Loewenthal, S. H., 1981, "Effect of Geometry and Operating Conditions on Spur Gear System Power Loss, " J. Mech. Des, **103**(95), pp. 151–159.

[48] Chanenet, C., Ville, F., and Velex, P., 2016, "Thermal Behavior of a High-Speed Gear Unit, " *GEAR Technology, January/February, 2016*, AGMA, Elk Grove Village, illinois, pp. 38–41.

[49] Hill, M. J., Kunz, R. F., Noack, R. W., Long, L. N., Morris, P. J., and Handschuh, R. F., 2008, "Application and Validation of Unstructured Overset CFD Technology for Rotorcraft Gearbox Windage Aerodynamics Simulation, " American Helicopter Soc. 64th Annual Forum, Montreal, Canada, April 29–May 1.

[50] Al. B. C., Simmons, K., Morvan, H. P., 2014, "Computational Investigation of Flows and Pressure Fields Associated With Spur Gear Meshing, " ASME Paper No. GT2014-26145.

[51] Fondelli, T., Massini, D., Andreini, A., Facchini, B., 2018, "Three-Dimensional CFD Analysis of Meshing Losses in a Spur Gear Pair, " ASME Paper No. GT2018-77141.

[52] Concli, F., Gorla, C., Torre, A. D., and Montenegro, G., 2014, "Windage Power Losses of Ordinary Gears: Different CFD Approaches Aimed to the Reduction of the Computational Effort, " *Lubricants*, **2**(4), Basel, Switzerland, pp. 162–176.

[53] Fondelli, T., Andreini, A., Soghe, R. D., Facchini, B., Cipolla, L., 2015, "Volume of Fluid (VOF) Analysis of Oil-Jet Lubrication for High-Speed Spur Gears Using an Adaptive Meshing Approach, " ASME Paper No. GT2015-42461.

[54] Keller, M. C., Braun, S., Wieth, L., Chaussonnet, G., Dauch, T. F., Koch, R., Schwitzke, C., Bauer, H. J., 2017, "Smoothed Particle Hydordynamics Simulation of Oil-Jet Gear Interaction, " ASME Paper No. GT2017-63594.

[55] Ambrose, S., Morvan, H., Simmons, K., 2018, "Investigation of Oil Jet Impingement on a Rotating Gear Using Lattice Boltzman Method (LBM), " ASME Paper No. GT2018-76371.

[56] Concli, F. and Gorla, C., 2016, "Numerical Modeling of the Power Losses in Geared Transmissions: Windage, Churning and Cavitation Simulations with a New Integrated Approach that Drastically Reduces the Computational Effort, " Tribol. Intl. **103**(C), pp. 58–68.

[57] Liu, H., Arfaoui, G., Stanic, M., Montigny, L., Jurkschat, T., Lohner, T., and Stahl, K., 2019, "Numerical Modelling of Oil Distribution and Churning Gear Power Losses of Gearboxes by Smoothed Particle Hydrodynamics, " Proc. Inst. Mech. Eng., **233J**(1), pp. 74–86.

[58] Houjoh, H. and Iino, T., 2015, "Experimental Investigation of the Possibility of a Self-Vacuuming Gearbox for Reducing Windage Loss, " ASME Paper No. DETC2015-47257.

[59] Handschuh, R., and Kilmain, C., 2005, "Experimental Study of the Influence of Speed and Load on Thermal Behavior of High-Speed Helical Gear trains, " Cleveland, Ohio, Report No. NASA TM-2005-213632.

[60] Sheridan, W., McCune, M., and Winter, M., 2010, "Geared Turbofan Engine Driven by Innovation, " *Encyclopeida of Aerospace Engineering*, John Wiley & Sons, Hoboken, New Jersey.

[61] Reynolds, C. N., 1985, "Advanced Prop-Fan Engine Technology(APET) Single and Counter-Rotation Gearbox Pitch Change Mechanism, " Cleveland, Ohio, Report No. NASA CR-168114.

[62] Handschuh, R. F., Hurrell, M. J., 2011, "Initial Experiments of High-Speed Drive System Windage Losses, " Cleveland, Ohio, Report No. NASA TM-2011-216925.

[63] Delgado, I. R., Hurrell, M., J., 2017, "Baseline Experimental Eesults on the Effect of Oil Temperature on Shrouded Meshed Spur Gear Windage Power Loss, " ASME Paper No. DETC2017-67818.

[64] Luke, P., Olver, A. V., 1999, "A Study of Churning Losses in Dip-Lubricated Spur Gears, " Proc. Inst. Mech. Eng., **213G**(5), pp. 337–346.

[65] Kolekar, A. S., Olver, A. V., Sworski, A. E., and Lockwood, F. E., 2014, "Windage and Churning Effects in Dipped Lubrication, " J. Tribol., **136**(2), pp. 021801-1–021801-10.

[66] Seetharaman, S. and Kahraman, A., 2009, "Load-Independent Spin Power Losses of a Spur Gear Pair: Model Formulation, " J. Tribol. **131**(2), pp. 022201-1–022201-11.

[67] Seetharaman, S., Kahraman, A., Moorhead. M. D., and Petry-Johnson, T. T., 2009, "Oil Churning Power lossse of a Gear Pair: Experiments and Model Validation, " J. Tribol. **131**(2), pp. 022202-1–022202-10.

[68] Liu, H., Jurkschat, T., Lohner, T., and Stahl, K., 2018, "Detailed Investigations on the Oil Flow in Dip-Lubricated Gearboxes by the Finite Volume CFD Method, " *Lubricants*, **6**(2):47, Basel, Switzerland.

[69] Hartono, E. A., Golubev, M., and Chernoray, V., 2013, "PIV Study of Fluid Flow Inside a Gearbox, " 10th Intl. Symp. on Particle Image Velocimetry, Delft, Netherlands, Jul. 1–3.

[70] Makino, H., Kimoto, M., Tsuji, H., Yoshida, H., and Iinoya, K., 1992, "Investigation of the Measurement Method of Particle Concentration and Size Distributions on Anisokinetic Sampling (Part 1) — Concept and Performance of the Measurement Method, " Cen. Res. Inst. Electric Pwr Ind., Report No. W92003.

[71] Yang, Y., and Telionis, D., 2013, "Design and Testing of Instrumentation for Multi-Phase Flow Sampling and Local Void Fraction Measurement, " WIT Trans. Eng. Sci., **79**, pp. 311–322.

[72] Namie, S., and Ueda, T., 1972, "Droplet Transfer in Two-Phase Annular Mist Flow — Part 1: Experiment of Droplet Transfer Rate and Distributions of Droplet Concentration and Velocity, " Bull. JSME, **15**(90), pp. 1568–1580.

[73] Ishikawa, A., Imai, R., and Tanaka, T., 2013, "Experimental Study on Two-Phase Flow in Horizontal Tube Bundle Using SF6-Water, " IHI Tech. Rev., **46**(2), pp. 26–31.

[74] Coy, J.J., Townsend, D.P., and Zaretsky, E.V., 1985, "Gearing," Cleveland, Ohio, Report No. NASA RP-1152.

[75] American Gear Manufactures Association, 1982, "Contact Load Factor, K, " *AGMA Standard for Rating the Pitting Resistance and Bending Strength of Spur and Helical Involute Gear Teeth*, AGMA 218.01, Alexandria, Virginia, p. 8.

[76] Dudley, D.W., 2012, "Indexes of Tooth Loading for Preliminary Design Calculations, " *Dudley's Handbook of Practical Gear Design and Manufacture, Second Edition*, CRC Press, Boca Raton, Florida, p. 216.

[77] Bhandari, V. B., 2010, "Gear Blank Design, " *Design of Machine Elements Third Edition*, Tata McGraw Hill Education, New Delhi, India, pp. 667–670.

[78] American Gear Manufactures Association, 1982, *AGMA Standard for Rating the Pitting Resistance and Bending Strength of Spur and Helical Involute Gear Teeth*, AGMA 218.01, Alexandria, Virginia.

[79] American Gear Manufactures Association, 1965, *AGMA Information Sheet: Gear Scoring Design Guide for Aerospace Spur and Helical Power Gears*, AGMA 217.01, Alexandria, Virginia.

[80] American Gear Manufactures Association, 2004, *American National Standard: Fundamental Rating Factors and Calculation Methods for Involute Spur and Helical Gear Teeth*, ANSI/AGMA 2001-D04, Alexandria, Virginia.

[81] American Gear Manufactures Association, 2003, *AGMA Information Sheet: Effect of Lubrication on Gear Surface Distress*, AGMA 925-A03, Alexandria, Virginia.

[82] Höhn, B.R., Michaelis, K., and Vollmer, T., 1996, "Thermal Rating of Gear Drives: Balance between Power Loss and Heat Dissipation," AGMA Paper No. 96FTM8.

[83] Palmgren, A., 1959, *Ball and Roller Bearing Engineering, Third Edition*, S.H., Burbank, Philadelphia, Pennsylvania.

[84] Liu, S., Gatin, I., Obhrai, C., Ong, M. C., and Jasak, H., 2019, "CFD Simulations of Violent Breaking Wave Impacts on a Vertical Wall using a Two-Phase Compressible Solver, " Coastal Engineering, **154**, Elsevier, Amsterdam, Netherlands.

[85] Morikawa, K., Nishihara, R., and Matsumoto, S., 2012, "Estimation and Improvement Method of Mesh Efficiency of Cylindrical Gears, " Trans. JSME, **78**(788), pp. 1250–1259.

[86] Miedema, S. A., 2013, "An Overview of Theories Describing Head Losses in Slurry Transport: A Tribute to Some of the Early Reseachers, " ASME Paper No. OMAE2013-10521.

[87] Ushijima, T., 2004, "Dispersion and Mixing of Small Particles, Droplets and Bubbles in Turbulent Flows, " *Nagare*, **23**(3), J. Jpn. Soc. Fluid Mech., pp. 191–201.

[88] Mizota, T., and Okajima, A., 1981, "Experimental Studies of Time Mean Flows around Rectangular Prisms, " Proc. Jpn. Soc. Civil Engrs. **1981**(312), pp. 39–47.

[89] Hill, M. J. and Kunz, R. F., 2012, "A Computational Investigation of Gear Windage, " Philadelphia, Pennsylvania, Report No. NASA CR-2012-217807.

[90] Tatsumi, T., 1995, *Dynamics of the Continuum (Iwanami Fundamental Physics Series (2))*, Iwanami Shoten Publ., Tokyo, Japan.

[91] Sano, O., 2000, *Dynamics of the Continuum (Selection of Fundamental Physics No.26)*, Shokabo, Tokyo, Japan.

[92] Kleinstreuer, C., 2003, "Homogeneous Flow Models, " *Two-Phase Flow Theory and Applications 1st Edition*, CRC Press, Boca Raton, Florida, pp. 139–150.

[93] Totten, G. E., and Negri, V. J., 2012, "Physical Properties and Their Determination, " *Handbook of Hydraulic Fluid Technology Second Edition*, CRC Press, Boca Raton, Florida, p. 117.

[94] Furuya, K., 1938, "Experimental Research on the Lubricating Oil (1st Report): Measurement of Contact

Angle of Oil Drops, " Trans. JSME, **4**(14), pp. 78–83.

[95] Nabesaka, S., Etoh, T., and Takehara, K., 2002, "A New Technique to Separately Evaluate the Effects of Surface Tension and Viscosity on Rupture of a Bubble at Water Surface, " Proc. Jpn. Soc. Civil Engrs., **705**, pp. 19–29.

[96] Fukushi, K, and Iguchi, M., 2005, "The Effects of Wettability on the Flow Pattern and Rising Gas Velocity of Gas–Liquid Two-Phase Flow in Vertical Pipe, " *Tetsu-to-Hagane*, Iron Steel Inst. Jpn., **91**(5), pp. 465–470.

[97] Lockhart, R. W., and Martinelli, R. C., 1949, "Proposed Correlation of Data for Isothermal Two-Phase, Two-Component Flow in Pipes, " Chem. Engrs. Progr., **45**(1), pp. 39–48.

[98] Mandhane, J. M., Gregory, G. A., and Aziz, K., 1974 "A flow pattern map for gas–liquid flow in horizontal pipes, " Intl. J. Multiphase Flow, **1**(4), pp. 537–553.

[99] Ditect, 2017, *Dipp Motion User Manual ver. 1.1.29*, Ditect, Tokyo, Japan.

[100] Chandorkar, A., and Palit, S, 2009 "Simulation of Droplet Dynamics and Mixing in Microfluidic Devices Using a VOF-Based Method, " *Sensors & Transducers*, **7**(Special Issue), Intl. Frequency Sensor Assoc. Publ., Barcelona, Spain, pp. 136–149.

[101] Marchaterre, J. F., and Hoglund, B. M., 1962, "Correlation for Two-Phase Flow, " *Nucleonics*, **20**(8), McGraw-Hill Book Company, New York, p. 142.

[102] El Telbany, M. M. M., and Reynolds, A. J., 1980, "Velocity Distributions in Plane Turbulent Channel Flows, " J. Fluid Mech., **100**(1), pp. 1–29.

[103] Hirt, C. W., and Nichols, B. D., 1981, "Volume of Fluid (VOF) Method for the Dynamics of Free Boundaries, " J. Comput. Phys., **39**(1), pp. 201–225.

[104] Hirt, C. W., and Sicilian J. M., 1985, "A Porosity Technique for the Definition of Obstacles in Rectangular Cell Meshes, " Proc. 4th Intl. Conf. Numerical Ship Hydrodynamics, Washington D.C., Sep. 24–27.

[105] Flow Science, Inc., 2016, *FLOW-3D/MP®Users Manual Version 6.0*, Santa Fe, New Mexico. `https://www.flow3d.com`

[106] Tennekes, H., and Lumley, J. L., 1972, *A First Course in Turbulence*, MIT Press, Cambridge, Massachusetts.

[107] Rusche, H., 2002, "Computational Fluid Dynamics of Dispersed Two-Phase Flows at High Phase Fraction, " Ph.D. thesis, Imperial College London, London, UK.

[108] Hirt, C. W., 1993, "Volume-Fraction Techniques: Powerful Tools for Wind Engineering, " J. Wind Eng. Ind. Aerodyn., **46,47**, pp. 327–338.

[109] Smagorinsky, J., 1963, "General Circulation Experiments with the Primitive Equations, " Monthly Weather Rev., **91**(3), pp. 99–164.

[110] Sakai, 2016, "How Should the Descrete Element Method Be Applied in Industrial Systems: A Review, " KONA Powder & Particle J., **33**, pp. 169–178.

[111] Okamoto, T., and Yagita, M., 1972, "The Experimental Investigation on the Flow of a Circular Cylinder of Finite Length Placed Normal to the Plane Surface in a Uniform Stream, " Trans. JSME, **38**(313), pp. 2259–2267.

[112] Yeaple, F., 1995, "Hydraulic Fluids and Lubes, " *Fluid Power Design Handbook, Third Edition*, CRC Press, Boca Raton, Florida, p. 7.

[113] Rajaratnam, N., 1976, *Turbulent Jets*, Elsevier, Amsterdam, Netherlands.

[114] Hayward, A. T. J., 1962, "The Viscosity of Bubbly Oil, " J. inst. Petroleum, **48**(461), pp. 156–164.

[115] Bruno, L., Fransos, D., Coste, N., and Bosco, A., 2008, "3D Flow Around A Rectangular Cylinder: A gational Study, " Proc. 6th Intl. Coll. on Bluff Bodies Aerodyn. & App., Milano, Italy, Jul. 20–24.

[116] Idelchik, I. E., 1996, *Handbook of Hydraulic Resistance, Third Edition*, Begel House, Danbury, Connecticut.

[117] Bilgen, E., and Boulos, R, 1973, "Functional Dependence of Torque Coefficient of Coaxial Cylinders on Gap Width and Reynolds Numbers," J. Fluids Eng. **95**(1), pp. 122–126.

[118] Schlichting, H., 1978, "Axially Symmetrical and Three-Dimentional Boundary Layers," *Boundary-Layer Theory Seventh Edition*, McGraw-Hill Book Company, New York, pp. 225–264.

[119] Furukawa, F., Egashira, Y., and Tsutsumi, M., 1981, "Proposal and Application of Empilical Formula on Moment Coefficient of Coaxial Cylinders on Gap Width and Reynolds Numbers," Bull. Nagasaki Inst. Appl. Sci., **22**(1), pp. 1–12.

[120] Terashima, K., Tsukada, K., and Amagai, K., 2012, "Fundamental Study on Gear Lubrication by Oil-mist," Trans. Soc. Automot. Engrs. Jpn., **43**(4), pp. 893–898.

[121] Wright, D., 2005, "Gear meshing," *Notes on Design and Analysis of Machine Elements*, `http://www-mdp.eng.cam.ac.uk/web/library/enginfo/textbooks_dvd_only/DAN/gears/meshing/meshing.html`

[122] Benedict, G. H., and Kelley, B. W., 1961, "Instantaneous Coefficients of Gear Tooth Friction," ASLE Trans., **4**(1), pp. 59–70.

[123] Crook, A. W., 1963, "The Lubrication of Rollers. IV. Measurements of Friction and Effective Viscosity," Phil. Trans. Royal Soc. London, **255A**(1056), pp. 281–312.

[124] Hamrock, B. J., and Dowson, D., 1977, "Isothermal Elastohydrodynamic Lubrication of Point Contacts. III — Fully Flooded Results," J. Lubrication Tech, **99**(2), pp. 264–276.

[125] Cheng, H. S., 1974, "Prediction of Film Thickness and Traction in Elastohydrodynamic Contacts," ASME Des. Eng. Tech. Conf., New York, pp. 285–293.

[126] Kobayashi, R., 1985, "Turbulent Transition of Boundary Layer in a Rotating Axisymmetric Body," *Turbomachinery*, **13**(3), Turbomach. Soc. Jpn., pp. 180–185.

[127] Imai, H., Goi, T., Kijima, K., Nishida, T., Arisawa, H., Matsuda, T., and Sato, M., 2013, "Design and Test of Differential Planetary Gear System for Open Rotor Power Gearbox," ASME Paper No. DETC2013-12089.

[128] Clean Sky 2 Joint Undertaking, 2018, *Annual Activity Report*.

[129] Lemmers Jr., G. C., and Behling, D. S., 2009, "High to Low Pressure Spool Summing Gearbox for Accessory Power Extraction and Electric Start," U. S. Patent 7,882,691.

[130] Hield, P. M., Cundy, J. M., Midgley, R. A., Newton, A. C., and Rowe, A. L., 1997, "Shaft Power Transfer in Gas Turbine Engines with Machines Operable as Generators or Motors," U. S. Patent 5,694,765.

[131] Harnoy, A., 2002, "Short Journal Bearings," *Bearing Design in Machinery*, CRC Press, Boca Raton, Florida, pp. 147–155.

[132] EagleBurgmann, 2021, "Power consumption of the sliding faces: Example M7," *Mechanical seal technology and selection*, EagleBurgmann Japan, Tokyo, Japan.

[133] Michael, P., Khalid, H., and Wanke, T., 2012, "An Investigation of External Gear Pump Efficiency and Stribeck Values," SAE Commercial Vehicle Eng. Cong., Rosemount, Minnesota, Oct. 2–3, Paper No. 2012-01-2041.

[134] Manring, N. D., and Fales, R. C., 2019, "5.2 Pump Efficiency," *Hydraulic Control Systems, Second Edition*, John Wiley & Sons, Hoboken, New Jersey, pp. 233–239.

Appendix A

Simple Estimation Equations for Fluid Dynamic Loss and Simple Design Method for Optimum Shroud Shapes

A.1   Simple Estimation Method for Aerodynamic Loss

A simplified non-dimensional equation for estimating the aerodynamic loss is given as follows (see Section 5.1.4 for details).

$$\frac{P_{air}}{\lambda \frac{1}{2} \rho_{air} v_p{}^3 \frac{hB}{\cos\beta} n_G} = 3.522 \left(\frac{B}{D_p}\right)^{-0.436} \tag{A.1}$$

In the above, P_{air} is the aerodynamic loss, λ is the shroud coefficient (the empirical equation is shown in Section A.3), ρ_{air} is the air density, v_p is the pitch circle speed, h is the tooth depth, B is the tooth width, β is the helix angle, n_G is the number of gears (= 1 for a single gear, = 2 for a gear pair), and D_p is the pitch circle diameter. The left side of the above equation is the dimensionless number for the aerodynamic loss P_{air}, and is a function of the gear aspect ratio B/D_p (dimensionless number) on the left side.

The above equation was constructed based on the results from the two-axis helical gearbox experiment in this research and Dawson's single spur gear experiments [31]. Therefore, when the equation is applied beyond the range of these experiments, it is necessary to separately validate it by experiments or numerical simulations (as validated by experiments).

A.2   Simple Estimation Method for Oil Dynamic Loss

A simplified non-dimensional equation for estimating the oil dynamic loss is given as follows (see Section 5.2.4 for details).

$$\frac{P_{oil}}{\rho_{oil} Q_s v_p{}^2 \cos\beta / \lambda} = -63.59 \frac{Q_s}{v_p B M_g} + 1.674 \tag{A.2}$$

Here, P_{oil} represents the oil dynamic loss, ρ_{oil} represents the density of the oil, Q_s represents the oil supply flow rate, and M_g represents the gear module. The left side of the equation is the dimensionless number for the oil dynamic loss (oil supply acceleration ratio), and the right side $Q_s/(v_p B M_g)$ is the dimensionless number for the oil supply flow rate Q_s (dimensionless oil supply flow rate).

The above equation was constructed based on the results from the two-axis helical gearbox experiment in this

research. Therefore, when the equation is applied beyond the range of these experiments, it is necessary to separately validate it by experiment or numerical simulation (as validated by experiments).

A.3 Experimental Equations for Shroud Coefficient

The empirical equation for the shroud coefficient λ is as follows (see Section 6.4.6 for details).

$$\lambda = \kappa\lambda_{\theta r} + (1 - \kappa)\lambda_x \tag{A.3}$$

In the above, $\lambda_{\theta r}$ represents the shroud coefficient on the gear peripheral surface, and λ_x represents the shroud coefficient on the gear side surface. κ represents the ratio of the air vortex loss on the peripheral surface of the gear to the total air vortex loss. $\lambda_{\theta r}$ and λ_x are calculated as follows.

$$\lambda_{\theta r} = a_w^{-b_w R_{w\_eff}}(1 - \lambda'_{\theta r}) + \lambda'_{\theta r} \tag{A.4}$$
$$\lambda'_{\theta r} = (\lambda_r - 1)(1 - R_\theta)^{n_\theta} + 1 \tag{A.5}$$
$$\lambda_r = (1 - a_r^{-b_r R_r})^{n_r} \tag{A.6}$$
$$\lambda_x = (1 - a_x^{-b_x R_x})^{n_x} \tag{A.7}$$

Here, R_r is the radial relative clearance, R_θ is the peripheral opening ratio, R_x is the axial relative clearance, and R_{w_eff} is the side wall coefficient (a factor related to the presence or absence of the side wall). R_r, R_θ, R_x, and R_{w_eff} are calculated as follows.

$$R_r = \frac{2C_{rr}}{D_p} \tag{A.8}$$

$$R_\theta = \frac{\sum_i \Delta\theta_{op,i}}{2\pi} \tag{A.9}$$

$$R_x = \frac{2C_{rx}}{D_p} \tag{A.10}$$

$$R_{w\_eff} = \begin{cases} \frac{\text{the width of the peripheral wall of the shroud}}{B} & \text{(without the side walls of the shroud)} \\ \infty & \text{(with side walls of shroud)} \end{cases} \tag{A.11}$$

where $\sum_i \Delta\theta_{op,i}$ is the total peripheral opening angle of the shroud (per gear).

κ, a_w, a_r, and a_x are the coefficients, and $b_w, n_\theta, b_r, n_r, b_x$, and n_x are the exponents. The corresponding values are shown in the table below.

Table A.3-1 Coefficients for evaluating shroud coefficient

Parameter	Value
κ	0.7875
a_w	3.5295
b_w	0.5627
n_θ	1.8365
a_r	53.3096
b_r	0.3186
n_r	0.2942
a_x	12.8704
b_x	2.6370
n_x	15.3235

The above equations were constructed from Dawson's experimental results regarding the effects of shrouds on a single spur gear [31]. Therefore, when the equations are applied beyond the range of that experiment, it is necessary to validate them separately by experiment or by numerical simulation (as validated by experiments).

A.4   Simple Design Method for Optimal Shroud Shapes

The following is a simplified design method for the shroud that minimizes the fluid dynamic loss (providing an optimal shroud) under the conditions of the two-axis helical gearbox studied in this research.

$R_r + R_x$ (the sum of the radial relative clearance and the axial relative clearance) and the oil supply flow rate with respect to the gear aspect ratio changes are shown in Fig. A.4-1 . In Fig. A.4-1 , two cases with $C_{rr} = C_{rx}$ and $C_{rr} = 0.5 C_{rx}$ are shown. $R_r + R_x$ is 0.65–0.75 at the gear aspect ratio of 0.3 or higher, in which the maximum efficiency exists. $R_r + R_x$ increased when the gear aspect ratio was 0.3 or less, but this was because the oil supply flow rate increased as the efficiency decreased. That is, to maintain the difference between the oil supply temperature and scavenging temperature at 30°C, it is considered to be the result of increased the clearance to improve oil discharge performance from the shroud. Optimum $\Delta\theta_{op}$ of the peripheral opening angle was approximately a constant value (60°) even in the gear aspect ratio changes. This is the angle at which the oil reacceleration loss becomes approximately zero and does not depend on the gear aspect ratio or the clearances.

From these results, it was found that the optimal shroud shape can be obtained by setting the sum of the radial relative clearance R_r (Eq. A.8) and axial relative clearance R_x (Eq. A.10) to 0.65–0.75, and the peripheral opening angle to 60°.

This design method is obtained from the fluid dynamic loss model as validated by the experimental results for the two-axis helical gearbox studied in this research. Strictly speaking, the method requires experimental validation, because the range of parameters is beyond the validated range.
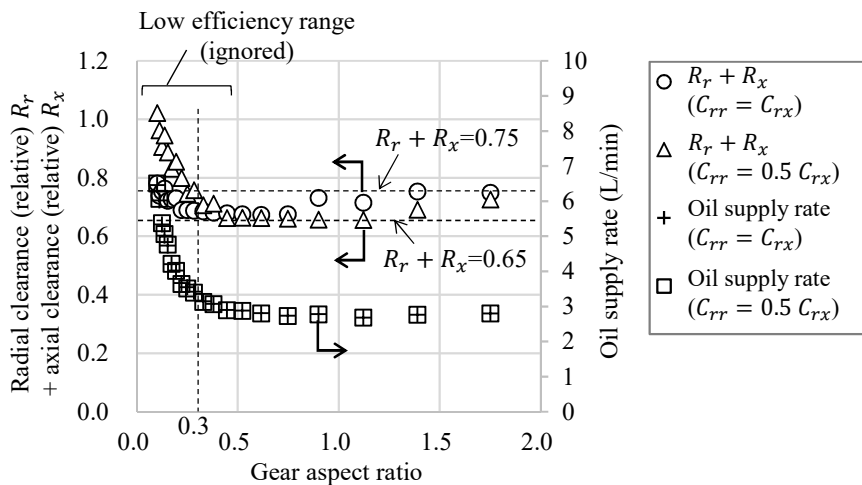
Fig. A.4-1 Trend of clearances for a simple design method of an optimal shroud (obtained using loss models)

A.5   Investigating the Influences of Parameters

Parameter studies were conducted using the simple estimation equations shown in A.1 and A.2 for the fluid dynamic loss.

The default parameters are shown in Table A.5-1 . The results from changing only one of the parameters are shown in Fig. A.5-1 . The horizontal axis shows the changed parameter, and the vertical axis shows the relative value when the default value is set to 1.0. Figures A.5-1 (a) to (d) exhibit the parameters for the gear shape, (e) and (f) shows the fluid densities, (g) and (h) address the operating conditions, and (i) displays the influence of the shroud coefficient.

Notably, of the parameters in Eqs. A.1 and A.2, the helix angle β can be excluded, because the change in the air side-flow loss is large, and therefore, the error is large for a simple estimation equation.

Table A.5-1 Default values of parameters to study the influence of parameters on fluid dynamic loss

Items	Simbol	Value	Unit	Source
Shroud coefficient	λ	0.58	–	Shroud 1
Air density	ρ_{air}	1.06	kg/m3	1 atm
Oil density	ρ_{oil}	971	kg/m3	MIL-PRF-23699
Pitch line speed	v_p	100	m/s	Two-axis helical gears, 10000 rpm of input gear
Tooth height	h	11.3	mm	Two-axis helical gears
Gear width	B	34.0	mm	Two-axis helical gears
Helix angle	β	30.0	deg	Two-axis helical gears
Pitch circle diameter	D_p	191	mm	Two-axis helical gears, input gear
Number of gears	n_G	2	–	Two-axis helical gears
Oil supply rate	Q_s	7.40	L/min	Two-axis helical gears
Gear module	M_g	5.00	mm	Two-axis helical gears

Regarding the influences of the parameters on the gear shape (Figs. A.5-1 (a) to (d)), all parameters affect the fluid dynamic loss, but the influence of the tooth width is relatively larger. In Section 7.4.1, the influence of the gear diameter was larger than that of the tooth width. This is because in Section 7.4.1, the gear peripheral speed increased as the gear diameter increased, whereas in this section, only the gear diameter was increased (the rotational speed was decreased to maintain the peripheral speed).

As to increasing the operating torque, one of the parameters of the gear shape, i.e., the (a) tooth width, (b) gear diameter, or (c) tooth height should be increased. That is, increasing the operating torque increases the fluid dynamic loss.

Regarding the influence of the fluid density (Figs. A.5-1 (e) and (f)), the influence of the air density is large. Insofar as the operating conditions (Figs. A.5-1 (g) and (h)), the influence of the gear peripheral speed is relatively large. However, the influence of the shroud coefficient (Fig. A.5-1 (i)) to the fluid dynamic loss P_{fluid} is relatively small compared to the other parameters. This is because the oil supply flow rate is high under the conditions of Table A.5-1 , and the influence of the increased oil dynamic loss owing to the installation of the shroud becomes large.

The results in this section have not been validated by either experiments or numerical simulations, so the results obtained should be carefully treated, for example, by conducting a separate validation.
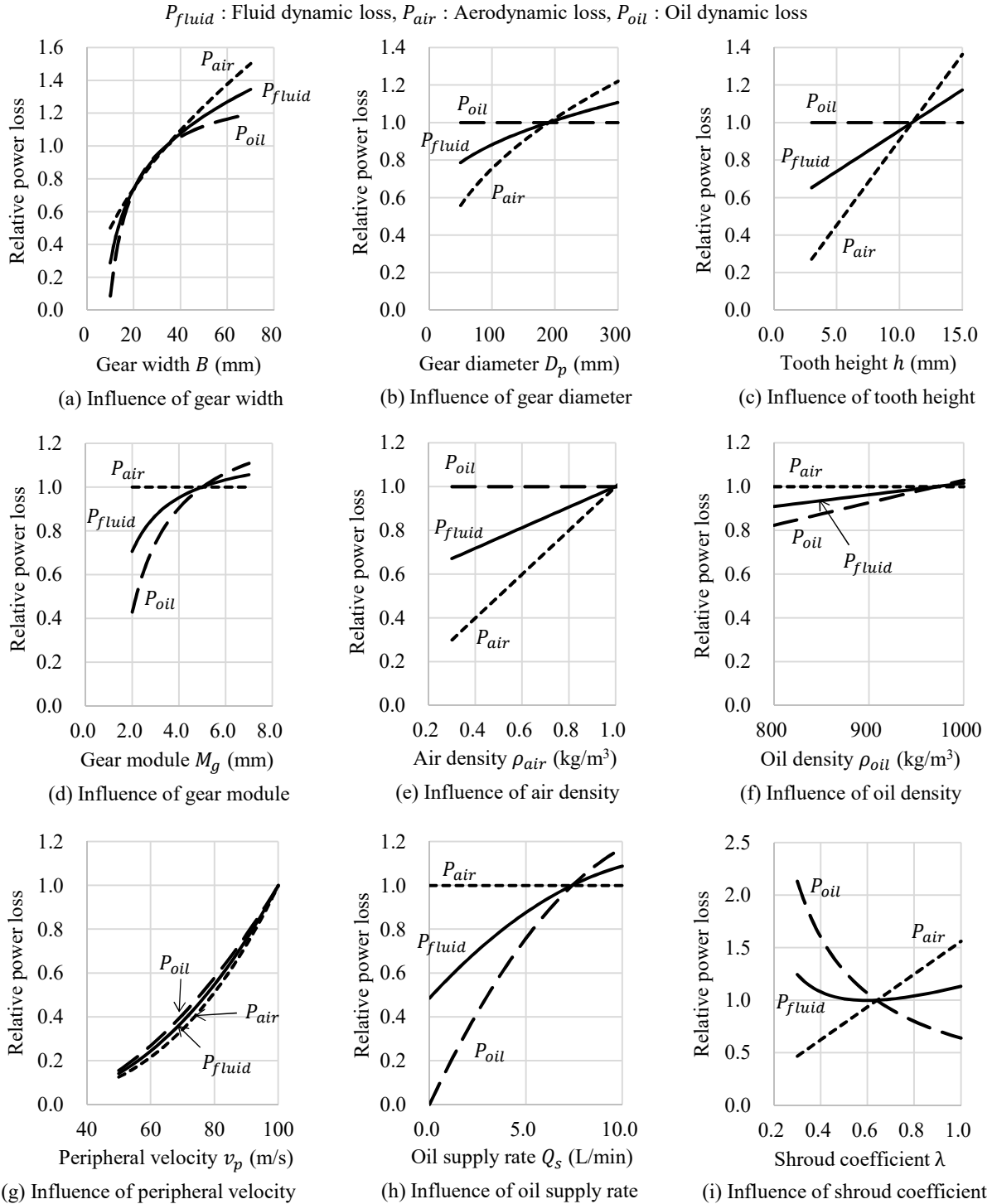
P_{fluid} : Fluid dynamic loss, P_{air} : Aerodynamic loss, P_{oil} : Oil dynamic loss

(a) Influence of gear width

(b) Influence of gear diameter

(c) Influence of tooth height

(d) Influence of gear module

(e) Influence of air density

(f) Influence of oil density

(g) Influence of peripheral velocity

(h) Influence of oil supply rate

(i) Influence of shroud coefficient

Fig. A.5-1 Results of the study conducted on the influence of various parameters on the fluid dynamic loss (obtained using non-dimensional equations)

Appendix B

Gear Friction Loss, and Power losses in Other Parts of Gearbox

The power losses except for fluid dynamic loss include the power loss at the gear contact surface (gear friction loss), the power losses in the rolling bearings and journal bearings, power losses in the seals, and power losses in the oil pumps. The methods for calculating these losses and their characteristics are described below.

B.1 Gear Friction Loss

There are two methods used for the calculation of gear friction loss: a simple method that calculates the friction coefficient at the contact surface by a time-averaged equation, and a detailed method that calculates the friction coefficient by considering the unsteady state of contact. This section describes both methods. Before that, an unsteady phenomenon at the gear contact surfaces is described.

B.1.1 Unsteady Phenomena at Gear Contact Surface

Examples of time changes in the load applied to gear tooth surfaces are shown in Fig. B.1-1 . In gear meshing, the gears mesh along the line of action. In Fig. B.1-1 (a), the tooth "A" is meshed with "Mesh 1" and the tooth "B" is meshed with "Mesh 2". That is, in this phase, the number of meshing teeth is 2. In Fig. B.1-1 (b), where the gear moves to the right from the state of (a), the tooth "B" is meshed with "Mesh 2". That is, in this phase, the number of meshing teeth is 1. In Fig. B.1-1 (c), where the gear is further moved to the right, the tooth "B" is meshed with "Mesh 2" and the tooth "C" is meshed with "Mesh 3". That is, in this phase, the number of meshing teeth is 2. Thus, the number of teeth of the gear to be meshed changes from 1 to 2 to 1 depending on the phase.

Changes in the load due to changes in the number of teeth meshed are shown in Fig. B.1-1 (d). "(a)", "(b)", and "(c)" in Fig. B.1-1 (d) correspond to Fig. B.1-1 (a), (b), and (c) respectively. For example, in the case of Mesh 2, the load per tooth is 1/2 because two teeth are meshed in the phase of (a). In the phase of (b), the load on the gear is fully applied to the tooth surface because one tooth is meshed. In the phase of (c), the load per tooth is 1/2 because two teeth are meshed. Thus, the load on the gear tooth surface varies depending on the phase.

In addition to the unsteady changes in the load described above, the relative velocity of the contact surface changes. For example, the sliding velocity of the tooth surface (the relative velocity of the tooth surface) is large

at the tip and root of the gear tooth. On the pitch circle, the sliding velocity becomes zero. If there is a relative velocity at the contact surface, it is necessary to consider the loss caused by the sliding between the contact surfaces (sliding loss at the contact surface). In addition, regardless of the presence or absence of the relative velocity, it is necessary to consider the loss that results from drawing oil into the gap between the contact surfaces (rolling loss at the contact surface).

The simple calculation method for the gear friction loss uses an equation that averages the unsteady phenomena at the contact surface, and the detailed calculation method uses an equation that takes into account the load on the tooth surface and the sliding speed that varies unsteadily with the phase.
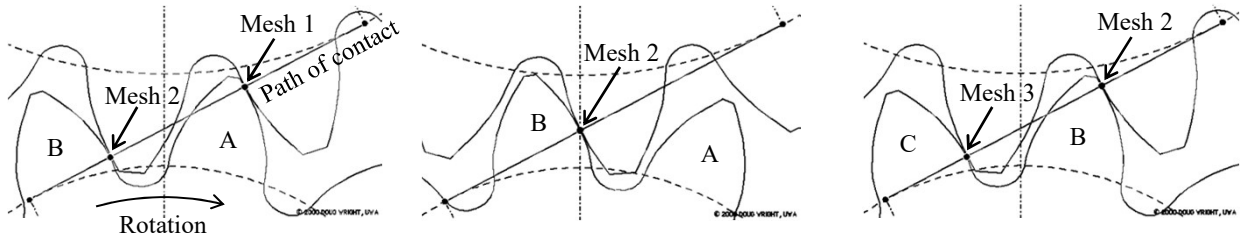
(a) Two meshings with Mesh 1 and Mesh 2   (b) One meshing with Mesh 2   (c) Two meshings with Mesh 2 and Mesh3
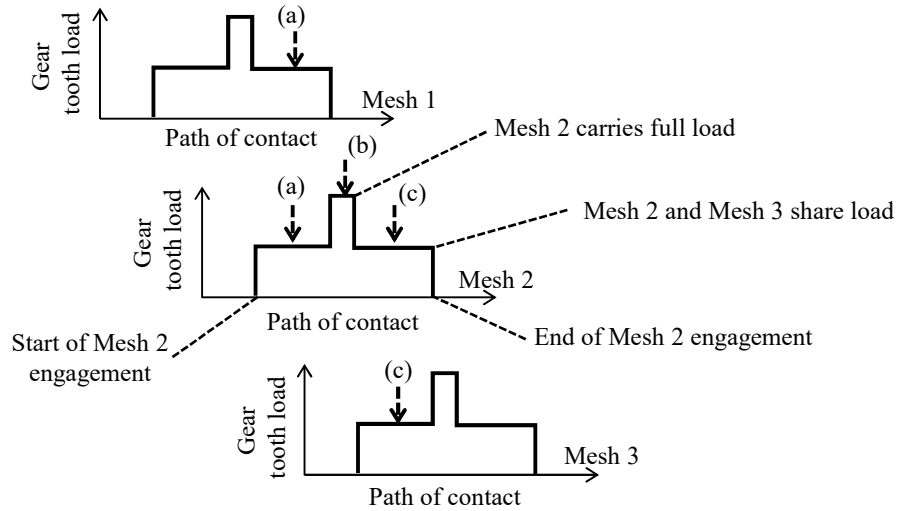
(d) Time history of load on gear teeth

Fig. B.1-1 Concept of tooth load sharing [22] [121]

B.1.2   Simple Calculation Method for Gear Friction Loss

The simplified equation proposed by Höhn et al. [82] for the gear friction loss, P_{mesh}, is given by the following equation.

$$P_{mesh} = P_A \mathfrak{f}_{mesh} H_V = \mathscr{F}_A v_p \mathfrak{f}_{mesh} H_V \tag{B.1}$$

where P_A is the transmitted power ($P_A = \mathscr{F}_A r_p \omega = \mathscr{F}_A v_p$, peripheral speed on the pitch circle $v_p = r_p \omega$, r_p is the radius of the pitch circle, ω is the rotational angular velocity), $\mathfrak{f}_{mesh}$ is the averaged friction coefficient on the tooth surface, and H_V is the loss coefficient calculated from the gear specifications. The value of $\mathfrak{f}_{mesh}$ is

expressed by the following equation.

$$\mathfrak{f}_{mesh} = 0.048 \left(\frac{\mathscr{F}_t/B}{v_{sum}\varrho_c} \right)^{0.2} \mu_{oil}^{-0.05} R_a^{0.25} X_L \tag{B.2}$$

where v_{sum} is the sum of the velocities at the pitch points of the gears (e.g., the sum of velocities of the surfaces of the two meshing gears), $\mathscr{F}_t$ is the force in the direction perpendicular to the tooth surface, B is the tooth width, μ_{oil} is the oil viscosity, and ϱ_c, R_a and X_L are the constants determined by the gear specifications. Equation B.2 is an empirical equation that considers the local oil shear at the contact line of the tooth as well as the local oil drawing. As v_{sum} is proportional to the peripheral speed of the pitch circle, $\mathfrak{f}_{mesh} \propto v_p^{-0.2}$ can be surmised from Eq. B.2. The friction coefficient $\mathfrak{f}_{mesh}$ decreases as the peripheral speed v_p increases because the tooth surface is in the mixed lubrication condition. From Eqs. B.1 and B.2, the relationship between v_p and P_{mesh} is as follows.

$$P_{mesh} \propto v_p \cdot v_p^{-0.2} \propto v_p^{0.8} \tag{B.3}$$

From the above equation, it can be seen that the proportional exponent of the peripheral velocity on the pitch circle with respect to the gear friction loss is 0.8. Considering the temperature dependence of the gear friction loss, from Eqs. B.1 and B.2, $P_{mesh} \propto \mu_{oil}^{-0.05}$ indicates that the oil viscosity μ_{oil} and the gear friction loss change as the temperature changes.

The averaged friction coefficient (Eq. B.2) used in the simplified calculation method in this section is assumed to have large error as, for example, the contact ratio (the time-averaged value of the number of meshing teeth shown in Fig. B.1-1) is neglected. Therefore, in the next section, we introduce a method that considers the local phenomena on the gear contact surface.

B.1.3   Detailed Calculation Method for Gear Friction Loss

In this study, the method proposed by Anderson et al. [22] is used to perform the calculations. An outline of this method is shown below.

(1)   Calculation of Sliding Loss at Gear Contact Surface

The following equation details the instantaneous frictional force $\mathscr{F}_S$ caused by the slippage between the two gear tooth surfaces that come into contact with each other.

$$\mathscr{F}_S(X) = \mathfrak{f}_c(X)w_c(X) \tag{B.4}$$

where X represents the coordinates on the line of action, $\mathfrak{f}_c$ is the instantaneous friction coefficient, and w_c is the load that acts perpendicular to the tooth surface. The Benedict and Kelley method [122] is used to calculate the instantaneous friction coefficient $\mathfrak{f}_c$ according to the following equation.

$$\mathfrak{f}_c(X) = 0.0127 \log \frac{29.66 w_c(X)/B}{\mu_{oil}V_S(X)\left\{V_T(X)\right\}^2} \tag{B.5}$$

where B is the tooth width, μ_{oil} is the oil viscosity, V_S is the sliding speed between the tooth surfaces (= difference in speed between the two tooth surfaces = $V_1 - V_2$, V_1 and V_2 are the speeds of each gear), and V_T is the rolling speed between the tooth surfaces (= total speed of two tooth surfaces = $V_1 + V_2$). By calculating $w_c(X)$, $V_S(X)$, and $V_T(X)$ on the line of action, the instantaneous friction coefficient $\mathfrak{f}_c(X)$ can be calculated using Eq. B.5. The minimum value of the friction coefficient (the boundary value between

mixed lubrication and hydrodynamic lubrication in the Stribeck Curve (Fig. 1.1-20)) was set to 0.01 from the experiment by Matsumoto et al. [46].

The instantaneous friction force $\mathscr{F}_S(X)$ can be calculated from Eq. B.4 using the instantaneous friction coefficient $\mathfrak{f}_c$ and the load w_c.

The instantaneous sliding loss P_S at the gear contact surface is calculated using the following equation.

$$P_S(X) = V_S(X)\mathscr{F}_S(X) \tag{B.6}$$

The above is the loss per contact surface. The sliding loss of the entire gear mesh needs to be the sum of the sliding losses at each contact surface.

(2) Calculation of Rolling Loss at Gear Contact Surface

The Crook method [123] is used to calculate the instantaneous traction force $\mathscr{F}_R$ due to rolling on the gear contact surface, and this is shown in the following equation.

$$\mathscr{F}_R(X) = 9.0 \times 10^7 h_c(X)\varphi_t(X)B \tag{B.7}$$

where h_c is the central oil film thickness for a uniform temperature, and φ_t is the thermal reduction coefficient.

Hamrock and Dowson's oil film thickness at the contact surface of the gear [124] is applied to h_c.

$$h_c = 2.69 \, U_c^{0.67} G_c^{0.53} W_c^{-0.067} \left(1 - 0.61e^{-0.73k}\right) R_X \tag{B.8}$$

U_c is the dimensionless velocity parameter, G_c is the dimensionless material coefficient, W_c is the dimensionless load coefficient, k is the ellipticity parameter (= semi-major axis / semi-minor axis of the contact ellipse), and R_X is the equivalent rolling radius. U_c, G_c, and W_c are calculated by the following equation.

$$U_c = \frac{\frac{V_1+V_2}{2}\mu_{oil}}{\mathscr{E}'R_X} \tag{B.9}$$

$$G_c = \mathscr{E}'\mathscr{A} \tag{B.10}$$

$$W_c = \frac{\mathscr{F}_t}{\mathscr{E}'R_X{}^2} \tag{B.11}$$

where $\mathscr{E}'$ is the equivalent stiffness coefficient expressed by the following equation, $\mathscr{A}$ is the pressure viscosity coefficient of oil, and $\mathscr{F}_t$ is the vertical load on the tooth surface.

$$\mathscr{E}' = \frac{2}{(1-\gamma_1{}^2)/\mathscr{E}_1 + (1-\gamma_2{}^2)/\mathscr{E}_2} \tag{B.12}$$

where γ_1 and γ_2 are the Poisson's ratios of each gear, and $\mathscr{E}_1$ and $\mathscr{E}_2$ are the Young's modulus of each gear. Cheng's diagram [125] is used to evaluate the thermal reduction factor φ_t. The coefficients used in the diagram are the functions of oil viscosity μ_{oil}, average velocity of contact surface $(V_1 + V_2)/2$, temperature viscosity coefficient of oil, and thermal conductivity of oil.

The instantaneous rolling loss P_R at the gear contact surface is calculated by the following equation.

$$P_R(X) = V_T(X)\mathscr{F}_R(X) \tag{B.13}$$

This equation represents the loss per contact surface. The rolling loss for the meshing of the entire gear must be summed up by the rolling loss at each contact surface.

311

(3)   Sample Calculation for Gear Friction Loss

An example of the calculation by Anderson et al. [22] based on the above method is shown. The calculation conditions are shown in Table B.1-1 . The change in the number of meshed teeth is the same as in Fig. B.1-1 (d) (according to gear rotation, two tooth contacts → one tooth contact → two tooth contacts). The results of the calculation are shown in Fig. B.1-2 .

The changes in sliding speed on the line of action are shown in Fig. B.1-2 (a). The sliding speed becomes maximum at the tooth tip and root, and reduces to zero on the pitch circle.

The changes in the rolling speed on the line of action are shown in Fig. B.1-2 (b). The rolling speed reaches the maximum value on the pitch circle and decreases slightly at the tooth tip and root.

The change in the friction coefficient along the line of action is shown in Fig. B.1-2 (c). The friction coefficient reaches its maximum value on the pitch circle. This is mainly because the friction coefficient increases (Eq. B.5) due to a decrease in the sliding speed (Fig. B.1-2 (a)).

The change in sliding loss on the line of action at the gear contact surface is shown in Fig. B.1-2 (d). The sliding loss reduces to zero on the pitch circle because the sliding speed becomes zero at this position. In addition, the loss decreases around the pitch circle because the contact area is reduced as only one gear is in mesh.

The change in rolling loss on the line of action at the gear contact surface is shown in Fig. B.1-2 (e). As in the case of the sliding loss, the rolling loss decreases around the pitch circle because the contact area is reduced by having only one gear meshing.

(4)   Validation of Calculation Program for Gear Friction Loss

The detailed method introduced in this section is used to calculate the gear friction loss.

To validate the program created using this method, the calculation was performed using the conditions specified in Anderson et al. (Table B.1-1). The obtained results agreed with Anderson et al. (Fig. B.1-2), and the validity of the calculation program was confirmed.

Table B.1-1 Gear geometry and operating parameters [22]

Pitch diameter	Pinion	152 mm
	Gear	254 mm
Number of teeth	Pinion	48
	Gear	80
Diametral pitch		8 inch^{-1}
Pressure angle		20°
Width		40 mm
Lubricant	Mineral oil with antioxidant additive	
Viscosity at oil jet temperature of 333 K		60 mm^2/s
Pinion speed		2000 rpm
Pinion torque		271 Nm

(a) Sliding velocity (b) Rolling velocity (c) Coefficient of friction

(d) Sliding power loss (e) Rolling power loss
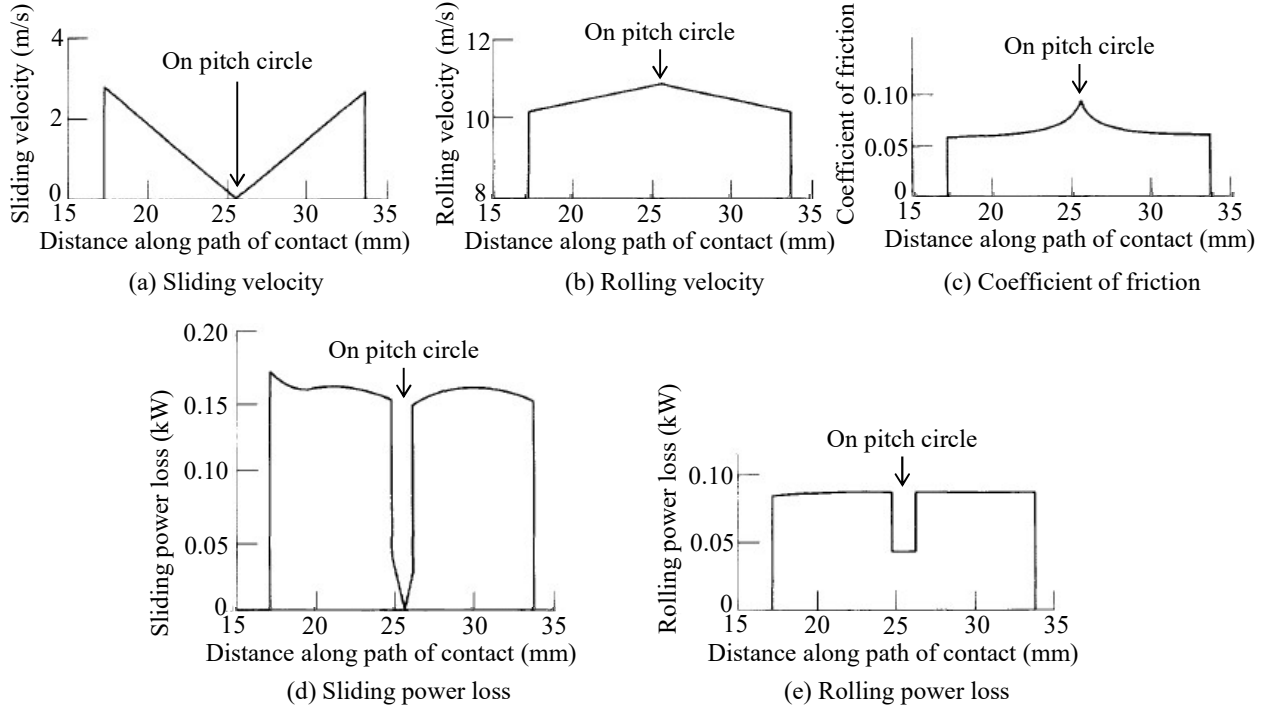
Fig. B.1-2 Instantaneous values of sliding velocity, rolling velocity, coefficient of friction, sliding power loss, and rolling power loss on the path of contact (calculation results) [22]

B.2 Power Loss in Bearings

(1) Power Loss in Rolling Bearings

The simplified equation of Palmgren [83] regarding the power loss P_{BR} of the rolling bearings is shown in the following equation.

$$P_{BR} = T_{BR}\omega = \left\{ f_0(\nu_{oil}\ N)^{2/3}d_{pb}{}^3 \times 10^{-7} + f_1\mathscr{F}_b d_{pb} \right\} \omega \tag{B.14}$$

In the above, T_{BR} is the friction torque, f_0 is a coefficient related to the bearing, f_1 is a coefficient related to the lubrication method, ν_{oil} is the kinematic viscosity of the oil, d_{pb} is the pitch circle diameter of the bearing, and $\mathscr{F}_b$ is the load.

From Eq. B.14, it can be seen that the power loss P_{BR} is proportional to the 5/3 power of the rotation speed N, as shown in the following equation ($\omega = 2\pi N$).

$$P_{BR} \propto N^{2/3} \cdot N \propto N^{5/3} \tag{B.15}$$

Regarding the temperature dependence of the power loss of the rolling bearings, from $P_{BR} \propto \nu_{oil}{}^{2/3}$ in Eq. B.14, it can be seen that the kinematic viscosity of the oil and power loss of the rolling bearings change when the temperature changes.

(2) Power Loss in Journal Bearings

The power loss P_{BJ} of a journal bearing and load capacity W_j of the bearing can be obtained by solving

the Reynolds equation using the short-width assumption and the half-Sommerfeld condition (e.g., [131]).

$$P_{BJ} = \frac{\mu_{oil} B r_j v_j{}^2}{C_j} \frac{2\pi}{(1-\varepsilon^2)^{1/2}} \tag{B.16}$$

$$W_j = \frac{\mu_{oil} v_j B^3}{4 C_j{}^2} \frac{\varepsilon}{(1-\varepsilon^2)^2} \left\{ \pi^2 (1-\varepsilon^2) + 16\varepsilon^2 \right\}^{1/2} \tag{B.17}$$

Here, B is the bearing width, r_j is the bearing radius, v_j is the surface speed of the bearing (proportional to the rotational speed), C_j is the radial clearance of the bearing, and ε is the eccentricity ratio ($\varepsilon = \mathcal{E}/C_j$, where $\mathcal{E}$ is the eccentricity). Equation B.17 becomes the following equation when the order is evaluated with $1 - \varepsilon = \mathcal{X}$.

$$W_j = \frac{\mu_{oil} v_j B^3}{4 C_j{}^2} \frac{\sqrt{1-\mathcal{X}}}{\mathcal{X}^2} \left\{ 16 - (16 - \pi^2)\mathcal{X} \right\}^{1/2} \propto v_j \frac{-\mathcal{X}^{0.5}}{\mathcal{X}^2} \left(-\mathcal{X}^{0.5} \right) = v_j/\mathcal{X} \tag{B.18}$$

Here, if the load capacity W_j is constant, then $\mathcal{X} \propto v_j$. Using this result, the order evaluation of Eq. B.16 yields as follows.

$$P_{BJ} \propto v_j{}^2 \mathcal{X}^{-0.5} \propto v_j{}^2 v_j^{-0.5} \propto v_j^{1.5} \tag{B.19}$$

From the above, it can be seen that the power loss P_{BJ} of the journal bearing is proportional to the 1.5th power of the surface speed v_j of the bearing (proportional to the 1.5th power of the rotation speed). Regarding the temperature dependence of the power loss of the journal bearing, from $P_{BJ} \propto \nu_{oil}$ in Eq. B.16, it can be seen that the kinematic viscosity of the oil and power loss of the journal bearing change when the temperature changes.

B.3   Power Loss in Seals

In general, the materials and shapes of seals are designed so that the friction coefficient does not increase significantly as the rotational speed increases. An example of a mechanical seal is shown in Fig. B.3-1 . A seal ring is attached to the rotary shaft, and a mating ring is attached to the housing. By pressing the seal ring against the mating ring with a spring, the sealing performance is achieved. A power loss is generated by friction between the rings. Examples of power losses are shown in Fig. B.3-2 [132]. The power loss equation for this seal is as follows.

$$P_{seal} = (\Delta p_{seal} \cdot k_{seal} + p_{spring}) v_{slide} A_{slide} \mathfrak{f}_{seal} \tag{B.20}$$

Here, Δp_{seal} is the pressure difference of the seal, k_{seal} is the balance distribution coefficient, p_{spring} is the pressure generated by the spring, v_{slide} is the sliding speed of the contact surface (proportional to the rotational speed), A_{slide} is the area of the contact surface, and $\mathfrak{f}_{seal}$ is the friction coefficient. In Fig. B.3-2 , k_{seal} and p_{spring} are kept constant. Figure B.3-2 shows that the power loss increases in proportion to the increase in the rotational speed, and that the power loss increases as the shaft diameter increases and/or pressure difference increases. In this example, the power loss of the seal is proportional to the rotational speed.

With regard to the temperature dependence of the power loss of the seal, Eq. B.20 shows that the temperature dependence of the power loss is small. However, if thermal deformation occurs owing to the temperature change of the gear shaft and housing and the extension of the spring changes, the power loss of the seal may change owing to the change in the spring load.
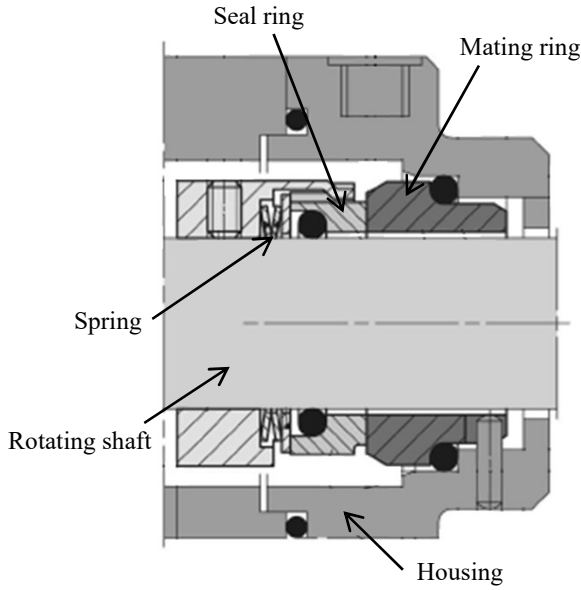
Fig. B.3-1 Example of a mechanical seal [132]
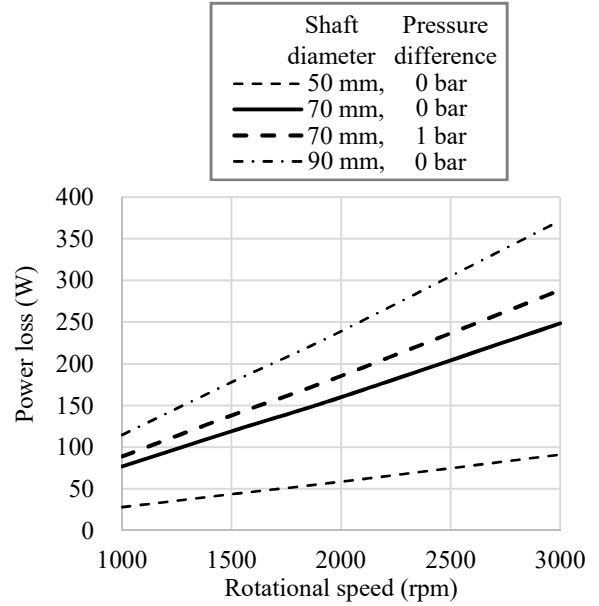
Fig. B.3-2 Examples of power losses in the mechanical seal (calculation results) [132]

B.4 Power Loss in Oil Pump

The calculation method for the power loss of an external gear pump (commonly used as an oil pump for aircraft engines) is shown below.

A schematic diagram of an external gear pump is shown in Fig. B.4-1 [133]. Oil sucked from the pump inlet is discharged from the pump outlet through the outside of a pair of meshing gears.

Manring et al. [134] divided the efficiency η_{gp} of an external gear pump into a torque efficiency $\eta_{gp,T}$ and volumetric efficiency $\eta_{gp,V}$, and made them a function of the oil viscosity $\mu_{oil} \times$ rotational angular velocity $\omega/$ differential pressure Δp_{gp} at the inlet and outlet of the pump.

The efficiency η_{gp} of the pump is shown by the following equation.

$$\eta_{gp} = \frac{\Delta p_{gp} Q_{gp}}{T_{gp} \omega} \tag{B.21}$$

Here, Q_{gp} is the discharged volume flow rate, and T_{gp} is the torque.

As mentioned above, the pump efficiency η_{gp} can be divided into the torque efficiency $\eta_{gp,T}$ and volumetric efficiency $\eta_{gp,V}$.

$$\eta_{gp} = \eta_{gp,T} \ \eta_{gp,V} \tag{B.22}$$

The torque efficiency $\eta_{gp,T}$ is expressed as follows:

$$\eta_{gp,T} = \frac{V_{gp} \Delta p_{gp}}{T_{gp}} \tag{B.23}$$

Here, V_{gp} is the unit theoretical discharge flow rate per radian, and the discharge flow rate per revolution is $2\pi V_{gp}$.

The volumetric efficiency $\eta_{gp,V}$ is expressed as follows:

$$\eta_{gp,V} = \frac{Q_{gp}}{V_{gp}\omega} \tag{B.24}$$

$V_{gp}\omega$ in the denominator is the theoretical discharged flow rate.

The volumetric efficiency $\eta_{gp,V}$ and torque efficiency $\eta_{gp,T}$ are modeled as follows.

$$\eta_{gp,V} = 1 - C_{V1}\frac{\Delta p_{gp}}{\mu_{oil}\omega} - C_{V2}\sqrt{\frac{\Delta p_{gp}}{\mu_{oil}\omega}} \tag{B.25}$$

$$\eta_{gp,T} = 1 - C_{T1} - C_{T2}\frac{\mu_{oil}\omega}{\Delta p_{gp}} - C_{T3}\sqrt{\frac{\mu_{oil}\omega}{\Delta p_{gp}}} \tag{B.26}$$

In the above, C_{V1} is a coefficient related to the influences of the fluid compressibility and leakage at a low Reynolds number, C_{V2} is a coefficient related to the leakage at high Reynolds number, C_{T1} is a coefficient related to torque loss at start-up, C_{T2} is a coefficient for the Coulomb friction torque loss (proportional to the load applied to the inside of the pump), and C_{T3} is a coefficient for the fluid dynamic torque loss caused by the fluid friction.
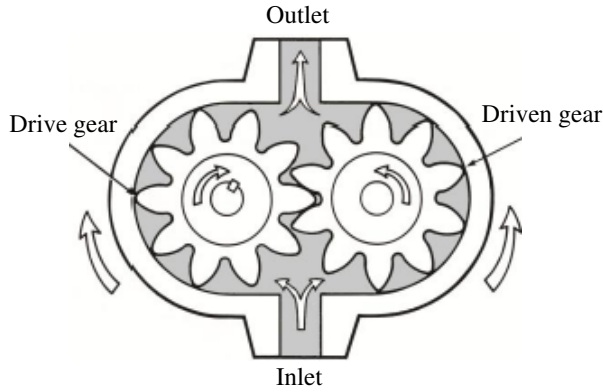
Fig. B.4-1 Schematic of an external gear pump [133]
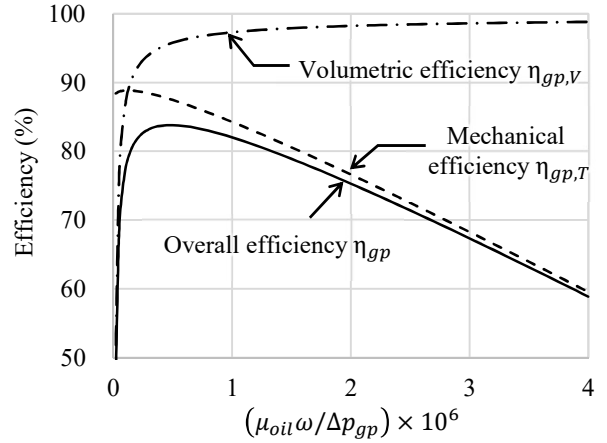
Fig. B.4-2 Volumetric, mechanical, and overall efficiency curves (representative) of external gear pumps for displacement of 31.8 to 56.5 cc, speed of 600 to 3000 rpm, and differential pressure of 1.38 to 27.6 MPa (approximation curve of experimental results) [133]

Michael et al. [133] obtained empirical equations for the volumetric efficiency $\eta_{gp,V}$ and torque efficiency $\eta_{gp,T}$ from experimental results concerning actual gear pumps (discharge flow rate was 31.8–56.5 cc, rotational speed was 600–3000 rpm, differential pressure between inlet and outlet was 1.38–27.6 MPa), as shown below.

$$\eta_{gp,V} = 1 - 6.8 \times 10^{-9}\frac{\Delta p_{gp}}{\mu_{oil}\omega} - 2.0 \times 10^{-5}\sqrt{\frac{\Delta p_{gp}}{\mu_{oil}\omega}} \tag{B.27}$$

$$\eta_{gp,T} = 1 - 0.124 - 1.07 \times 10^5\frac{\mu_{oil}\omega}{\Delta p_{gp}} - 73.78\sqrt{\frac{\mu_{oil}\omega}{\Delta p_{gp}}} \tag{B.28}$$

The curves from drawing the results of these empirical equations are shown in Fig. B.4-2 .

The oil supply pumps for aeroengine gearboxes have high rotational speeds, for miniaturization. In addition, the rotation speed of the pump varies with changes in the engine speed. For example, if the kinematic viscosity of the oil is 26 mm^2/s, density is 981 kg/m^3, rotation speed is 300 to 3000 rpm, and pump discharge pressure is 2 MPa (set to a constant for simplification), then $\mu_{oil}\omega/\Delta p_{gp} = 0.4 \times 10^{-6} \sim 4.0 \times 10^{-6}$. The volumetric efficiency in this range is approximately constant, as shown in Fig. B.4-2 . Therefore, the volumetric flow rate discharged by the pump is approximately proportional to the rotational speed. The power consumed by the pump under these conditions is calculated from Eqs. B.21 to B.28 as 0.1 kW (2 L/min, 2 MPa) to 1.1 kW (20 L/min, 2 MPa).

Using the pump power as P_{gp}, the rotational speed exponent can be calculated. Using Eq. B.21, the pump flow rate $Q_{gp} = \eta_{gp,V}V_{gp}\omega$ (Eq. B.24), and the pump discharge pressure $\Delta p_{gp} \propto Q_{gp}^2$ (general piping pressure loss).

$$P_{gp} = T_{gp}\omega = \frac{\Delta p_{gp}Q_{gp}}{\eta_{gp}} \propto \frac{Q_{gp}^3}{\eta_{gp}} = \frac{(\eta_{gp,V}V_{gp}\omega)^3}{\eta_{gp}} \propto \frac{(\eta_{gp,V})^3}{\eta_{gp}}\omega^3 \qquad (B.29)$$

Figure B.4-3 shows the results from calculating the coefficients $(\eta_{gp,V})^3/\eta_{gp}$ from Fig. B.4-2 (Eqs. B.22, B.25, and B.26). In addition, it shows that the coefficient $(\eta_{gp,V})^3/\eta_{gp}$ is approximately on the order of 1. Therefore, from Eq. B.29, the power for driving the pump is roughly proportional to the cube of the rotational speed.
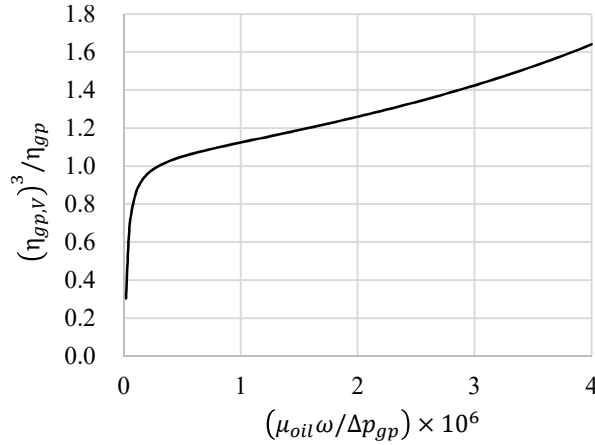
Fig. B.4-3 Variation of the coefficient $(\eta_{gp,V})^3/\eta_{gp}$ in the power loss equation (estimation)

B.5   Rotational Speed Exponent Characteristics of Gearbox Power Loss

The features of the power loss by each loss element (gear contact surfaces, air and oil flows, bearings, seals, oil pump) in the gearbox are summarized by focusing on the rotational speed (peripheral speed) exponents. Figure B.5-1 shows the rotational speed exponent of the power loss for the loss element.

1. As a simple calculation method for the power loss at the gear contact surface, Section B.1.2 describes a method based on using the average friction coefficient on the tooth surface. In this calculation, the power loss at the gear contact surface is proportional to the 0.8th power of the rotational speed (peripheral speed).

2. For the loss owing to the flow of air and oil in the gearbox (fluid dynamic loss), the aerodynamic loss is proportional to the cube of the rotational speed, and the oil dynamic loss is proportional to the 2–3th power of the rotational speed.

3. The power loss in the rolling bearings is proportional to the 5/3th power of the rotational speed according

to the empirical equation, and the power loss in the journal bearings is proportional to the 1.5th power of the rotational speed according to the theoretical equation.

4. Regarding the power loss in the seal, in the example of the mechanical seal (Section B.3), the power loss is proportional to the rotational speed.

5. In the example of power loss of an oil supply pump (an external gear pump) (Section B.4), the power loss is approximately proportional to the third power of the rotational speed.
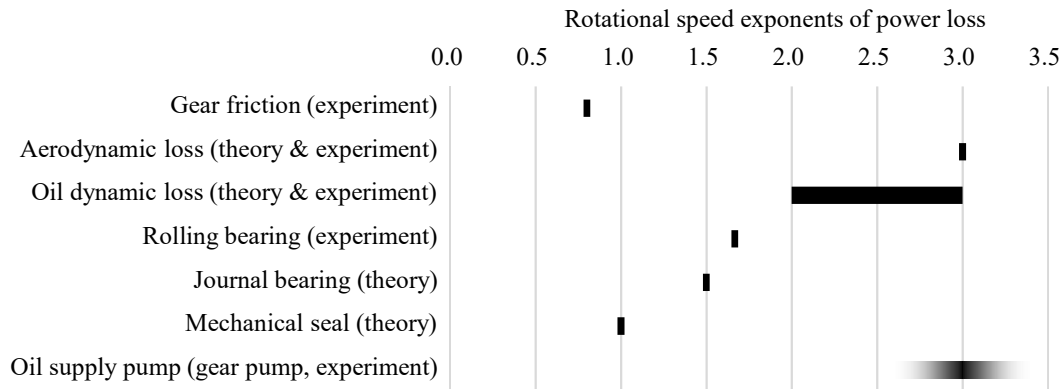
Fig. B.5-1 Rotational speed exponents of power loss on each loss component in a gearbox

Appendix C

Additional Validation of the Fluid Dynamic Loss Model

C.1 Validation of Fluid Dynamic Loss Model for Gear Aspect Ratio

Figure C.3-1 shows a comparison of the calculation results of the loss model with the numerical simulation results to ensure the reliability of the influence of the gear aspect ratio on the fluid dynamic loss (Section 7.4.2). Figure C.3-1 (a) shows the fluid dynamic loss, (b0) shows the aerodynamic loss, (b1)–(b3) show elements of the aerodynamic loss, (c0) shows the oil dynamic loss, and (c1)–(c3) show elements of the oil dynamic loss.

From Fig. C.3-1 , it is found that the trend of the loss model results and the trend of the numerical simulation results agree. Because the numerical simulation method is considered to have a certain reliability due to agreeing well with the experimental results, the loss model detailed in Section 7.4.2 is considered to be valid.

C.2 Validation of Fluid Dynamic Loss Model for Shroud Opening Angle

Figure C.3-2 shows a comparison of the calculation results of the loss model with the numerical simulation results to ensure the reliability of the influence of the shroud opening angle on the fluid dynamic loss (Section 7.4.3). The method of comparison is the same as in Fig. C.3-1 .

Because Fig. C.3-2 shows that the trend of the loss model results agrees with the trend of the numerical simulation results, the loss model explained in Section 7.4.3 is considered valid.

C.3 Validation of Fluid Dynamic Loss Model for a Spur Gear Pair

The loss model is validated for the fluid dynamic loss of a spur gear pair. In this paper, the experimental result of Delgado et al. [63] was used as validation data. Table C.3-1 shows the gear specifications, operation conditions, and shroud conditions. The gearbox is shown in Fig. C.3-3 .

A comparison of the calculation results of the loss model results with the experimental results is shown in Fig. C.3-4 . Figure C.3-4 shows that the loss model results and the experimental results correspond roughly. Possible reason for the differences between the loss model results and the experimental results are the error of the influence coefficient Z_β (Eq. 6.18) of the helix angle coefficient.

(a) Fluid dynamic loss

(b0) Aerodynamic loss

(c0) Oil dynamic loss

(b1) Air side-flow loss

(b2) Air pumping loss

(b3) Air vortex loss

(c1) Oil-jet acceleration loss

(c2) Oil reacceleration loss

(c3) Oil churning loss
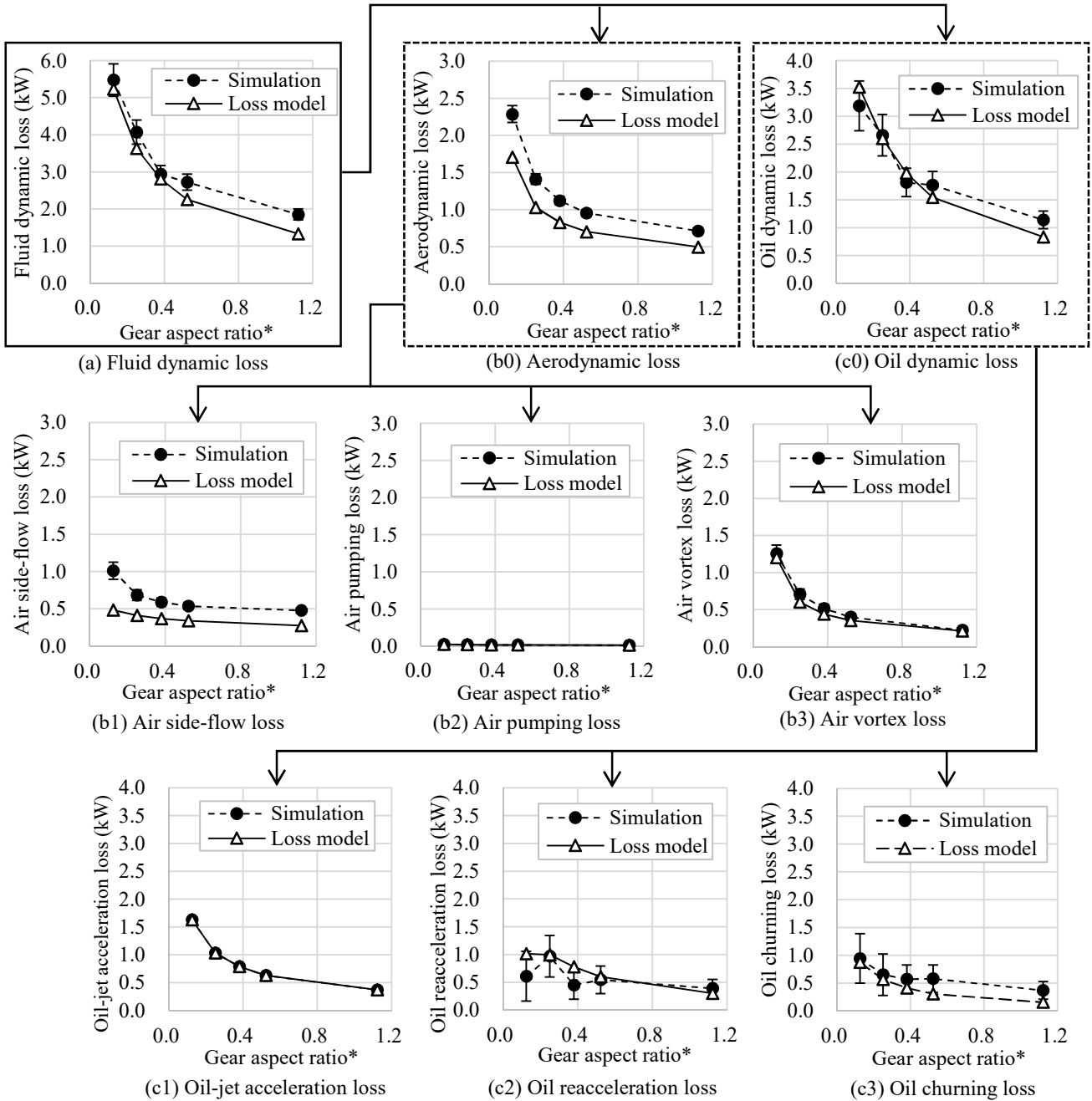
* Averaged value of input gear and output gear

Fig. C.3-1 Validation of changes in fluid dynamic loss according to gear aspect ratio changes
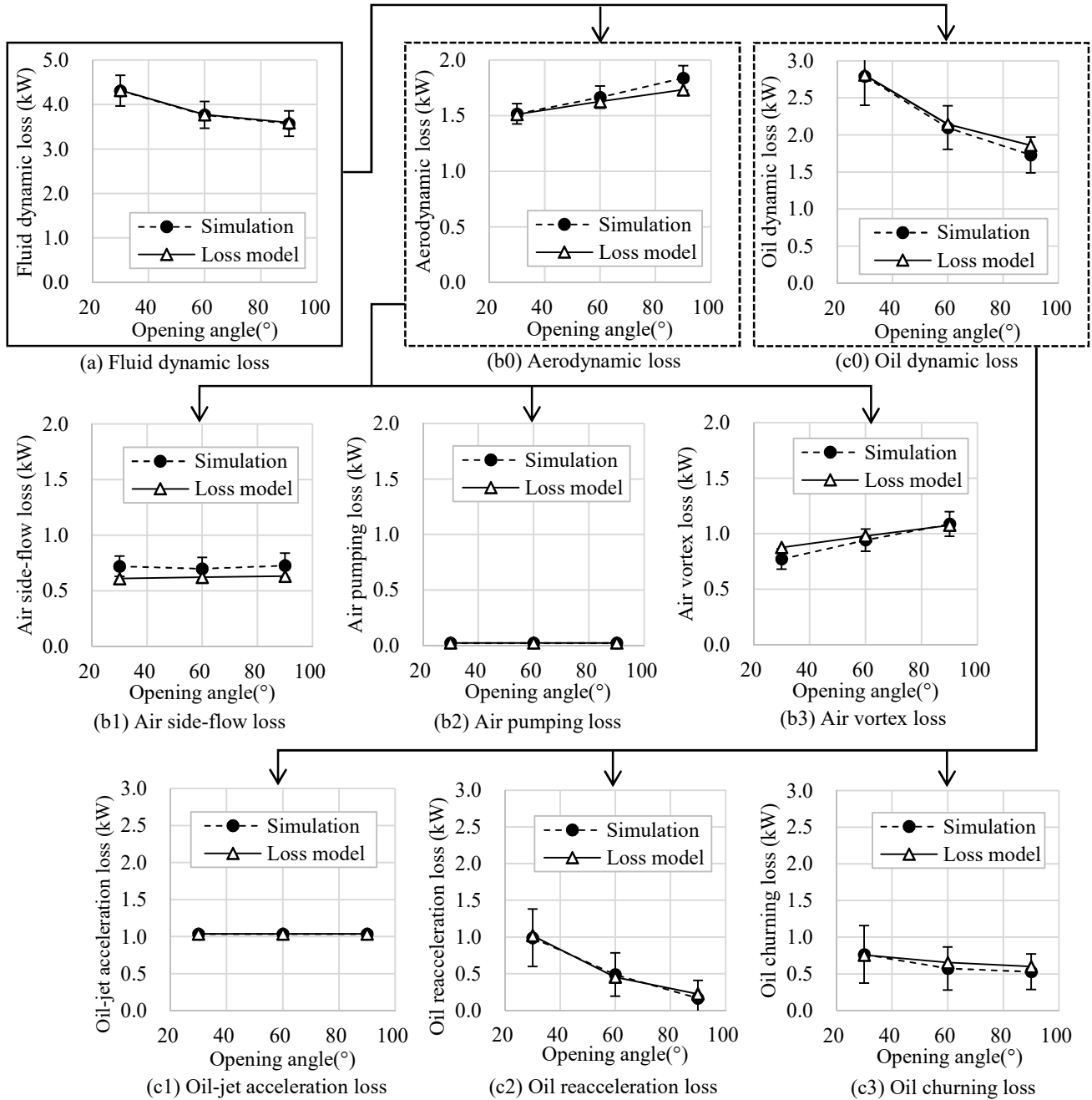
Fig. C.3-2 Validation of changes in fluid dynamic loss according to shroud opening angle changes

Table C.3-1 Calculation conditions for validating the fluid dynamic loss of a spur gear pair

(a) Gear specifications

Parameter	Drive-side	Driven-side
Number of teeth	44	52
Module (mm)	6.35	
Face width (mm)	28.4	
Pitch diameter (mm)	279.4	330.2
Pressure angle (°)	25	
Outside diameter (mm)	291.85	342.65

(b) Operation conditions

Parameter	Value
Lubricant	Royco 555
Temperature (°C)	39.4
Oil supply flow rate (L/min)	3.2

(c) Shroud conditions

Shroud	Parameter	Drive-side	Driven-side
U	Radial clearance (mm)	63.5	25.4
	Axial clearance (mm)	57.2	
C36	Radial clearance (mm)	16.8	
	Axial clearance (mm)	29.7	
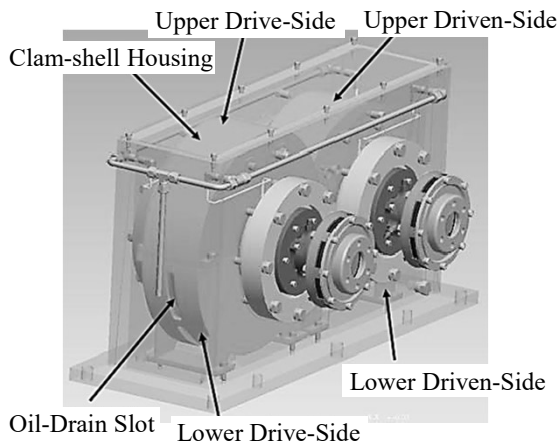
Fig. C.3-3 Spur gearbox [63]
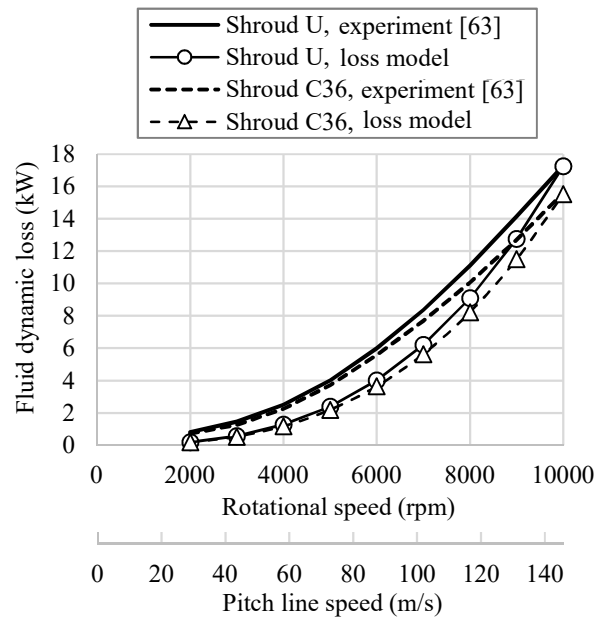
Fig. C.3-4 Validation of changes in the fluid dynamic loss of a spur gear pair

322

Appendix D

Fraction and Trend of Elements of Fluid Dynamic Loss

To understand the fraction and trends of the elements of fluid dynamic loss, the rotational speed characteristics and the oil supply flow-rate characteristics of the elements were investigated using the two-axis helical gearbox (GA) in this research.

D.1   Rotational Speed Characteristics of Elements of Fluid Dynamic Loss

The rotational speed characteristics of the elements of the fluid dynamic loss are shown in Fig. D.1-1 . Figure D.1-1 (a1)–(a6) shows the results of Shroud 1 and the oil supply flow rate of 7.40 L/min, (a1) shows the rotational speed change of the aerodynamic and oil dynamic losses, (a2) shows the rotational speed change of the elements of aerodynamic loss, (a3) shows the rotational speed change of the elements of oil dynamic loss, (a4) shows the rotational speed change of loss in the gear meshing part and loss in the gear peripheral part, (a5) shows the fraction of the losses at a rotational speed of 7000 rpm of the input gear, and (a6) shows the fraction of the losses at 10000 rpm of the input gear. Figure D.1-1 (b1)–(b6) shows the results of Shroud 2 and an oil flow rate of 7.40 L/min are similar to the results of Shroud 1.

Based on the results of Shroud 1, as shown in Fig. D.1-1 (a1)–(a4), each element of the loss increases as the rotational speed increases. Figure D.1-1 (a5) shows that the fraction of air side-flow loss (21%) and that of air vortex loss (23%) are equivalent (air pumping loss is sufficiently small) for the elements of aerodynamic loss, and that the fraction of oil-jet acceleration loss (31%) is dominant for the elements of oil dynamic loss. From a comparison of (a5) and (a6) in Fig. D.1-1 , the fraction of aerodynamic loss increases as the rotational speed increases (44% (air side-flow loss 21% + air vortex loss 23%) → 50% (23% + 27%)), and the fraction of loss around the gear periphery increases (37% (air vortex loss 23% + oil churning loss 14%) → 42% (27% + 15%)).

Based on the results of Shroud 2, as shown in Fig. D.1-1 (b1)–(b4), each element of the loss increases as the rotational speed increases. Figure D.1-1 (b5) shows that the fraction of air side-flow loss (14%) and the fraction of air vortex loss (17%) are equivalent (air pumping loss is sufficiently small) for the elements of aerodynamic loss, and that the fraction of oil-jet acceleration loss (28%) is dominant for the elements of oil dynamic loss. From a comparison of (b5) and (b6) in Fig. D.1-1 , the fraction of aerodynamic loss increases as the rotational speed increases (31% (air side-flow loss 14% + air vortex loss 17%) → 36% (15% + 21%), and the fraction of the loss around the gear periphery increases (34% (air vortex loss 17% + oil churning loss 17%) → 40% (21% + 19%).

Comparing Fig. D.1-1 (a5) of the loss fraction results at a rotational speed of 7000 rpm in Shroud 1, with the

323

loss fraction results in Shroud 2 as shown in Fig. D.1-1 (b5), shows a significant increase in oil reacceleration loss (11% → 23%) and an increase in oil churning loss (14% → 18%). These trends are similar to those of the loss fraction at 10000 rpm (Fig. D.1-1 (a6) and (b6)).

D.2   Oil Supply Flow Rate Characteristics of Elements of Fluid Dynamic Loss

The oil supply flow rate characteristics of the elements of the fluid dynamic loss are shown in Fig. D.2-1 . Figure D.2-1 (a1)–(a6) shows the results of Shroud 1 and the rotational speed of 10000 rpm of the input gear, (a1) shows the oil supply flow rate change of aerodynamic and oil dynamic losses, (a2) shows the oil supply flow rate change of the elements of aerodynamic loss, (a3) shows the oil supply flow rate change of the elements of oil dynamic loss, (a4) shows the oil supply flow rate change of loss in the gear meshing part and loss in the gear peripheral part, (a5) shows the fraction of the losses at an oil supply flow rate of 1.48 L/min, and (a6) shows the fraction of the losses at an oil supply flow rate of 7.40 L/min. Figure D.2-1 (b1)–(b6) shows the results of Shroud 2 and the rotational speed of 10000 rpm of the input gear, in the same way as the results of Shroud 1.

Based on the results of Shroud 1, as shown in Fig. D.2-1 (a1)–(a3), only the elements of the oil dynamic loss increased with an increase in the oil supply flow rate. Figure D.2-1 (a4), which is the diagram of oil supply flow rate change of the loss in gear meshing part and the loss in the gear peripheral part, shows that the loss in the gear meshing part increases significantly. In Fig. D.2-1 (a5) of the result at an oil supply flow rate of 1.48 L/min, the fraction of aerodynamic loss was large (79% (air side-flow loss 36% + air vortex loss 43%)). However, as illustrated in Fig. D.2-1 (a6) of the result at the oil supply flow rate of 7.40 L/min, the fraction of oil dynamic loss increases (50% (oil-jet acceleration loss 26% + oil reacceleration loss 9% + oil churning loss 15%)).

Based on the results of Shroud 2, as shown in Fig. D.2-1 (b1)–(b3), only the elements of the oil dynamic loss increased with an increase in the oil supply flow rate. Figure D.2-1 (b4), which is the diagram of oil supply flow rate change of the loss in gear meshing part and the loss in the gear peripheral part, shows that the loss in the gear meshing part increases significantly. In Fig. D.2-1 (b5) of the result at an oil supply flow rate of 1.48 L/min, the fraction of aerodynamic loss was large (67% (air side-flow loss 29% + air vortex loss 38%)). However, as illustrated in Fig. D.2-1 (b6) of the result at the oil supply flow rate of 7.40 L/min, the fraction of oil dynamic loss increases (64% (oil-jet acceleration loss 25% + oil reacceleration loss 20% + oil churning loss 19%)).

Comparing Fig. D.2-1 (a5) of the loss fraction results at an oil supply flow rate of 1.48 L/min in Shroud 1, with Fig. D.2-1 (b5) Shroud 2 shows an increase in the oil reacceleration loss (0% → 6%) and oil churning loss (13% → 18%). These trends were similar when comparing the loss fraction at an oil supply flow rate of 7.40 L/min (Fig. D.2-1 (a6) and (b6)).
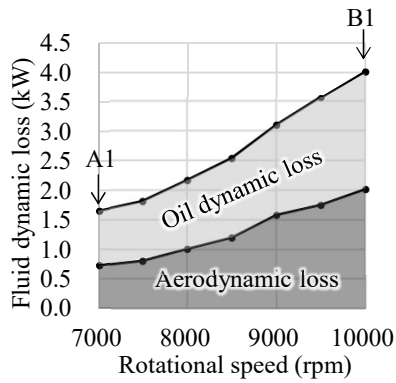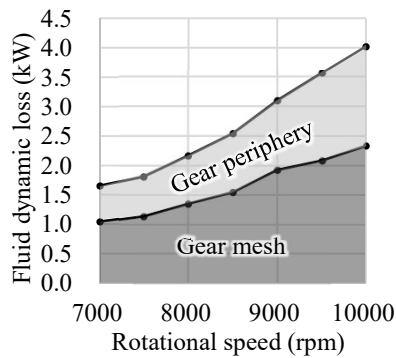
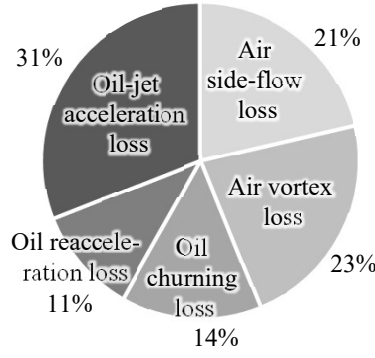(a1) Breakdown of fluid dynamic loss,
Shroud 1
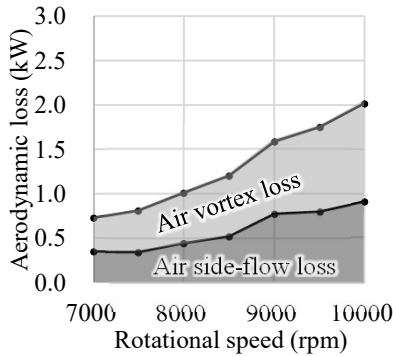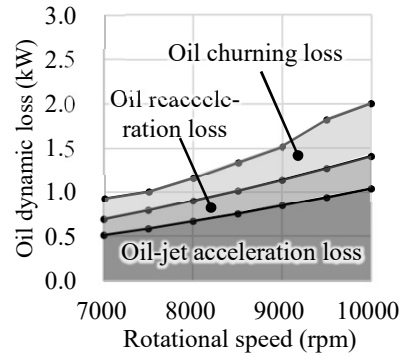
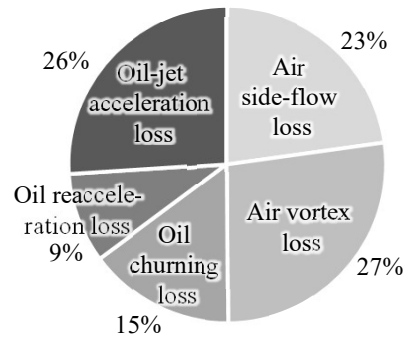(a2) Breakdown of aerodynamic loss,
Shroud 1

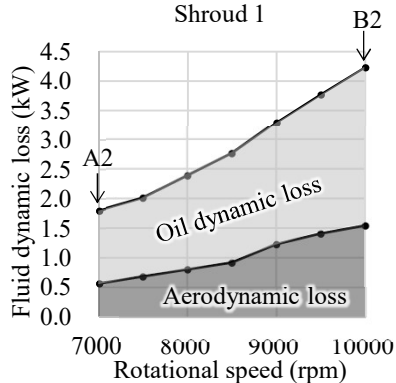(a3) Breakdown of oil dynamic loss,
Shroud 1

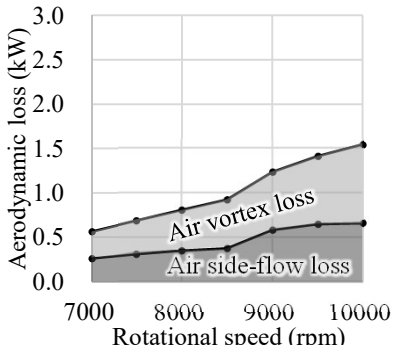(a4) Breakdown for loss location,
Shroud 1

(a5) Fraction of loss elements,
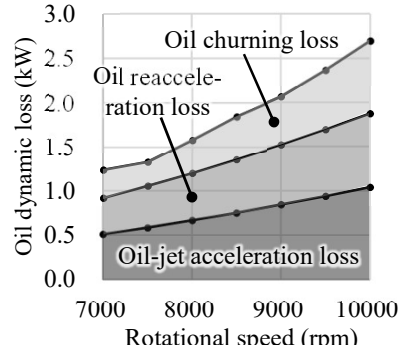Shroud 1, 7000 rpm ("A1" in (a1))

(a6) Fraction of loss elements,
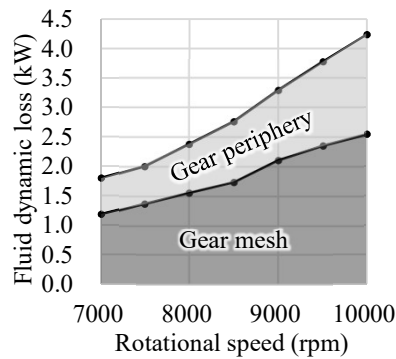Shroud 1, 10000 rpm ("B1" in (a1))

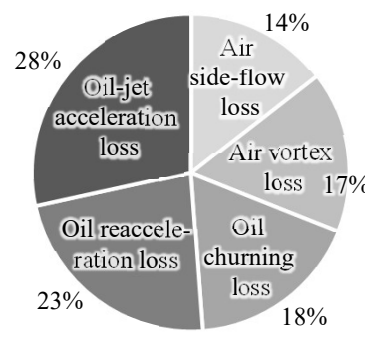(b1) Breakdown of fluid dynamic loss,
Shroud 2
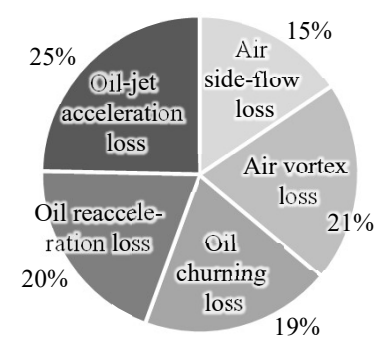
(b2) Breakdown of aerodynamic loss,
Shroud 2

(b3) Breakdown of oil dynamic loss,
Shroud 2

(b4) Breakdown for loss location,
Shroud 2

(b5) Fraction of loss elements,
Shroud 2, 7000 rpm ("A2" in (b1))

(b6) Fraction of loss elements,
Shroud 2, 10000 rpm ("B2" in (b1))

Fig. D.1-1 Breakdown of fluid dynamic loss elements with respect to rotational speed changes (experimental results decomposed using the experimental classification method)

(a1) Breakdown of fluid dynamic loss,
Shroud 1

(a2) Breakdown of aerodynamic loss,
Shroud 1

(a3) Breakdown of oil dynamic loss,
Shroud 1

(a4) Breakdown for loss location,
Shroud 1

(a5) Fraction of loss elements,
Shroud 1, 1.48 L/min ("A1" in (a1))

(a6) Fraction of loss elements,
Shroud 1, 7.40 L/min ("B1" in (a1))

(b1) Breakdown of fluid dynamic loss,
Shroud 2

(b2) Breakdown of aerodynamic loss,
Shroud 2

(b3) Breakdown of oil dynamic loss,
Shroud 2

(b4) Breakdown for loss location,
Shroud 2

(b5) Fraction of loss elements,
Shroud 2, 1.48 L/min ("A2" in (b1))

(b6) Fraction of loss elements,
Shroud 2, 7.40 L/min ("B2" in (b1))
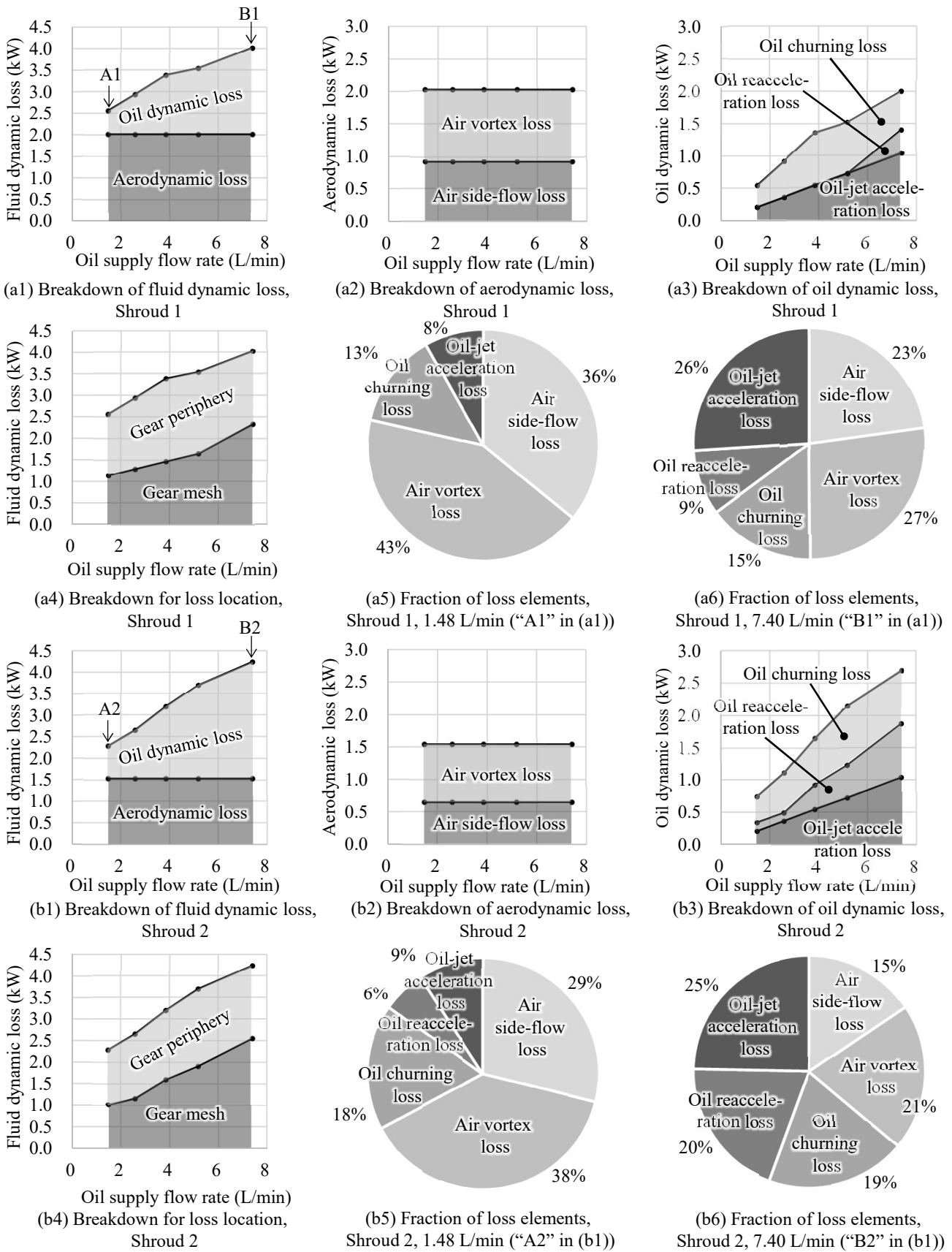
Fig. D.2-1 Breakdown of fluid dynamic loss elements with respect to oil supply flow rate changes (experimental results decomposed using the experimental classification method)

Appendix E

Example of Calculations of Fluid Dynamic Loss Model

The following tables show the results for the two-axis helical gearbox with "Shroud 2" (see Section 3.1.1 for details), as an example of calculations from the fluid dynamic loss model.

E.1   Gear Specifications and Operating Conditions

Table E.1-1 Specifications of gears and shroud (an example calculation with fluid dynamic loss model)

Item	Variable	Value	Unit	Reference
Pitch diameter, input gear	$D_{p,in}$	191	mm	Section 3.1.1, Fig. 1.2-2
Tip diameter, input gear	$D_{t,in}$	201	mm	Section 3.1.1, Fig. 1.2-2
Root diameter, input gear	$D_{f,in}$	179	mm	Section 3.1.1, Fig. 1.2-2
Pitch diameter, output gear	$D_{p,out}$	81.2	mm	Section 3.1.1, Fig. 1.2-2
Tip diameter, output gear	$D_{t,out}$	91.2	mm	Section 3.1.1, Fig. 1.2-2
Root diameter, output gear	$D_{f,out}$	68.7	mm	Section 3.1.1, Fig. 1.2-2
Number of tooth, input gear	z_{in}	33	–	Section 3.1.1
Number of tooth, output gear	z_{out}	14	–	Section 3.1.1
Gear module	M_g	5.00	mm	Section 3.1.1
Face width, input gear & output gear	B_{in}, B_{out}	34.0	mm	Section 3.1.1, Fig. 1.2-2
Tooth height, input gear & output gear	h	11.3	mm	Fig. 5.1-12
Backlash	j	0.181	mm	Fig. 6.3-1
Pressure angle	–	20.0	deg	–
Helix angle	β	30.4	deg	Fig. 5.1-12
Tip clearance, input gear & output gear	$C_{h,in}, C_{h,out}$	1.25	mm	Fig. 6.3-1
Shaft diameter, input gear	$D_{a,in}$	70.0	mm	Section 3.1.1, Fig. 1.2-2
Shaft diameter, output gear	$D_{a,out}$	51.0	mm	Section 3.1.1, Fig. 1.2-2
Shaft distance	L_a	136	mm	Section 3.1.1
Shroud radial clearance, input gear & output gear	C_{rr}	5.00	mm	Section 3.1.1
Shroud side clearance, input gear & output gear	C_{rx}	5.00	mm	Section 3.1.1
Shroud opening angle, input gear & output gear	$\Delta\theta_{op}$	30.0	deg	Section 3.1.1
Phase of Shroud opening center	θ_{op}	180	deg	Section 3.1.1

Table E.1-2 Operating conditions (example calculation with fluid dynamic loss model)

Item	Variable	Value	Unit	Reference
Rotational speed, input gear	N_{in}	10000	rpm	Section 3.1.1
Rotational speed, output gear	N_{out}	23571	rpm	Section 3.1.1
Pitch line velocity	v_p	100	m/s	Section 3.1.1
Oil density	ρ_{oil}	971	kg/m^3	Section 3.1.1
Air density	ρ_{air}	1.06	kg/m^3	Section 3.1.1
Oil supply rate, volumetric (total)	Q_s	7.40	L/min	Section 3.1.1

E.2   Calculation Results

Table E.2-1 Typical variables and values in aerodynamic loss model

Item	Variable	Value	Unit	Reference
Pressure loss coefficient during gear meshing	ζ_s	5.40	–	Section 6.2.2, Eq. 6.6
Velocity coefficient	Z_v	0.25	–	Section 6.2.2, Eq. 6.17
Helix angle coefficient	Z_β	1.00	–	Section 6.2.2, Eq. 6.18
Air drag coefficient	$C_{D,s}$	1.35	–	Section 6.2.2, Eq. 6.5
Pressure due to the airflow through gear mesh sides	p_s	15.9	kPa	Section 6.2.2, Eq. 6.4
Air side-flow loss, input gear	$P_{s,in}$	0.306	kW	Section 6.2.2, Eq. 6.23
Air side-flow loss, output gear	$P_{s,out}$	0.305	kW	Section 6.2.2, Eq. 6.23
Air side-flow loss, total	P_s	0.611	kW	Section 6.2.2, Eq. 6.24
Air pumping flow rate at gear mesh, volumetric	Q_{pump}	161	L/min	Section 6.3, Eq. 6.25
Air pumping loss	P_{pump}	0.0246	kW	Section 6.3, Eq. 6.30
Shroud coefficient, input gear	λ_{in}	0.434	–	Section 6.4, Eq. 6.39
Shroud coefficient, output gear	λ_{out}	0.516	–	Section 6.4, Eq. 6.39
Peripheral angle ratio, input gear	$\epsilon_{\theta,in}$	0.922	–	Section 6.4, Eq. 6.48
Peripheral angle ratio, output gear	$\epsilon_{\theta,out}$	0.821	–	Section 6.4, Eq. 6.49
Air vortex loss, input gear	$P_{v,peri,in}$ $+P_{v,sides,in}$	0.520	kW	Section 6.4, Eqs. 6.32 and 6.34
Air vortex loss, output gear	$P_{v,peri,out}$ $+P_{v,sides,out}$	0.355	kW	Section 6.4, Eqs. 6.32 and 6.34
Air vortex loss, total	P_v	0.876	kW	Section 6.4, Eq. 6.35

Table E.2-2 Typical variables and values in the oil dynamic loss model

Item	Variable	Value	Unit	Reference
Oil-jet acceleration loss	P_{jac}	1.04	kW	Section 6.5, Eq. 2.6
Oil re-inflow rate to gear mesh	Q_{re}	7.26	L/min	Section 6.6, Eq. 6.67
Oil reacceleration coefficient	χ_{re}	0.981	–	Section 6.6, Eq. 6.68
Oil reacceleration loss	P_{rac}	1.02	kW	Section 6.6, Eq. 6.61
Non-dimensional oil inflow rate to gear mesh, input gear & output gear	$\frac{Q_s+Q_{re}}{v_p B M_g}$	0.0143	–	Section 6.7, Eq. 6.77
Oil mist coefficient, input gear	$(\Phi-1)_{in}$	0.979	–	Section 6.7, Eq. 6.71
Oil mist coefficient, output gear	$(\Phi-1)_{out}$	0.693	–	Section 6.7, Eq. 6.71
Oil churning loss	P_{ch}	0.76	kW	Section 6.7, Eq. 6.70

Table E.2-3 Aerodynamic loss, oil dynamic loss, and fluid dynamic loss

Item	Variable	Value	Unit	Reference
Aerodynamic loss	P_{air}	1.51	kW	Section 6.1, Eq. 6.2
Oil dynamic loss	P_{oil}	2.81	kW	Section 6.1, Eq. 6.3
Fluid dynamic loss	P_{fluid}	4.32	kW	Section 6.1, Eq. 6.1

Nomenclature

A	Area
A_0	Cross-sectional area of the small diameter side of the pipe (sudden expansion pipe)
A_2	Cross-sectional area of the large diameter side of the pipe (sudden expansion pipe)
A_{B0}	Cross-sectional area of gear meshing part
A_{B1}, A_{B2}	Cross-sectional area through which the air flows according to move of the gear teeth
A_{hole}	Cross-sectional area of the measurement hole of the two-phase flow probe
A_{re}	Oil re-inflow reduction coefficient
A_x, A_y, A_z	Area of the cell surface in the x direction, y direction, and z direction, respectively
$\mathscr{A}$	Pressure viscosity coefficient of oil
a_r, a_w, a_x	Coefficients of the air vortex loss model
α_{ch}	Coefficients of the oil churning loss model
α_{oil}	Oil fraction in a two-phase flow of air and oil
B	Tooth width, Bearing width
b_1	Thickness of gear web
$b_{i,j}$	Block in gear mesh
b_r, b_w, b_x	Exponents of the air vortex loss model
β	Helix angle
β_{ch}	Coefficient of the oil churning loss model
C_α	Sharpening coefficient of gas–liquid interface
C_D	Drag coefficient of flow
C_h	Tip clearance of gears
C_j	Radial clearance of the bearing
C_M	Rotational moment coefficient
C_ν	Coefficient on the temperature dependence of oil viscosity
C_{re}	Coefficient of the oil reacceleration loss model
C_{rr}	Radial clearance between gear and shroud
C_{rx}	Axial clearance between gear and shroud
C_{T1}, C_{T2}, C_{T3}	Coefficients for torque efficiency of gear pump
C_{V1}, C_{V2}	Coefficients for volumetric efficiency of gear pump
c	Momentum conversion coefficient
c_a	The speed of sound of fluid
c_g	Smagorinsky constant
c_{flange}	Influence coefficient of flange near the side of the gear
c_p	Local pressure coefficient
D_a	Shaft outer diameter
D_{a1}	Shaft inner diameter
D_f	Root circle diameter
D_e	Equivalent diameter of a circular pipe
D_p	Pitch circle diameter
D_t	Tooth tip diameter
d_1, d_2	Hub outer diameter, and pitch circle diameter of weight reduction holes, respectively
d_3, d_4	Rim inner diameter, and diameter of weight reduction holes, respectively
d_{pb}	Pitch diameter of bearing

d_R	Rivet Diameter
Δp	Pressure drop, pressure difference
$\Delta\theta_{op}$	Shroud peripheral opening angle (one opening)
$\Delta\theta_{\sum op}$	Shroud peripheral opening angle (sum in one gear)
δ	Thickness of the oil layer
δp	Pressure change
δv	Deviation of velocity from mean velocity
$\delta x, \delta y, \delta z$	Calculation mesh size in the x direction, y direction, and z direction, respectively
E_2	Coefficient of squared proportional component of rotational speed
E_3	Coefficient of cubic proportional component of rotational speed
E_{ff_ch}	Conversion coefficient of shroud opening phase (oil churning loss model)
$E_{2\sigma}$	Standard error of 2σ
E_σ	Standard error of σ
E'_σ	Relative standard error of σ
$\mathcal{E}$	Eccentricity
$\mathscr{E}_1, \mathscr{E}_2$	Young's modulus
$\mathscr{E}'$	Equivalent stiffness coefficient
e_{ij}	Strain rate tensor
ϵ_θ	Angle range coefficient on gear periphery (air vortex loss model)
ε	Eccentricity ratio
η_{gp}	Efficiency of the gear pump
$\eta_{gp,T}$	Torque efficiency of gear pump
$\eta_{gp,V}$	Volumetric efficiency of gear pump
F	The force that the gear receives from the fluid
Fr	Froude number
$\mathcal{F}$	Volume of Fluid in the calculation cell
$\mathcal{F}_{jet}$	Oil jet source
$\mathscr{F}_A$	Transmitted force
$\mathscr{F}_b$	Load on the bearing
$\mathscr{F}_R$	Instantaneous traction force owing to rolling on the gear contact surfaces
$\mathscr{F}_S$	Friction force generated by sliding between the gear tooth surfaces
$\mathscr{F}_t$	Force in the vertical direction of the tooth surface
f_0	Coefficient for bearing (Palmgren's equation)
f_1	Coefficient for lubrication method (Palmgren's equation)
f_A	Small flow rate function (oil churning loss model)
f_B	Large flow rate function (oil churning loss model)
f_α	Calibration function for oil fraction α_{oil}
$f_{Ga,P}$	Gaussian distribution of power loss P
$f_{um,s}$	Simple calibration function of mixture velocity u_m
$f_{um,p}$	High accuracy calibration function of mixture velocity u_m
f_x, f_y, f_z	Viscous acceleration term in the x direction, y direction, and z direction, respectively
$\mathfrak{f}_c$	Instantaneous friction coefficient on tooth surface
$\mathfrak{f}_{mesh}$	Average friction coefficient on tooth surface
G_c	Dimensionless material coefficient
g	Gravitational acceleration
γ_1, γ_2	Poisson's ratio
γ_{ch}	Coefficients in the oil churning loss model
H	Transition function from small and large flow rate functions (oil churning loss model)
H_V	Gear friction loss coefficient (Höhn's equation)
h	Tooth height (tooth depth)
h_c	Central oil film thickness under uniform temperature assumption

h_R	Rivet height
j	Backlash
K	Index for tooth surface strength
$\mathcal{K}$	Volume force
k	Ellipticity parameter
k_{seal}	Balance distribution coefficient of the seal
κ	Fraction of loss on gear peripheral surface in air vortex loss
L	Calculation mesh size
L_a	Distance between input and output axes
L_R	Distance between rivets
λ	Shroud coefficient
$\lambda_{\theta r}$	Shroud coefficient of the gear peripheral surface
$\lambda'_{\theta r}$	Shroud coefficient of the gear peripheral surface for the effect of radial clearance and axial clearance
λ_r	Shroud coefficient of the gear peripheral surface for the effect of radial clearance
λ_x	Shroud coefficient of the gear sides
M_A, M_{B1}, M_{B2}	Increase ratio of pressure loss coefficient owing to velocity deviation (air side-flow loss model)
M_g	Gear module
m	Mass
m_G	Gear ratio or reduction ratio (not less than 1.0)
μ	Dynamic viscosity
N	Rotational speed
N_{rot}	Number of rotations
$\mathcal{N}_{mes}$	Number of measurement conditions
$\mathcal{N}_{pos}$	Number of measurement locations
$\mathcal{N}_{rep}$	Number of measurement iterations (same measurement condition)
n_G	Number of gears ($= 1$ for a single gear, $= 2$ for a gear pair)
n_h	Number of weight reduction holes
n_{op}	Number of peripheral openings in the shroud
n_r, n_θ, n_x	Exponents of the air vortex loss model
ν	Kinematic viscosity
ν_T	Eddy viscosity
ω	Rotational angular velocity
P	Power loss
P_A	Transmitted power
P_{BJ}	Power loss of journal bearing
P_{BR}	Power loss of rolling bearings
P_R	Instantaneous rolling power-loss on the gear tooth surface
P_S	Instantaneous sliding power-loss on the gear tooth surface
p	Pressure
Φ	Ratio of apparent fluid density around the gear to air density
Φ'	Density of the fluid around the gear
$\Phi - 1$	Oil mist coefficient (oil churning loss model)
Ψ'	Ratio of drag coefficient in two-phase flow to drag coefficient in air
φ_t	Thermal reduction coefficient
Q	Volumetric flow rate
Q'	Sum of volumetric oil supply flow rate and re-inflow rate of oil into gear meshing ($= Q_s + Q_{re}$)
Q_a	Volumetric flow rate around gear
Q_{cr}'	Flow rate at which the small flow rate function is equal to the large flow rate function (oil churning loss model)
Q_{re}	Re-inflow rate of oil into gear meshing
Q_s	Volumetric oil supply flow rate

R	Disk radius
R_A	Ratio of outlet cross-sectional area and inlet cross-sectional area in sudden expansion pipe or sudden contraction pipe
R_a	Constant determined by gear specifications (Höhn's equation)
Re	Rotational Reynolds number
R_r	Radial relative clearance of the shroud
R_{jet}	Source term of the oil jet
R_{sor}	Source of the fluid
R_θ	Peripheral opening ratio of the shroud
R_X	Equivalent rolling radius
R_x	Axial relative clearance of the shroud
R_{w_eff}	Side wall coefficient (air vortex loss model)
r	Radial distance
r_d	Cylindrical radius
r_f	Base circle radius
r_j	Bearing radius
r_p	Pitch circle radius
ρ	Density
ϱ_c	Constant determined by gear specifications (Höhn's equation)
S	Tooth tip length
s	Gas–liquid slip ratio
σ	Standard deviation
σ_c	Surface roughness
T	Torque
T_{BR}	Friction torque of rolling bearing (Palmgren's equation)
$\mathscr{T}$	Temperature
t	Time
t_{ij}	Stress tensor ($i = 1, 2, 3$, $j = 1, 2, 3$)
t_r	Rim thickness of gear
τ	Shear stress of flow
θ	Phase in the rotational direction, or phase in the rotational direction from gear meshing
θ_0	Phase from the stagnation point of the cylinder
θ_{max}	Maximum phase from gear meshing ($= 2\pi$)
U	Velocity of the oil particles
U_a	Axial velocity (on the surface of blocks of gear meshing)
U_c	Dimensionless velocity parameter
U_r	Radial Velocity (on the surface of blocks of gear meshing)
u	Velocity, or velocity in x direction
u_e	Density-weighted average velocity of the oil layer
V	Volume
V_1, V_2	Velocity of the tooth surfaces
V_f	Volume of the fluid in the cell (porosity method)
V_S	Sliding speed between tooth surfaces
V_T	Rolling speed between tooth surfaces
v	Velocity, or velocity in y direction
v_f	Root circle speed
v_∞	Axial flow velocity to disk
v_j	Bearing surface speed
v_a	Apparent velocity
v_p	Pitch circle speed
v_{sum}	Total speed at the gear pitch point

W	Shroud wall width (inner width)
W_c	Dimensionless load coefficient
W_j	Load capacity of the bearing
$WOBS$	Velocity in the z-direction of the object surface
w	Velocity in z direction
w_c	Force loading perpendicular to the tooth surface
w_{n+1}	Velocity in the z direction for the next time step
wsx, wsy, wsz	Wall shear force in the x direction, y direction, and z direction, respectively
X	Coordinates on the line of action
X_L	Constant determined by gear specifications (Höhn's equation)
$\mathscr{X}$	Lockhart-Martinelli parameter
x_i	Spatial Coordinates ($i = 1, 2, 3$)
χ_{re}	Oil reacceleration coefficient (oil reacceleration loss model)
y	Tooth face height direction
Z_β	Helix angle coefficient (air side-flow loss model)
Z_v	Velocity coefficient (air side-flow loss model)
z	Number of teeth
z'	Radial distance from shroud inner wall
z_h	Distance from shroud inner wall to gear tooth tip
ζ	Pressure loss coefficient
ζ_A	Pressure loss coefficient owing to changes in the volume between teeth (air side-flow loss model)
ζ_{B1}, ζ_{B2}	Pressure loss coefficient owing to changes in air flows according to move of gear teeth (air side-flow loss model)
$\zeta_{B,contraction}$	Pressure loss coefficient in sudden contraction pipe
$\zeta_{B,expansion}$	Pressure loss coefficient in sudden expansion pipe
ζ_M	Pressure loss coefficient of flow with velocity deviation
ζ_s	Pressure loss coefficient through the sides of gear mesh (air side-flow loss model)

Accent symbol

¯	Time Average
˙	Time derivative
ˆ	Ensemble Average
˜	Dimensionless

Superscript

$*$	Measured value

Subscript

$aeration$	Aeration of oil
air	Air
CFD	Computational fluid dynamics
cal	Calculated value
ch	Parameters for the oil churning loss model
$corr$	Calibrated value
cyl	Cylinder
exp	Experimental value

$fluid$	By means of a fluid (of air and oil)
gp	Gear pump
hom	Homogeneous distribution
in	Input gear
∞	Atmosphere
$inside$	Inside
jac	Parameters for the oil-jet acceleration loss model
jet	Oil jet
l	Peripheral direction
m	Mixed fluid of air and oil
mes	Measured value
$mesh$	Gear meshing
mod	Modified
$msides$	The sides of gear meshing
oil	Oil
out	Output gear
$outside$	Outside
org	Before calibration (original)
P	Power loss
par	Particle
$peri$	Gear peripheral part (excluding gear meshing part)
$pipe$	Circular pipe
$pressure$	Pressure induced
$pump$	Pumping
r	Radial direction, or relative velocity of gas and liquid
rac	Parameters for the oil reacceleration loss model
rep	Repetitive
re	Oil re-inflow into gear meshing
s	Parameters for the air side-flow loss model
$seal$	Seal
set	Setting value
$sh1$	Shroud 1
$sh2$	Shroud 2
$shear$	Caused by shear
$sides$	Gear sides (both sides)
$slide$	Sliding speed of the contact surface
$spring$	Spring
$stag$	Stagnation point
sum	Sum total
$surface$	Gear surface
θ	Peripheral direction
$total$	Total pressure
um	Parameters for the mixture velocity
up	Parameters for particle velocity
v	Parameters for the air vortex loss model
vac	Zero absolute pressure (vacuum)
w	Sidewall
x	Axial direction
$zero-oil$	Zero oil supply
$*$	in (input gear) or out (output gear)

Research achievement

Author's chief papers comprising this research

[A1] Arisawa, H., Shinoda, Y., Noguchi, Y., Goi, T., Banno, T., and Akahori, H., 2019, "Development of a Flow Visualization Borescope and a Two-Phase Flow Probe for Aeroengine Transmission Gears, " J. Eng. Gas Turbines Power, **141**(9), pp. 091013-1–091013-16.

[A2] Arisawa, H., Shinoda, Y., Tanaka, M., Goi, T., Akahori, H., and Yoshitomi, M., 2019, "Classification and Modeling of Fluid Dynamic Loss in Aeroengine Transmission Gears, " J. Eng. Gas Turbines Power, **141**(6), pp. 061012-1–061012-14.

[A3] Arisawa, H., Shinoda, Y., Noguchi, Y., Goi, T., Banno, T., and Akahori, H., 2018, "Developments of a Flow Visualization Borescope and a Two-Phase Flow Probe for Aeroengine Transmission Gears, " ASME Paper No. GT2018-75083.

[A4] Arisawa, H., Shinoda, Y., Tanaka, M., Goi, T., Akahori, H., and Yoshitomi, M., 2017, "Classification of Fluid Dynamic Loss in Aeroengine Transmission Gears, Experimental Analysis and CFD Validation," ASME Paper No. GT2017-63208.

[A5] Arisawa, H., Nishimura, M., Imai, H., and Goi, T., 2014, "Computational Fluid Dynamics Simulations and Experiments for Reduction of Oil Churning Loss and Windage Loss in Aeroengine Transmission Gears, " J. Eng. Gas Turbines Power, **136**(9), pp. 092604-1–092604-9.

[A6] Arisawa, H., Nishimura, M., Imai, H., Tanaka, K., and Goi, T., 2013, "CFD Simulations and Experiments for Reduction of Oil Churning Loss and Windage Loss on Aeroengine Transmission Gears, " Trans. JSME, **79C**(800), pp. 1213–1225.

[A7] Arisawa, H., Nishimura, M., Imai, H., and Goi, T., 2009, "CFD Simulation for Reduction of Oil Churning Loss and Windage Loss on Aeroengine Transmission Gears, " ASME Paper No. GT2009-59226.

Author's chief papers and co-authored papers as references of this research

[B1] Ogasawara, K., Arisawa, H., Hashimoto, H., Hayasaka, A., Shinoda, Y., and Yamamoto, H., 2020, "Computational Thermal Analysis and Testing to Improve Loss of Lubrication Performance of Helicopter Transmissions, " Vertical Flight Soc. 76th Annual Forum, Virginia, USA, Oct. 6-8.

[B2] Sato, K, Goi, T, Taguchi, T, Nishida, T, Arisawa, H, Matsuoka, T, Imai, H, and Banno, T. 2015, "Design, Analysis, and Tests of Differential Planetary Gear System for Open Rotor Power Gearbox (Final Report), " ASME Paper No. DETC2015-46414.

[B3] Imai, H., Goi, T., Kijima, K., Nishida, T., Arisawa, H., Matsuoka, T., and Sato, M., 2013, "Design and Test of Differential Planetary Gear System for Open Rotor Power Gearbox, " ASME Paper No. DETC2013-12089.

[B4] Arisawa, H., Nishimura, M., Tanaka, K., Imai, H., and Goi, T., 2011, "Oil Scavenging CFD Simulations and Experiments in the Accessory Gearbox of an Aircraft Engine," Intl. Gas Turbine Cong., Osaka, Japan, Nov. 13–18, Paper No. IGTC2011-0214.

[B5] Imai, H., Goi, T., Arisawa, H., and Nishimura, M., 2009, "GLE-02 Reduction in Gear Windage and Churning Loss by Optimum Shroud Design with aid of CFD (Gear Lubrication and Efficiency), " Proc. JSME Intl. Conf. Motion & Power Transmissions, Sendai, Japan, May 13–15, pp. 469–474.

[B6] Arisawa, H., Nishimura, M., Watanabe, H., Ueshima., A., Arima., K., and Yamasaki, A., 2009, "Study on Similarity of Pumping Flow in Engine Crankcase, " Small Engine Tech. Conf., Penang, Malaysia, Nov. 3–5, Paper No. 2009-32-0051.

[B7] Arisawa, H., Umemoto, K., Takeuchi, H., Ueshima, A., Kawamoto, Y., 2005, "Application of Oil Dynamics Simulation to Motorcycle Oilpans, " Small Engin Tech. Conf., Bangkok, Thailand, Oct. 12–14, Paper No. 2005-32-0011.

[B8] Arisawa, H., Umemoto, K, Ueshima, A., and Kawamoto, Y., 2004, "Development of Oil Dynamics Simulation for Motorcycle Oilpan, " Kawasaki Tech. Rev., **156**, pp. 52–55.

[B9] Murakami, A., Ueda, K., Owaki, K., Umemoto, K., Arisawa, H., Hamabe, K., Takahashi, N., and Kamiya, S., 2004, "Japan's First Pressure Build-up Type LNG Carrier, " Kawasaki Tech. Rev., **154**, pp. 12–15.

[B10] Arisawa, H., Shimoyama, N., Ikebuchi, T., Shimodoi, H., and Nakamoto, Y., 2003, "Numerical Simulation Method of Seawater Exchange for Breakwaters, " Proc. Coastal Engrs., Jpn. Soc. Civil Engrs, **50**, pp. 46–50.

[B11] Arisawa, H., Umemoto, K., Ueshima, A., and Kawamoto, Y., 2003, "CFD Simulation of the Lubricating Oil Flow in Motorcycle Oilpan, " Small Engin Tech. Conf., Madison, Wisconsin, Sep. 15–18, Paper No. 2003-32-0080.

[B12] Kitabayashi, K., Nakamura, S., and Arisawa, H., 2002 "A Study on the Influence of Swash Bulkhead with a Large Opening on Sloshing Pressure, " Proc. 16th Asian-Pacific Technical Exchange & Advisory Meeting on Marine Structures in Asia Pacific Maritime Cong., Kobe, Japan, May 21–23.

[B13] Takaoka, Y., Shimizu, H., Kiyosue, T., and Arisawa, H., 2001, "A Study on the Design Load due to Sloshing in LNG Tanks, " Proc. 15th Asian-Pacific Technical Exchange & Advisory Meeting on Marine Structures in Asia Pacific Maritime Cong., Jochiwon, Korea, Oct. 15–18.

Awards received

[C1] ASME Intl. Gas Turbine Inst., Aircraft Engine Committee, 2009 Best Paper Award for the paper of "CFD Simulation for Reduction of Oil Churning Loss and Windage Loss on Aeroengine Transmission Gears, " ASME Paper No. GT2009-59226.

[C2] Small Engine Tech. Conf., 2003 High Quality Paper Award for the paper of "CFD Simulation of the Lubricating Oil Flow in Motorcycle Oilpan, " Small Engine Tech. Conf., Madison, Wisconsin, Sep. 15–18, Paper No. 2003-32-0080.

Acknowledgement

---

[1] Affiliation at the time